

LUND UNIVERSITY

Modelling of electric power systems in electric vehicles

Widek, Per

2026

Document Version:
Publisher's PDF, also known as Version of record

Link to publication

Citation for published version (APA):
Widek, P. (2026). *Modelling of electric power systems in electric vehicles*. [Doctoral Thesis (monograph), Division for Industrial Electrical Engineering and Automation]. Department of Biomedical Engineering, Lund university.

Total number of authors:
1

Creative Commons License:
CC BY

General rights
Unless other specific re-use rights are stated the following general rights apply:
Copyright and moral rights for the publications made accessible in the public portal are retained by the authors and/or other copyright owners and it is a condition of accessing publications that users recognise and abide by the legal requirements associated with these rights.
• Users may download and print one copy of any publication from the public portal for the purpose of private study or research.
• You may not further distribute the material or use it for any profit-making activity or commercial gain
• You may freely distribute the URL identifying the publication in the public portal

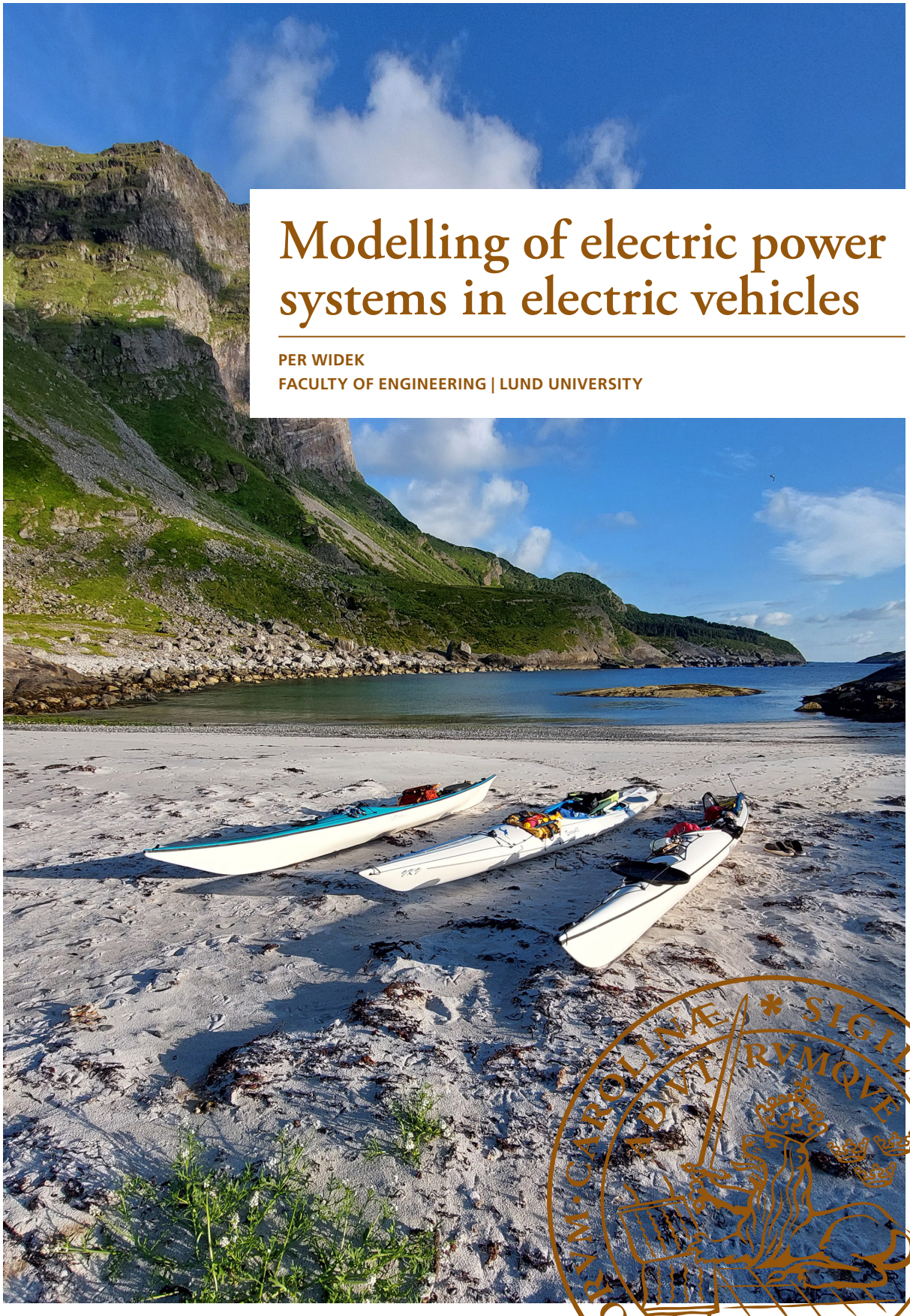
Read more about Creative commons licenses: https://creativecommons.org/licenses/

Take down policy
If you believe that this document breaches copyright please contact us providing details, and we will remove access to the work immediately and investigate your claim.

LUND UNIVERSITY

PO Box 117
221 00 Lund
+46 46-222 00 00

Download date: 16. Sep. 2026



Modelling of electric power systems in electric vehicles

PER WIDEK
FACULTY OF ENGINEERING | LUND UNIVERSITY

Printed by Media-Tryck, Lund 2026 NORDIC SWAN ECOLABEL 3041 0903



Faculty of Engineering
Department of Biomedical Engineering
Division of Industrial Electrical Engineering and Automation (IEA)

ISBN: 978-91-985110-9-3 (print)
ISBN: 978-91-985110-8-6 (pdf)
CODEN: LUTEDX/(TEIE-1102)/1-408/(2026)



Modelling of electric power systems in electric vehicles

Modelling of electric power systems in electric vehicles

by Per Widek



LUND
UNIVERSITY

Thesis for degree Doctor of Philosophy in Engineering
Thesis advisors: Prof. Mats Alaküla, Dr. Hans Bängtsson,
Dr. Sabine Alexandersson, Lic. Anders Lasson, Dr. Jonas Ottosson,
Dr. Zhe Huang, Dr. Dan Hagstedt
Faculty opponent: Prof. Dr.-Ing. Eckart Hoene

To be presented, with the permission of the Faculty of Engineering of Lund University, for public criticism in the M:B lecture hall. Electrical Engineering Buildning. Ole Römers väg 1, Lund Sweden, on Monday the 8th of June 2026 at 09:15

Organization	Document name
LUND UNIVERSITY Department of Biomedical Engineering Box 118, SE–221 00 LUND, Sweden www.iea.lth.se	**DOCTORAL DISSERTATION** Date of disputation 2026-06-08 Sponsoring organization Volvo Group
Author(s) Per Widek	

Title and subtitle

Modelling of electric power systems in electric vehicles:

Abstract

The rapid electrification of heavy-duty vehicles has introduced traction voltage systems (TVS) with electrical scale and complexity not previously seen in on-road applications. Multiple power electronic subsystems interact through long cables and frequency-dependent impedances, making conducted electromagnetic interference (EMI) a system-level phenomenon. Differential-mode (DM) and common-mode (CM) disturbances generated by converter switching propagate through intentional and parasitic impedances up to approximately 200 kHz for DM behaviour and 3 MHz for CM behaviour.

This thesis combines measurements on commercial battery-electric vehicles with physically based modelling and system-level simulation. A dedicated 96-channel, 60 MS/s measurement system is developed to capture CM and DM quantities across the distributed TVS with ability to record up to one hour of full resolution data. The results show that CM behaviour is governed by the ratio between symmetric CM capacitances and asymmetric parasitic capacitances, referred to as the *X*-factor. Both the CMDC voltage and the resulting CM current paths depend on capacitance placement, cable and junction-box impedances and non-ideal semiconductor behaviour.

A library of validated subsystem models is developed and calibrated with measurements, including converters, batteries, cables, filters and interconnection components. State-space reduction and eigenvalue analysis preserve the required bandwidth while enabling computationally feasible vehicle-level simulations. The simulations reproduce the measured CM and DM behaviour, quantify the influence of distributed impedances and measurement artefacts such as Break-Out Boxes and demonstrate how phase-shifted switching suppresses CM disturbances. The combined results provide system-level guidelines for EMI-aware design, including CM capacitance placement, use of damped DM filters and strategies that reduce sensitivity to subsystem interaction.

The thesis establishes a system-level framework for analysing, modelling and mitigating conducted EMI in commercial battery-electric vehicles and demonstrates how measurement, modelling and simulation must be integrated to understand and control behaviour in electrically large traction voltage systems.

Key words

Battery Electric Vehicles, Power electronic converters, Electromagnetic interference, Electromagnetic modelling, Harmonic analysis, Harmonic filters, Parasitic capacitance, Common-mode current, Differential-mode current.

Classification system and/or index terms (if any)

Supplementary bibliographical information	Language
	English
ISSN and key title	ISBN
	978-91-985110-9-3 (print) 978-91-985110-8-6 (pdf)
Recipient's notes	Number of pages: 408 / Price
	Security classification

I, the undersigned, being the copyright owner of the abstract of the above-mentioned dissertation, hereby grant to all reference sources the permission to publish and disseminate the abstract of the above-mentioned dissertation.

Signature _____ Date 2026-04-22

DOKUMENTDATABLAD enl SIS 61 41 21

Modelling of electric power systems in electric vehicles

by Per Widek



LUND
UNIVERSITY

Cover illustration front: Helgeland, Norway
(Credits: Per Widek).

Funding information: The thesis work was financially supported by
Volvo Group Trucks Technology AB.

© Per Widek 2026

Faculty of Engineering
Department of Biomedical Engineering
Division of Industrial Electrical Engineering and Automation (IEA)

ISBN: 978-91-985110-9-3 (print)
ISBN: 978-91-985110-8-6 (pdf)
CODEN: LUTEDX/(TEIE-1102)/1-408/(2026)

Printed in Sweden by Media-Tryck, Lund University, Lund 2026









Den som simulerar tror på det,
men ingen annan.
Den som mäter tror alla på,
utom han som mätte.

Branschuttryck, ursprung okänt

Om du inte vet hur du skall tolka en undersökning,
gör den inte.

Henrik Widegrens överläkare

Contents

Acknowledgements . . . vii
Populärvetenskaplig sammanfattning . . . xi
Popular scientific summary . . . xiii
Nomenclature . . . xv

1 Introduction 1
1.1 Background . . . 2
1.2 Goal, objective, and scope . . . 3
1.3 Contributions and publications . . . 3
1.3.1 Publications . . . 4
1.4 Disposition of the thesis . . . 5

2 Electric power systems in electric vehicles 7
2.1 Traction Voltage System (TVS) . . . 8
2.2 Other systems . . . 11
2.3 Important sources and loads . . . 12
2.3.1 Electric Machine Drive - (EMD) . . . 13
2.3.2 Electric Machine - (EM) . . . 14
2.3.3 Machine Drive System - (MDS) . . . 14
2.3.4 Energy Storage - Batteries . . . 14
2.3.5 Charging systems . . . 14
2.3.6 24 V DC/DC . . . 15
2.3.7 Air Condition - (HVAC) . . . 15
2.3.8 Air compressor . . . 15
2.3.9 ePTO . . . 15
2.4 CM and DM . . . 15
2.4.1 CM capacitance unbalance . . . 18
2.4.2 Asymmetric parasitic capacitances . . . 20
2.4.3 Common Mode DC voltage (U_{CMDC}) . . . 21
2.4.4 CM currents cause and effect . . . 24
2.4.5 DM current . . . 29
2.4.6 DM filter . . . 32
2.4.7 Conclusion . . . 36

2.5 Conclusion . . . 37

3 Vehicle measurement system **39**
3.1 Measurement system requirements . . . 41
3.2 Measurement system overview . . . 43
3.3 Break-Out Boxes (BoB) . . . 45
3.3.1 CM current sensor (Rogowski coil) . . . 46
3.3.2 DM current sensor (Rogowski coil) . . . 48
3.3.3 Differential voltage probe . . . 49
3.3.4 Conclusion . . . 50
3.4 NI data acquisition and recording platform (PXI) . . . 51
3.4.1 PXI chassis and included modules . . . 51
3.4.2 Streaming rate . . . 52
3.4.3 Synchronization and system architecture . . . 53
3.4.4 Accuracy . . . 55
3.4.5 Bandwidth BW . . . 56
3.4.6 Nyquist sampling theorem . . . 57
3.4.7 Anti-aliasing filter . . . 58
3.4.8 Anti-aliasing filter in measurements . . . 60
3.4.9 Resolution . . . 61
3.4.10 Conclusion . . . 61
3.5 Post-processing . . . 61
3.5.1 Total accuracy for HF . . . 64
3.5.2 FFT of the measured signals . . . 65
3.5.3 Conclusion . . . 66
3.6 Conclusion . . . 67

4 Measurements on a truck and a bus **69**
4.1 Results from impedance measurements of the cables and junction boxes on a bus and a truck . . . 71
4.2 Measurements affected by the break-out boxes . . . 75
4.3 Results from CMDC voltage measurements on a truck . . . 85
4.3.1 CMDC voltage compared to theory and simulations with varied factor X . . . 89
4.3.2 CMDC voltage and current elimination at simultaneous 180° phase-shifted switching . . . 91
4.3.3 Measured CM current maximum due to simultaneous in-phase switching . . . 93
4.3.4 Delayed switching to and from $(0, 0, 0)$ and $(1, 1, 1)$ . . . 95
4.3.5 CM frequency content at the DC side . . . 99
4.3.6 Conclusion . . . 109
4.4 Results from differential mode measurements on a truck . . . 110

4.4.1 DM frequency content at the DC side . . . 112
4.4.2 Conclusion . . . 115
4.5 Verification of FFT implementation . . . 116
4.6 Conclusion . . . 117

5 Sub system simulation model and model calibration 119
5.1 Measurement methods required . . . 120
5.1.1 Kelvin fixture . . . 122
5.1.2 Kelvin leads . . . 123
5.1.3 4-wire method with separate current probe . . . 125
5.1.4 Measuring on high voltage batteries with an HV interface . . . 126
5.1.5 Measuring with a high-current supply for DC resistance . . . 127
5.1.6 Conclusion . . . 127
5.2 System simulation tool – PLECS . . . 128
5.3 State space matrices and eigenvalues . . . 128
5.3.1 Eigenvalues, natural frequencies and damping in PLECS . . . 131
5.3.2 Validation of script . . . 132
5.3.3 Model simplification method . . . 133
5.3.4 Conclusion . . . 140
5.4 Measurement and modelling of subsystems . . . 141
5.4.1 Measurements and modelling of the EMD (CM and DM behaviour) 143
5.4.2 Reduced modelling of the EMD for DM behaviour . . . 146
5.4.3 Measurements and modelling of the EM (CM behaviour) . . . 147
5.4.4 Measurements and modelling of the battery (CM and DM behaviour) . . . 151
5.4.5 Reduced modelling of the battery from manufacturer 2 for DM behaviour . . . 157
5.4.6 Measurements of the battery for charging parameters . . . 159
5.4.7 Measurements and modelling of the DCDC (CM and DM behaviour) . . . 161
5.4.8 Reduced modelling of the DCDC for DM behaviour . . . 167
5.4.9 Measurements and modelling of the Air Compressor (AirComp) (CM and DM behaviour) . . . 168
5.4.10 Measurements and modelling of the On Board Charger (OnBC) (CM and DM behaviour) . . . 171
5.4.11 Measurements and modelling of the ESS and Cab Heater (CM and DM behaviour) . . . 175
5.4.12 Measurements and modelling of the AC compressor (CM and DM behaviour) . . . 178
5.4.13 Measurements and modelling of the On-board Charger and Electric Power Supply (OCEPS) (CM and DM behaviour) . . . 180

5.4.14 Measurements and modelling of the Cables 182
5.4.15 Measurements and modelling of the Junction Box 206
5.4.16 Measurements and modelling of the Break Out Box 209
5.5 Conclusion 211

6 System simulation **213**
6.1 Complexity of the CM (Common Mode) model 216
6.1.1 Part of Full Model for Verification of Non-Ideal vs. Ideal IGBTs . 216
6.1.2 Part of Full Model for Verification of the Impact of the Impedance in the Junction Box (JB) 223
6.1.3 Part of Full Model for Verification of Combining JB Impedance in the Cable Model 225
6.1.4 Part of Full Model for Verification of Merging Cables of Different Area and Junction Boxes 227
6.1.5 Part of Full Model for Verification of 6 BPs vs. 1 Equivalent 6BP . 228
6.1.6 Impact of cables and JBs on CM simulations 231
6.1.7 Conclusion 235
6.2 Results from CM Simulations 236
6.2.1 CMDC voltage – cause and effect 239
6.2.2 CM currents – importance of the position of CM capacitors and the X-factor 243
6.2.3 Delayed switching to and from $(0, 0, 0)$ and $(1, 1, 1)$ 245
6.2.4 Comparison between delayed switching and impact of X-factor . . 250
6.2.5 Conclusion 252
6.3 Common Mode Simulations of Full and Reduced Vehicle Models 252
6.3.1 Common-mode simulation of complete vehicle with full and reduced models 253
6.3.2 Common-mode simulation of part of the vehicle with full and reduced models 260
6.3.3 Conclusion 263
6.4 Differential-mode simulations 264
6.4.1 Subsystem simplification for DM simulation in PLECS 264
6.4.2 System simulation model in PLECS for DM 266
6.4.3 Conclusion 277
6.5 Differential-mode simulations compared to measurements in different load conditions 278
6.5.1 Overview of different load conditions 279
6.5.2 Challenge in comparing simulations of different load conditions . 286
6.5.3 Simulation of load conditions 14 FM1156 SteadyState HighTorque FixGear 290

6.5.4 Comparison of measurement and simulation for load condition 14 FM1156 SteadyState HighTorque FixGear 295
6.5.5 Analysis of discrepancies between simulation and measurement . . 300
6.5.6 Conclusion 314
6.6 EMI mitigation with differential-mode filters 315
6.6.1 Introduction of differential-mode (DM) filters and their effect on EMI currents 315
6.6.2 Analysis of how DM filtering influences the system's resonance point 320
6.6.3 Sensitivity analysis for cable length and junction box configuration 321
6.6.4 Conclusion 325
6.7 Summary and conclusion 325

7 Line impedance stabilization network (LISN) 327
7.1 Characteristics of a TVS 329
7.2 Characteristics of a LISN 332
7.3 Impedance comparison of an artificial network, a LISN, and measurements on a real truck 334
7.4 Alternative LISN 336
7.5 Conclusion 339

8 Conclusion, discussions and future work 341
8.1 Conclusions 342
8.2 Discussion 344
8.3 Future work 347

Appendix 349

A How to derive the parameters in the models from measurements with Zview 351

B FFT of pulses, FFT windowing and axis scaling 355
B.1 Frequency-domain behaviour of short pulses. 355
B.2 Spectral characteristics of short-duration current pulses 357
B.2.1 Broadband spectrum of a single short pulse 357
B.2.2 Spectral behaviour of polarity-alternating pulse trains 358
B.3 FFT windowing: Hanning and Flattop 358
B.3.1 Hanning window 358
B.3.2 Flattop window 358
B.4 Axis scaling: semilogx and loglog 359
B.4.1 Semilogx scaling 359
B.4.2 Loglog scaling 359
B.5 Full-record FFT versus pulse-segment FFT 359
B.5.1 Full-record FFT 359
B.5.2 Pulse-segment FFT 359

C Complementary simulation and measurement graphs from Chapter 6 **361**
C.1 Graphs from common mode simulation of complete vehicle with full and reduced models 361
C.2 Graphs from common mode simulation of part of the vehicle, with full and reduced models 367
C.3 Additional DM behaviour during dynamic operation (acceleration runs) . 372

Acknowledgements

Finally, it is time to write the last chapter of this thesis before a new chapter begins. It has now been eight years since I began this journey — a journey filled with new insights, new connections with fantastic people, joy, and sorrow. Having the opportunity to study at my age has been a true challenge. The theoretical courses were demanding after almost thirty years away from school. In the research work itself, however, my professional experience more than outweighed it.

Knowing the problem and seeking the answer. Looking at graphs and understanding them, rather than relying on mathematical formulas.

The journey started at Volvo Buses, where I discussed EMI with Mats Alaküla. Mats asked if I knew someone who wanted — and was capable of — doing a PhD in the EMI field for commercial vehicles. I had not been in academia and had no idea of the challenge ahead. Mats described the qualifications and added *"but it can be you as well,"* and here I am.

My reference group

Mats Alaküla has been by my side as my main supervisor throughout these eight years — through courses, papers, my thesis for the licentiate degree, and now my PhD thesis. He always has good ideas and offers endless encouragement. Whenever I doubt myself, he is the one who lifts my confidence.

Hans (Trisse) Bängtsson, an old colleague from Adtranz in Västerås. I spent a few years in Philadelphia working on a suburban tram delivery to a customer. There were many challenging problems to solve, and Trisse always supported me from Sweden. "Per, this is how it works!" A wealth of knowledge, and I am so grateful to have Trisse as my co-supervisor. Trisse is always the one who understands and explains how it works.

Jonas Ottosson has been part of my reference group from the beginning, and I am now fortunate to be in the same team as him at Volvo. He is a specialist within power electronic converters and is always helpful, contributing valuable ideas and questions. A small question from Jonas resulted in a patent application and a paper.

Sabine (Mäthäxan) Alexandersson is an EMC specialist working at the Swedish Defence Materiel Administration (FMV - Försvarets materielverk). I was honoured when she accepted to be part of my reference group and she has contributed significant expertise. Sabine has been important in keeping the scope concrete. I am also grateful for all her telephone calls when she realised I was feeling low.

Anders Lasson, system specialist at Volvo Cars, is encouraging and asks the trickiest yet very valid questions.

Zhe has been part of my reference group from the beginning, and I am now fortunate to be in the same team as her. She is always positive and has brought my ideas into projects at Volvo, which I am truly grateful for.

Dan Hagstedt, who is also my highly appreciated manager (you really are the best), has always been supportive and has given me the conditions I need to do my work.

Beyond my reference group

Marco Lind, previously manager at Volvo Buses and at Volvo GTT, encouraged me to start studying ”Chalmers Professionals”, which later gave me the courage to take the step and become a PhD student.

Daniel Pehrman, former PhD student at Chalmers, was one of the teachers and an endless source of support to me in the ”Chalmers Professionals” course.

David Hellstedt, former head of Volvo Electromobility, encouraged me to start the PhD studies and gave me the prerequisites in terms of funding from Volvo and encouragement.

My colleagues at Volvo

Tommy Strömborg supported me with the vehicle measurements and the new measurement system.

My team at Volvo, “MDS & Platform Design”, you are simply the best. I could not have wished for better colleagues — both as people and as professionals. On top of that, thank you for all the support with PLECS and Python.

And to all other colleagues at Volvo who have supported me along the way — thank you.

All staff in Lund

Carina Lindström, I would have missed many important things without your help.

Francisco Marquez invited me to speak at inspiring meetings at the Swedish Electromobility Centre.

Philip Abrahamsson was co-supervisor to my first master’s thesis students. He was always very helpful, and I greatly enjoyed the time we shared an office and exchanged ideas.

And to all other colleagues in Lund — thank you for always making me feel welcome whenever I am there.

Magnus Pihl is a former classmate from Chalmers, a former colleague at ABB, and above all, a good friend. We have had many fruitful discussions, and through his work at Micropower he has offered valuable insights from a supplier perspective.

The most important things in life are health, friends, and love

In the summer of 2025, I underwent hip resurfacing in Belgium. The hip pain is now gone, and I am again able to exercise and perform cross-country skiing without pain or fear of falling. Living without pain is something you easily take for granted—until you no longer have it. Over the years, I have spent at least one week off-site working in Dalarna, combining cross-country skiing with work. The value of exercise and work cannot be overstated. It is remarkable how new ideas appear and problems solve themselves during exercise.

I am so grateful for my old friends

I am deeply grateful to many friends I have met over the years. Among them, a few groups deserve special mention.

”Fallskärmsgänget” - I started skydiving just before I started at Chalmers. I quit skydiving a long time ago but the friendships remain. Now mostly skiing and kayaking with them. Thank you, all of you.

“Chalmersgänget” — we have our yearly get-together, a tradition since 1993. And on top of that, we still meet for parties or just small gatherings. Thank you, all of you.

Jonas Ebbesson is my oldest friend from Jönköping, and I am so grateful we reconnected.

There are, of course, many more friends who have been important in my life, and although I cannot mention everyone by name, you are all remembered with gratitude.

Finally my family

With love to my father Bertil who passed away, at the age of 95, between the licentiate presentation and the printing of the licentiate thesis book. He encouraged me all the time. He translated my first papers with Google Translate and was looking forward to translating this book as well. The last weekend we met, we celebrated with champagne. Love you!

My mother Gunvor passed away during my first year as PhD student. Love you!
Miss you both!

Ida och Tor, my lovely children.

Tor finished school in June 2025 and has started his first employment. I am so proud of him — he is a lovely son who cares deeply for his family and friends. Love you!

Ida, min älskade dotter som jag inte sett så mycket de senaste åren. Älskar dig, saknar dig och hoppas vi får mer tid framöver.

Tor och Ida, ni betyder allt för mig. Ni skulle bara veta hur mycket jag älskar er och inget är viktigt i jämförelse med er. Älskar er!

My sister Eva, she is always there for me. Love you!

Eva’s family, I am so grateful for you. Love you!

Marie, my newfound love. “Tinkering with my curves,” as Marie likes to say when she sees me running simulations. We take every day as it comes. Grateful for what we have found and for what lies ahead — wherever the journey may take us. Love you!

Music is important to me while I work, as it helps me shut out noise and distractions so I can focus. When writing, I need instrumental music that is just "there" and creates a pleasant feeling. When working with simulations, I prefer music that keeps my spirits up. A song that became something of an anthem for me during my PhD studies is *Only the Dead Fish Follow the Stream* by Louise Hoffsten. I listened to Louise Hoffsten twice, in 2023 and 2025, at a dinner show at Slussens Pensionat.
Listen to the song and its lyrics, and you will understand. Thanks to Louise for allowing me to use the lyrics in my thesis when we met at Slussens Pensionat in September 2025.

Only the Dead Fish Follow the Stream
Song by Louise Hoffsten

If you don't fight no one else will
Give it a try, keep it alive
To see the view you got to climb the hill
Give it a try, get to know why

It's been a long way coming
But you got to know why and when

Only the dead fish follow the stream
No, nothing is ever what it seems
You can do whatever if you know when and why
Only the dead fish follow the stream

Don't go and get too comfortable
You can't keep it alive
If you're not awake
I keep a smile through success and mistakes
Come hell or high water
I'm ready, I'm ready

It's been a long way coming

Only the dead fish follow the stream
No, nothing is ever what it seems
You can do whatever if you know when and why
Only the dead fish follow the stream

Populärvetenskaplig sammanfattning

Elfordon uppfattas ofta som en modern uppfinning, men elektriskt drivna fordon har funnits sedan slutet av artonhundratalet. De första helelektriska personbilarna, bussarna och lastbilarna utvecklades redan innan förbränningsmotorn slog igenom.

För att förstå varför elektriska störningar spelar en så viktig roll i dagens elfordon kan man börja med en enkel bild. Tänk dig en hamn en stilla dag. Båtarna ligger lugnt vid bryggorna och allt är stilla. Men när vinden ökar, eller en större båt passerar, bildas vågor som rullar in, studsar mellan båtar och bryggor och får allt att gunga. På samma sätt kan modern elektronik som styr en elmotor skapa små elektriska "vågor" i fordonets elsystem. Dessa elektriska "vågor" är en förenklad bild av det som i facklitteraturen kallas elektromagnetiska störningar – *Electromagnetic Interference (EMI)*. Hur mycket dessa vågor sprider sig beror på elsystemets motstånd mot sådana svängningar – det som i elektrotekniken kallas *impedans*. Det kan jämföras med hur lätt vatten rör sig i ett trångt eller brett rör: ett smalt rör bromsar flödet, ett bredare släpper igenom det lättare.

Dessa tidiga elfordon var dock tekniskt enkla: begränsad effekt, få delsystem, ingen avancerad elektronik och mycket små möjligheter till att sådana elektriska "vågor" uppstod mellan komponenter. Elektromagnetiska störningar utgjorde därför sällan några avgörande konstruktionsproblem.

Dagens elfordon representerar en helt annan komplexitet. Särskilt tunga fordon, såsom bussar och lastbilar, innehåller många elektriska delsystem som alla är kopplade till samma likspänningsnät. Batterier, elektroniska omvandlare som gör växelström av likström eller tvärtom, hjälplastssystem och omfattande kablage arbetar samtidigt. Delsystem som luftkonditionering, luftkompressor, värmare och DC/DC-omvandlare delar samma elektriska infrastruktur, vilket gör att störningar lätt sprider sig mellan komponenterna. Utvecklingen går dessutom mot elektronik som arbetar allt snabbare, vilket ytterligare förstärker problemet.

Elektriska störningar – det som på fackspråk kallas *Electromagnetic Interference (EMI)* – är inte något nytt. I system som tåg och spårvagnar har ledningsbundna störningar, impedanskopplingar och resonansfenomen studerats och hanterats i många decennier. Men i moderna elfordon uppträder dessa störningar i en mycket tätare och mer komplex elektrisk miljö.

För att kunna studera dessa elektriska "vågor" i verkliga fordon krävdes ett mätsystem som både kunde registrera mycket snabba och mycket små variationer i spänning och ström – och samtidigt tåla de höga strömmarna och spänningarna i ett tungt elfordon. Ett sådant system fanns inte att tillgå, och därför utvecklades det som en del av detta arbete. Mätsystemet är i sig inget forskningsresultat, men det var en nödvändig förutsättning för att förstå hur störningarna faktiskt uppstår och sprider sig i ett verkligt fordons elsystem.

Den snabba elektrifieringen av fordon, särskilt inom tunga transporter, innebär att dessa utmaningar nu uppträder i en bransch som historiskt har förlitat sig på mekanisk kraftöverföring eller enklare generatorbaserade elsystem. För att verifiera elektriska delsys-

tem används ofta standardiserade provmetoder. En vanlig metod är att mäta störningar genom ett *Line Impedance Stabilization Network (LISN)* – ett instrument som ger en fast och reproducerbar elektrisk miljö för testning. Syftet är att säkerställa jämförbarhet mellan olika tester, men metoden bygger på antagandet att denna standardiserade miljö liknar den verkliga miljön i ett fordon.

Denna avhandling visar att så inte alltid är fallet. Genom modellering och analys av kompletta fordonssystem kan man se att den impedans som ett delsystem faktiskt upplever beror starkt på fordonets konfiguration: antal och typ av batterier, olika omvandlare, kablarnas längder och deras inbördes placering. Både impedansens storlek och dess resonansbeteende skiljer sig ofta markant från den miljö som skapas av ett LISN – både i differential- och common-mode-fall.

Sammanfattningsvis presenterar avhandlingen ett systemorienterat ramverk för att förstå och analysera ledningsbundna elektromagnetiska störningar i elfordon. Genom att kombinera modellering, mätning och analys av fordonets impedans tydliggörs begränsningarna med att testa komponenter isolerat och vikten av att betrakta fordonet som ett integrerat elektriskt system. Simuleringarna överensstämmer sällan exakt med mätningarna, men de hjälper till att förstå hur systemet fungerar. Avhandlingen visar också att det som uppmäts i ett system som på något sätt är påverkat av mätinstrument inte alltid speglar det sanna beteendet när dessa instrument kopplats bort.

Arbetet är avsett att fungera som ett uppslagsverk och en praktisk vägledning för ingenjörer och forskare som vill förstå hur delsystemsinteraktioner, elektrisk impedans och resonanser påverkar EMI-beteendet i moderna elfordon.

Popular scientific summary

Electric vehicles are often regarded as a modern invention, but electrically powered road vehicles have existed since the late nineteenth century. The first fully electric cars, buses and trucks were developed even before the internal combustion engine became dominant.

A useful way to understand the behaviour of electrical disturbances is to think of the sea. The sea is not necessarily simpler, but it is easier to grasp because you can see what is happening. Boats may lie calmly by a jetty and everything appears peaceful. But when the wind rises, or when a larger vessel passes by, waves travel into the harbour, reflect between boats and quays, and make the boats move – sometimes enough to risk damage. That is why most harbours have breakwaters, the maritime equivalent of electrical filters.

Those early electric vehicles were technically simple: limited power levels, no advanced electronics, only a few subsystems, and very little opportunity for electrical interaction between components. Electromagnetic disturbances were therefore rarely a major design concern.

Today's electric vehicles are something completely different. Heavy–duty vehicles such as buses and trucks contain a large number of electrical subsystems, all connected through a shared high–voltage direct–current network. Batteries, advanced electronic converters, auxiliary loads and extensive cabling all operate at the same time. This creates a tightly coupled environment where electrical interaction between components is unavoidable.

In much the same way as in the harbour analogy, a single electrical component can create "waves" in a vehicle's electrical system – waves that travel through the cabling and affect completely different subsystems, even if all components functioned perfectly when tested on their own. Just as small waves from a passing ship can cause problems in a harbour without a breakwater, electrical disturbances can build up and interact when nothing is present to damp or redirect them.

Electrical disturbances – technically known as electromagnetic interference (EMI) – have been understood for many decades in other electric transport systems, such as trains and trams. In those fields, conducted disturbances, impedance coupling and resonance phenomena have been studied and managed for a long time.

Studying these electrical "waves" in real vehicles required a measurement system capable of capturing fast and very small variations in voltage and current, while also tolerating the high currents and high voltages found in heavy–duty electric vehicles. No such system existed, so one had to be developed as part of this work. The measurement system is not a research result in itself, but it was essential for understanding how disturbances actually arise and propagate in real vehicles.

The rapid electrification of vehicles, particularly in the heavy–duty sector, means that these challenges now appear in an industry that has historically relied on mechanical power-trains or relatively simple generator–based electrical systems. To verify electrical subsystems, standardised test methods are commonly used today. A typical method is to test components using a Line Impedance Stabilisation Network (LISN), which provides a fixed and

repeatable impedance for measuring conducted disturbances. The idea is to ensure comparability between tests, but the method also relies on the assumption that this standardised impedance represents the electrical environment of the vehicle.

This thesis shows that this assumption is often not valid. Through modelling and analysis of complete vehicle systems, it is demonstrated that the impedance experienced by a subsystem depends strongly on the vehicle's configuration – including the number and type of energy storages, converters and connecting cables. Both the magnitude of the impedance and its resonance behaviour differ substantially from those imposed by a standardised LISN, for both differential–mode and common–mode conditions.

In summary, this thesis provides a system–level framework for understanding conducted electromagnetic disturbances in electric vehicles. By combining modelling, measurement and impedance analysis, it highlights the limitations of testing components in isolation and the importance of viewing the vehicle as an integrated electrical system. Simulations rarely match measurements exactly, but they help build an understanding of how the system behaves. At the same time, measured results may not fully reflect reality once the measurement equipment has been removed.

This work is intended to serve as a reference and practical guide for engineers and researchers who wish to understand how subsystem interactions, impedance characteristics and resonance phenomena influence EMI behaviour in modern electric vehicles.

Nomenclature

AC comp	Air Conditioning Compressors
BB	Body Builders
BEV	Battery Electric Vehicle
BJB	Battery Junction Box
BoB	Break Out Box
BP	Battery Pack
BW	Band Width
C	Capacitance
CAN	Controller Area Network
Ch	Channel
CM	Common-Mode
CMDC	Common-Mode DC
CSU	Charging Switch Unit
DCDC	Converter from DC to DC
DM	Differential-Mode
DUT	Device Under Test
DYNO	Dynamometer
EM	Electrical Machine
EMC	Electromagnetic compatibility
EMD	Electrical Machine Drive
EMI	Electromagnetic Interference
ePTO	electrical Power Take Out
EV	Electric Vehicle
FFT	Fast Fourier transform
Gen	Generator
HEV	Hybrid Electric Vehicle
HF	High Frequency
HV	High Voltage
HVAC	High Voltage Air Condition
IAI 2	Impedance Analysis Interface 2
IGBT	Insulated Gate Bipolar Transistor
IP	Intellectual Property
JB	Junction Box
L	Inductance
LCR	Inductance Capacitance Resistance
LISN	Line Impedance Stabilisation Network
OCEPS	Onboard Charger and Electrical Power Supply
OEM	Original Equipment Manufacturer
OnBC	On Board Charger

PCI	Peripheral Component Interconnect
PEC	Power Electronic Converter
PHEV	Plug-in Hybrid Electric Vehicle
PMSM	Permanent-Magnet Synchronous Machine
PSM	Phase Sensitive Multi-meter
PXI	PXI (PCI eXtensions for Instrumentation)
R	Resistance
SC	Short Circuit
SiC	Silicon Carbide
TVS	Traction Voltage System

Chapter 1

Introduction

The rapid introduction of battery-electric commercial vehicles has created electrical architectures of a scale and complexity not previously encountered in on-road applications. A commercial battery-electric vehicle contains several traction battery packs, multiple electric machine drives, DC/DC converters, on-board and off-board charging systems, auxiliary loads, extensive cabling, all interconnected through a common traction voltage system (TVS). Unlike laboratory-scale powertrain rigs, a complete vehicle constitutes a distributed, multi-node DC network extending over tens of metres, in which subsystem interactions cannot be understood independently of the surrounding electrical environment.

Although academic literature contains important contributions to the understanding of conducted electromagnetic interference (EMI), the available work focuses predominantly on isolated subsystems. Representative examples include system-level conducted EMI modelling of high-voltage electric drive systems [27], conducted EMI prediction in on-board chargers [35], and EMI analysis in motor-drive subsystems [34]. These references are included not because they are directly relevant to the methods or results of this thesis, but because they clearly illustrate that existing EMI research addresses individual subsystems rather than complete commercial vehicles. This contrast is essential: it demonstrates the narrow subsystem-oriented scope of the current literature and highlights the absence of full-vehicle EMI studies that incorporate multiple interacting subsystems within an electrically large traction voltage system.

A broad literature search confirms that publicly available research on full-vehicle EMI modelling and measurement remains extremely limited. This lack of system-level studies may be attributed to intellectual property constraints, the industrial sensitivity of high-voltage architectures, and the practical difficulty of performing high-bandwidth measurements with a sufficiently large number of channels. Regardless of the underlying cause, the research gap is clear: subsystem-level EMI compatibility does not ensure system-level compatibility.

This gap is critical because differential-mode (DM) disturbances may coincide with resonance frequencies in the TVS, causing a subsystem to perform adequately in one vehicle

configuration while generating excessive differential-mode current ripple in another. Common-mode (CM) disturbances may propagate over long distances along cable shields and chassis structures if not mitigated at the disturbance source, thereby exciting unintended return paths and stressing components far from the originating converter. Such effects originate from the distributed impedance of the complete vehicle and cannot be predicted from isolated subsystem measurements.

The work presented in this thesis addresses this gap by combining broad, high-resolution EMI measurements on a complete commercial vehicle with system-level modelling of its traction voltage system. A dedicated measurement system is developed to capture the high-frequency behaviour of a full-scale vehicle, enabling synchronous sampling of up to 96 channels at rates up to 60 MS/s. This measurement architecture provides a unique dataset characterising both DM and CM behaviour across the entire TVS under representative operating conditions. The resulting data form the empirical foundation for the modelling, calibration, and simulation methodology developed in the thesis.

In this thesis, the term "high-frequency (HF) parameters" refers to the frequency-dependent intentional and parasitic elements that influence the conducted CM and DM behaviour within the modelling bandwidths established in the work. These bandwidths extend up to 2 MHz on the DC side of the traction voltage system and up to 3 MHz on the AC side between the EMD and EM. This definition differs from radio-frequency terminology, where the term HF typically denotes substantially higher frequency ranges. Within the scope of this thesis, HF therefore denotes the specific frequency region relevant for conducted-EMI mechanisms in commercial battery-electric vehicles.

A central methodological position in this work is that the depth of the research arises directly from its breadth. System-level EMI behaviour is governed by the electrical interactions across the complete traction voltage system rather than by the isolated details of individual components. A holistic perspective is therefore necessary to understand how disturbances propagate between subsystems, how cable and component impedances shape return paths, and how CM and DM mechanisms couple across the vehicle. While any individual subsystem can be modelled in further detail, such detail does not necessarily increase predictive capability unless the system context is preserved.

This thesis focuses exclusively on conducted EMI. The aim is to improve system-level understanding and predictive capability rather than to assess compliance with electromagnetic compatibility (EMC) standards. The work therefore emphasises impedance-driven interactions, DM and CM coupling mechanisms, measurement-supported model development, and the system-level behaviour of the traction voltage system.

1.1 Background

The background of this thesis builds on long-standing experience from industrial power electronics and railway traction systems, where system-level electromagnetic interference (EMI) is a recurring challenge. In these applications, the interaction between converters,

machines, cables and auxiliary equipment is extensively studied, and system integration is recognised as a critical aspect of reliable operation.

In contrast, the electrification of road vehicles introduces a development environment that is significantly more fragmented. Subsystems are often designed and delivered by different suppliers, each with limited insight into the characteristics, constraints and operating conditions of the complete vehicle. This situation imposes increased demands on system-level modelling, measurement and verification methods in order to ensure electromagnetic compatibility (EMC) and robust vehicle operation.

1.2 Goal, objective, and scope

The goal of the work presented in this thesis is to establish a solid understanding of how differential-mode (DM) and common-mode (CM) voltages and currents are generated within the traction voltage system (TVS) of a Class B vehicle, how they propagate through the system and how interactions between subsystems can give rise to EMI-related performance limitations.

The objective is to provide this understanding through design guidelines and modelling tools that enable prediction of TVS behaviour from an electromagnetic interference (EMI) perspective. These tools aim to support EMC considerations early in the vehicle development process, before physical prototypes are constructed.

One scope of the work is the development of simulation models of the electric power system that represent DM behaviour in the frequency range from 1 kHz to 200 kHz, and CM behaviour from 1 kHz up to 3 MHz. These models are calibrated and validated using measurements performed on a commercial electric vehicle.

Another scope is the development of a measurement system capable of providing the data required for such model validation, including sufficient bandwidth, dynamic range and channel count to capture relevant EMI phenomena across the distributed TVS.

1.3 Contributions and publications

The primary contribution of this thesis is the development of system-level methods and tools that enhance the ability of engineers to analyse and mitigate electromagnetic interference (EMI) in electric vehicles. Particular emphasis is placed on the interplay between wideband measurement techniques and physically based simulation models, and on the fundamental insight that any measurement inherently perturbs the electrical system under investigation. The integration of a new component influences the behaviour of the complete system, and conversely, the system constrains the behaviour of each individual component. The work presented in this thesis therefore advances both the methodological understanding and the practical capabilities required for system-level EMI analysis.

During the course of the work, an extensive high-bandwidth measurement system is developed, capable of recording up to 96 channels simultaneously, with sampling rates of up to 60 MS/s on 72 channels and 2 MS/s on 24 channels, and with a total storage capacity corresponding to approximately one hour of continuous acquisition.

In addition, a new high-voltage measurement interface is developed that enables safe blocking of the traction battery DC voltage, thereby allowing battery impedance measurements using an LCR instrument. No such interface was commercially available at the start of this work. This development makes it possible to derive impedance-based models of high-voltage vehicle batteries operating at voltages of up to approximately 750 V.

A new simulation environment based on PLECS is also integrated into the industrial development workflow at Volvo. While several commercial simulation tools exist, PLECS is found to be particularly well suited for system-level simulation of electric power systems; this assessment is acknowledged to be partly subjective but is supported by extensive practical use throughout the project.

In total, four scientific papers are authored during the work, including publications in peer-reviewed journals and presentations at international conferences.

1.3.1 Publications

Modelling of electric power system in electric vehicles

The Speedam 2020 conference paper [30] is developed in collaboration with Mats Alaküla. The technical content, modelling approach, simulations and analysis are performed by the author of this thesis. Mats Alaküla contributes primarily through critical review, structural guidance and language refinement, and by posing clarifying questions that support the development of the technical discussion. The paper is presented online at the SPEEDAM conference in 2020 during the COVID-19 pandemic.

Common Mode Current Measurements in Traction Systems for Electric Vehicles

The journal paper [29] is an extended and substantially expanded version of the conference paper [30]. The author develops the measurement methodology, experimental work, data analysis and technical conclusions. Mats Alaküla contributes through editorial support, structural improvements and critical discussion of the presented results.

Common Mode Current Reduction in Traction Systems for Electric Vehicles

The Speedam 2024 conference paper [32] is developed in collaboration with Jonas Ottosson. The initial observation of time-varying common-mode behaviour is made by the author of this thesis, who proposes that the behaviour can be influenced through converter control. Jonas Ottosson identifies the underlying cause as noise in the current measurement and develops the control software enabling experimental validation. The author writes the manuscript and performs the analysis and interpretation of the results.

Methods for the Investigation and Mitigation of Conducted Differential-Mode Electromagnetic Interference in Commercial Electrical Vehicles

Following the SPEEDAM 2024 conference [32], an invitation is received from the journal *Energies* to contribute to a peer-reviewed article. The resulting publication [31] is developed in collaboration with Mats Alaküla. The author carries out the modelling, simulations, measurements and analysis, while Mats Alaküla contributes through editorial review, improvements in structure and clarity, and critical feedback. This article forms an important basis for parts of Subsections 2.4.5 and 2.4.6 and Chapter 7 in this thesis.

1.4 Disposition of the thesis

Chapter 1 introduces the motivation and background for the thesis, with particular emphasis on the rapid electrification of road vehicles and the associated challenges related to electromagnetic interference (EMI). The chapter defines the problem context, outlines the traction voltage system (TVS) as a system-level entity, and motivates the need for early prediction of differential-mode (DM) and common-mode (CM) disturbances.

Chapter 2 describes the traction voltage system in electric vehicles, including batteries, power electronic converters, cables and auxiliary subsystems. The chapter introduces and formalises fundamental concepts related to DM and CM phenomena, forming the theoretical foundation for the remainder of the thesis.

Chapter 3 presents the development of a dedicated measurement system designed to capture high-frequency electrical behaviour in large-scale traction voltage systems. Design considerations such as bandwidth, channel count, isolation and synchronisation are discussed, together with validation of the measurement approach.

Chapter 4 presents extensive measurement results obtained from a full-scale commercial electric truck. Voltage and current waveforms are analysed at multiple subsystem interfaces, and their frequency content is examined to provide empirical insight into EMI-related behaviour in the vehicle.

Chapter 5 focuses on modelling techniques for deriving system-relevant electrical models from measurement data. Emphasis is placed on balancing model accuracy and complexity to enable computationally feasible system-level simulations.

Chapter 6 applies the developed models in system-level simulations of the traction voltage system. Simulation results are compared with measurements and theoretical analyses to investigate subsystem interactions and resonance phenomena.

Chapter 7 examines standardised artificial networks, such as line impedance stabilisation networks (LISNs), and compares their fixed test impedances with vehicle-representative conditions. The chapter has a limited, illustrative function and does not constitute one of the main contributions of the thesis.

Chapter 8 summarises the main findings and contributions of the thesis and outlines recommendations for future research, including implications for EMI-aware design, modelling, measurement and standardisation.

Chapter 2

Electric power systems in electric vehicles

Commercial electrified vehicles are available in different variants such as hybrid electric vehicles (HEV), plug-in hybrid electric vehicles (PHEV) and pure battery electric vehicles (BEV). This thesis focuses exclusively on BEV class B voltage systems with different charging solutions. The 24 V system is not included.

The focus on BEV class-B systems reflects the current state of practice in heavy-duty electric vehicles. Commercial trucks and buses operate almost exclusively at class-B voltage levels, where higher DC voltages are required to keep current magnitudes at reasonable levels for the traction power demanded in these applications. The industry trend is a transition from earlier 600-700 V platforms toward 800-1000 V architectures, reducing conductor cross-section, copper losses and thermal stress.

Hybrid architectures such as HEV and PHEV are becoming less relevant in heavy-duty applications, and most manufacturers—including Volvo—have transitioned to fully electric powertrains for new platforms. The analysis in this chapter therefore concentrates on BEV class-B, which is both the dominant architecture today and the most technically relevant for understanding high-power traction systems.

While the underlying physical mechanisms—parasitic capacitances, common-mode voltage generation, differential-mode ripple and impedance interaction—exist in all electrified powertrains, their magnitude and practical impact scale strongly with system voltage, cable length and converter power. BEV class-B systems therefore provide a representative and technically demanding environment for analysing the EMC behaviour addressed throughout this chapter.

To provide clarity and structure, this chapter gives a system-level introduction to the traction voltage system (TVS) and its interaction with surrounding electrical subsystems in an electric vehicle. The chapter explains how voltage distribution, current flow, resonances and parasitic parameters emerge in the DC network, and how these factors influence both

steady-state behaviour and the switching dynamics of the connected converters.

The chapter is organised into the following sections:

1. **Traction Voltage System (TVS)** – introduces the architecture, operating principles and electrical characteristics of the TVS, including its natural resonances and operating constraints.

2. **Other system** – describes external electrical systems connected to the TVS, outlining their intended functionality and the boundary conditions they impose on the traction voltage environment.

3. **Important sources and loads** – identifies the major subsystems interfacing with the TVS, including batteries, traction inverters, DC/DC converters and auxiliary loads, and explains their mutual electrical influence.

4. **CM and DM** – provides a detailed analysis of common-mode and differential-mode phenomena, including their origin, propagation mechanisms and the role of parasitic capacitances and impedances.

Together, these sections establish the foundation for the modelling, measurements and system-level analysis presented in the subsequent chapters.

2.1 Traction Voltage System (TVS)

This section builds on the introduction in Chapter 2 and focuses on the structure and operating characteristics of the Traction Voltage System (TVS). The purpose is to establish the system-level electrical environment in which all high-voltage subsystems operate, forming the basis for the analyses in the subsequent sections.

The Traction Voltage System (TVS) is the DC, class B [11] voltage system that connects all traction batteries, electric machines, charging systems, compressor drives, DC/DC converters and other units involved in the main power conversion processes on board a commercial electric vehicle. The TVS operates in the range of 600-700 V DC but varies between systems depending on the intended battery voltage as well as the state of charge (SOC), temperature and power loading of the vehicle.

This section uses the Traction Voltage System (TVS) of a Volvo FE280 (see Figure 2.1) and an FM1156 (see Figure 2.2) as the representative DC system for measurements and analysis.



Figure 2.1: Volvo FE electric.



Figure 2.2: Volvo FM electric.

The power levels of the included subsystems vary from 5 kW to more than 150 kW with switching frequencies from a few kHz up to almost 100 kHz. Depending on the vehicle layout, the 600 V cables that interconnect the different subsystems can range from 1 m to more than 20 m in an articulated bus.

In practical vehicle development, the individual subsystems connected to the TVS—such as traction inverters, DC/DC converters, chargers and auxiliary drives—are often supplied by different manufacturers. While this thesis does not describe supplier-specific details, the modelling assumptions reflect the industrial reality that subsystems are typically

delivered with limited information about switching behaviour, internal parasitics and impedance characteristics. This assumption is therefore used as an analytical framing rather than a statement about any specific supplier. The consequence is that the TVS must be analysed as a system in which converters with unknown and potentially mismatched characteristics interact electrically through a shared DC network.

Using modelling to understand and predict the behaviour of the TVS in all operating conditions requires detailed representation of all subsystems, both with respect to DM and CM aspects. The purpose of the work described in this thesis is to build understanding of the relationships between disturbances as well as providing guidelines to prevent harmful interference. This also results in the development of a simulation model library with all relevant subsystems and interconnections, represented in a LEGO®-like manner, enabling a wide range of TVS configurations and parameter sets to be modelled. The analysis investigates models that must be possible to construct in collaboration with suppliers prior to delivery to reduce development time.

The following subsections present the most important loads and sources in Figure 2.3. In the figure, the models denoted BP1-BP4 are battery packs, the DC/DC units supply the 24 V DC system, the OnBC units are on-board chargers, the JBs are junction boxes acting as electrical connection points, the EMDs are electric traction machine drives and the ePTO unit is an electrically driven mechanical PTO. The cables are shielded coaxial cables for high power subsystems and twin-axial shielded cables for low power subsystems, with the cable shield connected to the subsystem chassis via the connector.

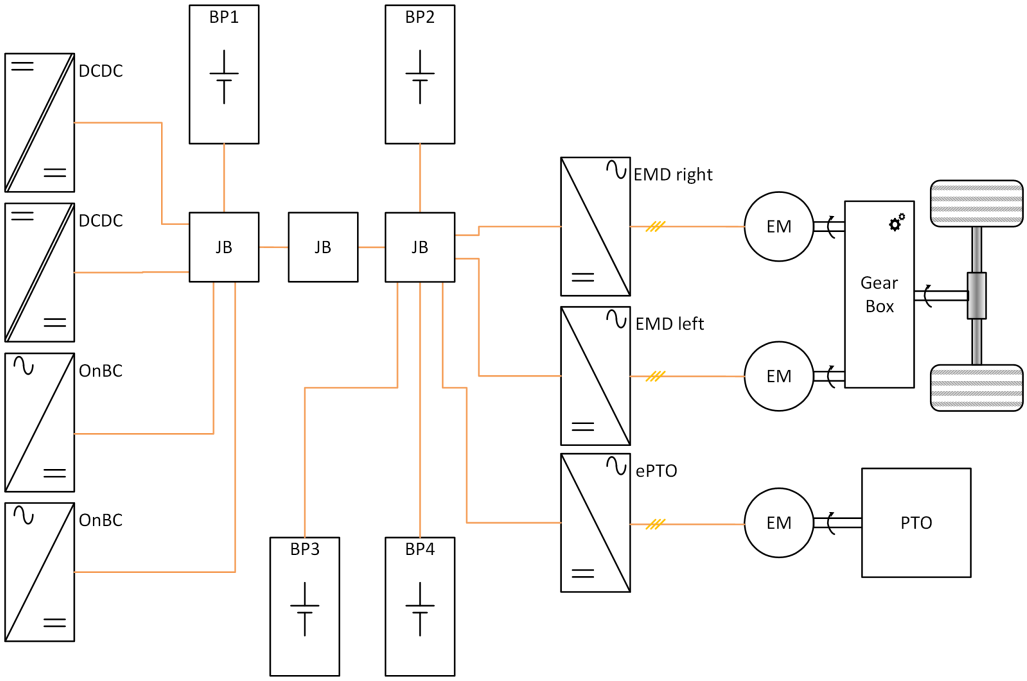


Figure 2.3: Volvo truck FE280 traction system layout (TVS). The orange connections represent the shielded cables connecting the subsystems. The cables between the electric machine drive (EMD) and the electric machine (EM) are denoted with three parallel lines for the three-phase cable. All other connections are DC cables with plus and minus poles.

Conclusion

The Traction Voltage System (TVS) forms the electrical backbone of the vehicle, integrating the traction batteries, converters and electric machines into a unified high-voltage architecture. This section has introduced the operating range, physical layout and key subsystems of the TVS, establishing the system-level environment required for the remaining sections of this chapter. The behaviour of each subsystem influences the electrical characteristics of the others, underscoring the need for consistent and system-aware modelling in all subsequent analyses.

2.2 Other systems

Building on the system-level description of the Traction Voltage System (TVS) in the previous section, this section expands the analysis by considering external electrical interfaces and operating conditions. These aspects define the boundary within which the TVS operates and clarify which interactions fall outside the scope of this thesis.

This thesis includes only a stand-alone vehicle in operation and the corresponding electrical dynamics on the TVS. The vehicle can be connected to the grid via the on-board or

off-board chargers. The charger can, but must not, be galvanically isolated from the grid. Galvanic isolation is used to break the electrical potential between two systems, for example between the grid and the vehicle, to increase the electric safety level. With galvanic isolation in the on-board charger, the TVS system is electrically separate with respect to the ground of the grid supply.

Vehicles can also be used for power supply in island operation, i.e. supplying electric energy where there is no connection to an electric grid. This can be done with or without galvanic isolation between the vehicle TVS and the externally driven load, which may be a DC load or a single- or three-phase AC load.

Body builders (BB) have historically connected loads mechanically to the combustion engine PTO or the transmission PTO to supply hydraulic pumps or air compressors. In a BEV an alternative to providing a mechanical PTO is to supply the loads directly with electric energy. However, the vehicle manufacturer has no knowledge of the BB subsystem and how the external load may interfere with the TVS. This implies that an electric supply to a BB load requires an appropriate safety level, potentially galvanic isolation.

This thesis therefore focuses entirely on the vehicle TVS without any connection to other vehicles, the power grid or BB loads.

Conclusion

This section has clarified the external electrical interfaces relevant to a TVS-equipped vehicle and the conditions under which galvanic isolation may or may not be present. The discussion establishes the operational boundaries for the remaining sections of this chapter and emphasises that the thesis exclusively considers the stand-alone vehicle case.

2.3 Important sources and loads

In the previous section, Section 2.2, the focus is on external electrical interfaces, stand-alone operation and boundary conditions that influence the Traction Voltage System (TVS). Building on that system-level perspective, this section introduces the main 600 V DC sources and loads that are directly connected to the TVS. These subsystems form the basis of the dynamic interactions analysed in Section 2.4.

The most relevant sources and loads are those directly connected to the TVS, i.e. 600 V DC loads and sources. The following description list introduces the subsystems

and guides the reader to their respective subsections:

Subsection 2.3.1 Electric Machine Drive (EMD), the main traction converter interfacing the TVS and the electric traction machine.

Subsection 2.3.2 Electric Machine (EM), the permanent-magnet synchronous traction machine.

Subsection 2.3.3 Machine Drive System (MDS), the combined system formed by the EM and the EMD.

Subsection 2.3.4 The traction batteries, serving as the primary energy storage units.

Subsection 2.3.5 Off-board and on-board charging systems interfacing with the TVS.

Subsection 2.3.6 The 24 V DC/DC converter supplying the low-voltage system.

Subsection 2.3.7 Air Conditioning (HVAC), the high-voltage air-conditioning compressor drive.

Subsection 2.3.8 The air compressor subsystem supplying compressed air for braking and auxiliary functions.

Subsection 2.3.9 Electric Power Take-Off (ePTO) units providing mechanical, DC or AC power to external Body Builder (BB) equipment.

With the exception of the batteries and the cables that connect these subsystems, all loads connected to the TVS incorporate a Pulse Width Modulated (PWM) converter as the interface between the TVS and the subsystem. These PWM converters generate both DM and CM harmonics that propagate through the TVS, including cables, batteries and other connected units. The selection of switching frequency represents a balance between switching losses and the required size of the DC-link capacitor on the TVS side of each converter. The switching frequencies used by the various subsystems span a wide interval, from a few kilohertz up to nearly 100 kHz.

2.3.1 Electric Machine Drive - (EMD)

The Electric Machine Drive (EMD) is the most powerful converter in the vehicle and operates in the power range of 150 kW and above. The TVS contains at least one EMD that transfers power between DC and AC, with the direction determined by the wheel torque. The EMD is a three-phase converter using insulated-gate bipolar transistors (IGBTs), although future designs may employ faster SiC devices, which could increase high-frequency harmonic emission. The total power handled by the EMD exceeds 150 kW, and the switching frequency typically remains below 10 kHz. Depending on vehicle configuration, multiple EMDs may operate in parallel on the TVS, each feeding its own traction machine.

2.3.2 Electric Machine - (EM)

The Electric Machine (EM) is a permanent-magnet synchronous machine (PMSM). Although induction machines or reluctance machines can also be applied, PMSMs are preferred due to their high torque-to-volume ratio. In this thesis, the term EM refers exclusively to the traction machine, as it plays a central role in the harmonic analysis. Other machines exist in subsystems such as the air compressor, the HVAC unit and potential ePTO interfaces, but these are not traction machines and are therefore not included in the harmonic modelling.

2.3.3 Machine Drive System - (MDS)

The Machine Drive System (MDS) is the combined system formed by the Electric Machine Drive (EMD) and the Electric Machine (EM).

2.3.4 Energy Storage - Batteries

The traction batteries constitute the primary energy storage units, either delivering or receiving electrical energy. Batteries exist in multiple chemistries and design types. For EV applications, energy-optimised batteries are preferred due to their high energy density, whereas hybrid vehicles may employ power-optimised batteries to support high peak-power requirements. In this thesis, the electrical behaviour of the battery is not modelled in detail, except for its TVS-relevant characteristics. A commonly raised concern is whether batteries tolerate current ripple. As indicated in [2], lithium-ion batteries are generally not negatively affected by such ripple.

2.3.5 Charging systems

Charging systems exist in several variants with distinct characteristics:

- Off-board DC chargers supplying the traction battery directly with galvanically isolated DC power from the AC grid.
- Isolated On-Board Chargers (OnBC) that receive AC power from the grid, provide galvanic isolation and rectify the output to DC for the traction battery.
- Non-isolated On-Board Chargers, which do not provide galvanic isolation and therefore create a low-impedance path between the grid and the TVS.

Charging operation and grid interaction fall outside the scope of this thesis. However, the DC side of the OnBC remains connected to the TVS during driving and its impedance must therefore be included in the simulation models.

2.3.6 24 V DC/DC

The DC/DC converter supplies the 24 V system from the traction batteries. The power consumption varies significantly depending on vehicle type and installed loads but is typically 7 kW or higher.

2.3.7 Air Condition - (HVAC)

The HVAC converter supplies the high-voltage air-conditioning compressor. The power level is typically 10 kW or higher, depending on vehicle size and climatic operating conditions.

2.3.8 Air compressor

The air compressor converter drives the pneumatic compressor used in the braking system. In Volvo vehicles, some compressors operate from the 24 V system, whereas others operate directly from the TVS.

2.3.9 ePTO

- Mechanical ePTO - a mechanical interface supplying rotational power.
- DC ePTO - an electric DC interface supplying power.
- AC ePTO - an electric AC interface supplying power.

The mechanical ePTO allows the Body Builder (BB) to request a specific shaft speed via a defined interface. The DC ePTO is more complex because the BB subsystem is externally defined and may interfere with the TVS. A galvanically isolated 600 V DC/600 V DC converter is therefore recommended. For AC ePTO, a power electronic converter is required, and galvanic isolation is recommended for the same reason.

2.4 CM and DM

Following the description of the TVS architecture in Section 2.3, the next step is to examine how electrical behaviour propagates through the system. This section introduces the two fundamental current modes that govern electromagnetic behaviour in the TVS: differential-mode (DM) and common-mode (CM) currents. Understanding these modes is essential before addressing capacitance asymmetry, CMDC voltage generation and the resulting current paths.

The following description list summarises the subsections in this section and guides the reader to their content:

Subsection 2.4.1 CM capacitance unbalance caused by asymmetric switching states in the EMD.

Subsection 2.4.2 Additional asymmetric parasitic capacitances contributing to CM behaviour.

Subsection 2.4.3 Definition and derivation of the common-mode DC voltage U_{CMDC}.

Subsection 2.4.4 CM current paths and their dependence on EM and battery parasitics.

Subsection 2.4.5 Origin and propagation of DM current ripple between subsystems.

Subsection 2.4.6 DM filter behaviour, resonance points and damping requirements.

There are two different types of currents flowing in the TVS: common-mode (CM) and differential-mode (DM) currents. DM current is the desired current that supplies the loads with energy. A DM current flows from the energy source, i.e. the battery, to the converter and back, as illustrated in Figure 2.4. The DM current normally includes an unwanted ripple component caused by switching events in the converters. This ripple causes losses in capacitors and inductors and may shorten component lifetime or, in the worst case, cause immediate failure if it exceeds the nominal design limits.

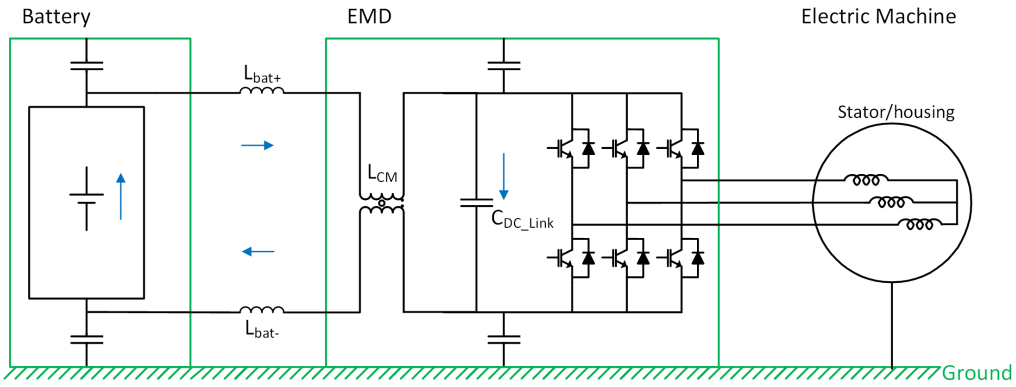


Figure 2.4: Differential-Mode (DM) current supplies the electric machine with the average power or receives energy from the EM during braking.

CM current leaks through, for example, the parasitic capacitances between the EM windings and the EM core, as illustrated by the red capacitors in Figure 2.5. The CM currents flow in the main conductors from the EMD to the EM and return in the cable

shields and chassis, via intentional pole-to-chassis capacitors (C_{CM_EMD}, i.e. Y-capacitors) and through parasitic battery capacitances (C_{CM_BAT}).

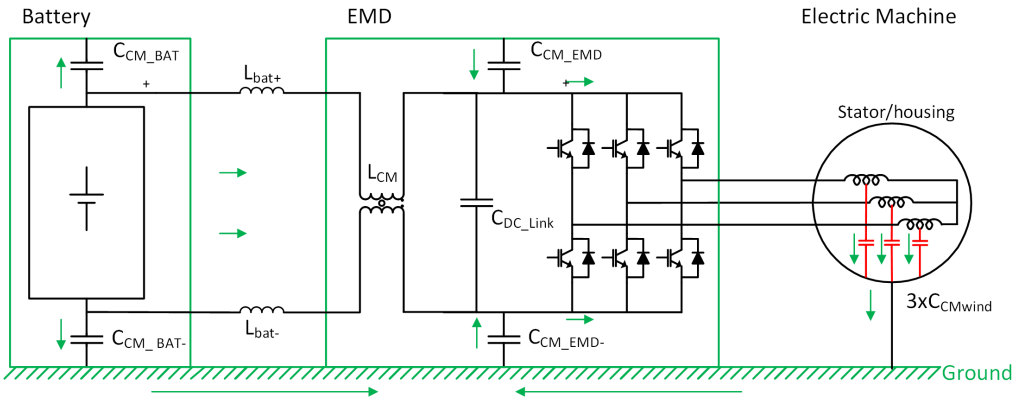


Figure 2.5: common-mode (CM) current.

Two CM current paths exist, as illustrated in Figure 2.6:

1. A CM current path involving the EMD and EM, driven by charge and discharge of the EM winding parasitic capacitances C_{CMwind}.
2. A CM current path involving the battery arises indirectly from variations across the CM capacitances of the EMD caused by path 1.

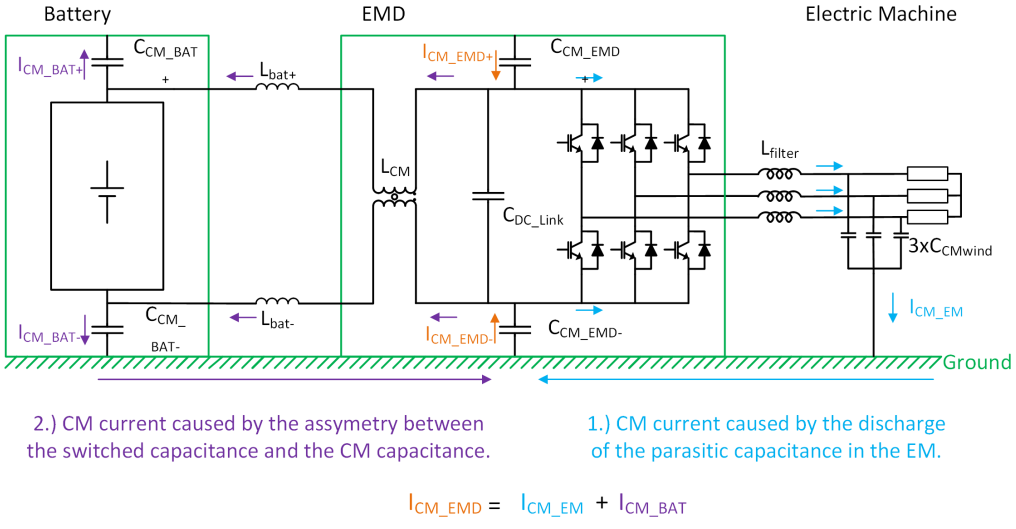


Figure 2.6: Two different CM currents and their paths.

None of the CM current would exist without the asymmetric parasitic capacitance C_{CMwind}. With careful system design, however, the resulting battery CM current I_{CM_BAT} can be minimised. Other asymmetric capacitances are present in the TVS, but the traction machine capacitances dominate due to their large magnitude. Therefore, C_{CMwind} is used as the representative example in the following explanations.

A subsystem supplier does not necessarily have insight into the behaviour of neighbouring subsystems. It is therefore the responsibility of the vehicle manufacturer to ensure system-level EMC characteristics and to specify appropriate requirements to suppliers.

2.4.1 CM capacitance unbalance

Following the definition of the two CM current paths in Section 2.4, this subsection examines how the parasitic EM winding-to-core capacitances, C_{CMwind}, become asymmetrically connected to the DC link depending on the switching state of the EMD. Each switching state redistributes the common-mode capacitances in a unique manner and therefore produces a distinct CM imbalance.

A two-level three-phase voltage source converter switches between eight possible switching-state combinations: $(0,0,0)$, $(0,0,1)$, $(0,1,0)$, $(0,1,1)$, $(1,0,0)$, $(1,0,1)$, $(1,1,0)$ and $(1,1,1)$. Each switching state creates a specific unbalance of the common-mode capacitances because the parasitic EM capacitances are alternately connected to either the positive or the negative pole of the EMD DC terminals. This unbalance is illustrated in the eight figures below.

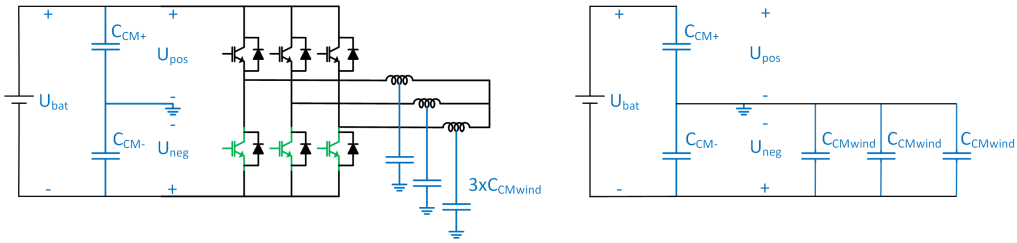


Figure 2.7: Unbalance when the converter is in the switching combination (0,0,0).

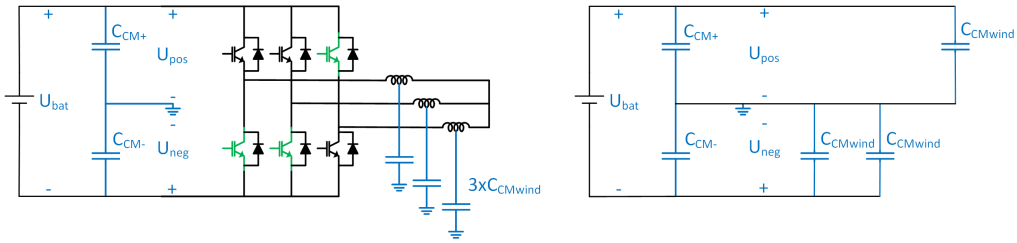


Figure 2.8: Unbalance when the converter is in the switching combination (0,0,1).

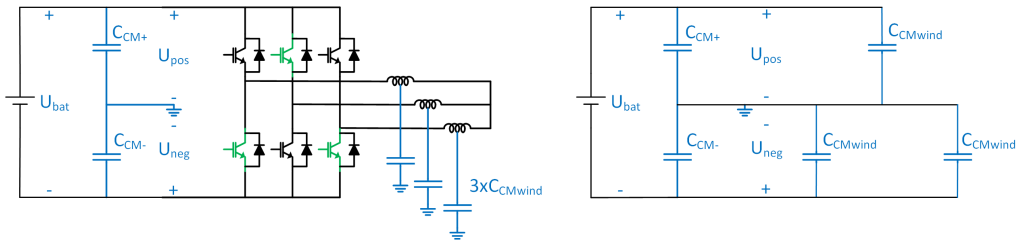


Figure 2.9: Unbalance when the converter is in the switching combination (0,1,0).

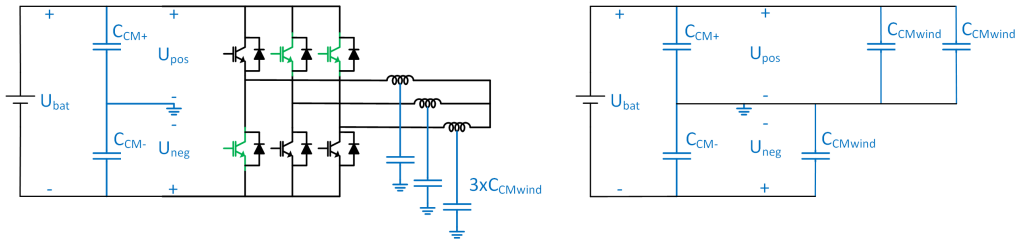


Figure 2.10: Unbalance when the converter is in the switching combination (0,1,1).

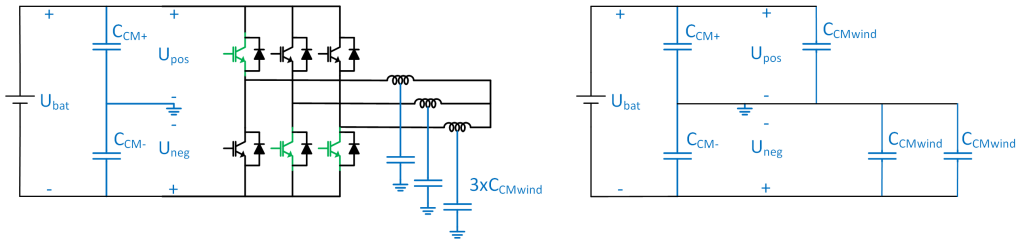


Figure 2.11: Unbalance when the converter is in the switching combination (1,0,0).

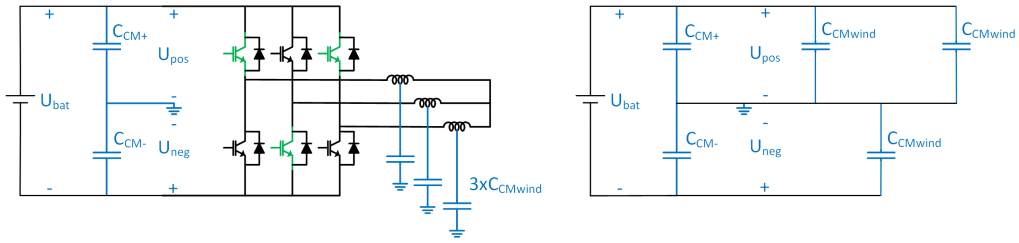


Figure 2.12: Unbalance when the converter is in the switching combination (1,0,1).

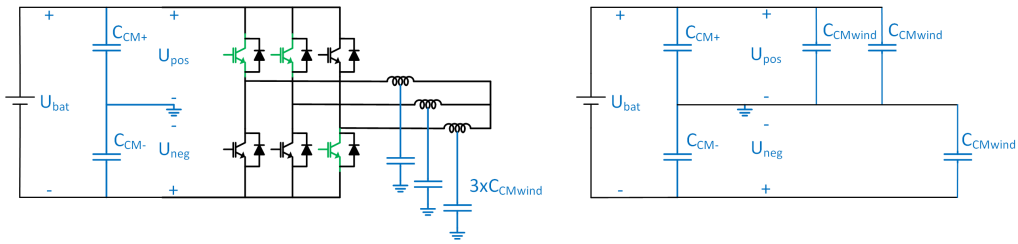


Figure 2.13: Unbalance when the converter is in the switching combination (1,1,0).

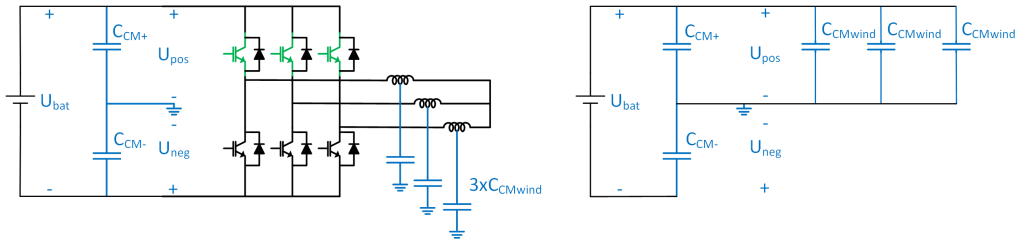


Figure 2.14: Unbalance when the converter is in the switching combination (1,1,1).

Note that with normal PWM the switching typically occurs between consecutive states, as illustrated in Figures 2.7 and 2.14. As a consequence, every switching event inherently modifies the asymmetry of the winding capacitances C_{CMwind}; the EM parasitics change their association to either the positive or negative DC pole at every transition of the EMD.

Conclusion

The eight switching states of the EMD create eight unique configurations of the EM parasitic capacitances. Each configuration produces a distinct redistribution of C_{CMwind}, resulting in an unavoidable CM capacitance unbalance at every switching event. This switching-dependent asymmetry forms the basis for understanding both the origin of the CMDC voltage and the characteristic CM current paths analysed in the following subsection.

The behaviour described here is only one source of asymmetry in the TVS. Additional parasitic capacitances elsewhere in the system also contribute to CM effects, and the next subsection introduces these capacitances.

2.4.2 Asymmetric parasitic capacitances

Following the demonstration of how the switching states of the EMD create a capacitance unbalance in the EM winding-to-core capacitances, this subsection broadens the scope to other parasitic capacitances in the TVS that may introduce similar asymmetries. While C_{CMwind} is used as the representative example throughout this thesis due to its dominant

magnitude, several additional parasitic capacitances can also contribute to asymmetric CM behaviour.

This thesis uses C_{CMwind} to study the dynamic effects arising from an asymmetric parasitic capacitance in the TVS. Several additional examples of asymmetric capacitances include:

- Between the winding and core in the transformer of the H-bridge in an isolated DC/DC converter.
- Between any semiconductor device in a converter and its heat sink.
- Between the main conductors and the shield in a three-phase cable.
- Between the windings and the core of other electrical machines connected to the TVS, such as the machines driving the HVAC compressor or the air compressor of a potential ePTO. These machines are generally smaller than the traction machines and are therefore expected to have smaller parasitic capacitances. Their capacitances remain relevant, even though they are not modelled in this thesis.

Conclusion

A range of parasitic capacitances in the TVS can introduce asymmetries during switching, although C_{CMwind} remains the dominant contributor due to the size of the traction machines. These capacitances introduce charge–discharge dynamics that affect the instantaneous CM voltage. The implications of this behaviour are examined in Subsection 2.4.3, where the resulting common-mode DC voltage U_{CMDC} is defined and its dependency on the system capacitances is derived.

2.4.3 Common Mode DC voltage (U_{CMDC})

Following the system-level discussion in Subsection 2.4.2, this subsection quantifies the DC component of the common-mode voltage that appears when the EMD toggles between asymmetric switching states. When the EMD switches, the EM winding-to-core parasitic capacitances alternate between two asymmetric positions in the circuit. As a consequence, the electric potentials of the battery terminals vary slightly depending on which asymmetric switching state the EMD operates in and how this state connects the parasitic EM capacitances. This variation is referred to as the common-mode DC (CMDC) voltage of the battery.

The common-mode (CM) voltage is defined as:

$$u_{cm} = \frac{u_{pos} + u_{neg}}{2} \tag{2.1}$$

where u_{pos} and u_{neg} are the battery terminal potentials relative to chassis. When the EMD switches one phase at a time, u_{CM} generally shows a quasi-square waveform. The most

pronounced case appears when all three phase legs switch simultaneously, which occurs when the EMD output voltage is zero. At standstill, the CM voltage is a square wave with amplitude U_{CMDC}, as shown in Figure 2.15. When the EM operates at speed, or when several EMDs operate with unsynchronised modulation, the measurements show a quasi-square waveform.

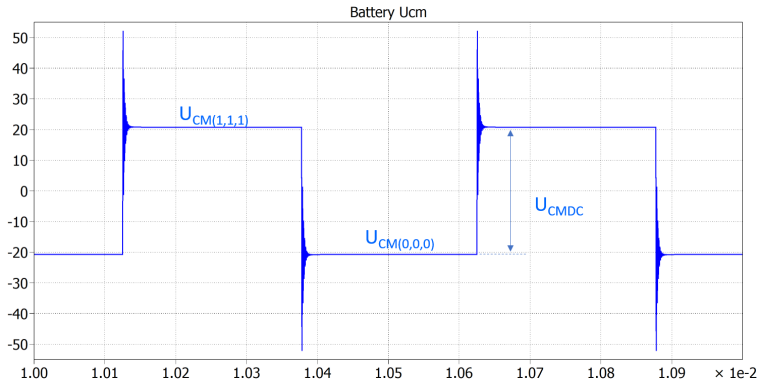


Figure 2.15: References for CM voltages and CMDC voltage U_{CMDC}.

The CMDC voltage originates from switching between asymmetric states of the parasitic EM capacitance C_{CMwind}. The symmetric CM capacitances C_{CM_BAT+}, C_{CM_BAT-}, C_{CM_EMD+} and C_{CM_EMD-} are grouped into C_{CM+} and C_{CM-} according to:

$$C_{CM+} = C_{CM_BAT+} + C_{CM_EMD+} \tag{2.2}$$

$$C_{CM-} = C_{CM_BAT-} + C_{CM_EMD-} \tag{2.3}$$

At standstill, with zero EM output voltage, the three C_{CMwind} capacitances are asymmetrically connected to either the positive or negative pole of the TVS. The sum of C_{CM+} and the asymmetric elements thus becomes unequal to C_{CM-}, as illustrated in Figure 2.16.

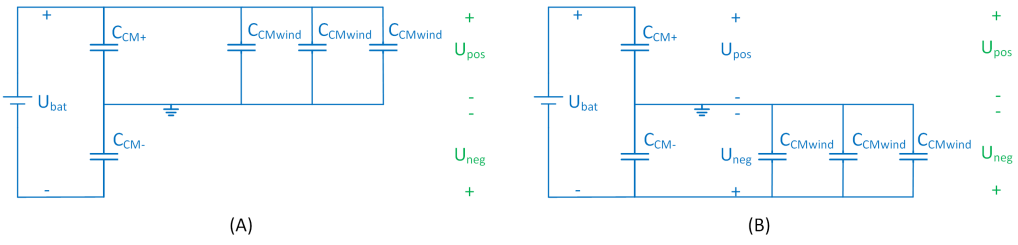


Figure 2.16: Equivalent circuit for parameters included in the definition of U_{CMDC}.

For analytical clarity, C_{CM+} and C_{CM-} are assumed equal and denoted C_{CM}:

$$C_{CM} = C_{CM+} = C_{CM-} \tag{2.4}$$

The three EM parasitic capacitances are combined into:

$$C_{CMasym} = 3C_{CMwind} \tag{2.5}$$

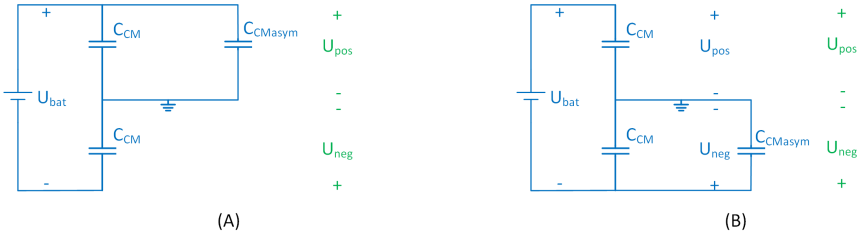


Figure 2.17: Equivalent circuit using the aggregated C_{CMasym}.

Define:

$$X = \frac{C_{CM}}{C_{CMasym}} \tag{2.6}$$

From Figure 2.17, the battery terminal voltages satisfy:

$$U_{bat} = U_{pos} - U_{neg} \tag{2.7}$$

Using the capacitor charge relations yields:

$$Q = C\,U \tag{2.8}$$

$$Q = C_1 U_1 = C_2 U_2 \tag{2.9}$$

Applying the relations above to switching state $(1, 1, 1)$ yields:

$$U_{pos(1,1,1)}(C_{CM} + C_{CMasym}) = -U_{neg(1,1,1)} C_{CM} \tag{2.10}$$

Solving these relations gives:

$$U_{pos(1,1,1)} = \frac{U_{bat}}{2 + \frac{1}{X}} \tag{2.11}$$

$$U_{neg(1,1,1)} = -U_{bat}\frac{1 + \frac{1}{X}}{2 + \frac{1}{X}} \tag{2.12}$$

Similarly, applying these relations to state $(0, 0, 0)$ yields:

$$U_{pos(0,0,0)} = U_{bat}\frac{1 + \frac{1}{X}}{2 + \frac{1}{X}} \tag{2.13}$$

$$U_{neg(0,0,0)} = -\frac{U_{bat}}{2 + \frac{1}{X}} \tag{2.14}$$

Inserting the expressions in Equations (2.11) to (2.13) into the CM definition yields:

$$U_{cm(1,1,1)} = -\frac{U_{bat}}{2(2X+1)} \tag{2.15}$$

$$U_{cm(0,0,0)} = \frac{U_{bat}}{2(2X+1)} \tag{2.16}$$

Thus, the CMDC voltage is:

$$U_{CMDC} = U_{cm(0,0,0)} - U_{cm(1,1,1)} = \frac{U_{bat}}{2X+1} \tag{2.17}$$

From Equation (2.17), it follows that U_{CMDC} is lower for larger values of X. Figure 2.18 shows example values.

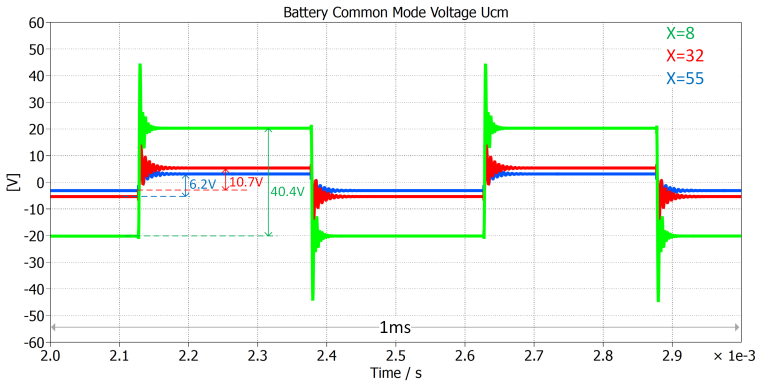


Figure 2.18: Illustration of U_{CMDC} for different values of X.

Conclusion

Asymmetric reconnection of the EM parasitic capacitances results in a switching-dependent DC offset on the battery terminals. The derived expression for U_{CMDC} demonstrates that increasing the symmetric common-mode capacitance relative to the asymmetric parasitic capacitance reduces this offset. This forms the foundation for understanding how the CMDC voltage influences CM current paths, and Subsection 2.4.4 analyses these paths.

2.4.4 CM currents cause and effect

The previous subsection introduces the mechanisms behind the common-mode DC voltage U_{CMDC} and the X-factor. This subsection examines how different CM current paths behave in the system. The CM current can be divided into two current paths, as mentioned in

Section 2.4 and shown in Figure 2.6. For convenience, the same figure appears again in Figure 2.19.

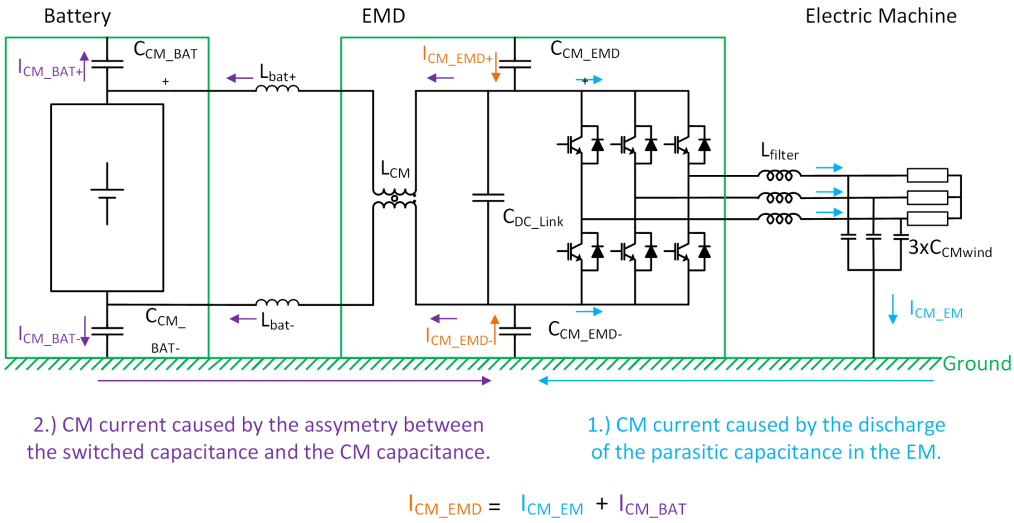


Figure 2.19: Two different CM currents and paths.

Cause and effects of I_{CM_EM}

This subsection begins with I_{CM_EM}, which always flows and cannot be avoided as C_{CMwind} alternates between the positive and negative poles. This current can be reduced by:

- reducing the size of C_{CMwind}
- reducing the voltage derivative at the phase output, limited by the semiconductor's loss dissipation
- reducing the voltage derivative at the phase winding due to the impedance in the circuit
- avoiding switching between $(0, 0, 0)$ and $(1, 1, 1)$ directly in the modulation.

The size of the parasitic capacitance in the EM depends on physical laws. Suppliers are expected to keep C_{CMwind} as low as possible. However, reducing this capacitance requires thicker winding insulation, which reduces the cooling capability for the phase winding losses. The C_{CMwind} also varies over time due to insulation wear, but this is not discussed further in this thesis.

The current is determined by Equation (2.18) where the voltage derivative over C_{CMwind} is defined as:

$$i_{CM_EM} = C\frac{du}{dt} \tag{2.18}$$

The voltage derivative at the EM depends on the inductive CM filter after the EMD, represented by L_{filter} in Figure 2.19. It is also worth noting that parasitic capacitances exist within the semiconductors and that these are only limited by the dv/dt capability of the semiconductor.

Modulation does not directly limit the current. At zero output voltage, when the switch state is $(0, 0, 0)$ or $(1, 1, 1)$, all three C_{CM_wind} change polarity in the same direction, increasing the total I_{CM_EM} and resulting in the highest CM current. When the output voltage to the EM is greater than zero, the EMD can switch according to Subsection 2.4.1. This has the effect that when switching between active states (all states except $(0, 0, 0)$ and $(1, 1, 1)$), charge is transferred between the C_{CMwind} capacitances, lowering the total I_{CM_EM}. Figure 2.20 shows how I_{CM_EM} changes when du/dt is lowered by decreasing the inductance L_{filter} to one third. The ratio of the frequencies f(L_{filter}) and f(0.33 L_{filter}), shown in the lower graph of Figure 2.20, is 3.1. Figure 2.19 also shows that an LC circuit consists of C_{CMwind}, C_{CM_EMD} and L_{filter}.

The resonance frequency of an LC circuit is given by:

$$f_{res} = \frac{1}{2\pi\sqrt{LC}} \tag{2.19}$$

When the ratio of L changes to $1/3$, the ratio of f changes by $\sqrt{1/3} = 0.58$, which is the same factor shown in Figure 2.20.

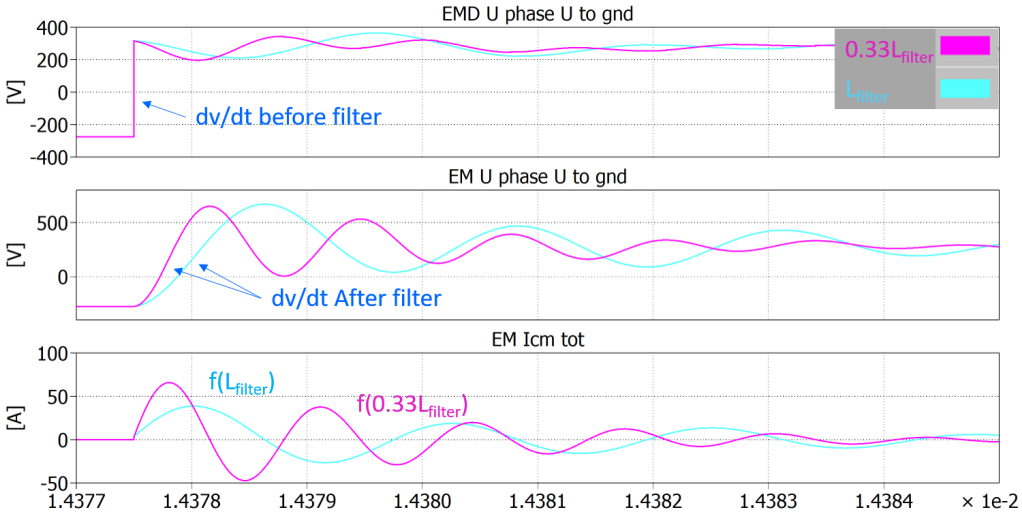


Figure 2.20: CM current from the EM when the inductance is decreased to 1/3.

The rise and fall times of the IGBT, t_r and t_f, can also be modified to lower the di/dt. In this example, however, t_r and t_f would need to be at least 50 times longer to have any appreciable effect. Such long rise and fall times, t_r and t_f, are unrealistic due to high switching

losses that cause excessive temperatures in the IGBT. This further illustrates the importance of a CM filter after the three-phase bridge of the EMD.

Conclusion

The behaviour of I_{CM_EM} is governed by the parasitic capacitances and the inductive CM filter. Lower inductance increases the resonance frequency and thereby the CM current frequency, whereas modulation and semiconductor dv/dt have limited impact.

Cause and effects of I_{CM_BAT}

The only change of potential in the system occurs when the EMD switches. Considering the same operating point as in Figure 2.20, but including the battery CM voltage and current (see Figure 2.21), the measurements show that the frequency f_{bat} for the battery CM current I_{CM_BAT} remains unchanged in frequency despite the change in frequency in the EM's CM current. The frequencies are also entirely different. The frequency of I_{CM_BAT} is determined by the circuit in Figure 2.19, consisting of C_{CM_BAT}, L_{BAT}, L_{CM} and C_{CM_EMD}.

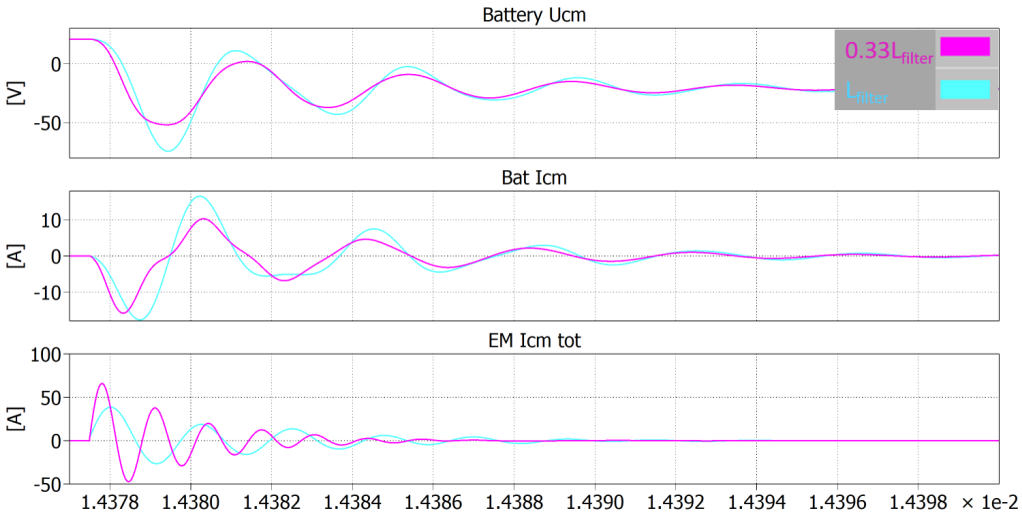


Figure 2.21: CM current from the battery when the dv/dt is changed to the EM by changing the inductance.

The CMDC voltage depends on the X factor as given in Equation (2.17). The CMDC voltage is changed by adjusting the X-factor (Equation (2.6)). X can be changed via C_{CM_EMD}, C_{CM_BAT} or a combination thereof. Figure 2.22 shows three combinations of capacitances: C_{CM_EMD} increased by a factor of 5, C_{CM_BAT} increased by a factor of 5, and unchanged values as a reference. The lower graph clearly shows that I_{CM_EM} is unchanged when C_{CM_EMD} and C_{CM_BAT} are varied. The upper graph shows that U_{CMDC} is lower for larger values of X.

The middle graph shows that I_{CM_BAT} increases when C_{CM_BAT} increases and that I_{CM_BAT} decreases when C_{CM_EMD} increases.

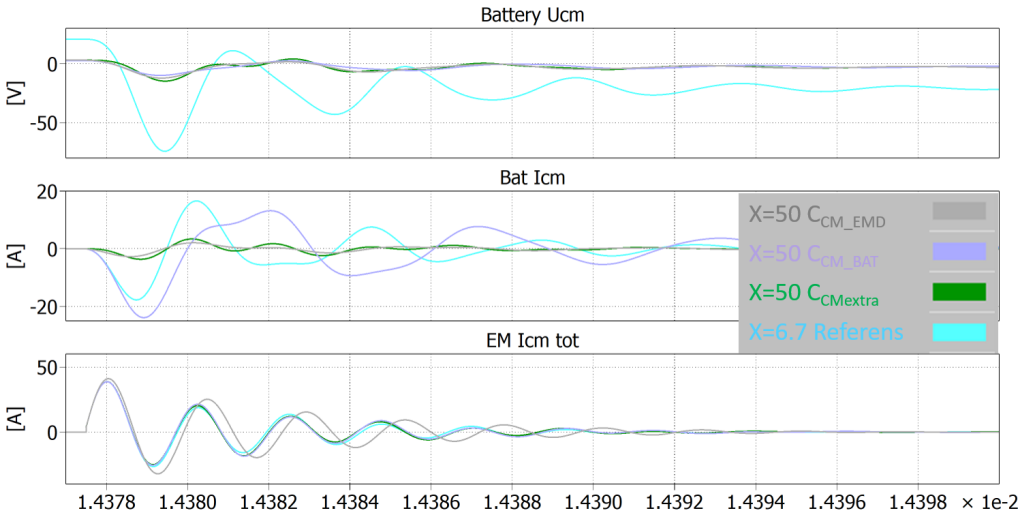


Figure 2.22: CM current from the battery when the CM capacitances are varied to achieve X=50.

The conclusion is that X shall be as high as possible to reduce U_{CMDC} and that the capacitance shall be increased in the EMD to avoid CM currents in the system. However, standards impose constraints, since the total capacitance from the poles to the ground/chassis is limited during charging as specified in [13].

An alternative solution is to add extra connectable capacitances, $C_{CMextra}$ in Figure 2.23, and connect these capacitances only after the charger is disconnected and the EMD starts to operate. This yields a robust system if CM capacitances, such as those in the batteries, cannot be kept sufficiently low and the ratio $X = 50$ cannot be achieved without additional measures.

Figure 2.23 shows three possible ways to add extra CM capacitance $C_{CMextra}$:

1. Inside the EMD, the preferred option, where $C_{CMextra}$ is marked with ① in Figure 2.23.

2. Outside the EMD but connected to the poles after the inductive CM filter, where $C_{CMextra}$ is marked with ②. A drawback is the long wiring to $C_{CMextra}$.

3. Outside the EMD and connected to the poles before the inductive CM filter, where $C_{CMextra}$ is marked with ③ in Figure 2.23. A drawback is that resonances may occur with the CM inductor in the EMD.

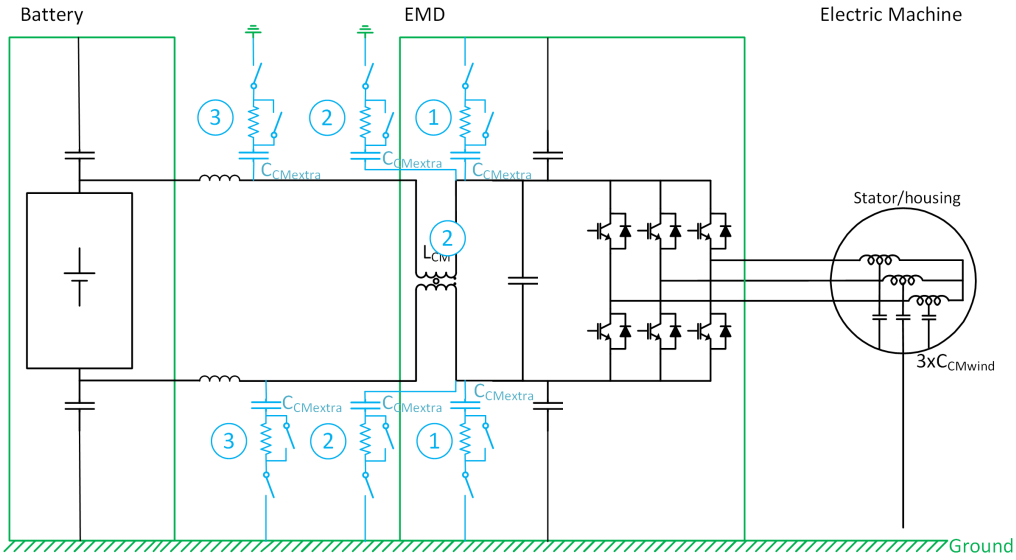


Figure 2.23: Possible solutions to mount the extra CM capacitance $C_{CMextra}$. The connection of the extra CM capacitors is illustrated with relays in the figure. However, it can also be achieved using semiconductors, and precautions shall be taken not to introduce stray inductance in the circuit.

Placing the filter inside the EMD minimises the risk of oscillation caused by additional LC circuits. The extra CM capacitance is connected through a pre-charge circuit, and a switch disconnects it when the EMDs are not in operation.

Conclusion

The CM currents I_{CM_EM} and I_{CM_BAT} depend on different circuit elements and therefore behave independently. I_{CM_EM} is strongly influenced by L_{filter} and the parasitic capacitances in the EM, whereas I_{CM_BAT} is determined by the CM network around the battery. Increasing C_{CM_BAT} increases I_{CM_BAT}, while increasing C_{CM_EMD} reduces I_{CM_BAT}. A high X-factor is essential to achieve a lower U_{CMDC} and to improve system performance. The next subsection, Subsection 2.4.5, analyses the behaviour of DM currents and their impact on subsystem interaction and component lifetime.

2.4.5 DM current

In the previous subsection, the analysis of the common-mode currents shows how the CM network influences the CMDC voltage and how the EM and battery CM currents interact. The present subsection shifts focus to the differential-mode (DM) behaviour of the system. While CM currents are driven by parasitic capacitances and switching-node dv/dt, DM currents arise from the energy transfer performed by the converters themselves. Because all subsystems in the TVS—except the battery—are switching, their DM behaviour determ-

ines how much current ripple is exchanged between subsystems. This ripple may propagate through the TVS depending on the impedance levels and filtering, and therefore represents a major interaction mechanism between otherwise independent converters.

All subsystems in TVS are switching except the battery. The switching causes a current ripple in the TVS between subsystem at the DC side of the converter. Depending on filters and TVS impedance, a voltage ripple appears in the TVS. It is impossible to tell what can happen when current ripple flows between the converters but following can be stated:

- Current ripple in the DC link capacitor causes heat and decreased lifetime. Suppliers dimension the capacitor for the load current and not for extra ripple from the system.
- Current ripple in the inductive filters causes heating and can change their inductance as well as decrease their lifetime.
- Current ripple is highest at duty cycle 0.5. See [1] and Figure 2.25.

To illustrate the DM current, a simple circuit with two step-down converters (buck converters) is used. See Figure 2.24. The upper buck converter in Figure 2.24 is active, hence it transfers energy in the converter to the load. The lower buck converter is passive and therefore does not transfer energy to the load.

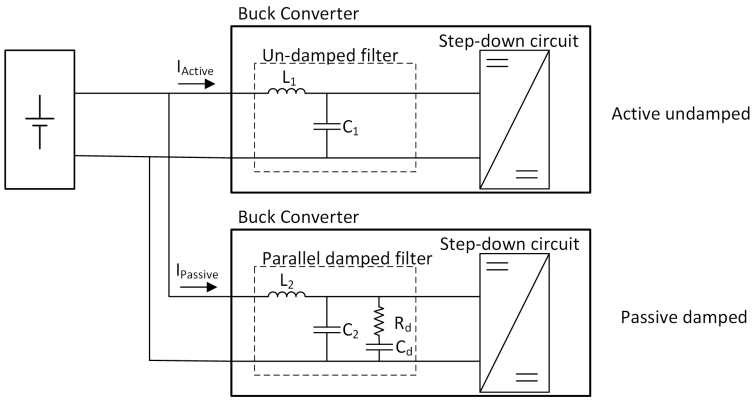


Figure 2.24: Simple two buck converter circuit with a battery supply.

An illustration of the worst current ripple when the duty cycle D varies from 0–1 is shown in Figure 2.25. Both buck converters show a cigar-shaped current waveform. The active buck converter has an increasing DC component of the current as it transfers energy to the load. Further details are given in [1]. The time scale makes it impossible to see the individual switching periods. The illustrations should rather be interpreted as an envelope of the current ripple. The highest current ripple occurs when $D = 0.5$.

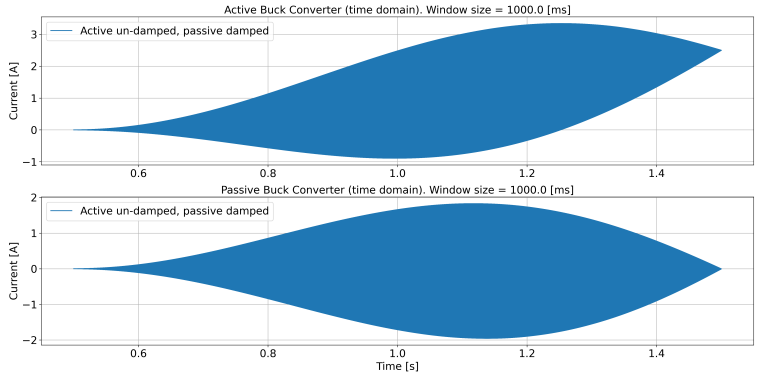


Figure 2.25: Current ripple in the active switching buck converter and the passive non switching buck converter.

An ideal situation is when the current ripple, caused by the switching buck converter, is damped within the active buck converter. This is how some suppliers believe the system behaves, as if it were an ideal DC network with smooth DC voltage.

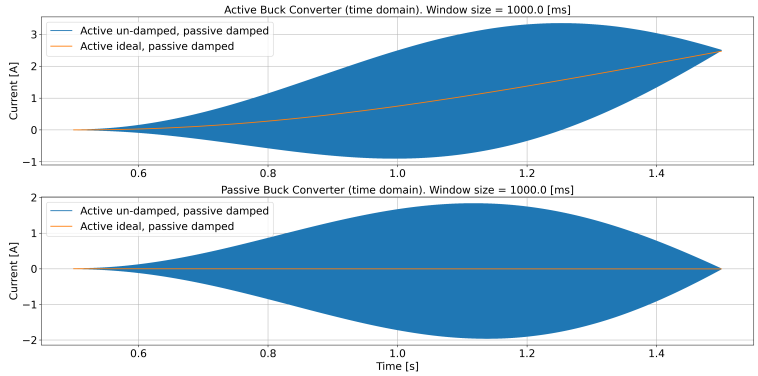


Figure 2.26: Current ripple in the active switching buck converter and the passive non switching buck converter. The graph with the largest current ripple, "Active un-damped, passive damped", is a "normal" case of the appearance. A more ideal situation is when all the current ripple is damped within the DC-link capacitor C_1. Then the passive converter is not affected by the active one; however, this is the ideal situation.

Although the system in this example consists only of two buck converters and a battery, it serves as a purely pedagogical simplification. Heavy-duty traction systems do not employ such converters, and real TVS installations typically include multiple high-power EMDs together with numerous auxiliary subsystems. Using a full TVS model would obscure the fundamental DM mechanisms, since several parallel current paths, interacting filters and cable impedances make it difficult to attribute ripple propagation to specific causes. By reducing the system to two converters, the essential resonance mechanisms and current-sharing behaviour become visible. In real vehicles, the DC network is never ideal, and the ripple propagation is generally larger and more complex than in this reference case.

Conclusion

The DM current behaviour is governed by the switching action of the active converter and the impedance of the surrounding TVS. Without sufficient filtering, a significant portion of the ripple generated by one converter propagates to neighbouring subsystems, potentially reducing component lifetime or causing unstable interactions.

The next Subsection 2.4.6, examines how DM filters can be used to limit this ripple. Since each subsystem may be sourced from different suppliers—with different switching frequencies, unknown impedance characteristics and no common requirements on DC voltage quality—DM filters become essential to protect both the active and neighbouring converters. The following subsection therefore analyses the behaviour of un-damped and damped DM filters, their resonance characteristics and how improper filtering can amplify the very ripple that the filter is intended to mitigate.

2.4.6 DM filter

The previous subsection demonstrates how differential-mode currents naturally circulate between subsystems when their switching behaviour interacts through the shared DC network. It also shows that the magnitude and distribution of this ripple current strongly depend on the impedance seen from each converter.

A direct consequence of this is that each subsystem requires a controlled and predictable DM impedance in order to avoid excessive heating, lifetime reduction or unwanted coupling from neighbouring converters. This subsection therefore examines DM filters—the primary means of shaping the local DM impedance of a converter—and shows how damping fundamentally changes their system-level behaviour.

It is normal that the subsystems are sourced from different suppliers, and there is no clear requirement regarding the TVS voltage quality or the switching frequency of each subsystem. One way to protect a subsystem and to reduce disturbances from neighbouring subsystems is to include a DM filter at each converter. A filter always introduces a resonance point. Since the relevant frequencies in the TVS are not always known by the suppliers or the OEMs, the filter is recommended to be damped.

In Figure 2.27, an un-damped and a parallel-damped filter are shown. It should be clear to the reader that this section does not provide a design guide for filters; instead, it highlights how different filter types influence system behaviour.

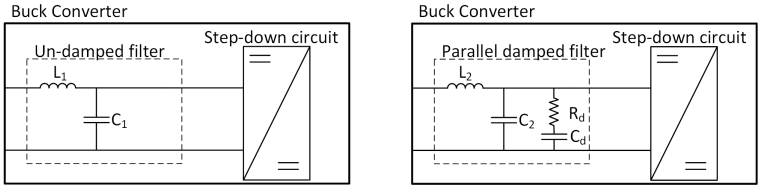


Figure 2.27: Un-damped and parallel-damped filter within a subsystem.

The resonance points for the two buck-converter filters in Figure 2.27 are:

$$f_0 = \frac{1}{2\pi\sqrt{L_1 C_1}}\,,\; f_0 = \frac{1}{2\pi\sqrt{L_2 C_2}} \tag{2.20}$$

The numerical values used in the following examples—such as the 10 kHz resonance—are representative and chosen for pedagogical clarity. Their purpose is to illustrate how resonance points in DM filters amplify or attenuate ripple currents. The exact resonance frequencies in a given subsystem depend on its component values, cable lengths and supplier-specific design choices, and are therefore system dependent.

In [23], optimal damping parameters are described. The transfer function for the parallel-damped and un-damped circuits is shown in Figure 2.28, and the corresponding DM impedance is shown in Figure 2.29.

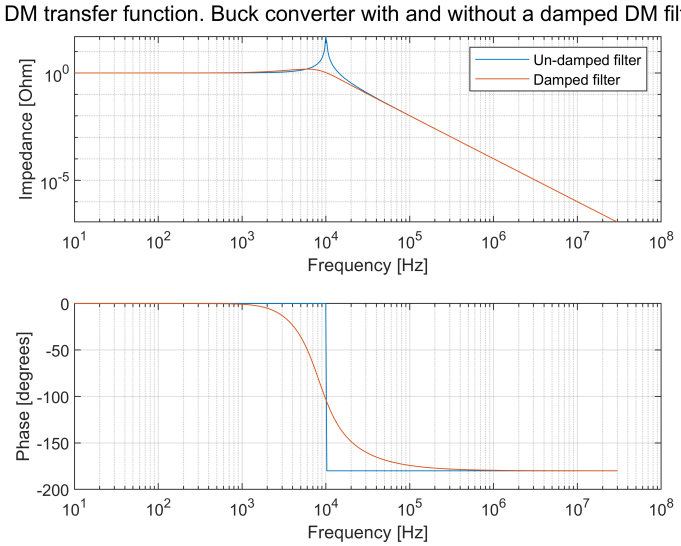


Figure 2.28: Transfer function for a parallel un-damped and damped filter. The resonance point at 10 kHz is clearly visible for the un-damped filter.

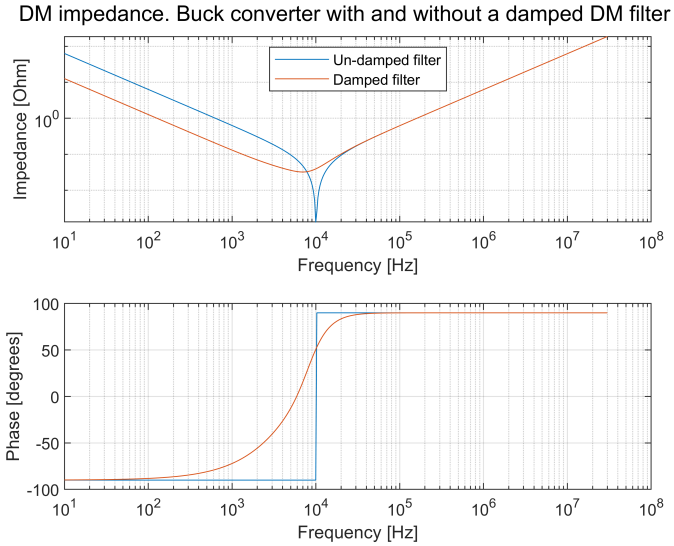


Figure 2.29: DM impedance for a parallel un-damped and damped filter.

If a converter has the switching frequency f_s, the TVS experiences the frequency $2f_s$ for three-phase converters and f_s for the buck converter in the example here. In the transfer function in Figure 2.28, the resonance frequency is 10 kHz. Imagine that a neighbouring converter switches at 10 kHz and the filter is un-damped: then the DC-link capacitor C_1 in Figure 2.27 will be exposed to a high ripple current that may destroy it. If the filter is damped according to Figure 2.27, the series damping network C_d and R_d will attenuate the resonance.

If there is no filter at all, the resonance frequency may be almost arbitrary, depending mainly on the total inductance of the TVS and especially on the cable between the source and the victim.

For high-power subsystems such as batteries and traction converters, adding filters may be inconvenient and costly. Protecting low-power systems can therefore be a reasonable compromise. In Figure 2.30, three variants of filters in the system are shown.

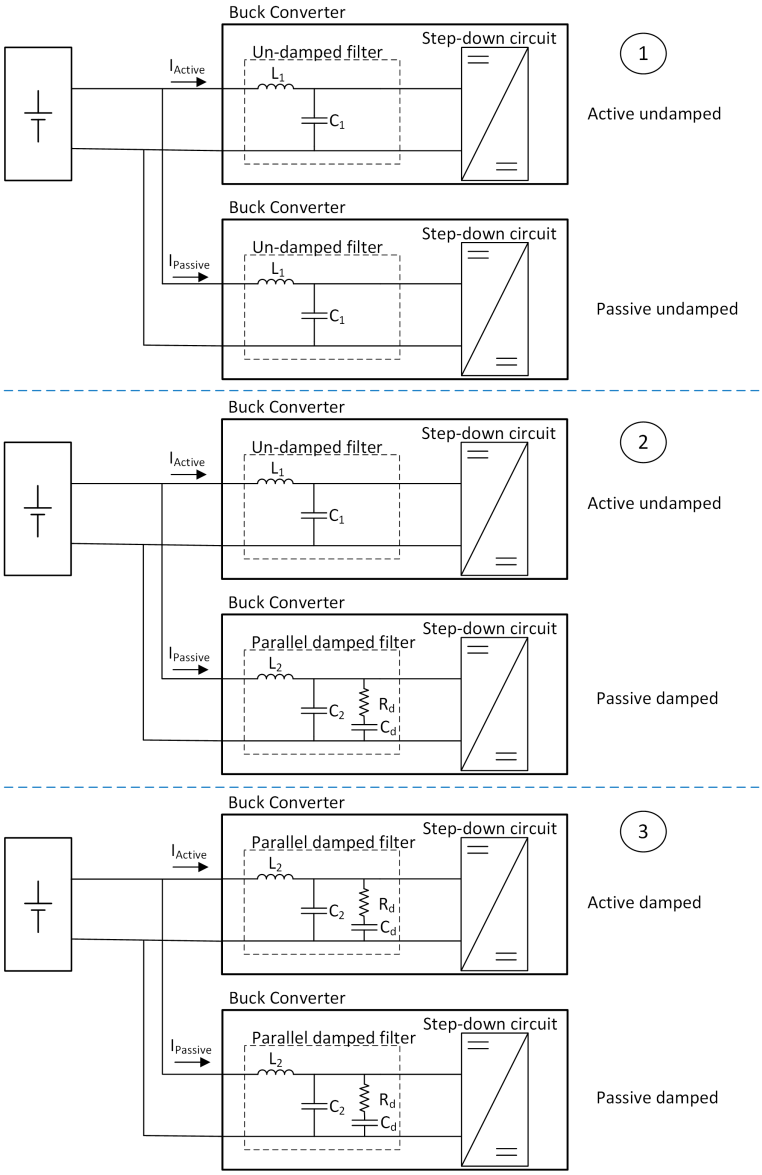


Figure 2.30: Three variants of the two buck converters. In (1) both converters are un-damped, in (2) the active converter is un-damped and the passive converter is damped, and in (3) both converters are damped.

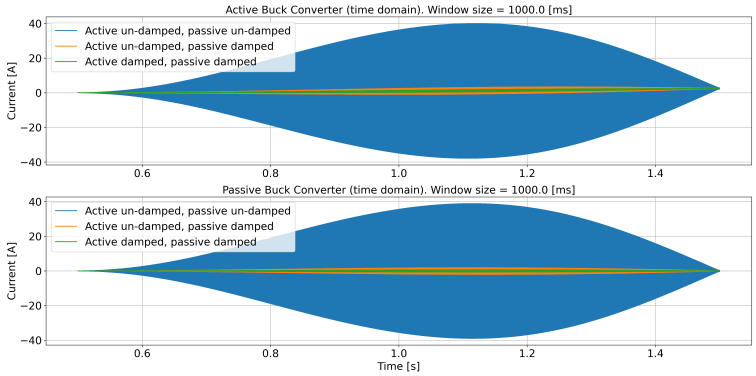


Figure 2.31: Current ripple for the three variants of filtering in Figure 2.30. Applying a filter in the passive circuit only significantly reduces the ripple. Adding filters to both the active and passive circuits reduces it further, but the primary goal is to protect each subsystem.

Even though damped filters are recommended, precautions must be taken regarding system parameters such as the total capacitance in the TVS (relevant for the pre-charge circuit) and the total inductance (important in case of a short circuit). Battery contactors must be able to interrupt the resulting inductive current.

Conclusion

The behaviour of DM filters strongly influences how ripple currents propagate between subsystems in the TVS. Un-damped filters introduce sharp resonance points that may expose components such as the DC-link capacitor to excessive stress, especially when neighbouring converters switch close to the resonance frequency. Adding damping effectively attenuates these resonances and reduces current ripple, thereby improving subsystem robustness. Although filters can be costly for high-power converters, protecting low-power subsystems remains a reasonable compromise. Care must also be taken to ensure that total system capacitance and inductance remain compatible with pre-charge requirements and short-circuit interruption capability.

2.4.7 Conclusion

The analyses in Subsections 2.4.1 to 2.4.6 collectively describe how common-mode (CM) and differential-mode (DM) behaviour emerges in the traction voltage system as a consequence of subsystem parasitics, switching dynamics and impedance interactions. The switching states of the electric machine drive inherently recreate asymmetric reconnections of the machine's parasitic capacitances, ensuring that CM capacitance unbalance is unavoidable. These asymmetries are further reinforced by several additional parasitic capacitances distributed throughout the TVS, with the machine windings remaining the dominant contributor due to their magnitude.

The combined effect of these parasitics is the generation of a switching-dependent CMDC voltage at the battery terminals. Its magnitude is governed by the ratio between symmetric and asymmetric capacitances, showing that increased symmetric capacitance can effectively reduce the resulting DC offset. The resulting CM current is shaped primarily by the total parasitic capacitances and the inductive CM filtering in the system, while the semiconductor dv/dt capability and the modulation strategy play comparatively minor roles.

In parallel, the DM behaviour of the system is driven by the switching action of each converter and the surrounding system impedance. Without appropriate filtering, ripple currents originating in one subsystem propagate into others, risking reduced component lifetime or unstable cross-coupling effects. The role of DM filters therefore becomes central. However, un-damped filters introduce sharp resonances that may severely stress components if excited by neighbouring converters. Damped filters, in contrast, effectively attenuate these resonances and substantially reduce ripple propagation, although practical constraints such as subsystem cost, total system capacitance and short-circuit interruption capability must be considered.

Overall, Section 2.4 demonstrates that both CM and DM phenomena arise from fundamental system properties rather than from specific converter designs. Their mitigation requires an understanding of how parasitics, switching states and impedance networks interact across the complete traction voltage system.

2.5 Conclusion

The analyses presented in this chapter provide a system-level understanding of the traction voltage system (TVS) and its interaction with electrical components. The chapter begins by defining the structure, operating principles and electrical characteristics of the TVS in Section 2.1, establishing the environment in which all onboard converters operate and the natural resonances that arise in the DC network.

In Section 2.2, the external electrical systems connected to the vehicle are described, such as the grid, chargers and functionalities available when the vehicle is parked. Although these systems are not part of the onboard TVS, their behaviour and connection characteristics influence the boundary conditions under which the TVS operates, including charging constraints, grounding structure and permissible current levels.

Section 2.3 then characterises the major power sources and loads internal to the vehicle. The behaviour of the battery, traction machine drive (EMD) and auxiliary converters is described, highlighting how their switching behaviour, impedance properties and operating points shape both steady-state and transient conditions in the TVS.

The remainder of the chapter, summarised in Section 2.4, analyses the phenomena of common-mode (CM) and differential-mode (DM) disturbances. Starting from the unavoidable CM capacitance unbalance created by the eight switching states of the EMD, it is shown how asymmetric parasitic capacitances generate the common-mode DC voltage.

This voltage offset, derived in detail in the chapter, depends on the ratio between symmetric and asymmetric CM capacitances.

The interaction between U_{CMDC}, the parasitic elements and the CM filter inductance explains the resulting CM currents, their frequency content and their impact on EMC performance, subsystem stress and component lifetime. For DM behaviour, the chapter demonstrates how switching ripple from one converter can propagate into other subsystems if the TVS impedance is low or insufficiently damped. The role of DM filters is therefore analysed, showing how un-damped filters may amplify ripple through resonance effects, whereas damped filters effectively limit ripple propagation.

Beyond these detailed CM and DM mechanisms, an important methodological aspect should be emphasised. The purpose of the modelling work in this chapter is not to reproduce every high-frequency detail of each converter but to build a system-level understanding of how disturbances propagate through the TVS. The strength of the approach lies in its breadth rather than depth: by modelling all major subsystems, their parasitic elements and their interaction pathways, the chapter establishes a holistic perspective that remains valid even when exact parameter values vary between platforms or suppliers. This system-oriented methodology provides the conceptual foundation used later in the thesis for measurements, validation and mitigation strategies.

Overall, this chapter demonstrates that the TVS must be regarded not merely as a distribution bus but as a coupled electromechanical system where converter switching, parasitic parameters and subsystem design interact across multiple frequency domains. These interactions determine current ripple, voltage stress, EMC robustness and long-term reliability. The results presented in Chapter 2 form the foundation for the modelling, measurements and mitigation strategies developed in the subsequent chapters.

Chapter 3

Vehicle measurement system

The previous chapter provides the system-level context required before introducing the measurement approach. This chapter continues from that perspective and describes how the electrical quantities of interest are captured experimentally. It presents the measurement system used throughout the thesis.

This chapter introduces the measurement system developed for capturing conducted electromagnetic interference (EMI) in both common-mode (CM) and differential-mode (DM). The purpose is to outline the constraints associated with distributed, wide-band and time-synchronised measurements on a large commercial vehicle.

Early investigations show that short recordings of approximately 100 ms do not capture the behaviour of interest. Slight differences in switching frequency between electric machine drives generate low-frequency beating, which causes the EMI signature to vary over time. Long recordings and sub-nanosecond synchronisation are therefore required.

The measurement task is further influenced by the physical scale of a heavy-duty vehicle: a complete traction voltage system (TVS) spans up to 30 m, and approximately 20 TVS nodes must be measured simultaneously. Each node includes one Break-Out Box (BoB) providing five measurements: two DC voltages to chassis, one DC and low-frequency AC current, one CM current and one DM current. In total, 100 channels must be sampled in synchronisation.

To illustrate the physical distribution of the TVS nodes in a challenging configuration, an articulated bus is shown in Figure 3.1. Most TVS components are located along the roof and at the rear of the vehicle, resulting in cable lengths approaching 30 m.

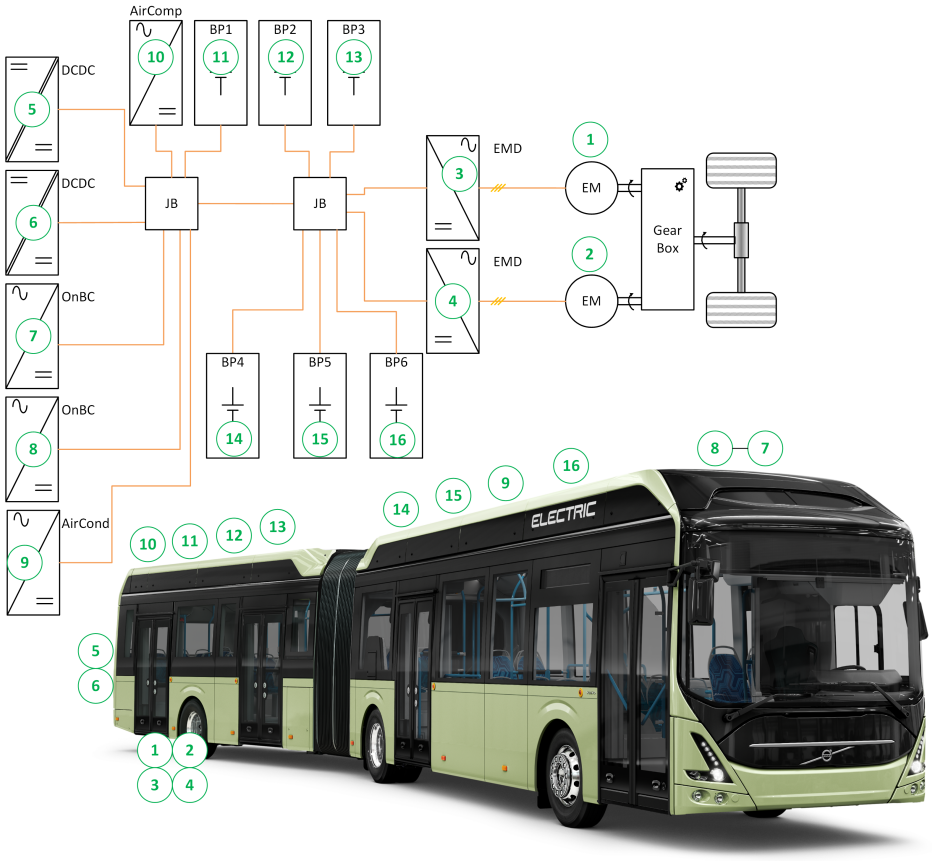


Figure 3.1: Distributed TVS on an articulated bus. The vehicle has a length of approximately 24 m.

Several vehicle platforms are used throughout this thesis for illustration. A Volvo FE280 truck is used during the early development phase to evaluate installation aspects. The thesis includes measurements on articulated buses, representing the largest TVS distribution. The thesis presents measurement results from a Volvo FM1156 truck, which serves as the primary platform for the dynamometer-based campaign. Although different vehicles appear in figures and examples, the TVS architecture and the measurement principles remain identical.

The EMI characteristics follow from the traction power, vehicle speed and operating point. To capture the full behaviour, the measurement system must record complete driving cycles, including acceleration, cruising, regenerative braking and standstill. A single acquisition may last up to five minutes, and the total recording capacity must reach one hour to support a full dynamometer session.

Although sometimes referred to as a ”measurement system”, ”data-acquisition system” or ”DAQ system”, the system does not include a graphical display such as an oscilloscope.

All waveform inspection is performed in post-processing. Throughout this thesis, the term *measurement system* is used consistently.

The chapter is organised into the following sections:

1. **Measurement system requirements** — Functional, electrical and practical constraints that define the system design.
2. **Measurement system overview** — A high-level view of the complete setup on a heavy-duty vehicle.
3. **Break-Out Boxes (BoB)** — Sensor integration at each TVS node, including CM, DM, DC current and voltage measurements.
4. **Measurement acquisition platform (PXI-based system)** — Synchronised sampling, timing architecture, streaming, accuracy, bandwidth and sampling theory.
5. **Post-processing of measurement data** — File indexing, channel reconstruction, frequency-domain analysis and accuracy evaluation.

3.1 Measurement system requirements

The analyses in Chapter 2 and the introduction of Chapter 3 show that the relevant common-mode (CM) and differential-mode (DM) phenomena are distributed along the full traction voltage system (TVS). They arise from parasitic elements and depend strongly on switching behaviour and operating-point variations. To characterise these effects experimentally, the measurement system must satisfy a set of functional and physical requirements that follow directly from the system-level behaviour identified earlier.

The purpose of the vehicle measurement system is to perform simultaneous measurements of key electrical quantities at approximately 20 nodes distributed throughout the TVS in a large commercial vehicle. Each node is equipped with one Break-Out Box (BoB), and each BoB measures five electrical quantities:

- Two DC potentials to chassis, used to calculate the CM and DM voltage,
- One DC and low-frequency AC current (this thesis does not include this sensor in the analysis),
- One CM current,
- One DM current,
- One DC–200 kHz voltage measurement (not used for analysis in this thesis).

This results in 100 signals, 5 measurement points and 20 nodes that must be sampled in synchronisation. The physical size of the vehicle requires that these measurement nodes are located over up to 30 m.

In laboratory setups, CM frequencies up to 7 MHz have been observed. To ensure that switching harmonics, beating phenomena and transient EMI behaviour are captured, a complete acceleration and deceleration cycle must be recorded. The measurement system must therefore support individual recordings of up to 5 minutes, and the total recording capacity must reach 1 hour in order to complete a full dynamometer test sequence.

The key requirements for the measurement system are therefore:

- Frequency band from DC to 30 MHz (implying a sampling rate of 60 MSamples/s),
- Physically distributed sensors over up to 30 m,
- Approximately 100 synchronised channels,
- Cable-delay compensation,
- Safe and convenient sensor connection,
- DC and low-frequency current measurement,
- High-frequency CM current measurement,
- High-frequency DM current measurement,
- High-frequency CM voltage measurement(1),
- High-frequency DM voltage measurement(2),
- CAN-signal acquisition with analogue presentation,
- Post-processing capability for all channels,
- Up to 1 hour total recording time,
- Oscilloscope-like operation (trigger, zoom, scaling) in post-processing,
- Suitability for indoor dynamometer testing.

(1) According to Equation (2.1), the CM voltage follows from the positive and negative potentials to chassis. (2) According to Equation (3.3), the DM voltage follows from the same potentials.

At the time of development, no oscilloscope or commercial data acquisition system fulfils these requirements. The thesis presents a custom measurement system based on modular PXI hardware from National Instruments (NI).

The measurement system fulfils several requirements only partially:

- The figure-eight geometry limits the DM-current sensor bandwidth (see Figure 3.3 and Equation (3.2)), although this deviation is acceptable because CM bandwidth is more critical,
- The hardware limitations prevent real-time viewing of all channels,
- Neither the NI hardware nor the sensors are weatherproof; therefore all tests take place on a chassis dynamometer for repeatability and safety.

The requirements defined in this section specify what the measurement system must achieve in terms of bandwidth, synchronisation, number of channels and operating constraints. They also imply a distributed architecture in which sensors, cabling and central acquisition operate as a cohesive measurement chain rather than as separate subsystems. As several requirements interact—such as synchronisation, bandwidth, sensor placement and data throughput—the thesis describes each subsystem from a system-level perspective. To understand how these requirements translate into a practical implementation on a heavy-duty vehicle, the next section presents an overview of the complete measurement system architecture and its physical integration into the traction voltage system (TVS).

Conclusion

This section summarises the functional and physical requirements that the measurement system must fulfil to capture CM and DM behaviour reliably. These requirements specify the performance limits and sensing capabilities that form the basis for the subsequent system-level architecture.

3.2 Measurement system overview

The previous section defines the functional and physical requirements that the vehicle measurement system must satisfy. Building on these requirements, this section provides a system-level overview of how the complete measurement architecture is realised in practice.

To satisfy the requirements in Chapter 3, the measurement system follows a distributed architecture in which sensing, signal transport, central acquisition and post-processing form an integrated measurement chain. Before each subsystem is analysed in detail, this overview links the earlier requirement analysis to its physical implementation on the vehicle.

The measurement system is intended for use both on full-scale vehicles and on laboratory rigs. Its primary purpose is to capture CM and DM quantities with simultaneous sampling at distributed nodes of the traction voltage system (TVS), while ensuring mechanical robustness, electrical safety and minimal interference with the original vehicle architecture.

Figure 3.2 shows a block diagram of the TVS of a Volvo FE280 truck used during the early development phase to validate sensor installation, cabling strategies and BoB placement. The vehicle carries multiple Break-Out Boxes (BoB) mounted at selected TVS nodes, together with a PXI-based measurement platform installed inside the cab. The electrical connections between the BoB sensors and the PXI system are not shown in the figure.

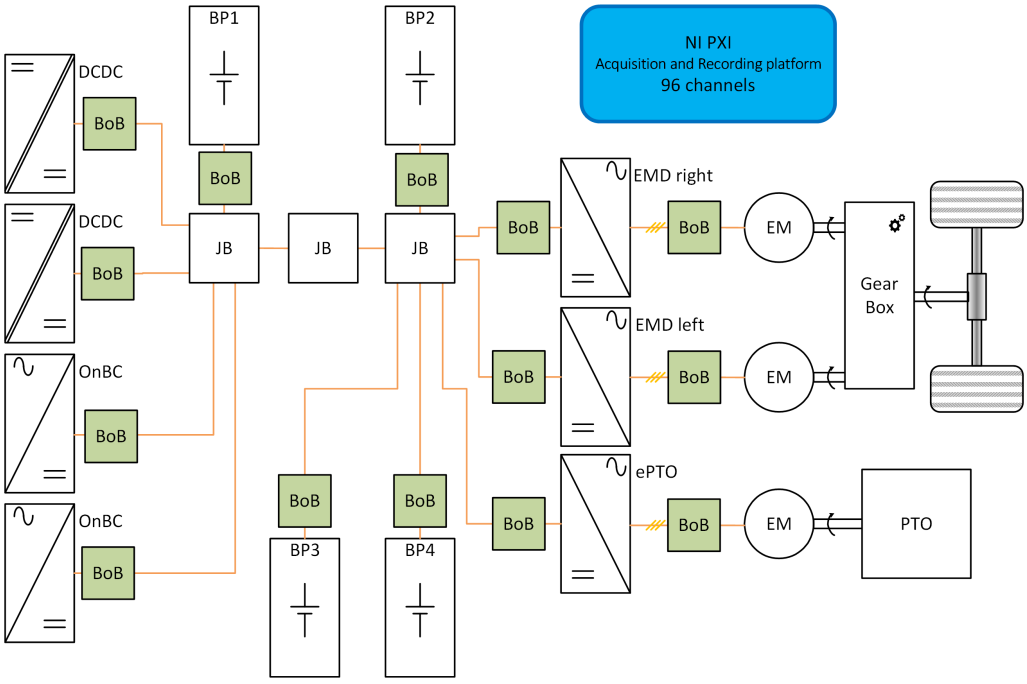


Figure 3.2: Volvo FE280 truck with Break-Out Boxes and PXI-based measurement system during early development.

The FE280 platform is representative of a mid-size heavy-duty vehicle and serves as an illustrative example of how BoBs and the acquisition hardware are physically arranged. As stated in the chapter introduction, several vehicle platforms are used throughout the development and measurement campaign, but the overall measurement architecture remains consistent across all platforms.

The measurement system consists of four main elements:

1. **Break-Out Boxes (BoB):** Installed at selected TVS nodes to measure DC voltage, DC and low-frequency AC current, CM current and DM current.

2. **High-bandwidth coaxial cabling:** Connecting the BoB sensors to the central PXI measurement system while preserving signal integrity and synchronisation.

3. **PXI-based acquisition platform:** Providing simultaneous sampling of all channels

with sub-nanosecond timing alignment, high data throughput and continuous streaming capability.

4. **Post-processing environment:** Used for waveform inspection, reconstruction of CM and DM quantities, spectral analysis and validation of measurement accuracy.

This section introduces the BoB only at a conceptual level, as the measurement interface between the TVS and the central acquisition platform. The next section presents the detailed electrical design, sensing functions and mechanical integration.

Conclusion

This section provides a system-level overview of the vehicle measurement architecture. It outlines the main structural elements of the system and describes how distributed sensing, cabling, centralised acquisition and post-processing operate together as a coherent measurement chain. These principles form the basis for the detailed subsystem descriptions that follow.

3.3 Break-Out Boxes (BoB)

The previous section introduces the overall structure of the complete measurement system and its installation on a heavy-duty vehicle. Building on that foundation, this section presents the Break-Out Box (BoB), which serves as the interface between the traction voltage system (TVS), the sensors and the PXI-based measurement platform.

The design of the BoB is critical, as it determines both measurement quality and electrical safety. Within the distributed measurement architecture outlined in Section 3.2, each BoB functions as a local measurement node that provides the electrical quantities required for CM and DM analysis from the TVS. These quantities include i_{cm} and i_{dm}, measured directly by dedicated Rogowski coils, a DC and low-frequency AC current (not evaluated in this thesis), and the positive and negative pole voltages to chassis from which the CM and DM voltages are reconstructed during post-processing. The following subsections describe the BoB architecture and its associated sensors.

The purpose of a BoB is to interrupt the traction voltage system (TVS) at a selected node and insert a measurement interface that enables sensing of all required electrical quantities without compromising personnel safety or significantly altering the electrical behaviour of the system. The BoB is positioned between the junction box (JB) and the device under test (DUT), and its physical geometry and electrical layout must preserve the original current paths and parasitic characteristics as far as possible.

Each BoB measures five quantities: a DC and low-frequency AC current (not evaluated in this thesis), common-mode (CM) current, differential-mode (DM) current, the positive pole voltage to chassis and the negative pole voltage to chassis. In laboratory experiments,

CM currents have been observed with spectral content up to 7 MHz, and the target bandwidth for all quantities is therefore extended to 30 MHz to ensure sufficient measurement margin.

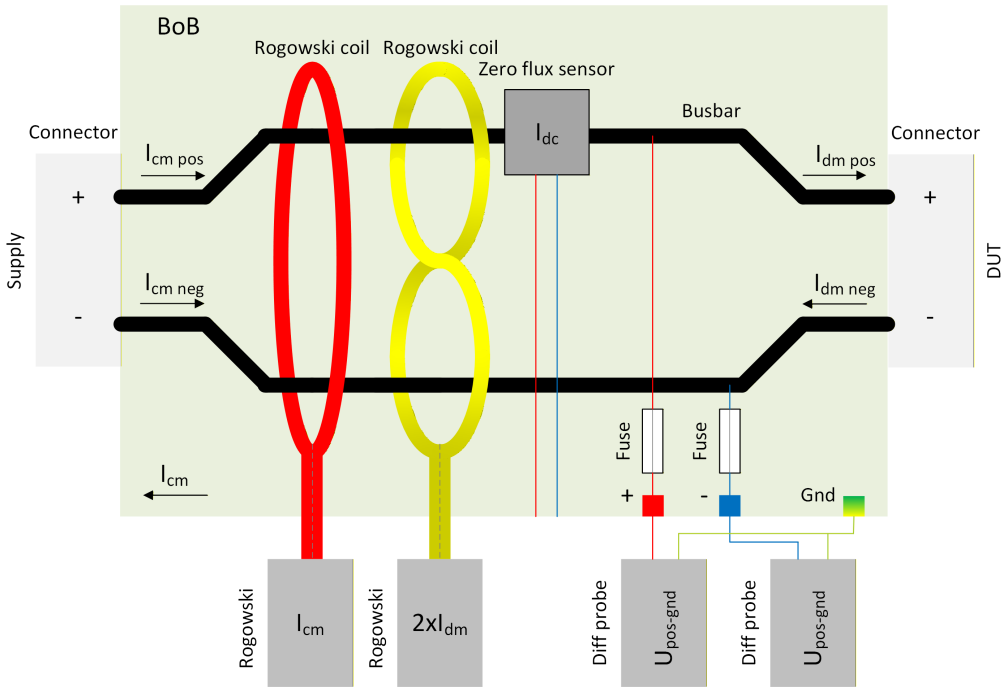


Figure 3.3: Break-Out Box (BoB) with Rogowski coils for i_{cm} and i_{dm}, a zero-flux sensor for i_{dc} (capable of measuring DC and low-frequency AC currents), and fused connections for differential voltage sensing of u_{pos} and u_{neg}.

The following subsections describe each sensor type and measured quantity in detail.

3.3.1 CM current sensor (Rogowski coil)

The previous subsection introduces the BoB as the local measurement interface in the distributed architecture. Building on this context, this subsection focuses on the sensor used to measure the common-mode (CM) current extracted at each BoB.

The common-mode (CM) current is the part of the total current that returns through the vehicle chassis or surrounding conductive structures. In the two conductors of the traction voltage system (TVS), the CM current appears as equal-direction components in the positive and negative poles. The CM current is defined as:

$$i_{cm} = i_{cm_pos} + i_{cm_neg} \tag{3.1}$$

In practice, the Rogowski coil measures the CM current by enclosing both conductors simultaneously, as illustrated by the red coil in Figure 3.3. The Rogowski coil used in the

measurement system is the PEMUK CWTHF 015x/B/2.5/300, selected for its bandwidth, accuracy and mechanical robustness. For measurements at the connection between the electric machine drive (EMD) and the electric machine (EM), a coil with a higher current rating is used because the CM components in this region are significantly larger.

The key specifications of the CM Rogowski coil are:

- Bandwidth (−3 dB): 300 Hz to 30 MHz,
- Traceable accuracy: ±0.2% (with the conductor centred in the loop),
- Position-dependent variation: ±1%,
- Sensitivity: 200 mV/A,
- Coil length: 300 mm,
- Insulation rating: 10 kV,
- Coil thickness: 8.5 mm.



Figure 3.4: PEMUK CWT Rogowski coil. Picture from PEMUK.

The next subsection describes the Rogowski coil configuration used to measure the differential-mode (DM) current, which complements the CM measurement presented here.

Conclusion

The Rogowski coil measures the CM current by enclosing both TVS conductors simultaneously and provides the bandwidth, sensitivity and positional stability required to capture fast transients and wideband CM behaviour. Its performance characteristics ensure reliable extraction of CM quantities within the distributed measurement system.

3.3.2 DM current sensor (Rogowski coil)

The previous subsection introduces the CM current sensor and its role in extracting the common-mode component from the traction voltage system (TVS). Building on this context, this subsection focuses on the Rogowski coil configuration used to measure the differential-mode (DM) current within each BoB.

The differential-mode (DM) current is the current that flows in the positive conductor and returns in the negative conductor. When the current in only one conductor is measured, the resulting signal contains both the DM component and the common-mode (CM) component. To reduce the influence of the CM component, the DM current is measured in both conductors and calculated as:

$$i_{dm} = \frac{i_{dm_pos} + i_{dm_neg}}{2} \tag{3.2}$$

This expression removes the CM contribution only if the CM current is identical in both conductors, which is not always the case in practice.

The Rogowski coil measures the DM current using a figure-of-eight geometry that encloses both conductors, as illustrated by the yellow coil in Figure 3.3. This geometry enhances sensitivity to the DM component while suppressing the CM component due to the opposing field contributions.

The selected Rogowski coil is the PEMUK CWTMiniHF 03/B/2.5/400/5. A coil with a higher current rating is used for DM measurements between the electric machine drive (EMD) and the electric machine (EM), where significantly larger current components occur.

The key specifications of the DM Rogowski coil are:

- Bandwidth (-3 dB): 100 Hz to 12 MHz,
- Traceable accuracy: ±0.2% (conductor centred),
- Sensitivity: 100 mV/A,
- Coil length: 400 mm,
- Insulation rating: 5 kV,
- Coil thickness: 4.5 mm.

The next subsection describes how the BoB measures the positive and negative pole voltages to chassis, which form the basis for reconstructing the CM and DM voltages.

Conclusion

The Rogowski coil measures the DM current by enclosing both TVS conductors in a figure-of-eight geometry that suppresses CM interference and strengthens the differential signal. Its bandwidth, sensitivity and mechanical properties enable accurate extraction of DM quantities within the distributed measurement system.

3.3.3 Differential voltage probe

The previous subsection introduces the DM current sensor and describes how the differential-mode component is extracted from the traction voltage system (TVS). Building on this context, this subsection presents the differential voltage probe used to measure the voltage quantities required for reconstructing the CM and DM voltages.

The differential voltage is measured using a high-bandwidth differential voltage probe. In addition to meeting the bandwidth requirement, the probe must interface with the PXI-based measurement system using a BNC connector. The selected probe is the Testec TT-SI 9010, with key parameters specified in [24].

- Bandwidth (-3 dB): DC to 70 MHz,
- Attenuation: $x100/x1000$,
- Accuracy: ±2%,
- Input impedance: 10 MΩ, 10 pF,
- Differential-mode input voltage, $x100$: ±700 V (DC + peak AC) or 700 Vrms,
- Differential-mode input voltage, $x1000$: ±7000 V (DC + peak AC) or 2500 Vrms.



Figure 3.5: Testec TT-SI-9010 differential voltage probe.

The differential voltage probe measures the quantities u_{dm} and u_{cm}. The common-mode voltage u_{cm} is defined in Equation (2.1), and the differential-mode voltage u_{dm} is defined as:

$$u_{dm} = u_{pos} - u_{neg} \tag{3.3}$$

Conclusion

The differential voltage probe provides the bandwidth, attenuation settings and input characteristics required to measure the voltages used to reconstruct the CM and DM quantities. Its interface and performance ensure accurate extraction of differential and common-mode voltages within the distributed measurement system.

3.3.4 Conclusion

The Rogowski coils and the differential voltage probe installed inside each Break-Out Box (BoB) provide the current and voltage quantities required for CM and DM analysis. The CM and DM coils measure the corresponding current components, while the differential voltage probe enables accurate reconstruction of u_{dm} and u_{cm}. Together, these sensors form the local measurement interface that extracts the electrical quantities from the traction voltage system (TVS) for subsequent acquisition and post-processing.

3.4 NI data acquisition and recording platform (PXI)

The previous section describes the sensing interface provided by each Break-Out Box (BoB) and the quantities extracted from the traction voltage system (TVS). Building on that foundation, this section introduces the PXI-based acquisition platform that samples, synchronises and records all measurement channels.

The measurement signals from all BoBs need to be collected and sampled in a synchronised way. For this purpose, the measurement system requires a signal sampling system functionally equivalent to a 100-channel oscilloscope. The modular instrumentation platform PCI eXtensions for Instrumentation (PXI) fulfils the requirements for this purpose. It is a rugged platform offering high-performance measurement and control capabilities. Integrated timing and triggering features in the PXI backplane provide precise inter-module synchronisation. The developed PXI-based measurement system, which provides oscilloscope-class sampling performance, supports up to 96 channels at a sampling rate of 60 MS/s using four PXI chassis in the configuration shown in Figure 3.6.

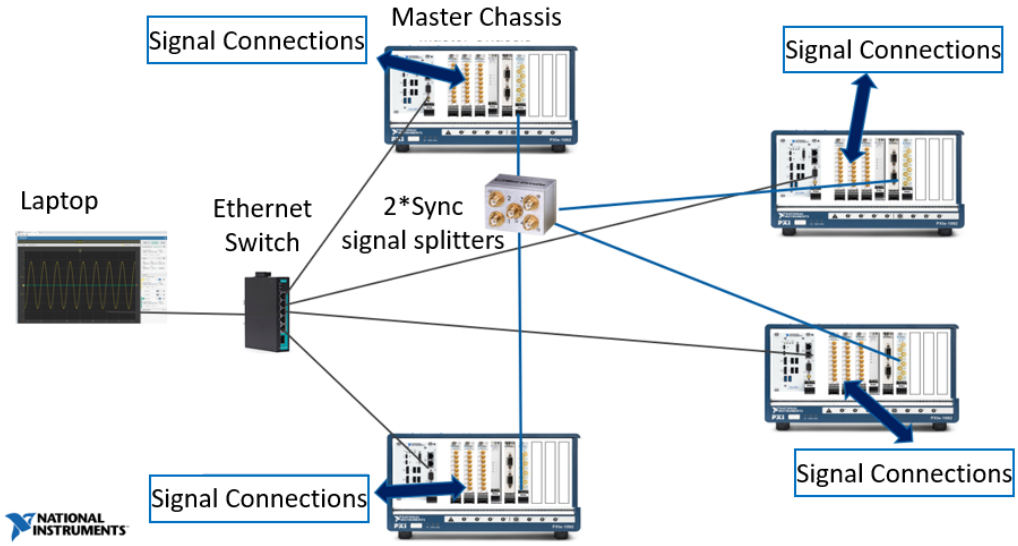


Figure 3.6: PXI solution architecture with four PXI chassis, signal synchronisation switch, Ethernet hub and laptop.

3.4.1 PXI chassis and included modules

The PXI chassis (PXIe-1092) shown in Figure 3.7 contains the following components, listed from left to right:

- PXI controller (PXIe-8861),
- 4 oscilloscope modules with 8 channels each (PXIe-5105), providing 12-bit resolution and synchronised using a common sampling clock at a maximum of 60 MS/s/ch*,

- Timing module (PXIe-6674T). Analogue channels are synchronised across modules within each chassis and to an external master clock to enable multi-chassis acquisition,
- 4 TB SSD disk (PXIe-8267),
- 6-channel X-NET board (PXI-8510) equipped with 5 CAN adapters (TRC-8542),
- Adapter plate for the CAN adapters.

*Each module streams data to the PXI backplane through a dedicated PCIe x4 Gen1 lane (theoretical bandwidth 1 GB/s). In practice, the effective bandwidth is below 1 GB/s, limiting continuous streaming to 6 full-speed channels per module. Therefore, four analogue input modules are required.



Figure 3.7: PXI backplane with mounted modules.

Conclusion

The PXI chassis integrates the controller, oscilloscope modules, timing module, storage and CAN interface required for synchronised high-speed acquisition. Its modular architecture provides the sampling capacity and timing precision needed to record all analogue and digital channels within the distributed measurement system.

3.4.2 Streaming rate

The previous subsection describes the PXI chassis and its installed modules. Building on that context, this subsection explains the streaming rate required to sustain continuous high-speed acquisition.

The key goal of the streaming architecture is to transmit data from an instrument fast enough to maintain continuous acquisition. During an acquisition task, the data produced by the instrument is transferred through the PCIe bus to the host computer, where it is placed in memory.

The required bandwidth of 30 MHz implies a sampling frequency greater than 60 MS/s. A 12-bit sample is stored on disk as 2 bytes, which results in a data stream greater than 120 MB/s per channel. With 24 channels running at full speed, the total required data rate is 2.9 GB/s. The PXIe-1092 chassis supports a total backplane bandwidth of 24 GB/s.

To store continuous data, a high-speed storage device is required. The PXIe-8267 provides 4 TB of storage with a sustained streaming capability of 5 GB/s. If the maximum sampling rate is used on all 24 channels, approximately 22 minutes of continuous recording are possible. The sensors used for DC quantities require significantly lower sampling rates, which allows some channels to operate at reduced sampling frequency.

Conclusion

The required streaming rate is determined by the sampling frequency, sample size and number of channels operating at full speed. The PXI storage and backplane bandwidth support continuous recording for the intended high-speed channels while allowing reduced sampling for low-frequency measurements.

3.4.3 Synchronization and system architecture

The previous subsection explains the streaming rate required for continuous acquisition. Building on that context, this subsection describes the timing and synchronisation architecture used to align all PXI modules during high-speed measurement.

With PXI timing and synchronisation modules, advanced multi-device synchronisation can be implemented by using the trigger bus, star trigger and system reference clock features of the PXI platform, as illustrated in Figure 3.8.

In an NI PXI signal-based timing and synchronisation architecture, clocks and triggers are physically connected between subsystems, which synchronise the sample clocks of the individual modules. This achieves the highest synchronisation precision and is required in this measurement system to reach below 1 ns of alignment between samples, as shown in Figure 3.9.

With the timing and synchronisation capabilities built into the PXI platform, a 10 MHz and/or 100 MHz system reference clock can be distributed on the backplane to synchronise modules within a single PXI chassis. In the same way, the 10 MHz reference clock can be distributed between multiple chassis to achieve synchronisation across several PXI systems, as shown in Figure 3.10.

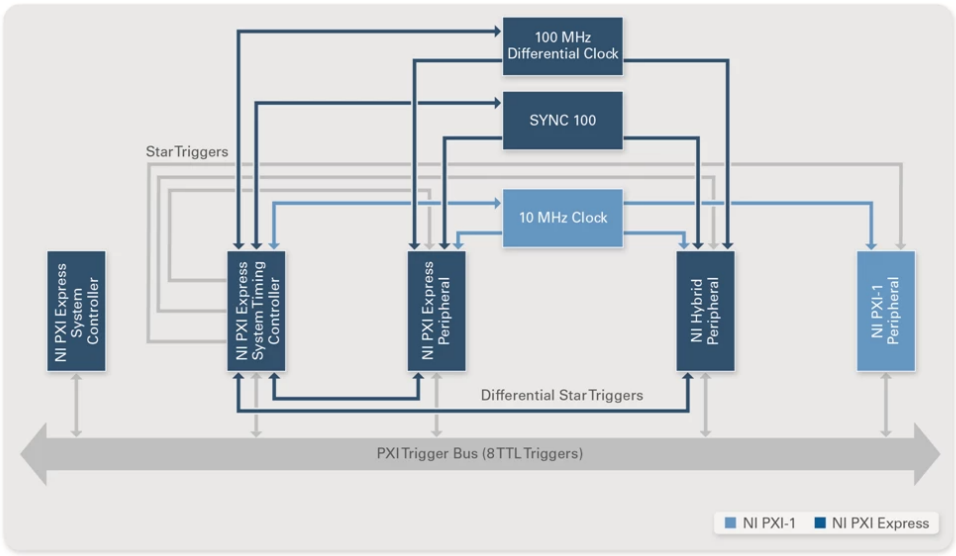


Figure 3.8: PXI timing and synchronisation modules.

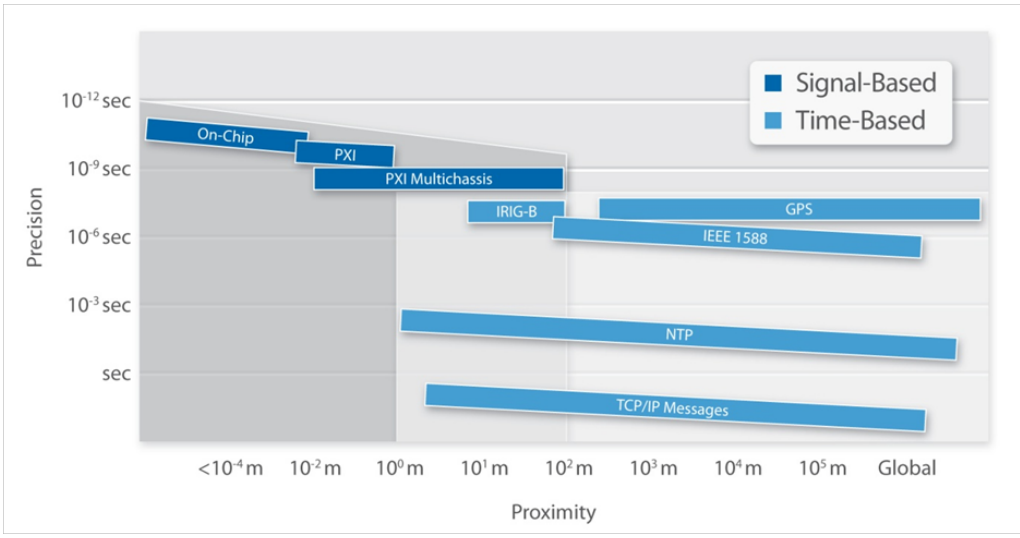


Figure 3.9: PXI precision versus proximity for signal-based and time-based synchronisation.

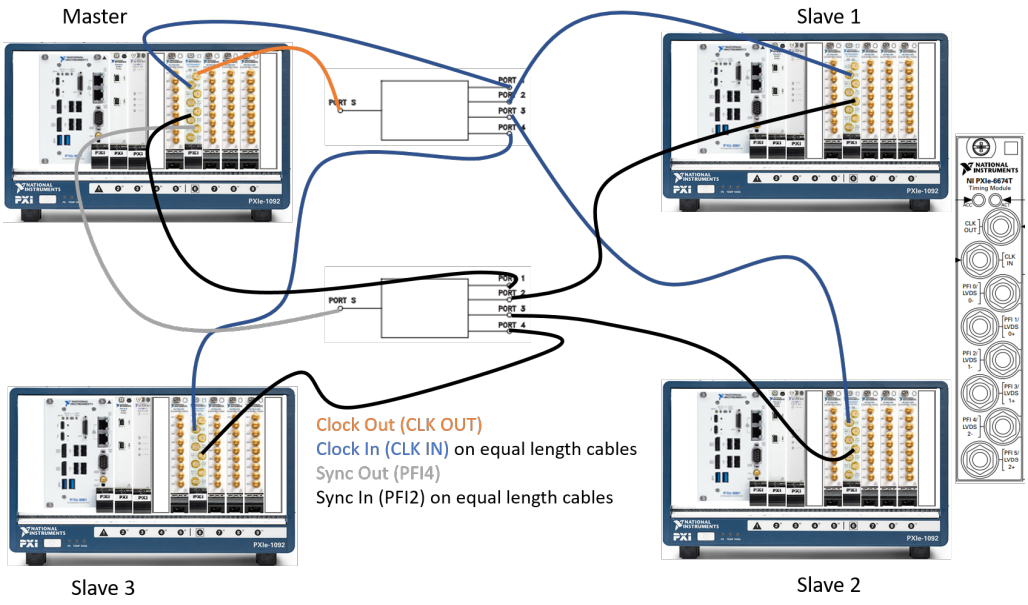


Figure 3.10: Synchronisation of multiple PXI chassis. The PXI system supports operation as a single chassis or in configurations with two, three or four chassis.

Conclusion

The PXI timing architecture distributes clocks and triggers through the backplane and between chassis to align all modules during acquisition. The combination of signal-based synchronisation, reference clocks and triggering ensures sub-nanosecond alignment across all PXI systems in the measurement setup.

3.4.4 Accuracy

The previous subsection describes the timing and synchronisation architecture of the PXI system. Building on that context, this subsection summarises the accuracy characteristics of the oscilloscope modules used in the measurement system.

The differential voltage probes and the Rogowski coils are connected to the oscilloscope inputs with an impedance of 1 MΩ. Table 3.1 lists the accuracy for the DC measurements, and Table 3.2 lists the accuracy for the AC measurements. The tables originate from [10].

Table 3.1: Accuracy for DC measurements.

Input Impedance	Input Range ($V_{pk\text{-}pk}$)	DC Accuracy, Warranted
50 Ω	All	±(1% × *Reading* + 0.25% of FS + 600 µV)
1 MΩ	0.05 V	±(1% × *Reading* + 0.25% of FS + 600 µV)
	0.2 V, 1 V, and 6 V	±(0.65% × *Reading* + 0.25% of FS + 600 µV)
	30 V	±(0.75% × *Reading* + 0.25% of FS + 600 µV)

Table 3.2: Accuracy for AC measurements at 50 kHz.

Input Impedance	Input Range ($V_{pk\text{-}pk}$)	AC Amplitude Accuracy
50 Ω	All	±0.1 dB (±1.2%) of *Reading*
1 MΩ	0.05 V	±0.2 dB (±2.3%) of *Reading*
	0.2 V and 1 V	±0.13 dB (±1.5%) of *Reading*
	6 V and 30 V	±0.4 dB (±4.7%) of *Reading*

In practice, the accuracy for AC measurements follows the last row of Table 3.2, corresponding to ±4.7% of the reading.

Conclusion

The accuracy of the oscilloscope modules is defined by the DC and AC performance listed in the NI specifications. The AC measurement accuracy typically follows the highest error band, while DC accuracy is determined by the specified gain and offset limits. These accuracy values apply to all channels connected through the differential probes and Rogowski coils.

3.4.5 Bandwidth BW

The previous subsection summarises the accuracy of the PXI-based measurement system. Building on that context, this subsection defines the corner frequency, centre frequency and bandwidth used in signal analysis.

The corner frequency is defined as the frequency at which the input signal is attenuated to -3 dB or 70.7 percent of the original amplitude. This normally occurs at a lower frequency f_1 and an upper frequency f_2.

$$-3\ dB = 20\log\left(\frac{V_{out}}{V_{in}}\right) \tag{3.4}$$

The centre frequency is defined as:

$$f_0 = \sqrt{f_1 f_2} \tag{3.5}$$

Finally, the bandwidth is defined as:

$$BW = f_2 - f_1 \tag{3.6}$$

Conclusion

The definitions of corner frequency, centre frequency and bandwidth describe the frequency range over which a signal or system operates. These quantities are used to characterise attenuation behaviour and usable measurement bandwidth.

3.4.6 Nyquist sampling theorem

The previous subsection defines the corner frequency, centre frequency and bandwidth. Building on that context, this subsection provides a brief reminder of the Nyquist sampling theorem.

The Nyquist sampling theorem explains the relationship between the sampling frequency f_s and the frequency content of the signal. The limiting frequency is referred to as the Nyquist frequency f_N:

$$f_s > 2f_N \tag{3.7}$$

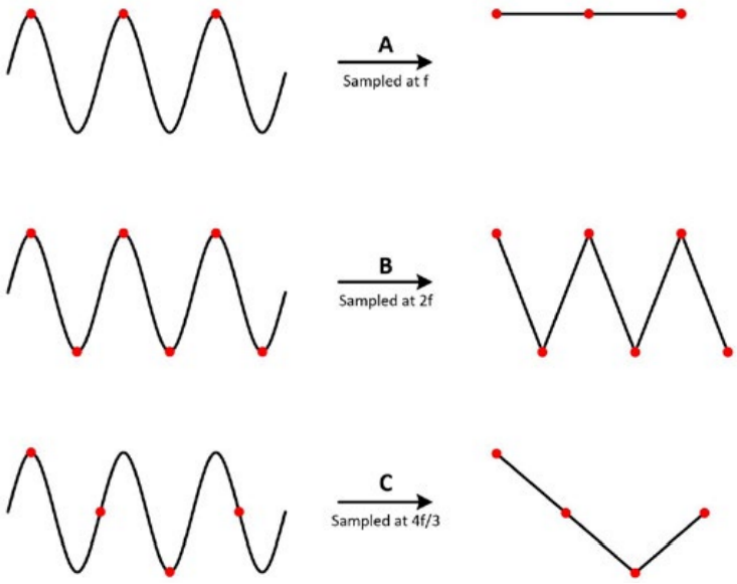


Figure 3.11: Too low sampling frequency can cause an incorrect waveform. Figure from [9].

This subsection is included only as a brief reminder of the concept and is not intended to be exhaustive.

Conclusion

The Nyquist sampling theorem states that the sampling frequency must exceed twice the highest frequency present in the signal to avoid aliasing. This criterion provides the basis for selecting appropriate sampling rates within the measurement system.

3.4.7 Anti-aliasing filter

The previous subsection explains the Nyquist sampling theorem and its implication for selecting appropriate sampling frequencies. Building on that context, this subsection describes the anti-aliasing filter available in the PXI oscilloscope modules.

The NI oscilloscope offers an anti-aliasing filter at 24 MHz, which can be enabled or disabled. As shown in Subsection 3.4.6, a sampling frequency that is too low results in incorrect waveform reconstruction. If the measured signal is sampled at a frequency lower than twice the highest present signal frequency, false low-frequency components appear in the sampled data. This phenomenon is called aliasing, and an illustration is shown in Figure 3.12.

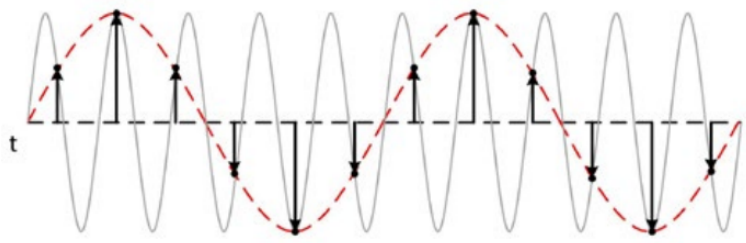


Figure 3.12: Aliasing caused by too low sampling frequency. Figure from [9].

In practice, this means that the anti-aliasing filter is required for sampling frequencies $f_s < 48$ MHz, which corresponds to 60 MSamples/s on the PXI.

The next lower sampling rate available is 30 MSamples/s. This would require an anti-aliasing filter of 15 MHz, which is not available on the PXI. Another possible way to reduce f_s is to reduce the bandwidth of the sensor.

If the anti-aliasing filter is not used, aliasing may occur. According to [9], the alias frequency can be calculated as

$$f_a = |nf_s - f| \tag{3.8}$$

n closest integer such that nf_s is the nearest multiple of the sampling frequency to f.

A few examples are shown in Figure 3.13.

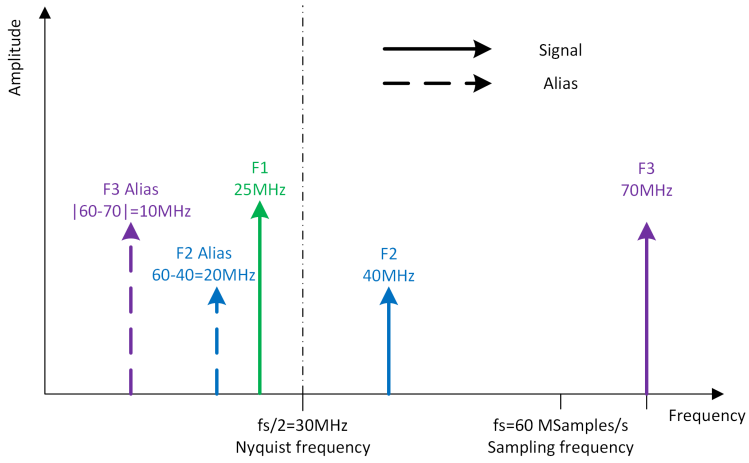


Figure 3.13: Alias frequencies for three input tones at different sampling rates.

In this example, the signal in Figure 3.13 contains the frequencies F1 = 25 MHz, F2 = 40 MHz and F3 = 70 MHz.

F1 Represented accurately because it is below the Nyquist frequency.

F2 Alias: $|1 \cdot 60 - 40| = 20$ MHz.

F3 Alias: $|1 \cdot 60 - 70| = 10$ MHz.

This subsection is a brief summary of the topic and is not intended to be exhaustive.

Conclusion

The anti-aliasing filter prevents false low-frequency components when the sampling frequency is insufficient relative to the highest signal frequency. It is required for sampling below 48 MHz and complements the Nyquist criterion to ensure correct waveform reconstruction.

3.4.8 Anti-aliasing filter in measurements

The previous subsection describes aliasing and the role of the anti-aliasing filter. Building on that context, this subsection summarises how the sensor bandwidths determine the minimum required sampling frequency.

According to Subsections 3.3.1 to 3.3.3, the bandwidths for the sensors are:

- BW (-3 dB): 300 Hz to 30 MHz for the CM current sensor,
- BW (-3 dB): 100 Hz to 12 MHz for the DM current sensor,
- BW: DC to 70 MHz for the differential voltage sensor.

This leads to the lowest possible sampling frequency f_s:

- 60 MSamples/s for the CM current,
- 30 MSamples/s (e.g. $2 \cdot 12$ MHz) for the DM current,
- 60 MSamples/s for the differential voltage.

A small loss may occur for the CM current above 24 MHz. However, using the anti-aliasing filter at all times reduces the risk of aliasing.

Conclusion

The sensor bandwidths determine the required sampling frequencies for the CM current, DM current and differential voltage measurements. Using the anti-aliasing filter minimises the risk of aliasing whenever the sampling frequency approaches the upper limit of the sensor bandwidth.

3.4.9 Resolution

The previous subsection describes how the anti-aliasing filter relates to sensor bandwidth and sampling frequency. Building on that context, this subsection summarises the resolution characteristics of the PXI oscilloscope modules.

The eight-channel oscilloscope modules (PXIe-5105) have a 12-bit resolution, corresponding to 2^{12} or 4096 discrete levels of the measured signal. Assume that an input channel is set to a range of 30 V. The resolution of the measured signal is then 30/4096, which corresponds to 7.3 mV.

Consider a measurement scenario where a voltmeter with 100x attenuation is used. The test object delivers a voltage of 50–700 V. This results in a signal of 0.5–7 V at the oscilloscope input. The available oscilloscope input ranges are 30 V, 6 V, 1 V, 0.2 V and 0.05 V. These ranges are symmetric around zero, meaning that the 30 V range corresponds to ±15 V of available measurement span.

This equals a ±1500 V measurement span on the sensor (in this example, the differential voltage probe). The next lower oscilloscope range, 6 V, is too narrow because it corresponds to only ±300 V on the sensor. The resolution of the 30 V oscilloscope range is therefore 3000 V/4096, or 0.73 V. This is relatively coarse, but it is necessary to accommodate the full input range. The noise in this range is dominated by digital quantisation noise.

Conclusion

The oscilloscope resolution is determined by the selectable input range and the 12-bit quantisation. Higher ranges allow large input signals but reduce amplitude resolution, while lower ranges improve resolution but may not accommodate the full signal span. Quantisation noise dominates when using the largest input ranges.

3.4.10 Conclusion

The PXI-based acquisition platform provides the synchronised sampling, bandwidth, storage capacity and timing precision required for high-speed measurements in the distributed system. The chassis modules, timing architecture, streaming rate, bandwidth definitions, sampling considerations, anti-aliasing functions and resolution constraints together establish the performance limits of the acquisition chain. These characteristics define how the measurement system captures the electrical quantities delivered from the Break-Out Boxes (BoB) with consistent accuracy and synchronisation.

3.5 Post-processing

The previous section describes the PXI-based acquisition platform and how data are sampled, synchronised and stored. Building on that context, this section outlines the post-processing

workflow required to handle the large data volumes generated during a measurement session.

Post-processing of the recorded data is a practical challenge. Each oscilloscope card in the PXI chassis stores its data on an internal 4 GB SSD. The file size is fixed by the firmware, which means that the duration of each file depends on the number of active channels and the sampling rate. When the maximum size is reached, the system automatically creates the next consecutive file. An example of the raw file structure is shown in Figure 3.14.

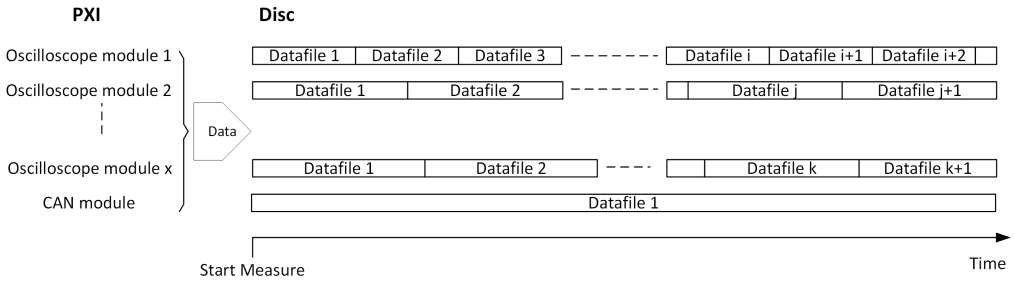


Figure 3.14: Data files stored on disk. High sampling rates generate many consecutive files, whereas low sampling rates may result in only one file per channel.

Assume that a specific time interval is of interest, as illustrated in Figure 3.15.

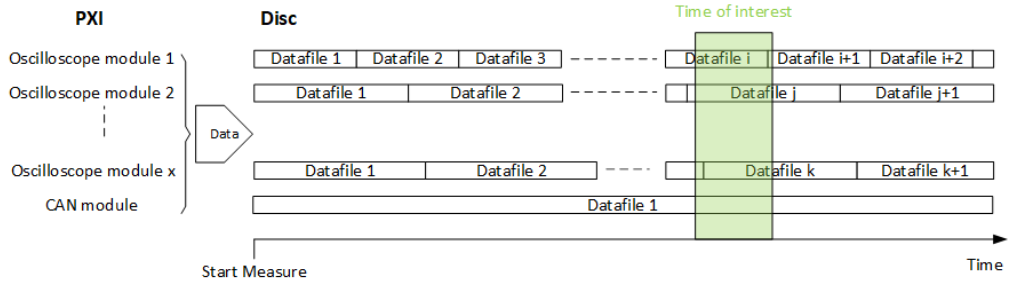


Figure 3.15: Specific time interval of interest for analysis.

It is not feasible to open the individual files manually and view them in a synchronised manner. To address this, a post-processing tool has been developed that indexes all files generated by the measurement system (*Indexer.exe*). Each channel is represented as one continuous file in the index, as shown in Figure 3.16.

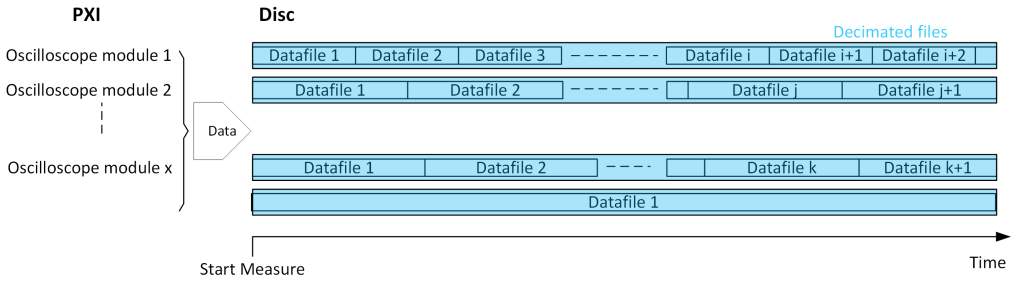


Figure 3.16: Indexed representation of the raw files. Each channel appears as one continuous file.

Any channel can be inspected individually, and when an interesting phenomenon is identified, all channels or a selected subset of channels can be exported to a new file using *Datalogger Viewer.exe*. The exported file contains only the time interval of interest but includes all selected channels with full resolution, as illustrated in Figure 3.17.

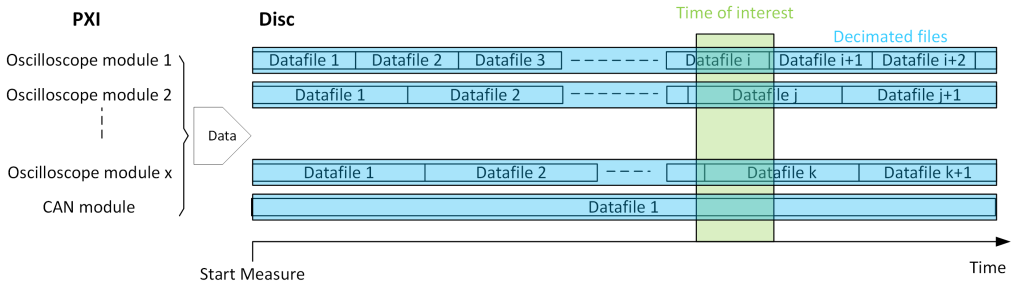


Figure 3.17: New file created from the indexed dataset, containing all selected channels within the chosen time interval.

The exported file can then be evaluated using external tools, such as Python-based scripts or other time-domain analysis software capable of handling multi-channel data.

When the full measurement system is used, with four PXI chassis and associated CAN boards, each PXI produces five parallel files. This results in twenty parallel files for a complete configuration. To illustrate the scale, Figure 3.18 shows a 600 s measurement of one channel. The complete dataset consists of 72 consecutive files. For all channels in a full system, this corresponds to 72 files per board $\times$ 5 boards/PXI $\times$ 4 PXIs $=$ 1440 files.

The data displayed in the viewer are decimated, as 60 MS/s cannot be visualised in real time. When a relevant event is identified, the post-processing tool exports only the desired time span, with all channels aligned and stored at full sampling resolution. From the original 1440 files, a single synchronised dataset can be created that contains only the channels and time interval of interest.

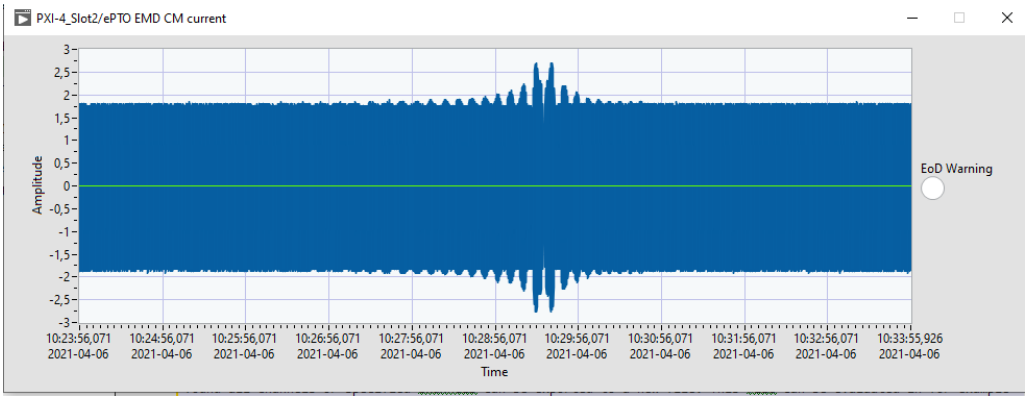


Figure 3.18: One channel recorded for 600 s, displayed in *Datalogger Viewer.exe*. The measurement is divided into 72 raw files, which are indexed and decimated for viewing.

3.5.1 Total accuracy for HF

The previous subsection introduces the post-processing workflow and how raw measurement data are indexed and handled. Building on that context, this subsection summarises the total high-frequency (HF) accuracy obtained from combining oscilloscope and sensor uncertainties.

According to Subsection 3.4.4, the AC accuracy for the oscilloscope is 4.7 % at 50 kHz. No information from NI specifies what should be considered DC or AC.

According to Subsections 3.3.1 to 3.3.3, the accuracy of the sensors is 1 %, 2 % and 2 %, respectively.

The total HF accuracy for oscilloscope and sensor is obtained by combining the individual uncertainties using the root-sum-square (RSS) method:

$$\sigma_{\text{total}} = \sqrt{\sigma_1^2 + \sigma_2^2 + \dots} \tag{3.9}$$

For the calculated HF voltage quantities u_{cm} and u_{dm}, two independently measured voltage signals U_{pos} and U_{neg} contribute to the result. Since both signals have the same uncertainty, the propagated uncertainties become:

$$\begin{aligned} \sigma_{u_{cm}} &= \frac{\sqrt{\sigma_1^2 + \sigma_2^2}}{2}, \\ \sigma_{u_{dm}} &= \sqrt{\sigma_1^2 + \sigma_2^2}. \end{aligned} \tag{3.10}$$

Applying this to the HF measurements in this thesis, the total uncertainties are:

$$\begin{aligned} i_{cm} &= \sqrt{(4.7\%)^2 + (1\%)^2} \approx 4.81\%, \\ i_{dm} &= \sqrt{(4.7\%)^2 + (2\%)^2} \approx 5.11\%, \\ u_{pos} &= \sqrt{(4.7\%)^2 + (2\%)^2} \approx 5.11\%, \\ u_{neg} &= \sqrt{(4.7\%)^2 + (2\%)^2} \approx 5.11\%. \end{aligned} \tag{3.11}$$

$$\begin{aligned} u_{cm} &= \frac{\sqrt{(5.11\%)^2 + (5.11\%)^2}}{2} \approx 3.61\%, \\ u_{dm} &= \sqrt{(5.11\%)^2 + (5.11\%)^2} \approx 7.23\%. \end{aligned} \tag{3.12}$$

These values represent the total HF measurement accuracy for the CM and DM quantities. Although the absolute uncertainty is not extremely small, it is sufficient for evaluating relative changes in EMI, studying the effect of system modifications and comparing with simulation results.

The RSS formula assumes that the individual uncertainties are independent and random. Correlated errors are neglected, which is standard practice in measurement uncertainty analysis.

In practice, the derived total accuracies indicate that the measured HF CM and DM current signals can be trusted within approximately 5.1 %, whereas the calculated HF CM and DM voltage signals can be trusted within approximately 3.6 % and 7.2 %, respectively. This accuracy is adequate for comparative and qualitative analysis in this thesis.

Conclusion

The total HF accuracy is obtained by combining oscilloscope and sensor uncertainties using the RSS method. The resulting accuracy is approximately 5.1 % for CM and DM current measurements, 3.6 % for CM voltage and 7.2 % for DM voltage. These values are sufficient for relative comparisons and for evaluating system-level behaviour.

3.5.2 FFT of the measured signals

The previous subsection derives the total HF accuracy for the measured quantities. Building on that context, this subsection describes the FFT processing used to extract frequency-domain information from the recorded signals.

The measurements are analysed to retrieve the frequency content and the amplitude. In the analysis, an FFT window function is used to evaluate the measurement signal. Several window functions exist, such as Hanning and FlatTop. FlatTop is known for its good amplitude accuracy, whereas Hanning typically provides better frequency accuracy. FlatTop is chosen here due to its amplitude accuracy.

To verify that the FFT script in Python performs correctly, a synthetic signal is created, shown in Figure 3.19, consisting of five frequencies: 100 Hz, 1 000 Hz, 10 kHz, 50 kHz and 100 kHz. Each component has an amplitude of $\sqrt{2}$. The RMS FFT of the combined signal should therefore contain five distinct peaks in the frequency spectrum.

The advantages and disadvantages of the window functions are described in [7] and [25].

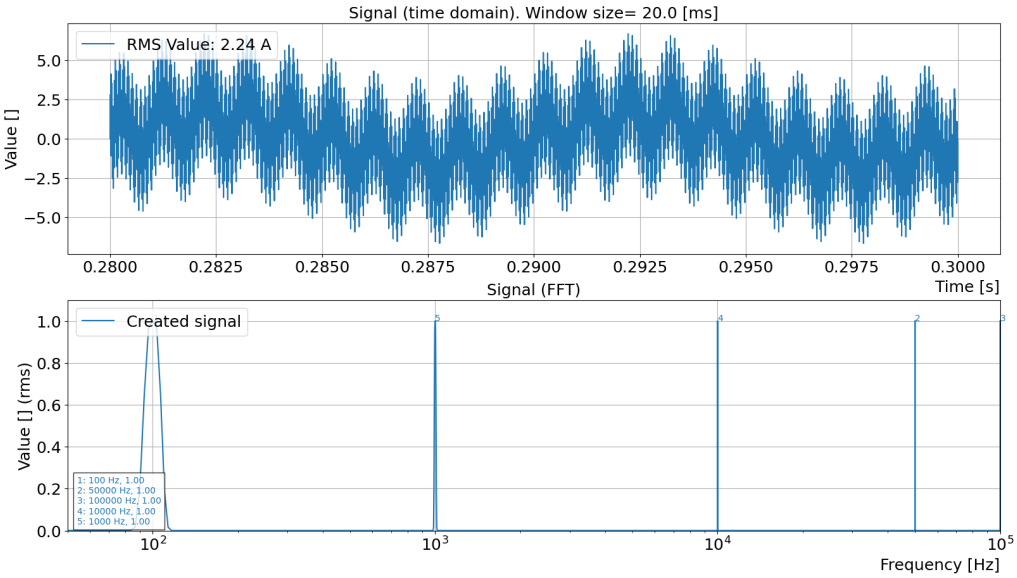


Figure 3.19: Five sinusoidal signals combined into one waveform. Each has an amplitude of $\sqrt{2}$. The lower graph shows the FFT of the same signal, where each component has an RMS value of 1, verifying the correctness of the RMS FFT calculation.

Conclusion

FFT analysis is used to identify the frequency components of the measured signals. The choice of window function affects amplitude and frequency accuracy, and verification with a synthetic signal confirms that the RMS FFT calculation performs as intended.

3.5.3 Conclusion

The post-processing workflow enables efficient handling of the large data volumes generated by the PXI-based measurement system. By indexing all files and treating each channel as an individual data stream, the developed tool reconstructs fully synchronised datasets for any selected time interval, regardless of sampling rate or file fragmentation. This capability is essential for analysing transient CM and DM phenomena in long measurements.

The total HF accuracy is determined by the combined tolerances of the oscilloscope and the sensors, resulting in a practical accuracy of approximately ±5 %. Although not extremely

high, this accuracy is sufficient because EMI evaluations rely primarily on relative changes rather than absolute amplitude verification.

The FFT verification demonstrates that the analysis method retrieves both frequency and amplitude content correctly when an appropriate window function is used. The Flat-Top window is selected due to its superior amplitude accuracy, ensuring that the extracted spectral magnitudes reliably represent the measured signals.

3.6 Conclusion

Chapter 3 presents the complete measurement system developed to capture common-mode (CM) and differential-mode (DM) electrical quantities in a full traction voltage system (TVS) under realistic vehicle operating conditions. The system requirements defined in Section 3.1 establish the need for a synchronised, high-bandwidth and mechanically robust platform capable of recording nearly one hundred distributed signals with sub-nanosecond alignment across a 30 m vehicle.

The physical arrangement and functional architecture of the system are described in Section 3.2, showing how the measurement platform integrates into different heavy-duty vehicle types and how the distributed Break-Out Boxes (BoB) enable local sensing without disturbing the TVS. The detailed design of each BoB and its sensors is presented in Section 3.3, where the Rogowski coils and differential voltage probes provide i_{cm}, i_{dm}, u_{cm}, u_{dm} and a DC and low-frequency current (not evaluated in this thesis) required for subsequent EMI analysis.

The PXI-based acquisition platform is analysed in Section 3.4. This section explains why commercially available oscilloscopes or DAQ systems cannot meet the required combination of bandwidth, synchronisation accuracy, channel count and continuous streaming capability. The chapter further reviews the timing architecture, sampling limitations, anti-aliasing behaviour, accuracy, bandwidth definitions and practical considerations such as resolution, all of which determine how the raw signals are interpreted during analysis.

Finally, Section 3.5 describes the post-processing environment required to handle the very large data volumes generated during long vehicle measurements. The indexing approach enables reconstruction of fully synchronised datasets from thousands of fragmented files, and the FFT verification confirms that spectral content and amplitudes are retrieved with the required accuracy.

In summary, Chapter 3 establishes the complete foundation on which all later measurement-based analysis in this thesis is built. The system does not evaluate EMI by itself, but it provides accurate, time-aligned and bandwidth-correct signals for subsequent analysis. The chapter therefore serves both as a technical reference for the measurement system and as a methodological basis for interpreting the results presented in the following chapters.

Chapter 4

Measurements on a truck and a bus

The previous chapter presents the measurement system that enables consistent observation of common-mode and differential-mode behaviour across the traction voltage system. This chapter uses that system to characterise full-vehicle behaviour. This shift ensures that the measurements presented here follow a coherent and validated methodological foundation.

In this chapter, conducted common-mode (CM) and differential-mode (DM) measurements are presented, primarily from an FE280 truck but also from a bus installation. Chapter 3 describes the measurement system and its validation in a bus environment, motivated by the wide physical separation of traction-voltage nodes. The FE280 truck uses a similar traction-voltage architecture but with a more compact layout, which enables observation of CM behaviour in a configuration closer to a production vehicle.

Although the measurement system captures CM and DM quantities simultaneously, DM currents do not offer meaningful information on a stationary vehicle, since they depend strongly on the operating point of the traction system. Full DM measurements therefore use a chassis dynamometer (DYNO), where speed, load and power flow define the operating point. DM measurements appear briefly in Section 4.4, and Chapter 6 evaluates them together with simulation results.

The present chapter focuses on CM measurements performed on a stationary vehicle and on vehicle-level impedance characterisation. These results form an intermediate validation step between the standalone component and subsystem characterisation presented earlier and the combined CM/DM comparison in Chapter 6.

The purpose of this chapter is to establish the dominant vehicle-level CM and DM mechanisms across the entire traction voltage system. Consequently, the chapter adopts a broad, system-oriented perspective rather than analysing each subsystem in exhaustive geometric detail, since it is this breadth that determines the relevant physical trends and the modelling requirements addressed in Chapter 5.

The overall structure of this thesis follows a measurement-modelling-simulation sequence. Chapter 4 examines experimental observations and traction voltage behaviour, Chapter 5 develops models that reproduce the measured phenomena and Chapter 6 uses

these models in system-level simulations and compares them with measurements.

During the measurement campaign, several phenomena occur that do not follow directly from the recorded data. Targeted analytical reasoning and simplified investigations therefore support interpretation of the physical origin of the observed behaviour and ensure correct understanding.

As a consequence, some analyses in this chapter anticipate concepts that Chapter 6 treats in a more systematic and comprehensive manner. These analyses appear here because they validate the measurement approach and distinguish genuine system behaviour from artefacts introduced by the measurement interface.

This chapter is organised in the following sections:

1. **Results from impedance measurements of the cables and junction boxes on a bus and a truck**: Presents differential-mode impedance measurements of cables and junction boxes performed on both a bus and a truck installation, providing insight into the frequency-dependent behaviour of distributed vehicle components and forming a basis for subsequent modelling work.

2. **Measurements affected by the break-out boxes**: Investigates how the introduction of break-out boxes influences measured CM quantities, highlighting the extent to which the measurement setup itself can perturb the system under investigation.

3. **Results from CMDC voltage measurements on a truck**: Presents common-mode DC voltage measurements obtained on a stationary FE280 truck, analysing their temporal and spectral characteristics and identifying dominant CM phenomena at vehicle level.

4. **Results from differential mode measurements on a truck**: Provides a brief presentation of differential-mode measurements obtained under controlled operating conditions, serving as a link to the more detailed DM analysis and simulations in Chapter 6.

5. **Verification of FFT implementation**: Verifies the correctness of the implemented FFT processing used throughout the measurement analysis, ensuring that the reported frequency-domain results are reliable.

6. **Conclusion**: Summarises the measurement findings of the chapter and prepares the transition to the modelling and simulation work presented in the subsequent chapters.

Throughout this work, all voltages use a local chassis reference as defined by the measurement or simulation setup. This applies to both AC and DC quantities.

On the AC side, voltages appear between a phase conductor and the local chassis reference, referred to as phase-to-chassis voltages. In figures and plots, this quantity may appear as U_{phase}, but it always represents a phase-to-chassis voltage.

On the DC side, voltages appear between the positive or negative DC conductor and the local chassis reference, referred to as DC(+)-to-chassis, DC(-)-to-chassis or pole-to-chassis voltages. Differential-mode (DM) and common-mode (CM) voltages follow from these pole-to-chassis voltages.

Since the chassis and cable screens do not form an ideal equipotential reference, the term chassis refers to a local reference node rather than an absolute ground, and its voltage may vary spatially within the vehicle. This definition ensures consistent interpretation of both measured and simulated results.

4.1 Results from impedance measurements of the cables and junction boxes on a bus and a truck

This section builds on the modelling structure introduced in previous chapters and prepares the ground for the validation steps that follow.

The models of cables and junction boxes (JBs), which are used for comparison in this section, are developed in detail in Chapter 5, Subsection 5.4.14 for the cables and Subsection 5.4.15 for the junction box. The purpose here is not to introduce the modelling methodology itself, but to provide a reference for evaluating how well the simplified model structure matches the measured impedance of the real vehicle harness. This comparison serves as an early validation step before the complete modelling framework is presented in Chapter 5. The simulation model of the cable is frequency dependent but cannot handle this dependency dynamically; therefore, the frequency of interest is set explicitly in the simulation model for each simulation.

The first comparison originates from differential-mode (DM) impedance measurements performed on a bus, according to Figure 4.1. All junction boxes (JBs) and charging switch units (CSUs) have more connections than those shown in Figure 4.1, but these are disconnected during the measurement in order not to interfere with the measurement loop. The purpose is to measure the impedance of a combined circuit that could, in principle, have been assembled outside the vehicle. The results are shown in Figure 4.2 for a model valid at 1 kHz and in Figure 4.3 for a model valid at 1 MHz.

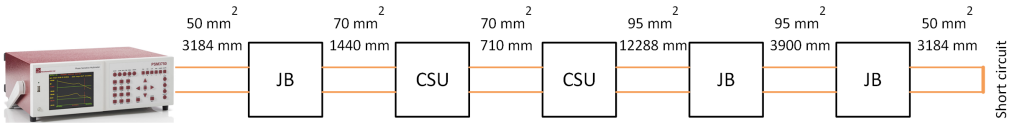


Figure 4.1: Circuit diagram of the measured cable–JB structure on the bus platform. The CSU is a junction-box variant containing an internal contactor that isolates the charging inlet. The diagram shows the measurement configuration used for comparing the real vehicle impedance with the LCR characterisation and the PLECS-based model. Other subsystems are disconnected from JBs and CSUs in order not to interfere with the measurement. This circuit represents the connections from an EMD to the battery.

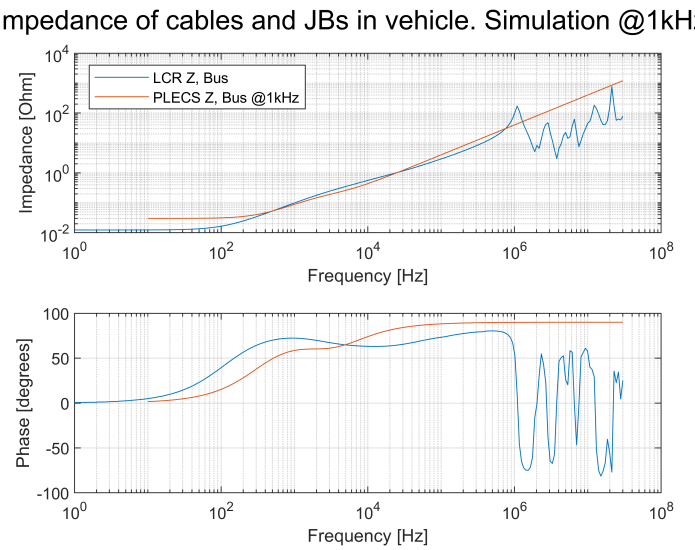


Figure 4.2: Low-frequency differential-mode impedance at 1 kHz of the measured cable–JB structure on the bus. The impedance is primarily resistive in this range, and the simulated model aligns closely with both the LCR measurement and the PLECS representation.

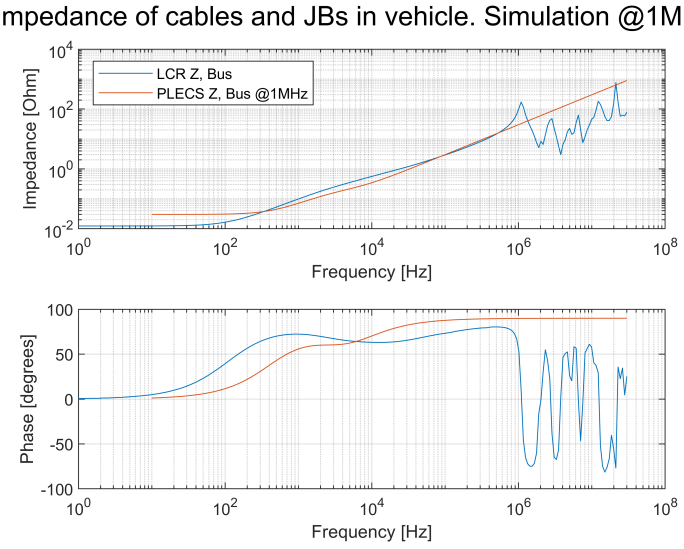


Figure 4.3: High-frequency differential-mode impedance at 1 MHz of the same cable–JB structure. In this frequency range, parasitic effects such as connector inductance and distributed capacitance dominate. Small deviations between simulation and measurement occur due to simplified high-frequency assumptions in the model, while the overall trend is preserved.

The second comparison is based on differential-mode impedance measurements per-

formed on a truck platform, shown in Figure 4.4. The results are presented in Figure 4.5 at 1 kHz and in Figure 4.6 at 1 MHz.

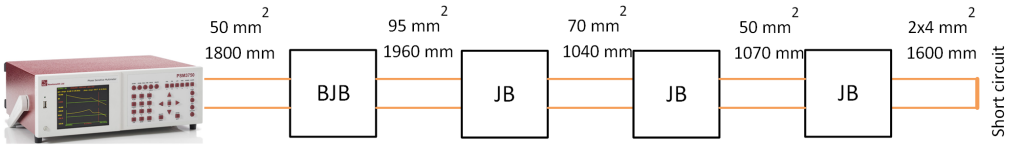


Figure 4.4: Circuit diagram of the measured cable–JB structure in the FH2592 truck platform. A BJB variant is used for the battery-side connection, and several JB types appear along the measurement path. The diagram shows how DCDC1, BP3, and the intermediate JB structures are interconnected for impedance measurement. Other subsystems are disconnected from JBs and the BJB in order not to interfere with the measurement. This circuit represents the connections from an EMD to the battery.

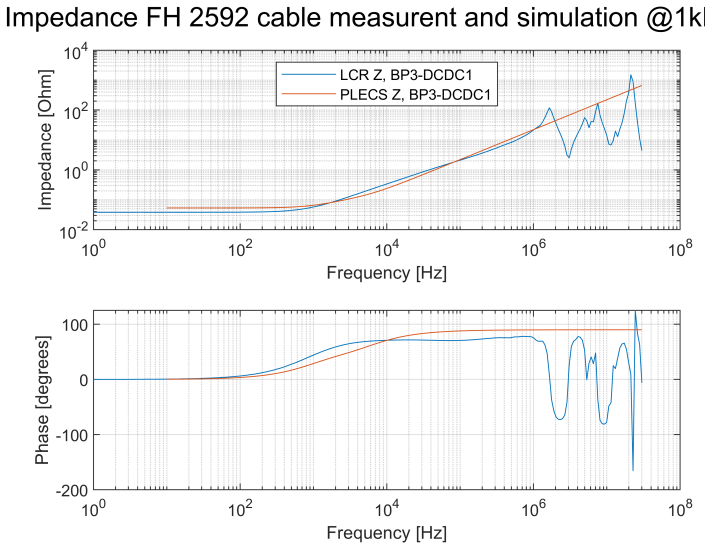


Figure 4.5: Differential-mode impedance comparison at 1 kHz for the FH2592 truck harness. The measured impedance aligns well with the simulated model, confirming that the low-frequency resistive–inductive behaviour is captured accurately.

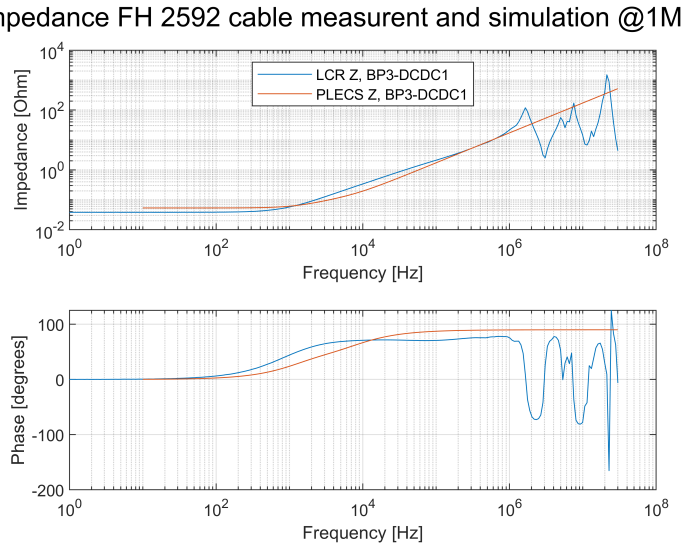


Figure 4.6: Differential-mode impedance comparison at 1 MHz for the FH2592 truck harness. High-frequency deviations occur due to parasitic effects in connectors and JB geometries and due to simplified high-frequency assumptions in the model. The overall trend is, however, preserved.

Although the impedance comparison is shown only at 1 kHz and 1 MHz, this does not imply that the model is valid only at these discrete frequencies. The cable model used in this work is frequency dependent, and each simulation uses an explicitly set frequency point, whereas the junction box models are frequency independent within the considered range. Each selected frequency point therefore represents a limited frequency region around that point, in which the cable impedance behaviour is governed by the same dominant physical mechanisms. The validation at 1 kHz and 1 MHz thus demonstrates that the model captures the correct impedance trends in the frequency regions most relevant for subsequent differential-mode and common-mode analyses. At low frequencies around 1 kHz, the differential-mode behaviour is dominated by the resistive–inductive structure of the harness, whereas the common-mode behaviour of interest occurs primarily in the higher-frequency range above 100 kHz, where parasitic capacitances, connector inductances, and cable geometry dominate. The implications of this validation, and the application of the frequency-point-based cable modelling approach in system-level simulations, are discussed in detail in Chapter 5. A full wideband characterisation on a complete vehicle is not practically feasible, but the adopted approach provides sufficient accuracy for the intended CM and DM analyses.

Conclusion

When the cable and junction box models evaluated in this chapter are compared with measured impedances of real cable–JB structures, good agreement is obtained across the dominant frequency range of interest. Deviations above 1 MHz are observed and can be attributed to simplified assumptions in the cable and junction box representations. These simplifications are deliberate, as more detailed high-frequency models would significantly increase simulation complexity without providing commensurate benefit for the intended system-level analyses.

The comparison at 1 kHz and 1 MHz demonstrates that the measured and simulated impedances exhibit consistent behaviour in the frequency regions that are most relevant for differential-mode and common-mode phenomena, respectively. In this chapter, the agreement between measurement and simulation is used to establish confidence that the simplified cable and junction box representations capture the dominant physical effects governing impedance behaviour. The formal development and validation of the underlying modelling approach are presented in Chapter 5.

Although the models are applied over a wider frequency range in subsequent analyses, the key requirement for common-mode investigations is not exact wideband impedance matching, but the correct representation of how impedance magnitude and phase evolve with frequency in the regions where common-mode coupling is significant. The results presented here therefore provide a sufficient and physically consistent basis for the system-level simulations and comparisons with measurements presented in the later chapters.

4.2 Measurements affected by the break-out boxes

This section follows naturally from the previous discussion on impedance validation and examines how the measurement interface itself influences the observed behaviour.

Although some of the investigations presented in this section are performed in a laboratory environment, the purpose is to quantify the influence of the measurement setup on vehicle-level common-mode (CM) measurements. The laboratory experiments are therefore not intended to replicate the full traction voltage system (TVS), but to isolate and characterise the contribution of the break-out box (BoB) itself.

During vehicle measurements, unexpected results are observed that cannot be explained by the anticipated behaviour of the TVS alone. The unexpected behaviour becomes visible in the common-mode voltage u_{cm} for the electrical machine drives EMD1–EMD3, measured in the break-out boxes shown in Figure 4.7, together with the corresponding common-mode current i_{cm}.

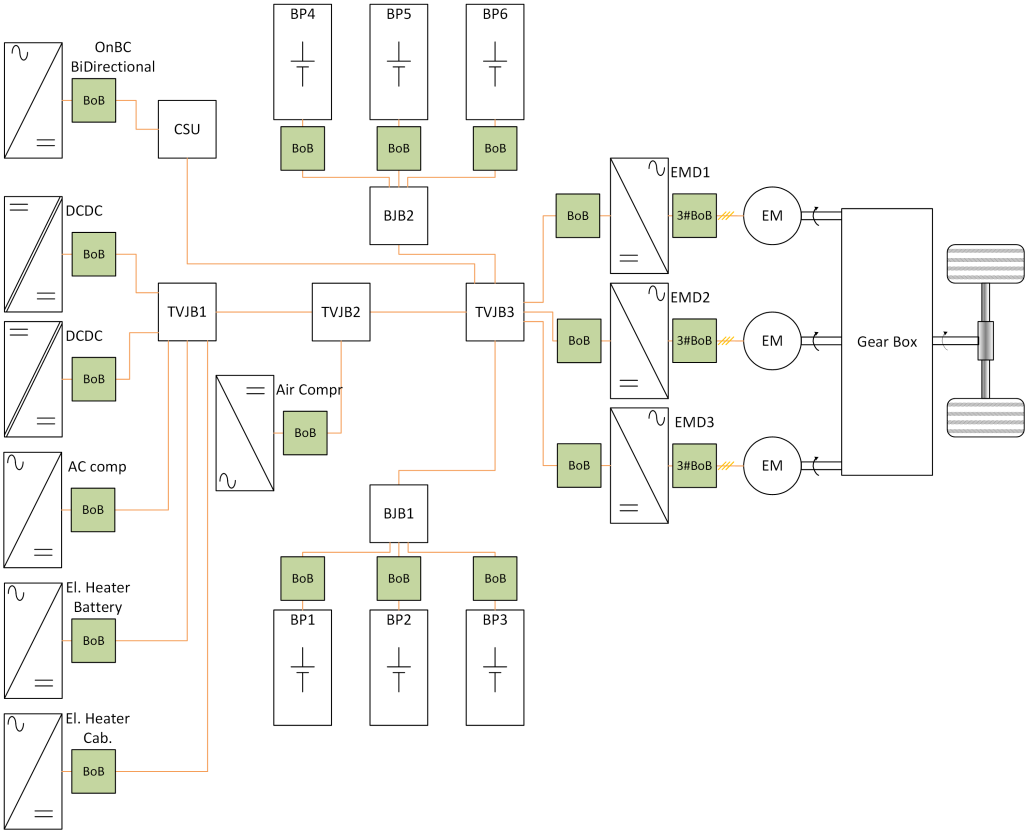


Figure 4.7: FM1156 truck architecture with break-out boxes.

The unexpected result is illustrated for EMD1 in Figure 4.8. At first glance, u_{cm} measured at EMD1–EMD3 appears similar, whereas the magnitude measured at the battery BP4 is higher. This behaviour is not immediately intuitive, as the battery is located further away from the switching units and might therefore be expected to exhibit a lower voltage level.

The explanation is that the common-mode current is primarily returned through the parasitic capacitance of the battery. The battery therefore acts as the effective common-mode reference point, and the common-mode voltage is established there before the current propagates back towards the electrical machine drives. As the common-mode current flows through the connecting cables and junction boxes, a voltage drop appears across their impedance. Consequently, the common-mode voltage measured at the EMDs is reduced relative to that measured at the battery. If the cable and junction box impedances between the battery and the EMDs were ideal, the measured common-mode voltage levels would coincide.

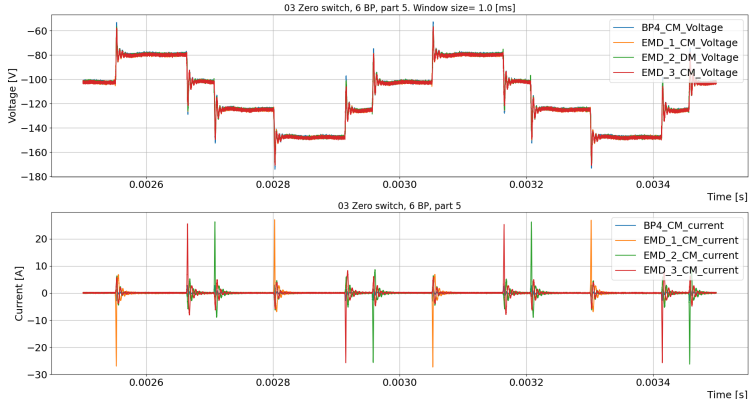


Figure 4.8: Common-mode voltage at EMD1–EMD3 and BP4 (upper graph), and corresponding common-mode currents (lower graph). The common-mode voltage at BP4 is higher due to cable voltage drops.

The three EMDs switch at different instants, which is visible in the lower graph of Figure 4.8. The EMD that switches exhibits a higher amplitude in i_{cm}. A closer inspection of the switching event for EMD1, slightly after 3 ms, is shown in Figure 4.9.

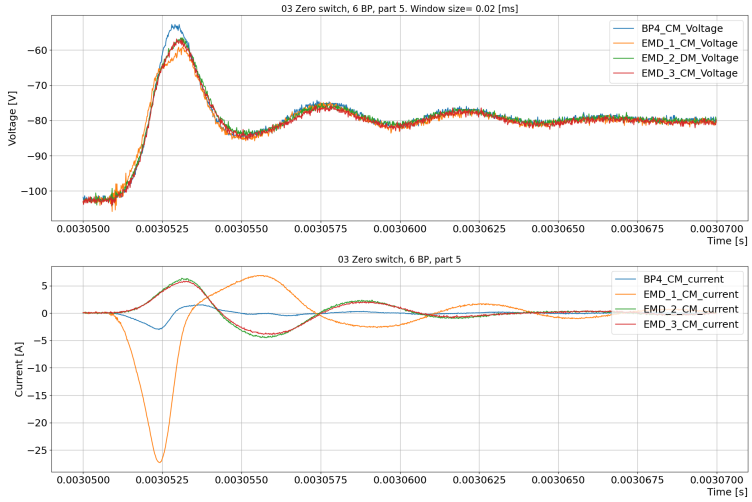


Figure 4.9: Zoom-in around the switching instant of EMD1. The battery voltage remains the highest, but a skewed shape in u_{cm} for EMD1 becomes visible.

A further zoom in Figure 4.10 reveals two distinct effects for EMD1:

(1) a skewed top-left corner of u_{cm}, and

(2) an earlier voltage rise compared with EMD2, EMD3, and BP4.

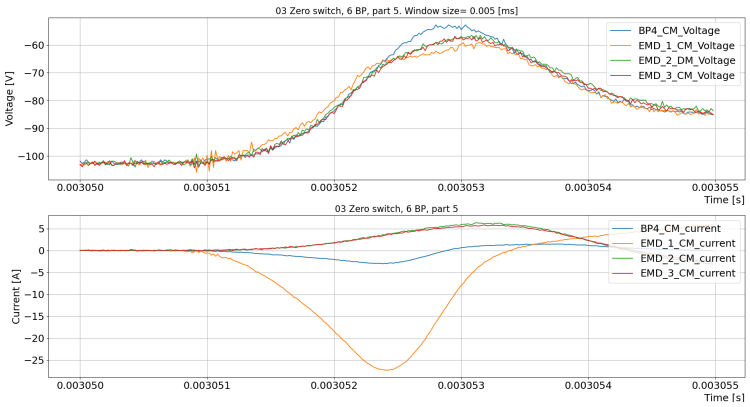


Figure 4.10: Further zoom of the switching event. The common-mode voltage at EMD1 exhibits a skewed leading edge and a premature voltage rise compared with EMD2, EMD3, and BP4.

These observations suggest that the deviation in u_{cm} for EMD1 depends on the sign of the current derivative. The skewed shape appears when the derivative of i_{cm} is positive, whereas the premature voltage rise appears when the derivative is negative. A plausible hypothesis is that parasitic inductance in the break-out box introduces a voltage drop when the common-mode return current flows through the busbar structure.

To investigate this effect, dedicated laboratory measurements are performed with the break-out box itself as the device under test (DUT). These tests demonstrate that magnetic fields in the busbars, together with the inductance of conductors and measurement leads, induce voltages on the measurement outputs.

To reproduce the high current derivatives present in the TVS, a test setup is constructed using an H-bridge and an inductor, as shown in Figure 4.11. In the vehicle measurements, current derivatives of approximately 20 A/µs are observed, while the laboratory setup generates a representative derivative of 16 A/µs.

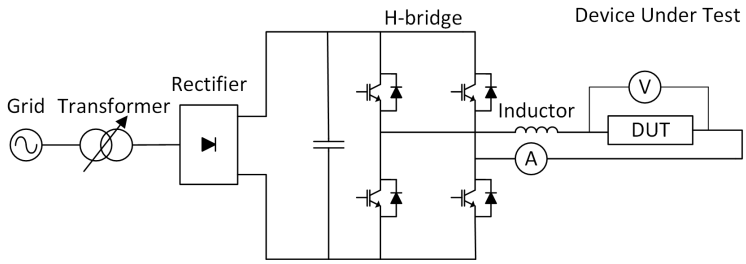


Figure 4.11: Test setup used to generate current pulses with high current derivative using an H-bridge and an inductor.

In Figure 4.12, the setup from Figure 4.11 is simplified into a generic pulse generator to emphasise the measurement connections used to characterise the influence of the BoB.

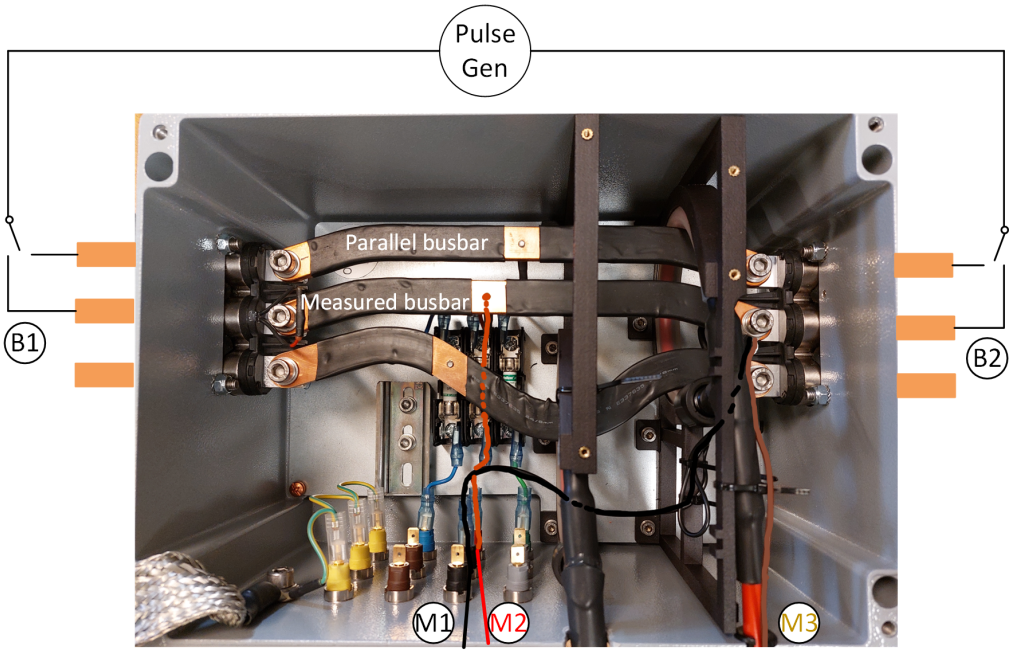


Figure 4.12: Measurement setup for examining induced voltages in the break-out box busbar and measurement wires. M1, M2 and M3 represent measurement points along different wires. B1 and B2 represent the busbar terminals. Measurements are performed with current either in the measured busbar or in the parallel busbar.

All measurements below are performed both with current in the measured busbar or with current in the parallel busbar:

- B1–B2: voltage over the busbar with and without current,
- M1–B2: voltage over the black measurement wire,
- M2–B2: voltage over the red wire and part of the busbar,
- M3–B2: voltage over the brown measurement wire,
- M1–M2: voltage between black and red wires through the busbar,
- M2–M3: voltage between red and brown wires through the busbar.

The measurement results corresponding to the above list are presented below. In each diagram, the upper trace shows that the current ramp is essentially identical regardless of whether the excitation current flows in the measured busbar or in the parallel busbar. The lower trace shows that non-zero voltages are measured along the measured busbar in both cases, that is, both when the excitation current flows in the measured busbar and when it flows in the parallel busbar. This demonstrates that the measured voltages are influenced by

magnetic coupling and inductive effects in the break-out box, independently of the location of the excitation current.

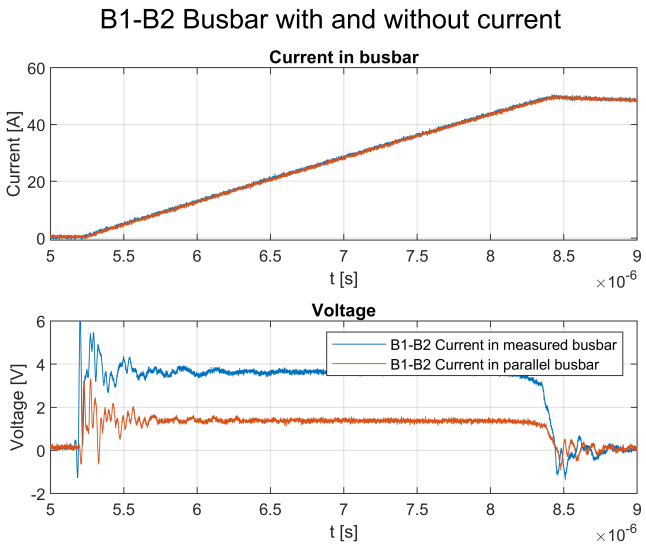


Figure 4.13: Measured voltage over the busbar (B1–B2) with current in the measured busbar and in the parallel busbar.

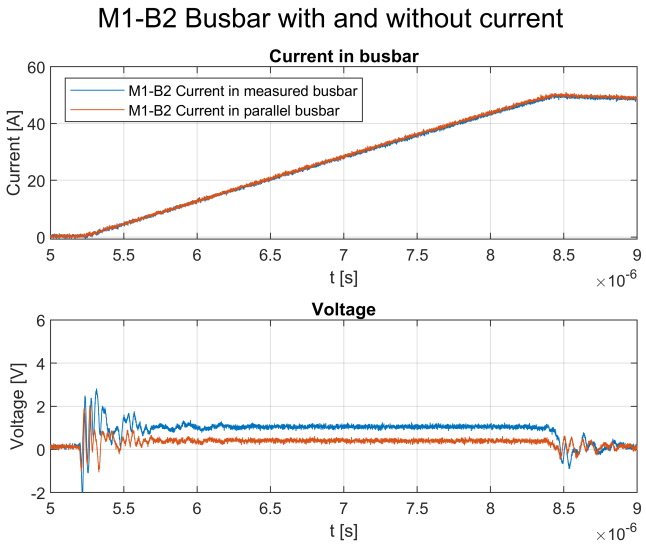


Figure 4.14: Measured voltage from M1 to B2 (black wire). Measurements are performed with current in both the measured busbar and the parallel busbar.

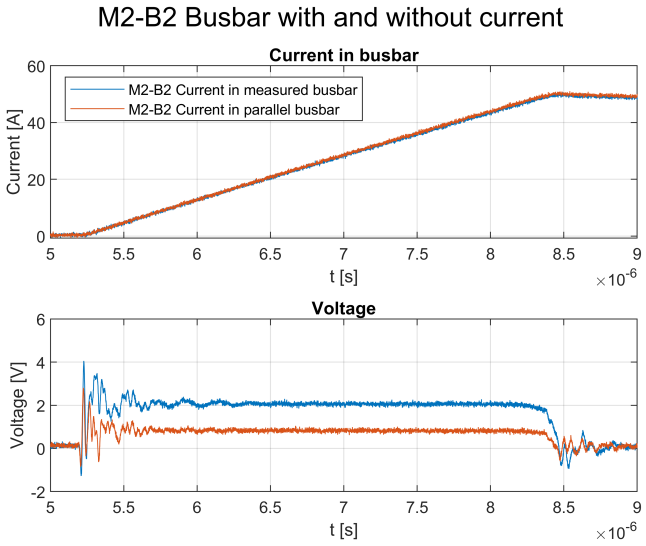


Figure 4.15: Measured voltage from M2 to B2 (red wire and part of the busbar), with current in the measured and parallel busbars.

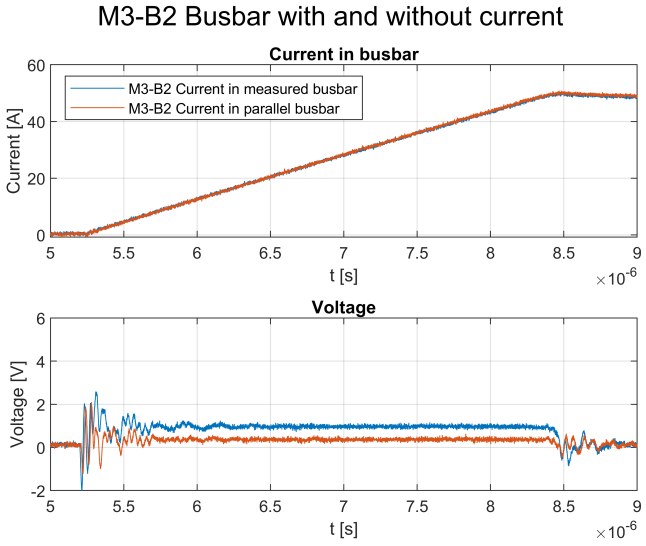


Figure 4.16: Measured voltage from M3 to B2 (brown wire), with current in the measured and parallel busbars.

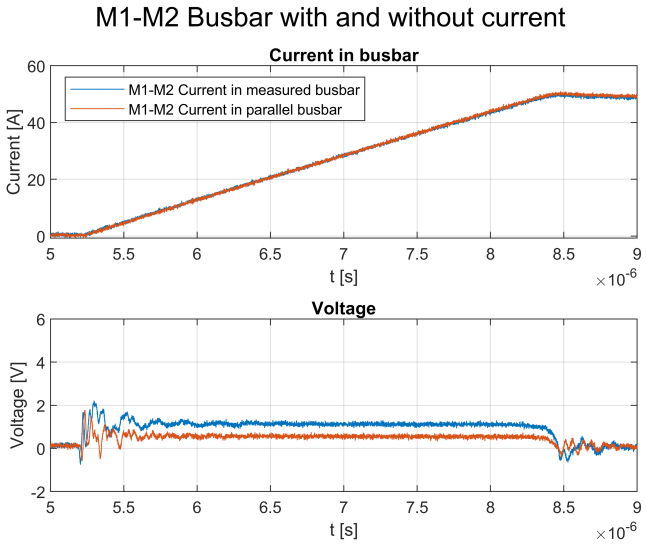


Figure 4.17: Measured voltage from M1 through the busbar section and over the red wire to M2. Measurements are performed with both busbars energised separately.

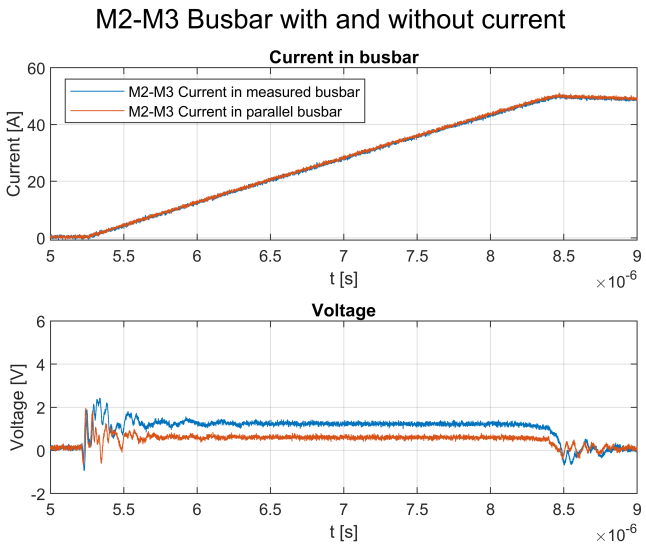


Figure 4.18: Measured voltage between M2 and M3 via the busbar section. Currents flow either in the measured busbar or in the parallel busbar.

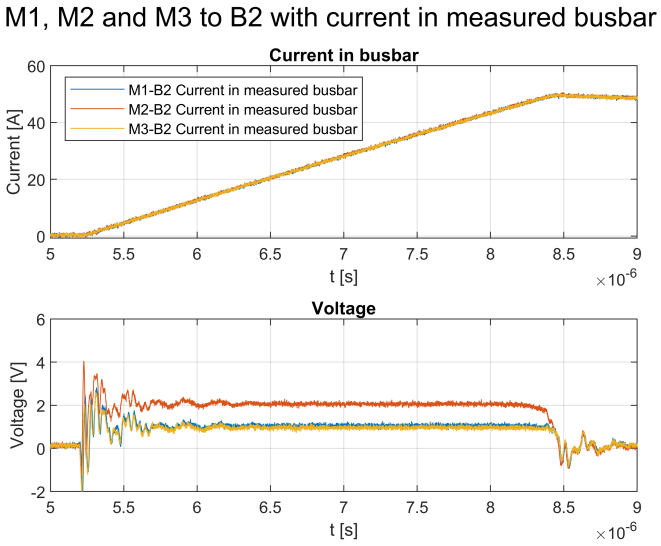


Figure 4.19: Voltages M1–B2, M2–B2 and M3–B2 with current in the measured busbar. M1–B2 and M3–B2 exhibit similar induced voltages. M2–B2 also includes a busbar segment, contributing to an additional inductive drop.

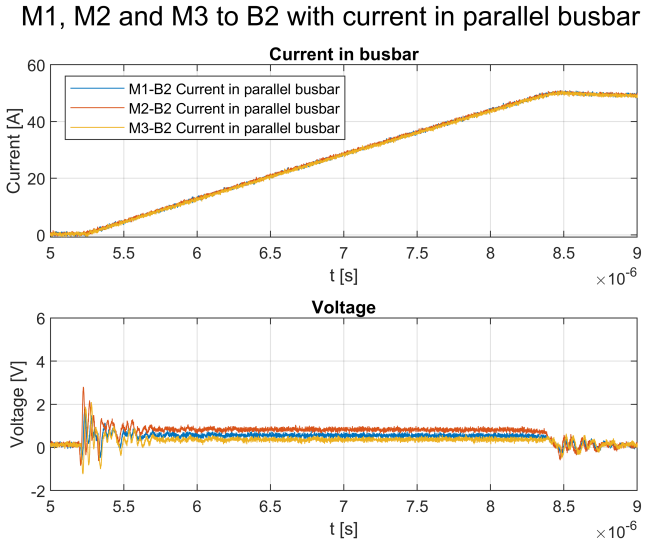


Figure 4.20: Voltages M1–B2, M2–B2 and M3–B2 with current in the parallel busbar. Without inductive voltage drop along the measured busbar, the remaining induced voltages reflect magnetic coupling from the parallel conductor.

The results show that induced voltages appear both when the current flows in the measured busbar and when it flows in the parallel busbar. In both cases, magnetic coupling generates voltages in the measurement wires and in the break-out box busbar. However, when

the current flows in the measured busbar, the inductive voltage drop along the conductor adds to the magnetic coupling, resulting in a larger measured voltage.

The high di/dt currents that occur in the TVS are superimposed AC components, and their influence on the break-out box cannot be disregarded. Awareness of these effects is essential when interpreting CM and DM measurements. A detailed quantitative explanation of the skewed behaviour is presented in Chapter 6.

Conclusion

The measurements demonstrate that the break-out box introduces systematic deviations caused by magnetic coupling and busbar inductance. These deviations, on voltage measurements, appear both when current flows in the measured busbar and when it flows in the parallel busbar. When the current flows in the measured busbar, the inductive voltage drop along the conductor adds to the magnetically induced voltage, leading to a higher measured value.

A key implication is that the measurement system itself becomes part of the electrical circuit. The BoB modifies the local voltage distribution, meaning that alterations in the measured waveform do not necessarily originate from the TVS but may instead arise from the measurement interface. This is clearly illustrated in Figures 4.8 to 4.10, where the common-mode voltage of EMD1 shows a skewed leading edge and a premature rise compared with EMD2, EMD3 and BP4.

The magnitude of this deviation is approximately 10 V between the switching and non-switching cases when measured on the vehicle. Interpreted in relation to the full CM transient of roughly 50 V, the deviation is moderate in absolute terms but significant because it affects the shape of the CM waveform and may lead to incorrect interpretation if not accounted for.

Importantly, the order of magnitude of the deviation observed on the vehicle aligns with the laboratory characterisation of the BoB itself. The induced voltages measured in Figures 4.13 to 4.20 reach levels of approximately 4 V when a single BoB is included in the laboratory setup. In the vehicle architecture, shown in Figure 4.7, two BoBs are included in the return path. This naturally leads to a larger cumulative voltage offset of around 10 V, which agrees with the deviation observed in the vehicle measurements.

The consistency between the one-BoB laboratory characterisation and the two-BoB vehicle behaviour confirms that the skewed voltage shape observed in the TVS is not caused by the TVS architecture itself, but by the measurement interface. Awareness of these effects is essential for accurately interpreting CM and DM measurements and for the subsequent comparison between measurements and simulations in Chapter 6.

4.3 Results from CMDC voltage measurements on a truck

This section follows the impedance and break-out box investigations and introduces the measured CMDC voltage behaviour at vehicle level. It provides the link between subsystem effects and complete-system behaviour.

The purpose of this section is to present the measured common-mode DC (CMDC) voltage and common-mode current behaviour in a full heavy-duty electric truck under zero-torque operating conditions. These measurements constitute the empirical foundation for the CM simulation analysis in Chapter 6.2. While the simulations in Chapter 6.2 provide insight into the physical mechanisms behind CM disturbances, the results in this section present the corresponding behaviour as measured in the complete vehicle.

The theoretical background for CMDC voltage generation is given in Chapter 2, and switching-state dependent CM behaviour is analysed later in this thesis. In the vehicle, the CMDC voltage arises from the interaction between the switching states of the electric machine drives (EMDs), the parasitic capacitances in the EMDs, cables and EM windings, and the return capacitances distributed throughout the traction voltage system (TVS). These measurements capture these effects exactly as they appear in the real TVS.

The measurements presented in this chapter are obtained on different heavy-duty vehicle platforms (FE280, FM1156 and FH2592). This is a natural consequence of the multi-year development of the measurement system and the varying availability of vehicles. The traction voltage system (TVS) architecture is, however, functionally equivalent across all platforms, ensuring that the measured CM phenomena are directly comparable.

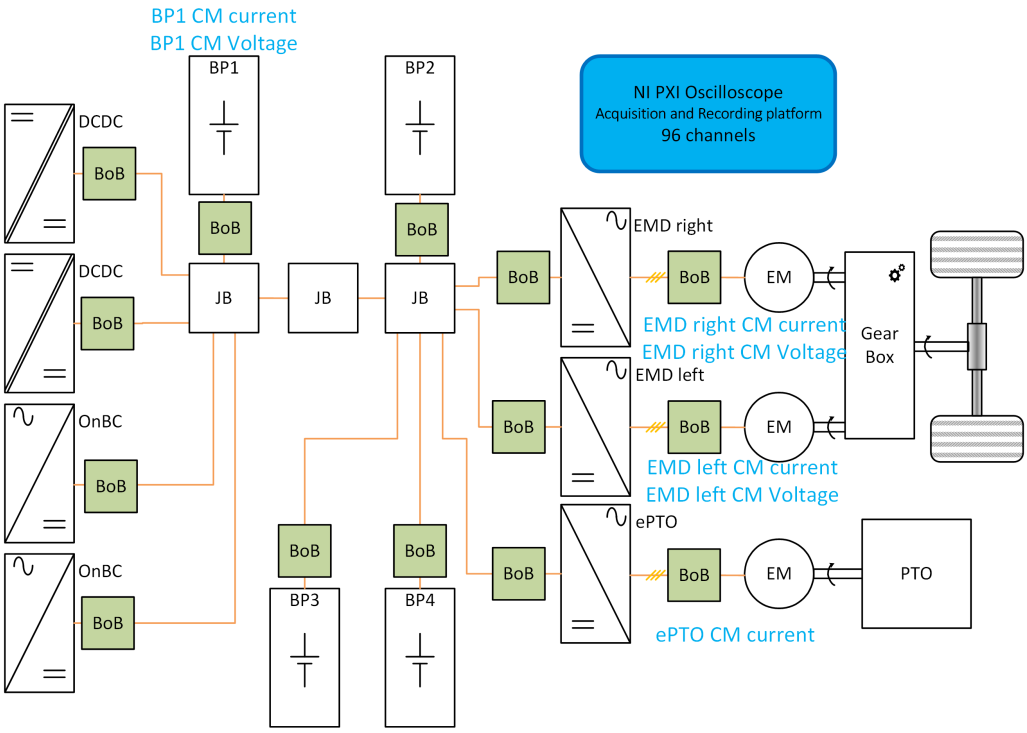


Figure 4.21: Measured common-mode related quantities in the Volvo FE280 truck. The system contains DCDC converters, electric machine drives (EMD), the ePTO EMD, onboard charger (OnBC), batteries, junction boxes (JB), and break-out boxes (BoB).

All measurements in this chapter are performed with the truck standing still and with zero torque command, meaning that the three-phase output voltage of each EMD is the zero voltage vector, i.e. all three phases of the same electric machine drive switch at essentially the same instant. Under these operating conditions, the CMDC voltage and the corresponding common-mode currents are determined by the switching states of the electric machine drives and by asymmetries in the parasitic capacitances and inductances of the traction voltage system (TVS).

The measurement results in this section cover three phenomena:

- The dependency of the CMDC voltage on the X-factor, i.e. the ratio between the AC side of the EMD common-mode capacitance, C_{wind} in Figures 4.22 to 4.25, and the battery/system return capacitances, C_{CM} in Figures 4.22 to 4.25 (Section 4.3.1).
- The elimination of CMDC voltage and CM current when the two traction EMDs switch with a relative phase shift of 180°, causing their CM contributions to cancel (Section 4.3.2).
- The amplification of CM current when the traction EMDs switch in phase, producing maximal simultaneous asymmetry (Section 4.3.3).

To aid interpretation of the following measurement plots, the four possible zero-voltage switching states that occur when two EMD converters operate simultaneously are illustrated below:

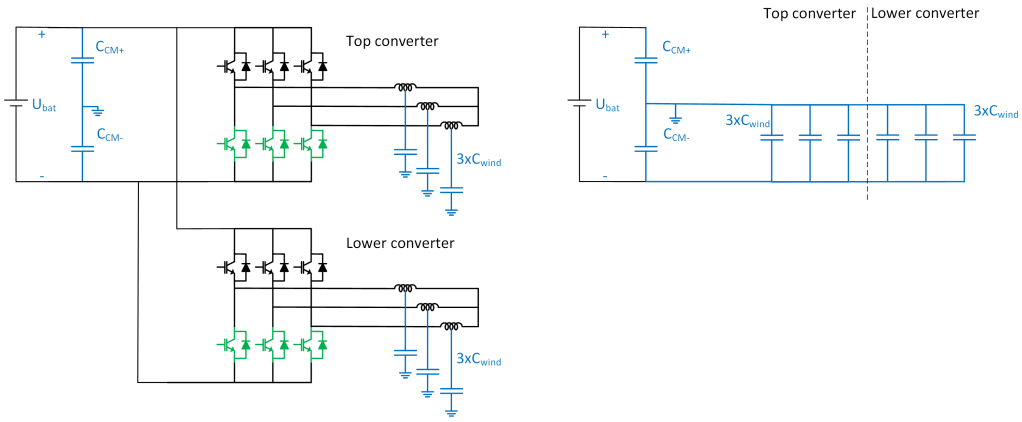


Figure 4.22: Both converters in the zero-vector state $(0, 0, 0)$.

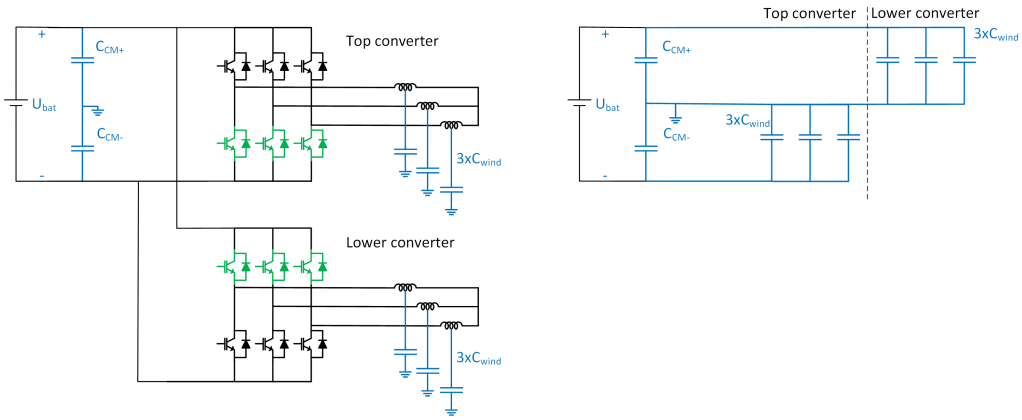


Figure 4.23: Upper converter in $(0, 0, 0)$ and the lower converter in $(1, 1, 1)$.

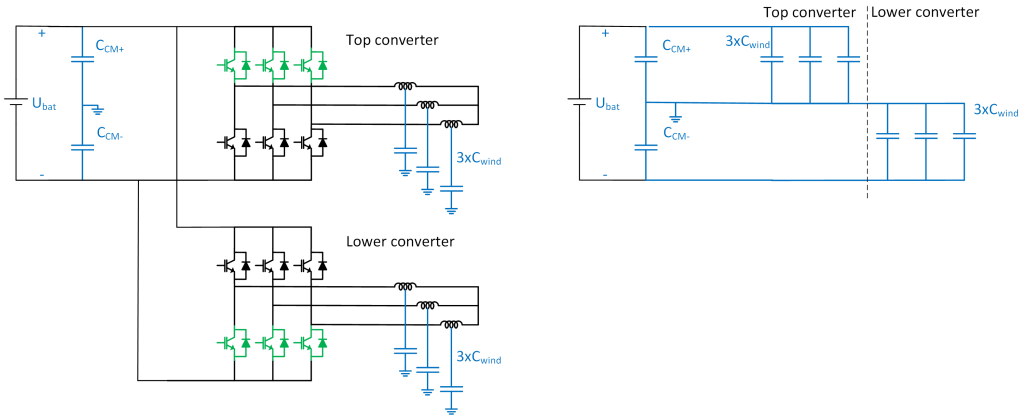


Figure 4.24: Upper converter in $(1, 1, 1)$ and the lower converter in $(0, 0, 0)$.

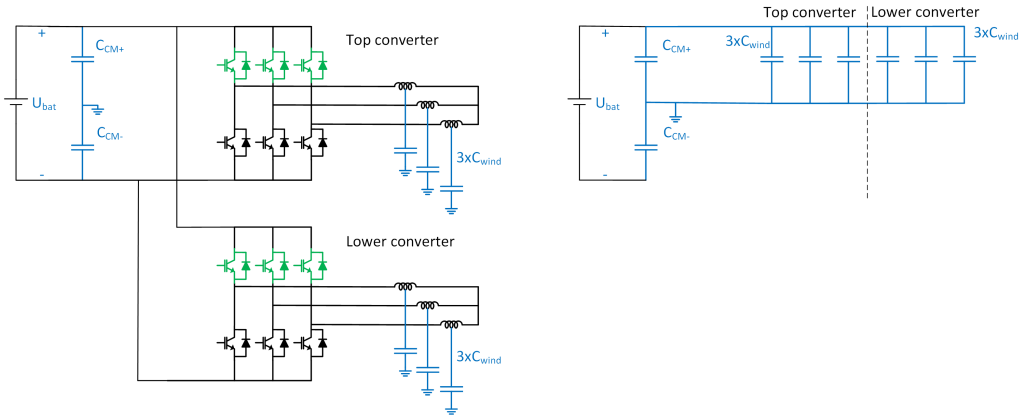


Figure 4.25: Both converters in the zero-vector state $(1, 1, 1)$.

These switch-state combinations occur with different relative timing depending on the phase relationship between the EMD modulation carriers. Note that the timing circuits defining the modulation of each EMD are not perfectly synchronised. As a result, the modulation waves drift slowly relative to each other, giving rise over time to the different switching patterns shown in Figures 4.22 to 4.25. The measured CM behaviour in the subsequent subsections reflects these switching patterns exactly as they appear in the real vehicle.

This section is organised as follows:

1. **CMDC voltage compared to theory and simulations with varied X-factor**: Investigates the dependency of the CMDC voltage on the X-factor, defined as the ratio between machine-side and return-path common-mode capacitances, and compares measurements with analytical expressions and simulations.

2. **CMDC voltage and current elimination**: Examines the operating condition where two traction EMDs switch with an approximate 180° phase shift, leading to cancellation of their common-mode contributions.

3. **Measured CM current maximum**: Analyses the opposite case, where the traction EMDs switch in phase.

4. **Delayed switching to and from** $(0, 0, 0)$ **and** $(1, 1, 1)$: Studies how intentional delays influence transient CM behaviour.

5. **CM frequency content at the DC side**: Characterises the frequency content of the measured CM currents using FFT analysis and defines upper frequency limits for modelling.

4.3.1 CMDC voltage compared to theory and simulations with varied factor X

This subsection presents measurements of the common-mode DC (CMDC) voltage at the battery terminals for two different values of the X-factor. According to Equation (2.17), the CMDC voltage depends directly on the value of X. To investigate this dependency experimentally, additional common-mode (CM) capacitance is inserted in the Break-Out Boxes (BoB) on the DC side of the electric machine drives (EMDs), see Figure 4.21. This increases the CM-capacitance in the return path and modifies the effective X-factor of the traction voltage system (TVS).

Two operating points are investigated, corresponding to the measured values $X_1 = 11.5$ and $X_2 = 31.1$. The traction battery voltage is 650 V. Using Equation (2.17), the expected BP1 CMDC voltages are:

$$u_{CMDC} = \frac{U_{bat}}{2X_1 + 1} = \frac{650}{2 \cdot 11.5 + 1} = 27 \text{ V} \tag{4.1}$$

$$u_{CMDC} = \frac{U_{bat}}{2X_2 + 1} = \frac{650}{2 \cdot 31.1 + 1} = 10.3 \text{ V} \tag{4.2}$$

The corresponding measured CMDC voltages are 30.4 V for X_1 and 11.9 V for X_2, shown as "BP1 CM voltage" in Figures 4.26 and 4.27. The deviation between measured and calculated values is within ten per cent, which is acceptable given the system complexity and parasitic elements not included in the analytical expression.

The waveform behaviour differs from the idealised analytical case. In the truck, two EMDs switch independently with slightly different switching frequencies and with drifting modulation carrier phases. As a consequence, the machine-side common-mode capacitances C_{asym} are sometimes connected to the same pole of the TVS and sometimes to opposite poles. When they connect to opposite poles, their contributions partially cancel each other. This explains the quasi-square-wave CMDC voltage shape observed in the measurements.

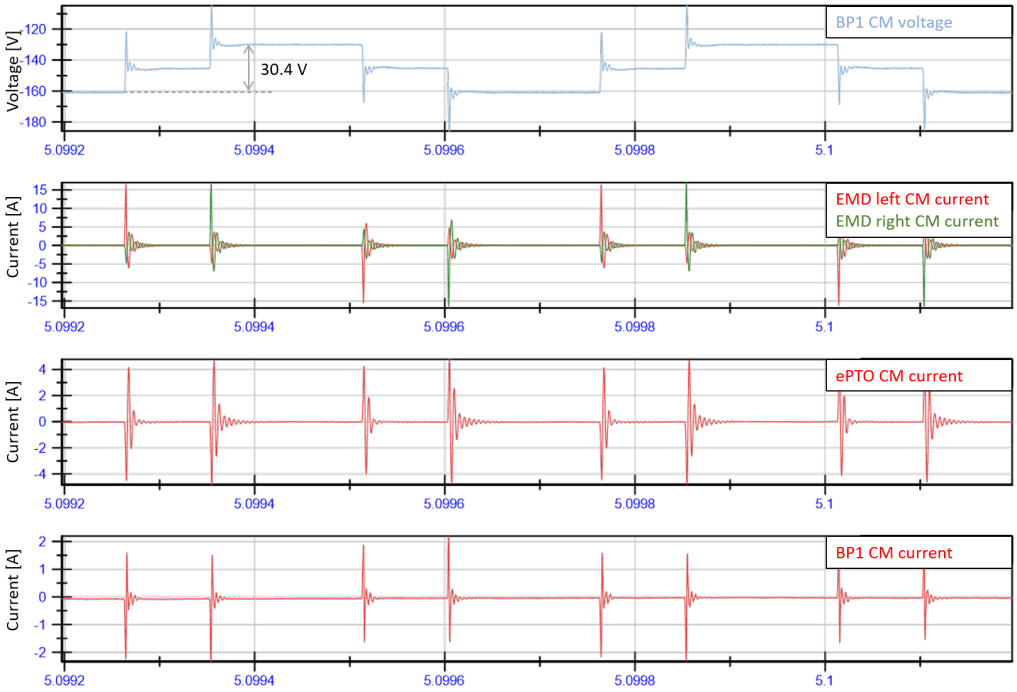


Figure 4.26: Original configuration with X_1 = 11.5.

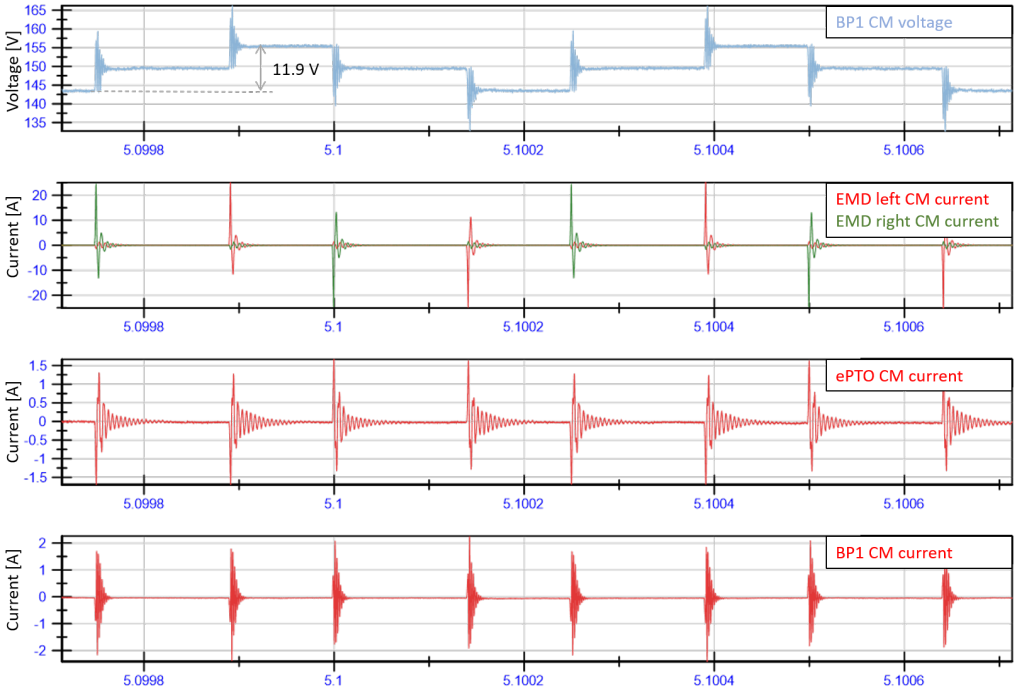


Figure 4.27: Configuration with increased CM-capacitance giving X_2 = 31.1.

Conclusion

The measurements confirm the theoretical dependency between the CMDC voltage and the X-factor. Increasing the CM-capacitance on the EMD side reduces the CMDC voltage in accordance with Equation (2.17). The measured values agree with the analytical prediction within ten per cent. Independent switching of the two EMDs explains the observed quasi-square-wave behaviour due to intermittent cancellation of the machine-side asymmetry contributions.

4.3.2 CMDC voltage and current elimination at simultaneous 180° phase-shifted switching

In Subsection 4.3.1, the CMDC behaviour is examined as a function of the X-factor. This subsection instead considers the case where the two traction converters switch simultaneously but in opposite phase.

Unless the modulation of the two EMDs is intentionally synchronised, their switching instants drift relative to each other. This behaviour is already visible in Subsection 4.3.1, and is illustrated here by examining the CM currents measured on the right EMD, left EMD and ePTO EMD, see Figure 4.21. Only EMD1 and EMD2 switch in this measurement. The ePTO EMD is passive, and no switching is performed. Over a time interval of

approximately 8 s, the switching of the two traction EMDs gradually drifts in and out of phase, as shown in Figure 4.28.

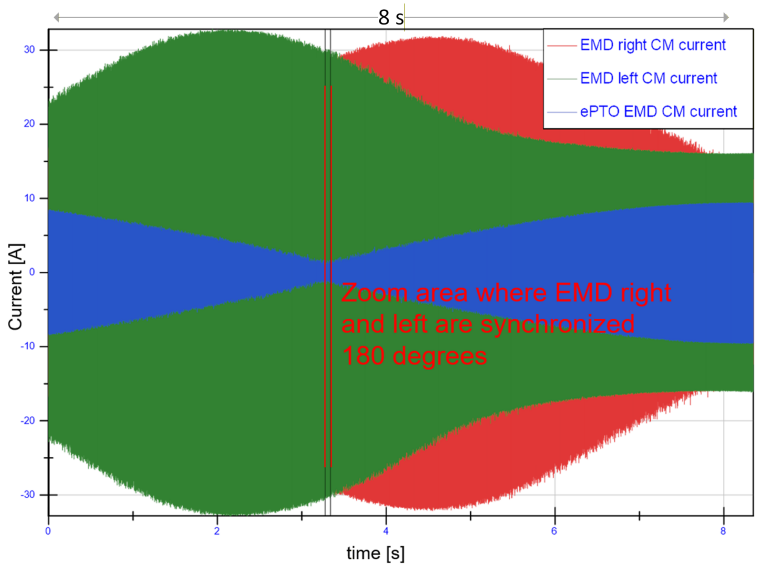


Figure 4.28: Common-mode currents of the right EMD, left EMD and ePTO EMD, see Figure 4.21. The ePTO EMD does not switch. The left and right EMDs switch with a drifting phase relationship. At the cursor position, the switching instants are separated by approximately 180°. The magnified region is shown in Figure 4.29.

The enlarged region in Figure 4.29 shows the instant at which the switching of the two traction EMDs is nearly 180° phase-shifted. Under this condition, the CM current contributions from the two EMDs oppose each other. Since the CM disturbances arise from the asymmetric switching states $(0, 0, 0)$ and $(1, 1, 1)$ (see Figures 4.23 and 4.24), a 180° phase shift means that when one EMD applies state $(0, 0, 0)$, the other applies $(1, 1, 1)$, and vice versa. The resulting asymmetry currents cancel to a high degree, reducing the net CM current in the system.

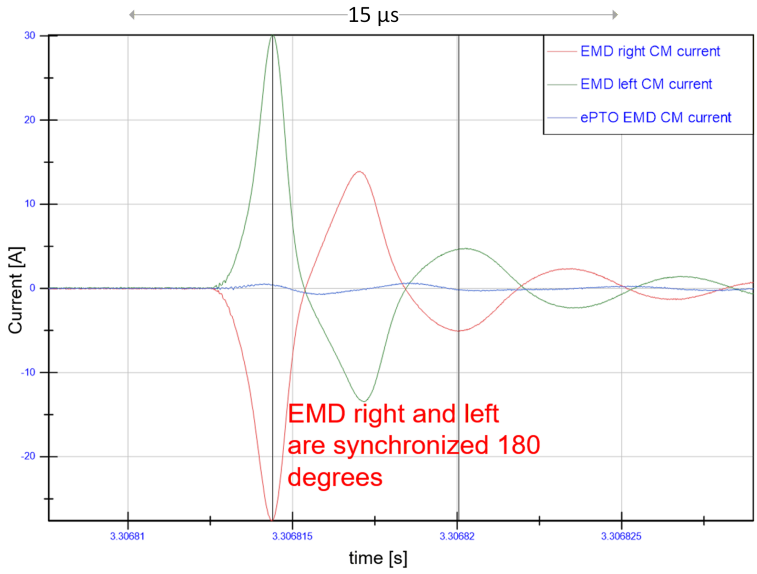


Figure 4.29: Zoom of the 180°phase-shifted switching condition. When one EMD applies the zero vector (0,0,0) while the other applies (1,1,1), the CM current contributions oppose each other. This produces near-elimination of the resulting CM current, here observed on the ePTO EMD channel.

This operating point represents an *optimal* switching condition from a CM perspective: the excitation responsible for CMDC voltage and CM current is minimised due to cancellation of the machine-side asymmetries. In contrast, the opposite case—simultaneous in-phase switching—is addressed in Subsection 4.3.3, where the CM contributions instead add constructively and the peak CM current becomes maximal.

Conclusion

When the two traction EMDs switch with an approximately 180° phase shift between their modulating waves, their CM excitation cancels almost completely. This demonstrates experimentally that the relative switching phase between converters has a decisive influence on the CMDC voltage and the resulting CM currents. By controlling or constraining the relative switching phase, CM disturbances can be significantly reduced in multi-converter traction systems.

4.3.3 Measured CM current maximum due to simultaneous in-phase switching

After examining the 180° phase-shifted case in Subsection 4.3.2, this subsection turns to the complementary condition: simultaneous in-phase switching.

In contrast to the 180° phase-shifted case discussed in Subsection 4.3.2, this subsection examines the situation in which the two traction EMDs switch *in phase*. The common-mode (CM) currents of the right EMD, left EMD and ePTO EMD are measured on the

FM280 truck, see Figure 4.21. Over a time interval of approximately 8 s, the relative phase between the left and right EMD switching drifts, and intervals of near in-phase operation can be identified, as illustrated in Figure 4.30.

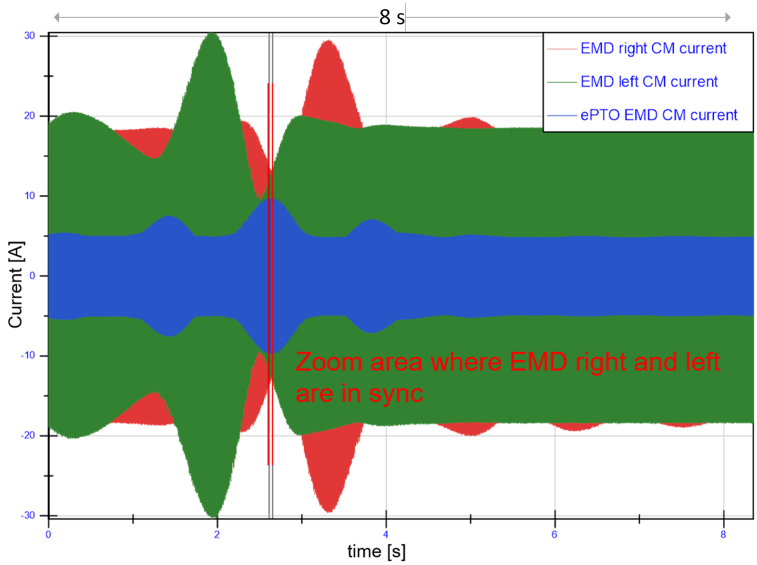


Figure 4.30: Common-mode currents of the right EMD, left EMD and ePTO EMD, see Figure 4.21. The ePTO EMD does not switch. The left and right EMDs switch with nearly in-phase modulation, which causes their CM current contributions to add constructively.

The region around the cursor in Figure 4.30 is expanded in Figure 4.31. Here, the switching of the two traction EMDs is nearly synchronised in phase. Under this condition, both converters apply the same zero vector sequence, i.e. they switch between $(0, 0, 0)$ and $(1, 1, 1)$ simultaneously, as illustrated in Figures 4.22 and 4.25. Since the asymmetry in each machine generates a CM excitation of similar polarity, the resulting CM currents from the two EMDs add rather than cancel. This leads to a pronounced increase in the net CM current observed in the system.

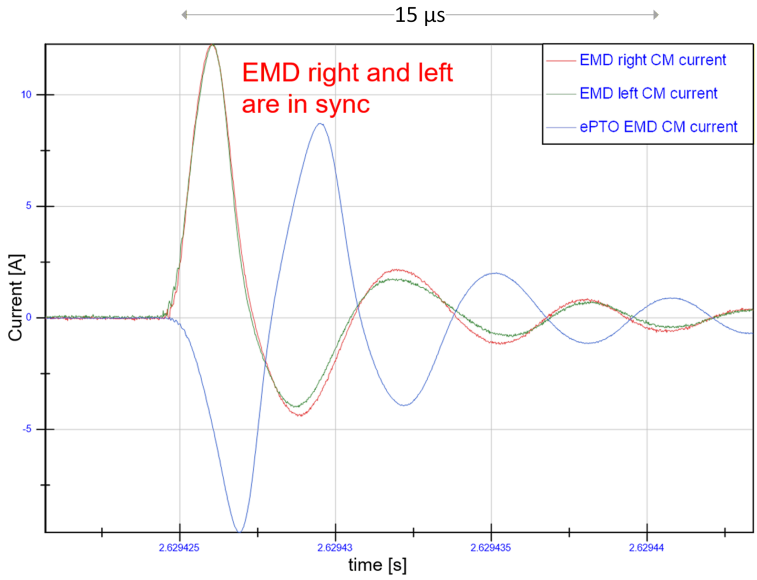


Figure 4.31: Zoom of the near in-phase switching condition. When both EMDs switch simultaneously between (0,0,0) and (1,1,1), their CM current contributions add constructively. This results in a maximum observed CM current level in the system.

Comparing Figure 4.31 with the 180° phase-shifted case in Figure 4.29 demonstrates the sensitivity of the CM behaviour to the relative switching phase. In the 180° case, the CM excitations from the two EMDs oppose each other and largely cancel, resulting in a strongly reduced CM current. In the in-phase case studied here, the CM excitations instead add constructively, leading to the highest CM current levels observed in these measurements.

Conclusion

When the two traction EMDs switch nearly in phase, their common-mode excitations add constructively and the resulting CM current in the system reaches a maximum. Together with the 180° phase-shifted case in Subsection 4.3.2, this demonstrates that the relative switching phase between converters is a key parameter for controlling CM disturbances in multi-converter traction systems.

4.3.4 Delayed switching to and from $(0, 0, 0)$ and $(1, 1, 1)$

After examining the 180° phase-shifted case in Subsection 4.3.2, this subsection turns to the complementary condition: simultaneous in-phase switching.

The common-mode DC (CMDC) voltage, defined in Subsection 2.4.3, represents the steady value reached after the switching transition is complete. Therefore, the CMDC voltage is not affected by whether the three phase legs switch simultaneously or with a delay. However, the transient common-mode (CM) voltage and current are influenced by

the timing of the phase-leg transitions. This subsection investigates how a deliberate delay between the phase legs affects the transient CM behaviour during the zero-vector transition between $(0, 0, 0)$ and $(1, 1, 1)$.

Two cases are analysed experimentally:

1. nearly simultaneous switching of all three phase legs,
2. switching with a delay of 0.4 µs between the phase legs.

The CM current is measured both with and without this delay. The measurement system layout is shown in Figure 4.32.

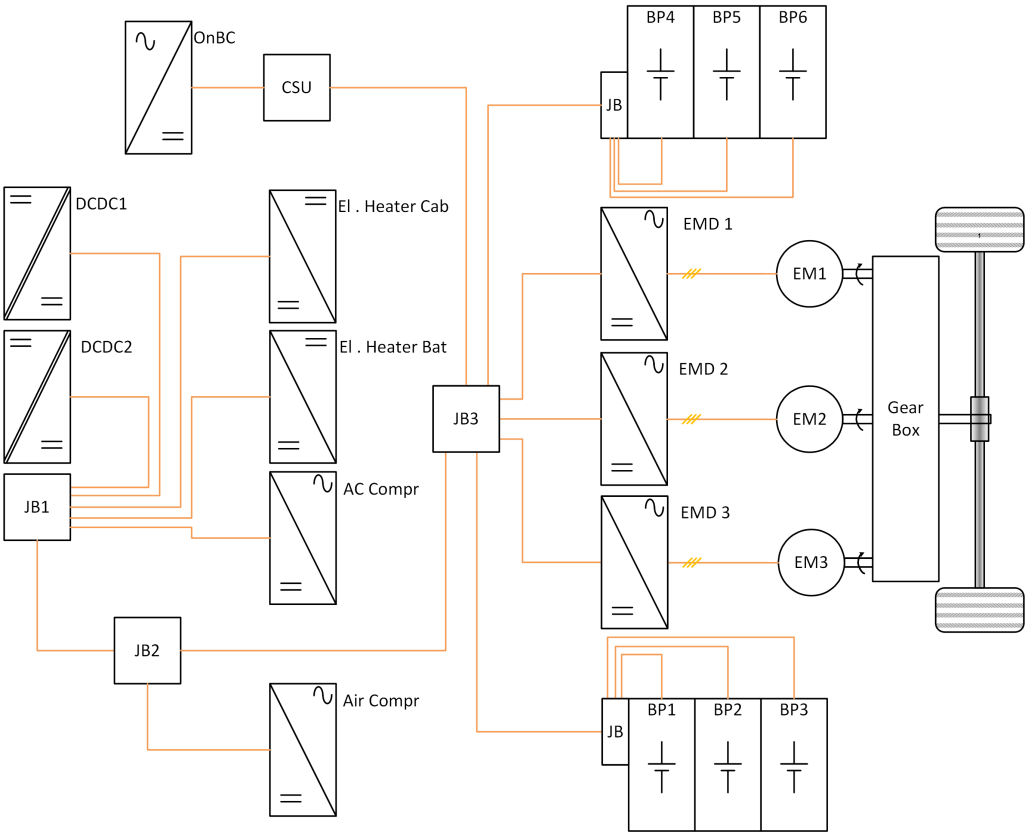


Figure 4.32: Volvo FM1156 truck with converters (DCDC, EMD, ePTO), chargers (OnBC), batteries, Charging Switch Unit (CSU) and junction boxes (JB).

Measurement results for switching with almost no delay are shown in Figure 4.33, and the results for switching with a 0.4 µs delay are shown in Figure 4.34. Note that ESS4 (Energy Storage System 4) is the same as BP4 (Battery Pack 4). The calculation of u_{cm} for the three-phase side is described in Equation (6.15).

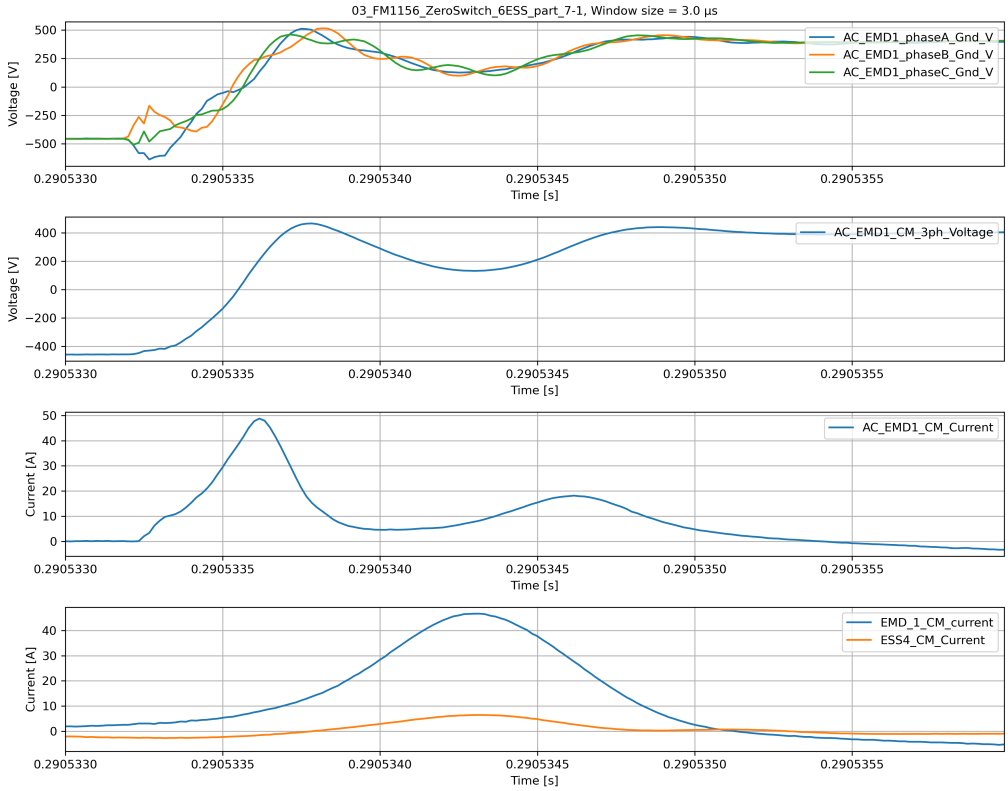


Figure 4.33: Transition from (0,0,0) to (1,1,1) with negligible separation between the switching instants of the phase legs. The simultaneous charge redistribution over the parasitic capacitances results in pronounced CM voltage and current transients.

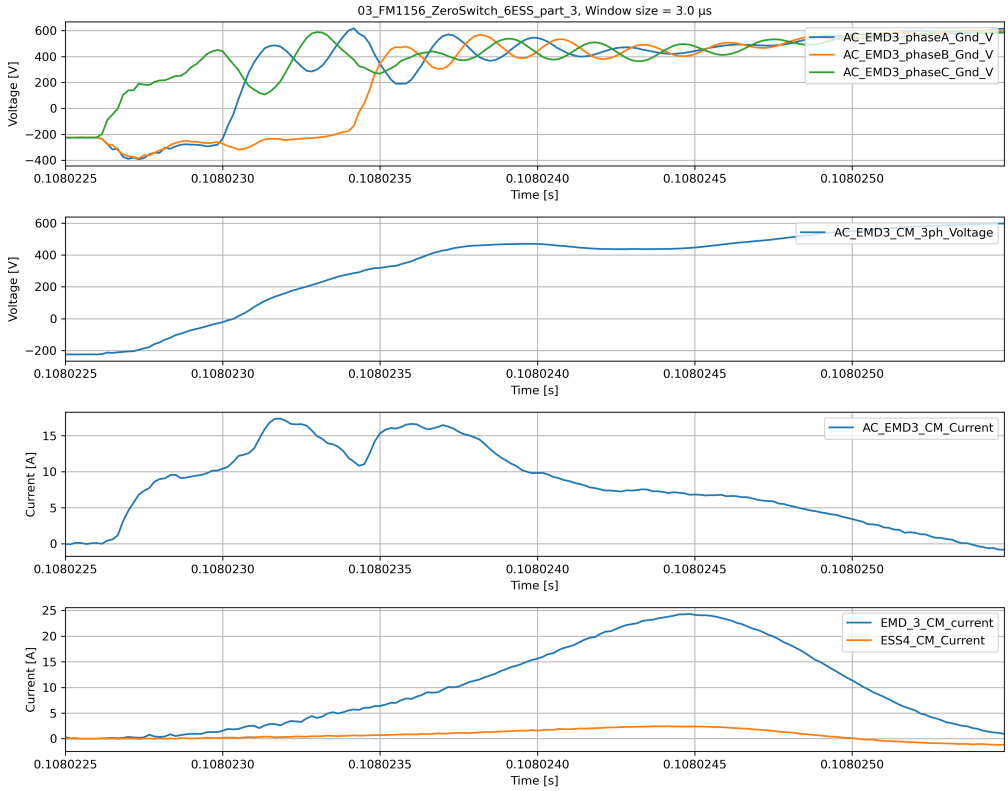


Figure 4.34: Transition from (0,0,0) to (1,1,1) with a delay of 0.4 µs between the switching instants of the phase legs. The staggered excitation reduces the simultaneous dv/dt seen by the parasitic capacitances, resulting in lower CM voltage and current transients.

The comparison between Figure 4.33 and Figure 4.34 shows that:

- the CM three-phase voltage decreases when a delay is introduced between the switching of the phase legs,
- the CM three-phase current decreases with increased switching delay,
- the CM current on the DC side also decreases when the phase-leg transitions are not simultaneous.

This behaviour is expected because the CM transients are driven by the simultaneous excitation of the parasitic capacitances in the EMD (C_{par_igbt}), the three-phase cable ($C_{CM3phcable}$), and the electric machine windings (C_{CMwind}). When all three phase legs switch at the same instant, these capacitances experience the same dv/dt, resulting in a large, concentrated CM current pulse. Introducing a delay distributes the charge displacement over time and lowers the effective peak dv/dt, thereby reducing the CM transient.

Conclusion

Delayed switching between the phase legs during transitions between $(0, 0, 0)$ and $(1, 1, 1)$ does not affect the stationary CMDC voltage but has a significant impact on the transient CM behaviour. A delay of 0.4 µs substantially reduces both CM voltage and CM current peaks on the AC and DC sides by eliminating the simultaneous excitation of the parasitic capacitances. This confirms that phase-leg timing is an effective mechanism for mitigating CM disturbances during zero-vector switching.

4.3.5 CM frequency content at the DC side

Following the time-domain investigations in Subsection 4.3.4, this subsection addresses the frequency-domain characteristics that define the bandwidth relevant for subsequent modelling work.

To construct simulation models of the truck and its subsystems, it is essential to determine the actual frequency content of the measured common-mode (CM) currents. The frequency content is obtained from FFT analysis. The upper frequency limit extracted from the FFT guides the bandwidth and parameterisation of the subsystem-level models. The truck architecture is shown in Figure 4.7. All measurements are performed on the DC side of the subsystems, except for the EMD, which is evaluated on both its DC side and its AC side (between the EMD and EM).

Both CM and differential-mode (DM) disturbances are analysed; for the DM analysis, see Subsection 4.4.1. Window functions such as flattop or Hanning may be applied depending on the intended amplitude accuracy. A brief theoretical motivation for FFT behaviour and windowing is given in Appendix B. The Python script that is used for performing the FFT is validated in Section 4.5.

Measurements are performed at three locations in the FM1156 truck (see Figure 4.7):

- Common-mode current on the AC side between EMD1 and EM1, denoted AC_EMD1_CM_Current.
- Common-mode current on the DC side of EMD1, denoted EMD1_CM_Current.
- Common-mode current at battery 4 (BP4), denoted ESS4_CM_Current.

Each of the three measurement points is recorded under three operating conditions: two cases of zero switching at standstill, and one case of high-torque operation. In this test setup, there are three EMDs in operation for both zero switching and at high-torque operation.

The three measurement points are presented in three different operating points:

- Zero switching when the three EMDs are switching almost perfectly separated. This is clearly visible in the battery common-mode current in Figure 4.37. The subsets of the measurement points are shown in Figures 4.35 to 4.37.

- Zero switching when the three EMDs are switching almost at the same time. This is clearly visible in the battery common-mode current in Figure 4.40. The subsets of the measurement points are shown in Figures 4.38 to 4.40.
- High torque when the three EMDs are switching to produce a torque to the EM. That means that one EMD seldom, or never, switches from $(0, 0, 0)$ to $(1, 1, 1)$ resulting in a lower CM current for each EMD but also for the battery. The subsets of the measurement points are shown in Figures 4.41 to 4.43.

The figures below present the measurements in this order.

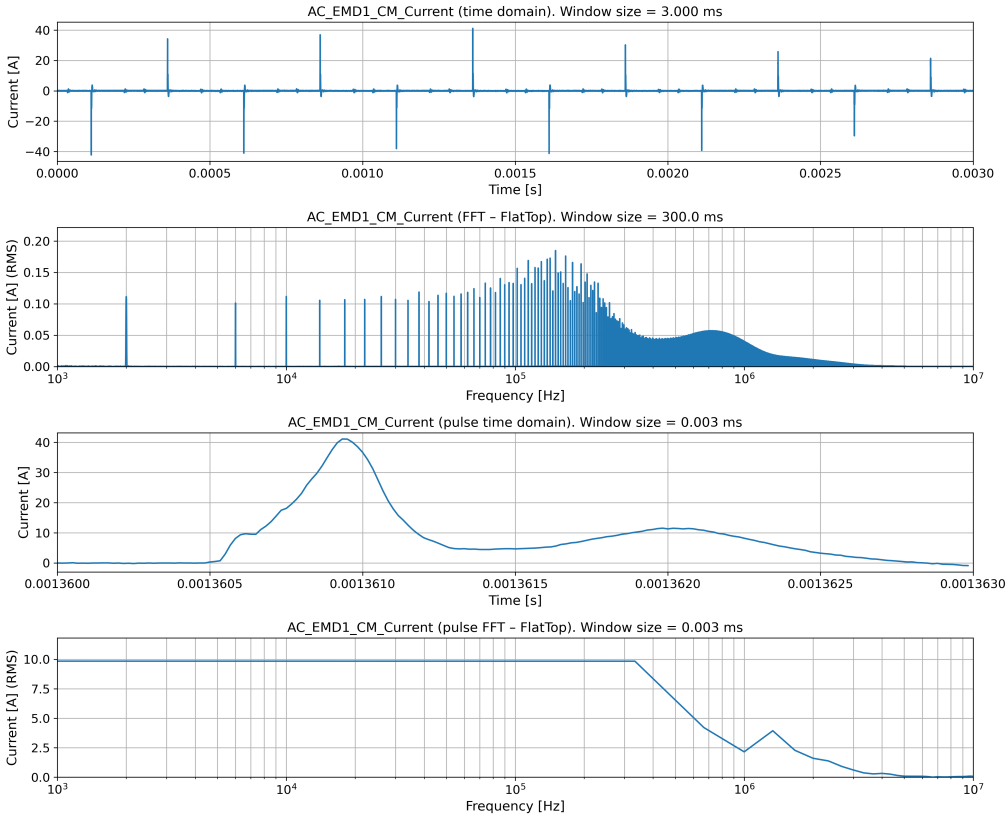


Figure 4.35: Common-mode current i_{cm} in time domain and FFT. Measured at the AC side (EMD1–EM1) during zero switching at standstill.

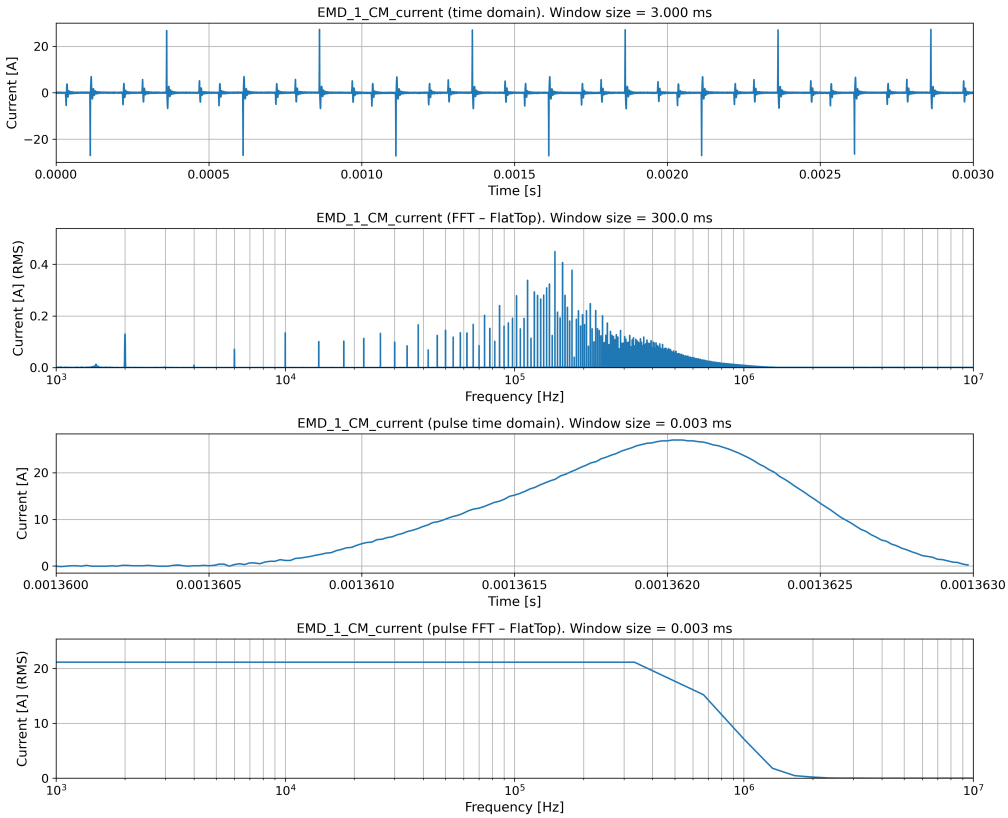


Figure 4.36: Common-mode current i_{cm} in time domain and FFT. Measured on the DC side of EMD1 during zero switching at standstill.

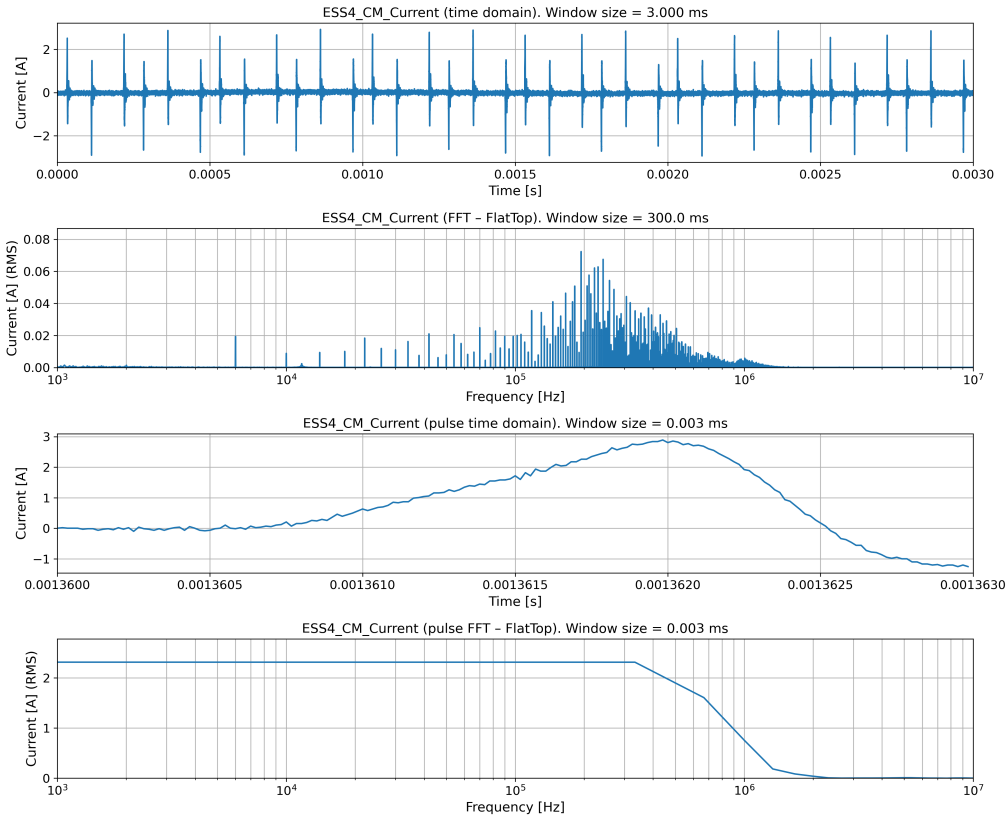


Figure 4.37: Common-mode current i_{cm} in time domain and FFT. Measured at battery 4 (BP4) during zero switching at standstill.

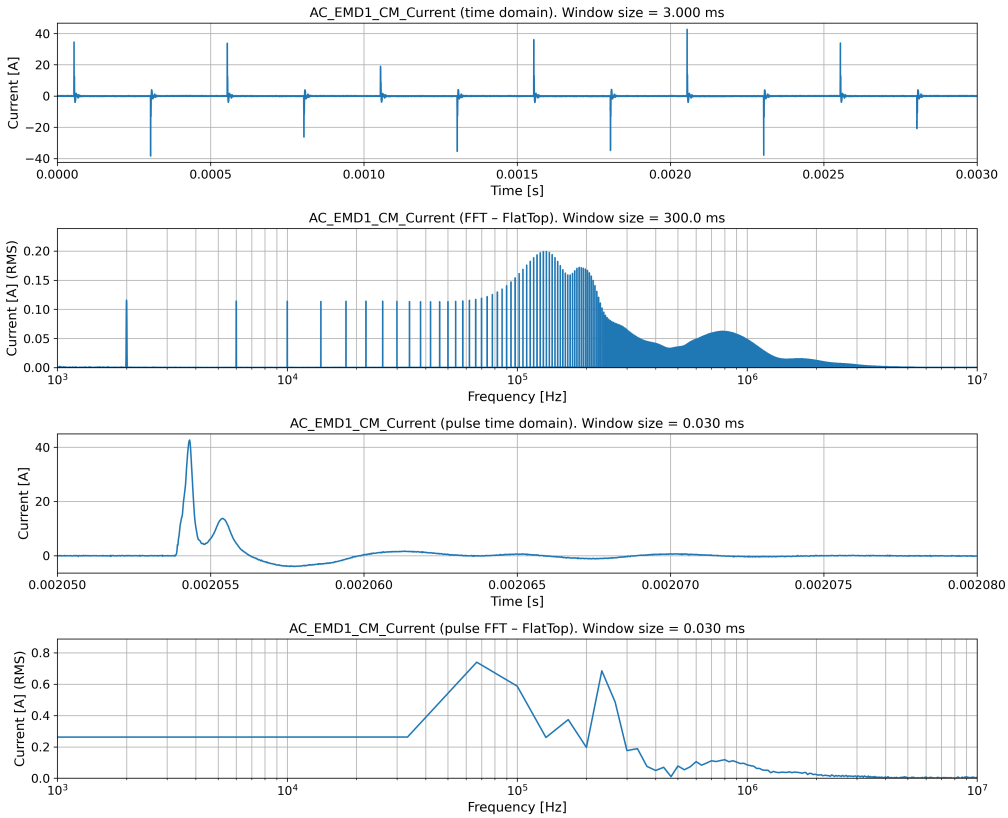


Figure 4.38: Common-mode current i_{cm} in time domain and FFT. Measured at the AC side (EMD1–EM1) during zero switching at standstill.

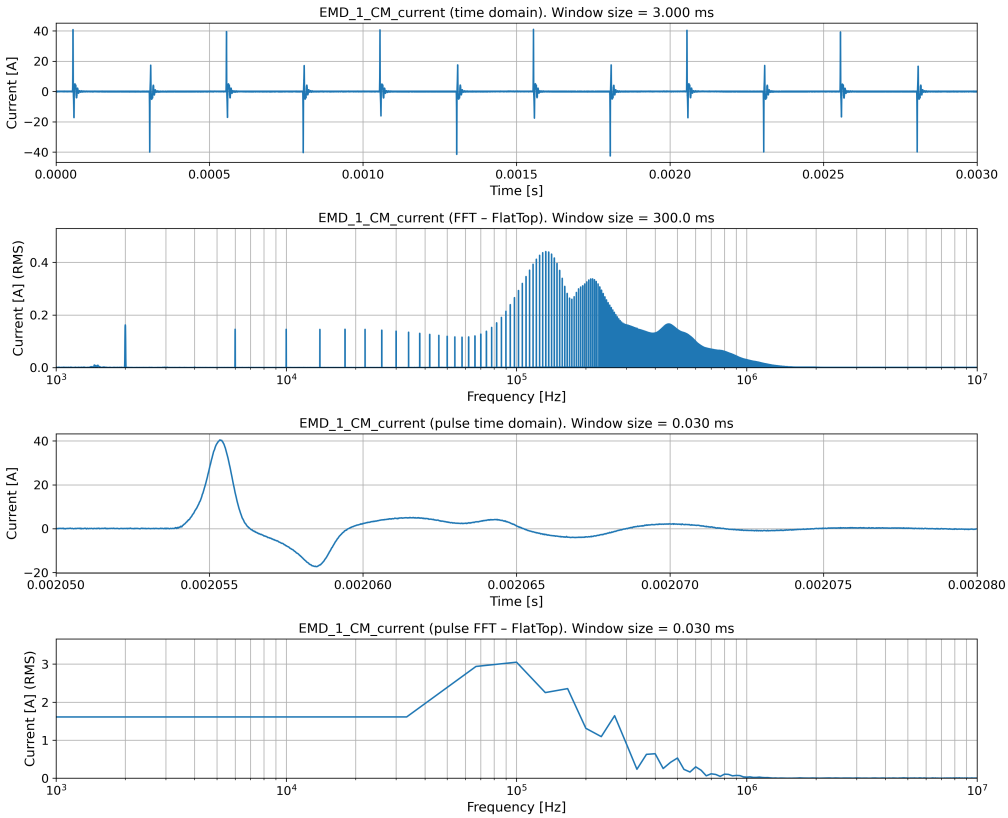


Figure 4.39: Common-mode current i_{cm} in time domain and FFT. Measured on the DC side of EMD1 during zero switching at standstill.

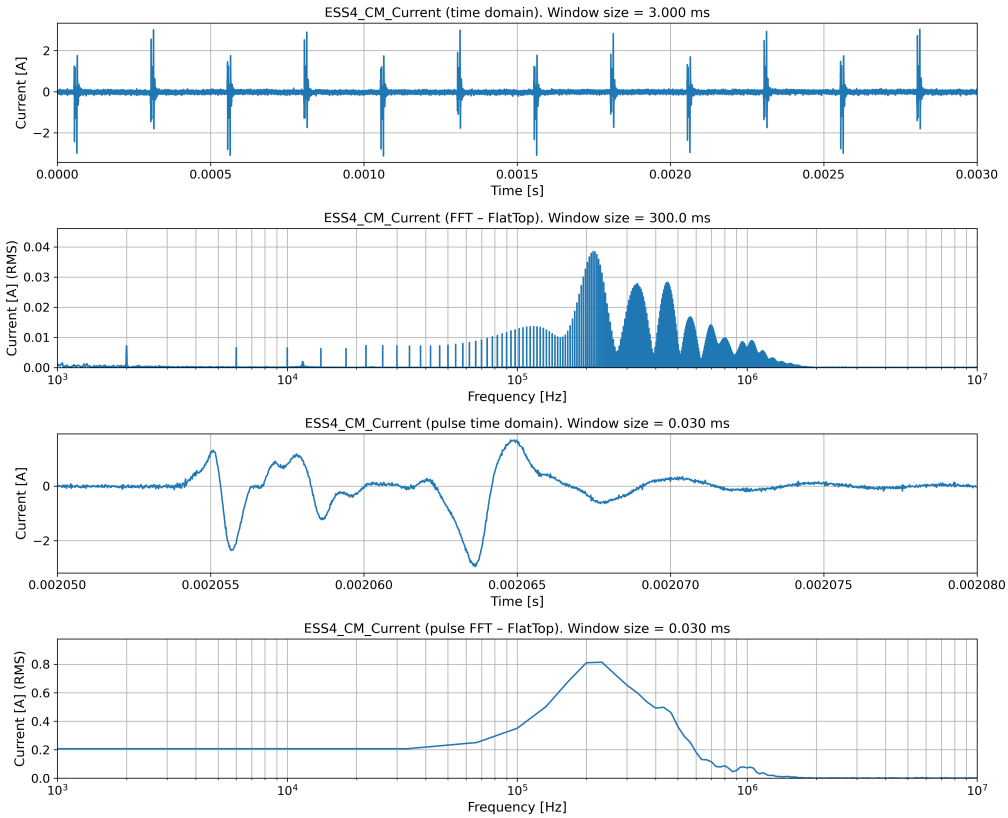


Figure 4.40: Common-mode current i_{cm} in time domain and FFT. Measured at battery 4 (BP4) during zero switching at standstill.

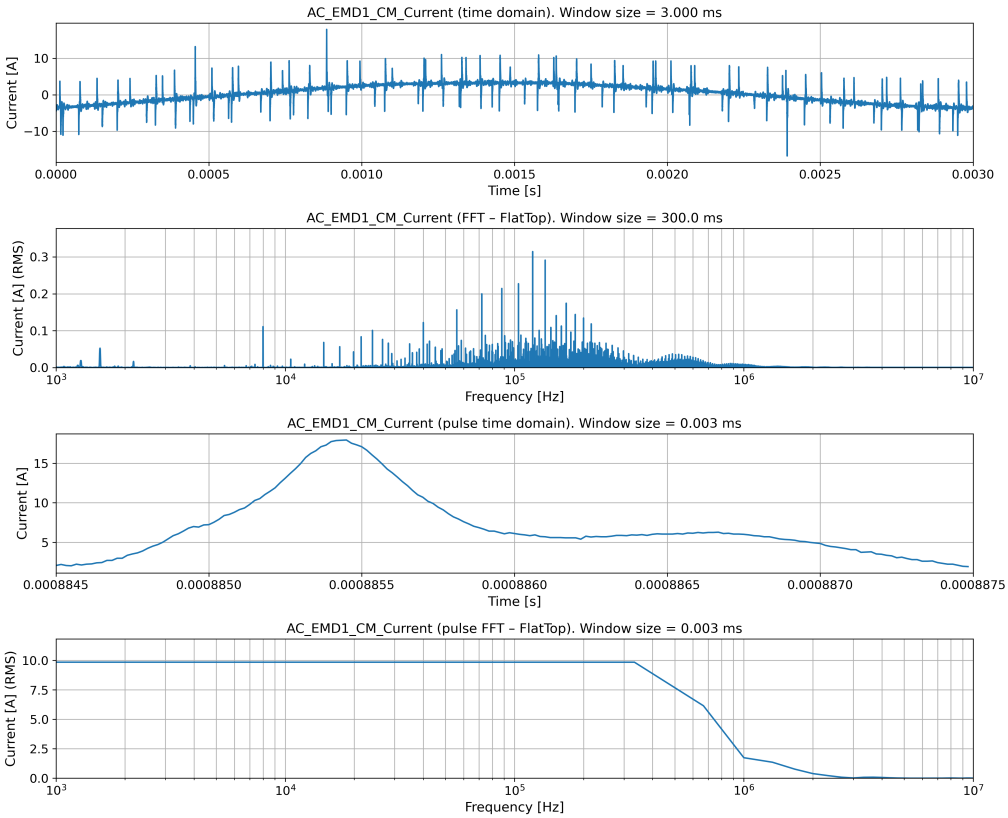


Figure 4.41: Common-mode current i_{cm} in time domain and FFT. Measured at the AC side (EMD1–EM1) during high-torque operation.

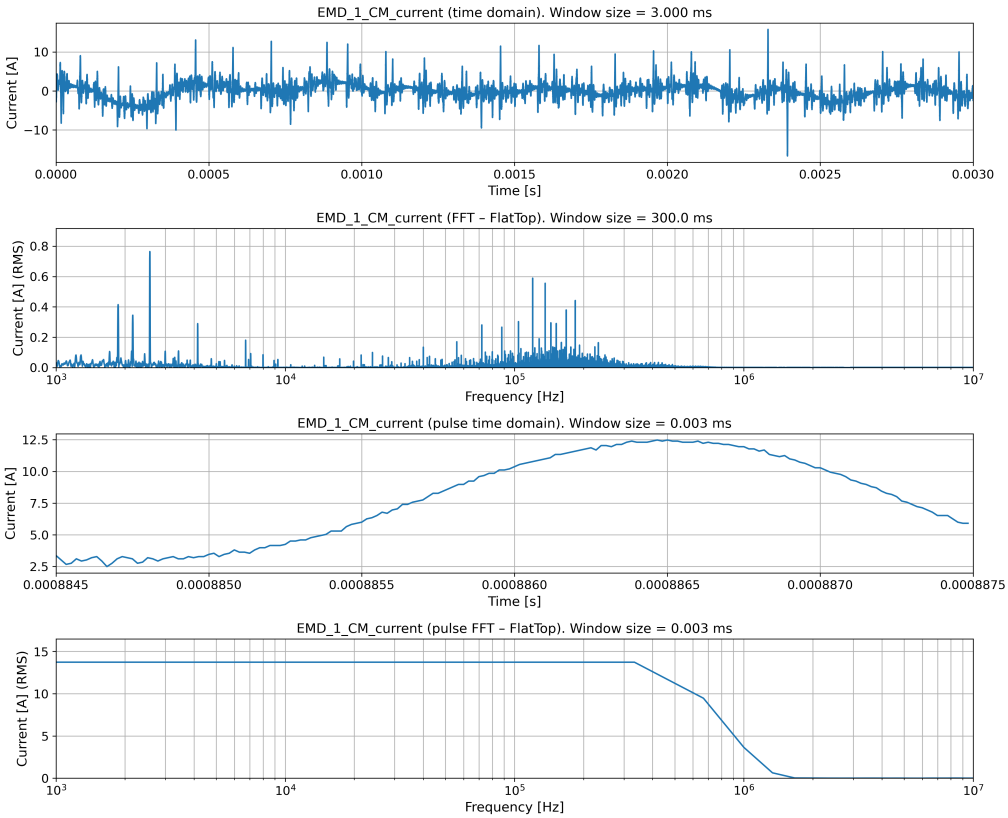


Figure 4.42: Common-mode current i_{cm} in time domain and FFT. Measured on the DC side of EMD1 during high-torque operation.

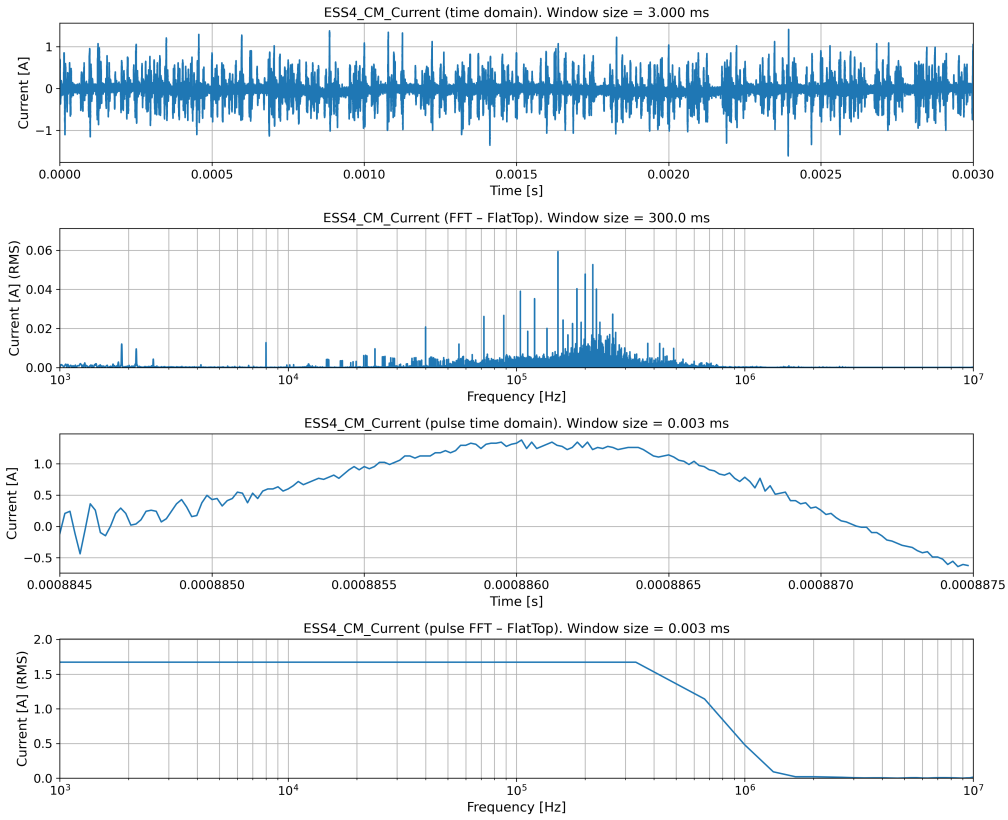


Figure 4.43: Common-mode current i_{cm} in time domain and FFT. Measured at battery 4 (BP4) during high-torque operation.

The measurements allow several observations:

- The highest CM current i_{cm} occurs during zero switching at standstill for all measurement positions, as all three phase legs switch simultaneously, Figures 4.38 to 4.40.
- For the AC-side measurement (EMD1–EM1), the FFT shows that the rms level above 3 MHz is negligible across all operating points, Figures 4.35, 4.38 and 4.41.
- On the DC side of EMD1, the highest i_{cm} also appears during zero switching at standstill. The level depends on neighbouring converter activity.
- At BP4, the highest i_{cm} again appears during zero switching at standstill. Pulse clustering increases when neighbouring EMDs switch simultaneously, as seen in Figure 4.40.
- The FFT at BP4 shows negligible rms content above 2 MHz for all operating conditions, Figures 4.37, 4.40 and 4.43.

Conclusion

The CM current is highest during zero switching at standstill for all measurement locations. Across all conditions, the rms current above 3 MHz on the AC side and above 2 MHz on the DC side is negligible. These results define the practical upper frequency limit required for CM-oriented subsystem modelling Chapter 5 where the simulation models are designed.

4.3.6 Conclusion

The measurements in Section 4.3 confirm the theoretical dependency between the common-mode DC (CMDC) voltage and the X-factor defined by the ratio between machine-side and return-path capacitances. By increasing the effective CM-capacitance associated with the traction system, the CMDC voltage at the battery is reduced from approximately 30 V to 12 V, in good agreement with the analytical expression in Equation (2.17). In principle, the additional CM-capacitance should be placed at the source, i.e. inside the EMD at the original capacitance location. However, this is not feasible in the test setup. Therefore, additional capacitance is instead introduced in a Break-Out Box (BoB) as a practical work-around to modify the effective X-factor of the traction voltage system. This demonstrates that the X-factor is a practical design parameter for controlling CMDC voltage levels in the traction voltage system.

The timing of the EMD switching is shown to be equally important. When two EMDs switch with a phase shift of approximately 180°, the common-mode currents largely cancel and the resulting i_{cm} is minimised. In contrast, when the EMDs switch in phase, the CM currents add constructively and the measured i_{cm} reaches its maximum. These observations confirm that synchronisation strategies for zero-vector transitions can be used to either mitigate or, unintentionally, aggravate CM disturbances.

The transient CM behaviour is also influenced by the timing between the phase-leg transitions. A deliberate phase-leg delay of 0.4 µs during the zero-vector transition between $(0, 0, 0)$ and $(1, 1, 1)$ does not affect the stationary CMDC voltage, but it substantially reduces the transient CM voltage and CM current peaks on both the AC and DC sides. This confirms that phase-leg timing is an effective mechanism for mitigating CM disturbances during zero-vector switching.

Finally, FFT-based analysis of the CM currents at several locations in the truck shows that the dominant CM spectral energy is concentrated below a few megahertz. The rms CM current above 3 MHz on the AC side and above 2 MHz on the DC side is negligible for both zero switching at standstill and high-torque operation. These results provide quantitative upper-frequency limits for model bandwidth and justify the modelling range employed in later chapters.

4.4 Results from differential mode measurements on a truck

This section shifts the focus from the common-mode behaviour analysed in Section 4.3 to the corresponding differential-mode behaviour examined in this part of the study.

Differential-mode (DM) measurements are performed on the FM1156 truck, see Figure 4.7, using a vehicle dynamometer (DYNO). The test environment and measurement equipment are shown in Figures 4.44 to 4.47.



Figure 4.44: FM1156 truck mounted in the vehicle dynamometer (DYNO).



Figure 4.45: The truck secured in the dynamometer using tie-down straps.

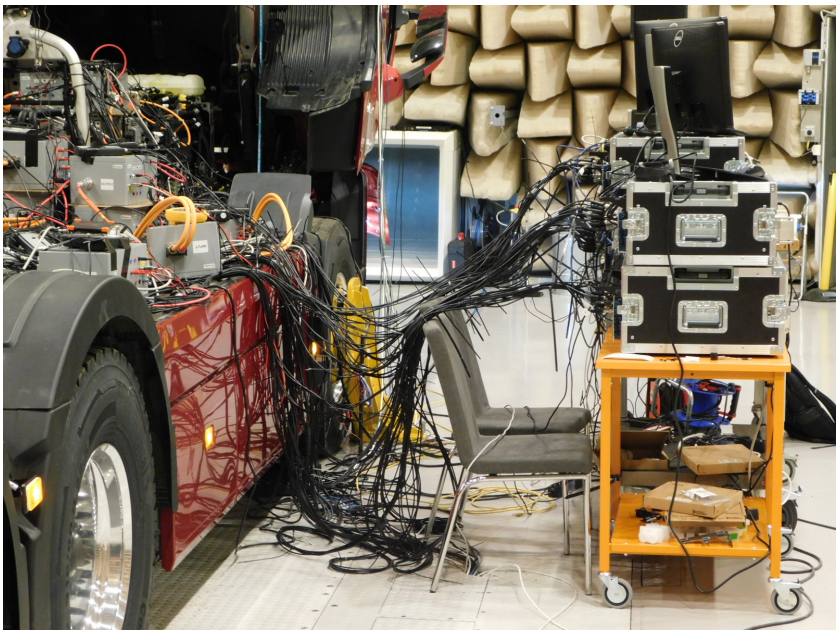


Figure 4.46: Measurement setup with break-out boxes (left) and data acquisition system (right).

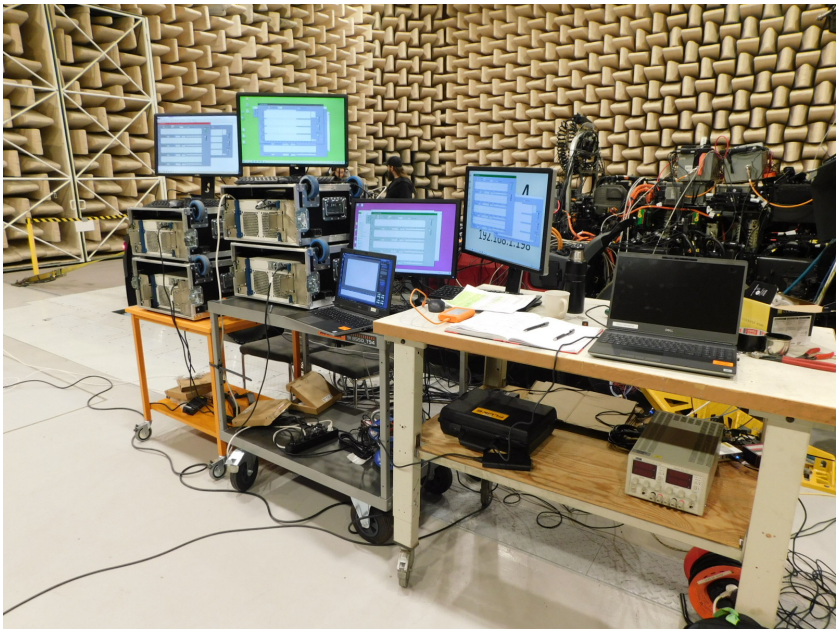


Figure 4.47: Measurement system used for recording the DYNO tests.

4.4.1 DM frequency content at the DC side

This subsection continues the analysis introduced in this section by examining the frequency-domain characteristics relevant for differential-mode behaviour.

To enable accurate differential-mode (DM) simulations of the truck subsystems, the actual frequency content of the measured DM currents must be determined. This is performed using FFT analysis. The upper frequency limit extracted from the FFT determines the bandwidth requirements for the subsystem-level models. The measurement points are located on the DC side of each subsystem, as the AC side is not included in the DM simulations.

FFT calculations use window functions such as Flattop or Hanning depending on the required amplitude accuracy. A theoretical motivation for FFT behaviour and windowing is provided in Appendix B. The Python FFT implementation used here is validated in Section 4.5.

Measurements are performed at two locations in the FM1156 truck:

- Differential-mode current on the DC side of EMD1, denoted EMD1_DM_Current.
- Differential-mode current at battery 4 (BP4), denoted ESS4_DM_Current.

Each measurement point is analysed under three operating conditions: low torque at 600 rpm (Figures 4.48 and 4.49), high torque at 2700 rpm (below base speed) (Figures 4.50 and 4.51), and high torque at 6400 rpm (above base speed) (Figures 4.52 and 4.53).

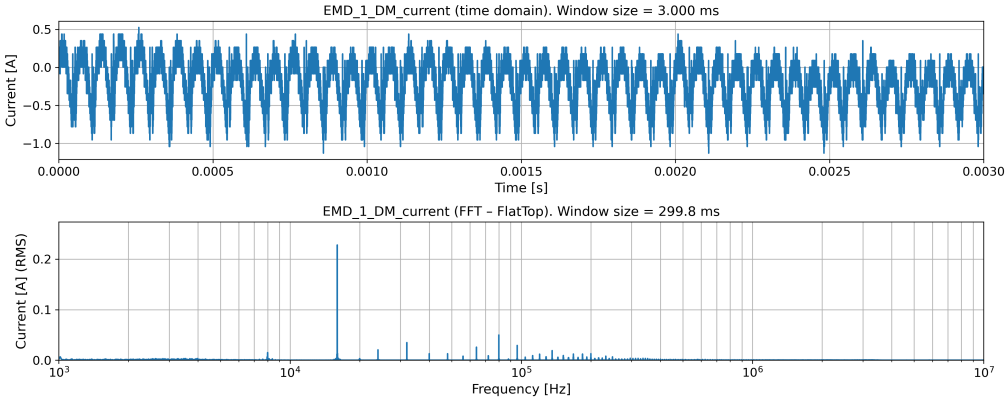


Figure 4.48: Differential-mode current in time domain and FFT. Measured on the DC side of EMD1 during low-torque operation at 600 rpm.

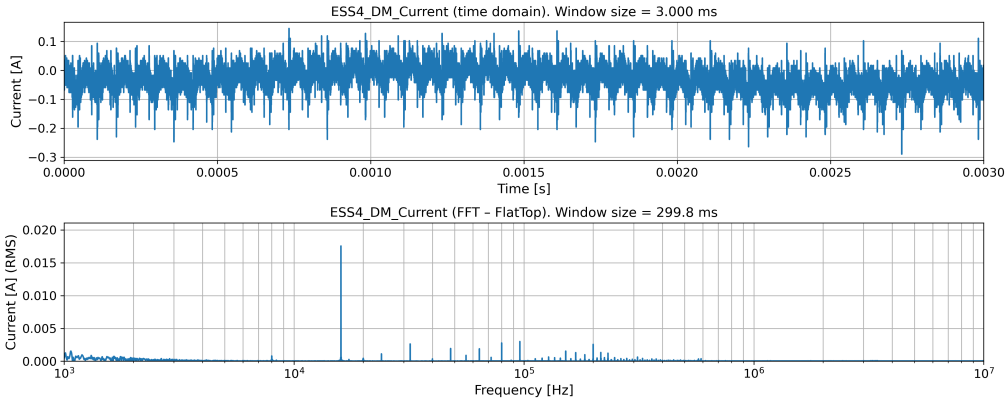


Figure 4.49: Differential-mode current in time domain and FFT. Measured at battery 4 during low-torque operation at 600 rpm.

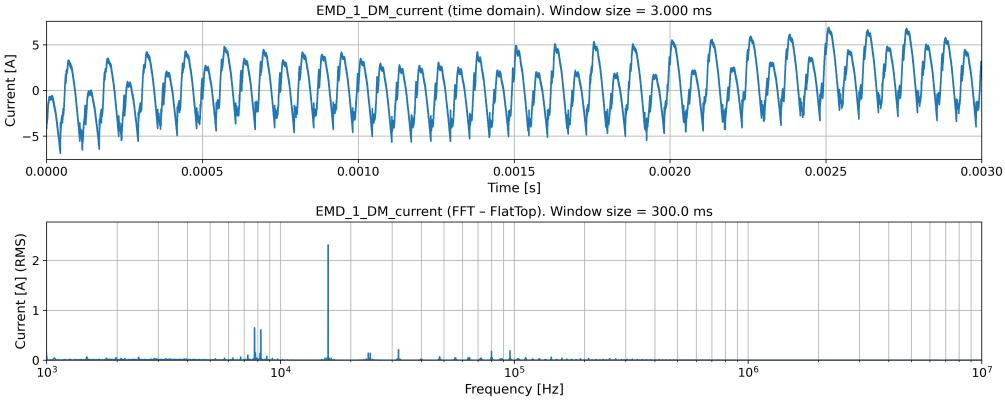


Figure 4.50: Differential-mode current in time domain and FFT. Measured on the DC side of EMD1 during high-torque operation at 2700 rpm.

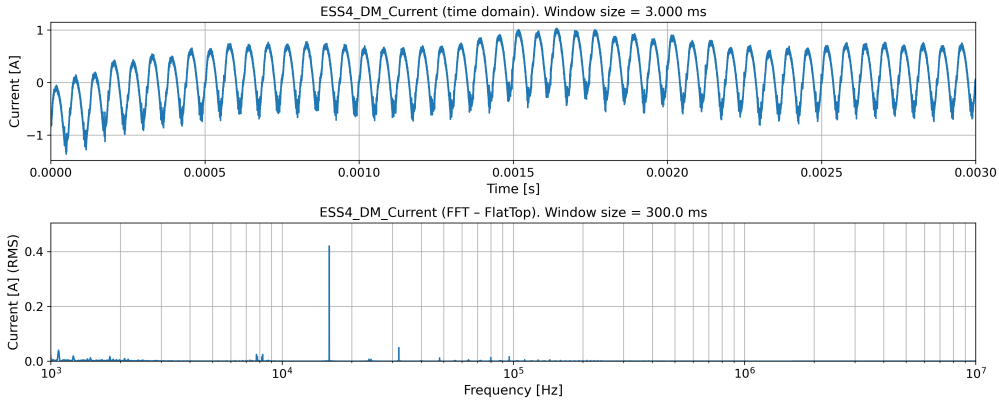


Figure 4.51: Differential-mode current in time domain and FFT. Measured at battery 4 during high-torque operation at 2700 rpm.

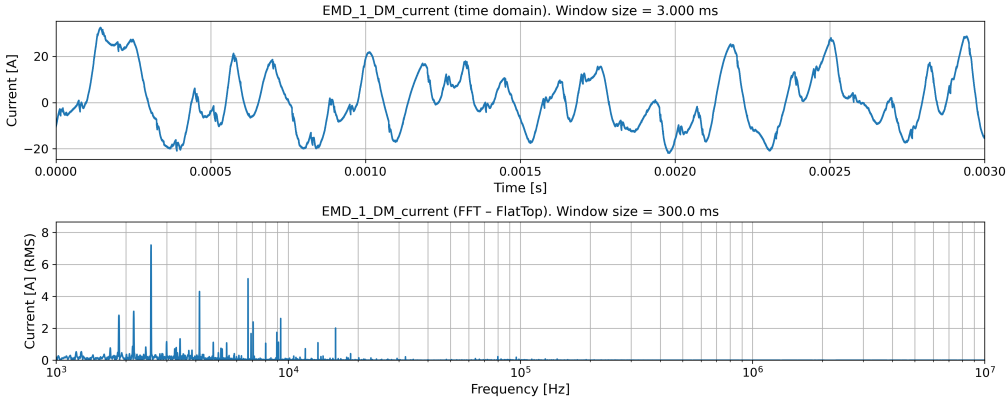


Figure 4.52: Differential-mode current in time domain and FFT. Measured on the DC side of EMD1 during high-torque operation at 6400 rpm.

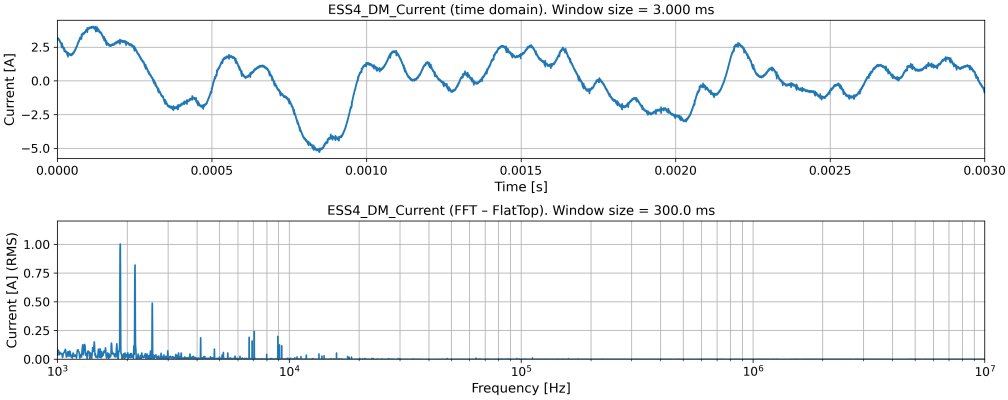


Figure 4.53: Differential-mode current in time domain and FFT. Measured at battery 4 during high-torque operation at 6400 rpm.

All differential-mode currents shown in Figures 4.48 to 4.53 exhibit negligible rms current above 200 kHz. This defines the practical upper frequency limit required for DM-oriented subsystem modelling in later simulation work.

4.4.2 Conclusion

This subsection summarises the differential-mode measurement results presented in Section 4.4.

The differential-mode measurements on the FM1156 truck demonstrate that the DM spectral content is strongly confined to frequencies below approximately 200 kHz for all operating conditions, including low torque, high torque below base speed, and high torque

above base speed. Above this frequency, the rms current contribution becomes negligible at both measurement locations (DC side of EMD1 and battery 4).

This establishes 200 kHz as the required upper modelling frequency limit for DM simulations of the traction voltage system. The results also confirm that, unlike the common-mode behaviour, the DM dynamics do not exhibit significant high-frequency components driven by switching transients. Consequently, the DM modelling bandwidth can be kept substantially lower than for CM modelling, thereby reducing computational complexity without sacrificing accuracy.

4.5 Verification of FFT implementation

To verify the correctness of the FFT implementation used throughout this thesis, a synthetic reference signal is generated consisting of eight sinusoidal components with known RMS amplitudes and known frequencies. Each sinusoid is constructed as $1.414\cos(2\pi f_i t)$, which corresponds to an exact RMS value of 1 A for each component.

The verification tones are:

- f_1 = 2 kHz
- f_2 = 5 kHz
- f_3 = 10 kHz
- f_4 = 50 kHz
- f_5 = 100 kHz
- f_6 = 500 kHz
- f_7 = 1 MHz
- f_8 = 5 MHz

As shown in Figure 4.54, the resulting FFT spectrum contains eight discrete lines located exactly at the expected frequencies, each with an RMS value of 1 A after flattop windowing and proper FFT normalisation. This confirms that the complete processing chain – including windowing, scaling and RMS conversion – is implemented correctly.

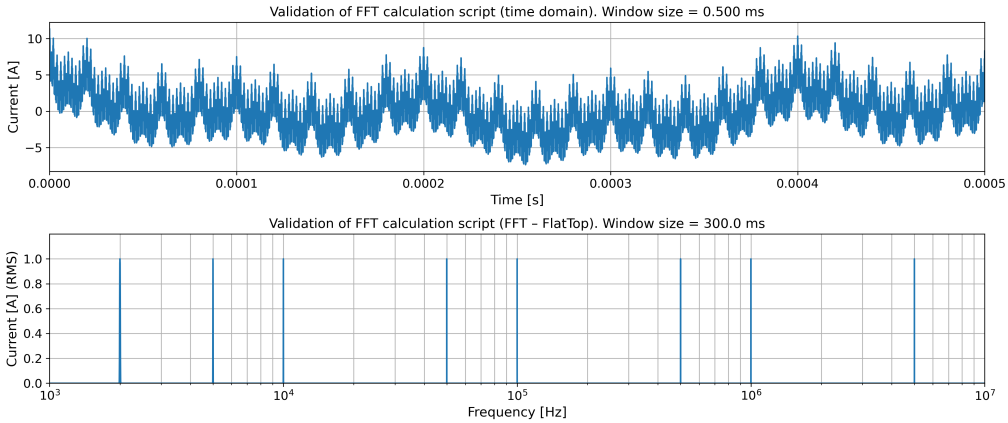


Figure 4.54: Verification result for the FFT implementation using a synthetic reference signal composed of eight sinusoidal components, each with an RMS magnitude of 1 A.

Conclusion

The FFT verification confirms that the implemented processing pipeline correctly identifies the frequency, amplitude and RMS value of known sinusoidal components from 2 kHz up to 5 MHz. The accuracy of the synthetic validation demonstrates that all FFT-based spectral analyses in this thesis are based on a fully validated methodology.

4.6 Conclusion

The measurements presented throughout this chapter provide a complete vehicle-level characterisation of the common-mode (CM) and differential-mode (DM) behaviour of a heavy-duty electric truck. The results confirm the theoretical mechanisms introduced in earlier chapters and establish the frequency ranges required for accurate subsystem modelling.

The CMDC voltage measurements verify the analytical dependency on the X-factor. Increasing the machine-side common-mode capacitance lowers the CMDC voltage in accordance with Equation (2.17). In these measurements, the X-factor variation is realised by adding CM-capacitance in the Break-Out Boxes (BoB) on the DC side as a practical workaround; in an optimised design, the added capacitance is placed at the disturbance source inside the EMD. The relative switching phase between the traction EMDs is shown to be equally important: a 180° phase shift produces near-complete cancellation of CM currents, whereas in-phase switching leads to maximum CM current levels. These findings demonstrate that both capacitance distribution and switching coordination are decisive parameters for CM mitigation in multi-converter traction systems.

The influence of the measurement interface itself is established through a detailed characterisation of the break-out boxes. High-di/dt current pulses induce voltages in the busbars and measurement wires, leading to measurable distortions of the CMDC waveform.

Laboratory tests reproduce the deviations observed in the vehicle, confirming that a significant part of the skewed behaviour originates from the measurement system rather than the traction voltage system. This insight is essential for correct interpretation of all subsequent CM and DM measurements.

The frequency-domain analysis shows that the CM spectral content is confined below approximately 3 MHz on the AC side and 2 MHz on the DC side. Above these limits, the rms current contribution becomes negligible. For DM behaviour, the upper relevant frequency is substantially lower: all measured DM currents show negligible spectral energy above 200 kHz across all operating conditions. These limits define the modelling bandwidths required for the CM and DM subsystem models developed in Chapter 5.

Finally, the FFT implementation used throughout the thesis is validated with synthetic reference signals containing known frequency components. The FFT successfully reproduces all amplitudes and frequencies, confirming that the spectral analyses presented in this chapter are based on a correct and reliable signal-processing chain.

The combined results of this chapter provide the empirical basis for the concept modelling in Chapter 5. The subsystem models developed there rely directly on the frequency limits, CM mechanisms and measurement insights established in this chapter.

Chapter 5

Sub system simulation model and model calibration

Chapter 4 provides a measurement-based characterisation of the common-mode (CM) and differential-mode (DM) behaviour of the traction voltage system. The results establish the frequency ranges that the subsystem models in this chapter must be constructed such that they preserve: the CM current exhibits relevant spectral content up to approximately 3 MHz on the AC side and 2 MHz on the DC side, while the DM current shows negligible spectral energy above 200 kHz. These limits form the basis for the subsystem modelling strategy applied here.

The purpose of the concept modelling is to analyse how CM and DM disturbances propagate in the traction voltage system and how design choices affect the electromagnetic interference (EMI) behaviour of the vehicle. Each subsystem is measured, and the equivalent circuits follow from the measured impedance and current–voltage behaviour. This includes battery packs operating at approximately 600–700 V, junction boxes, cables, electric machine drives (EMDs), auxiliary converters and other units connected to the traction voltage system. The equivalent circuits are implemented in suitable simulation tools, and Appendix A describes the parameter-extraction procedure used to construct the models, forming a modular model library that can be combined to represent different vehicle configurations.

Replacing full vehicle measurements with subsystem-based simulation reduces development time and cost, provided that the models are formulated to preserve the relevant CM and DM behaviour within the frequency ranges established in Chapter 4. Since a fully detailed model of a complete vehicle is computationally infeasible, simplified models are necessary. This chapter therefore introduces a method based on state-space matrices and eigenvalue analysis to derive reduced models that retain the resonant behaviour within the required CM and DM frequency ranges.

This chapter is organised in the following sections:

1. **Measurement methods required** – describes the measurement procedures and instrumentation used to characterise the subsystems.
2. **System simulation tool – PLECS** – introduces the simulation tool used to implement the subsystem models and to perform the system-level simulations.
3. **State-space matrices and eigenvalues** – presents the mathematical framework used to reduce subsystem model size while preserving relevant frequency content.
4. **Measurement and modelling of subsystems** – provides the detailed modelling of cables, battery packs, junction boxes, break-out boxes, filters and converter interfaces. This section forms the core of the chapter.
5. **Conclusion** – summarises the modelling outcome and prepares the transition to the system-level simulations presented in Chapter 6.

5.1 Measurement methods required

This section introduces the measurement methods used to measure the impedance required for constructing the subsystem models. The LCR measurements form the basis for extracting both DM and CM parameters, and the available methods differ significantly in accuracy, bandwidth and suitability for TVS-level subsystems. Since the subsystem models must be designed to preserve the behaviour within the frequency limits established in Chapter 4, the choice of measurement method directly determines the validity and resolution of the resulting models.

To measure the impedance, the measurement setup uses an LCR meter that analyses the frequency characteristics of the electrical subsystems. Given the intended validity range of the subsystem models (CM: DC–2 MHz on the DC side and AC–3 MHz on the AC side, DM: DC–200 kHz), the chosen LCR instrument is the PSM3750 Frequency Response Analyzer [20] together with the IAI2 Impedance Analyzer [19], shown in Figure 5.1. The instruments are provided with calibration within the Volvo calibration programme, and each individual measurement setup includes a calibration performed before use. Since the relevant impedances are low, the calibration is performed towards a short circuit to remove the influence of the cables in the measurement loop. At frequencies above approximately 5 MHz, the validity of the measurement becomes increasingly uncertain, and the origin of resonances above this frequency may be uncertain, as they can arise either from the measurement setup or from the device under test (DUT).

The LCR measurements provide impedance and phase as a function of frequency. These graphs provide the basis for the design of suitable equivalent circuits, as Appendix A describes. Zview [36] is used to extract parameters from the impedance measurements.

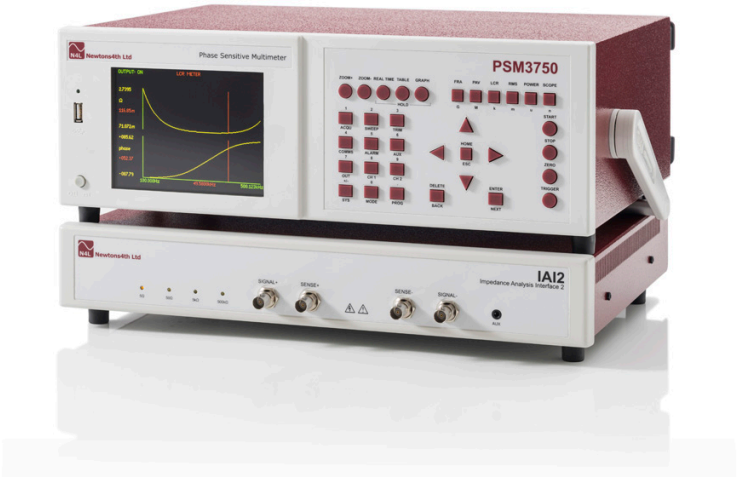


Figure 5.1: PSM3750 and IAI2 impedance analysis package capable of performing impedance measurements up to 35 MHz. Picture from newtons4th.com.

To provide clarity and structure, this section is organised into the subsections listed below:

Subsection 5.1.1 describes the Kelvin fixture method, which provides the highest accuracy and the best immunity to parasitics, but is limited to small DUTs due to mechanical constraints.

Subsection 5.1.2 presents the Kelvin lead method, which performs well at low frequencies, including the impedance region referred to as “DC”, but exhibits reduced accuracy above 4–5 MHz due to the lead-induced parasitic inductance and capacitance.

Subsection 5.1.3 introduces the four-wire method with a separate high-bandwidth current probe, which performs well up to 10–20 MHz but exhibits reduced accuracy at low frequencies, including the region referred to as ”DC”.

Subsection 5.1.4 describes the custom HV interface that enables impedance measurements on batteries and other DUTs containing internal DC voltage sources.

Subsection 5.1.5 explains the high-current supply method used for accurate measurement of DC cable resistance, compensating for the limitations of the LCR instrument at very low impedances.

Subsection 5.1.6 summarises how the different measurement methods complement each other and how their applicable frequency ranges support the subsystem modelling requirements in this chapter.

5.1.1 Kelvin fixture

For measurements requiring high accuracy, particularly in situations with very low or very high impedances, the impedance introduced by the connectors must be properly accounted for. The connections are arranged to minimise the introduced impedance and contact resistance while avoiding damage to the terminals of the device under test (DUT). The measurement arrangement is known as the four-wire method, in which two probes provide the excitation signal and two separate probes measure the voltage across the DUT. The exact placement and mechanical arrangement of the probes influence the accuracy of the measurement.

The most accurate method available in this setup is the Kelvin fixture, shown in Figure 5.2, which is attached to the IAI2 Impedance Analyzer, shown in Figure 5.3. The advantage of the Kelvin fixture is that the DUT is mounted between two circuit boards, which reduces the stray inductances and parasitic capacitances associated with the measurement arrangement. In the example shown, a cylindrical capacitor is mounted in the fixture. The Kelvin fixture is too small, however, to be used for TVS subsystems such as cables or converters operating at the TVS level of approximately 600–700 V.

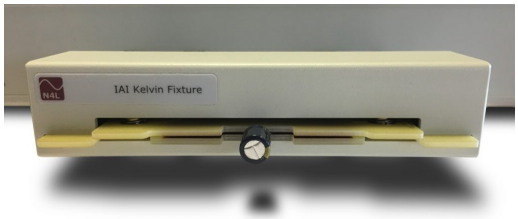


Figure 5.2: Kelvin fixture featuring four contact plates that provide true four wire impedance measurement. A cylindrical capacitor is used as the DUT in this example. Valid frequency range for this method is DC–35 MHz. Note: "DC" in this context refers to a very low frequency level, approximately 10 µHz.



Figure 5.3: IAI Kelvin fixture, DC–35 MHz.

Conclusion

The Kelvin fixture provides the most accurate impedance measurement method within the available setup by minimising stray inductance and parasitic capacitance. However, its physical size prevents its use for TVS subsystems operating at approximately 600–700 V. Within its dimensional limitations, the fixture provides high quality impedance data suitable for deriving equivalent circuits for small components such as capacitors, resistors and inductors that fit within the fixture. Although the measurement instrument itself supports frequencies up to 35 MHz, the physical size of the fixture prevents its use for the test objects investigated in this thesis.

5.1.2 Kelvin leads

Certain measurements require cables, including cases where long cable lengths are unavoidable. A common approach is the 4-wire Kelvin method using Kelvin leads, shown in Figures 5.4 and 5.5. Testing shows that the method performs well at low frequencies, including the frequency range referred to as "DC" in impedance measurements, but that its accuracy decreases above approximately 4–5 MHz. The reduced high frequency accuracy originates from the parasitic inductance and capacitance introduced by the leads. For this reason, the Kelvin lead method is not used for the high frequency measurements required for TVS subsystem modelling in this thesis.

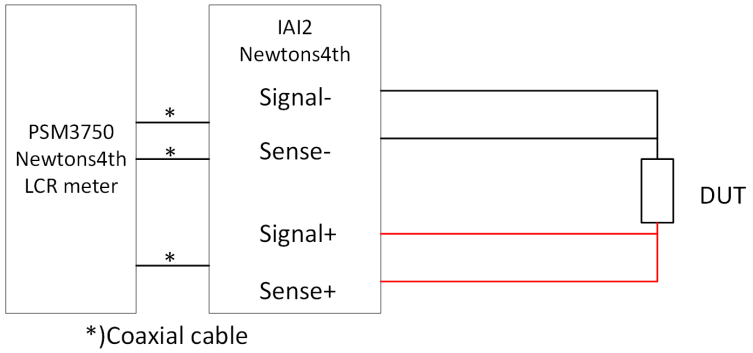


Figure 5.4: Four wire Kelvin method, valid up to approximately 5 MHz.

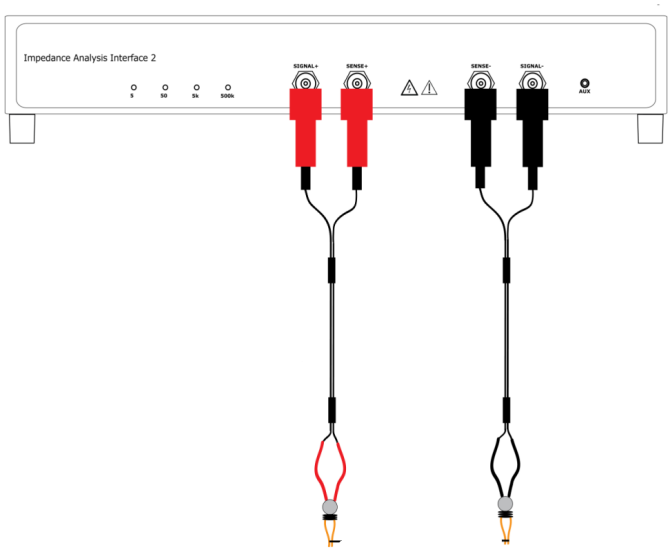


Figure 5.5: Four wire Kelvin leads.

Conclusion

The Kelvin lead method provides a practical four wire measurement arrangement and performs well at low frequencies, including the impedance region referred to as “DC”. However, the parasitic inductance and capacitance of the leads limit the usable frequency range to approximately 4–5 MHz. Consequently, the method is applied only to low frequency measurements, such as determining resistive parameters or supporting complementary measurements for subsystems where high frequency accuracy is not required.

5.1.3 4-wire method with separate current probe

A new test method is developed for the measurements reported in this thesis. The method is a four wire arrangement combined with a high bandwidth current probe, shown in Figure 5.6. The voltage of the device under test (DUT) is measured directly on the DUT, while the current is measured using a Pearson current probe, model 2877 [5], with a bandwidth of 300 Hz–200 MHz.

The method provides "good accuracy" up to the range 10–20 MHz in the impedance measurements. In this context, "good accuracy" refers to the absence of resonance points attributable to the measurement method within the instrument's usable range up to approximately 10–20 MHz for the test objects used in this thesis. This extended instrument bandwidth does not alter the model validity limits, which remain 2 MHz on the DC side and 3 MHz on the AC side for CM behaviour, as established in Chapter 4. The drawback of the method is its limited performance at lower frequencies and at the very low frequency region referred to as "DC". Kelvin leads introduce impedance in the measurement loop, and an alternative two-wire method (not described here) is also influenced by the impedance of the measurement leads.

The four wire method with a separate current probe is evaluated using a known reference DUT and compared with the alternative methods. It is found to be the best alternative within the available setup. For the TVS cables operating at the TVS level of approximately 600–700 V, the "DC" properties are of greatest interest and are measured instead using a high current supply, see Subsection 5.1.5.

This method using the Pearson probe is referred to as the "4-wire method with separate current probe".

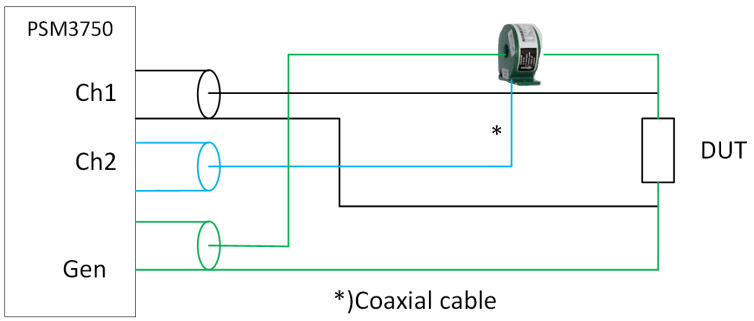


Figure 5.6: Four wire method with separate current probe, valid up to approximately 10–20 MHz.

Conclusion

The four wire method with a separate current probe provides reliable impedance measurements up to approximately 10–20 MHz and performs better than the alternative methods evaluated in this thesis. Its main limitation concerns poor accuracy at low frequencies,

including the region referred to as “DC”, and the method therefore cannot measure the low-frequency properties required for TVS subsystems. Those properties are instead measured using a dedicated high current supply.

5.1.4 Measuring on high voltage batteries with an HV interface

Measurements on a battery or a DC voltage source are not possible with the LCR instrument because the device under test (DUT) contains an internal DC voltage source that is far too high for the instrument. Measurements are not possible on AC sources either. The normal procedure is to measure passive circuits such as resistors, capacitors, inductors or combinations of these. If measurements are performed on devices with an internal DC voltage, the DC voltage must be blocked.

No HV LCR interfaces for voltages around 750 VDC are available on the market, or at least none are identified by the author. Therefore, an HV LCR interface is developed for the measurements in this thesis. A principal schematic is shown in Figure 5.7.

The bandwidth of the interface is estimated to be in the range 100 Hz to 1 MHz. The measurement current is supplied from the PSM3750 generator output and flows through a measurement resistor of 49.9 Ω to the DUT. The value 49.9 Ω must be entered as the scale factor in the LCR instrument. The voltage across the measurement resistor is measured at channel 2 and used to calculate the current. The AC voltage is measured at channel 1 after the capacitors block the DC voltage.

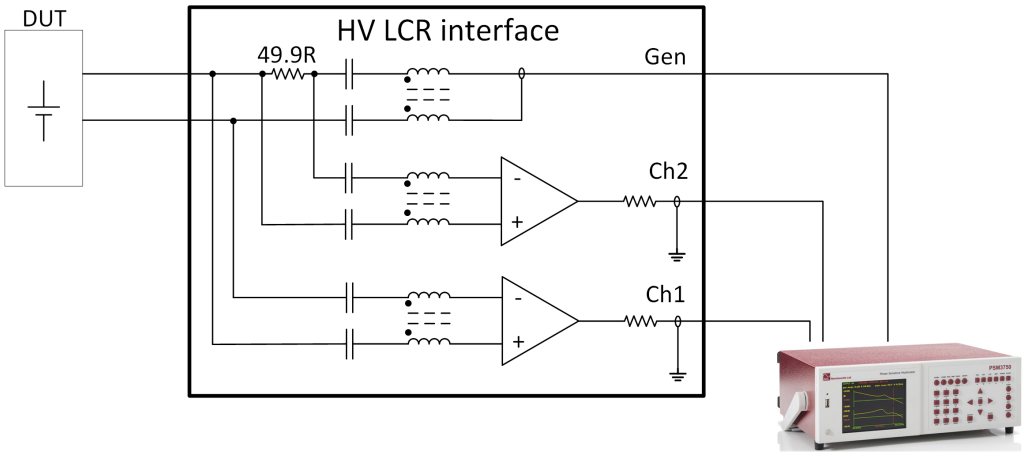


Figure 5.7: HV LCR interface with a bandwidth of approximately 600 Hz–1 MHz.

A battery has a short circuit current that must be handled safely, and the principal setup shown in Figure 5.7 cannot be used directly in a real measurement. A fuse between the DUT and the HV LCR interface protects the wires entering the interface.

Conclusion

The HV interface enables impedance measurements on devices containing an internal DC voltage, such as high voltage batteries. The method provides access to the required AC characteristics within an estimated bandwidth of approximately 100 Hz to 1 MHz. However, protective components such as fuses must be included before practical measurements are carried out to ensure safe operation of the setup.

5.1.5 Measuring with a high-current supply for DC resistance

To measure the DC resistance of the cables without the connectors, the measurement setup uses a current source to deliver a high current. As mentioned earlier in this chapter, the LCR method is not accurate at low impedances, and the cable resistance is low. The measurement circuit is shown in Figure 5.8.

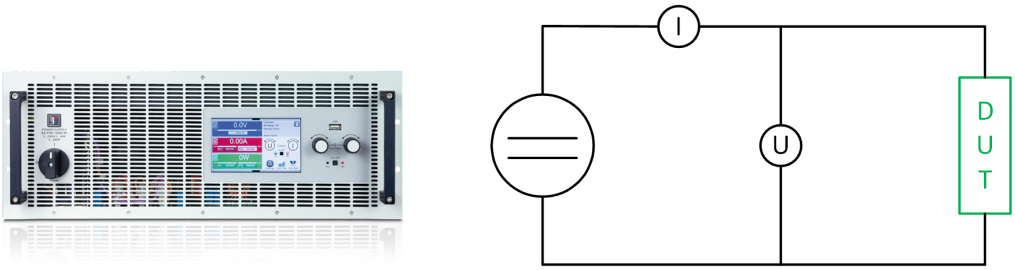


Figure 5.8: Measurement of the DC resistance.

By using a current density of approximately 0.5–2 A/mm2, a stable voltage is measured without heating the cable, and the resulting resistance remains consistent across the tested current range. The resistance is given by

$$R_{DUT} = \frac{U}{I} \tag{5.1}$$

Conclusion

The measurement setup uses a high-current supply to measure the DC resistance of the cables because the LCR method is not accurate at low impedances. By using a current density of approximately 0.5–2 A/mm2, a stable voltage is measured without heating the cable, and the resulting resistance remains consistent across the tested current range.

5.1.6 Conclusion

This section presents the measurement methods required for characterising the subsystems used in the TVS modelling. The Kelvin fixture provides the highest accuracy for small

components but cannot be used for TVS subsystems operating at the TVS level of approximately 600–700 V. Kelvin leads offer a practical four-wire method but are limited to approximately 4–5 MHz due to the inductance and capacitance of the leads. The four-wire method with a separate current probe enables accurate impedance measurements up to approximately 10–20 MHz and is therefore used for high-frequency measurements in this thesis. An HV interface has been developed to enable impedance measurements on devices with internal DC voltages, such as high-voltage batteries. Finally, the DC resistance of cables is measured using a high-current supply, as the LCR method is not accurate at low impedances.

5.2 System simulation tool – PLECS

The simulation tool PLECS [21] supports the implementation of all subsystem models used in this work. Although PLECS can operate inside the Matlab/Simulink environment, the standalone version is used here. The tool provides a user-friendly interface for system-level modelling and supports libraries that enable consistent reuse of model components.

In system-level simulations, the subsystem models use a level of detail that enables feasible full-vehicle simulation. PLECS therefore uses ideal semiconductor representations unless non-ideal behaviour is explicitly required. The tool also supports frequency-sweep analysis, which enables direct comparison with LCR-based impedance measurements, and its scripting functionality supports repeated simulations with modified parameter values.

5.3 State space matrices and eigenvalues

A model representing a discrete component, subsystem or vehicle-level system expresses its behaviour using state-space matrices. Although the matrices are not the primary modelling interface in the simulation tools used in this thesis, they are required to determine the eigenvalues of the circuit. To introduce the method, Figure 5.9 shows a simple RLC model that illustrates how the state-space matrices and eigenvalues are derived.

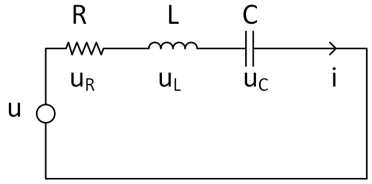


Figure 5.9: RLC circuit used to derive the state-space matrix.

From Figure 5.9, the following equations are derived:

$$u_R = Ri \tag{5.2}$$

$$u_L = L\frac{di}{dt} \tag{5.3}$$

$$i = C\frac{du_C}{dt} \tag{5.4}$$

$$u = u_R + u_L + u_C \tag{5.5}$$

Combining Equations (5.2), (5.3) and (5.5) yields

$$u = Ri + L\frac{di}{dt} + u_C \tag{5.6}$$

Rearranging Equation (5.6) yields

$$\frac{di}{dt} = \frac{1}{L}u - \frac{R}{L}i - \frac{1}{L}u_C \tag{5.7}$$

Rewriting Equation (5.4) yields

$$\frac{du_C}{dt} = \frac{1}{C}i \tag{5.8}$$

The state-space representation is given by

$$\dot{x} = Ax + Bu \tag{5.9}$$

$$y = Cx + Du \tag{5.10}$$

Combining Equations (5.7) and (5.9) yields

$$\dot{i} = -\frac{R}{L}i - \frac{1}{L}u_C + \frac{1}{L}u \tag{5.11}$$

Combining Equations (5.8) and (5.10) yields

$$\dot{u}_C = \frac{1}{C}i \tag{5.12}$$

Equations Equations (5.11) and (5.12) describe the complete state-space system

$$\begin{bmatrix} \dot{i} \\ \dot{u}_C \end{bmatrix} = \begin{bmatrix} -\frac{R}{L} & -\frac{1}{L} \\ \frac{1}{C} & 0 \end{bmatrix} \begin{bmatrix} i \\ u_C \end{bmatrix} + \begin{bmatrix} \frac{1}{L} \\ 0 \end{bmatrix} u \tag{5.13}$$

From Equations (5.9) and (5.13), the matrix A is given by

$$A = \begin{bmatrix} -\frac{R}{L} & -\frac{1}{L} \\ \frac{1}{C} & 0 \end{bmatrix} \tag{5.14}$$

The eigenvalues of A are the poles of the system. The eigenvalues follow from solving

$$\det(sI - A) = 0 \tag{5.15}$$

Using Equations (5.14) and (5.15) yields

$$\det \begin{bmatrix} s + \frac{R}{L} & \frac{1}{L} \\ -\frac{1}{C} & s \end{bmatrix} = 0 \tag{5.16}$$

$$\left(s + \frac{R}{L}\right) s + \frac{1}{LC} = 0 \tag{5.17}$$

$$s^2 + s\frac{R}{L} + \frac{1}{LC} = 0 \tag{5.18}$$

Solving Equation (5.18) yields

$$s = -\frac{R}{2L} \pm \sqrt{\left(\frac{R}{2L}\right)^2 - \frac{1}{LC}} \tag{5.19}$$

The roots from Equation (5.19) can be written using the damping factor ζ and the natural frequency ω_n

$$s = -\zeta\omega_n \pm \omega_n\sqrt{\zeta^2 - 1} \tag{5.20}$$

$$\omega_n = \frac{1}{\sqrt{LC}} \tag{5.21}$$

$$\zeta = \frac{R}{2}\sqrt{\frac{C}{L}} \tag{5.22}$$

To provide clarity and structure, this section is organised into the subsections listed below:

Subsection 5.3.1 Shows how eigenvalues, natural frequencies and damping are extracted using PLECS.

Subsection 5.3.2 Validates the script using analytical calculations, AC sweeps and frequency comparisons.

Subsection 5.3.3 Demonstrates how high-frequency resonances are eliminated to produce a reduced subsystem model.

5.3.1 Eigenvalues, natural frequencies and damping in PLECS

In the simulation program PLECS, the system poles are expressed directly as the eigenvalues of the state matrix. To analyse circuits, the natural frequency ω_n and the damping factor ζ are needed. From Equation (5.19), the two roots are

$$s_1 = -\frac{R}{2L} + \sqrt{\left(\frac{R}{2L}\right)^2 - \frac{1}{LC}} \tag{5.23}$$

$$s_2 = -\frac{R}{2L} - \sqrt{\left(\frac{R}{2L}\right)^2 - \frac{1}{LC}} \tag{5.24}$$

Combining Equations (5.23) and (5.24) gives

$$s_1 + s_2 = -2\frac{R}{2L} \tag{5.25}$$

$$s_1 - s_2 = 2\sqrt{\left(\frac{R}{2L}\right)^2 - \frac{1}{LC}} \tag{5.26}$$

Combining Equations (5.25) and (5.26):

$$s_1 - s_2 = 2\sqrt{\frac{(-(s_1 + s_2))^2}{4} - \frac{1}{LC}} \tag{5.27}$$

$$\frac{(s_1 - s_2)^2}{4} = \frac{(s_1 + s_2)^2}{4} - \frac{1}{LC} \tag{5.28}$$

$$\frac{1}{LC} = \frac{(s_1 + s_2)^2}{4} - \frac{(s_1 - s_2)^2)}{4} \tag{5.29}$$

Using Equations (5.21) and (5.29):

$$\omega_n = \sqrt{\frac{(s_1 + s_2)^2}{4} - \frac{(s_1 - s_2)^2}{4}} \tag{5.30}$$

$$\zeta = -\frac{s_1 + s_2}{2\omega_n} \tag{5.31}$$

A PLECS script evaluates the expressions in Equations (5.30) and (5.31). The implementation follows directly from the equations, and the script is therefore not included in the appendix.

5.3.2 Validation of script

The circuits in a vehicle are complex. Figure 5.10 analyses a simple circuit to verify the script.

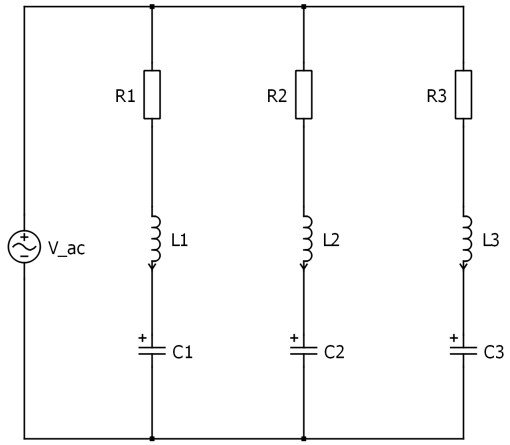


Figure 5.10: Three parallel RLC circuits.

For verification, the RLC values are selected such that the natural frequencies appear clearly separated

$$\begin{aligned} R_1 &= 1\ \Omega, & L_1 &= 100\ \mu H, & C_1 &= 100\ \mu F, \\ R_2 &= 0.1\ \Omega, & L_2 &= 10\ \mu H, & C_2 &= 1\ \mu F, \\ R_3 &= 0.01\ \Omega, & L_3 &= 10\ \text{nH}, & C_3 &= 10\ \text{nF}. \end{aligned}$$

The script in PLECS returns the following values

$$\begin{aligned} f_1 &= 1591\ \text{Hz}, & \zeta_1 &= 0.5, \\ f_2 &= 50329\ \text{Hz}, & \zeta_2 &= 0.0158, \\ f_3 &= 15915494\ \text{Hz}, & \zeta_3 &= 0.005. \end{aligned}$$

Using hand calculations of Equations (5.21) and (5.22) for each RLC branch in Figure 5.10 yields

$$\begin{aligned} f_1 &= 1591\ \text{Hz}, & \zeta_1 &= 0.5, \\ f_2 &= 50329\ \text{Hz}, & \zeta_2 &= 0.0158, \\ f_3 &= 15915494\ \text{Hz}, & \zeta_3 &= 0.005. \end{aligned}$$

An AC sweep analyses the circuit in Figure 5.10. Figure 5.11 shows the result.

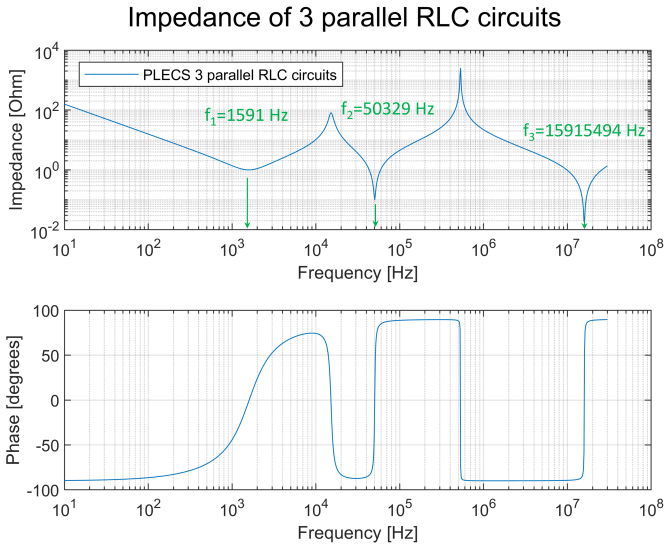


Figure 5.11: AC sweep of the circuit in Figure 5.10. The resonance frequencies are marked and align well with the script results.

The analysis considers the circuit in Figure 5.10 and uses an upper frequency of interest of 10 MHz. The script returns a natural frequency of 15.9 MHz. The components responsible for this high-frequency resonance can therefore be identified and removed from the model, since they lie outside the frequency range of interest.

Conclusion

The verification shows that the script, the AC sweep and the hand calculations produce identical values for both the natural frequency and the damping factor. The agreement between the script, the AC sweep and the hand calculations confirms the script's correctness.

5.3.3 Model simplification method

The model simplification uses the script to reduce a complex subsystem. The simplification reduces the size of the state-space matrix while retaining the natural frequencies within the range of interest. The procedure removes components that do not affect the resonances within this frequency range.

The model considered here is a subsystem that is not used in the vehicle and can therefore be shown in full detail. The complete model builds on the measurement results and adjusts to them accordingly. Figure 5.12 shows the subsystem.

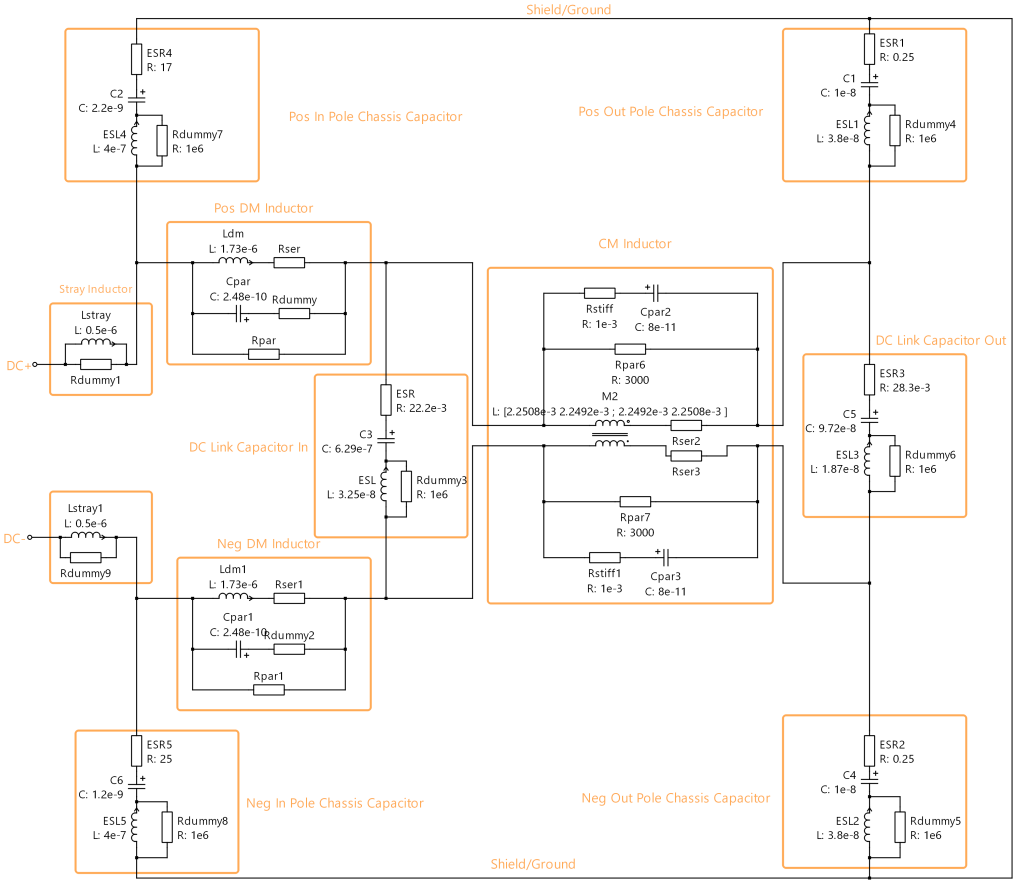


Figure 5.12: Subsystem in full resolution.

The subsystem is analysed under both differential-mode and common-mode conditions. Because the subsystem is unsymmetrical with respect to positive-to-ground and negative-to-ground, the analysis covers the three configurations: positive-to-negative, positive-to-ground and negative-to-ground. The state-space matrix has a size of 23×23. The natural frequencies for all three connections are presented in Table 5.1.

Table 5.1: Natural frequencies for the subsystem in Figure 5.12.

n	$f_{n\,\mathrm{pos-neg}}$ [Hz]	$f_{n\,\mathrm{pos-gnd}}$ [Hz]	$f_{n\,\mathrm{neg-gnd}}$ [Hz]
1	7.84E−10	2.15E−04	1.89E−10
2	6.04E+04	2.37E+04	2.37E+04
3	8.72E+04	2.98E+05	2.98E+05
4	3.00E+05	2.07E+06	1.58E+06
5	4.53E+06	3.74E+06	5.02E+06
6	6.69E+06	6.69E+06	6.67E+06
7	7.50E+06	7.50E+06	7.50E+06
8	2.21E+07	1.98E+07	1.94E+07
9	3.18E+07	3.68E+07	3.68E+07
10	1.19E+08	1.19E+08	1.19E+08
11	3.18E+14	3.18E+14	3.18E+14
12	2.29E+15	1.89E+15	1.89E+15
13	4.53E+15	4.96E+15	4.96E+15

A frequency sweep in PLECS analyses the subsystem in Figure 5.12. Figure 5.13 shows the natural frequencies from Table 5.1, marked with arrows and the corresponding index n. For the positive-to-ground and negative-to-ground cases, all curves overlap except the resonance corresponding to $n = 4$ and $n = 5$, highlighted in red. Frequencies for $n = 1, 11, 12$ and 13 fall outside the displayed frequency range.

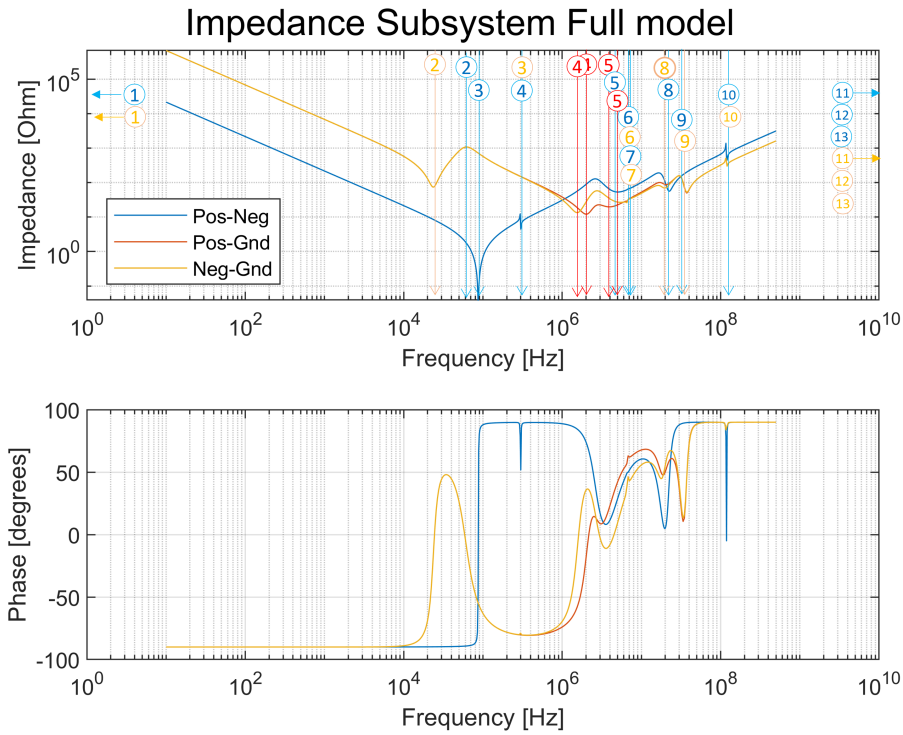


Figure 5.13: Frequency sweep of the subsystem in full resolution.

The first task is to identify the frequency range of interest for the simulation. Assume that 10 MHz is the upper frequency of interest. From Table 5.1, natural frequencies for $n \geq 10$ can be removed. From Equation (5.21), the product $1/(2\pi\sqrt{LC})$ must exceed 10^7. Inspection of Figure 5.12 shows that C_{par2} and C_{par3}, in series with L_{stray} and L_{stray1}, respectively, create small $L \cdot C$ products. The result after removing these components is shown in Figures 5.14 to 5.16.

At approximately 10^8 Hz, the simplification step removes a small resonance from all three graphs. At approximately $3 \cdot 10^7$ Hz, the simplification step removes another resonance in the positive-to-ground and negative-to-ground cases.

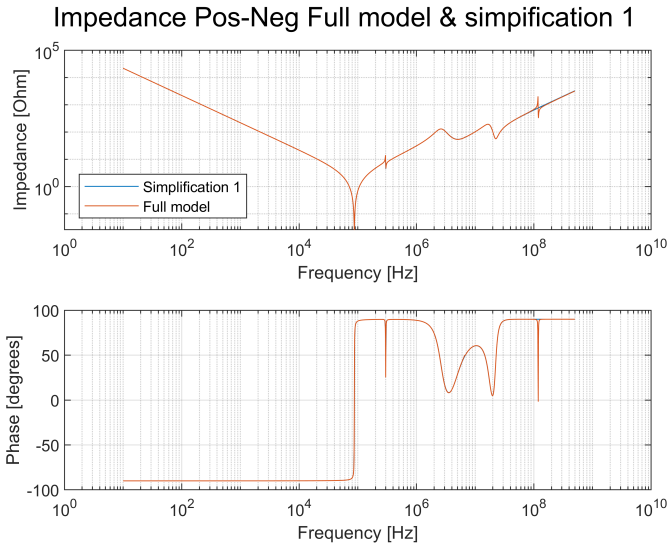


Figure 5.14: Frequency sweep (positive to negative pole) after removal of C_{par2} and C_{par3}.

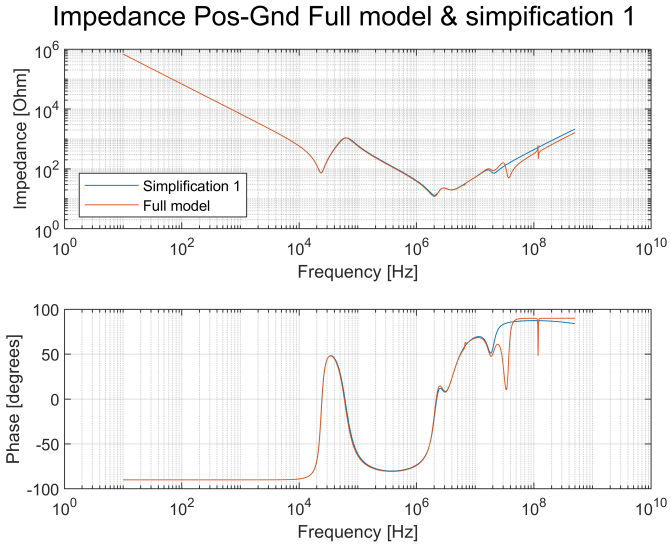


Figure 5.15: Frequency sweep (positive pole to ground) after removal of C_{par2} and C_{par3}.

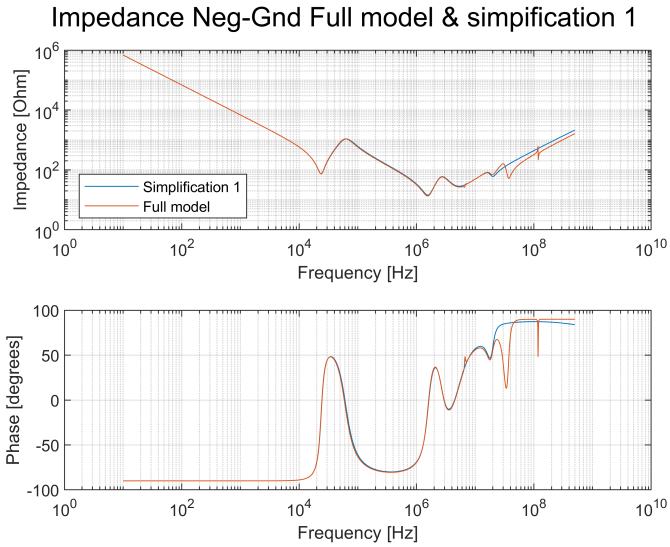


Figure 5.16: Frequency sweep (negative pole to ground) after removal of C_{par2} and C_{par3}.

A second simplification is performed by removing C_{par} and C_{par1}. At approximately $2 \cdot 10^7$ Hz, an additional resonance is removed in all three configurations. The resulting frequency sweeps are shown in Figures 5.17 to 5.19.

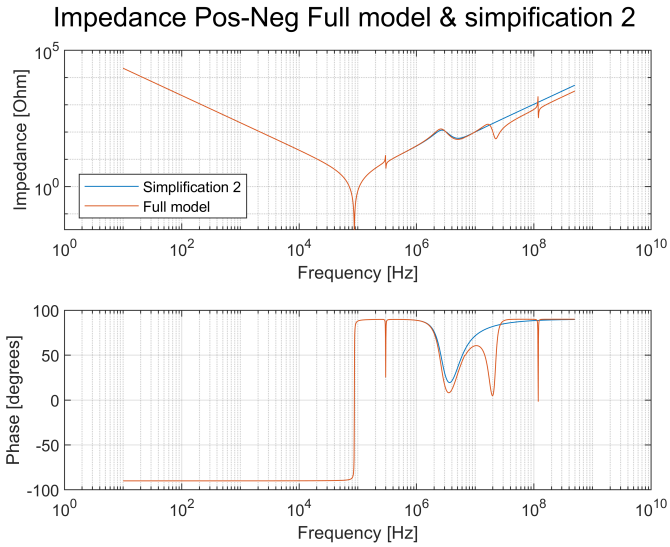


Figure 5.17: Frequency sweep (positive to negative pole) after removal of C_{par} and C_{par1}.

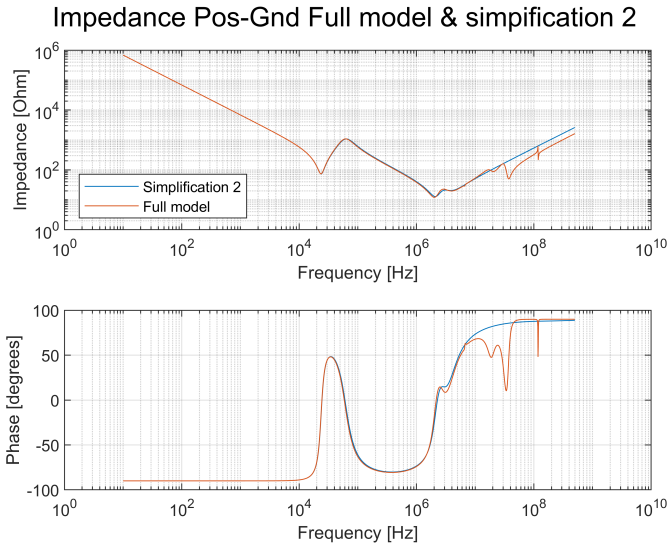


Figure 5.18: Frequency sweep (positive pole to ground) after removal of C_{par} and C_{par1}.

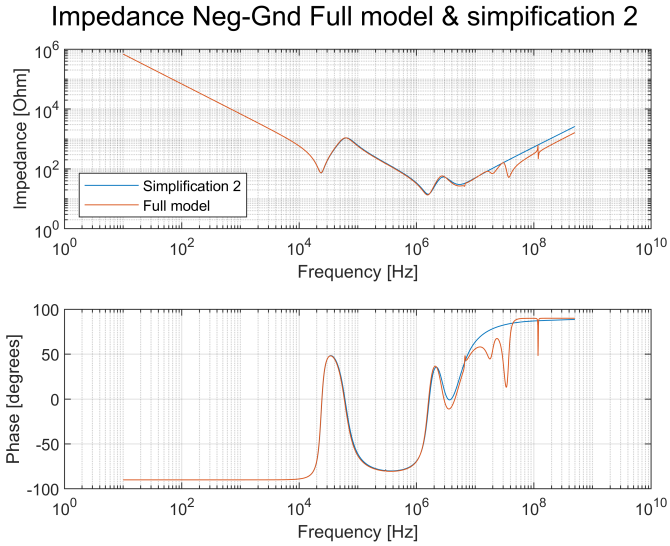


Figure 5.19: Frequency sweep (negative pole to ground) after removal of C_{par} and C_{par1}.

After the two simplifications, the state-space matrix decreases in size from 23×23 to 18×18. The resulting natural frequencies are shown in Table 5.2.

Table 5.2: Natural frequencies for the simplified subsystem after removing C_{par}, C_{par1}, C_{par2} and C_{par3}.

n	$f_{n\ \text{pos}-\text{neg}}$ [Hz]	$f_{n\ \text{pos}-\text{gnd}}$ [Hz]	$f_{n\ \text{neg}-\text{gnd}}$ [Hz]
1	7.38E−07	1.26E−04	4.66E−07
2	6.20E+04	2.38E+04	2.38E+04
3	8.72E+04	2.98E+05	2.98E+05
4	3.00E+05	2.15E+06	1.61E+06
5	4.55E+06	3.76E+06	5.02E+06
6	7.50E+06	7.50E+06	7.50E+06
7	2.21E+08	2.31E+08	2.31E+08
8	2.05E+10	2.05E+10	2.05E+10
9	4.56E+11	4.68E+11	4.68E+11
10	7.91E+11	7.49E+11	7.49E+11
11	3.18E+14	3.18E+14	3.18E+14
14	2.29E+15	1.89E+15	1.89E+15
15	4.53E+15	4.97E+15	4.97E+15

One natural frequency, $n = 7$, falls outside the frequency range of interest, together with the frequencies for $n = 8$–15. These resonances are more difficult to pinpoint than in simplification steps 1 and 2. A possible method is to scan the inductance and capacitance values in the subsystem to determine which component combinations affect the remaining natural frequencies.

Conclusion

The model simplification method demonstrates that natural frequencies outside the frequency range of interest can be systematically identified and removed. By iteratively analysing the state space matrices and performing frequency sweeps, components responsible for high-frequency resonances can be eliminated, resulting in a reduced and computationally efficient subsystem model.

5.3.4 Conclusion

This section shows how state space analysis, natural frequency calculation and targeted simplification techniques reduce the complexity of a subsystem model. By removing components responsible for high-frequency resonances outside the modelling bandwidth, the procedure reduces the state space matrices from 23×23 to 18×18. The method provides a structured approach that retains physical accuracy within the frequency range of interest while improving simulation efficiency.

5.4 Measurement and modelling of subsystems

External companies develop the subsystems used in Volvo vehicles, and this thesis presents their circuit diagrams in a generic format to avoid disclosing protected intellectual property. The measurement graphs are shown in full resolution, as the same electrical quantities can be measured directly on any vehicle of the same type, making these results non-proprietary even though the underlying circuit diagrams remain confidential. The modelling process develops all models from suitable LCR measurements, as described in Section 5.1, and the measurement current remains a small-signal excitation far from the nominal operating level and well below any overload condition. The measurement method cannot operate at operating points corresponding to high current levels, which makes it impossible to derive models that capture current-dependent behaviour. The modelling approach omits this dependency because it cannot be represented with the available measurement method. Inductors and capacitors must not be overloaded, as both lifetime and electrical characteristics change under overload conditions. Datasheet values typically originate from LCR measurements performed with small-signal excitation.

CM simulations use the full subsystem model. This model includes the required CM bandwidth (up to 2 MHz on the DC side and up to 3 MHz on the AC side), which makes it computationally demanding. Consequently, the CM simulation runs only over short time intervals of a few milliseconds.

DM simulations use two different modelling representations depending on the simulation objective. The full subsystem model is employed for high frequency impedance validation and frequency domain analysis, while a reduced subsystem model is used for time domain simulations over extended time scales. The reduced DM model is designed to be valid up to 200 kHz while significantly reducing the size of the state-space matrices. This simplification allows the complete TVS to be simulated over longer time intervals while preserving the DM behaviour within the frequency range of interest.

The following subsections provide the measurements and modelling results for the individual subsystems. For each component, the high-frequency impedance behaviour is described and modelled to capture both CM and DM behaviour over the relevant frequency range. Where required for long time simulations, a reduced DM model is subsequently introduced and validated against the full model within its intended frequency range.

All subsystems included in this section are available as reduced DM models for system-level time-domain simulations. While the full CM and DM impedance models are shown for all subsystems, only selected reduced DM models are documented in dedicated subsections. The remaining DM models follow the same reduction methodology and are omitted from detailed presentation to avoid redundancy.

To provide clarity and structure, this section is organised into the subsections listed

below:

Subsection 5.4.1 Measurements and modelling of the Electric Machine Drive (EMD), including CM and DM impedance characterisation and model validation.

Subsection 5.4.2 Development and validation of a reduced DM model of the Electric Machine Drive (EMD) for long time-domain simulations.

Subsection 5.4.3 CM-focused modelling of the Electric Machine (EM) based on parasitic capacitances and measured frequency response.

Subsection 5.4.4 High-frequency CM and DM impedance modelling of traction batteries from multiple manufacturers.

Subsection 5.4.5 Construction and validation of a reduced DM model of the battery from manufacturer 2.

Subsection 5.4.6 Measurements relevant to charging-standard requirements, including pole-to-chassis capacitance.

Subsection 5.4.7 High-frequency CM and DM impedance modelling and validation of the DC/DC converter (DCDC).

Subsection 5.4.8 Development of a reduced DM model of the DC/DC converter (DCDC) for long time-domain simulations.

Subsection 5.4.9 CM and DM impedance modelling of the Air Compressor subsystem (AirComp) and comparison with measurements.

Subsection 5.4.10 High-frequency modelling and simplification of the On-board Charger (OnBC) for CM and DM behaviour.

Subsection 5.4.11 CM and DM impedance modelling of the Energy Storage System (ESS) heater and the cab heater.

Subsection 5.4.12 Modelling of the Air Conditioning compressor (AC compressor) DC-link, including CM filter, parasitic elements and impedance validation.

Subsection 5.4.13 CM and DM modelling of the On-board Charger and Electric Power Supply (OCEPS) subsystem.

Subsection 5.4.14 Modelling, simplification and validation of coaxial, twin-axial and multi-core cables used in the Traction Voltage System (TVS).

Subsection 5.4.15 Modelling and impedance characterisation of the Junction Box (JB/HJB).

Subsection 5.4.16 Modelling of the Break Out Box (BoB) and evaluation of its influence on impedance measurements.

5.4.1 Measurements and modelling of the EMD (CM and DM behaviour)

The EMD is a four-quadrant three-phase converter that drives and brakes the electric traction machines in the vehicle. It is the converter with the highest power rating in the vehicle, up to 50 times the rated power of the auxiliary converters. Figure 5.20 shows a simplified schematic of the EMD.

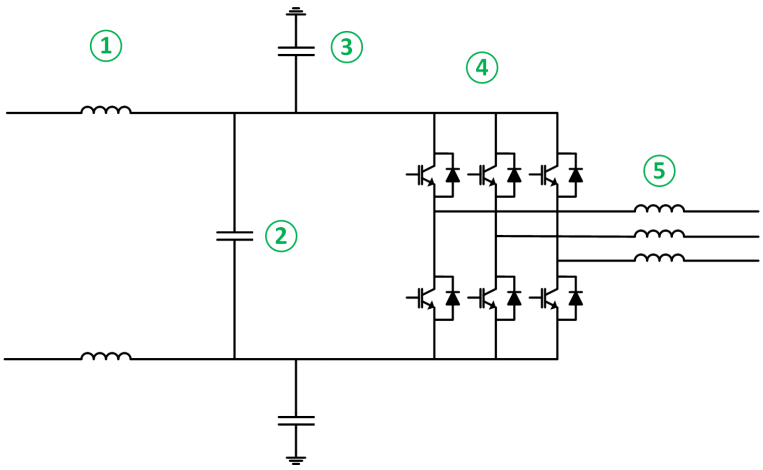


Figure 5.20: EMD main circuit.

The following parts are included in the EMD:

1. Input CM filter, reducing the CM currents.
2. DC-link capacitor, supplying and storing the switching power.
3. CM capacitor, providing a return path for CM currents.
4. Three-phase converter bridge.
5. Output CM filter, reducing the CM current to the EM.

The complete model of the EMD is highly complex and is not included here. However, the simulations presented in this thesis use the full model. The complete simulation model in PLECS contains over 50 discrete components. In this model, a physical capacitor is represented by five discrete components. The IGBT model used in the simulations is developed in co-operation with the supplier and includes, among other parameters, rise and fall time, stray inductance and forward voltage drop. Although PLECS prefers idealised semiconductor representations, non-ideal IGBT behaviour is essential when simulating CM currents, as variations in rise and fall time directly influence the CM current.

Three impedance measurements must agree with the simulation model, as shown in Figures 5.21, 5.23 and 5.25:

- Impedance from positive to negative pole (DM properties).
- Impedance from positive pole to vehicle chassis (CM properties).
- Impedance from negative pole to vehicle chassis (CM properties).

Figures 5.22, 5.24 and 5.26 show that the measured impedance correlates with the model up to 10 MHz for both DM and CM. A small resonance is observed in the DM curve at approximately 2–3 MHz. Figure 5.20 shows the capacitive structure between the positive and negative poles and ground, from which this resonance originates. The DM impedance is only relevant within the DM modelling range, i.e. up to 200 kHz.

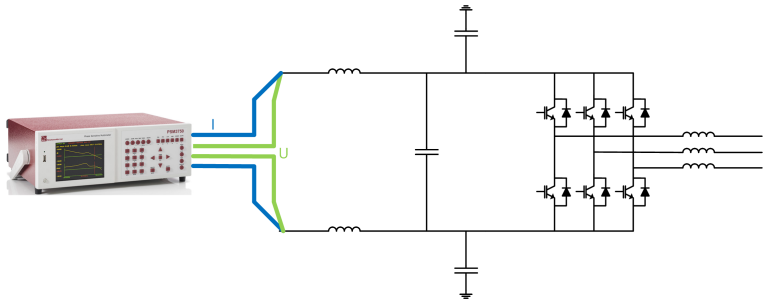


Figure 5.21: LCR measurement of the impedance and phase measured from positive to negative pole.

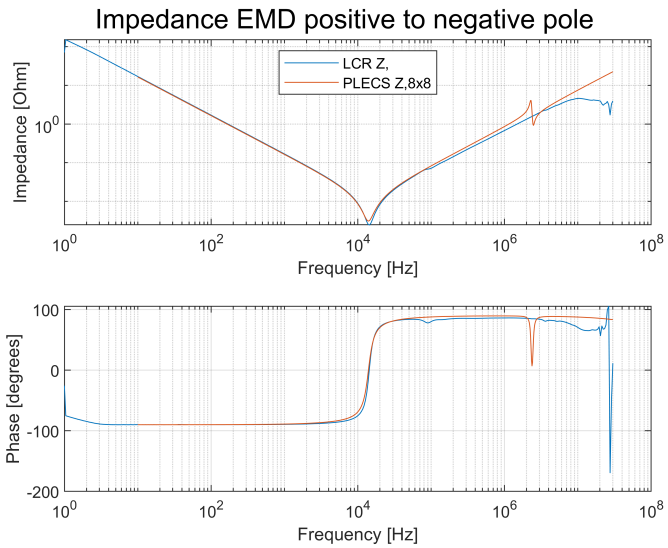


Figure 5.22: Impedance and phase as a function of frequency for the EMD measured from positive to negative pole.

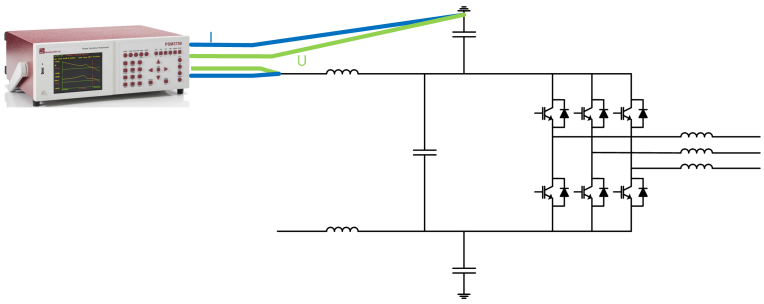


Figure 5.23: LCR measurement of the impedance and phase measured from positive pole to vehicle chassis.

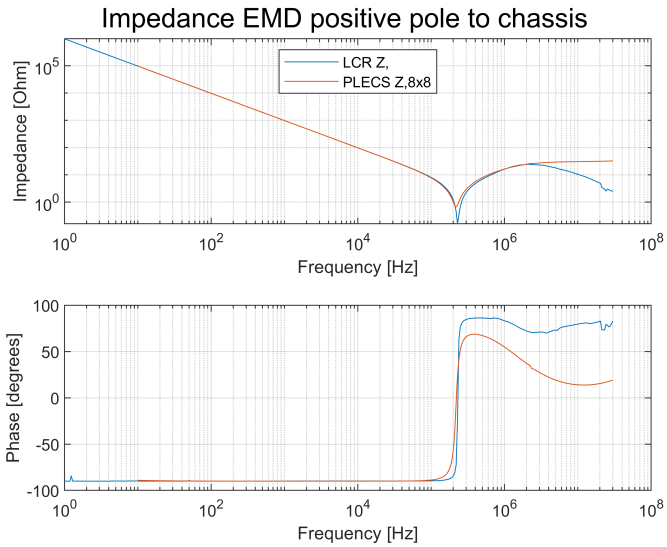


Figure 5.24: Impedance and phase as a function of frequency for the EMD measured from positive pole to vehicle chassis.

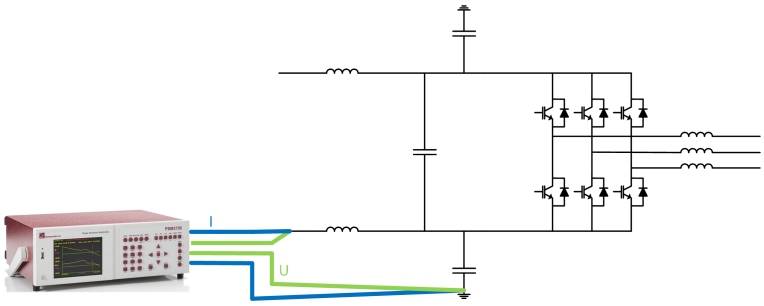


Figure 5.25: LCR measurement of the impedance and phase measured from negative pole to vehicle chassis.

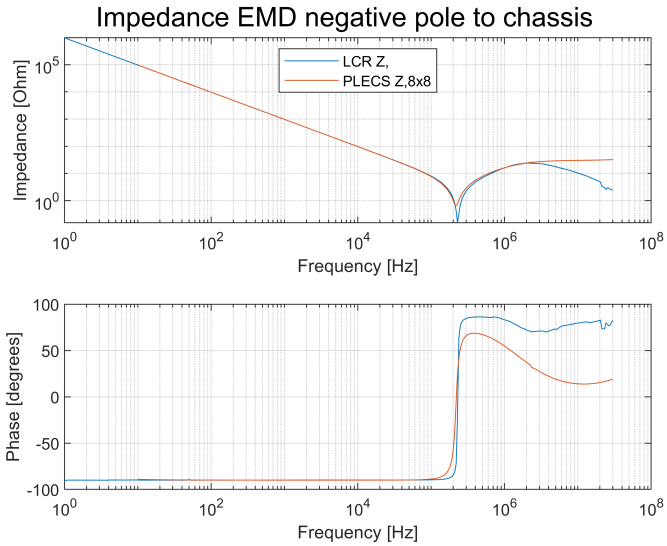


Figure 5.26: Impedance and phase as a function of frequency for the EMD measured from negative pole to vehicle chassis.

Conclusion

In the simulation model, the DC-link and the three-phase converter bridge are separated. The DC-link contributes an 8×8 state space matrix, and the converter bridge contributes a 12×12 matrix, resulting in a combined 20×20 state space model. The original model before reduction consists of a 65×65 state space matrix. The reduced model is valid up to approximately 4 MHz, and even up to 10 MHz the deviation from the measured impedance remains small.

5.4.2 Reduced modelling of the EMD for DM behaviour

In Subsection 5.4.7, the high-frequency parameters of the EMD come from the analysis described there and are required for CM simulations. However, the high-frequency model is too detailed to use for DM simulations. DM simulations run over time intervals of several seconds, whereas CM simulations run only over a few milliseconds. This subsection presents a model that is valid for DM behaviour only.

The reference for the DM model is the measured impedance of the full EMD model, shown in Figure 5.22. The main modification from the full model to the DM model is that all elements connected to ground, as well as all CM chokes, are removed, except for the DM-relevant values extracted from the CM choke.

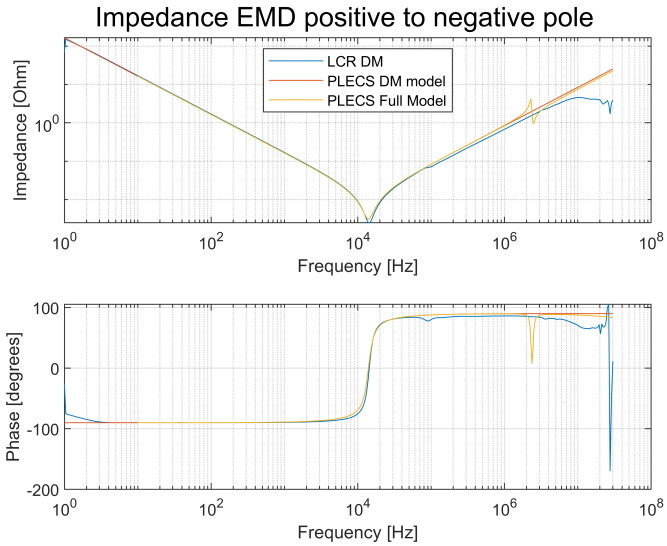


Figure 5.27: DM model of the EMD. The DM model is compared with the measured EMD and the full model with high-frequency parameters.

Figure 5.27 shows that the DM model exhibits good conformity with the full model within the DM modelling range (up to 200 kHz).

Conclusion

The derived DM model reproduces the DM-relevant impedance behaviour of the EMD and is therefore valid for simulations within the DM modelling bandwidth.

5.4.3 Measurements and modelling of the EM (CM behaviour)

This subsection develops the EM model from a CM perspective only. The CM currents leak to the chassis via the parasitic winding-to-core capacitances, making these capacitances of major importance. The characteristics related to EM torque or speed performance are not included in the CM simulations and therefore fall outside the scope.

An EM has three windings that may be connected in a Y or delta configuration, as shown in Figure 5.28.. The DUT is a Y-connected EM without an accessible neutral point. Figure 5.29 shows the simplified EM model used for the CM analysis. A more detailed model would include capacitances between individual winding turns and between each conductor and the stator. However, as shown in the impedance graph in Figure 5.33, the measured phase-to-ground impedance shows good agreement with the simplified model, even though some resonances are not captured. The absolute impedance level is sufficiently close to the measurements for CM analysis.

The measured CM current spectra reach up to approximately 10 MHz. In contrast, the CM modelling bandwidth follows the limits established in Chapter 4: up to 2 MHz for the DC side and up to 3 MHz for the AC side. The parasitic capacitances in the EM are symmetrical, i.e. identical for all three phases. Ageing effects may introduce small differences, but such deviations are difficult to predict. The measurements used for modelling are carried out on a new EM, and the resulting parasitic capacitances are found to be nearly identical across all phases.

Parasitic capacitances also exist between the stator windings and the rotor. The return path to chassis or ground goes through the bearings or the transmission. Since all measurements in this thesis occur with the EM at standstill, the resulting return-path behaviour is modelled as winding-to-chassis capacitances.

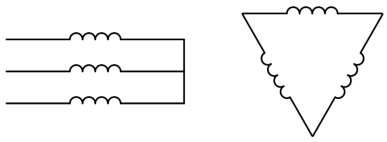


Figure 5.28: EM in a Y or Delta connection

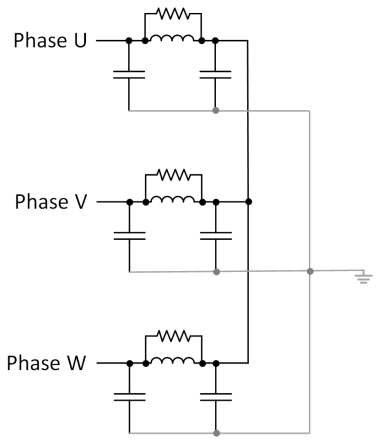


Figure 5.29: EM model structure adapted to the LCR measurement

The frequency response is measured using the Kelvin method and the 4-wire method with a separate current probe. The Kelvin method is used for the low-frequency range, while the 4-wire method with a separate current probe is used for the high-frequency range. The frequency response is measured in the following configurations, and the results are compared with simulations:

- One phase to ground, as shown in Figure 5.30.
- All phases short-circuited and measured to ground, as illustrated in Figure 5.31.

- Phase to phase, as presented in Figure 5.32.

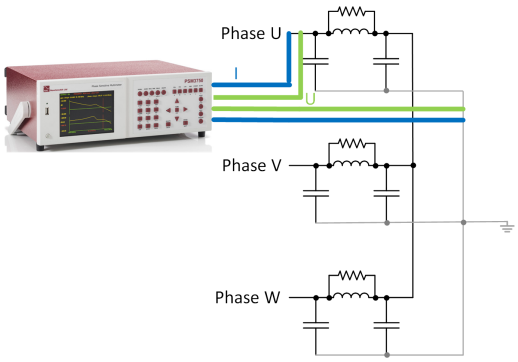


Figure 5.30: EM measured from one phase to ground

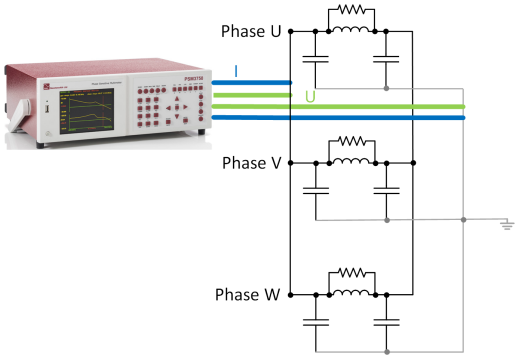


Figure 5.31: EM measured from all phases to ground

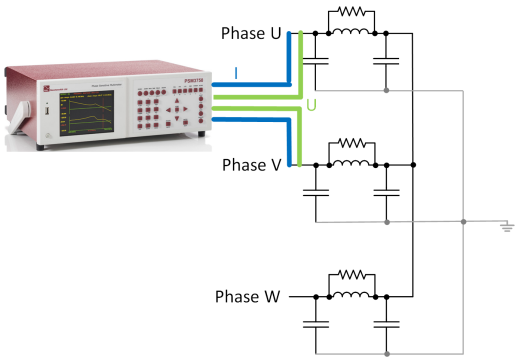


Figure 5.32: EM measured from phase to phase

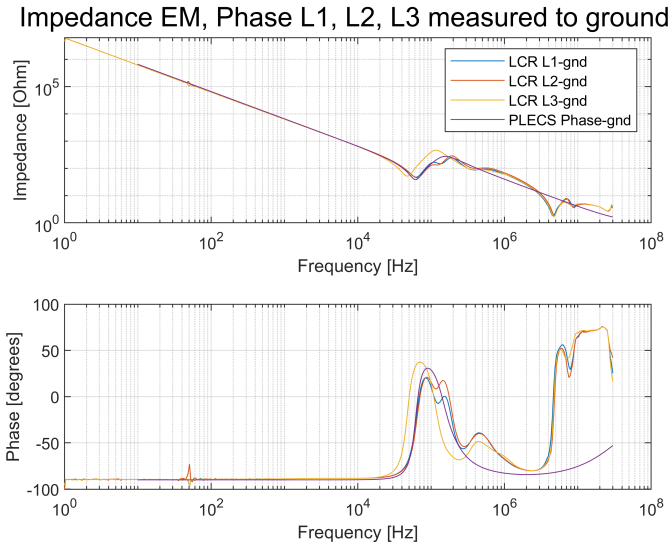


Figure 5.33: EM measured from one phase to ground. The slight deviation around 60 kHz originates from rotor position

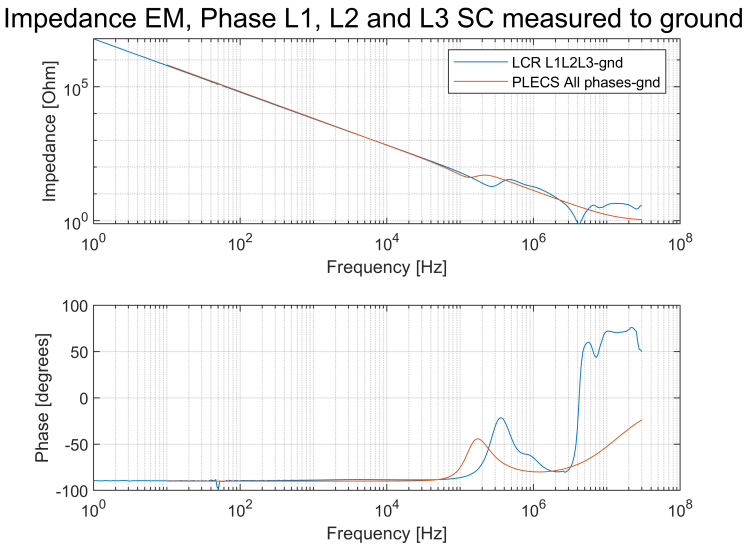


Figure 5.34: EM measured from all phases to ground. The small deviation shifts between phases when the rotor is rotated

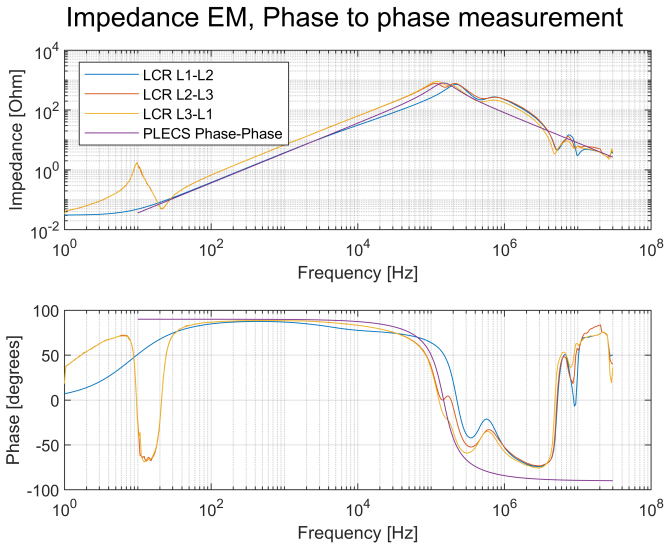


Figure 5.35: EM measured from phase to phase. The deviation between phases results from rotor position

Although the parasitic capacitances of the EM are symmetrical, the measured inductances show a slight variation with frequency between the phases. This variation is visible in Figure 5.33, where L2 deviates slightly around 60 kHz, and a similar deviation occurs between phases L3 and L1 in Figure 5.35. This variation does not result from winding asymmetry but rather from the rotor position during measurement. When the rotor angle changes by the smallest mechanical increment, the deviation shifts to a different phase. The effect is therefore periodic with the rotor position and does not indicate a permanent imbalance. In the model, this effect is modelled by assigning one of the three phase windings a slightly higher inductance, while the overall model remains symmetrical.

The resonance at approximately 4 MHz does not occur in the simplified model. However, at these high frequencies and with the EM at standstill, the model is sufficiently accurate for CM purposes.

Conclusion

The simplified CM model of the EM reproduces the measured phase-to-ground, phases-to-ground and phase-to-phase impedance with sufficient accuracy within the CM modelling bandwidth. It is therefore considered valid for CM simulations of the traction system.

5.4.4 Measurements and modelling of the battery (CM and DM behaviour)

Building the EM modelling in the previous subsection, this subsection presents measurements and modelling of the battery relevant to high-frequency behaviour.

The development of the battery model and the corresponding measurements serve two purposes. First, the analysis focuses on the HF parameters that influence the DM and CM impedance. Second, the parasitic capacitance from pole to chassis is important in the context of charging standards.

For this thesis, the battery models are developed from both DM and CM perspectives. The interface described in Subsection 5.1.4 is used to perform the measurements. The complete models are developed through reverse engineering of the impedance measurements, and a principal schematic is included in the measurement setup shown in Figure 5.36. The positive-to-negative pole measurement is shown in Figure 5.36, while the pole-to-chassis measurement is shown in Figure 5.37. For the battery from manufacturer 1, the impedance and frequency-response results are shown for DM in Figure 5.38 and for CM in Figure 5.39. For battery manufacturer 2, the positive-to-negative pole impedance is shown in Figure 5.40, while the pole-to-chassis impedance is shown in Figure 5.41.

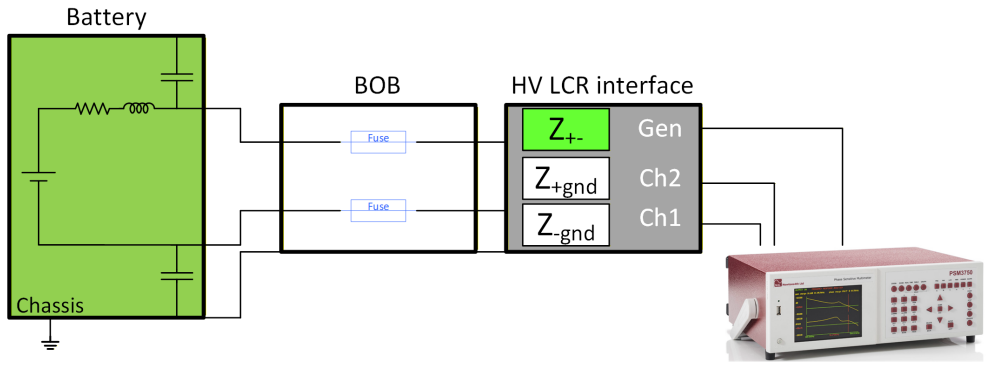


Figure 5.36: Measurement setup for pole-to-pole impedance measurement, including a simplified schematic of the battery. The HV LCR interface is configured to measure the impedance between the positive and negative poles.

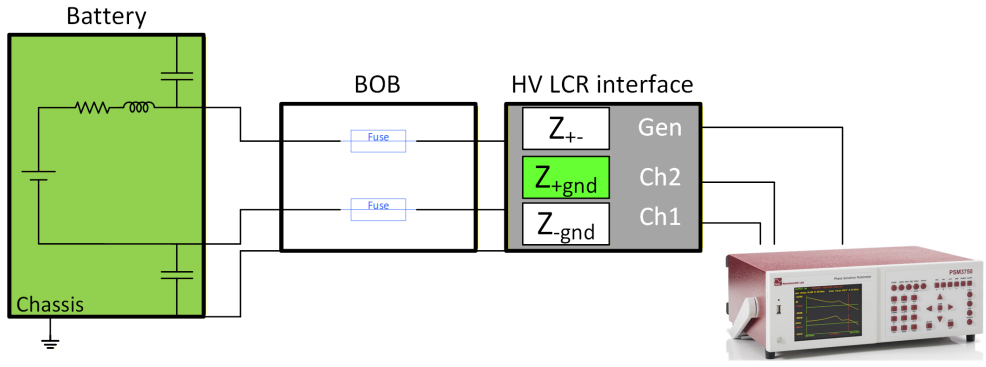


Figure 5.37: Measurement setup for pole-to-ground impedance measurement, including a simplified schematic of the battery. The HV LCR interface is configured to measure the impedance between the positive pole and ground.

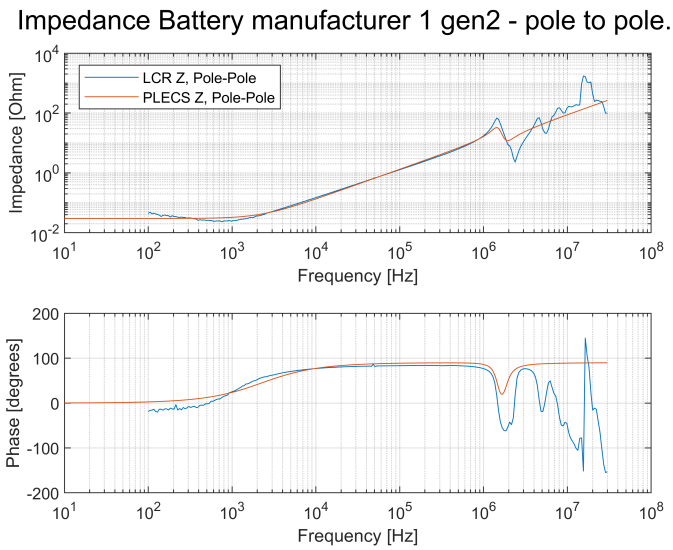


Figure 5.38: Battery from manufacturer 1 gen2 measured from pole to pole compared with the model.

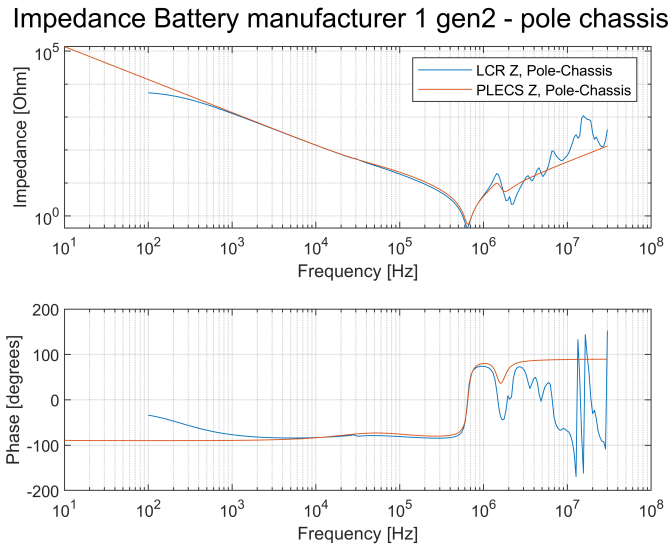


Figure 5.39: Battery from manufacturer 1 gen2 measured from pole to ground compared with the model.

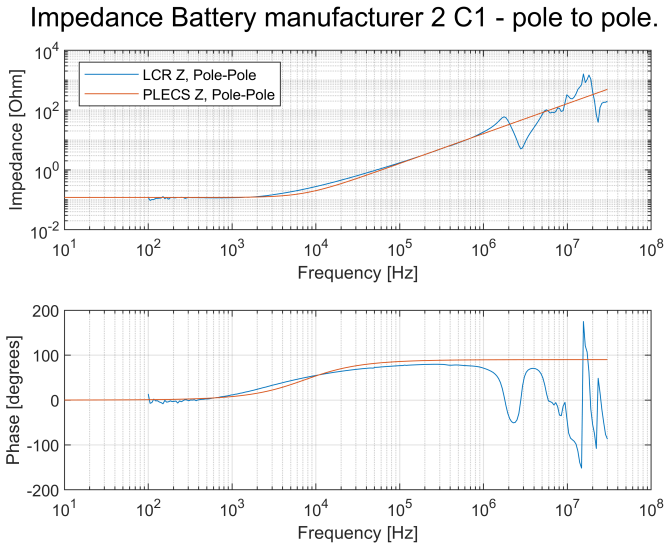


Figure 5.40: Battery manufacturer 2 measured from pole to pole and the PLECS model of the battery.

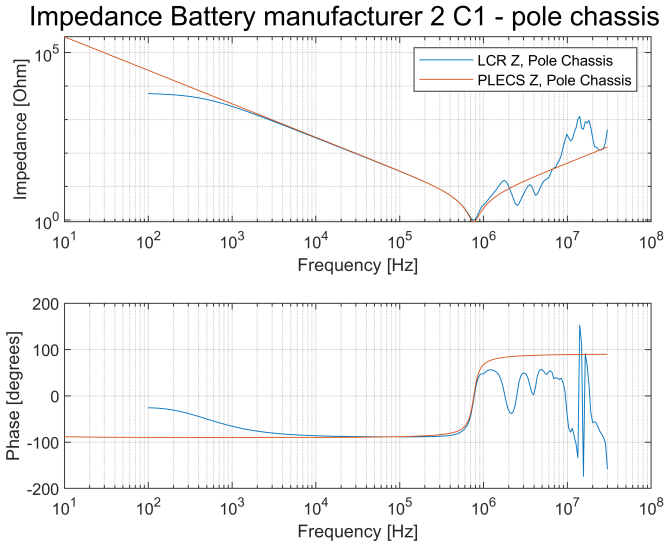


Figure 5.41: Battery manufacturer 2 measured from pole to ground.

In large vehicles, significant amounts of stored energy are needed, and the batteries are therefore connected in parallel. According to measurements, the voltage and current do not differ significantly between the parallel-connected batteries during vehicle operation, even though the cable lengths differ to a certain extent. As a further simplification, the model

is scalable to n batteries. Thus, n parallel-connected batteries in the vehicle model can be represented by a single scaled battery. Figures 5.42 and 5.43 shows that this simplification agrees well with the impedance comparison.

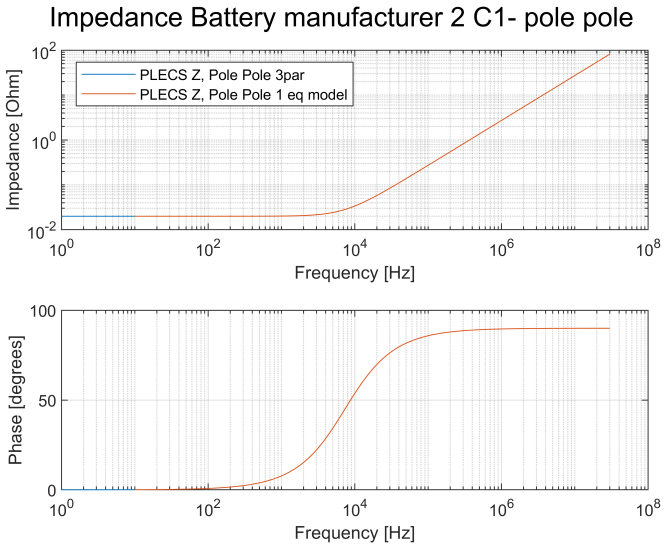


Figure 5.42: Comparison between battery manufacturer 2 model where three batteries are connected in parallel vs. one battery scaled with n=3.

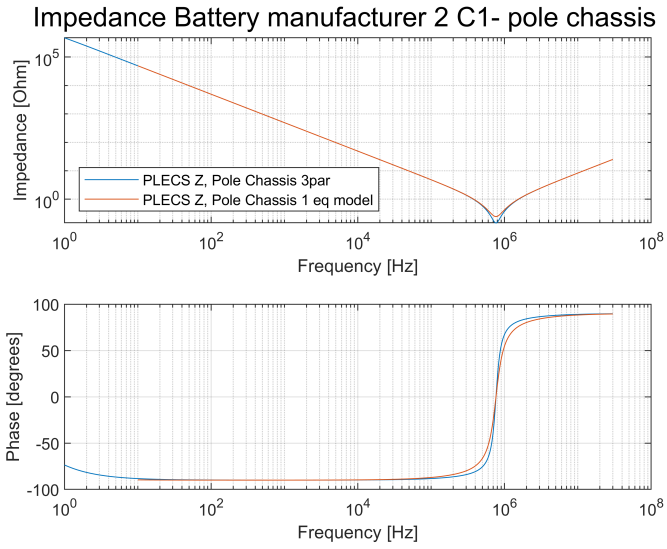


Figure 5.43: Comparison between battery manufacturer 2 model where three batteries are connected in parallel vs. one battery scaled with n=3.

A comparison of the impedances of the two batteries is shown in Figure 5.44 for the pole-to-pole measurement and in Figure 5.45 for the pole-to-chassis measurement.

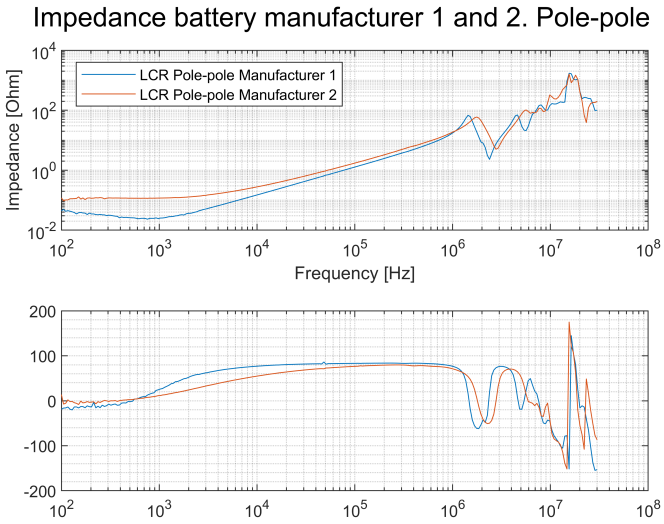


Figure 5.44: Comparison between battery manufacturer 1 and 2 measured from pole to pole.

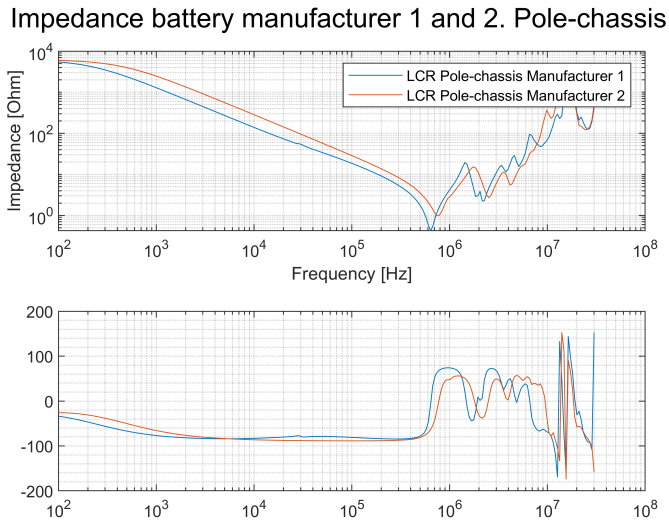


Figure 5.45: Comparison between battery manufacturer 1 and 2 measured from pole to chassis.

Based on measurements showing that the CM currents in the battery occur within

the range of 100–250 kHz, the model must be valid within this range. The measurement interface has an upper bandwidth of 1 MHz. Within this frequency interval, the model agrees well with the measurements.

The battery model, shown in simplified form in the left part of Figures 5.36 and 5.37, is implemented in PLECS using parameter values obtained through the extraction procedure in Appendix A.

Conclusion

The measurements show the pole-to-pole and pole-to-chassis impedances for the two battery manufacturers, and the developed CM and DM models match the measured impedances within the required frequency range. The simplification of parallel battery connections is validated through impedance comparison, and the resulting scalable battery model remains accurate across the relevant bandwidth. The measured CM currents fall within the range of 100–250 kHz, while the CM model is valid up to 2 MHz on the DC side and 3 MHz on the AC side, consistent with the modelling requirements.

5.4.5 Reduced modelling of the battery from manufacturer 2 for DM behaviour

Following the battery modelling for HF-parameters in the previous subsection, this subsection presents the development of a battery model intended specifically for DM-simulations.

In Subsection 5.4.4, the HF parameters of the battery are obtained from the measurements described there and are required for CM simulations. However, the HF-model is too detailed for DM-simulations. DM-simulations run over seconds, whereas CM-simulations run over milliseconds. This subsection presents a model that is valid for DM-parameters only. The reference is the measured parameters for the battery from manufacturer 2 and the full model of this battery shown in Figure 5.40.

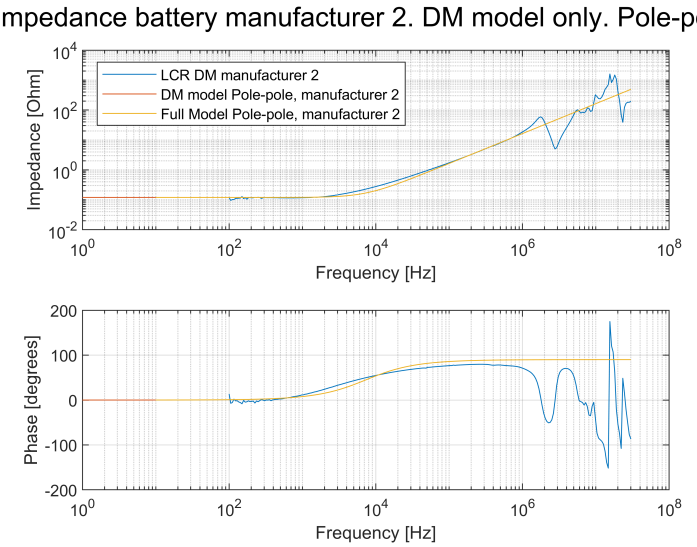


Figure 5.46: DM-model of the battery from manufacturer 2. The model is compared to the measured battery and the full model with HF-parameters.

Figure 5.47 shows a comparison between the six-BP equivalent full model and the DM-model.

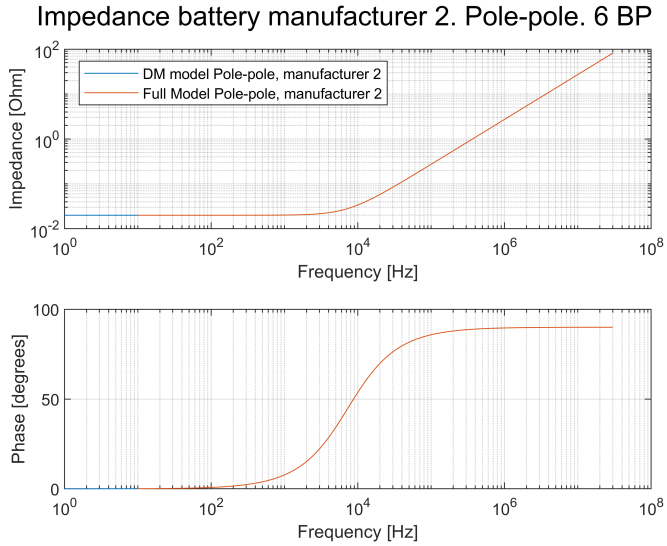


Figure 5.47: Comparison of the six-BP full model and the DM-model for the battery from manufacturer 2.

Figure 5.46 shows that the DM-model produces the same result as the full model when measured from pole to pole.

Conclusion

The DM model matches the full model when measured from pole to pole and is therefore suitable for DM simulations. The model is also valid for n-battery configurations.

5.4.6 Measurements of the battery for charging parameters

Building on the DM battery modelling in the previous subsection, this subsection presents measurements related to the charging requirements defined in international standards.

In Subsection 5.4.4, the HF-parameters of the battery come from the measurements described there. In the CCS charging standard, Electrically propelled road vehicles - Conductive power transfer - Safety requirements (ISO 17409:2020), a maximum pole-to-chassis capacitance is specified for the vehicle. The standard requires the use of the RC method to obtain the total pole-to-chassis capacitance of the battery. The RC method is applied using the setup shown in Figure 5.48.

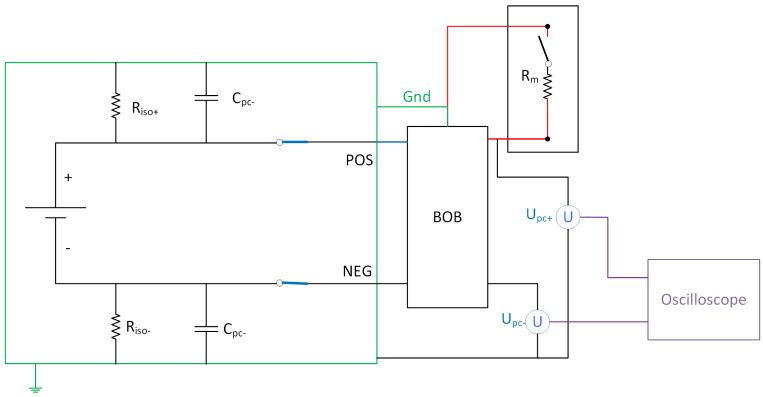


Figure 5.48: Measurement setup according to the charging standard ISO 17409:2020.

The measurements show that the parasitic capacitance measured with the RC method is higher than the capacitance measured with the LCR measurement. The parasitic capacitance also varies with the measurement resistance R_{m}. To enable comparison between the values, the RC method data are converted to frequency using the relationship between measurement resistance and cut-off frequency, as given in [33]. To correlate the frequency and the measurement resistance, the following expression is used:

$$f_c = \frac{1}{2\pi R_{\mathrm{m}} C} \tag{5.32}$$

where f_{c} is the cut-off frequency.

$$R_m = \frac{1}{2\pi f_{\mathrm{c}} C} \tag{5.33}$$

To enable comparison between the values, the two capacitance points obtained with the LCR measurement ($C = 88$ nF at $f_c = 10$ kHz and $C = 80$ nF at $f_c = 100$ kHz) are converted to the corresponding measurement resistances using the RC relationship, resulting in $R_m = 160\ \Omega$ and $16\ \Omega$.

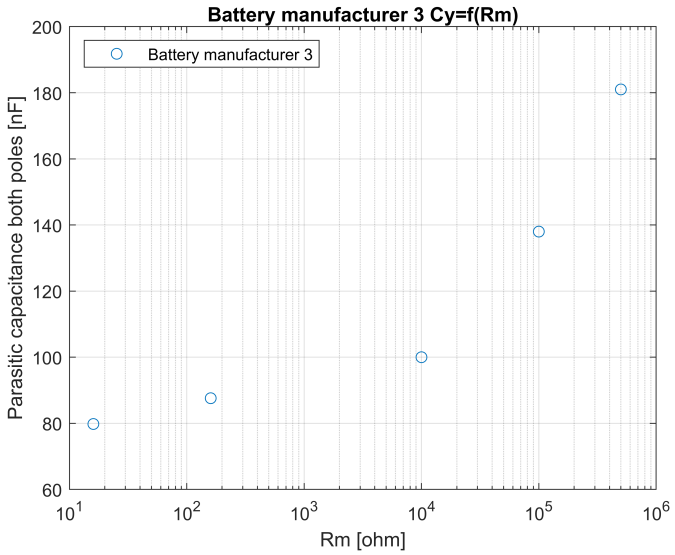


Figure 5.49: Summary of the measured parasitic capacitance from the RC-method and the LCR measurement. The two points on the left are obtained with the LCR method and the three points on the right are from the RC-method measurement.

The graph in Figure 5.49 may be plotted as a function of frequency instead of measurement resistance, as shown in Figure 5.50.

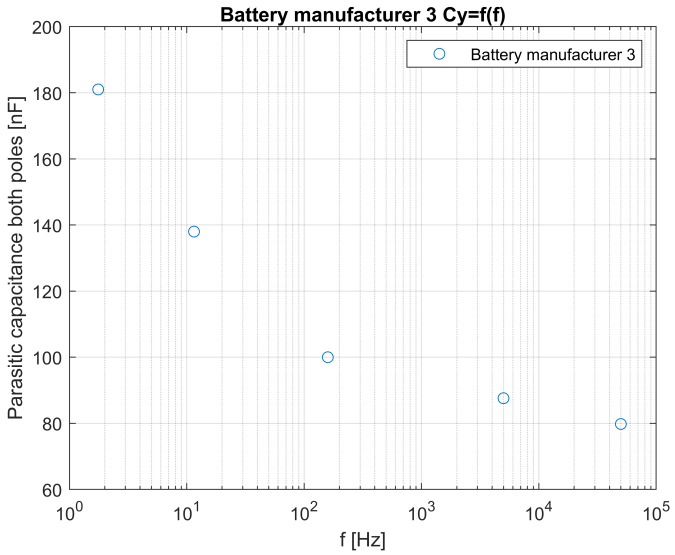


Figure 5.50: Summary of the measured parasitic capacitance from the RC-method and the LCR measurement plotted as a function of frequency. The two points on the right are obtained with the LCR method and the three points on the left are from the RC-method measurement.

The parasitic capacitance varies significantly depending on the frequency or the measurement resistance. The cause of this variation lies outside the scope of this thesis and is left for future work.

Conclusion

The measurements show that the parasitic pole-to-chassis capacitance takes different numerical values in the RC method and in the LCR measurement. This difference does not originate from the measurement methods themselves, but from the strong frequency dependence of the capacitance. In the LCR measurement, the capacitance is obtained directly at a fixed frequency, whereas the RC method determines the capacitance at a frequency corresponding to the applied measurement resistance. As a result, the two methods probe the battery at different effective frequencies, which explains the spread observed in the combined LCR and RC datasets. Since the capacitance varies substantially with frequency, the measurements exhibit nonlinear behaviour that simulations using fixed capacitance values cannot reproduce. Such frequency-dependent effects must therefore be taken into account when interpreting charging-related capacitance measurements.

5.4.7 Measurements and modelling of the DCDC (CM and DM behaviour)

Following the charging-parameter measurements in the previous subsection, this subsection presents the measurements and modelling of the DCDC unit.

The DCDC is a one-quadrant converter supplying the 24 V DC system in the vehicle. It provides galvanic isolation between the traction voltage system (TVS) and the 24 V DC system, which is directly connected to the vehicle chassis. The DCDC is rated at 7 kW. Figure 5.51 shows a simplified schematic of the DCDC.

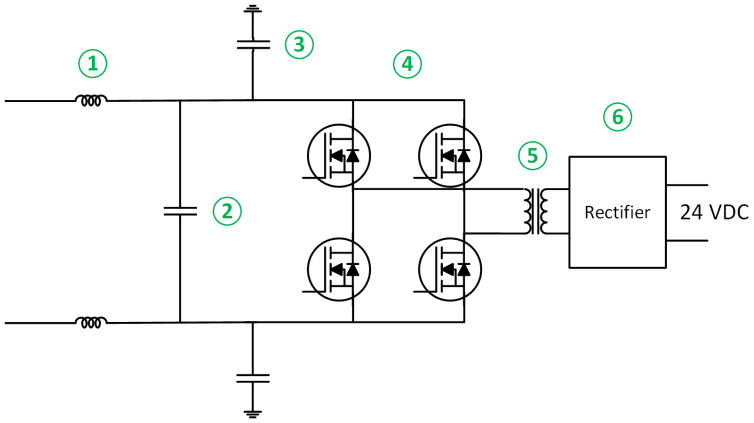


Figure 5.51: DCDC main circuit.

The major parts included in the DCDC are:

1. Input filter inductor, reducing both CM and DM currents.
2. DC-link capacitor, supplying and storing the switching power.
3. CM capacitor, providing a return path for CM currents.
4. H-bridge consisting of two phase legs.
5. Transformer, reducing the voltage and providing galvanic isolation.
6. Rectifier that rectifies and filters the AC current from the transformer. The secondary 24 V side is not part of this thesis.

The complete model of the DCDC is complex and is therefore not shown in full. Simulations nevertheless use the complete model, except for the H-bridge, transformer, and rectifier shown in Figure 5.51. The full simulation model implemented in PLECS contains more than 70 discrete components. The model runs without active switching; the modulation of the H-bridge remains disabled.

Three impedance measurements are of particular importance and are expected to correspond to the simulations, as illustrated in Figures 5.52, 5.54 and 5.56:

- Positive to negative pole, representing DM behaviour.
- Positive pole to vehicle chassis, representing CM behaviour.

- Negative pole to vehicle chassis, representing CM behaviour.

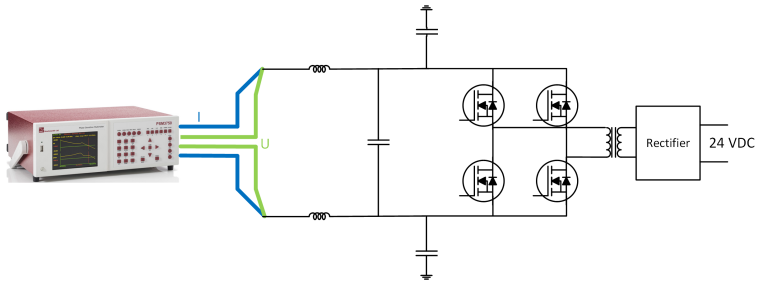


Figure 5.52: LCR measurement of impedance and phase measured from positive to negative pole.

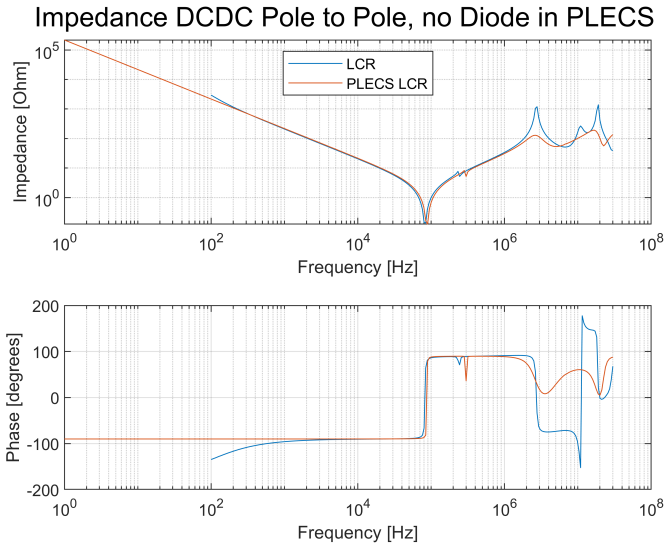


Figure 5.53: Impedance and phase as a function of frequency for the DCDC measured from positive to negative pole.

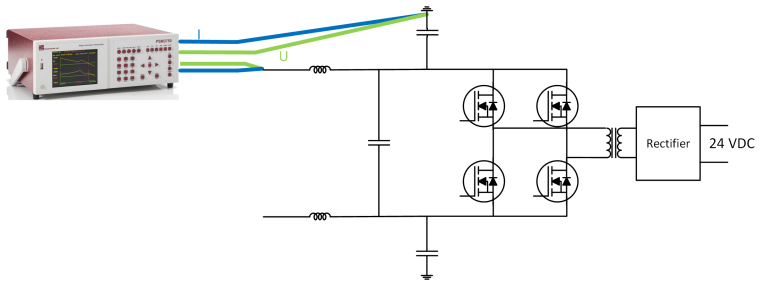


Figure 5.54: LCR measurement of impedance and phase measured from positive pole to vehicle chassis.

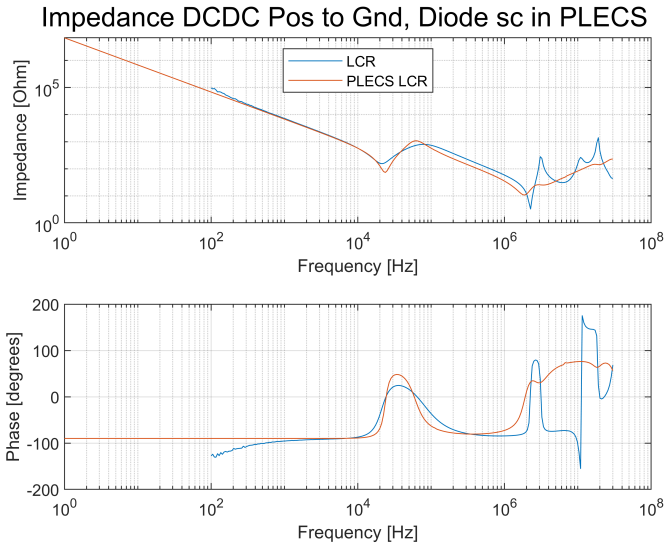


Figure 5.55: Impedance and phase as a function of frequency for the DCDC measured from positive pole to vehicle chassis.

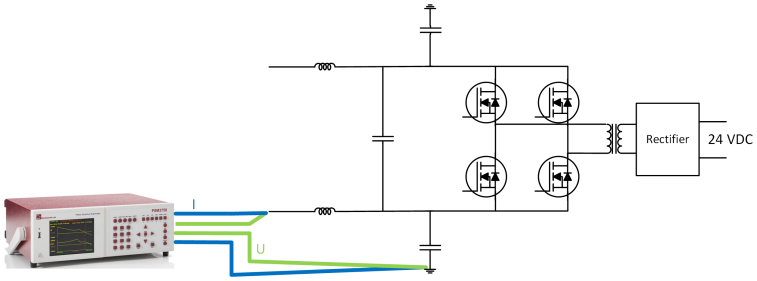


Figure 5.56: LCR measurement of impedance and phase measured from negative pole to vehicle chassis.

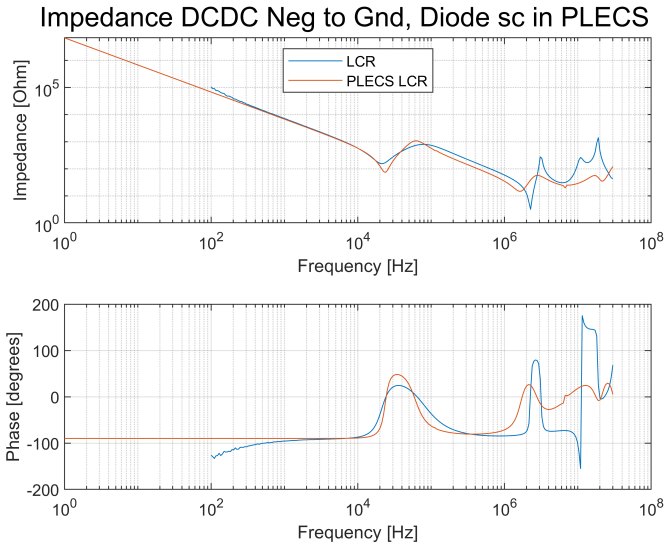


Figure 5.57: Impedance and phase as a function of frequency for the DCDC measured from negative pole to vehicle chassis.

The DCDC model, shown in simplified form in the left part of Figure 5.51, is implemented in PLECS using parameter values obtained through the extraction procedure in Appendix A.

Figures 5.53, 5.55 and 5.57 show that the measured impedance agrees well with the model up to approximately 2-3 MHz for both DM and CM. In the frequency range from approximately 70 kHz to 2 MHz, the deviation lies on the order of 30 %.

The state-space representation of the full DCDC model consists of a 29×29 matrix. Such a model is not computationally feasible for full-vehicle simulations. A reduced-order model is therefore derived, reducing the state-space size to 14×14 while preserving accuracy in the frequency range of interest. Figures 5.58 and 5.59 show the comparison between the full and reduced models.

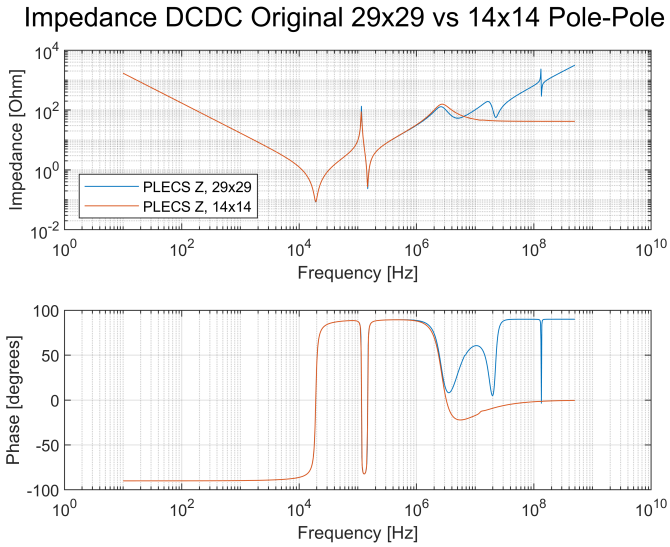


Figure 5.58: Impedance and phase as a function of frequency for the DCDC measured from positive to negative pole. Comparison between the original 29×29 state-space model and the simplified 14×14 model.

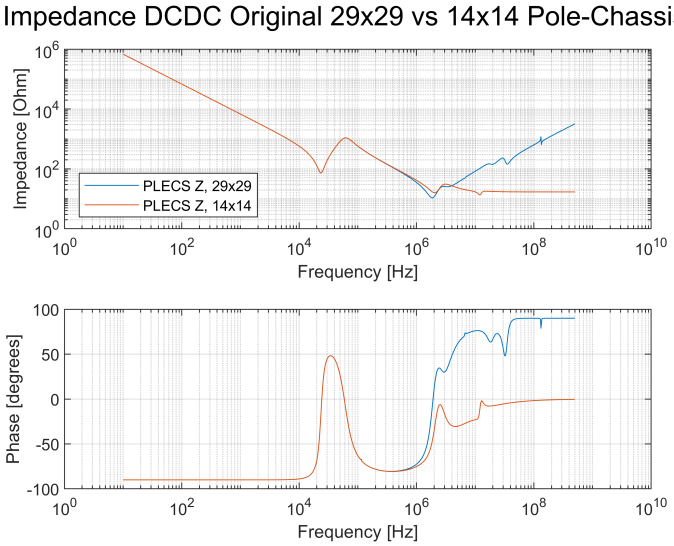


Figure 5.59: Impedance and phase as a function of frequency for the DCDC measured from pole to chassis. Comparison between the original 29×29 state-space model and the simplified 14×14 model.

Conclusion

The measurements show that the DCDC model agrees well with the measured impedance up to approximately 2-3 MHz for both DM and CM. The full model is too large for vehicle-level simulations, and a reduced state-space representation is therefore required. The simplified 14×14 model retains the accuracy of the original 29×29 model within the relevant frequency range and therefore enables feasible integration into complete vehicle simulations.

5.4.8 Reduced modelling of the DCDC for DM behaviour

In Subsection 5.4.7, the high-frequency impedance model of the DCDC is derived from the analysis described there and is required for CM simulations. However, this high-frequency model is too detailed to use for long time-domain DM simulations. While CM simulations run over milliseconds, DM simulations typically extend over several seconds. This subsection therefore presents a reduced model intended for DM behaviour only.

The reduced DM model is benchmarked against the complete DCDC model, which includes all high-frequency (HF) common-mode parameters derived from the measured impedance data shown in Figure 5.53. Compared to the full high-frequency model, the reduced DM model results from removing all elements connected to chassis ground as well as the common-mode chokes. The differential-mode parameter values of the common-mode choke are retained.

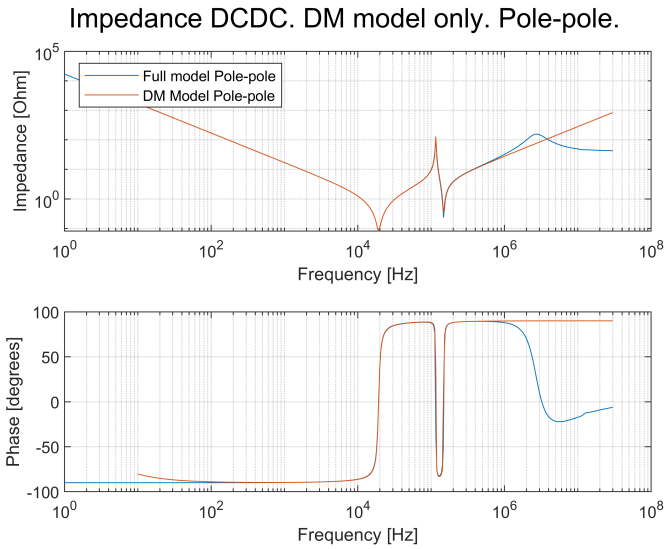


Figure 5.60: DM model of the DCDC. The DM model is compared to the full model with HF parameters.

Figure 5.60 shows that the reduced DM model agrees well with the full high-frequency

model for DM behaviour within the relevant frequency range up to approximately 200 kHz.

Conclusion

The reduced model captures the DM behaviour of the DCDC within the relevant frequency range up to approximately 200 kHz and is suitable for long time-domain DM simulations.

5.4.9 Measurements and modelling of the Air Compressor (AirComp) (CM and DM behaviour)

The Air Compressor converter supplies an electrical machine that mechanically drives the air compressor. Figure 5.61 shows a simplified representation of the air compressor DC link.

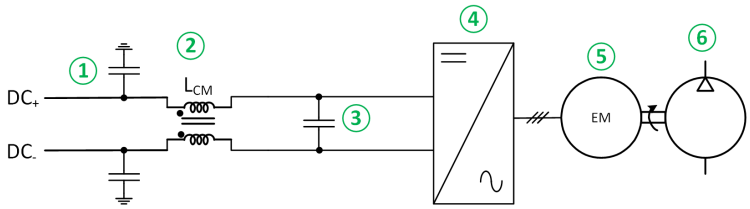


Figure 5.61: Air compressor main circuit.

1. CM capacitor, providing a return path for CM currents.
2. CM filter.
3. DC-link capacitor, supplying and storing the switching power.
4. Three-phase converter.
5. Electrical motor.
6. Air compressor.

The complete air compressor model is more complex than shown here; however, the full model is used in simulations, excluding the converter stage. The complete simulation model in PLECS contains more than 35 discrete components and functions solely as a passive load.

Two impedance measurements are of primary interest:

- Positive to negative pole, representing the DM properties.
- Positive pole to vehicle chassis, representing the CM properties. The negative pole to chassis impedance is identical due to symmetry.

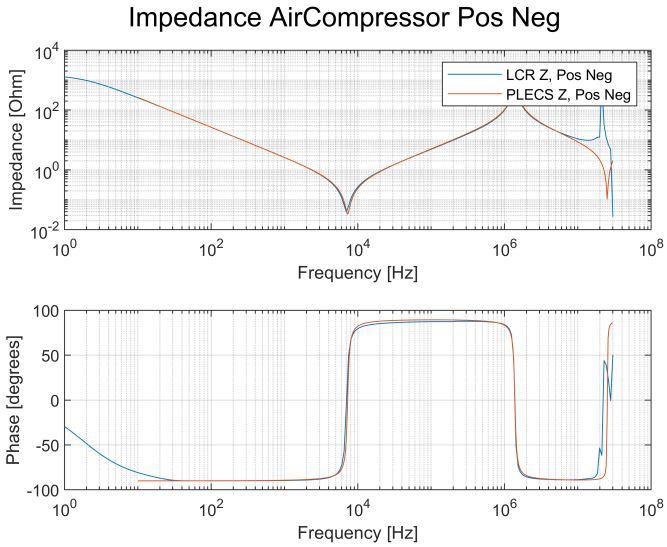


Figure 5.62: Impedance and phase as a function of frequency for the air compressor measured from positive to negative pole.

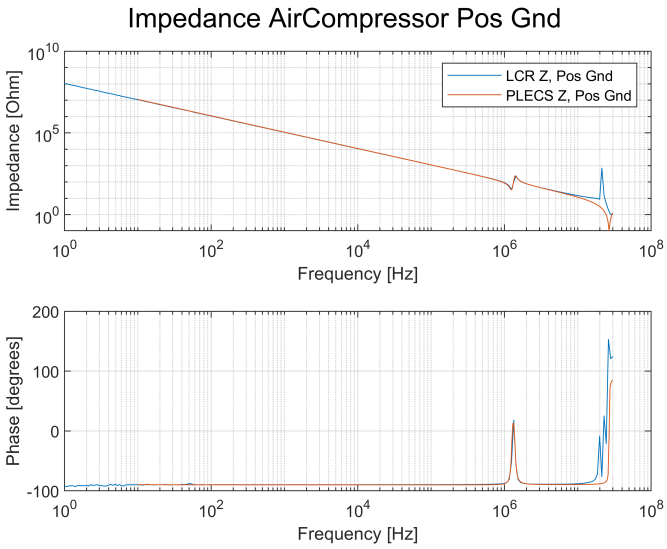


Figure 5.63: Impedance and phase as a function of frequency for the air compressor measured from positive pole to chassis.

The state-space representation of this model is comparatively compact, consisting of a 13×13 state-space matrix. The model reduces further to a 10×10 state-space representation while maintaining accuracy over the same frequency range. Figures 5.64 and 5.65 show the comparison between the original and reduced models.

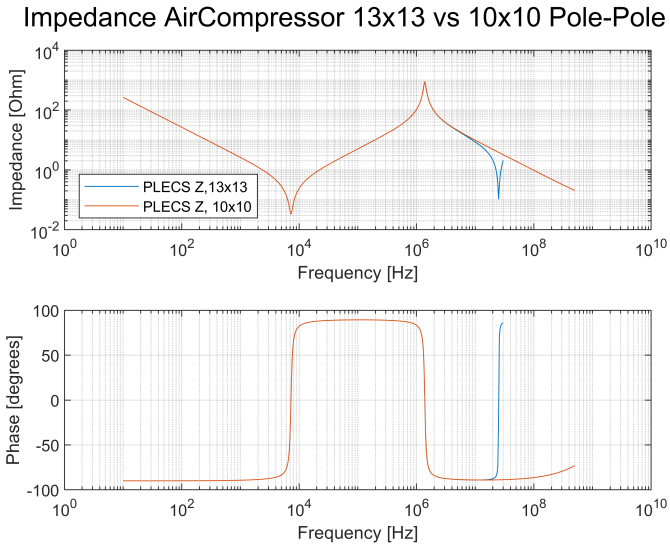


Figure 5.64: Impedance and phase as a function of frequency for the air compressor measured from positive to negative pole. Comparison between the original 13×13 state-space model and the reduced 10×10 model.

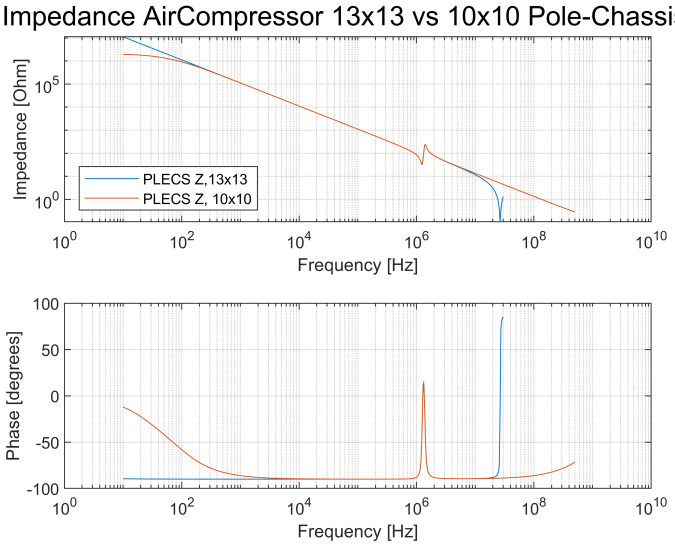


Figure 5.65: Impedance and phase as a function of frequency for the air compressor measured from pole to chassis. Comparison between the original 13×13 state-space model and the reduced 10×10 model.

Conclusion

The measurements show that the air compressor model correlates well with the measured impedance up to approximately 6 MHz for DM behaviour and up to 8 MHz for CM behaviour. In particular, the model remains valid well beyond the required frequency range on the DC side, which is limited to 2 MHz, and therefore fully satisfies the modelling requirements for system-level simulations.

The original model has a state-space size of 13×13 and reduces to a 10×10 representation while maintaining accuracy over the same frequency range. This reduction is necessary to enable feasible simulation of the complete vehicle model without compromising the relevant CM and DM impedance characteristics.

5.4.10 Measurements and modelling of the On Board Charger (OnBC) (CM and DM behaviour)

The OnBC is a one-quadrant converter that charges the TVS batteries in the vehicle. The OnBC provides galvanic isolation between the TVS and the grid and operates only at standstill when the electric traction machine(s) is deactivated. The power rating lies in the range of 11 kW. In some vehicles, multiple chargers are installed in parallel. Figure 5.66 shows a simplified schematic of the OnBC. Note that the power flow in this figure is from right to left.

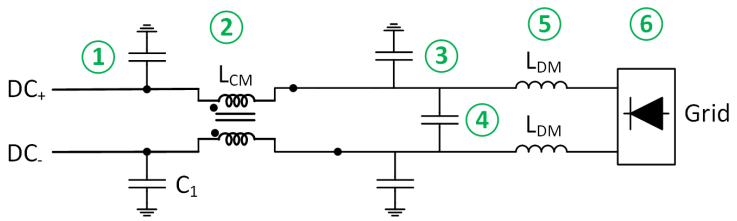


Figure 5.66: OnBC main circuit

The major parts included in the OnBC are:

1. CM capacitor. Return path for CM currents.
2. Output filter. Reduces the CM currents from the TVS to the OnBC.
3. CM capacitor.
4. DC link capacitor. Filters the output voltage.
5. Inductive input filter that smooths the output current.
6. Rectifier from the transformer that isolates the grid from the TVS.

The complete model of the OnBC is very complex and is therefore not shown here. Simulations use the full model, excluding the transformer and rectifier. The complete simulation model in PLECS contains more than 120 discrete components. As for the DCDC model, this model functions only as a passive load. Three impedance measurements are of primary importance:

- Positive to negative pole, for the DM properties.
- Positive pole to vehicle chassis, for the CM properties.
- Negative pole to vehicle chassis, for the CM properties.

The connection of the LCR meter follows the same procedure as described in previous subsections.

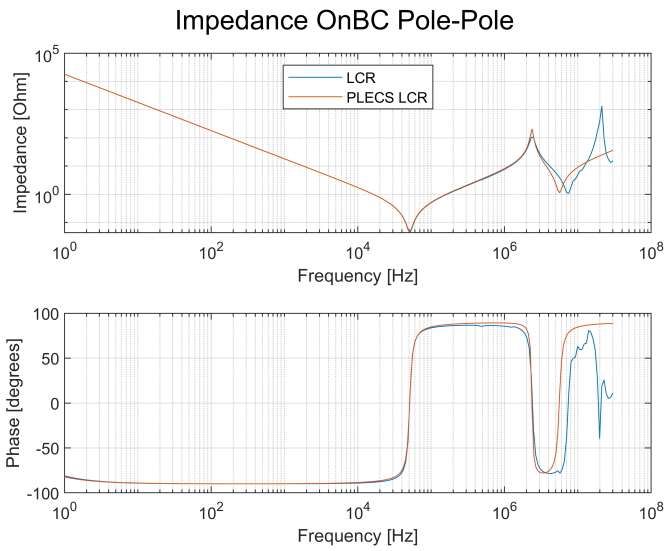


Figure 5.67: Impedance and phase as function of frequency for the OnBC measured from positive to negative pole.

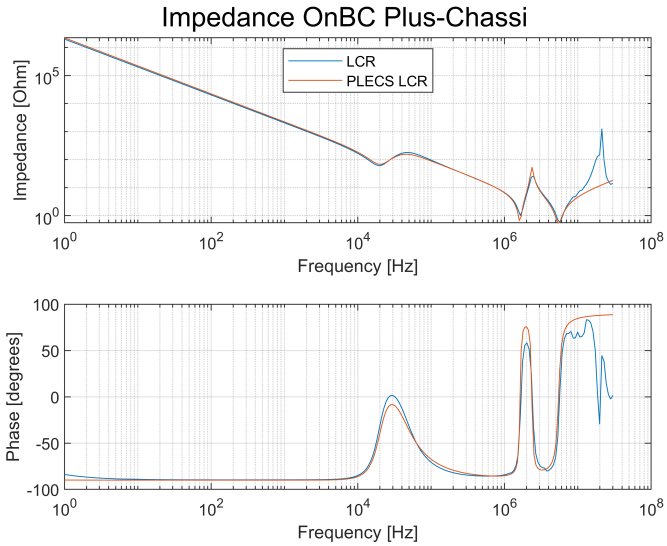


Figure 5.68: Impedance and phase as function of frequency for the OnBC measured from positive pole to vehicle chassis.

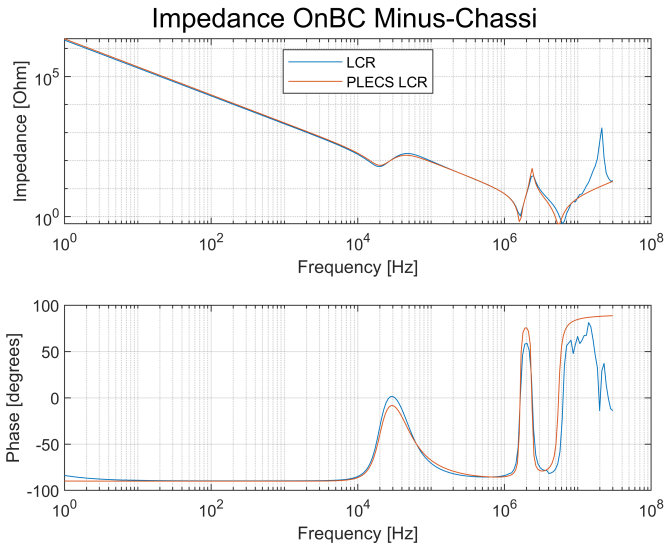


Figure 5.69: Impedance and phase as function of frequency for the OnBC measured from negative pole to vehicle chassis.

The OnBC model, shown schematically in the left part of Figure 5.66, is implemented in PLECS using parameter values obtained through the extraction procedure in Appendix A.

The state-space representation of the full OnBC model is expressed as a 50×50 state-

space matrix. Such a large model is not feasible for vehicle-level simulations, and the model therefore reduces while retaining accuracy over the required frequency range. The reduction decreases the state-space size from 50×50 to 11×11. Figures 5.70 and 5.71 show the comparison between the full and reduced models.

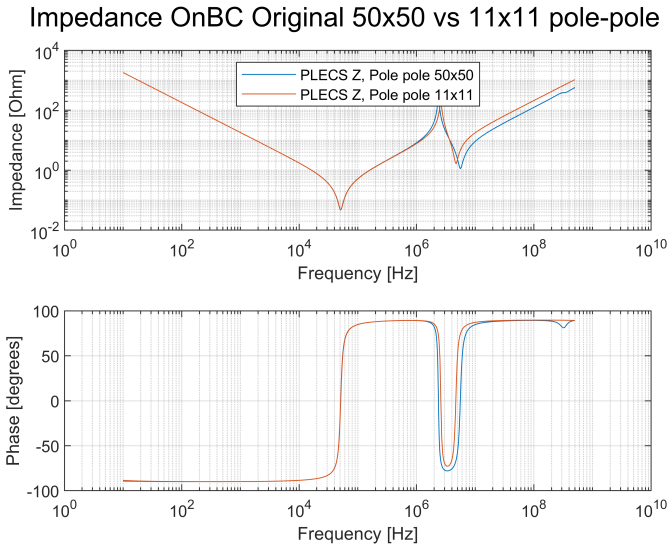


Figure 5.70: Impedance and phase as function of frequency for the OnBC measured from positive to negative pole. Comparison between the original 50×50 state-space model and the simplified 11×11 model.

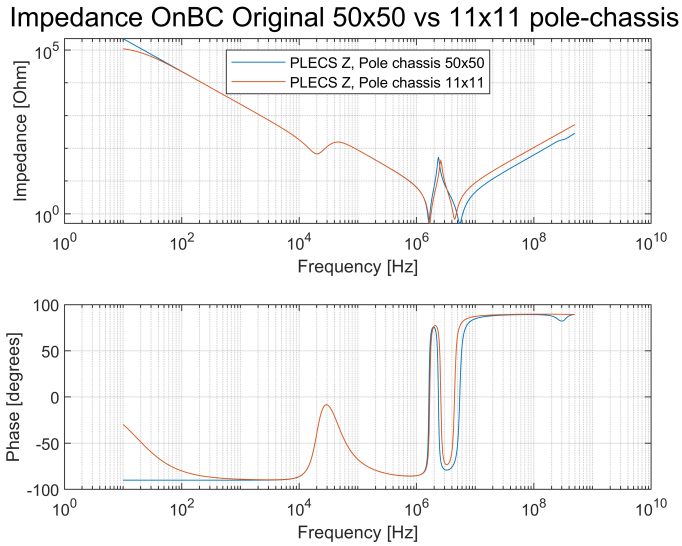


Figure 5.71: Impedance and phase as function of frequency for the OnBC measured from pole to chassis. Comparison between the original 50×50 state-space model and the simplified 11×11 model.

Conclusion

The measurements show that the OnBC impedance model correlates with the measured data up to 5 MHz for DM behaviour and up to 10 MHz for CM behaviour. This satisfies the CM modelling requirement of 2 MHz on the DC side. Deviations above 10 MHz cannot be reliably assessed due to increased measurement uncertainty at high frequencies. The full state-space model reduces from 50×50 to 11×11 while retaining accuracy within the required frequency range, as demonstrated in Figures 5.70 and 5.71. This reduction is necessary to enable feasible simulation of the complete vehicle.

5.4.11 Measurements and modelling of the ESS and Cab Heater (CM and DM behaviour)

The heater is a PWM on-off converter that controls the power delivered to a resistive load. Two physically separate heaters are installed in the vehicle—one for the ESS cooling circuit and one for the cab heating circuit—but the two units are electrically identical and use the same component design. The resistive load in each heater transfers heat to the respective fluid circuit. Figure 5.72 shows a simplified model.

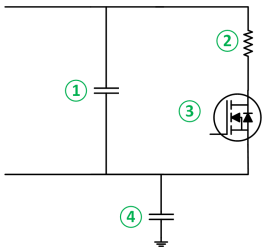


Figure 5.72: The main circuit of the Heater.

The included major parts in the Heater are:

1. DC link capacitor.
2. Heater resistor that heats the fluid for the ESS and cab heating circuits.
3. Semiconductor device that controls the power to the heater resistor.
4. CM capacitor.

Figure 5.73 shows the impedance measured from positive to negative pole in the Heater, compared with the PLECS model.

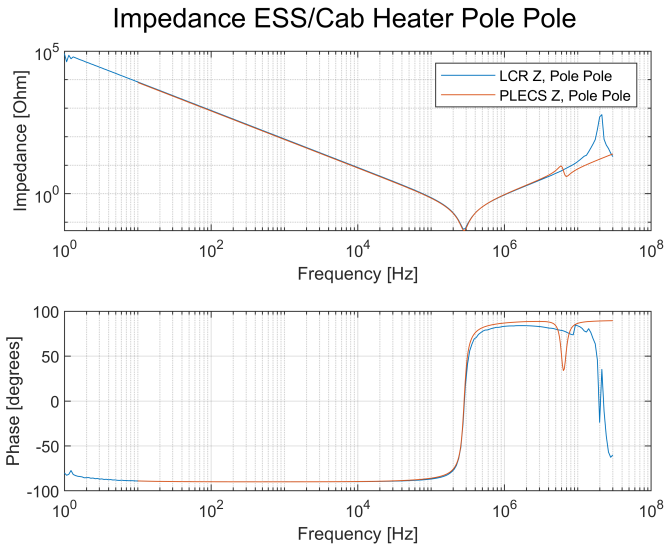


Figure 5.73: Impedance and phase as a function of frequency for the Heater, measured from positive to negative pole.

Figure 5.74 shows the impedance measured from positive pole to chassis in the Heater, compared with the PLECS model.

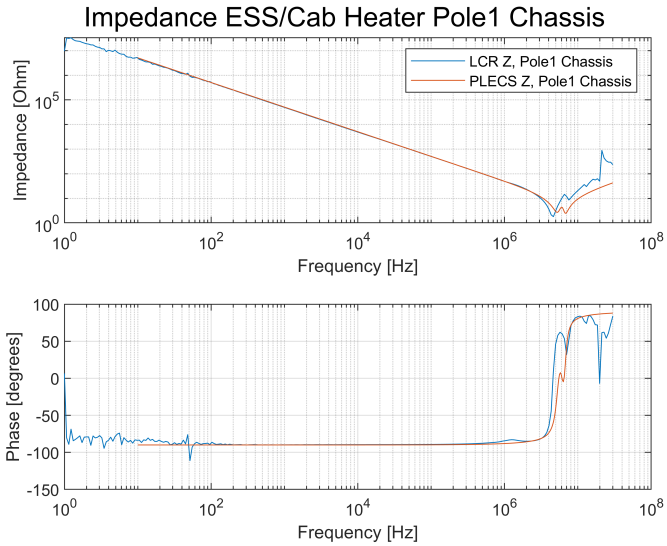


Figure 5.74: Impedance and phase as a function of frequency for the Heater, measured from positive pole to chassis.

Figure 5.75 shows the impedance measured from negative pole to chassis in the Heater, compared with the PLECS model.

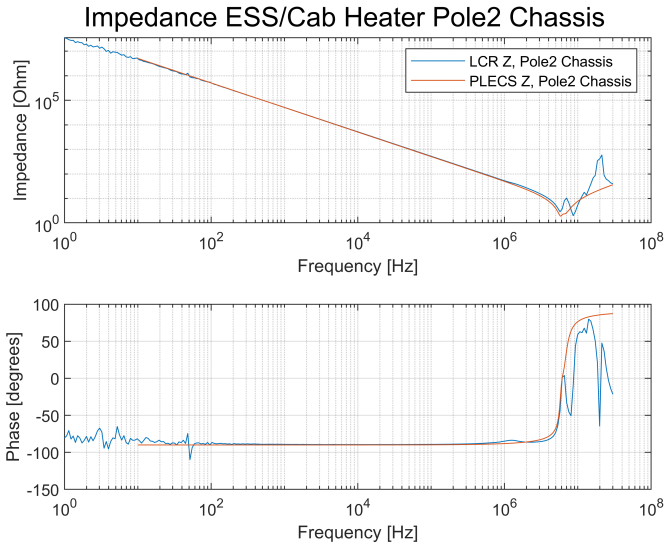


Figure 5.75: Impedance and phase as a function of frequency for the Heater, measured from negative pole to chassis.

Conclusion

The comparison between the simulation model and the measurements shows good correlation up to 5 MHz for both DM and CM behaviour. The resulting state-space representation has size 6×6 and cannot reduce further without loss of accuracy within the required frequency range. The model therefore fulfils the DC-side CM modelling requirement up to 2 MHz and is suitable for integration in vehicle-level simulations.

5.4.12 Measurements and modelling of the AC compressor (CM and DM behaviour)

The Air Condition compressor (AC compressor drive) consists of an inverter and an electric motor that supports the compressor. For this investigation, the AC compressor functions only as a passive load; only the DC-link behaviour is required in the system simulation model. For the AC compressor, a schematic was not supplied by the manufacturer, and the circuit diagram is developed through reverse engineering. Figure 5.76 shows a simplified model.

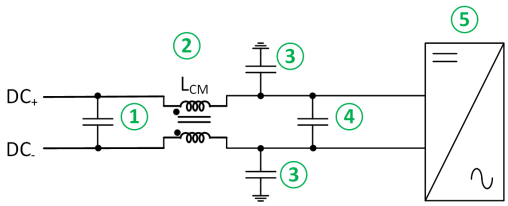


Figure 5.76: The main circuit of the AC compressor.

The included major parts in the AC compressor are:

1. DC-link capacitor.
2. Common-mode filter.
3. CM capacitor.
4. DC-link capacitor.
5. 3-phase converter.

Figure 5.77 shows the impedance measured from positive to negative pole in the AC compressor, compared with the PLECS model.

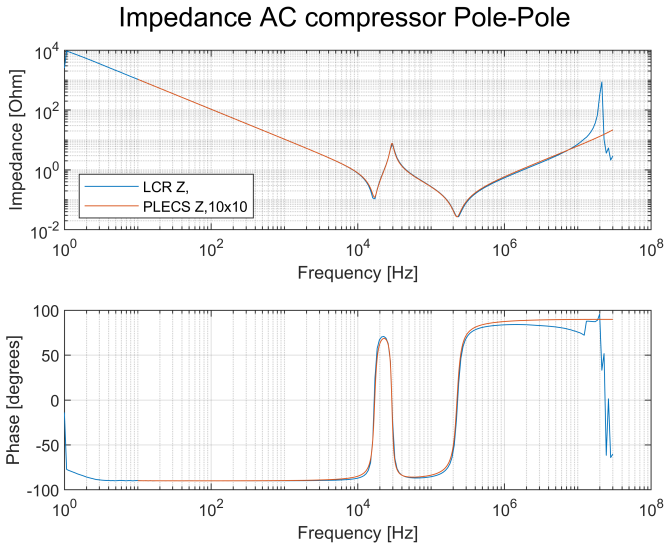


Figure 5.77: Impedance and phase as function of the frequency for the AC compressor, measured from positive to negative pole.

Figure 5.78 shows the impedance measured from the positive pole to the shield in the AC compressor, compared with the PLECS model.

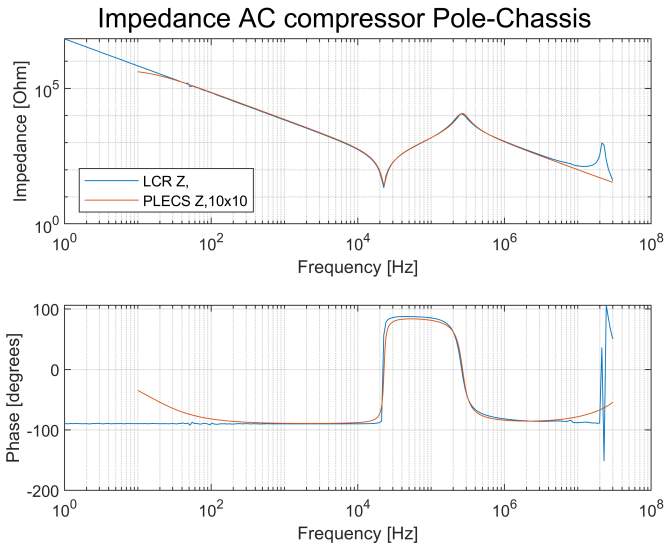


Figure 5.78: Impedance and phase as function of the frequency for the AC compressor, measured from positive pole to chassis.

Conclusion

The comparison between the simulation model and the measurements shows good correlation up to 10 MHz for both DM and CM behaviour. The resulting model is represented by a state-space matrix of size 10×10. This accuracy exceeds the required DC-side CM modelling limit of 2 MHz and the DM modelling limit of 200 kHz, making the model suitable for integration into complete vehicle-level simulations.

5.4.13 Measurements and modelling of the On-board Charger and Electric Power Supply (OCEPS) (CM and DM behaviour)

The OCEPS consists of two inverters: one providing DC supply to an ePTO and one providing three-phase supply to an ePTO, but it can also function as an on-board charger with the power direction from the grid. Both supplies are galvanically isolated from the TVS. For this investigation, the OCEPS operates only as a passive load, meaning that only the DC link behaviour is required in the system-level simulation model. The OCEPS does not correspond to the OnBC described in Subsection 5.4.10; a vehicle includes either an OnBC or an OCEPS, but never both. Figure 5.79 shows a simplified model of the OCEPS.

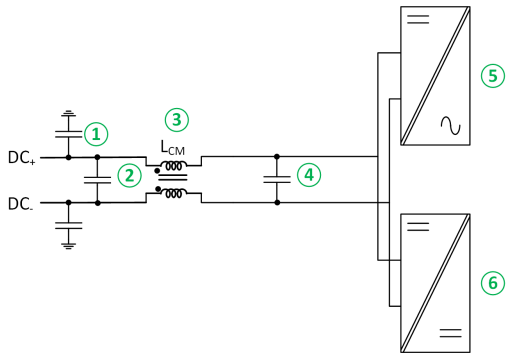


Figure 5.79: The main circuit of the OCEPS.

The included major parts in the OCEPS are:

1. CM capacitor.
2. DC-link capacitor.
3. Common-mode filter.
4. DC-link capacitor.
5. Three-phase converter for ePTO three-phase supply or, in reverse power direction, as an on-board charger.

6. DCDC converter for ePTO DC supply.

Figure 5.80 shows the impedance measured from positive to negative pole in the OCEPS, compared with the PLECS model.

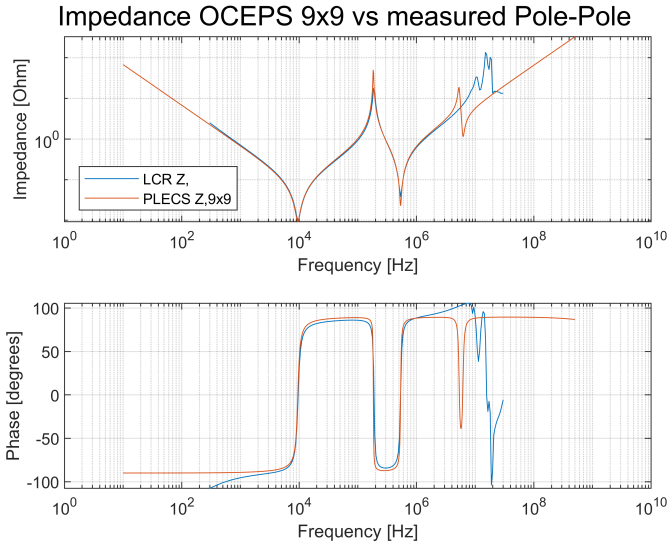


Figure 5.80: Impedance and phase as a function of frequency for the OCEPS, measured from positive to negative pole.

Figure 5.81 shows the impedance measured from positive pole to the shield in the OCEPS, compared with the PLECS model.

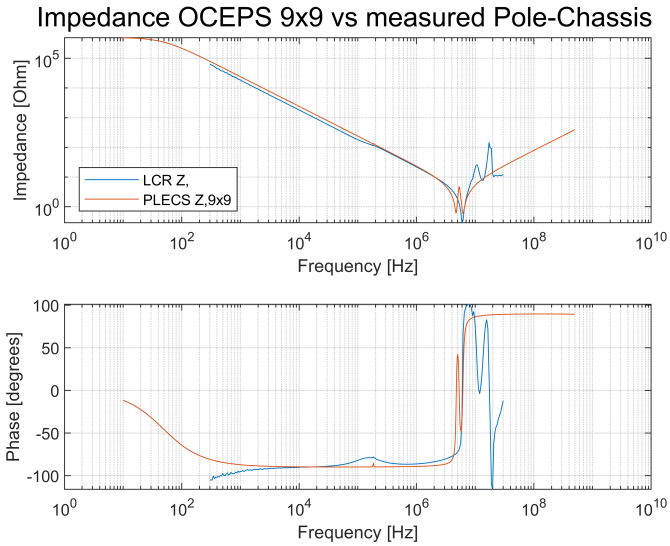


Figure 5.81: Impedance and phase as a function of frequency for the OCEPS, measured from positive pole to chassis.

Conclusion

The comparison between the simulation model and the measurements shows good correlation up to 4–5 MHz for both DM and CM behaviour. In this case, the model is simplified from the outset, resulting in a state-space representation of size 9×9. The achieved accuracy exceeds the required DC-side CM modelling limit of 2 MHz and the DM modelling range, making the model suitable for integration into complete vehicle-level simulations.

5.4.14 Measurements and modelling of the Cables

The 600 V cables in the vehicle are either of coaxial or twin-axial type. The twin-axial cables supply the low-power loads, while the coaxial cables supply the high-power loads. Figure 5.82 shows the cables.

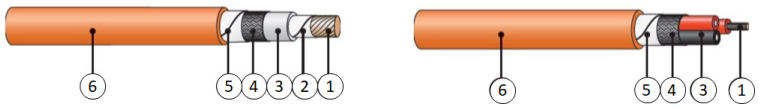


Figure 5.82: Coaxial and multi-core cable from Huber + Suhner. The cable used in the vehicles has two conductors, while the cable shown in the picture has three. Picture from Huber + Suhner.

The cable consists of the following parts:

1. Conductor
2. Tape

3. Insulation
4. EMC screen
5. Tape
6. Sheath

The cable model is based on a master's thesis carried out during this research [4]. In the master's thesis, the aim is to build a cable model that fits the LCR measurements and to calculate the same parameters by modelling in COMSOL [3]. A central challenge is to determine the required parameters and simplify the models so that they remain as small as possible. Simulating the vehicle with all subsystems and cables results in a large and very complex model. If all subsystems, including cables, are too detailed, the simulation becomes infeasible.

The subsection presents a full cable model together with a simplified model that provides acceptable accuracy for further use. The model is parameterised for a chosen frequency to account for the skin effect.

The master's thesis [4] describes how the different parameters and the complete model are built. The full model of the coaxial and twin-axial cable, shown in Figures 5.83 to 5.85, is built as a π-model where the parameters are divided symmetrically around the inductance and resistance. Therefore, some of the parameters are divided by 2. The model contains the following parameters:

R_C	Conductor resistance
R_S	Shield resistance
C_{cs}	Capacitance between conductor and shield, parasitic capacitance
L_m	Self and mutual inductance of the conductor and shield
C_{sg}	Capacitance between shield and ground, parasitic capacitance
L_g	Self-inductance of the ground plane.
R_{dummy}	Dummy resistance to avoid infinite voltage or current

R_{dummy} for capacitors is $\mu\Omega$ and for inductors $M\Omega$.

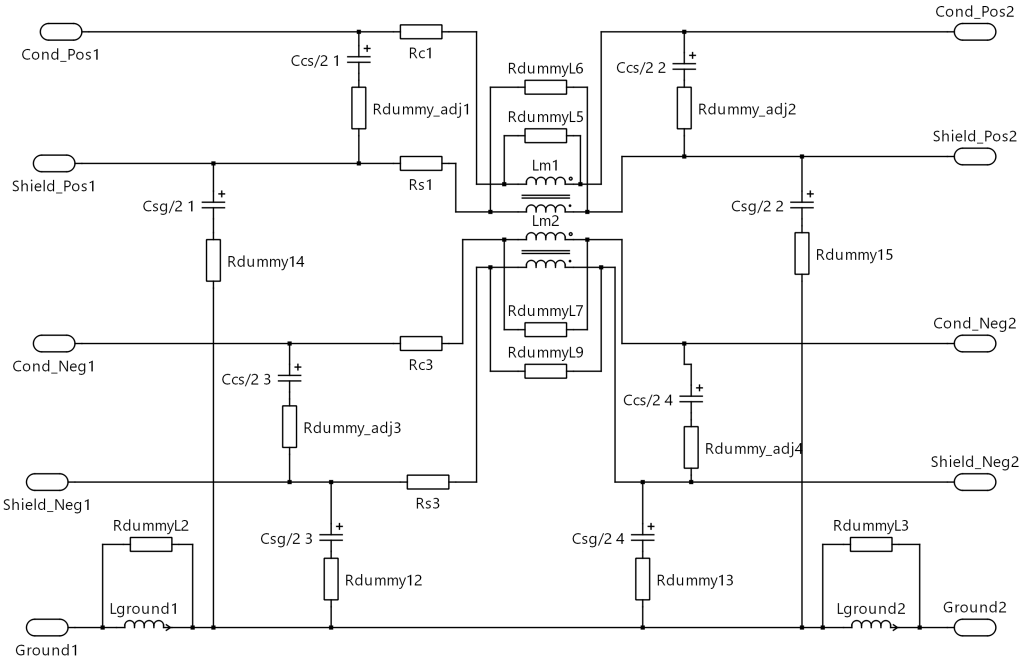


Figure 5.83: Full model of the coaxial cable. Note that the model represents two coaxial cables, one for the positive conductor and one for the negative conductor. This model is used on the DC side for cables of 50, 70 and 95 mm².

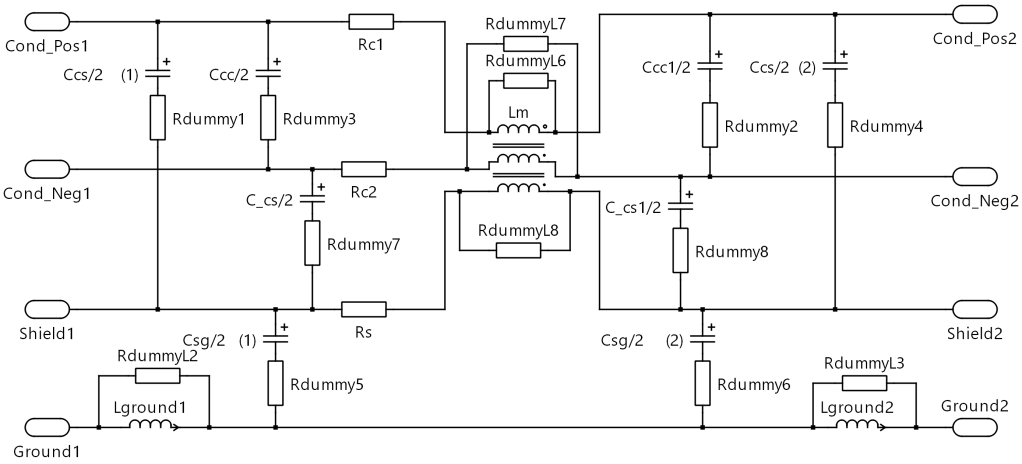


Figure 5.84: Full model of the twin-axial cable. This model is used for low power subsystems.

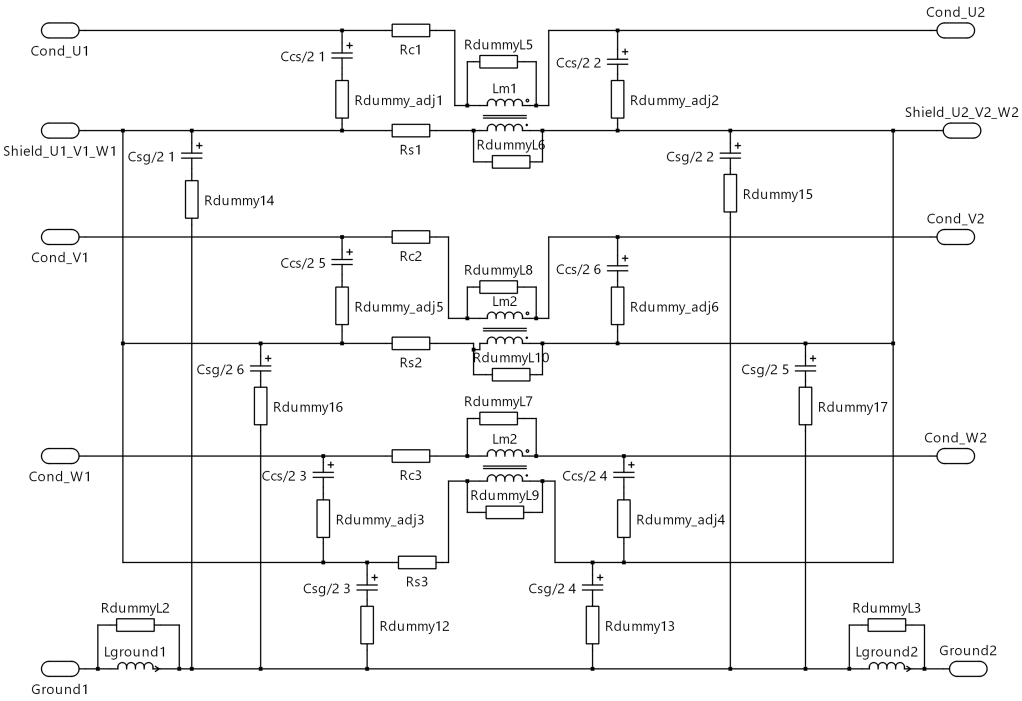


Figure 5.85: Full model of the three-phase cable. Note that the model represents three coaxial cables, used for the connection between the electrical machine (EM) and the electrical machine drive (EMD).

Apart from shielding the conductor and reducing emitted disturbances, the shield also provides a low-impedance return path for CM currents. A common approach when building models is to introduce simulation ground connections everywhere, which would short-circuit the return path of the shield. The present model therefore contains a ground impedance L_g. The ground impedance is derived through LCR-based impedance measurements.

Frequency dependence

The measurements show that the reactance does not increase with ω. In [28], the cable models are adapted for a frequency around 100 kHz. The cable models in this thesis use the frequency f as an input parameter, in addition to the cable length. The model is valid only for a fixed frequency and cannot represent variations across frequency. The impedance is frequency dependent, and in this case the inductance is frequency dependent as well. This makes the model represent only the frequency range that is relevant for the specific simulation. For DM behaviour (typically 1–50 kHz) and CM behaviour (100 kHz–3 MHz), the cable model therefore uses an input frequency chosen for the relevant range. A simulation may produce incorrect results at lower frequencies if the input frequency is 1 MHz, or incorrect results at higher frequencies if the input frequency is 10 kHz.

The inductance of a cable can be divided into

$$L = L_{int} + L_{ext} \tag{5.34}$$

where L_{int} is the inductance inside the conductor and L_{ext} is the inductance outside the conductor. When the frequency is low, the current flows symmetrically in the conductor since the penetration depth is larger than the radius of the conductor, $\delta > r$. When the frequency is high, the penetration depth is much smaller than the radius of the conductor, $\delta \ll r$, and $L_{int} \to 0$. Between these extremes, $L_{int} \propto \frac{1}{\sqrt{f}}$, which is described in [22, 6].

Simplifications

The models of the coaxial, twin-axial and three-phase cables shown in Figures 5.83 to 5.85 are complex. By comparing the parameters in the cable models with the corresponding parameters of the connected subsystems, it becomes evident that several simplifications are possible.

The measured parasitic capacitance between the shield and ground lies in the range of 0.2 nF/m. Assuming a large vehicle with 50 m of coaxial cables, the total parasitic capacitance C_{sg} lies in the range of 10 nF. The voltage difference between the shield and ground remains low, and any current flowing through C_{sg} becomes negligible. Consequently, C_{sg} is omitted in a medium-simplified model. Figure 5.86 shows an example for a coaxial cable. The same simplification applies to the twin-axial cable and the three-phase cable, but they are not shown here.

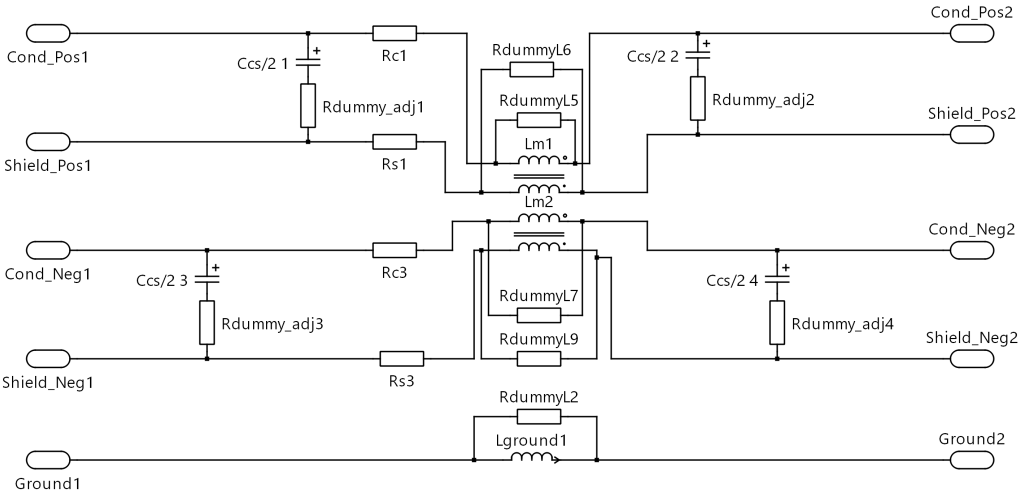


Figure 5.86: Medium model of the coaxial cable, where the shield-to-ground capacitance is omitted.

The parasitic capacitance between the conductor and the shield lies in the range of 0.6 nF/m for the coaxial cable and 0.2 nF/m for the twin-axial cable. A typical cable

between the battery and a converter is 1–10 m long, which results in a total parasitic capacitance from pole to shield of 0.6–6 nF for the coaxial cable. The corresponding value for the twin-axial cable is 0.2–2 nF. The parasitic capacitance to ground in high-power subsystems typically lies in the range of 50–500 nF, and for low-power subsystems 10–100 nF.

As a further simplification, the parasitic capacitance of the cables is omitted to reduce the model complexity. This simplification additionally allows the split ground inductance L_g to be combined. Figure 5.87 shows the resulting minimum model for the coaxial cable. The twin-axial cable and the three-phase cable simplify accordingly, but are not shown here.

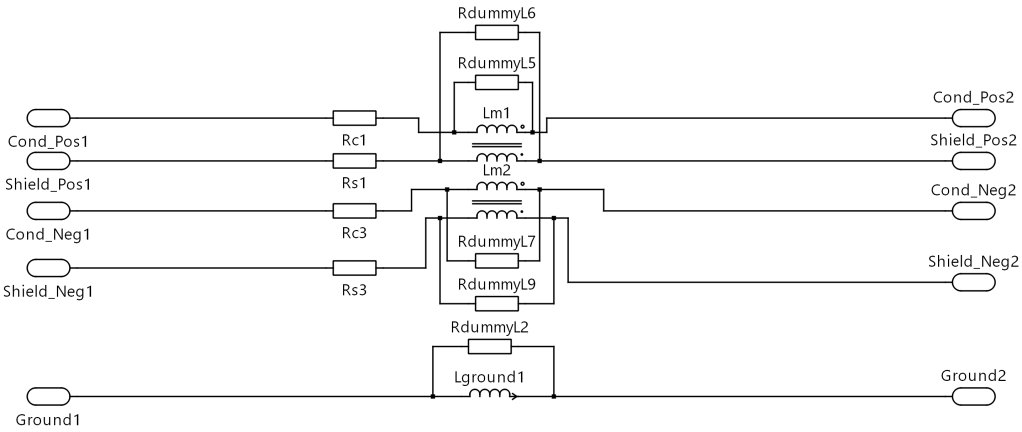


Figure 5.87: Minimum model of the coaxial cable, where the conductor-to-shield capacitance is omitted.

To reduce the model further, the ground impedance is considered before being omitted. The return path for CM currents is through the shield and the ground plane (vehicle chassis). A coaxial or twin-axial cable exhibits a low inductance between the conductor and the shield compared with the inductance between the conductor and the ground plane, as the latter forms a significantly larger current loop. By comparing the impedance of a conductor current returning via the shield with that of a current returning via the ground plane, the comparison shows that the impedance is much larger for the ground-plane return path.

Based on this observation, the minimum models are designed by omitting the ground plane. Figures 5.88 to 5.90 show the resulting models for the coaxial cable, the twin-axial cable and the three-phase cable, respectively.

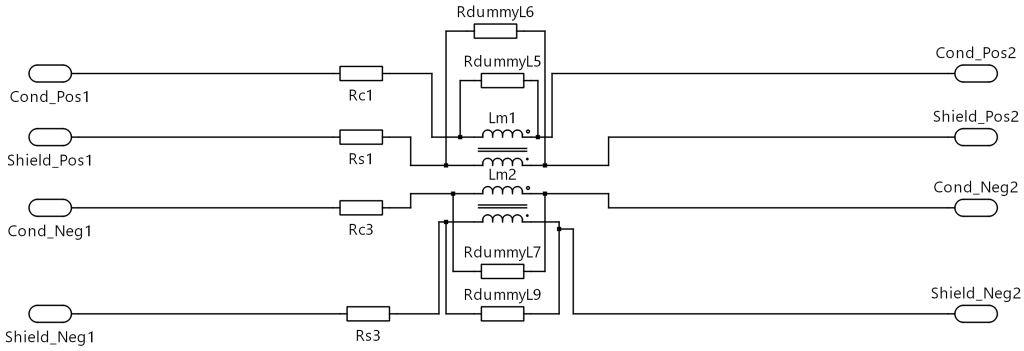


Figure 5.88: Minimum model of the coaxial cable, where the ground plane is omitted.

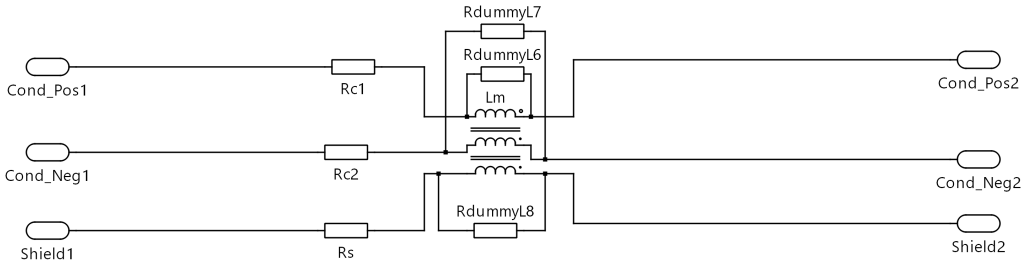


Figure 5.89: Minimum model of the twin-axial cable, where the ground plane is omitted.

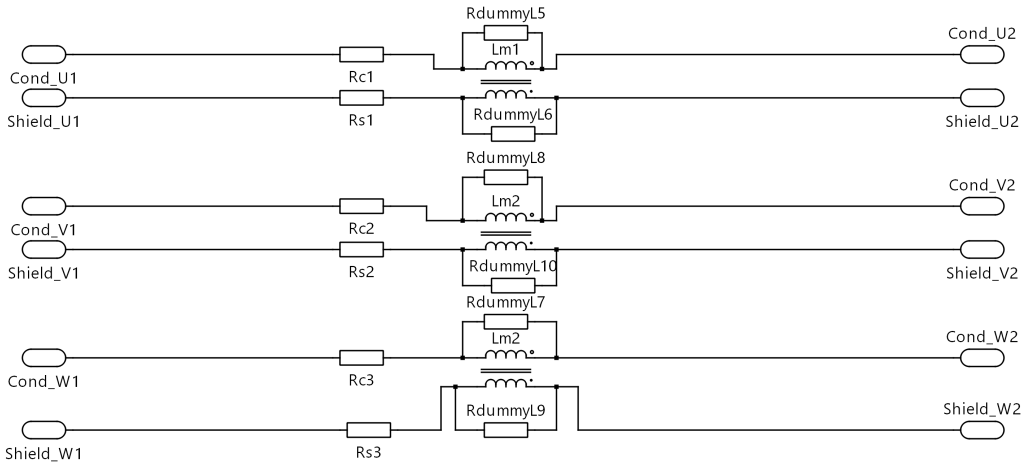


Figure 5.90: Minimum model of the three-phase cable, where the ground plane is omitted. For simplicity, the shields are connected within the model.

Based on the measured parasitic values and the observed impedance behaviour, the minimum cable models are sufficient within the frequency ranges relevant for common-

mode analysis. In particular, the simplifications applied do not affect the model validity up to 2 MHz on the DC side and 3 MHz on the AC side, which corresponds to the CM modelling requirements used throughout this thesis.

In Subsection 5.4.14, simulations of the three cable models (full, medium, and minimum models) are presented and compared with the corresponding measurement data.

Coaxial cable measurements – L_{11}

The next step is to compare the different models with the measured data. The first comparison, shown in Figures 5.92 and 5.93 at 1 kHz and 1 MHz respectively, concerns the impedance of the conductor with an open shield, L_{11}, as illustrated in Figure 5.91. The comparison shows that the three cable models shown in Figures 5.83, 5.86 and 5.87 give the same result up to 3 MHz. Above 3 MHz, all models deviate to some extent.

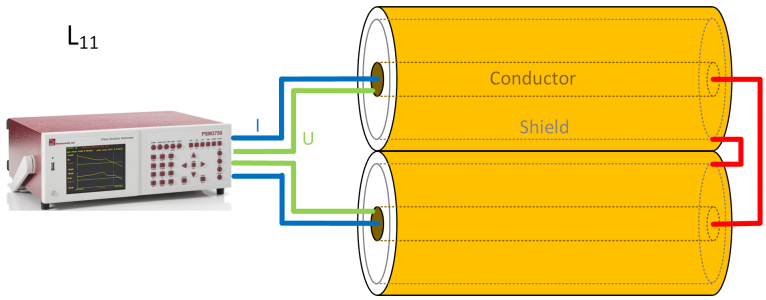


Figure 5.91: Measurement of the conductor impedance.

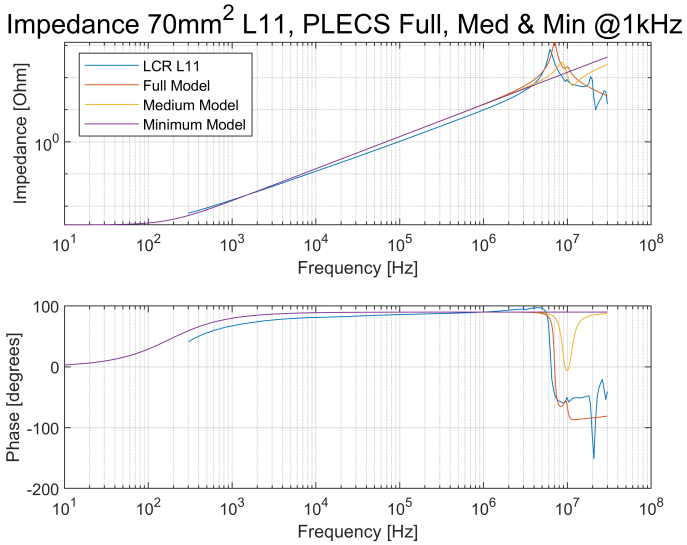


Figure 5.92: Comparison of the impedance from measurements and from the three different models at 1 kHz.

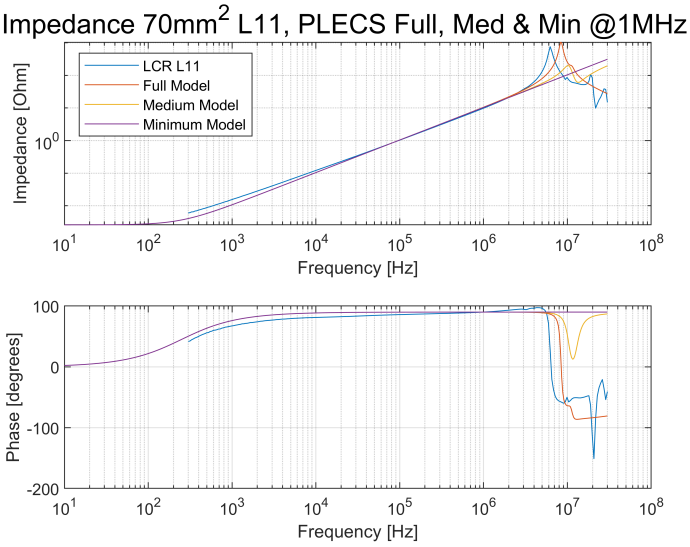


Figure 5.93: Comparison of the impedance from measurements and from the three different models at 1 MHz.

These results show that the minimum cable model remains suitable for system-level simulations. All cable models provide identical results up to 3 MHz, which exceeds the required frequency range for common-mode modelling on the DC side, limited to 2 MHz in this thesis. The minimum model therefore provides sufficient accuracy for DC-side CM

simulations while significantly reducing model complexity.

For differential-mode simulations, the choice of the frequency parameter f remains important. As the DM modelling requirement is limited to 200 kHz, the reduced cable model remains valid within the frequency range relevant for DM analysis.

Coaxial cable measurements – L_C

The second comparison concerns the self-inductance of the conductor. The comparison is shown in Figures 5.95 and 5.96 at 1 kHz and 1 MHz, respectively. The self-inductance becomes visible when the shield is short-circuited, as illustrated in Figure 5.94. The comparison shows that the full model in Figure 5.83 and the medium model in Figure 5.86 give identical results. Furthermore, all three models—full, medium and minimum—show the same behaviour up to 2 MHz. The full and medium models are also in close agreement with the measured impedance.

For differential-mode operation, the current sees the inductance L_C. Based on these observations, the minimum cable model remains sufficient for all subsequent simulations. For both DM and CM simulations, the choice of the frequency parameter f remains important.

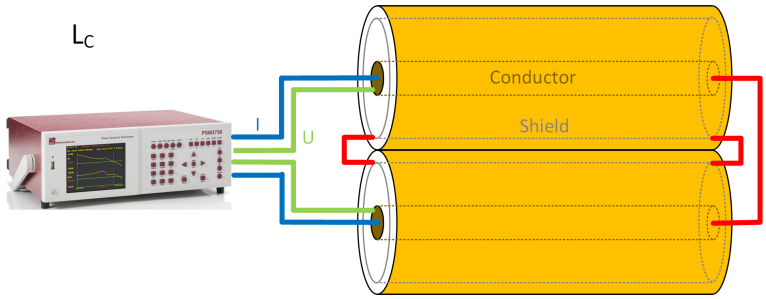


Figure 5.94: Measurement of the conductor self-inductance.

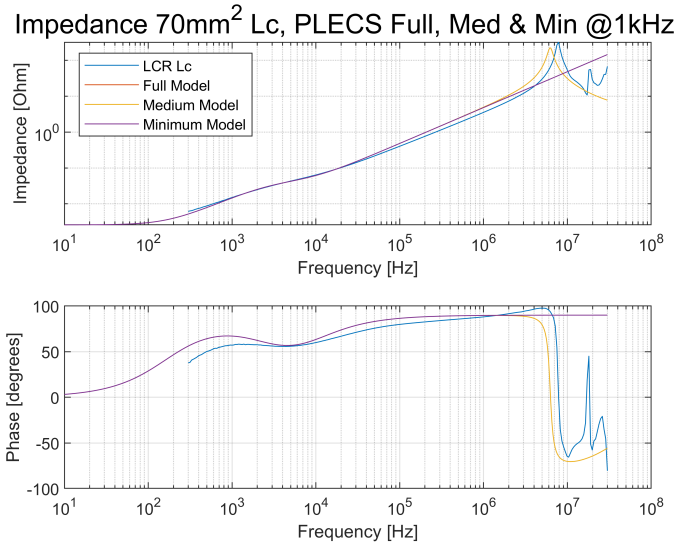


Figure 5.95: Comparison between measured impedance and the three cable models at 1 kHz.

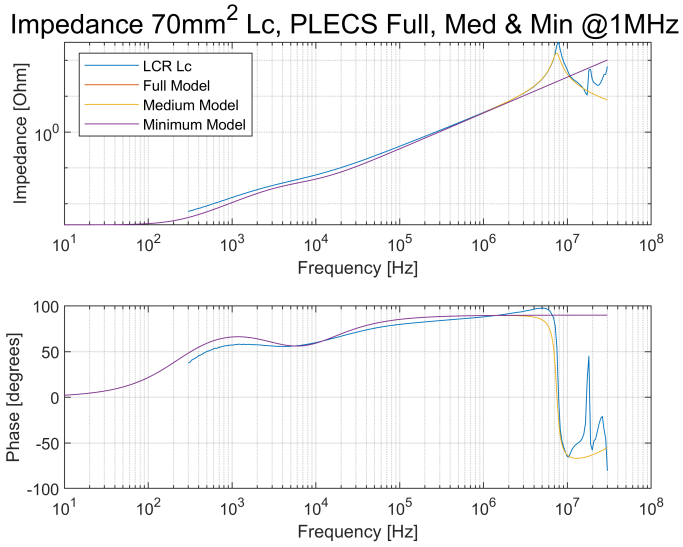


Figure 5.96: Comparison between measured impedance and the three cable models at 1 MHz.

Coaxial cable measurements – L_{22}

The third comparison concerns the shield impedance, shown in Figures 5.98 and 5.99 at 1 kHz and 1 MHz, respectively; see Figure 5.97. The comparison shows that the medium

and minimum models give identical results. All models agree up to 2 MHz. Between 3 and 8 MHz, both the medium and full models deviate to some extent from the measured response. Above 8 MHz, all models deviate from the measured response. These observations support the use of the minimum model for subsequent simulations, where the choice of frequency parameter f remains important for both DM and CM simulations.

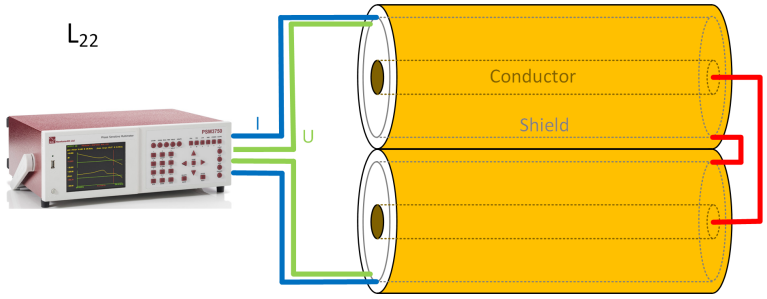


Figure 5.97: Measurement of the shield inductance.

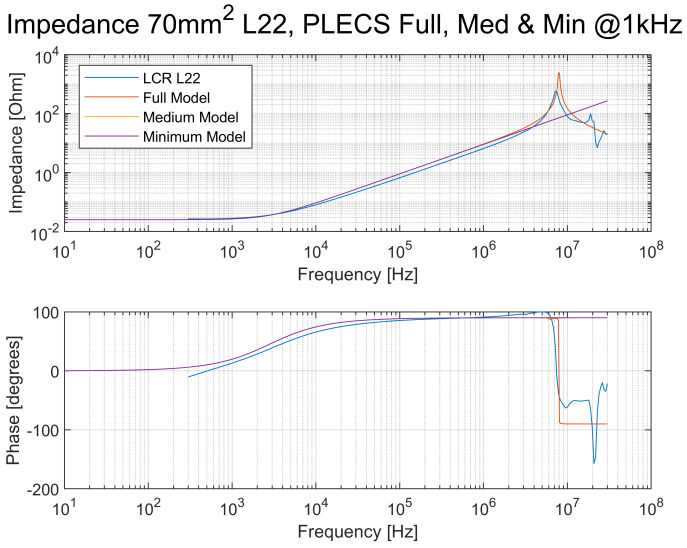


Figure 5.98: Comparison between measured impedance and the three cable models at 1 kHz.

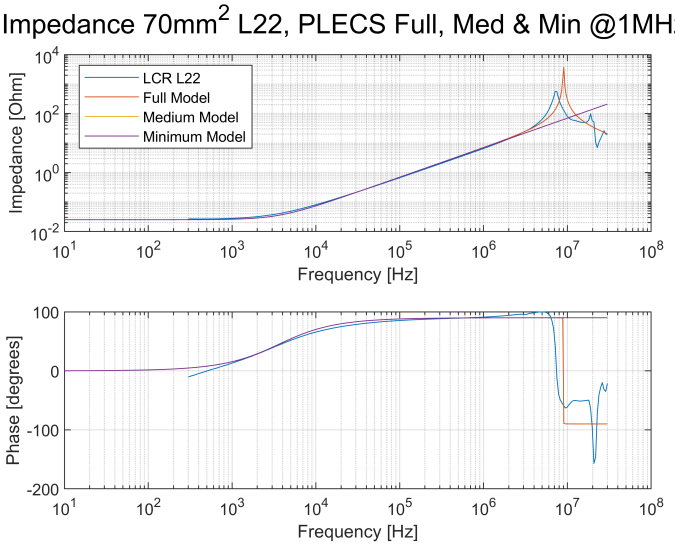


Figure 5.99: Comparison between measured impedance and the three cable models at 1 MHz.

Coaxial cable measurements – L_{11}–L_{22}

The fourth comparison concerns the combined impedance of the conductor and the shield. The results are shown in Figures 5.101 and 5.102 at 1 kHz and 1 MHz, respectively. The corresponding measurement configuration for the combined conductor and shield impedance, L_{11}–L_{22}, is illustrated in Figure 5.100.

The comparison shows that the full and medium cable models give identical results. All three models provide the same impedance response up to 2 MHz. In the frequency range from 1 MHz to 4 MHz, the full and medium models show the closest agreement with the measurements. Above 4 MHz, all models deviate from the measured impedance to a similar extent. These results indicate that the minimum model provides sufficient accuracy for system-level simulations, while the choice of the frequency parameter f remains important for both DM and CM simulations.

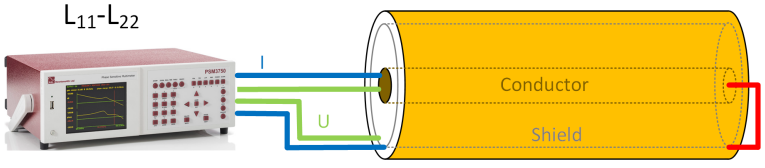


Figure 5.100: Measurement of the combined conductor and shield impedance.

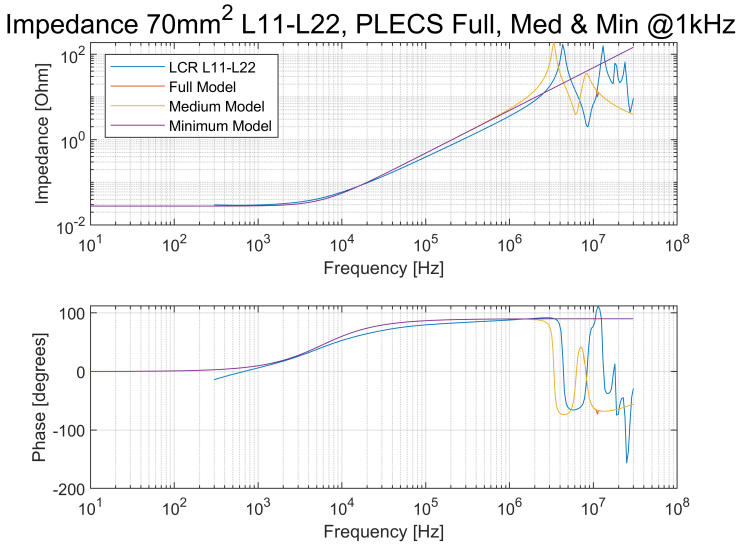


Figure 5.101: Comparison between measured impedance and the three cable models at 1 kHz.

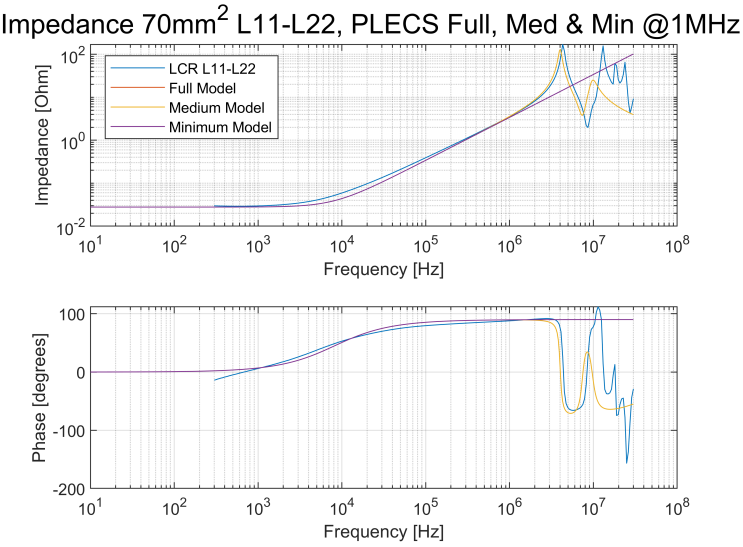


Figure 5.102: Comparison between measured impedance and the three cable models at 1 MHz.

Coaxial cable measurements – L_{11} + L_g

The fifth comparison concerns the combined impedance of the conductor and the ground plane. The results are shown in Figures 5.104 and 5.105 at 1 kHz and 1 MHz, respectively.

This impedance becomes visible when the conductor is connected directly to the ground plane, as illustrated in Figure 5.103.

The comparison shows that the different cable models exhibit similar behaviour over the investigated frequency range. The minimum model provides sufficient accuracy for system-level simulations, while the choice of the frequency parameter f remains important for both DM and CM simulations.

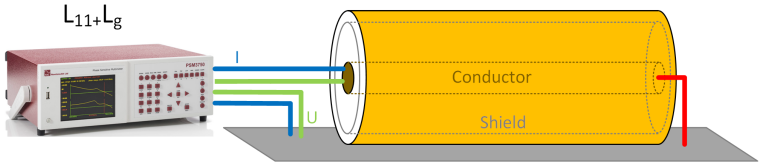


Figure 5.103: Measurement of the ground and conductor inductance.

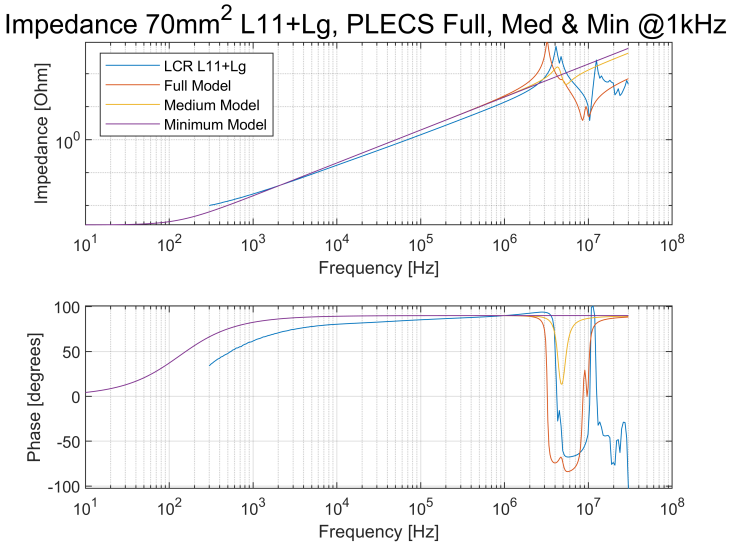


Figure 5.104: Comparison between measured impedance and the three cable models at 1 kHz.

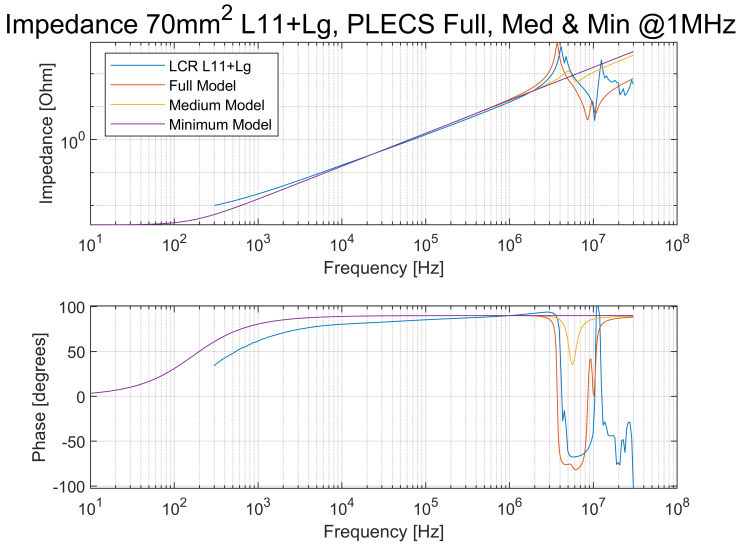


Figure 5.105: Comparison between measured impedance and the three cable models at 1 MHz.

Coaxial cable comparison – $L_{11} - L_{22}$ vs. $L_{11} + L_g$ and $L_{11} + (L_g \parallel L_{22})$

The purpose of this subsection is to demonstrate that the impedance of the ground plane is considerably higher than that of the shield. Furthermore, Figures 5.106 and 5.107 shows that the impedance remains unchanged when the shield and the ground plane are connected in parallel compared to the case where only the shield is used as the return path.

This observation shows that the ground plane does not contribute significantly to the return path impedance when the shield is present. Consequently, the ground plane can be omitted in the simulation models, and the shield alone can be used as the return path for CM currents.

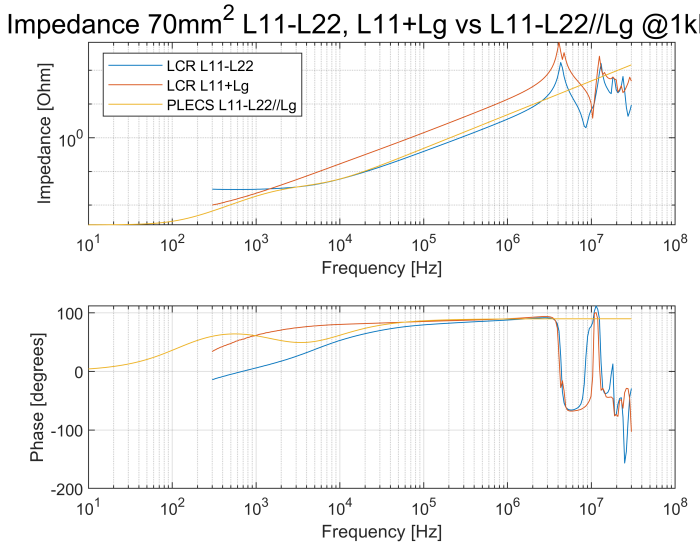


Figure 5.106: Comparison between ground plane impedance, shield impedance, and the parallel combination of ground plane and shield at 1 kHz.

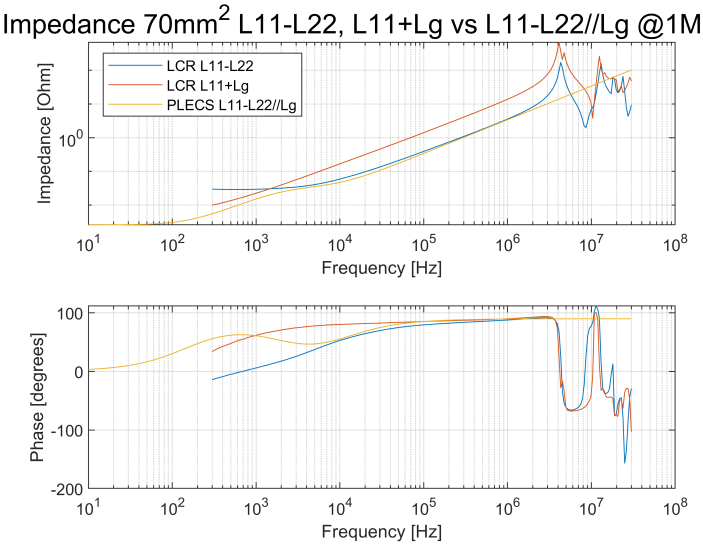


Figure 5.107: Comparison between ground plane impedance, shield impedance, and the parallel combination of ground plane and shield at 1 MHz.

Coaxial cable measurements - C_{cs}

The sixth and final comparison concerns the parasitic capacitance between the conductor and the shield, as illustrated in Figures 5.108 and 5.109. This comparison is not applicable to the minimum model, since C_{cs} is removed in that model. The results show that the full and medium models produce identical results.

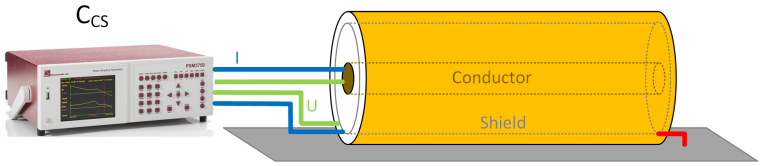


Figure 5.108: Measurement of the shield-to-conductor parasitic capacitance.

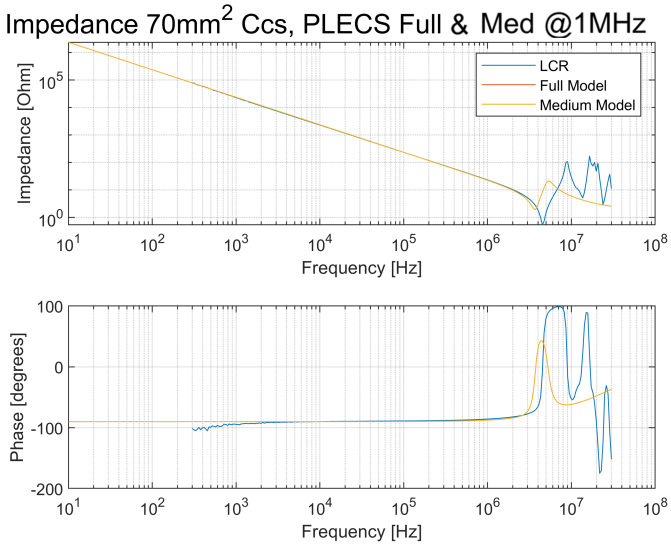


Figure 5.109: Comparison of the impedance from measurements and from the two different models at 1 MHz; measurements at 1 kHz show the same behaviour.

Twin-axial cable measurements – $2L_c$

The next step is to perform corresponding comparisons for the twin-axial cable models using measured data. The measurements show that the conductor impedance is reduced due to the skin effect. The reactance X_L normally increases with frequency f; however, the impedance magnitude increases proportionally to $\sqrt{f}$. The full and medium models yield identical results and therefore overlap in the plots.

The first comparison concerns the impedance of the conductor with an open shield, $2L_c$, as illustrated in Figure 5.110. Figures 5.111 and 5.112 show that all three cable models

(full, medium and minimum) produce identical results up to 2 MHz. Up to 7 MHz, the full and medium models follow the measured impedance closely, whereas the minimum model deviates at higher frequencies.

Within the frequency range relevant for DC-side CM analysis, limited to 2 MHz, the agreement between measurements and all model variants demonstrates that the minimum model provides sufficient accuracy for representing the conductor impedance of the twin-axial cable.

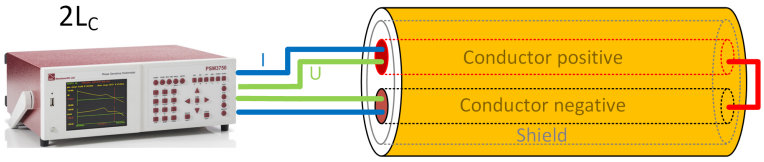


Figure 5.110: Measurement of the conductor impedance.

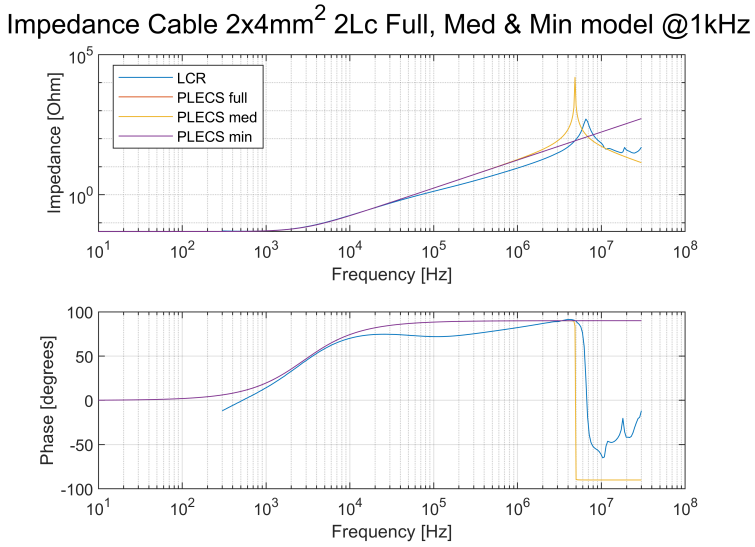


Figure 5.111: Comparison of the impedance from measurements and from the three different models at 1 kHz.

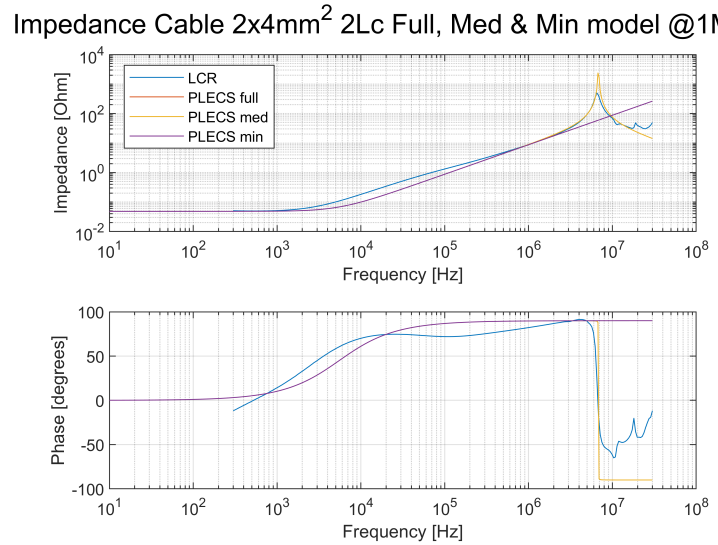


Figure 5.112: Comparison of the impedance from measurements and from the three different models at 1 MHz.

Based on these results, a preference is given to using less complex cable models whenever possible. More complex cable models increase the overall system complexity, resulting in longer simulation times or, in some cases, models that are not possible to solve.

For simulations of the twin-axial cable, which is used exclusively on the DC side, the relevant frequency range is limited by the CM modelling requirement of up to 2 MHz. Within this frequency range, the minimum cable model provides sufficient accuracy. The agreement between measurements and all model variants demonstrates that the reduced representation is valid over the required frequency span.

Consequently, the minimum model is recommended for system-level simulations involving the twin-axial cable.

Twin-axial cable measurements – L_cL_s

The second step for the twin-axial cable is the conductor–shield measurement, L_cL_s. The return path through the shield is primarily due to unwanted CM currents. Figures 5.114 and 5.115 show that the measured impedance exhibits frequency-dependent behaviour.

Figure 5.113 shows the impedance of the conductor–shield path, L_cL_s. The comparison shows that all three twin-axial cable models (full, medium and minimum) produce the same result up to 2 MHz.

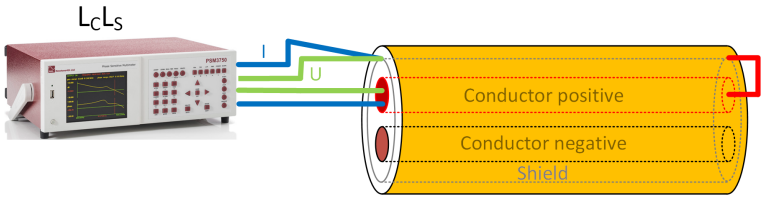


Figure 5.113: Measurement of the conductor–shield impedance.

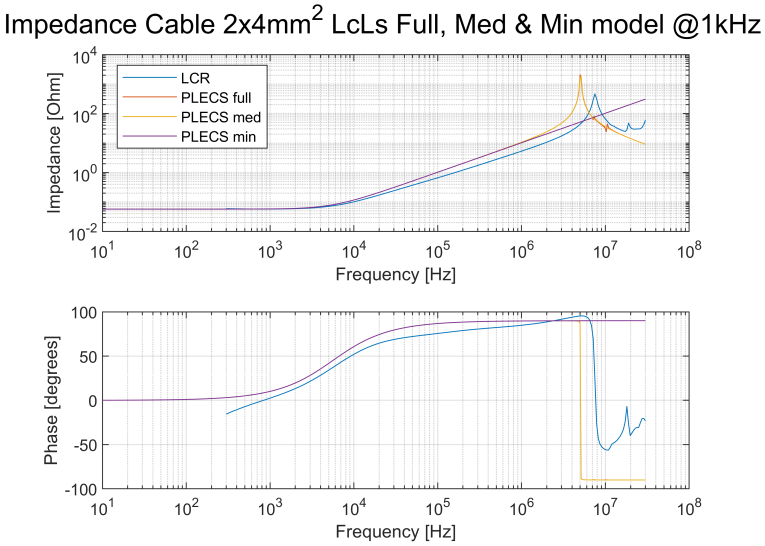


Figure 5.114: Comparison of the impedance from measurements and from the three different models at 1 kHz.

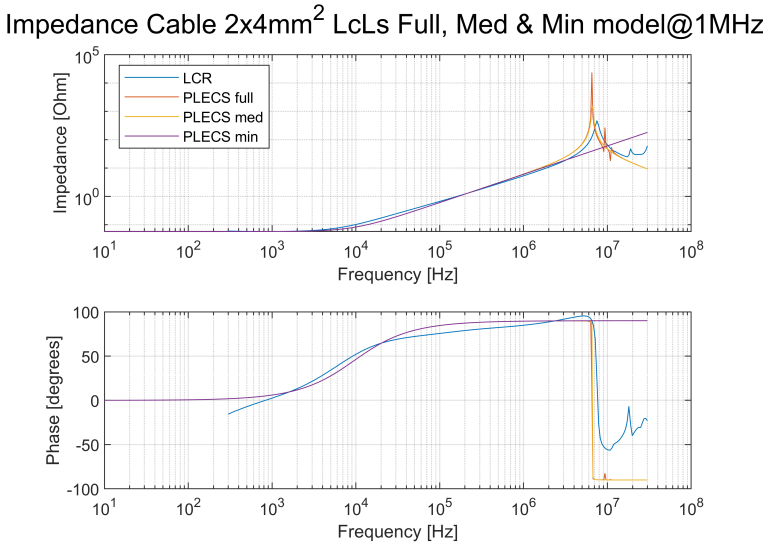


Figure 5.115: Comparison of the impedance from measurements and from the three different models at 1 MHz.

Twin-axial cable measurements – L_cL_g

The third step for the twin-axial cable is the conductor and ground impedance, L_cL_g. The return path of current in the ground plane is mainly associated with unwanted CM currents. In simulations, the ground is often connected at multiple points, which implies a negligible ground impedance and may effectively bypass the shield inductance L_s. Therefore, the simulation model shall use a single connection to the simulation ground point. Figures 5.117 and 5.118 show that the measured impedance exhibits frequency-dependent behaviour.

Figure 5.116 shows the impedance of the conductor and ground plane, L_cL_g. The comparison shows that all twin-axial cable models yield similar results up to 3 MHz.

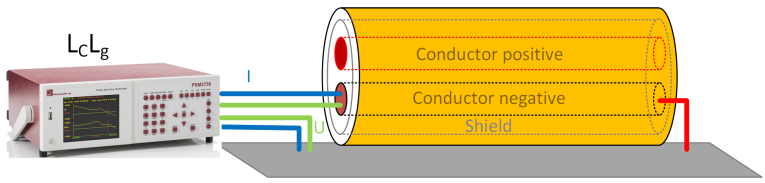


Figure 5.116: Measurement of the conductor and ground impedance.

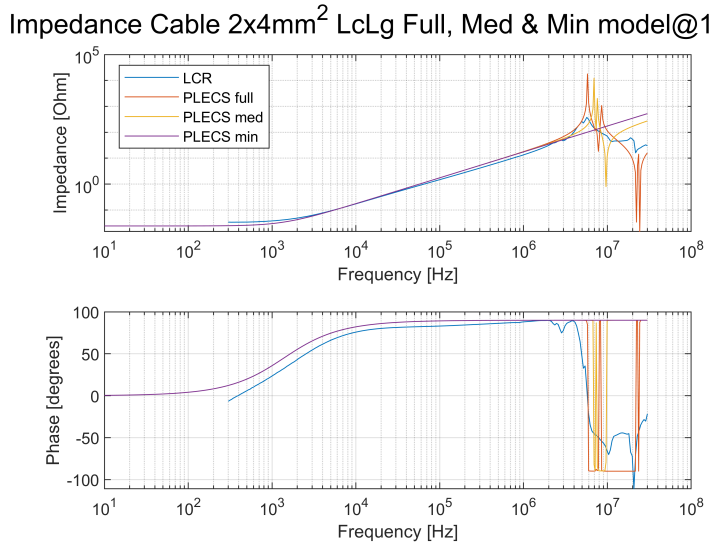


Figure 5.117: Comparison of the impedance from measurements and from the three different models at 1 kHz.

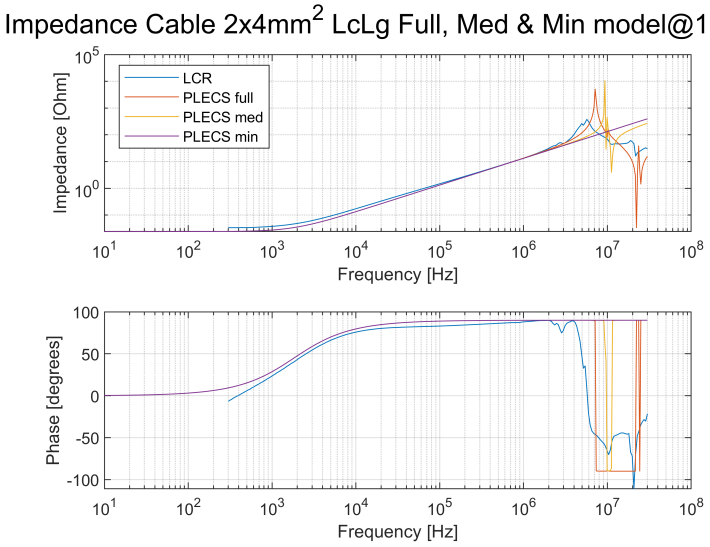


Figure 5.118: Comparison of the impedance from measurements and from the three different models at 1 MHz.

For the twin-axial cable used on the DC side, the relevant frequency range is limited by the CM modelling requirement of up to 2 MHz. Within this frequency range, all model variants show comparable agreement with the measurements.

This demonstrates that the minimum model provides sufficient accuracy for conductor–

ground impedance representation in DC side CM analysis.. Consequently, the minimum model is preferred for system-level simulations, as it satisfies the required frequency range while minimising model complexity.

Twin-axial cable comparison of L_cL_s, L_cL_g and $L_cL_sL_g$

By comparing the impedances of L_cL_s and L_cL_g, it is evident that the impedance associated with the shield return path, L_cL_s, is significantly lower than that associated with the ground plane return path, L_cL_g. The next step is to evaluate the three possible return-path configurations: the shield return path L_cL_s, the ground-plane return path L_cL_g, and the parallel combination $L_cL_sL_g$, in order to determine which representation is required in the model.

To carry out this evaluation, an additional comparison is performed where the conductor–shield–ground-plane configuration, $L_cL_sL_g$, is measured and compared with the two individual return paths. Figures 5.113, 5.116 and 5.119 show the measurements corresponding to L_cL_s, L_cL_g, and $L_cL_sL_g$. Figure 5.120 shows the direct comparison.

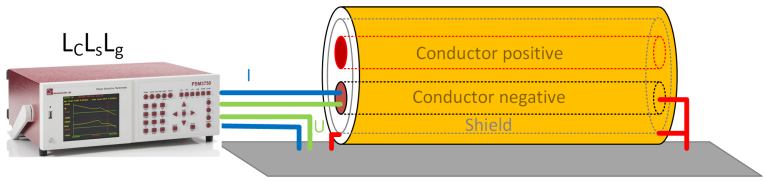


Figure 5.119: Measurement of the conductor, shield, and ground-plane impedance.

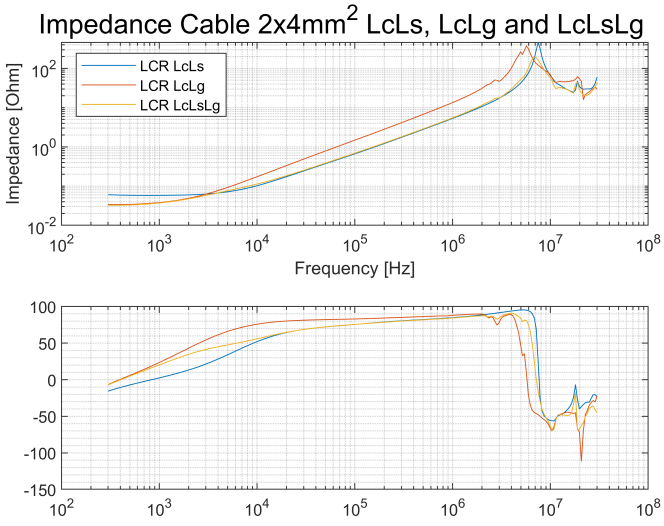


Figure 5.120: Comparison of the impedance from measurements for the three different return paths, L_cL_s, L_cL_g, and $L_cL_sL_g$, at 1 MHz.

The results clearly show that the ground plane impedance, $L_c L_g$, is considerably higher than the shield impedance, $L_c L_s$. The parallel combination of the ground plane and shield, represented by $L_c L_s L_g$, does not significantly change the overall impedance compared with using the shield return path alone. This indicates that the contribution of the ground plane to the total return-path impedance is negligible in comparison with that of the shield.

Conclusion

The cable modelling results in this section show that detailed representations of coaxial and twin-axial cables rapidly lead to large state-space systems. Although full models provide high fidelity, their size significantly increases the computational burden in system-level simulations. For example, the coaxial cable model leads to a state-space matrix of 14×14 in the full representation, whereas the corresponding minimum model reduces this to 4×4.

For vehicle-level simulations, this reduction is essential to ensure that time-domain computations remain tractable. The analyses show that the minimum cable models provide sufficient accuracy within the frequency ranges relevant to this thesis. Consequently, the minimum models remain preferred for system simulations.

The common-mode cable behaviour is explicitly modelled and validated up to 2 MHz on the DC side and 3 MHz on the AC side, in accordance with the modelling requirements used throughout this work. Differential-mode behaviour is not treated in dedicated subsections, as the differential-mode representation follows directly from consistent simplification of the same cable models and remains sufficient within the frequency range relevant for the analyses performed.

5.4.15 Measurements and modelling of the Junction Box

The Junction Box (JB), also referred to as the Hybrid Junction Box (HJB), is a connection and distribution unit in the vehicle. It connects the batteries to different electrical consumers. In addition to acting as a connection box, the JB provides fused connections for low-power loads. From a system-level perspective, the JB introduces additional impedance, primarily inductance, and therefore requires modelling.

The JB provides both High Current Connections (HCCs) and Low Current Connections (LCCs). The LCCs are protected by fuses. Figure 5.121 shows a schematic of a JB with a combination of HCCs and LCCs. The model includes the contact resistance of the connector.

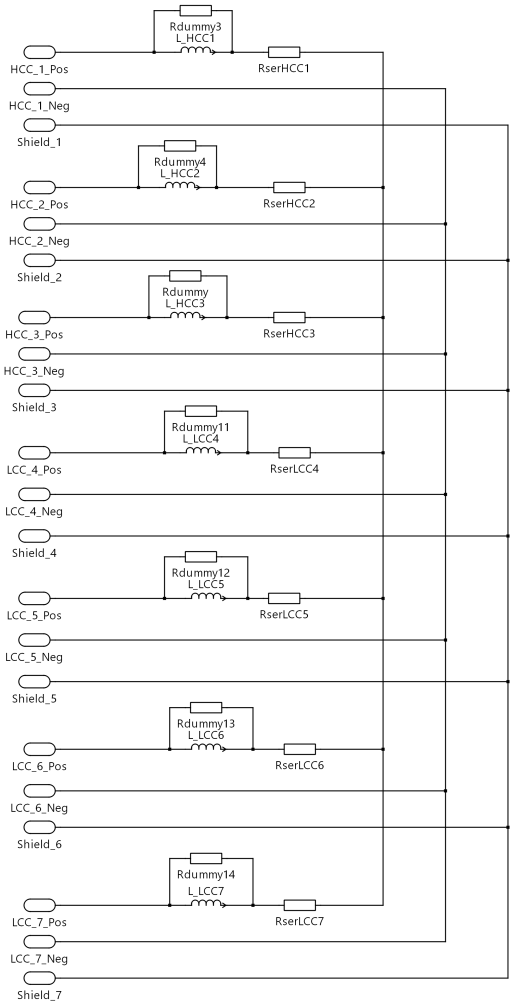


Figure 5.121: Schematic of the PLECS model of a Junction Box. Note that the fuse is not included in the model.

It is difficult to determine from the vehicle schematics where the individual cables inside the JB are connected. Some connections are physically close, while others are located further apart within the JB. In the present model, an approximation is used that does not account for these internal distances. The figures below illustrate different connection configurations and the comparison between measured impedances and simulation results. Figures 5.122 and 5.123 show the impedance between different connector combinations.

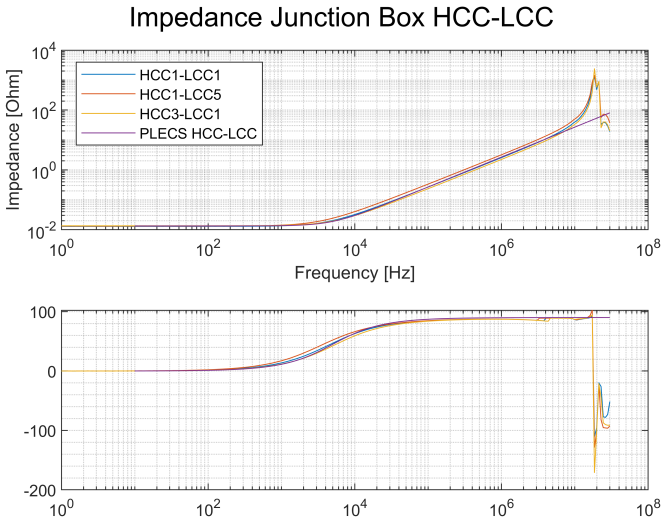


Figure 5.122: Comparison between measurements and simulation for different HCC-to-LCC connections in the Junction Box, and simulation of a generic outlet.

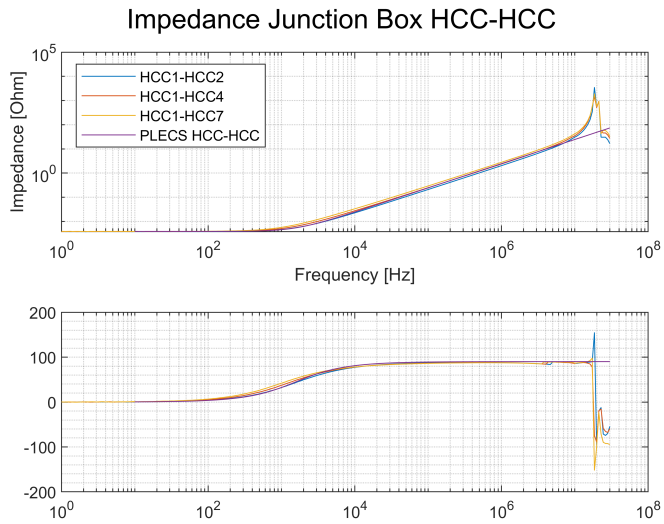


Figure 5.123: Comparison between measurements and simulation for different HCC-to-HCC connections in the Junction Box, and simulation of a generic outlet.

Figure 5.124 compares the JB impedance measured between an LCC and an HCC with the impedance of two parallel cables, each with a length of 3.1 m and a cross-sectional area of 70 mm².

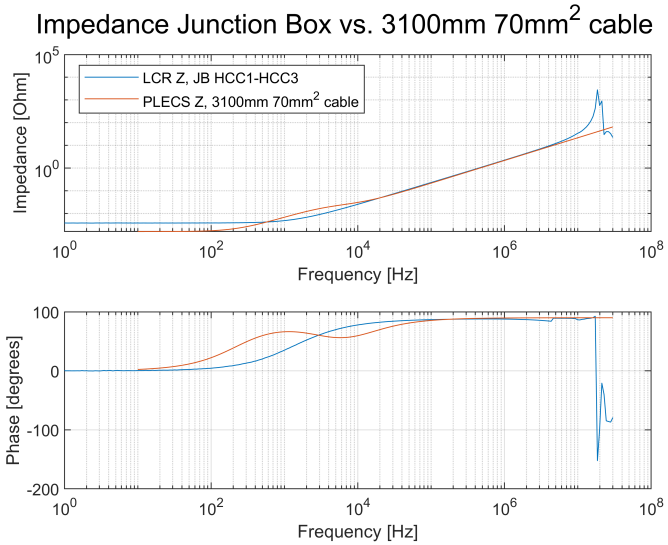


Figure 5.124: Comparison between the impedance of a Junction Box and a cable with a cross-sectional area of 70 mm². The result shows that a cable length of 3.1 m at 100 kHz produces approximately the same impedance as the Junction Box. The JB measurement is performed between HCC1 and HCC3.

Conclusion

The results demonstrate that the impedance introduced by the Junction Box is significant and comparable to that of two parallel cables with a length of 3.1 m and a cross-sectional area of 70 mm². Consequently, the Junction Box must be included as an explicit component in the system-level model to accurately represent its impact on the overall electrical behaviour.

5.4.16 Measurements and modelling of the Break Out Box

The Break Out Box (BoB) is a measurement unit that interrupts the cable and inserts a box equipped with voltage and current sensors. The BoB is only used during measurements and is not present when the vehicle operates in normal conditions. Figure 5.125 shows the schematic of the BoB. The purpose of modelling the BoB is to evaluate its impact on the measurement results. The model includes the contact resistance of the connector.

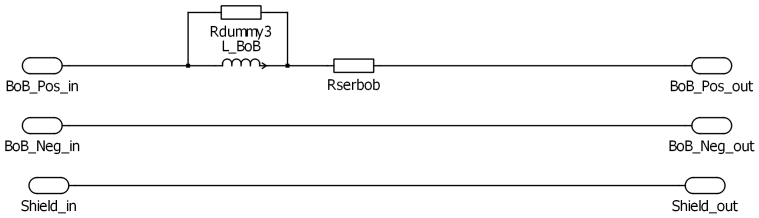


Figure 5.125: Schematic of the PLECS model of a Break Out Box.

Figure 5.126 shows a comparison between the BoB model and impedance measurements.

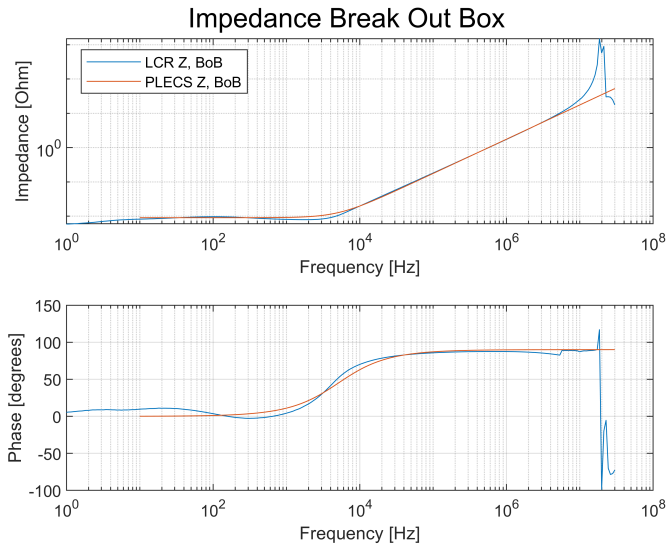


Figure 5.126: Comparison between measured and simulated impedance of the Break Out Box.

Figure 5.127 compares the BoB impedance with two parallel cables, each with a length of 2.7 m and a cross-sectional area of 70 mm².

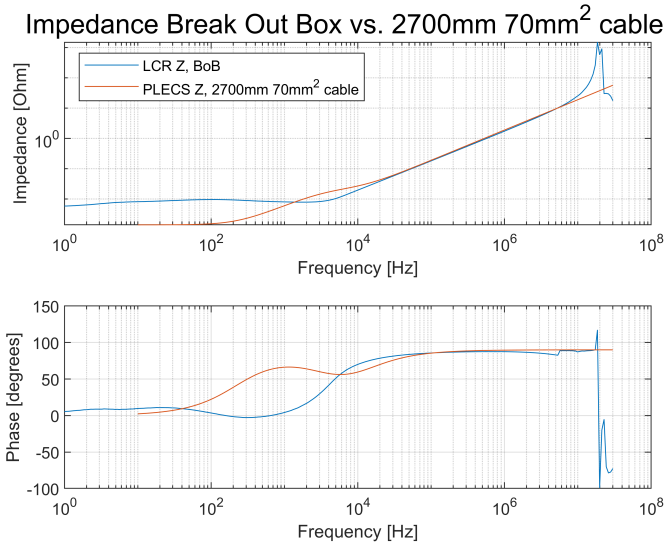


Figure 5.127: Comparison between the impedance of a Break Out Box and a cable with a cross-sectional area of 70 mm². The result shows that a cable length of 2.7 m at 100 kHz produces approximately the same impedance as the Break Out Box.

Conclusion

The results show that the impedance introduced by the Break Out Box is significant and comparable to that of two parallel cables with a length of 2.7 m and a cross-sectional area of 70 mm². Consequently, the Break Out Box must be included in the simulation model to ensure that the simulated impedance accurately reflects the measurements.

5.5 Conclusion

This chapter establishes a complete and measurement-based modelling framework for the electrical subsystems and interconnections in the vehicle. The chapter analyses both active and passive subsystems, including power electronic converters, electrical machines, batteries, filters, cables and interconnection components. For each subsystem, the chapter develops suitable modelling approaches, defines measurement methods, and assesses model validity through direct comparison with experimental data.

All subsystem models, full-order models and reduced-order models are implemented in PLECS, which supports the generation of state-space matrices, model reduction and complete vehicle-level simulation within feasible computation times.

The modelling work in Section 5.4 shows that individual subsystems already exhibit non-negligible impedance characteristics and frequency-dependent behaviour. When combined at vehicle level, these subsystems form a tightly coupled network in which parasitic

elements and interconnections significantly influence the overall system behaviour. Consequently, accurate subsystem modelling is a prerequisite for meaningful system-level analysis.

A central outcome of this chapter is the explicit relationship between model fidelity and state-space complexity. The cable models illustrate this clearly: the full coaxial representation results in a 14×14 state-space matrix, whereas the corresponding minimum model reduces the representation to 4×4. Similar trends apply to the other subsystem models introduced in this chapter.

Through systematic comparison between measurements and simulations, the chapter introduces several justified model reductions. These reductions preserve the dominant electrical behaviour within the frequency ranges relevant to this work, while significantly reducing the dimension of the state-space representation. For common-mode phenomena, the validated modelling range extends up to 2 MHz on the DC side and up to 3 MHz on the AC side. Differential-mode behaviour follows from consistent reduction of the same subsystem models and remains valid up to 200 kHz.

The results further show that interconnection elements such as cables, Junction Boxes and Break Out Boxes contribute impedances comparable to several metres of high-current cabling and must be included to obtain agreement between measurements and simulations. These components therefore form an integral part of the reduced system representation rather than remaining secondary modelling details.

In summary, this chapter provides a coherent set of validated, reduced-order models for all major electrical subsystems and interconnections in the vehicle. The resulting state-space models retain sufficient accuracy and remain computationally tractable for full vehicle-level simulations. These models form the foundation for the analyses presented in the following chapter, where subsystem interaction and conducted emission behaviour are investigated at system level.

Chapter 6

System simulation

This chapter builds on the subsystem modelling in Chapter 5 and extends the analysis to system level. It introduces the transition from validated subsystem representations to complete vehicle-level modelling, where interactions between components determine the behaviour of the traction voltage system.

The chapter examines how the combined subsystem models form a physically consistent representation of the vehicle and how system-level phenomena arise when the electric machine drives operate independently with non-synchronised modulation. It also establishes the frequency ranges of interest, the modelling constraints, and the need for reduced models that remain computationally feasible while retaining the essential CM and DM behaviour.

In Chapter 5, subsystem models are developed, calibrated, and validated against LCR measurements. These models provide a physically grounded representation of the electrical behaviour of each component within the traction voltage system (TVS). Building on this foundation, the present chapter assembles the validated subsystem models into complete vehicle-level simulation models. Two complementary system models are constructed: one representing common-mode (CM) behaviour and one representing differential-mode (DM) behaviour. Both model variants represent the same vehicle configuration used in the measurements presented in Chapter 4.

Moving from subsystem models to a complete vehicle model introduces a fundamental trade-off between model fidelity and computational feasibility. To enable system-level simulations within practical computation times, the full CM and DM models are therefore simplified. Each simplification is systematically compared with the corresponding full model to quantify the impact on accuracy and to identify which physical effects may be neglected without compromising the validity of the simulated behaviour. This approach enables a reduction in model complexity while retaining the essential system dynamics.

The electric machines operate at different rotational speeds and power levels due to differences in the drivetrain gear ratios. The machine drive systems are not synchronised, and

their PWM modulation may drift over time. As a consequence, each machine produces a distinct current pattern, which contributes to the variations observed in both measurements and simulations in this chapter.

The simulation model topology of the complete vehicle is illustrated in Figure 6.1, which appears after the chapter overview.

The upper frequency limit of interest is, as established in Chapter 4, up to 200 kHz for DM behaviour. For CM behaviour, the relevant frequency range extends up to 2 MHz on the DC side of the TVS and up to 3 MHz on the AC side of the TVS, i.e. at the interface between the electric machine drive (EMD) and the electric machine (EM). CM simulations are highly sensitive to small variations in subsystem parameters, such as C, L, and $\frac{dv}{dt}$, which arise from parasitic capacitances, stray inductances, and voltage derivatives. At the same time, the size of the complete vehicle model, defined by the number of interacting subsystems, conflicts with the detailed resolution required to capture semiconductor switching and high-frequency effects. Both simulations and measurements indicate that high-frequency effects remain largely confined within individual subsystems, whereas neighbouring subsystems are primarily influenced by a common-mode DC voltage that couples them through shared impedances. On this basis, comparisons between full and reduced models are performed to identify a practical balance between accuracy and simulation efficiency.

To manage the overall complexity of the simulation task, the simulations in this chapter are divided into two categories: common-mode (CM) simulations and differential-mode (DM) simulations. This separation enables targeted analysis of the dominant physical mechanisms in each mode. CM simulations focus on high-frequency interactions and coupling through shared impedances, whereas DM simulations concentrate on differential current paths and their associated dynamic behaviour. This division is essential for achieving both computational efficiency and physical relevance in system-level modelling.

To provide clarity and structure, the chapter is organised into the following sections:

1. **Complexity of the CM (Common Mode) model** – discusses the modelling challenges and frequency-dependent behaviour.

2. **Results from CM simulations** – presents key findings from the common-mode analysis.

3. **Common-mode simulations of the full and reduced models** – compares the complete vehicle model with reduced representations.

4. **Differential-mode simulations** – focuses on differential signal paths and their dynamic behaviour.

5. **Differential-mode simulations compared to measurements in different load conditions** – validates the DM models against experimental data.

6. **EMI mitigation with differential-mode filters** – presents mitigation strategies based on the DM analysis to reduce electromagnetic interference.

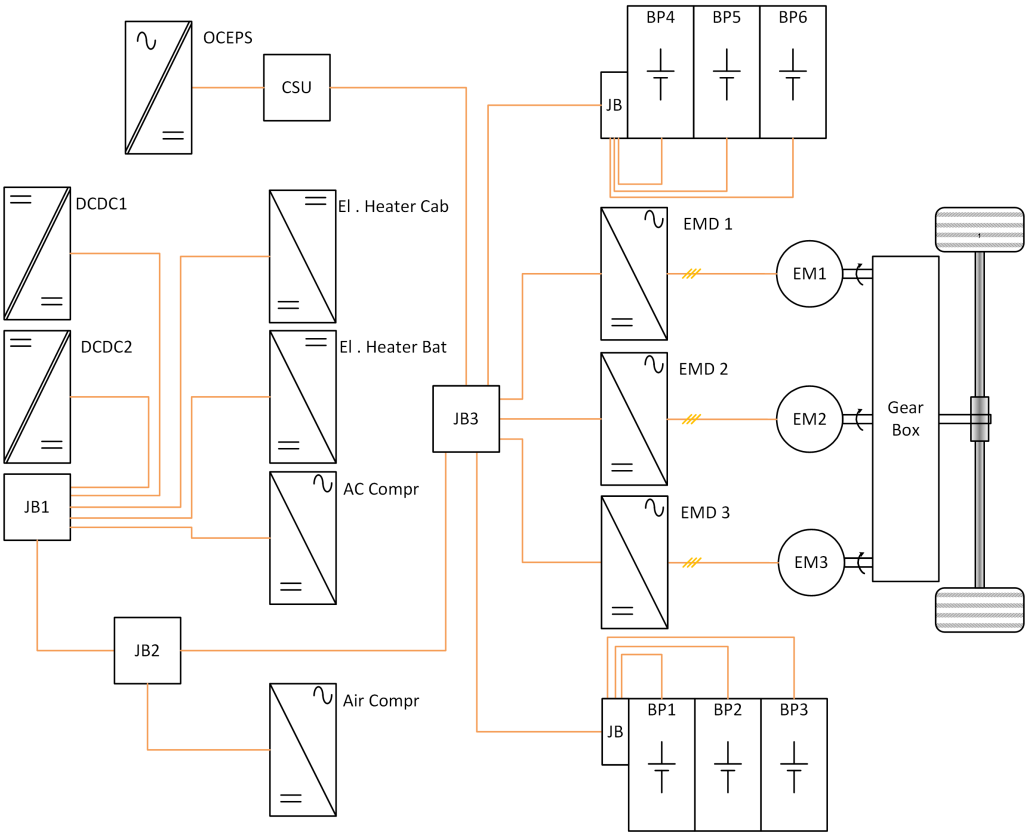


Figure 6.1: Vehicle topology for the vehicle FM1156. The vehicle contains several subsystems: EM (Electrical Machine); EMD (Electrical Machine Drive), which is the only subsystem actively switching in the model; DCDC converter that converts the traction voltage to 24 VDC; electrical heaters for cab and battery heating; AC compressor for climate control in the cab; air compressor supplying compressed air to the braking system; OCEPS (On Board Charger Electrical Propulsion System); CSU (Charging Switch Unit) connecting the charging power to the TVS (Traction Voltage System); and JB (Junction Boxes).

Throughout this chapter, the voltage definitions introduced in Chapter 4 are used consistently. All AC voltages refer to phase-to-chassis voltages measured or simulated between a phase conductor and a local chassis reference. All DC voltages refer to DC(+) to chassis or DC(-) to chassis (pole-to-chassis) voltages measured or simulated between the positive or negative DC conductor and a local chassis reference. Differential-mode (DM) and common-mode (CM) voltages are derived quantities calculated from these pole-to-chassis voltages.

6.1 Complexity of the CM (Common Mode) model

This section follows the system-level introduction in Chapter 6 and introduces the analysis of the common-mode (CM) modelling approach. It provides orientation before the technical evaluation begins.

PLECS, as described in Section 5.2, is a powerful simulation tool, although it has inherent limitations. The subsystem models developed in Section 5.4 are simplified according to the frequency content measured in Chapter 4. Combining all subsystems into a complete vehicle-level model nevertheless remains too complex for PLECS to solve. The resulting state-space matrix becomes large, and the system becomes stiff, meaning that the frequency span of the included nodes is wide.

The number of inductors, capacitors, and switch states determines the size of the state-space matrix. If the matrix becomes too large, PLECS is not able to solve it within a reasonable computation time. The term "reasonable time" is inherently subjective, but a full model cannot be solved for 5 ms within 2 weeks on a powerful DELL laptop. Section 5.3 describes the method used to determine the size of the state-space matrix.

The remainder of this section systematically evaluates different model simplifications that reduce simulation complexity while preserving the relevant CM behaviour.

Subsection 6.1.1 Examines the influence of ideal and non-ideal IGBT representations on CM voltage and current behaviour, establishing which semiconductor model is required to reproduce measured results.

Subsection 6.1.2 Assesses the impact of junction box impedance by comparing ideal and non-ideal JB models and determining whether JB impedance can be neglected in CM simulations.

Subsection 6.1.3 Investigates whether the JB impedance can be incorporated into the cable model as an equivalent representation without affecting simulation accuracy.

Subsection 6.1.4 Evaluates the validity of merging multiple cables with different cross-sectional areas and associated junction boxes into a single equivalent cable model.

Subsection 6.1.5 Compares the full battery configuration with multiple parallel battery packs (BP) to an equivalent reduced battery model, quantifying the impact on CM behaviour and simulation time.

6.1.1 Part of Full Model for Verification of Non-Ideal vs. Ideal IGBTs

The first step in the simplification process is to illustrate the difference between non-ideal and ideal IGBTs, including associated parasitic capacitances, in the EMD. The definitions used in this context are as follows:

Ideal An IGBT, including transistor and diode, with instantaneous switching, no stray inductances, no losses, and no voltage drop.

Non-ideal An IGBT with limited di/dt, forward voltage, on-resistance, stray inductance, reverse recovery time, and other non-ideal characteristics.

The part of the system used for simulation is shown in Figure 6.2.

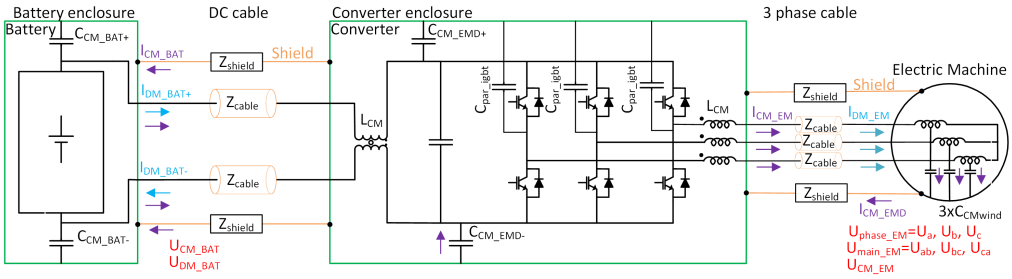


Figure 6.2: Circuit diagram for the simulation model comparing non-ideal and ideal IGBTs. The different components and variables are described below.

Key components and variables in the simulation model in Figure 6.2 are:

C_{CM_BAT+}, C_{CM_BAT-}	Parasitic capacitance in the battery from the positive and negative pole to chassis or ground.
I_{CM_BAT}	Common-mode current to or from the battery. Labelled as BP4_CM_current in Figure 6.4.
I_{DM_BAT}	Differential-mode current to or from the battery. Labelled as BP4_DM_current in Figure 6.4.
U_{CM_BAT}	Common-mode voltage at the battery, derived from the DC(+)-to-chassis and DC(-)-to-chassis voltages. Labelled as BP4_CM_voltage in Figure 6.4.
U_{DM_BAT}	Differential-mode voltage at the battery, derived from the DC(+)-to-chassis and DC(-)-to-chassis voltages. Labelled as BP4_DM_voltage in figures presented later.
Z_{shield}, Z_{cable}	Impedance of the cable and its shield.
C_{CM_EMD+}, C_{CM_EMD-}	Intentional Y-capacitance in the EMD.
I_{CM_EM}	Common-mode current on the AC side of the EMD. Labelled as AC_EM_CM_current.

$\mathbf{I_{DM_EM}}$	Differential-mode current on the AC side of the EMD. Labelled as AC_EM_DM_current.
$\mathbf{U_{phase_EM}}$	Phase-to-chassis voltage at the electric machine (EM). Labelled as AC_EM1_Ua_voltage, AC_EM2_Ub_voltage, and AC_EM3_Uc_voltage.
$\mathbf{U_{main_EM}}$	Line-to-line voltage at the electric machine (EM), derived from the corresponding phase-to-chassis voltages. Labelled as AC_EM1_Uab_voltage, AC_EM2_Ubc_voltage, and AC_EM3_Uca_voltage.
$\mathbf{U_{CM_3phase_EM}}$	Common-mode voltage on the AC side, derived from the phase-to-chassis voltages at the electric machine (EM). Labelled as AC_EM1_CM_voltage, AC_EM2_CM_voltage, and AC_EM3_CM_voltage.
$\mathbf{3xC_{CMwind}}$	Parasitic capacitance in the EM stator windings to ground.

The simulation compares non-ideal and ideal IGBTs. Ideal IGBTs lack properties such as voltage drop, rise-time t_r, fall-time t_f, and stray inductances. The only return path for the common-mode (CM) current is the cable shield, while the ground plane is excluded from the model. As described in Subsection 5.4.14, the impedance of the ground plane is significantly higher than that of the coaxial cable shield, which justifies its removal as a simplification. The ground current path originates from the capacitors C_{CM_BP}, C_{CM_EMD}, C_{par_IGBT}, and C_{CMwind} to the enclosures and returns via the cable shield.

Not all IGBT properties are shown in Figure 6.2. In Figure 6.3, the full non-ideal and ideal IGBT models are shown. Each topology (a–d) is simulated using both non-ideal and ideal semiconductor representations.

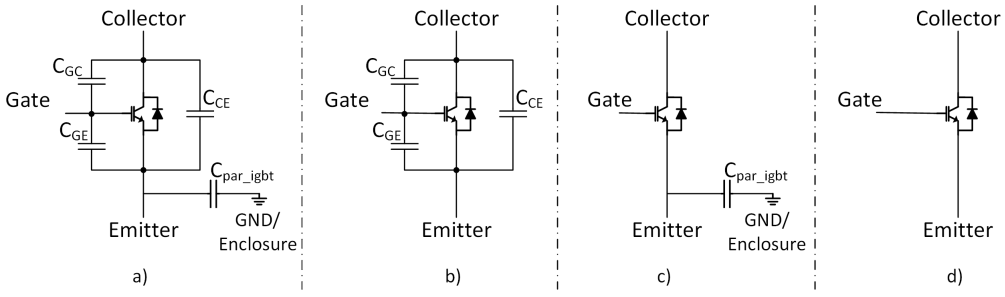


Figure 6.3: Ideal IGBT model and non-ideal model with properties such as rise-time and fall-time and parasitic capacitances. Each topology (a–d) is evaluated using two semiconductor representations: an ideal device model and a non-ideal device model. The surrounding capacitances, for example C_{GC} and C_{par}, are included in both cases. The distinction between ideal and non-ideal semiconductors is therefore not encoded in the subfigures (a–d), but in the device models applied to each topology.

(a) IGBT with all capacitors.

(b) IGBT with only C_{GC}, C_{GE}, and C_{CE}.

(c) IGBT with only C_{par_IGBT}.

(d) IGBT without any capacitors.

Simulations for each variant are shown in Figure 6.4 across two switching periods.

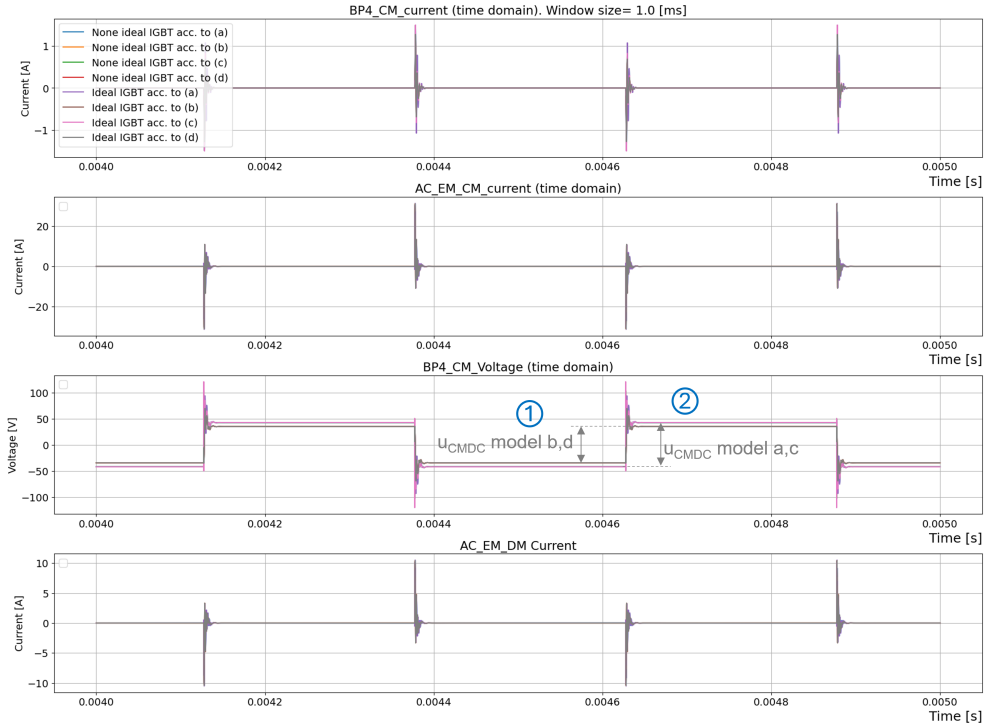


Figure 6.4: Simulations of the IGBT over two periods. (1) and (2) show that the common-mode DC voltage u_{CMDC}, see Subsection 2.4.3, is lower for models b and d than for models a and c. These results suggest that only models a and c provide behaviour consistent with measurements from a u_{CMDC} perspective.

A zoomed-in view of one switching event is shown in Figure 6.5.

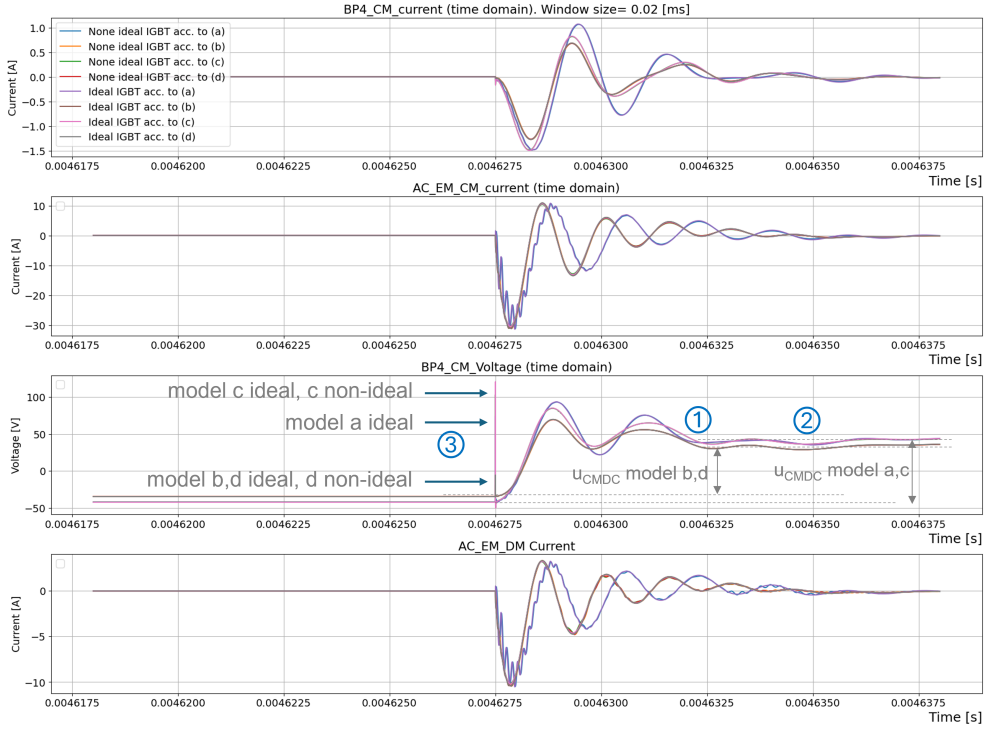


Figure 6.5: Simulation of one switching event. (3) shows that models a–d with ideal IGBTs and models c and d with non-ideal IGBTs exhibit fast transients that are not present in measurements from the actual vehicle. As shown in Figure 6.4, (1) and (2) indicate that the common-mode DC voltage U_{CMDC}, see Subsection 2.4.3, is lower for models b and d than for models a and c. These results suggest that only model a with a non-ideal IGBT exhibits behaviour consistent with measurements.

It is observed in Figure 6.5 that the common-mode DC voltage U_{CMDC} is significantly lower for models b and d. This deviation is caused by the absence of C_{par_IGBT}, which reduces the asymmetry in parasitic capacitance, see Subsections 2.4.2 and 2.4.3. However, this reduction in u_{CMDC} is not physically realistic, as C_{par_IGBT} is inherently present in real IGBTs. Fast transients are also observed in all ideal IGBT simulations, as well as in variants c and d. The only simulation that exhibits behaviour consistent with measurements is model a with the non-ideal IGBT, see Figure 6.6, where it is plotted stand-alone.

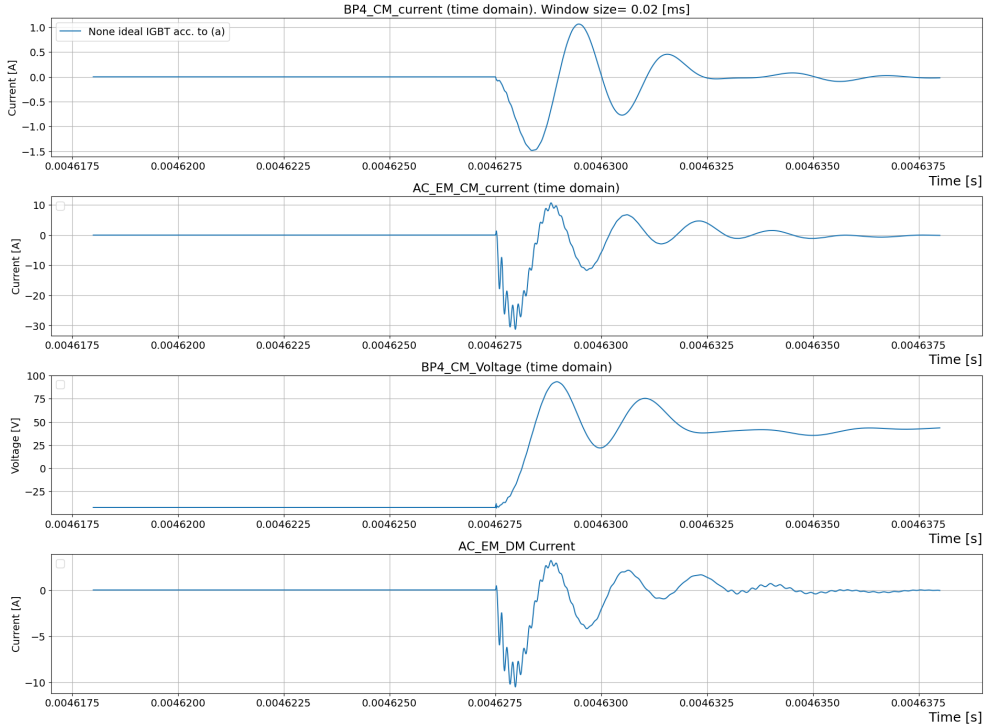


Figure 6.6: Simulation of one switching event for non-ideal IGBT model a, extracted from Figure 6.5.

A measurement on the complete vehicle is shown in Figure 6.7.

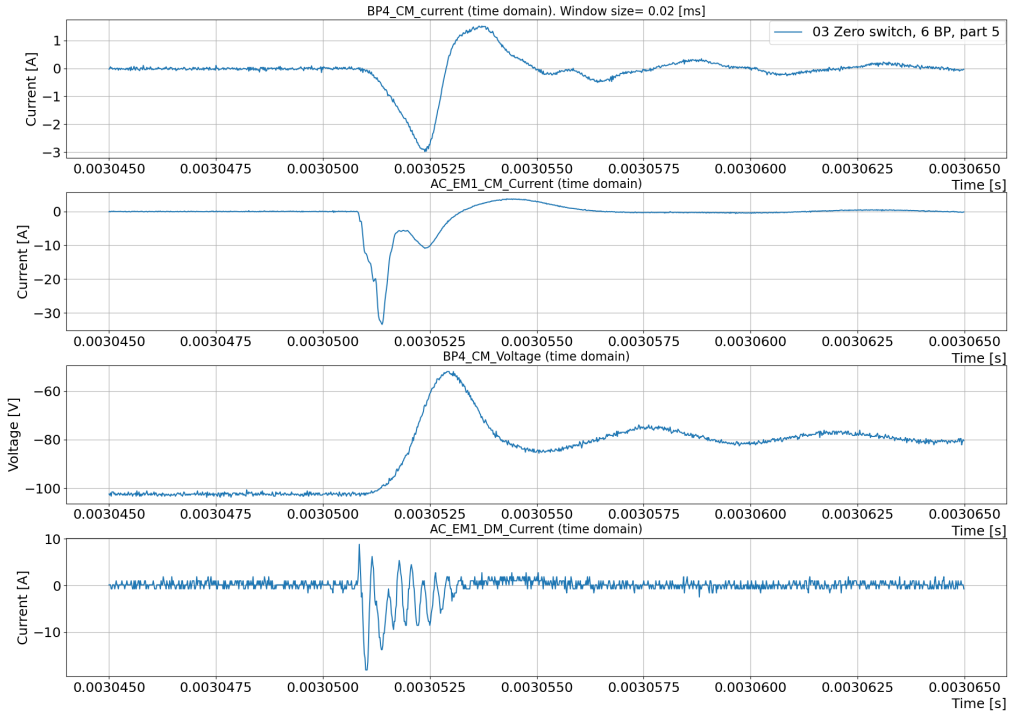


Figure 6.7: Measurement on the complete vehicle of the same parameters as in Figure 6.6.

The measured oscillation in the phase current is not captured in the initial simulation. Introducing a short delay between the switching events of each phase leg, which are expected to switch simultaneously, of t_d = 0.4 µs yields results that align more closely with the measured signal, as shown in Figure 6.8. This delay is based on observations from measurements, see Figure 4.34.

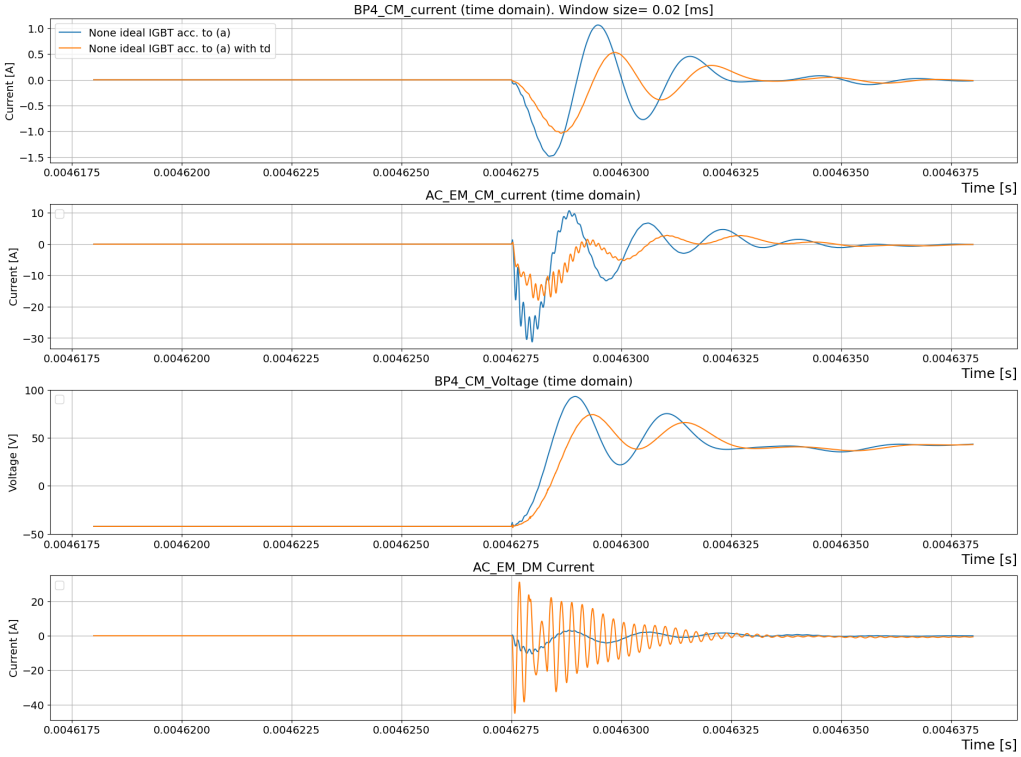


Figure 6.8: Simulation result with and without time delay t_d = 0.4 µs between IGBT legs.

In Figure 6.8, it is also observed that the common-mode current I_{CM} to the battery is significantly reduced. This behaviour is also confirmed by measurements, see Subsection 6.2.3.

Conclusion

The comparison between non-ideal and ideal IGBT models demonstrates that only the non-ideal model variant a, which includes all relevant parasitic capacitances and switching characteristics, provides results that align with measured data from the complete vehicle. The inclusion of a short switching delay further improves the simulation accuracy, particularly in reproducing observed oscillations in the phase current and reducing common-mode currents. The non-ideal model variant a with a non-zero t_d is therefore used in subsequent simulations to ensure realistic system behaviour.

6.1.2 Part of Full Model for Verification of the Impact of the Impedance in the Junction Box (JB)

The JB connects different subsystems to each other. The modelling shows that the impedance varies between connectors that are close to each other compared with connectors that

are farther apart within the same JB, depending on the busbar length. However, it is not possible to determine which connector is linked to a specific subsystem. The impedance is therefore set to an average value across all terminals. A principle sketch of the JB is shown in Figure 6.9.

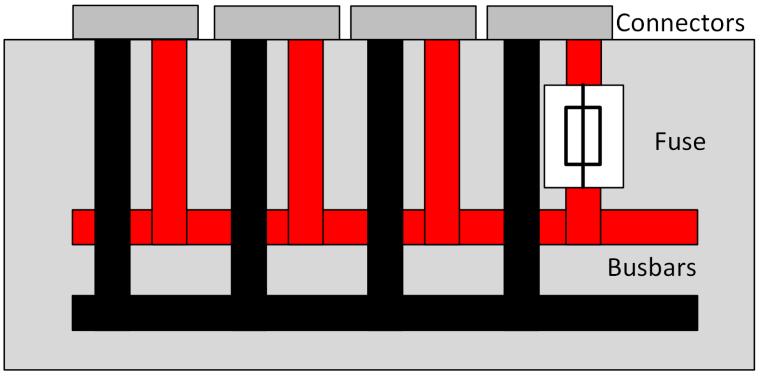


Figure 6.9: Principle layout of a junction box. High-current loads such as the battery and electrical machine drive (EMD) are connected in parallel via busbars. Low-current loads such as DCDC and air compressor are connected via a fuse.

The different loads are connected through the JB. High-current loads are connected via busbars only, while low-current loads are connected via a fuse. Batteries are connected via a battery junction box (BJB).

In this subsection, a comparison between an ideal and a non-ideal JB and BJB, shown in Figure 6.10, illustrates the impact of the JB impedance on a circuit in the vehicle. The JB model is described in Subsection 5.4.15. An ideal JB has no impedance, whereas the non-ideal JB includes the measured impedance.

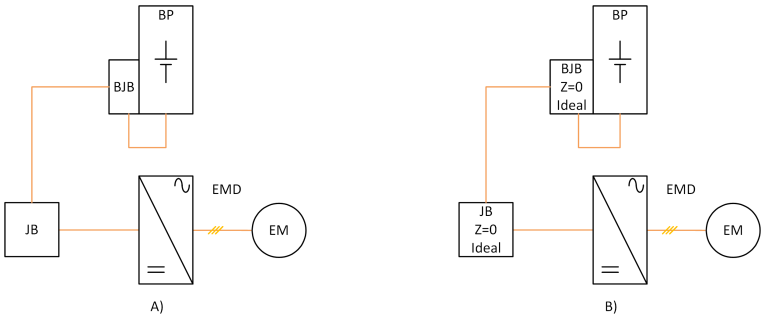


Figure 6.10: Circuits containing one JB, one BJB, and three cables: (A) with symmetrically-distributed impedance and (B) with an ideal JB without impedance.

In simulation, there is only a marginal difference between the ideal JB and the symmetric non-ideal JB. As this difference is barely visible in the time-domain response, the

corresponding waveform is not shown. However, an impedance analysis reveals a measurable deviation; therefore, the JB impedance cannot be omitted, see Figure 6.11.

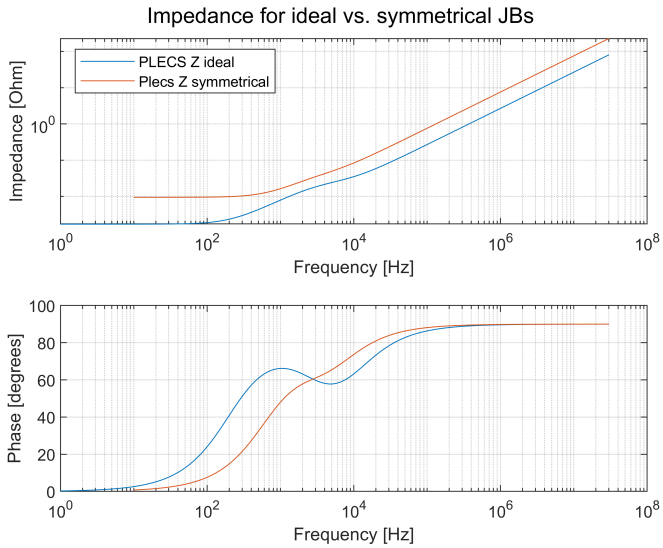


Figure 6.11: Impedance for three cables and two JBs, where the impedance sweep shows the difference between an ideal JB and a symmetrical JB. A symmetrical JB is defined as a JB where the impedance is evenly-distributed between the positive and negative poles.

Conclusion

Although the simulated current behaviour shows only a minor difference between an ideal and a non-ideal junction box (JB), the impedance analysis reveals measurable deviations. These differences, while not always visible in time-domain plots, affect the system frequency response and must be considered in CM simulations. The JB impedance therefore cannot be omitted, as it contributes to the overall system behaviour and ensures physical accuracy in the model.

6.1.3 Part of Full Model for Verification of Combining JB Impedance in the Cable Model

To mitigate the increased size of the state-space matrix described in Subsection 6.1.2, the impedance of the JB is incorporated into the cable model. In addition to the cable length, the number of JB connections, n_{JB}, is introduced as an input parameter. The reduction in model complexity results from replacing two serially connected inductances, namely the cable inductance and the JB inductance, with a single equivalent inductance. In Figure 6.12B, the cable from the battery to the battery junction box BJB has one JB connection ($n_{JB} = 1$), the cable between the BJB and the JB has two JB connections ($n_{JB} = 2$), and subsequent cables include an increasing number of JB connections.

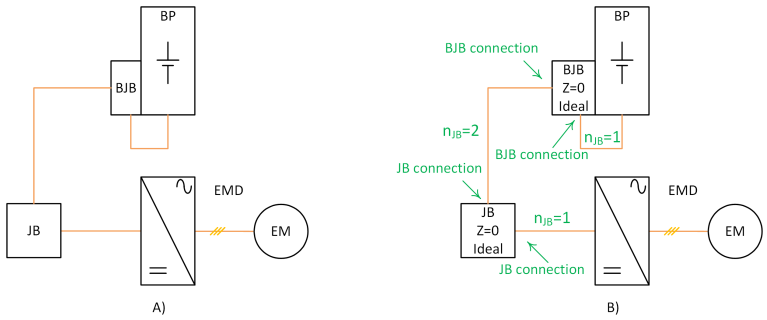


Figure 6.12: Part of the system showing the difference when JB properties are merged into the cable model. Figure A shows cables and JBs with impedance, and Figure B shows ideal JBs with cables including JB impedance scaled by the factor n_{JB}.

In Figure 6.13, the cable model including JB impedance together with ideal JBs is compared with a model consisting of cables and JBs with explicit impedance. No visible difference is observed between the two cases.

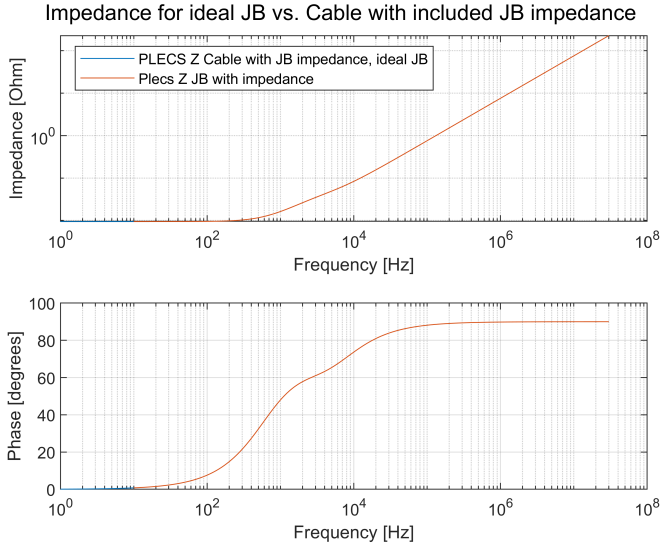


Figure 6.13: Impedance for three cables, one JB, and one BJB, where the impedance sweep shows the difference between an ideal JB/BJB and a cable model in which the JB impedance is included.

Conclusion

Incorporating the JB impedance directly into the cable model provides a practical simplification that preserves the electrical behaviour while significantly reducing the size of the state-space matrix. This approach enables faster simulations without compromising accuracy, making it suitable for system-level CM analysis where JB impedance is relevant but can be abstracted through parameter scaling.

6.1.4 Part of Full Model for Verification of Merging Cables of Different Area and Junction Boxes

In Figure 6.14B, the three cables from the BP to the EMD in Figure 6.14A are replaced by a single cable. The original cables have different cross-sectional areas, 50, 70, and 95 mm^2, and are replaced by one 70 mm^2 cable with the same total length. The JB impedance is included according to Subsection 6.1.3. The impedance response of the equivalent model matches that of the full model, see Figure 6.15.

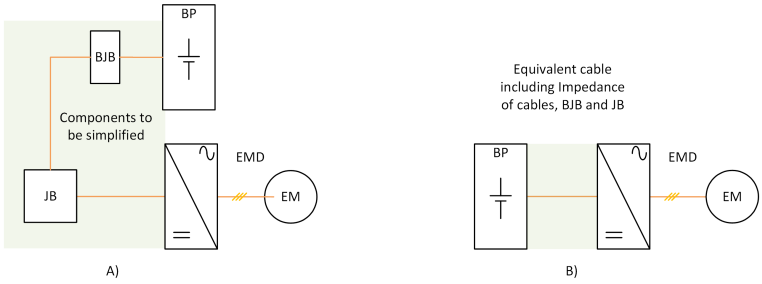


Figure 6.14: Part of the system simulated to show the impact of merging cables and junction boxes. Figure A illustrates the original configuration, and Figure B shows the equivalent model where cables and junction boxes are merged.

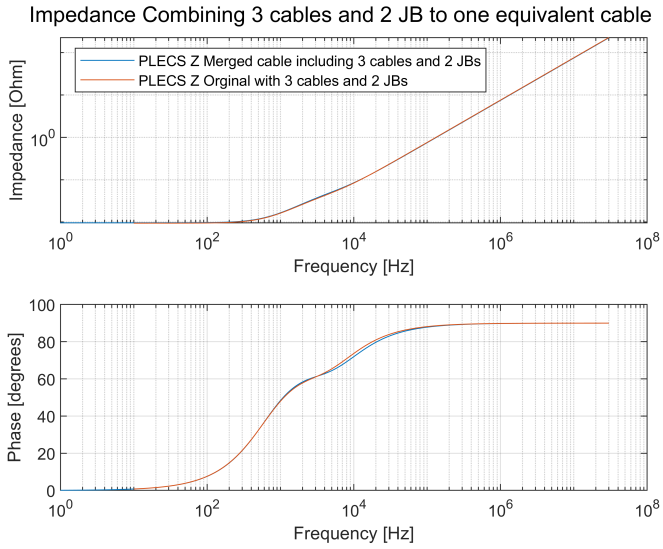


Figure 6.15: Impedance for three cables and two JBs, where the impedance sweep shows identical results for the full model and the equivalent cable configuration.

The simulation time for the equivalent cable model is 8 % of that required for the full model.

Conclusion

Replacing multiple cables with different cross-sectional areas by a single equivalent cable, while including the JB impedance, yields simulation results consistent with those of the full model. This simplification reduces the simulation time to 8 % of the original without loss of fidelity. It demonstrates that merging cable and JB models is an effective approach for reducing computational complexity in CM simulations.

6.1.5 Part of Full Model for Verification of 6 BPs vs. 1 Equivalent 6BP

This subsection compares 6 separate battery packs (BPs) with one equivalent battery pack. The equivalent battery model is developed in Subsection 5.4.4. In Figure 6.16, the simplification steps are illustrated. In Figure 6.16A, the reference case with 6 BPs is shown; in Figure 6.16B, the upper and lower batteries are replaced by equivalent BPs with $n = 3$, where n denotes the number of parallel battery packs; in Figure 6.16C, all batteries are replaced by one equivalent BP with $n = 6$. Finally, in Figure 6.16D, the cable from the JB to the BJB (95 mm²) and the cable from the BJB to the BP (50 mm²) are merged into one equivalent cable.

Comparing models A and B shows that the DM current is slightly lower.

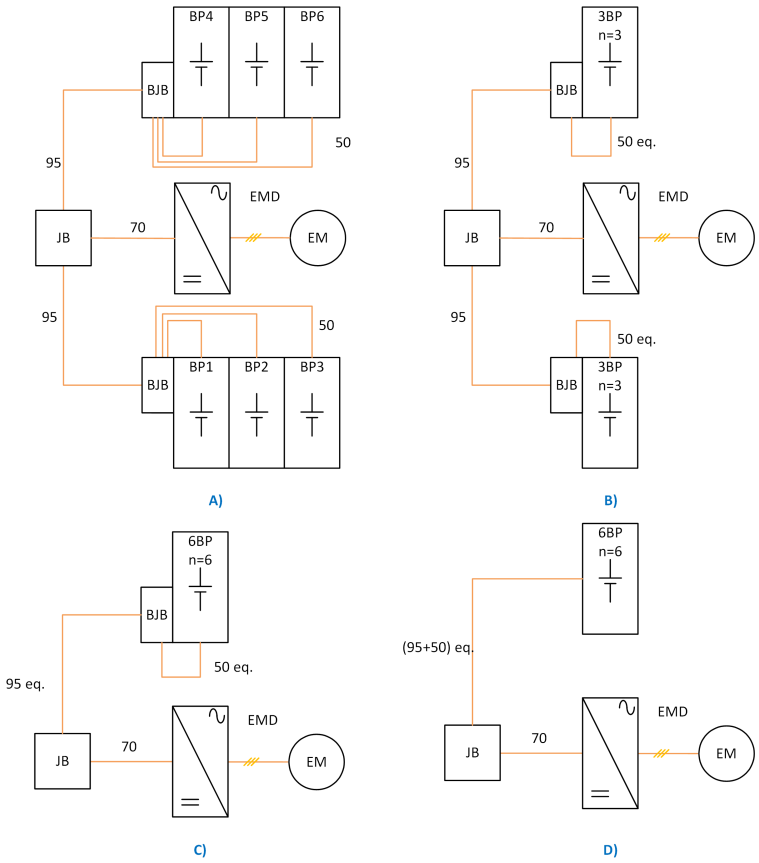


Figure 6.16: Part of the system simulated to show the effect of successive simplifications. Figure A shows 6 BPs. Figure B shows two equivalent 3BP configurations, where the 50 mm² cable represents three parallel cables. Figure C shows one equivalent 6BP configuration, where the 50 mm² cable represents three parallel cables and the 95 mm² cable represents two parallel cables. Figure D shows one equivalent 6BP configuration with the 95 mm² and 50 mm² cables merged.

Simulations of the different models in Figure 6.16 show full conformity for CM quantities. In Figures 6.17 and 6.18, the models in Figure 6.16A and D are simulated. The primary advantage is the significantly reduced simulation time.

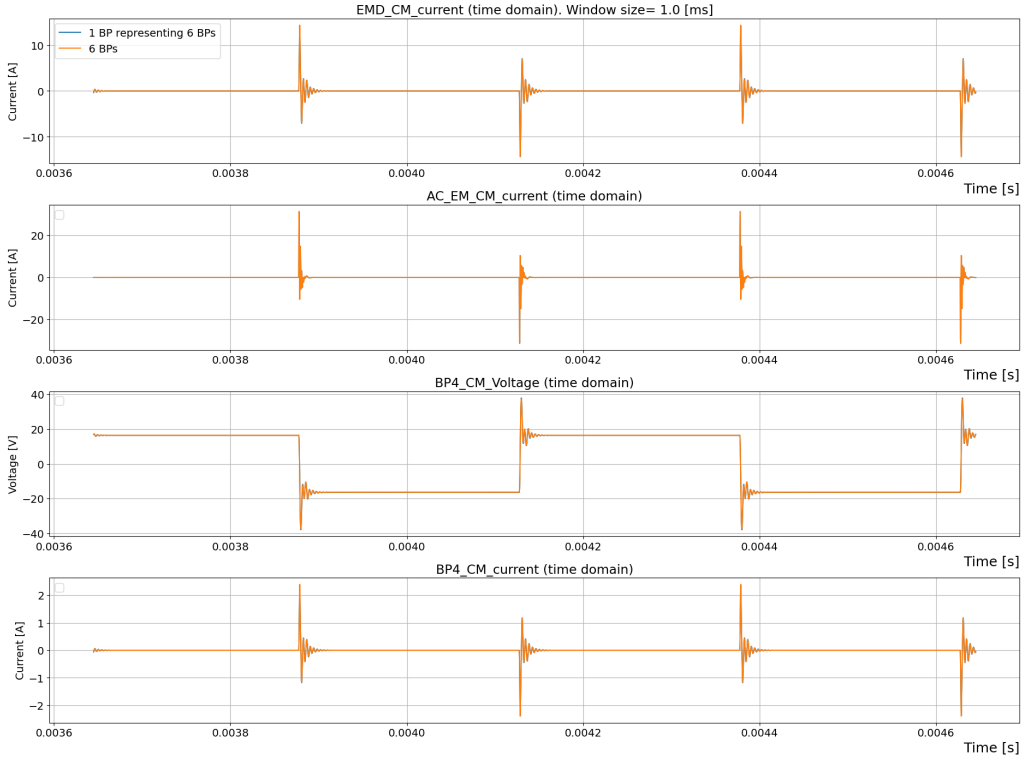


Figure 6.17: Simulation of the full model with 6 BPs compared with the simplified model using one equivalent BP ($n_{\text{bat}} = 6$), where the cables are scaled to an equivalent representation. All curves coincide, indicating no observable difference. The simulation covers one switching cycle. A zoomed-in view is provided in Figure 6.18.

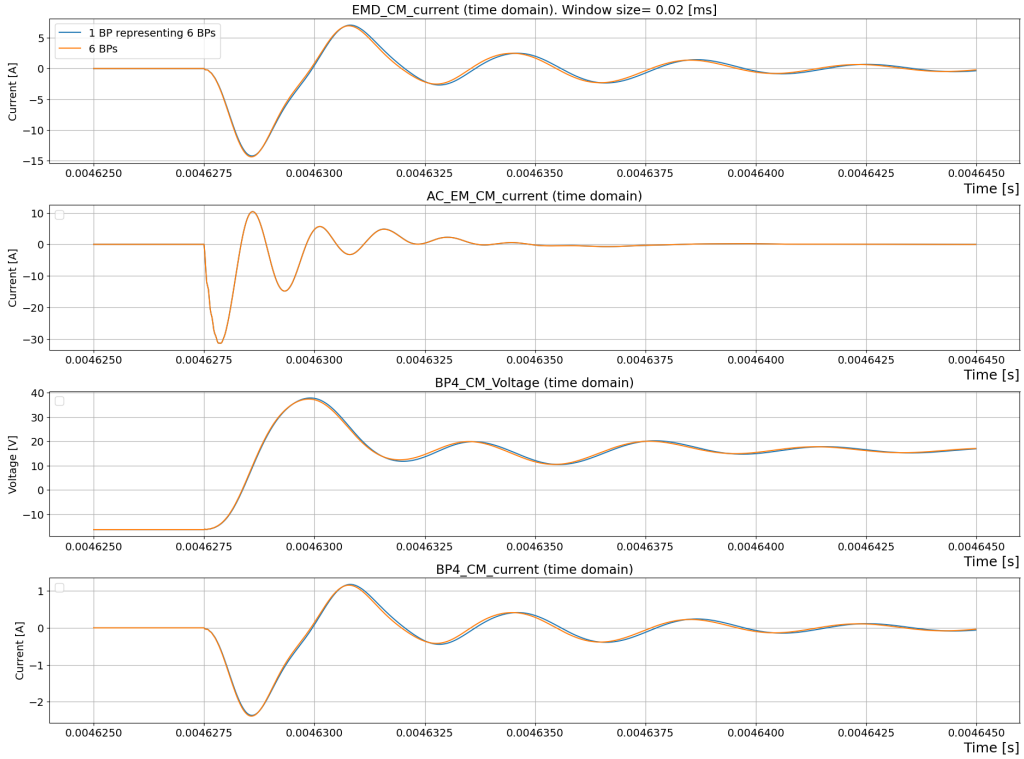


Figure 6.18: Zoomed-in simulation comparing the full model with 6 BPs and the simplified model with one equivalent BP ($n_{bat} = 6$). All curves overlap, confirming identical behaviour.

Conclusion

The simplified models in Figure 6.16B, C, and D can be used, as all exhibit conformity with model A. The simulation time is reduced to 42 % for model B, 4 % for model C, and 3 % for model D. Proper adjustment of the cable models for parallel and serial JB connections is therefore essential for achieving accurate and efficient CM simulations.

6.1.6 Impact of cables and JBs on CM simulations

As demonstrated in Section 4.2, the break-out boxes introduce measurable deviations in the common-mode voltage due to magnetic coupling and busbar inductance. Laboratory tests demonstrate induced voltages of approximately 4 V with a single BoB, and vehicle measurements show a corresponding deviation of around 10 V when two BoBs are included in the return path. This effect explains part of the skewed behaviour observed in the measured u_{CM} waveforms in Figures 4.8 to 4.10.

In the following comparison between measurements and simulations, these measurement-induced effects must therefore be distinguished from the intrinsic system behaviour caused by cable impedances, junction boxes, and asymmetries in the EMD DC-side

inductances. The simulations presented in this subsection isolate the physical mechanisms and allow the BoB-induced contributions identified in Section 4.2 to be separated from the true CM dynamics of the TVS.

In Subsection 6.1.3, it is shown that cables and JBs can be merged, and in Subsection 6.1.4, that series-connected cables can be merged into a single equivalent cable without affecting the simulation results. Even though the cables and JBs are merged, the CM simulation time remains long, reaching several days. This subsection therefore investigates the actual impact of cables and JBs on the complete CM simulation model.

For CM behaviour, a coaxial cable exhibits low impedance, and the converters include CM inductors. The comparison is made according to Figure 6.19, where the impedance difference between the BP and the EMD is illustrated. The simulated models are shown in Figure 6.20.

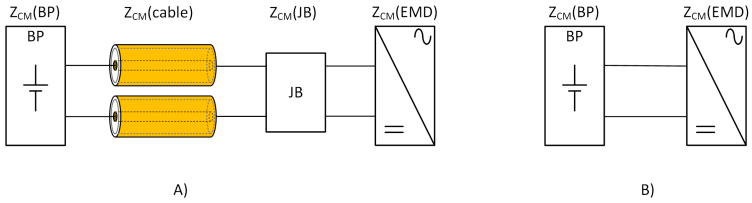


Figure 6.19: Comparison between the CM impedance between the BP and the EMD. In (A), impedance from the cable and junction box is present, whereas in (B) the connection between the BP and the EMD is ideal. The simulated models are shown in Figure 6.20.

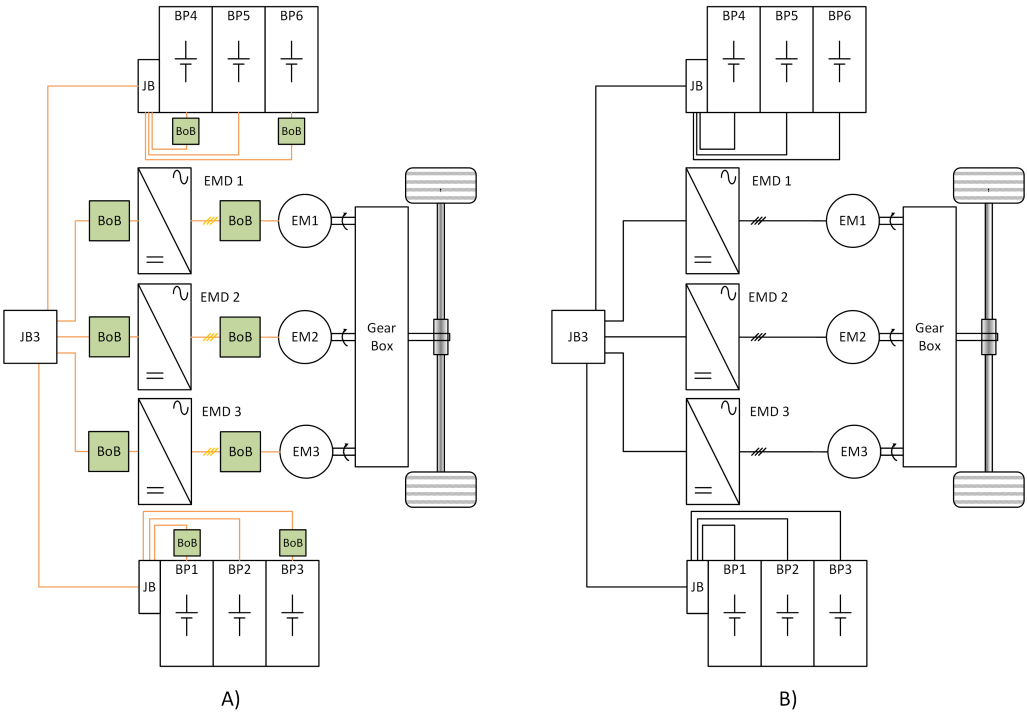


Figure 6.20: Comparison between the CM impedance between the BP and the EMD. The simulated model with and without impedance from the cables and junction boxes. The black connections in (B) illustrate ideal connections.

In Figures 6.21 and 6.22, simulations over 1 ms and 20 µs, respectively, are shown for a 3MDS system with and without cables, based on Figure 6.20. For sensitivity analysis, an additional simulation with cables is performed in which the CM choke inductance on the DC side of the EMD is reduced by 10 %.

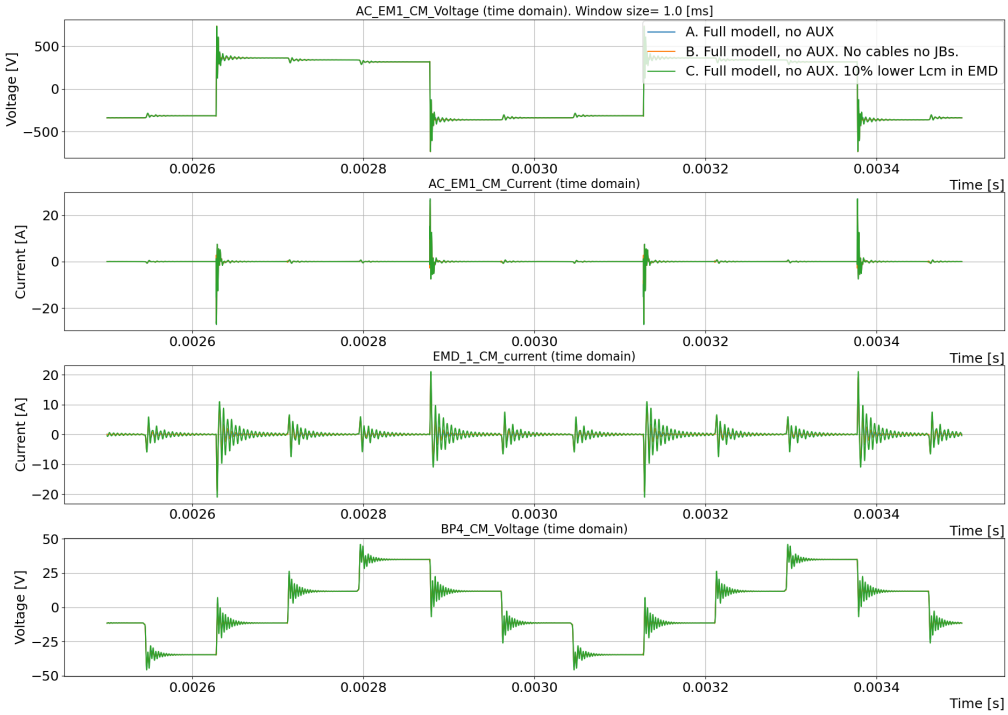


Figure 6.21: Comparison between a 3MDS system with and without cables. A sensitivity analysis is included in which the DC CM choke in the EMD is reduced by 10 %.

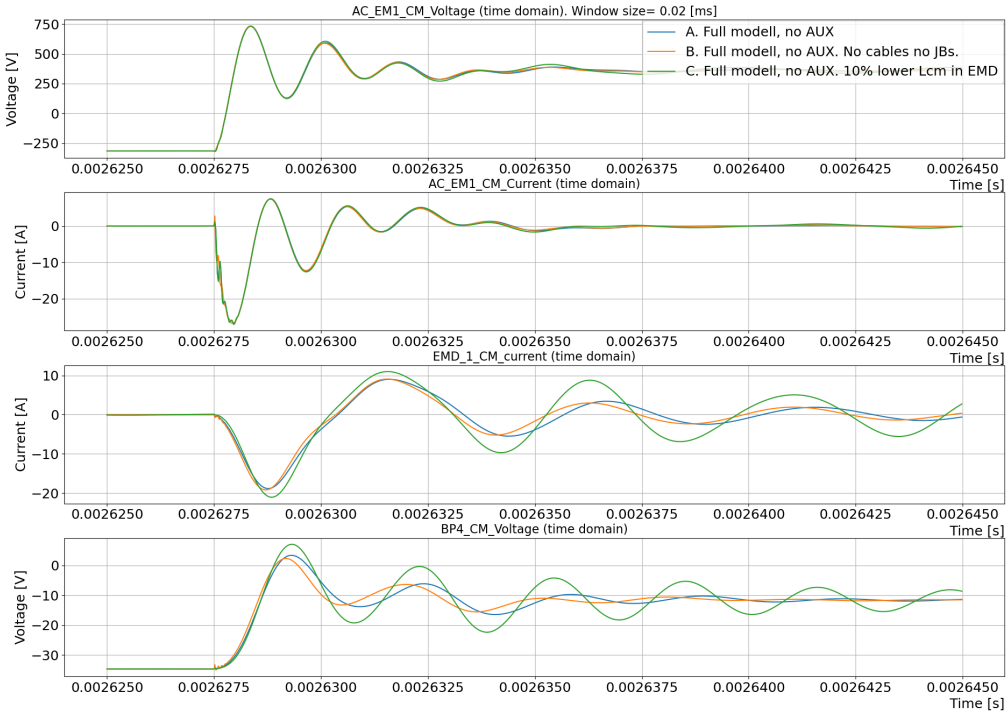


Figure 6.22: Comparison between a 3MDS system with and without cables. A sensitivity analysis is included in which the DC CM choke in the EMD is reduced by 10 %.

Conclusion

Figures 6.21 and 6.22 show that the difference on the three-phase (AC) side is negligible across all simulated cases. On the DC side, the difference between simulations with and without cables is minor compared with the effect of reducing the CM inductance by 10 %. Since the purpose of the simulation is to analyse CM behaviour, the impact of cables and JBs is negligible. This observation is explained by the low common-mode impedance of the cables relative to the impedance of the CM filter in the EMD, which also clarifies why a small change in CM inductance has a more pronounced effect.

6.1.7 Conclusion

This section investigates six key aspects of model simplification in common-mode (CM) simulations for a complete vehicle system:

1. Non-ideal versus ideal IGBT switching behaviour.
2. The impact of junction box (JB) impedance.

3. Combining JB impedance into cable models.
4. Merging cables of different cross-sectional areas.
5. Replacing multiple battery packs with one equivalent model.
6. The influence of cables and junction boxes on CM behaviour.

The results show that several simplifications, such as merging cables, combining JB impedance into cable models, and using an equivalent battery pack, can significantly reduce simulation time while maintaining conformity in CM behaviour. For example, replacing six battery packs with one equivalent model reduces the simulation time by up to 97 % without affecting accuracy.

The analysis also demonstrates that certain elements, in particular non-ideal IGBTs and JB impedance, must be modelled with care. Omitting these aspects leads to deviations from measured data, especially with respect to high-frequency oscillations and common-mode current return paths.

Overall, the section shows that model simplification is not merely a technical exercise but requires engineering judgement and domain expertise in power electronics. Simplifications must therefore be guided by measurement data and a detailed understanding of system behaviour to ensure that physically relevant phenomena are preserved.

The following section, Section 6.2, applies these validated simplifications to the complete CM model.

6.2 Results from CM Simulations

In the simulations presented here, the results focus on reduced system complexity to investigate the causes and effects of common-mode (CM) disturbances generated by EMD switching, and how these disturbances can be mitigated.

The PLECS models include the details described in Chapter 5. For the investigation of CM current distribution, a simplified system model is used, containing a limited set of subsystems. The system consists of one traction battery, DC cables, one EMD, three-phase cables, and one EM. This limitation arises because the full system, shown in Figure 6.1, cannot be simulated with the selected simulation tool and frequency range due to excessive complexity.

The source of CM disturbances is the interaction between the electric machine drive (EMD) and the parasitic capacitances to chassis in the IGBT (C_{par_igbt}), the three-phase cable ($C_{CM3phcable}$), and the EM windings (C_{CMwind}). When the EMD switches from one zero vector to the other, these parasitic capacitances are excited through four switch states, $(0,0,0)$, $(1,0,0)$, $(1,1,0)$, and $(1,1,1)$, depending on the modulation method. The switching pattern from $(0,0,0)$ to $(1,1,1)$ can also be realised through other intermediate transitions.

This switching causes the DC(+) to chassis and DC(-) to chassis voltages at the battery terminals to vary slightly depending on the active switch state. These voltage variations drive CM currents through the EM windings ($3\times$ C_{CMwind}), the three-phase cable ($C_{CM3phcable}$), and the parasitic capacitances within the IGBT (C_{par_igbt}). The return paths for the CM current are provided by the CM capacitances in the EMD (C_{CM_EMD}), the parasitic capacitance in the DC cables ($C_{CM_DCcable}$), and the parasitic capacitance in the battery (C_{CM_BAT}), as shown in Figure 6.23.

The worst case occurs when the EMD switches all phases simultaneously, corresponding to a zero output voltage of the EMD, that is, during transitions between the states $(0, 0, 0)$ and $(1, 1, 1)$.

The CM voltages are defined in Figure 6.23.

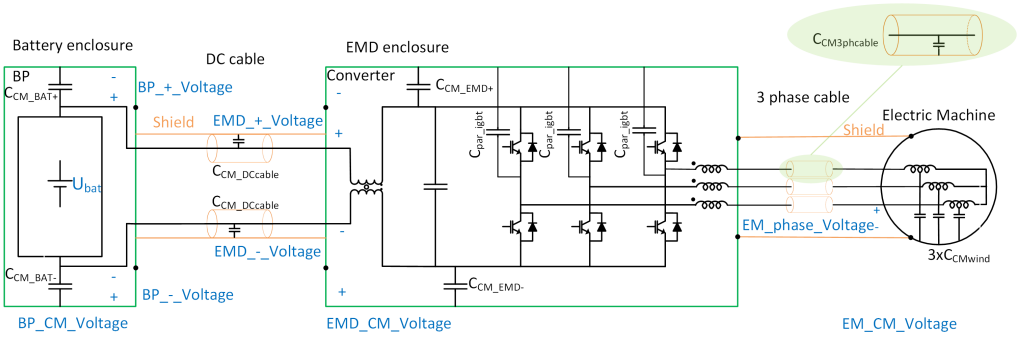


Figure 6.23: Circuit diagram for simulation with CM voltage references. Capacitance definition for the subsystem $C_{CM_capacitances}$.

The return paths for the CM currents are shown in Figure 6.24. All currents have the same reference direction, from the battery to the load and from the chassis to the TVS and load, which simplifies tracking of inbound and outbound currents. The naming conventions are shown in the figures.

The battery circuit is modelled as a voltage source with series inductance and resistance, and intentional CM capacitors connected from the positive or negative TVS pole to chassis.

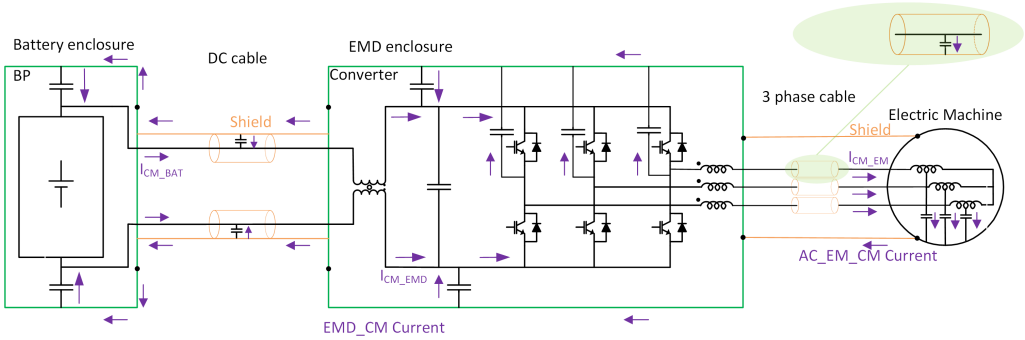


Figure 6.24: Circuit diagram with different CM currents. The CM current originates from the parasitic capacitance in the IGBTs, the parasitic capacitance in the three-phase cable to the shield, and from the EM winding to the stator. It returns via the cable shield to the EMD enclosure. Part of the CM current returns to the EMD via C_{CM_EMD}, continues in the shield to the battery enclosure, and returns to the positive and negative poles via the parasitic capacitance in the DC cable and the battery, through the parasitic capacitances C_{CM_BP}, and back via the positive and negative conductors to the EMD.

The winding-to-core capacitances in the EM are asymmetrically distributed relative to the DC link due to modulation, that is, the connection of these parasitic capacitances varies with the switch states. This asymmetry introduces a difference in common-mode voltage between two switch events, referred to as the Common-Mode DC voltage (u_{CMDC}), as described in Subsection 2.4.3. The CMDC voltage changes level due to the asymmetrically distributed CM capacitances (C_{par_igbt}, $C_{CM3phcable}$, and C_{CMwind}), according to Figure 6.23, as described in the following subsection.

Figure 6.25 provides an alternative representation of Figure 6.23, focusing on the CM capacitances.

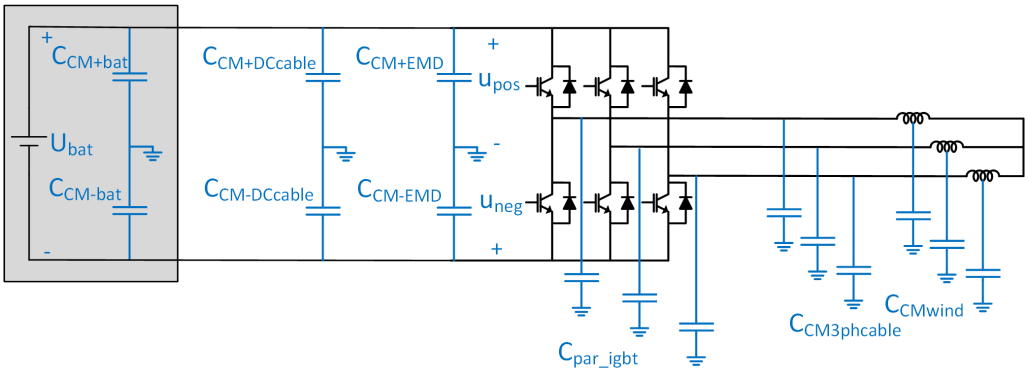


Figure 6.25: Equivalent circuit diagram for the $CM_{capacitances}$.

At standstill, with zero output voltage, the CMDC voltage is a square wave. It becomes a quasi-square wave when the EM rotates or in systems with multiple EMs using non-synchronised modulation of the EM drivers. This square or quasi-square waveform is

referred to as the CMDC voltage in this thesis.

The remainder of this section is structured to progressively analyse the mechanisms governing CM behaviour and the effectiveness of different mitigation strategies, moving from fundamental voltage generation mechanisms to practical mitigation techniques at system level.

Subsection 6.2.1 Analyses the origin of the CMDC voltage and quantifies its dependence on the ratio between symmetrical and asymmetrical CM-capacitances, introducing the X-factor as a key design parameter.

Subsection 6.2.2 Extends the analysis by distinguishing between subsystem-level and system-level X-factors, highlighting the importance of CM-capacitance placement for controlling current return paths.

Subsection 6.2.3 Investigates delayed switching between phase legs as a transient mitigation technique and analyses its impact on CM voltage and current during switching events.

Subsection 6.2.4 Provides a direct comparison of the relative influence of delayed switching and the X-factor on both the DC and AC sides.

Subsection 6.2.5 Summarises the combined implications of the results and formulates practical design guidelines for reducing CM disturbances in electric drive systems.

6.2.1 CMDC voltage – cause and effect

The common-mode (CM) voltage is defined as:

$$u_{cm} = \frac{u_{pos} + u_{neg}}{2} \tag{6.1}$$

The CMDC voltage originates from the winding-to-core capacitance of the EM and the cable-to-shield capacitance of the three-phase cable, denoted as C_{asym}.

$$C_{asym} = C_{par_igbt} + C_{CM3phcable} + C_{CMwind} \tag{6.2}$$

As C_{asym} is asymmetric with respect to either the positive or the negative pole of the TVS, the sum of the winding-to-core capacitances and the cable-to-shield capacitances of the three-phase cable towards the positive or negative poles of the TVS is asymmetric relative to the DC link for a certain switch state, see Figure 6.26. The sum of the CM-capacitances in this example—battery, DC cable, and EMD included but EM and three-phase cables excluded—is referred to as C_{pn}.

$$C_{pn} = C_{CM+bat} + C_{CM+DCcable} + C_{CM+EMD} = C_{CM-bat} + C_{CM-DCcable} + C_{CM-EMD} \tag{6.3}$$

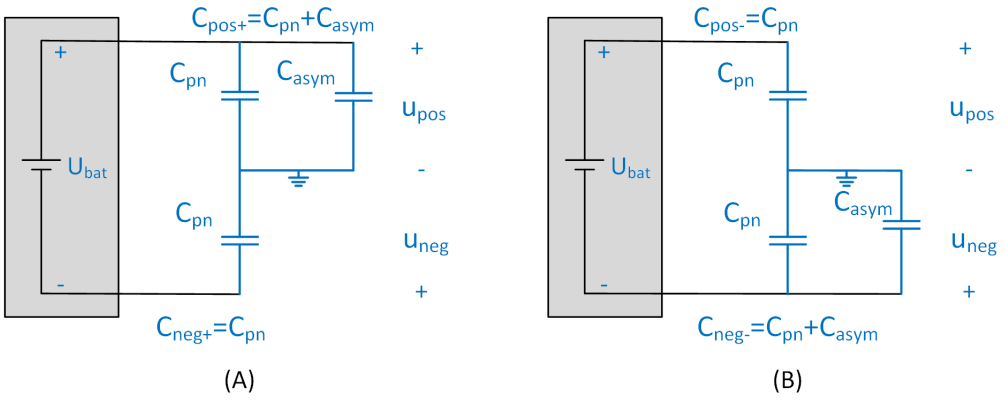


Figure 6.26: Equivalent circuit diagram for the CM-capacitances where (A) C_{asym} is asymmetric to the positive, or (B) to the negative pole of the TVS. C_{pos+} and C_{neg+} are the capacitances at switch state (1,1,1), and C_{pos-} and C_{neg-} at switch state (0,0,0).

Two configurations are analysed where the CM-capacitances, C_{CM+EMD} and C_{CM-EMD} (see Figure 6.25), are simultaneously increased by a factor of 16 in the EMD. The factor 16 is determined to achieve an X-factor of 50. The CM-capacitance of the EMD is intentionally changed to provide a significant but realistic shift in the balance between the CM-capacitances of the EMD and EM, to observe how the CM voltage changes, see Figure 6.27.

The total symmetrical CM-capacitances (C_{pn}, in Equation (6.3), Figure 6.26) in the system are related to the asymmetrical CM-capacitances (C_{asym}, in Equation (6.2), Figure 6.26). The ratio between them is:

$$X = \frac{C_{pn}}{C_{asym}} \tag{6.4}$$

The sum of the symmetrical CM-capacitances in the first configuration, obtained in an unaltered vehicle, results in X=8.1 using Equation (6.4). In the second configuration, with a 6× increased total CM-capacitance and 16× in the EMD, the corresponding value becomes X=50.

In parallel, the total CM-capacitance towards the positive TVS pole when all three phases of the EMD are connected to it (switch state $(1, 1, 1)$) is:

$$C_{pos+} = C_{pn} + \frac{C_{pn}}{X} = C_{pn} + C_{asym} \tag{6.5}$$

Simultaneously, the total CM-capacitance towards the negative TVS pole is:

$$C_{neg+} = C_{pn} \tag{6.6}$$

When all phases of the EMD are connected to the negative TVS pole (switch state $(0, 0, 0)$), the total capacitance from poles to chassis in the TVS swaps asymmetry.

The corresponding voltages when all phases of the EM winding are connected to the positive pole of the TVS are:

$$u_{pos} = \frac{U_{bat}}{2 + \frac{1}{X}} \tag{6.7}$$

$$u_{neg} = \frac{-U_{bat}\left(1 + \frac{1}{X}\right)}{2 + \frac{1}{X}} \tag{6.8}$$

The stationary CM voltage when all phases of the EM winding are connected to the positive pole of the TVS is:

$$u_{cm} = \frac{-U_{bat}}{2} \cdot \frac{1}{2X + 1} \tag{6.9}$$

The stationary CM voltage when all phases of the EM winding are connected to the negative pole of the TVS is:

$$u_{cm} = \frac{U_{bat}}{2} \cdot \frac{1}{2X + 1} \tag{6.10}$$

The CMDC voltage, illustrated for BP4_CM_Voltage in Figure 6.27, but also valid for EMD_Uout_CM and EMD_Uin_CM, is:

$$u_{CMDC} = \frac{U_{bat}}{2X + 1} \tag{6.11}$$

The CMDC voltage amplitude is illustrated for BP4_CM_Voltage in Figure 6.27 for two different X-values. For voltage definitions and references, see Figure 6.23. In the following graphs, the trace colour is blue for X=8.1 and orange for X=50.

For X=8.1, the CMDC voltage is 40.6 V. For X=50, the CMDC voltage is 6.9 V. See Figure 6.27.

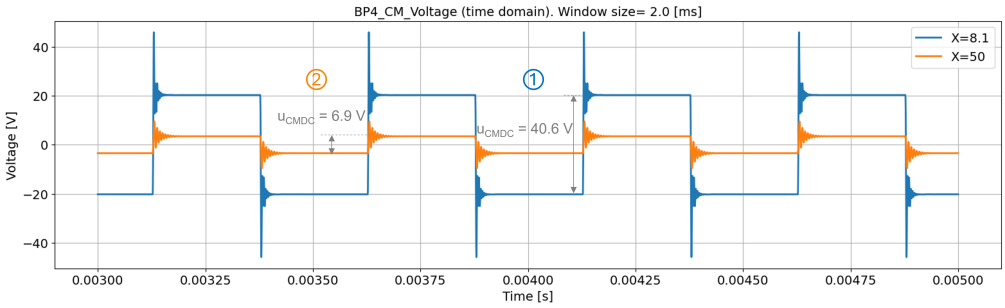


Figure 6.27: CMDC voltage caused by asymmetries where X=8.1, (1) in blue, and X=50 (2) in orange. The CMDC voltage decreased from 40.6 V to 6.9 V, which aligns with the theoretical value calculated using Equation (6.11). (U_{bat}=700 V).

Comparing the two simulations in Figure 6.27, the expanded view in Figure 6.28 shows that the peak of the ringing is substantially lower when the CMDC voltage is reduced at the battery. Since the battery should be protected from EMI, a proper relationship between the parasitic capacitance in the EM and the CM-capacitance in the EMD must be maintained. The blue graph corresponds to X=8.1 and the orange to X=50.

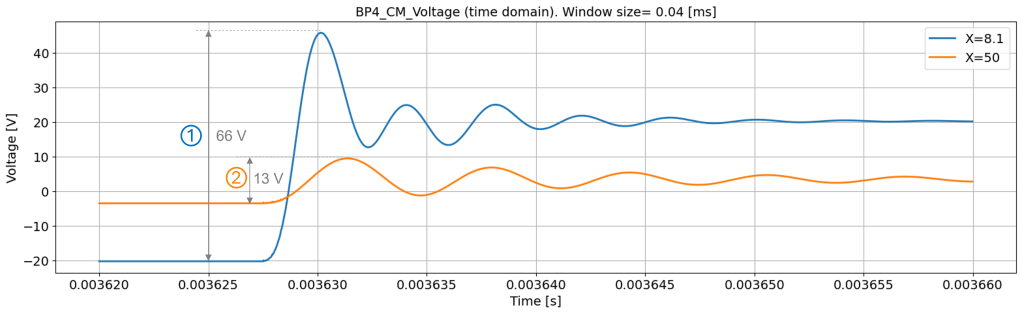


Figure 6.28: Voltage overshoot at the battery. The orange trace corresponds to X=50, obtained from a 16× increased CM-capacitance in the EMD or a 6× total increased CM-capacitance.

The rationale for increasing the CM-capacitance in the EMD rather than in the battery is that the CM current via the EM should return to the source as close as possible to its point of emission. That is, if the CM current leaves the EMD via the EM three-phase cable capacitance $C_{CM3phcable}$ and the EM winding-to-core capacitance C_{CMwind}, it should return to the EMD capacitances C_{CM+EMD} and $C_{CM\text{-}EMD}$. Increasing the CM-capacitance in the battery instead causes the CM current to travel a longer distance in the vehicle, which is from a few metres in a truck up to ten to fifteen metres in an articulated bus.

Based on these observations—reduced U_{CMDC} and reduced CM current—a rule of thumb for any EMD–EM combination is that the EMD CM-capacitance to chassis should be at least 50× higher than the CM-capacitance of the EM, three-phase cable, and IGBT together. This is valid for any type of TVS.

These findings are consistent with [15]. However, the maximum total CM-capacitance in the system is regulated by standards [13, 11], which limit the freedom to arbitrarily choose CM-capacitances. Without these limitations, the CM-capacitance in each converter could be easily adapted to meet the ratio of X=50. Designing commercial electric vehicles is therefore a trade-off to achieve an acceptable level of CMDC voltage and corresponding peak voltage.

Conclusion

This section has demonstrated how the CMDC voltage is governed by the ratio between symmetrical and asymmetrical CM-capacitances, expressed as the X-factor. A higher X-factor leads to a lower CMDC voltage and reduced voltage overshoot, which is essential for EMI mitigation.

The next section investigates the propagation of CM currents and how the physical placement of CM-capacitances influences current paths and system performance.

6.2.2 CM currents – importance of the position of CM capacitors and the X-factor

It is shown in Subsection 6.2.1 that a proper X-factor is essential to reduce the CMDC voltage. However, the distribution of CM-capacitances is equally important. Minimising ground and shield currents in the vehicle is critical, as CM currents should return to their source rather than propagate through other subsystems.

As demonstrated in Subsection 2.4.4 and Figure 2.22, the CM-capacitance should be placed close to the source. To clarify this concept, a refined naming convention for the X-factor is introduced.

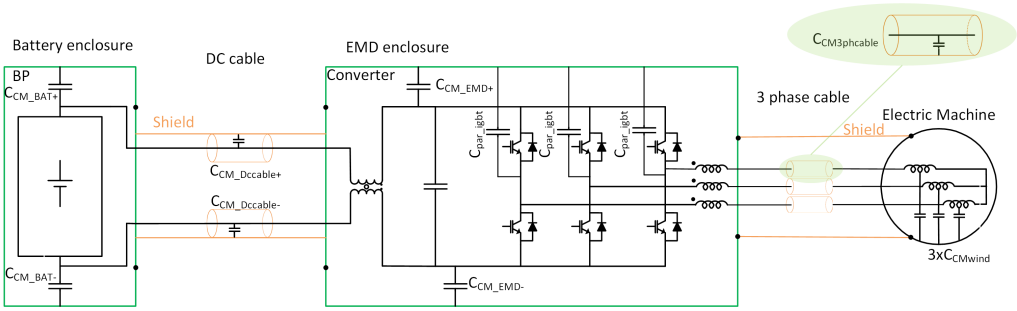


Figure 6.29: Circuit used to define the capacitances and X-factors.

X_{tot} Total X-factor for the complete system, previously referred to as the X-factor.

X_{EMD} X-factor within the EMD or another subsystem, defined as the ratio between parasitic capacitance and CM-capacitance.

For a symmetrical system, as illustrated in Figure 6.29, where $C_{CM_EMD+} = C_{CM_EMD-}$ and $C_{par} = 3\times C_{CMwind} + 3\times C_{par_igbt} + 3\times C_{CM3phcable}$, the subsystem X-factor is defined as:

$$X_{EMD} = \frac{C_{par}}{C_{CM_EMD+}} = \frac{C_{par}}{C_{CM_EMD-}} \tag{6.12}$$

For a symmetrical system where $C_{CM_tot+} = C_{CM_tot-}$, the total CM-capacitance is:

$$\begin{aligned} C_{CM_tot} &= C_{CM_BAT+} + C_{CM_EMD+} + C_{CM_DCcable+} \\ &= C_{CM_BAT-} + C_{CM_EMD-} + C_{CM_DCcable-} \end{aligned} \tag{6.13}$$

The total X-factor becomes:

$$X_{tot} = \frac{C_{par}}{C_{CM_tot+}} = \frac{C_{par}}{C_{CM_tot-}} \tag{6.14}$$

In Figures 6.30 and 6.31, simulations of the model in Figure 6.29 are shown with identical X_{tot}=50, but with different distributions resulting in X_{EMD}=45 and 2.7, respectively.

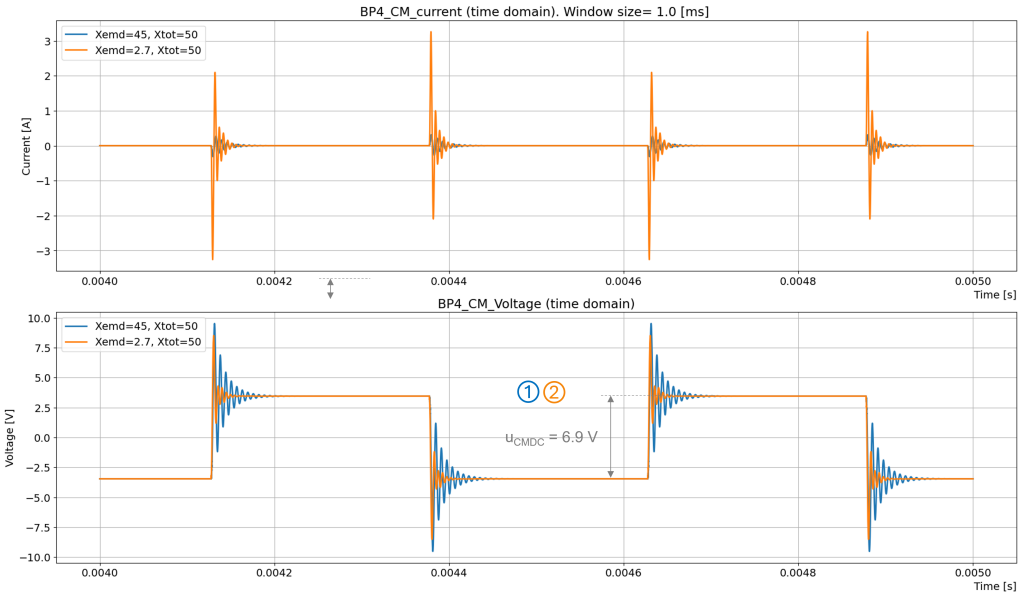


Figure 6.30: In the lower graph, U_{CMDC} remains constant as long as X_{tot} is unchanged. In the upper graph, the battery current is lower when X_{EMD} is higher. A zoomed view is shown in Figure 6.31.

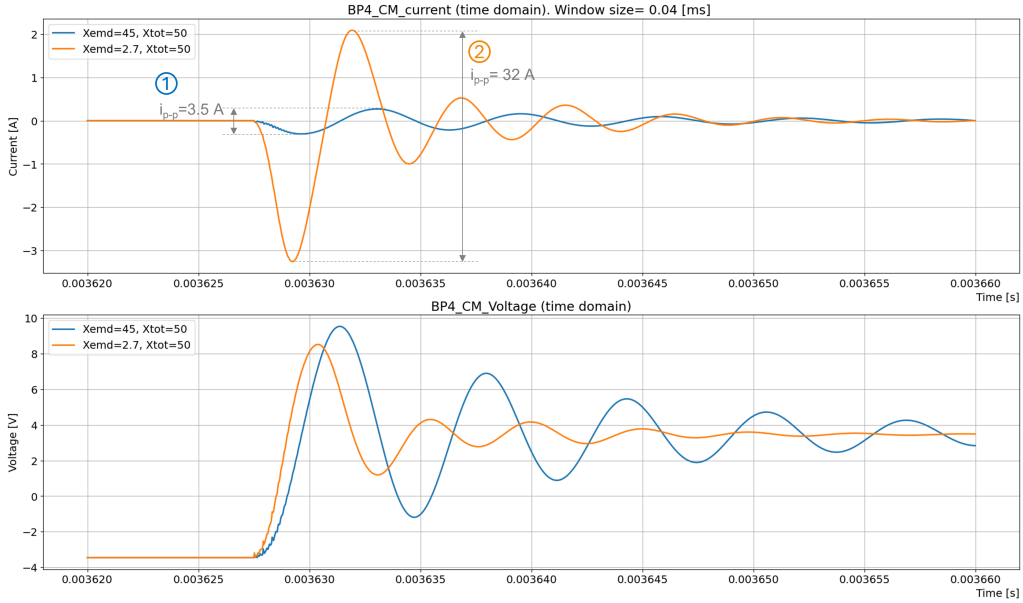


Figure 6.31: Zoomed view of battery current. The peak-to-peak current (i_{p-p}) is significantly lower when X_{EMD} is higher.

It is shown in Figure 6.30 that U_{CMDC} remains the same for both simulations. However, the CM current from the battery is notably higher when X_{EMD}=2.7 compared to X_{EMD}=45.

Conclusion

As concluded in Subsection 6.2.1, the EMD CM-capacitance to chassis should be at least 50× higher than the CM-capacitance of the EM. This subsection adds an important clarification: the X-factor is refined into X_{EMD} and X_{tot} to distinguish between subsystem-level and system-level design.

The results show that even with a constant X_{tot}, the distribution of CM-capacitance significantly affects CM current paths. A high X_{EMD} ensures that CM currents return locally within the EMD, reducing unwanted current flow through the battery and other subsystems. This insight is critical for EMI mitigation and robust system design.

In Subsection 6.2.3, measurements show that delayed switching between phase legs reduces CM currents and voltages on both the AC and DC sides of the EMD. The next subsection builds on this by simulating the same effect in a simplified system.

6.2.3 Delayed switching to and from $(0, 0, 0)$ and $(1, 1, 1)$

The delayed switching method, relevant to common-mode (CM) current reduction in electric drive systems, is published in [32].

In Subsection 6.2.3, measurements show that a delay in switching between phase legs reduces the CM current and voltage on the AC side of the EMD, as well as the CM current

on the DC side. Simulations are performed in this subsection using a simplified system, illustrated in Figures 6.24 and 6.29.

The CMDC voltage remains unchanged if the switching is performed with a delay between phase legs. The CMDC voltage remains stationary after the switching is complete. However, the transient CM voltage and current are affected by the delay, as the asymmetric capacitances are charged or discharged sequentially, resulting in lower peak currents.

Three scenarios are analysed for the transition between $(0, 0, 0)$ and $(1, 1, 1)$, see Figure 6.32:

1. Simultaneous switching: direct transition from $(1, 1, 1)$ to $(0, 0, 0)$, corresponding to A $\rightarrow$ D or vice versa in Figure 6.32.
2. Switching with a delay of 0.4 µs between phase legs. Transition from $(1, 1, 1)$ to $(0, 0, 0)$, corresponding to A $\rightarrow$ B $\rightarrow$ C $\rightarrow$ D or vice versa.
3. Switching with a delay of 1 µs between phase legs in the same transition pattern A $\rightarrow$ B $\rightarrow$ C $\rightarrow$ D.

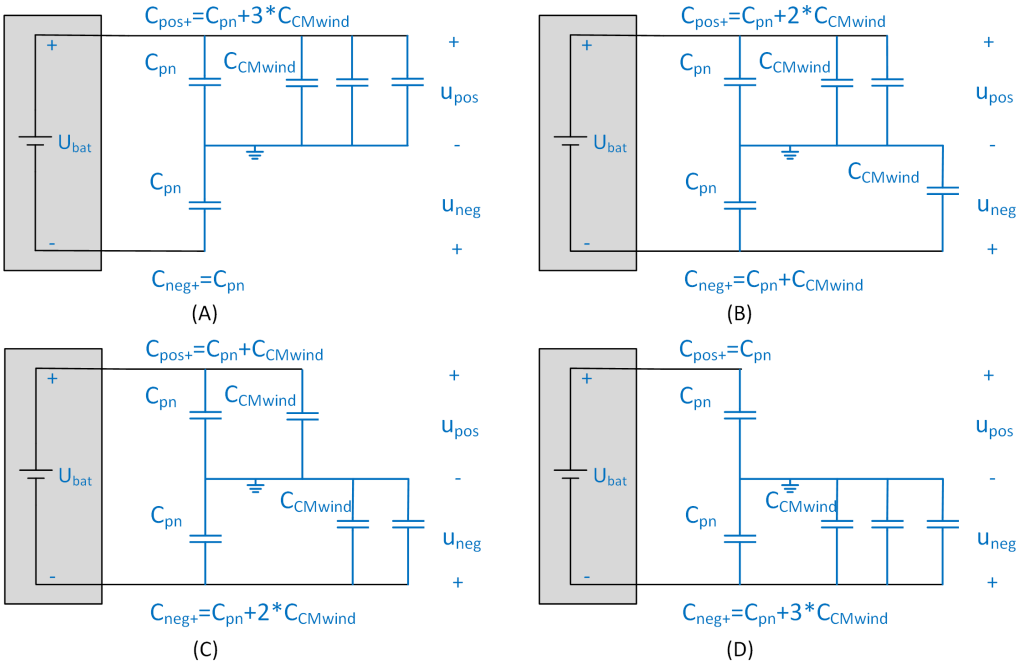


Figure 6.32: Equivalent circuit diagram for the CM-capacitances: (A) C_{asym} is asymmetric to the positive TVS pole (1,1,1), (B) partly asymmetric (1,1,0), (C) partly asymmetric to the negative pole (1,0,0), and (D) fully asymmetric to the negative pole (0,0,0).

In the first scenario, the asymmetric capacitance is $C_{asym} = 3\times C_{CMwind}$. In the second and third scenarios, $C_{asym} = 1\times C_{CMwind}$, as only one phase leg switches at a time. In

Figure 6.33, top graph, the U_{CMDC} voltage for BP4_CM_Voltage remains the same across all three switching delays.

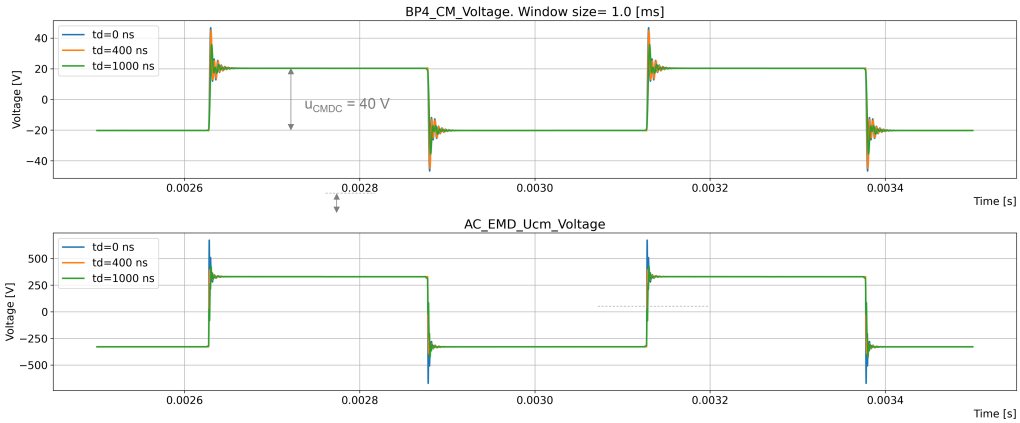


Figure 6.33: Common-mode voltage, U_{cm}, for the three scenarios for both BP4_CM_Voltage and AC_EMD_Ucm_Voltage, where t_d=0 µs, t_d=0.4 µs, and t_d=1 µs.

The peak values in Figure 6.34 show that the common-mode peak voltage on the DC side decreases when a time delay t_d is introduced between phase-leg switching. The same effect is observed on the AC side. The lower graph in Figure 6.34 illustrates the delay: the first switch occurs at mark (1), the second at (2), and the final switch at (3). At each step, one additional $C_{asym} = 1 \times C_{CMwind}$ changes position, resulting in a staircase-like transition.

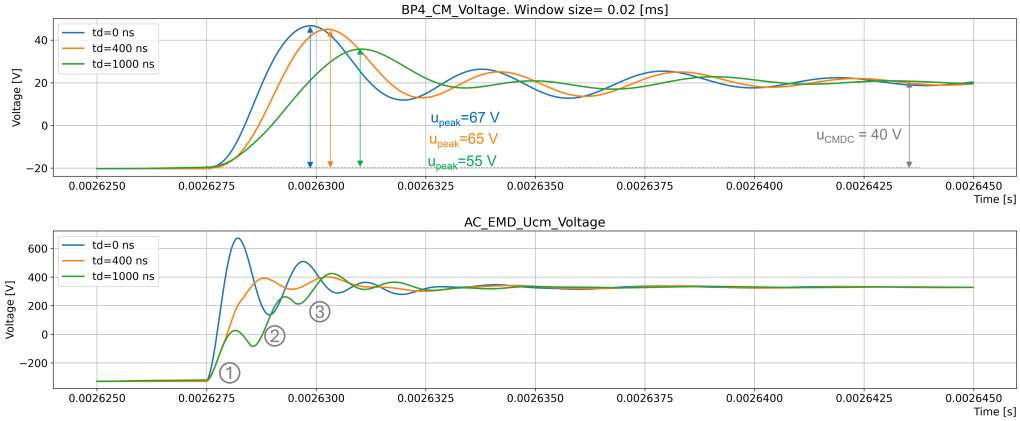


Figure 6.34: Zoomed view of the common-mode voltage at the battery (DC side) and the common-mode voltage on the AC side, derived from the three phase-to-chassis voltages, for the three scenarios: t_d=0 µs, t_d=0.4 µs, and t_d=1 µs. The common-mode peak voltage decreases on both the DC and AC sides.

The AC phase-to-chassis voltages, the AC common-mode voltage, the AC common-mode current, and the DC common-mode current, evaluated over the same time span as

in Figures 6.33 and 6.34, are shown in Figure 6.35. The three-phase AC common-mode voltage is defined as:

$$u_{cm} = \frac{u_u + u_v + u_w}{3} \tag{6.15}$$

Signal naming follows the schematics in Figures 6.24 and 6.29.

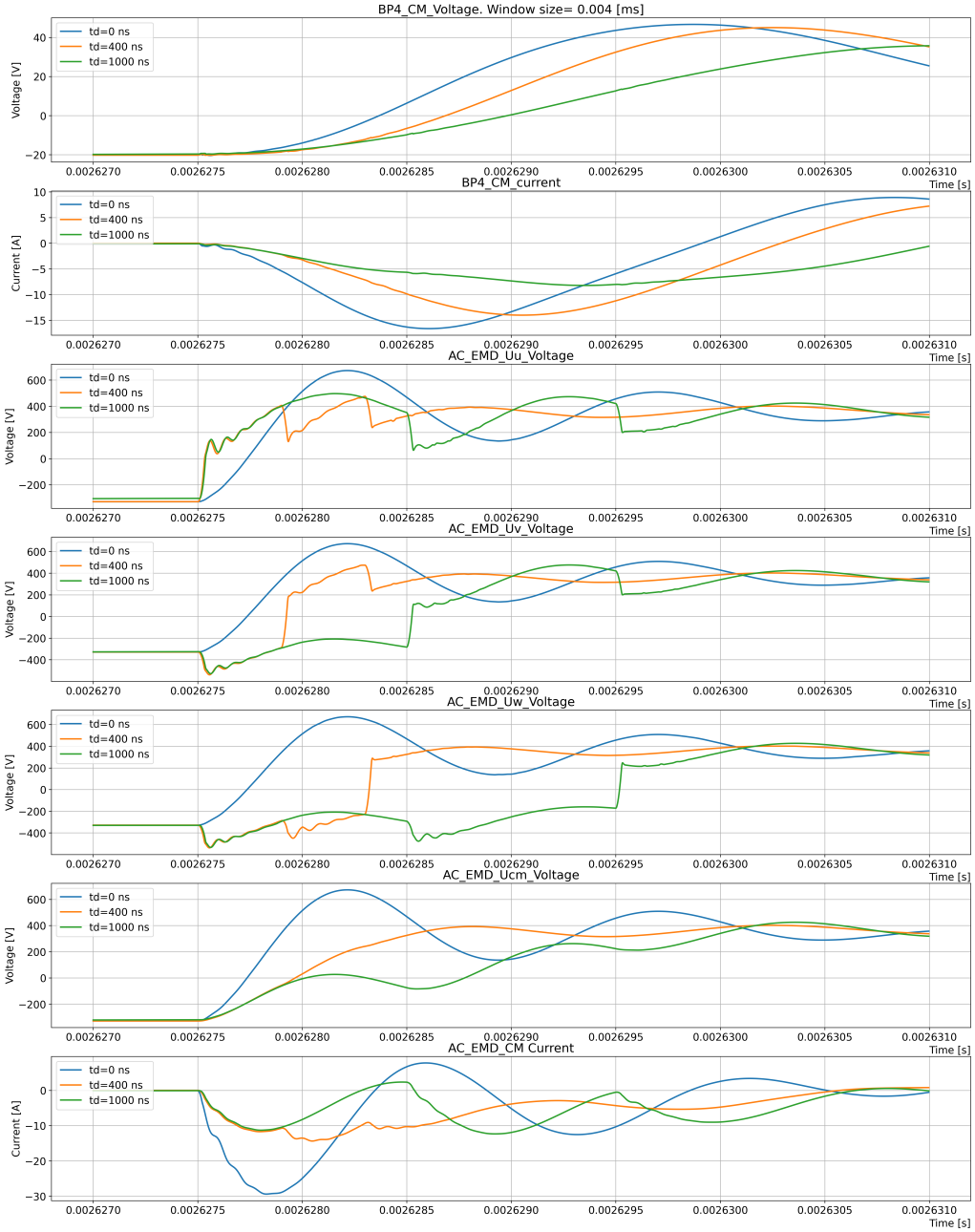


Figure 6.35: Zoomed view of the time span from Figure 6.33 with additional graphs, for the three scenarios where t_d=0 µs, t_d=0.4 µs, and t_d=1 µs. The third to fifth graphs show the phase voltages AC_EMD_Uu_Voltage, AC_EMD_Uv_Voltage, and AC_EMD_Uw_Voltage. The sixth graph shows the common-mode voltage on the AC side. The lowest graph shows that the AC_EMD_CM_Current peak value decreases with increased time delay.

- The CM peak voltage on the DC side, BP4_CM_Voltage, decreases with increased delay between the switching of the phase legs.
- The CM peak current on the DC side, BP4_CM_Current, decreases with increased delay between the switching of the phase legs.
- The phase voltages AC_EMD_Uu_Voltage, AC_EMD_Uv_Voltage, and AC_EMD_Uw_Voltage increase in a step-wise manner as each phase leg is switched.
- The CM three-phase voltage AC_EMD_Ucm_Voltage decreases with increased delay between the switching of the phase legs.
- The CM three-phase peak current AC_EMD_CM_Current decreases with increased delay between the switching of the phase legs.

Conclusion

The simulation results demonstrate that delayed switching between phase legs effectively reduces common-mode disturbances in electric drive systems. As the delay t_d increases, both the common-mode voltage and current on the DC and AC sides decrease. The phase voltages transition in a step-wise manner as each leg is switched sequentially, confirming that sequential switching reduces peak charging and discharging of the asymmetric capacitances. Delayed switching is therefore shown to be a practical method for mitigating transient effects and improving electromagnetic compatibility. The transition from $(1, 1, 1)$ to $(0, 0, 0)$, or vice versa, occurs mainly during standstill and zero output voltage. The impact on current control is left for future investigation.

6.2.4 Comparison between delayed switching and impact of X-factor

A comparison of the effects of delayed switching and the X-factor is presented in Figure 6.36 for the three-phase and DC-side properties.

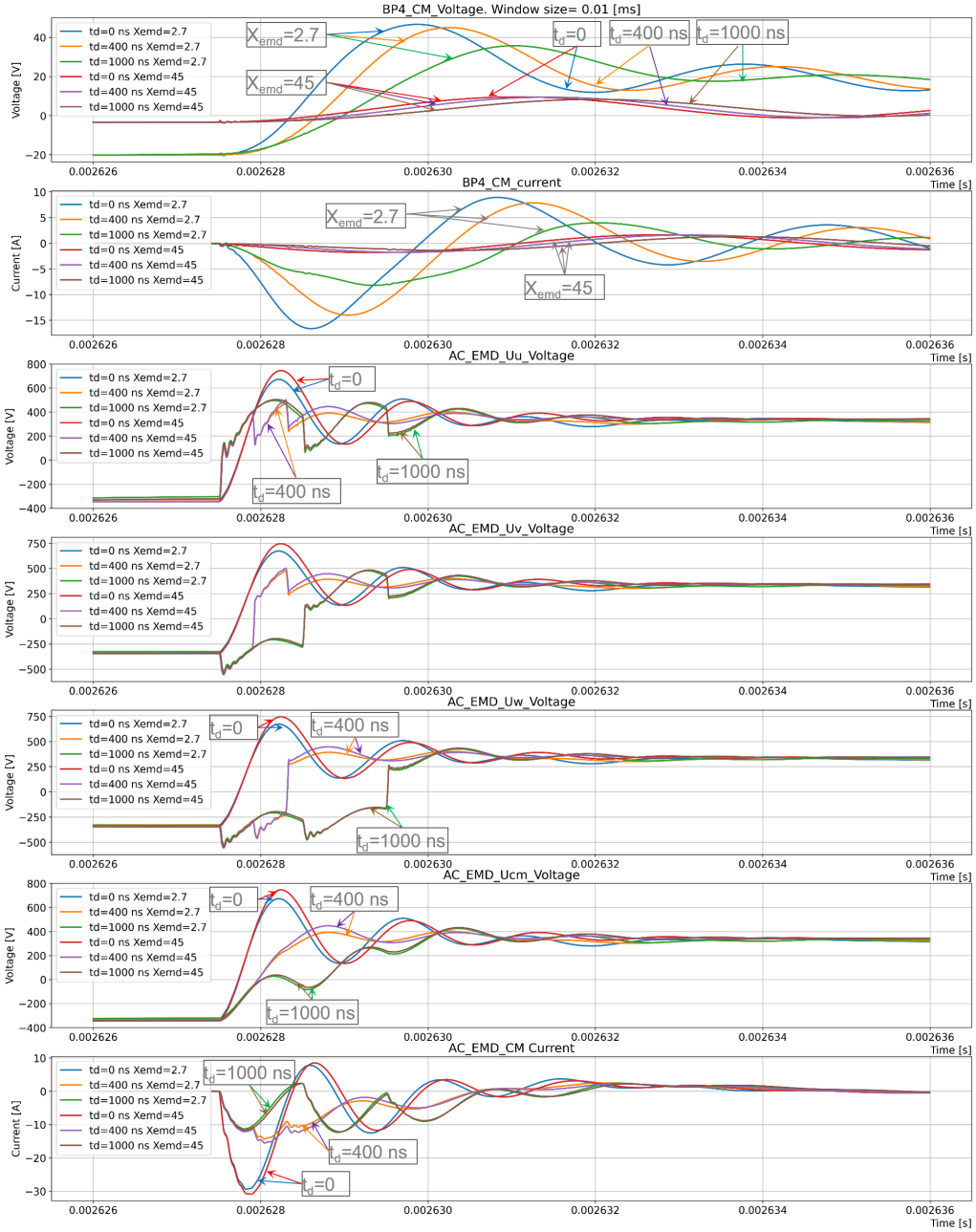


Figure 6.36: Comparison of changed X-factor and delayed switching for DC- and AC-side signals. The DC graphs show BP4_CM_Voltage and BP4_CM_Current for X_{EMD} = 2.72 and X_{EMD} = 50, with switching delays t_d = 0 µs, 0.4 µs, and 1 µs. The effect of increased X-factor is clearly noticeable, while the effect of delayed switching is present but less dominant. The AC graphs show AC_EMD_Uu_Voltage, AC_EMD_Uv_Voltage, AC_EMD_Uw_Voltage, AC_EMD_Ucm_Voltage, and AC_EMD_CM_Current for the same conditions. Here, the effect of delayed switching is more pronounced, while the impact of increased X-factor is minor.

Conclusion

The results show that, on the three-phase side, the effect of delayed switching is substantial, whereas the impact of changing the X-factor is minor. Conversely, on the DC side, the effect of delayed switching is relatively insignificant compared to the influence of the X-factor.

A combination of a properly selected X-factor and delayed switching enables improvements in both DC- and AC-side behaviour. Reducing the magnitudes and derivatives of the common-mode current and voltage is beneficial from an electromagnetic interference (EMI) perspective.

6.2.5 Conclusion

This chapter explores how common-mode (CM) disturbances in electric drive systems can be mitigated through strategic design of CM-capacitances and switching behaviour. The CMDC voltage is shown to be governed by the ratio between symmetrical and asymmetrical CM-capacitances, expressed as the X-factor. A higher X-factor reduces CMDC voltage and overshoot, which is essential for EMI mitigation.

The X-factor is further refined into X_{EMD} and X_{tot}, enabling a clear distinction between subsystem-level and system-level design. Even with a constant X_{tot}, the distribution of CM-capacitance significantly affects current paths. A high X_{EMD} ensures local current return within the EMD, thereby reducing interference in other subsystems.

Simulations confirm that delayed switching between phase legs reduces both CM voltage and CM current on the DC and AC sides. The step-wise transition of phase voltages, resulting from sequential switching, lowers peak values and derivatives of CM quantities. This behaviour is beneficial from an EMI perspective.

Finally, the combined effect of a properly selected X-factor and delayed switching enables improvements in both DC and AC properties. While the X-factor dominates the CM behaviour on the DC side, delayed switching has a greater impact on the AC side. Together, these methods provide a robust strategy for reducing CM disturbances and improving electromagnetic compatibility in electric drive systems. To further investigate how specific subsystems influence the overall CM behaviour, the next section analyses a reduced vehicle model in which auxiliary systems are removed while key electrical interfaces are preserved.

6.3 Common Mode Simulations of Full and Reduced Vehicle Models

As described in the introductory text of Chapter 6, the full vehicle model comprises several interacting subsystems represented with a high level of detail. While this level of fidelity is necessary to capture local high-frequency effects, it also results in excessive simulation times

and, in some cases, numerical infeasibility when analysing common-mode (CM) behaviour at system level.

To analyse CM behaviour efficiently, the complexity of the full vehicle CM model must therefore be carefully evaluated and, where possible, reduced without losing the dominant physical mechanisms. The purpose of reducing the full vehicle model is to shorten simulation time and ensure that the model can be solved in PLECS, while still preserving the relevant CM characteristics. This introduces an inherent trade-off between modelling the complete system with full detail and maintaining sufficient resolution of the phenomena of interest.

In this section, the full vehicle CM model is progressively reduced and compared against simplified representations. The comparisons aim to identify which subsystems and modelling details have a significant influence on CM behaviour and which can be simplified or omitted without compromising the validity of the results.

The remainder of this section is structured as follows:

Subsection 6.3.1 Compares CM simulations of the complete vehicle using the full model and selected reduced representations, quantifying the impact of model reduction on both CM behaviour and simulation time.

Subsection 6.3.2 Investigates CM behaviour for a reduced subset of the vehicle, enabling higher-frequency resolution and providing insight into how local subsystems contribute to the overall CM response.

Subsection 6.3.3 Summarises the findings and identifies which levels of model reduction are acceptable for system-level CM analysis.

6.3.1 Common-mode simulation of complete vehicle with full and reduced models

In Figure 6.37, the vehicle model is shown with Break Out Boxes (BoB) for measurements.

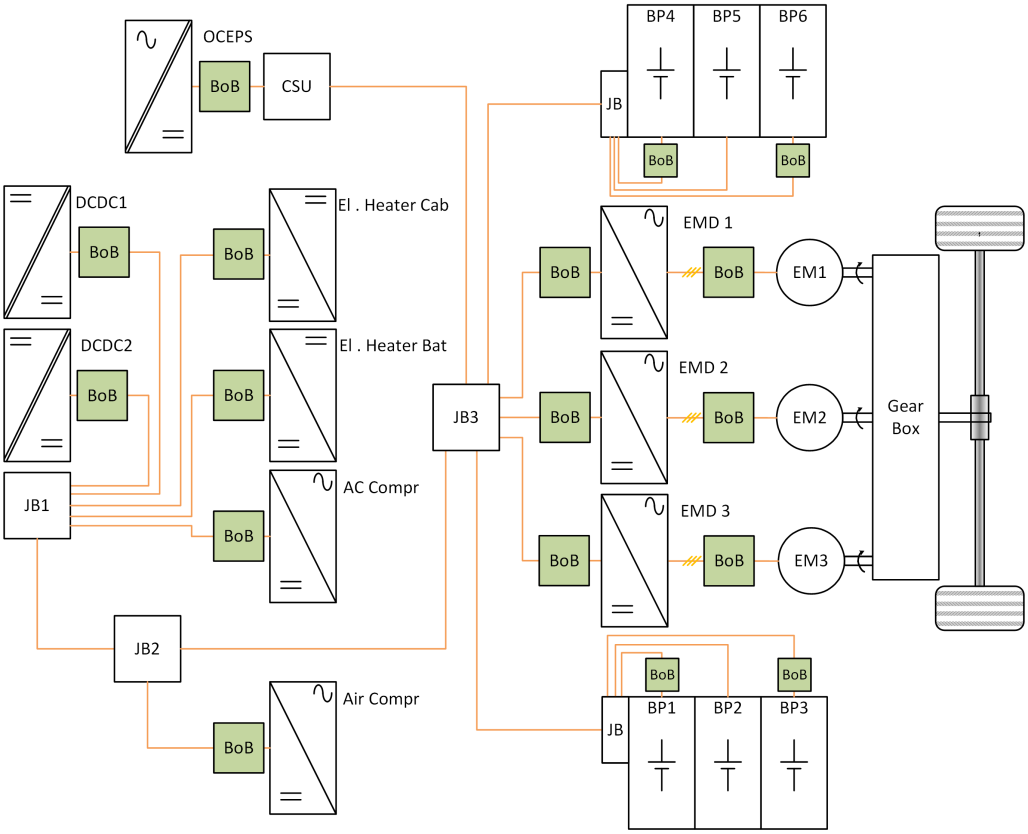


Figure 6.37: The vehicle FM1156 with Break Out Boxes (BoB) for measurements.

In each DC BoB, the following signals are simulated:

$\mathbf{I_{cm}}$ True common-mode current, as described in Subsection 3.3.1.

$\mathbf{U_{cm}}$ Common-mode voltage.

In each AC BoB, the following signals are simulated:

$\mathbf{I_{cm}}$ True common-mode current, as described in Subsection 3.3.1.

$\mathbf{U_{cm}}$ Common-mode voltage.

$\mathbf{U_{phase_ground}}$ Phase-to-ground voltages, e.g. U_{u_ground}, U_{v_ground}, and U_{w_ground}.

In the simulations, all three EMDs operate. Due to the high-resolution EMD model with non-ideal IGBTs (model a) in Figure 6.3, only EMD1 and EMD2 use non-ideal IGBTs. EMD3 uses an ideal IGBT model (model d). Comparisons of switching events are

made only for EMD1 and EMD2. The parasitic capacitances in EMD3 are identical to those in EMD1 and EMD2.

From the start, the impedance in the JB and BoB is merged into the cable model, as described in Subsection 6.1.3.

The following models are simulated:

Model A Full model including BoB, see Figure 6.37.

Model B As Model A, with 3-phase cables removed.

Model C As Model B, with the cable to the OCEPS merged with the cable between CSU and JB3.

Model D As Model C, with the cable between JB1 and JB2 merged with cables to DCDC1, DCDC2, AC compressor, El. Heater Cab, and El. Heater Bat.

Model E As Model D, but with all BoBs and corresponding extra cable impedances removed. This shows the system without measurement disturbance.

Only a few changes between Models A–E affect the simulation results. Models A–D give identical results, while Model E differs slightly. The differences are:

$\mathbf{U}_{\mathbf{cm_EMD1}}$ Lower magnitude and slightly slower frequency.

$\mathbf{U}_{\mathbf{cm_BP4}}$ and other U_{cm} signals (except U_{cm_EMD1}): slightly slower frequency, 284 kHz vs. 292 kHz.

$\mathbf{I}_{\mathbf{cm_Air_Compr}}$ Increased magnitude of high-frequency oscillations (10 MHz).

All simulations are performed for time spans of 1 ms, 100 µs (zoom area Z1), and 10 µs (zoom area Z2). Parameters that differ between models are shown below. All other graphs are presented in Section C.1.

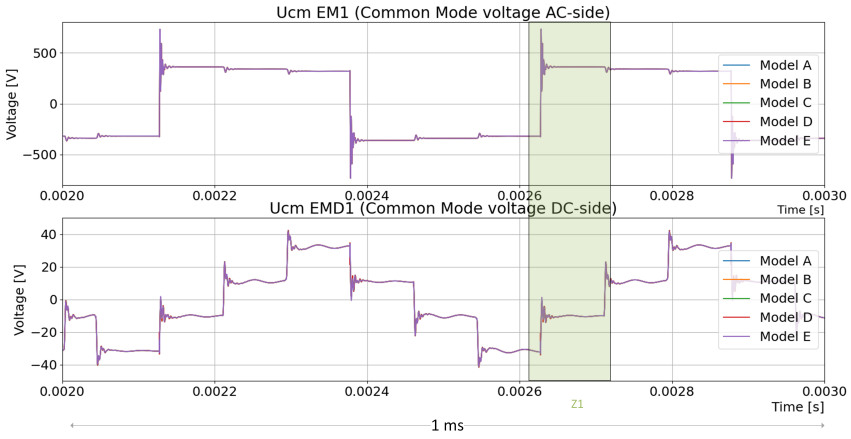


Figure 6.38: Common-mode voltage at EM1 (AC side) and EMD1 (DC side). This figure shows the full simulation time span. The green area marked Z1 indicates the zoomed-in region shown in Fig. Figure 6.39.

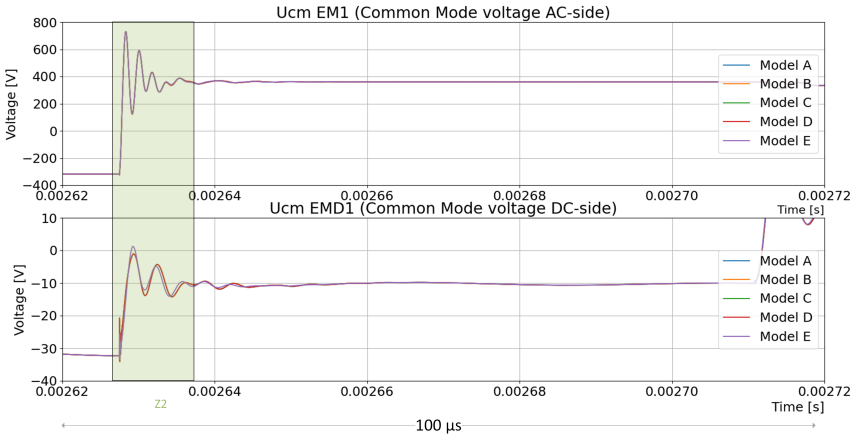


Figure 6.39: Common-mode voltage at EM1 (AC side) and EMD1 (DC side). This figure shows the zoomed-in time span Z1. The green area marked Z2 indicates the next zoom level shown in Fig. Figure 6.40.

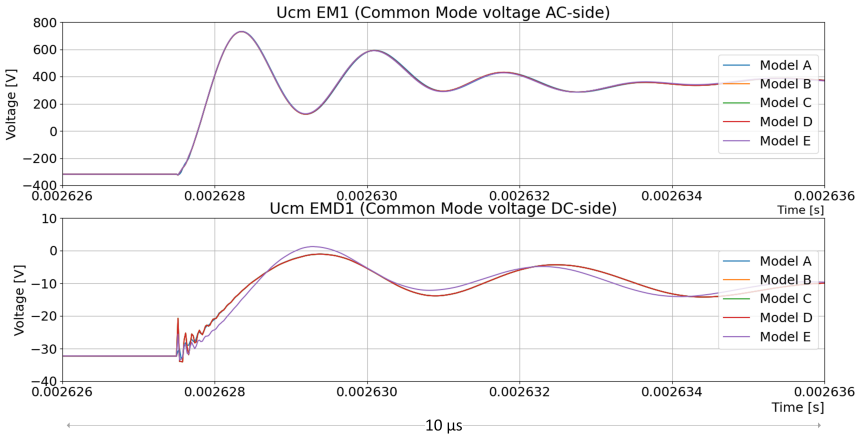


Figure 6.40: Common-mode voltage at EM1 (AC side) and EMD1 (DC side). This figure shows the zoomed-in time span Z2, which is the smallest time span used in the simulations.

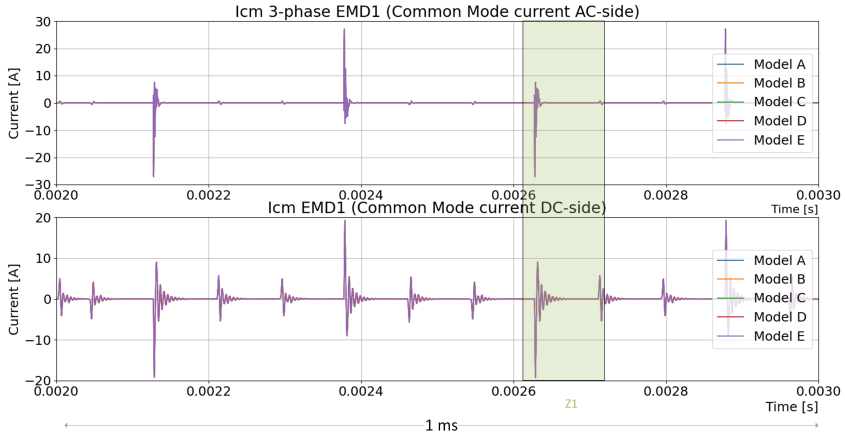


Figure 6.41: Common-mode current at EM1 (AC side) and EMD1 (DC side). This figure shows the full simulation time span. The green area marked Z1 indicates the zoomed-in region shown in Fig. Figure 6.42.

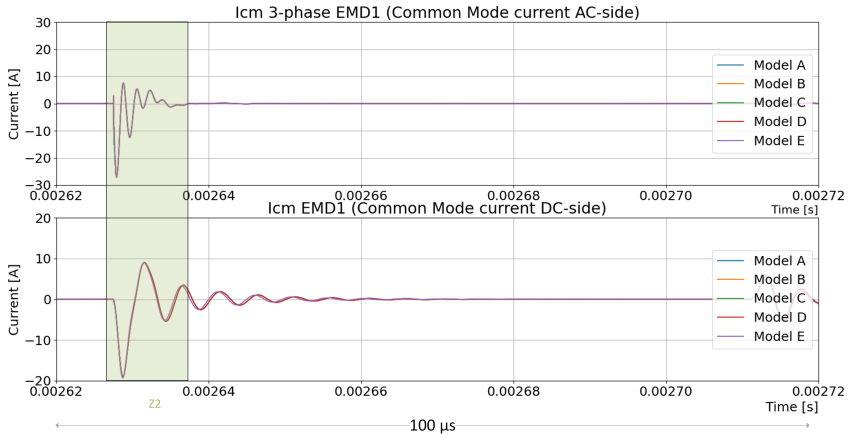


Figure 6.42: Common-mode current at EM1 (AC side) and EMD1 (DC side). This figure shows the zoomed-in time span Z1. The green area marked Z2 indicates the next zoom level shown in Fig. Figure 6.43.

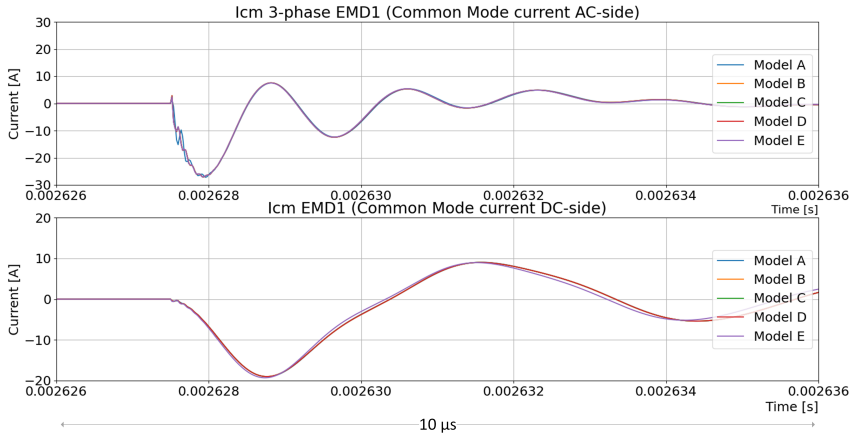


Figure 6.43: Common-mode current at EM1 (AC side) and EMD1 (DC side). This figure shows the zoomed-in time span Z2, which is the smallest time span used in the simulations.

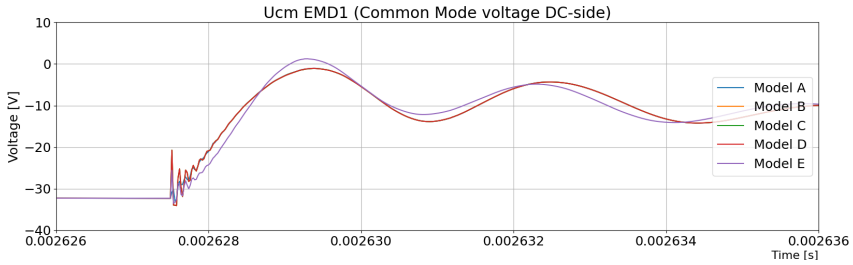


Figure 6.44: Common-mode voltage at EMD1 (DC side). The voltage is higher for Model E than for Models A–D. This figure shows the zoomed-in time span Z2.

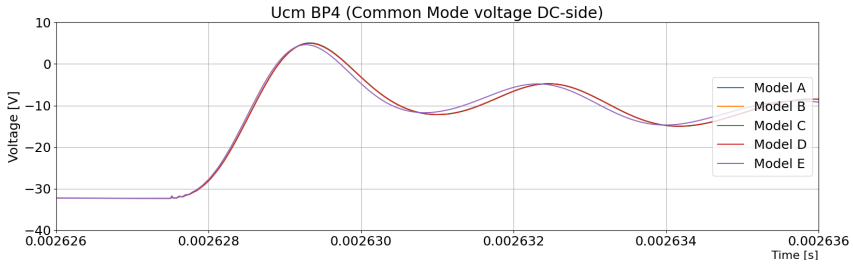


Figure 6.45: Common-mode voltage at BP4 (DC side). This figure shows the zoomed-in time span Z2.

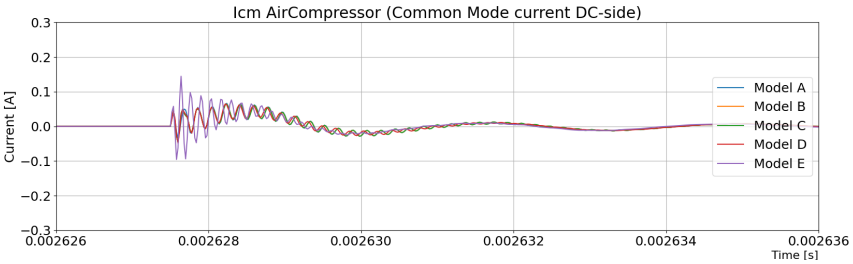


Figure 6.46: Common-mode current to the air compressor (DC side). The current increases by 250% between Models A–D and Model E. This figure shows the zoomed-in time span Z2.

Conclusion

The simulations show that removing measurement equipment such as Break Out Boxes (BoB) affects common-mode behaviour. Model E, which excludes BoBs, exhibits higher common-mode voltage at EMD1 and increased high-frequency oscillations in the current to the air compressor. These effects are caused by increased inductance in the return path and reduced damping before the pole-to-chassis capacitances. The results highlight that measurement setups can significantly influence observed EMI behaviour and must be considered when interpreting simulation data. While the simulations of the complete vehicle

provide valuable insights into the overall common-mode (CM) behaviour, it is also important to analyse how individual parts of the vehicle contribute to this behaviour. To achieve this, selected subsystems are simulated separately, with auxiliary components removed, to evaluate the impact on CM voltage and current paths. This approach significantly reduces simulation time while preserving the essential electromagnetic characteristics of the full model.

6.3.2 Common-mode simulation of part of the vehicle with full and reduced models

Following the analysis of the complete vehicle, this section focuses on a reduced model where all auxiliary systems are removed. The purpose is to investigate whether a simplified representation of the powertrain—consisting mainly of batteries, electric machines (EM), and electric motor drives (EMD)—can reproduce the essential CM behaviour while significantly reducing simulation time.

In Figure 6.47, the reduced vehicle model is shown with all auxiliaries removed and Break Out Boxes (BoB) included for measurements. In this configuration, EMD1 and BP4 are the primary source and sink for the common-mode (CM) current, as EMD1 is the main disturbance source and BP4 has the largest pole-to-chassis capacitance.

Note: The capacitance is sometimes referred to as Y-capacitance in the battery, but the dominant capacitance is parasitic. Y-capacitance is a protective capacitance and should not be confused with parasitic capacitance.

The simulated parameters that differ between the models are listed below. All other graphs are presented in Appendix C.2.

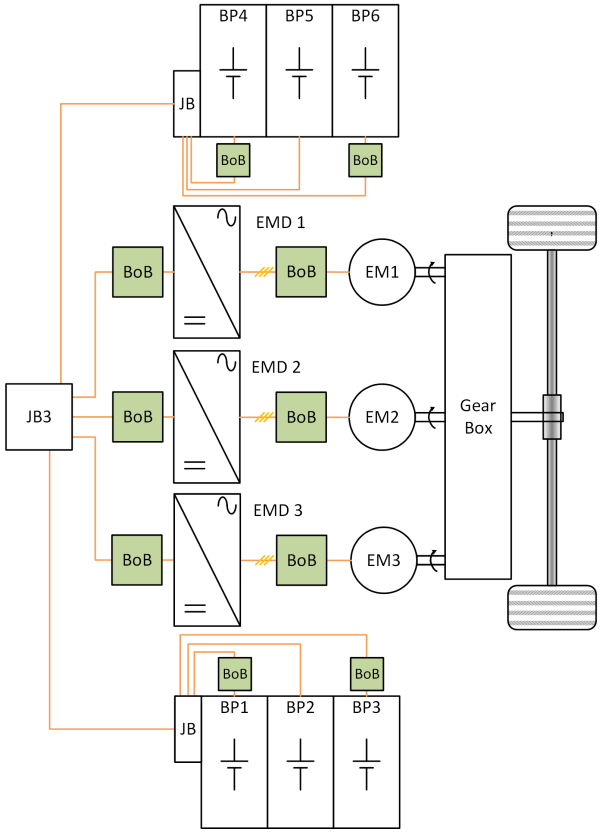


Figure 6.47: The vehicle FM1156 with all auxiliaries removed and break out boxes for measurements.

The following simulations and simplifications of the model are performed:

Model A Full model, including BoB, according to Figure 6.37.

Model I Based on Model E, with all auxiliaries removed, see Figure 6.47.

Model J Based on Model A, including BoB, but with all auxiliaries removed, see Figure 6.47.

Model K Based on Model J, but without 3-phase cables or cables between JB and batteries.

Model L Based on Model K, but without cables between JB3 and JB.

Model A is retained as a reference for the reduced vehicle model without auxiliaries.

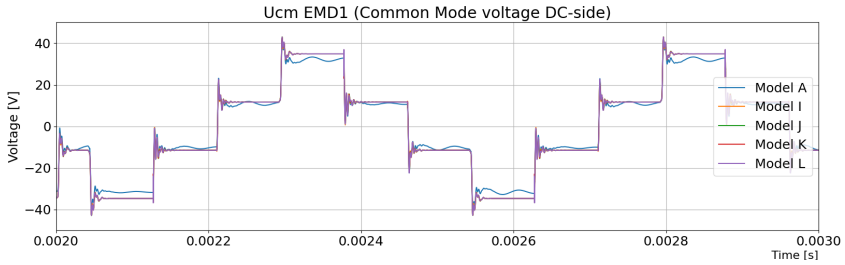


Figure 6.48: Common-mode voltage at EMD1 (DC side). It is observed that U_{cm} is higher for Model A than for Models I–L.

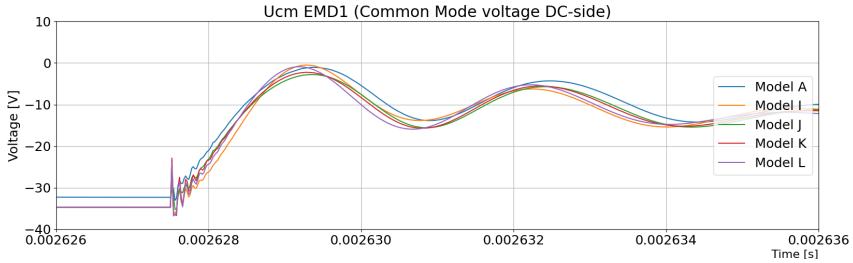


Figure 6.49: Common-mode voltage at EMD1 (DC side) during the Z2 time span. It is observed that U_{cm} is higher for Model A than for Models I–L.

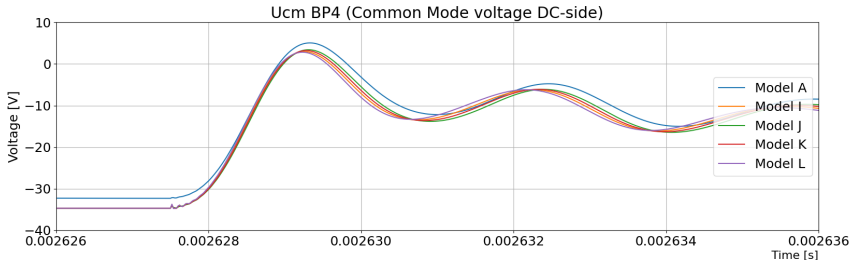


Figure 6.50: Common-mode voltage at BP4 (DC side) during the Z2 time span.

Only a few of the changes between Models A, I, J, K, and L affect the simulations. Model A differs because the total capacitance from pole to chassis is higher. This total capacitance is a combination of Y-capacitances and parasitic capacitances.

U_{cm_EMD1} An offset in U_{cm} due to the higher total capacitance from pole to chassis. A low-frequency ringing around 20 kHz is also observed in Model A, see Figure 6.48, which does not appear in models without auxiliaries (e.g. Model M9).

U_{cm_BP4} Other U_{cm} signals exhibit behaviour similar to that observed at EMD1.

The ringing at 20 kHz is identified as a common-mode resonance frequency in both DCDC1 and the AC compressor. If both components are removed, the ringing disappears, as shown in Model M9 in Figure 6.51.

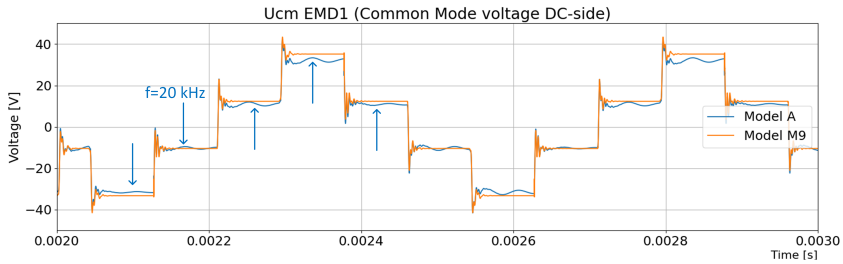


Figure 6.51: Common-mode voltage at EMD1 (DC side). If DCDC1 and the AC compressor are removed (Model M9), the ringing observed in models with auxiliaries disappears. The ringing is marked with blue arrows.

Conclusion

The simulations validate the theory described in Subsection 2.4.4. The introduced factor X highlights the importance of the ratio between CM capacitances and asymmetrical parasitic capacitances in determining the common-mode DC voltage level.

The results further show that the presence and location of CM-related capacitances in auxiliary subsystems influence the observed common-mode voltage behaviour and associated resonances in the vehicle. When subsystems such as the DCDC converter and the AC compressor are removed, the low-frequency ringing observed in the full model disappears, indicating that these components contribute to the overall CM resonance characteristics.

The reduced vehicle model can therefore be used to analyse dominant CM voltage behaviour and resonance phenomena with significantly reduced simulation time. While exact numerical values are not expected from the simulations, the model is well suited for identifying critical behaviours and resonances at an early design stage, enabling corrective actions before prototype vehicles are built.

6.3.3 Conclusion

The simulations demonstrate two key insights into common-mode behaviour in vehicle systems. First, the presence or absence of measurement equipment, such as Break Out Boxes (BoB), significantly influences the observed electromagnetic interference (EMI) characteristics. Model E, which excludes BoBs, shows elevated common-mode voltage at EMD1 and increased high-frequency oscillations in the current to the air compressor. These effects are attributed to increased inductance in the return path and reduced damping prior to the pole-to-chassis capacitances. This highlights the importance of accounting for measurement setups when interpreting simulation results.

Second, the simulations validate the theoretical framework described in Subsection 2.4.4. The introduced factor X illustrates the critical role of the ratio between common-mode capacitances and asymmetrical parasitic capacitances in determining the common-mode DC voltage level. In addition, the distribution of CM-related capacitances within the vehicle is shown to influence the observed common-mode voltage behaviour and associated resonance phenomena.

It should also be emphasised that the simulation of complete vehicle systems is not merely a matter of model construction. It requires a combination of theoretical understanding and practical experience in power electronics. Without this foundation, there is a risk of misinterpreting results or overlooking key behaviours. The model presented here is intended to support engineers with expertise in both simulation and measurement, enabling early identification and resolution of unwanted effects before prototype vehicles are built.

6.4 Differential-mode simulations

This section focuses on the modelling and calibration of the simulation models for the traction voltage system (TVS). The measurements and simulations are based on a commercial truck's TVS, as illustrated in Figure 6.1.

Following the validated simplifications and findings from the common-mode analysis in Section 6.2, the purpose of the DM simulations is to verify that subsystems within the TVS do not introduce unacceptable levels of conducted electromagnetic interference (EMI). Such interference may cause functional disturbances or reduce the lifespan of components. This section focuses on differential-mode (DM) disturbances. A related article is published in [31].

The remainder of this section is structured as follows:

Subsection 6.4.1 Describes how the full CM+DM subsystem models are reduced to DM-only models while preserving key impedance characteristics.

Subsection 6.4.2 Presents the system-level DM simulation model and explains the hybrid modelling approach combining ideal and non-ideal converter representations.

Subsection 6.4.3 Summarises the complete findings from the differential-mode modelling, subsystem reductions, system-level simulations, and validation against measurements. This section also defines the final DM reference model used in subsequent chapters.

6.4.1 Subsystem simplification for DM simulation in PLECS

Subsystem reduction of the vehicle model in Figure 6.1, following the approach in Chapter 5, includes both DM and CM parameters such as series resistance of inductors, cable induct-

ance, and the capacitance between the TVS and the chassis. This results in a complete state-space matrix of size 29×29. To model both CM and DM behaviour, the system can be reduced to 14×14 while preserving impedance characteristics within the relevant frequency range. For DM-only modelling, a further reduction to 4×4 is possible. The principle of reduction from a full CM model to a DM model is illustrated in Figure 6.52.

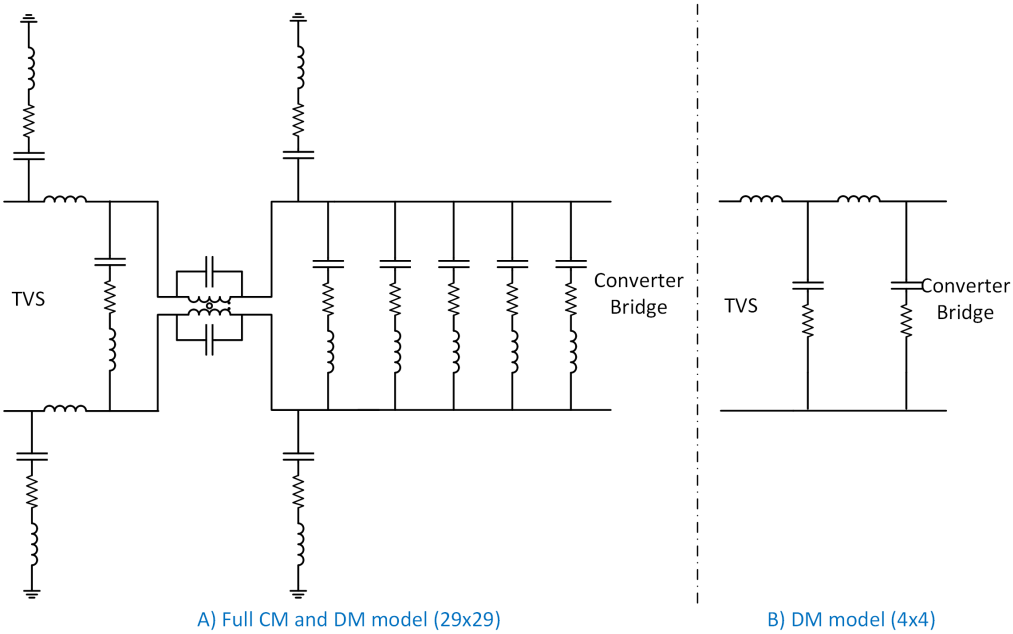


Figure 6.52: Principle of model reduction from a full common-mode (CM) and differential-mode (DM) representation (A) to a differential-mode (DM) model (B). The reduction is performed by removing all CM capacitances to chassis and combining the five DC-link capacitors into a single equivalent capacitance. Series inductances associated with the DC link are omitted, as their influence appears above the frequency range of interest for DM simulations.

Figure 6.53 compares the three models (29×29,14×14 and 4×4) from a DM perspective.

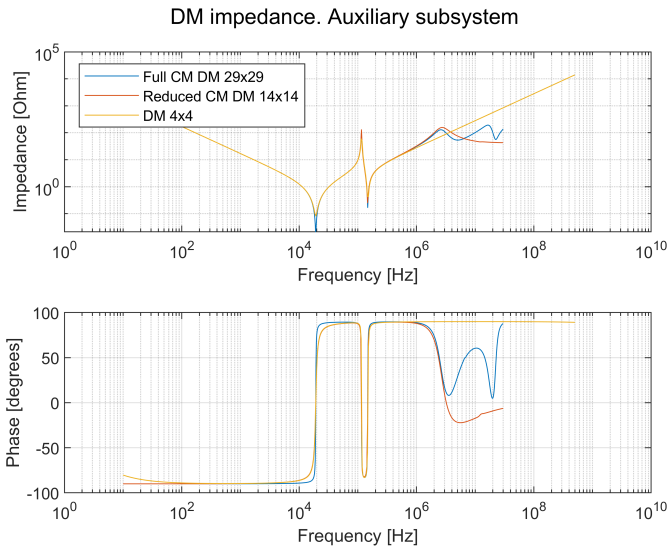


Figure 6.53: Terminal impedance characteristics of an auxiliary subsystem showing DM impedance magnitude and phase for the full CM+DM model, the reduced CM+DM model, and the DM-only model. The corresponding state-space matrix sizes are 29×29, 14×14, and 4×4.

The DM impedance of the auxiliary subsystem shown in Figure 6.53 is evaluated up to 200 kHz. Although the reduced model remains accurate up to 1 MHz, vehicle measurements presented in Section 4.4 indicate that RMS values of DM currents above 200 kHz in the TVS are negligible. This frequency range therefore defines the practical upper limit for the DM analysis.

All subsystems are subsequently integrated to form a complete simulation model of the TVS, as shown in Figure 6.1. This model serves as the basis for the system-level DM simulations presented in the following subsection.

Conclusion

The subsystem reduction yields models with state-space matrix sizes of 29×29, 14×14, and 4×4. The reduced CM+DM model preserves impedance characteristics within the relevant frequency range, while the DM-only model provides a compact and computationally efficient representation for differential-mode analysis. These reduced models form the foundation for the system-level DM simulations that follow.

6.4.2 System simulation model in PLECS for DM

At this stage, all subsystem DM models are available, and full system-level simulations are performed for the complete truck system shown in Figure 6.1.

Modelling power-electronic converters, such as the three-phase converter in an EMD, presents specific challenges. In system simulations, the switches and the DC-link capacitor are most conveniently modelled as ideal components, see Figure 6.54.

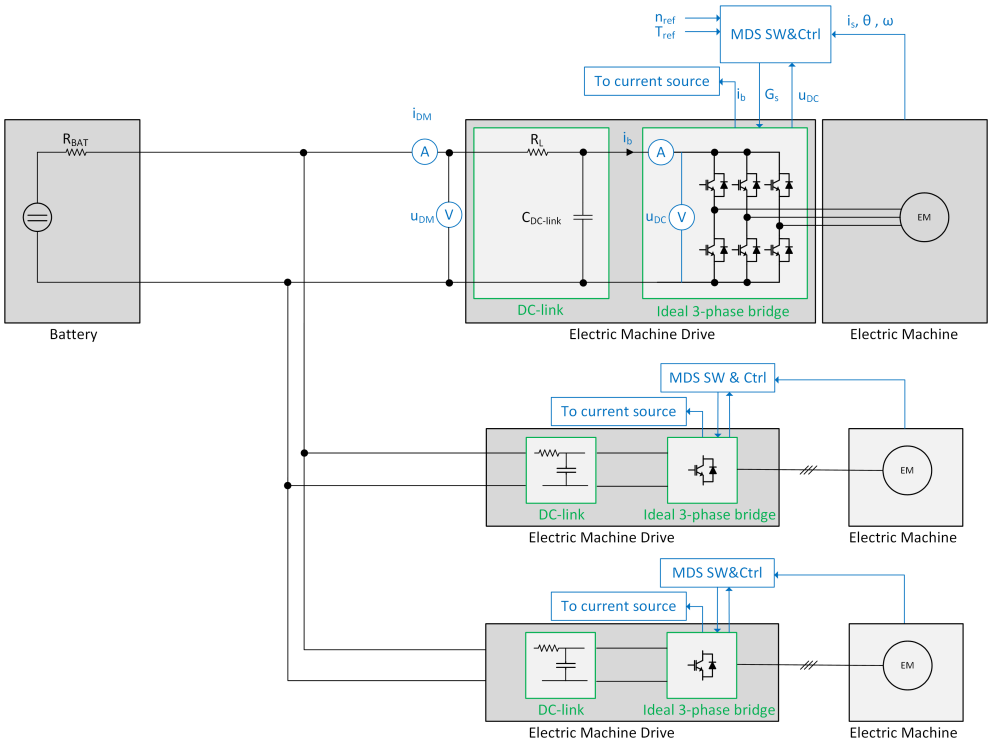


Figure 6.54: Reduced system model including a complete MDS and active feedback control implemented in the block "MDS SW & Ctrl". This configuration is used as the starting point for the differential-mode system simulations.

However, with ideal capacitor models, the simulated DC differential-mode (DM) currents differ from measured results. To accurately reproduce the DC-side DM current i_{DM}, the stray inductance of the DC-link capacitor must be included, as illustrated later in Figure 6.55.

Using ideal switches in a three-phase converter results in unrealistically high transient voltages across the DC link. When IGBTs are modelled in PLECS with limited rise and fall times, the simulation model becomes numerically stiff. To address this, an idealised simulation approach is adopted, in which the current i_b to the three-phase bridge in Figure 6.54 controls a current source in Figure 6.55.

The key signals and components used in Figures 6.54 to 6.56 and 6.58 are summarised in Table 6.1.

Table 6.1: Parameters for the simulations according to Figure 6.54.

Electrical Parameter	Description
n_{ref}	Reference speed for the control system
T_{ref}	Reference torque for the control system
i_s	Feedback of the three-phase current to the control system
Θ	Feedback of the phase angle to the control system
ω	Feedback of the electrical speed to the control system
G_s	Gate signal to the three-phase bridge from the control system
u_{DC}	DC voltage feedback to the control system, measured with a voltmeter
i_b	Current from the DC link to the three-phase converter, measured with an ammeter and used to control a current source
i_{DM}	Differential-mode current, measured on the DC side; main parameter under investigation
u_{DM}	Differential-mode voltage, measured on the DC side; main parameter under investigation
R_{BAT}	Series resistance of the battery
L_{BAT}	Series inductance of the battery
R_C	Series resistance of the cable
L_C	Series inductance of the cable
R_L	Series resistance of the EMD filter inductance
L_L	Series inductance of the EMD filter inductance
$C_{DC\text{-}link}$	DC-link capacitor; in ideal simulations, neither R_S nor L_S are included
R_S	Series resistance of the DC-link capacitor
L_S	Series inductance of the DC-link capacitor

To mitigate the limitations of ideal switch models and to accelerate the simulation process, the following steps are applied:

1. A reduced system model with a complete MDS and active feedback control is simulated with an ideal battery and ideal cables; see Subsection 6.4.2.

2. An extended system model, including DC cable models and refined battery and EMD models, is simulated. The full EMD from step 1 is replaced with a DC current source mimicking the DC-link current drawn by the MDS in step 1, and a slew rate is added to the DC-link current pulses; see Subsection 6.4.2.

3. An extended system model with a complete MDS and active feedback control is simulated; see Subsection 6.4.2. This configuration corresponds to step 2 but includes the full MDS.

4. The extended system model from step 3 is simulated again, replacing the MDS with a current source reproducing the DC current drawn by the MDS in step 1. A slew rate is added to the DC-link current pulses. This step evaluates to what extent the complete MDS can be substituted with a current source featuring an adjustable slew rate; see Subsection 6.4.2. Results from steps 3 and 4 are compared.

5. The DC DM current to the EMD, affected by the stray inductance of the DC-link capacitor, is compared with measurements from a real vehicle, as shown in Figure 6.1; see Subsection 6.4.2.

6. A conclusion is drawn based on the results from steps 1–5; see Subsection 6.4.2.

All simulations in Subsection 6.4.2 are carried out at an operating point corresponding to half the base speed and maximum torque.

Reduced system model with a complete MDS with active feedback control

The model shown in Figure 6.54 represents a reduced system with a complete MDS and active feedback control, corresponding to the implementation used in a physical EMD in a truck. The control structure originates from the block "MDS SW&Ctrl". The IGBTs are modelled as ideal devices with instantaneous turn-on and turn-off behaviour. No cables or stray inductances are included in the circuit.

The current to the three-phase bridge, i_b, as shown in Figure 6.54, is used to control a current source in the subsequent simulation step; see Subsection 6.4.2.

Extended system models where the EMD models are simulated with a current source and the DC current is drawn by the MDS

Building upon the reduced model presented in Subsection 6.4.2, this extended configuration introduces non-ideal components to more accurately represent system behaviour.

The simulation model shown in Figure 6.55 is a simplified representation of the model in Figure 6.54 with respect to the control system, the three-phase bridge, and the electric machine (EM). These components are replaced by a current source controlled by the current i_b, as output from the simulation model described in Figure 6.54. A rate limiter is applied to shape the current generated by the source, emulating the current slope of an IGBT with finite rise and fall times.

In this simulation model, non-ideal components are introduced. The DC-link capacitor includes a stray inductance L_s and a series resistance R_s, the cables are modelled as non-ideal, and the battery includes a series inductance. Subsystems with non-ideal circuits are also added.

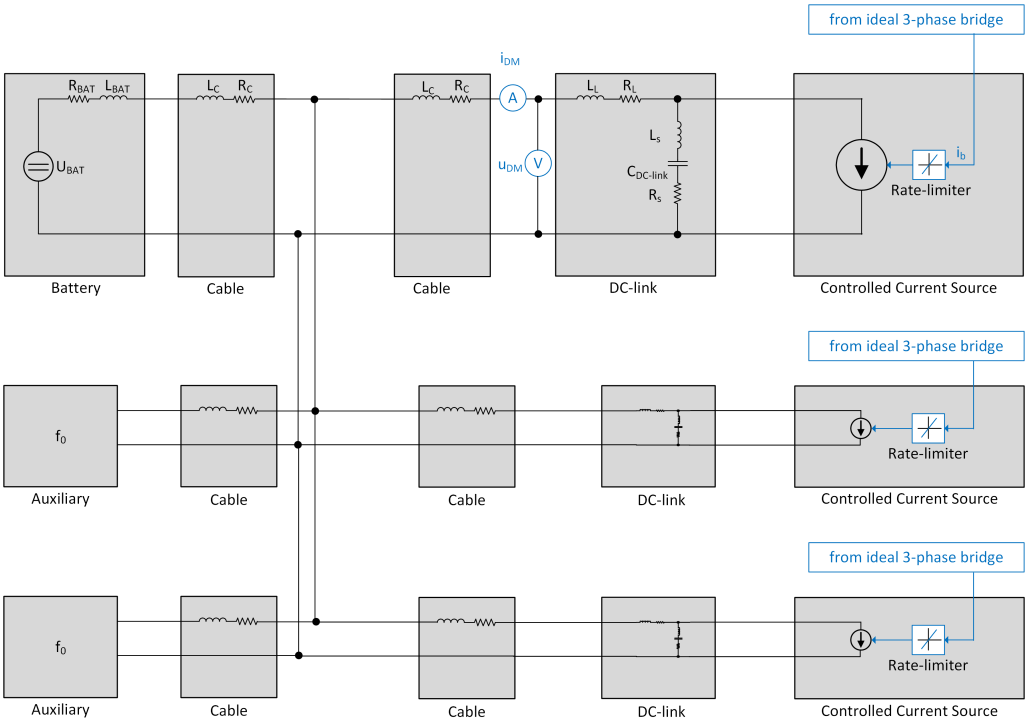


Figure 6.55: Simulation model with a current source whose current, i_b, is controlled by the current shown in Figure 6.54.

This extended model forms the basis for the subsequent simulations. It includes stray inductances and the subsystems to be analysed. The next subsection further extends this model to include the complete MDS with active feedback control under non-ideal conditions.

Extended system model with a complete MDS with active feedback control

Building upon the preceding subsection, where the EMD models were represented by controlled current sources, this part reintroduces the complete MDS and its active feedback control to assess its influence under more realistic conditions.

A natural question arises: is the current to the three-phase bridge affected when the system is varied, for example by adding auxiliaries that may influence the DC-link voltage and thereby, through the MDS feedback loops, indirectly affect the current drawn? To address this, an additional simulation model is constructed using the control configuration shown in Figure 6.54.

In this simulation, cables and inductances are introduced, as shown in Figure 6.55, with the only difference being that the DC-link capacitor remains ideal, i.e. without series inductance; see Figure 6.56.

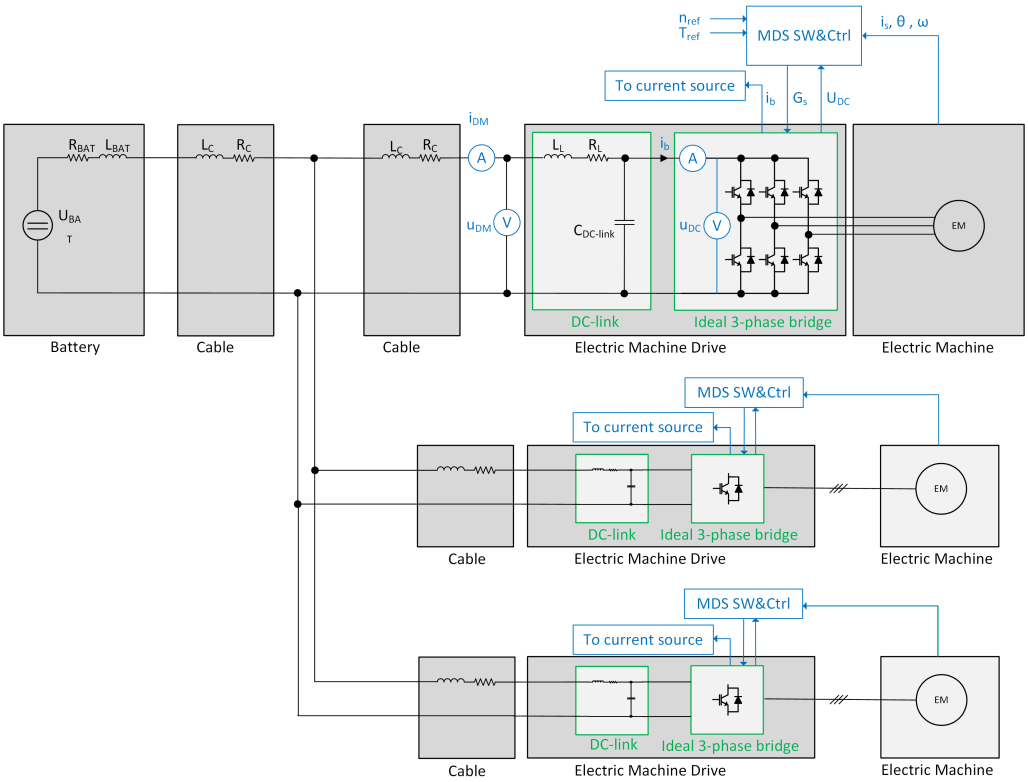


Figure 6.56: Extended system model with a complete MDS and active feedback control, including non-ideal cables and subsystems, while the DC-link capacitor remains ideal.

The current to the three-phase bridge, i_b, remains unaffected despite system variations; see Figure 6.57. This confirms that the differential-mode current to the three-phase bridge, i_b, is unchanged even when the system external to the bridge—including the MDS, cables, subsystems, and battery—is modified from ideal to non-ideal. The influence of the MDS feedback control on the DM current to the three-phase bridge is therefore negligible.

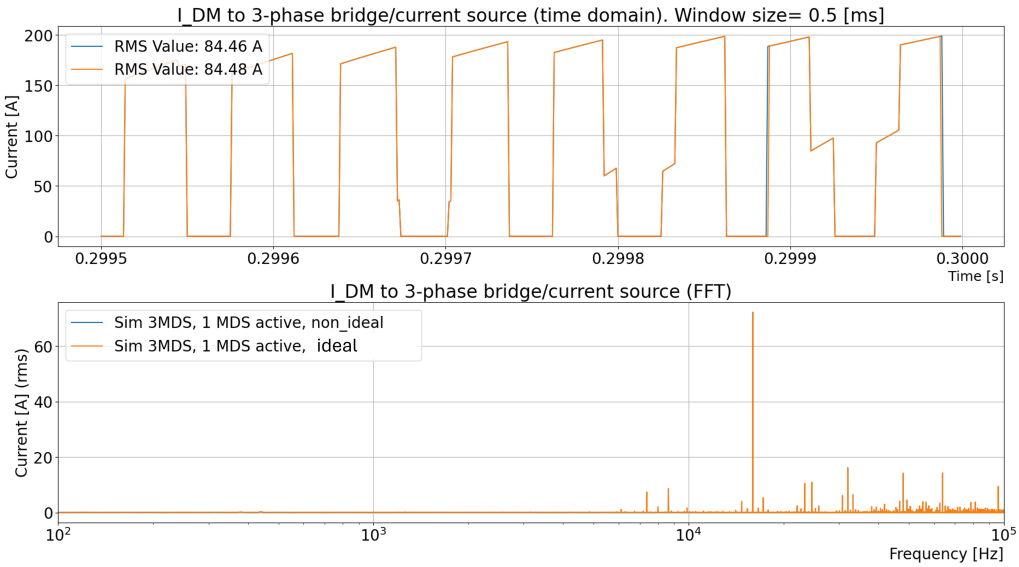


Figure 6.57: Current i_b to the three-phase bridge for the models shown in Figures 6.54 and 6.56, demonstrating that the bridge current is unaffected by non-ideal components external to the MDS.

These results justify replacing the complete MDS with a controlled current source in subsequent simulations, enabling a significant reduction in model complexity while preserving the relevant differential-mode behaviour.

Extended system model where the EMD model is simulated with a current source and the DC current is drawn by the MDS

Based on the results from Subsection 6.4.2, the next step is to investigate whether the same system response can be obtained using a simplified EMD representation based on a controlled current source.

It is essential to verify that the simulation results are not significantly affected by the differences between the models shown in Figures 6.56 and 6.58. This verification is performed by comparing the differential-mode DC current, i_{DM}, drawn by EMD1 (the upper unit in Figures 6.56 and 6.58) and the differential-mode DC-link voltage, u_{DM}, across the DC-link capacitor of EMD1. The comparison results are presented in Figures 6.59 and 6.60.

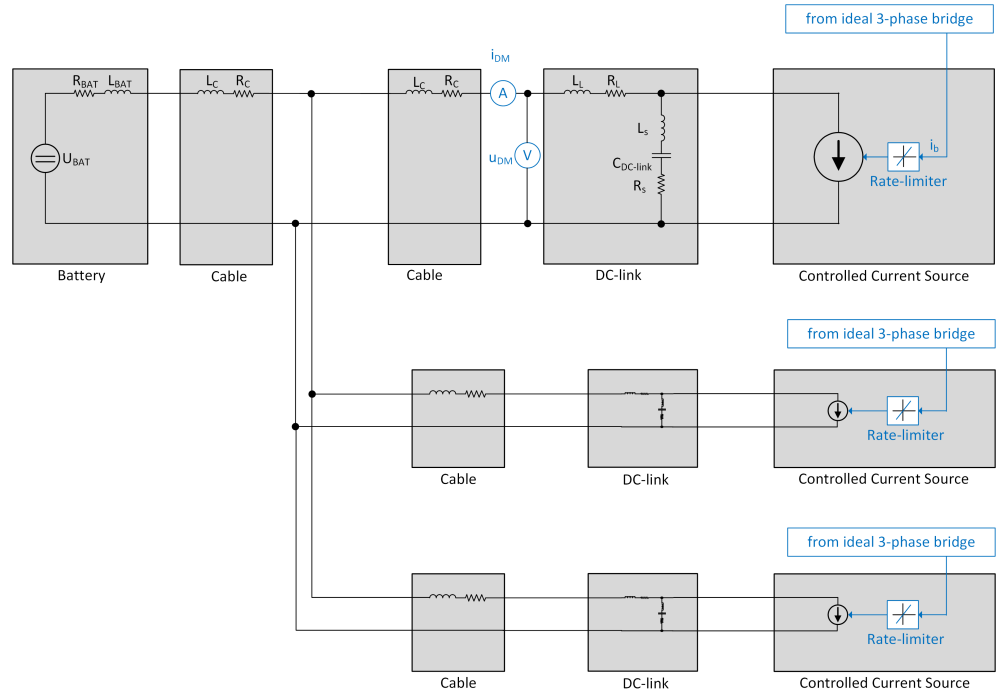


Figure 6.58: Simulation model where the EMD is represented by a controlled current source, replacing the complete MDS while retaining the surrounding non-ideal system components.

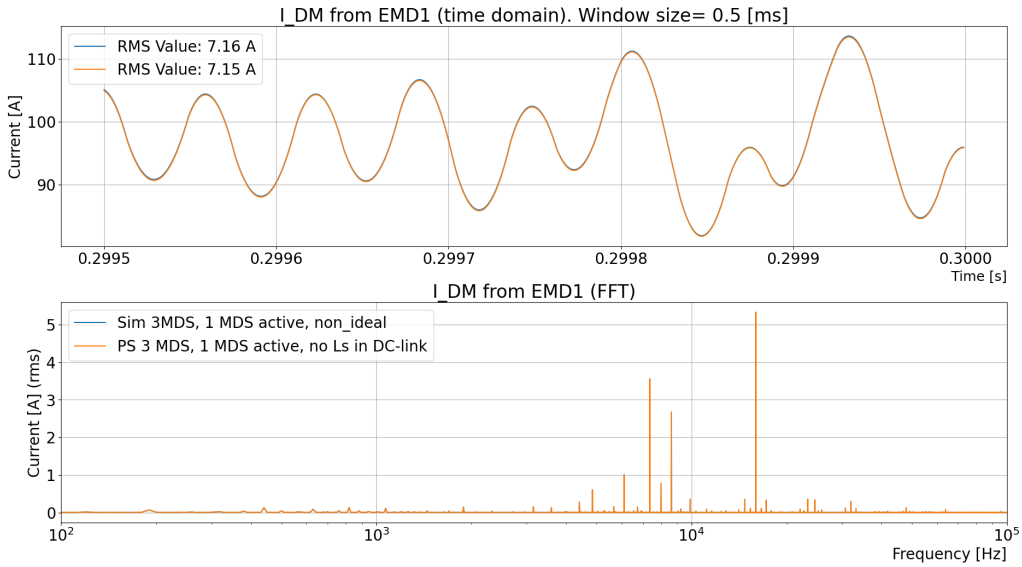


Figure 6.59: Comparison of the DC differential-mode current i_{DM} for the models shown in Figures 6.56 and 6.58, demonstrating negligible differences between the two configurations.

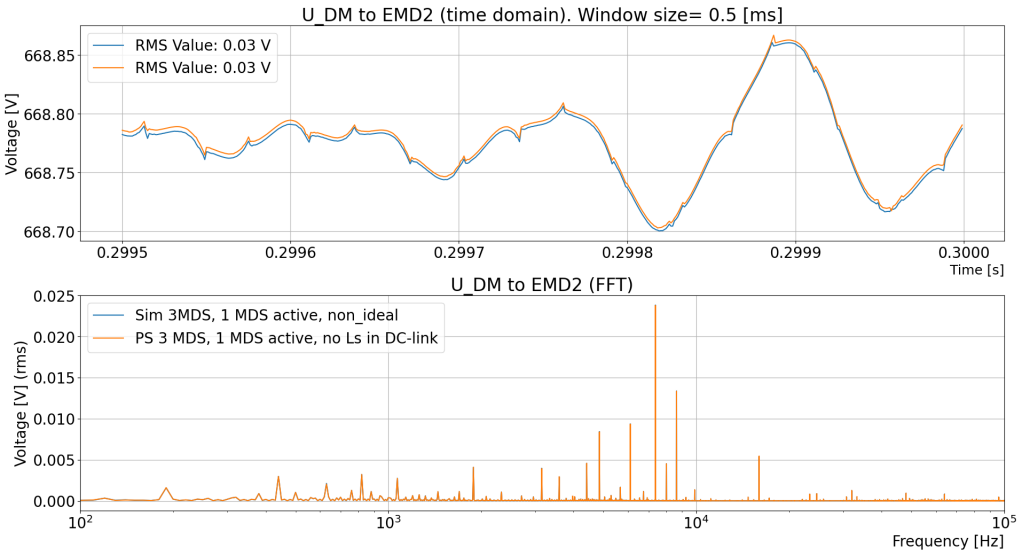


Figure 6.60: Comparison of the DC differential-mode voltage u_{DM} for the models shown in Figures 6.56 and 6.58, showing consistent voltage behaviour across both models.

The simulation results confirm that both models produce nearly identical differential-mode current and voltage waveforms. This verifies that a simplified EMD representation using the current i_b as control input can accurately reproduce the relevant system behaviour.

These results enable a more computationally efficient analysis in the subsequent subsection, where the model complexity is further reduced while preserving the accuracy of the differential-mode response.

Comparing the simulation models with measurements

Based on the previously verified simulation models, this subsection compares their behaviour with measurements from a real vehicle, with particular focus on how the DC differential-mode (DM) current depends on the stray inductance in the DC-link capacitor.

Measurements are performed on the DC side of EMD1, where the DC DM current is measured, while the corresponding phase-to-chassis voltage is measured on the AC side of EM1. This comparison provides a direct link between switching behaviour and the resulting DM current response.

As shown in Figure 6.61, the measured DC differential-mode current on the DC side of EMD1 is presented together with the phase-to-chassis voltage of EM1.

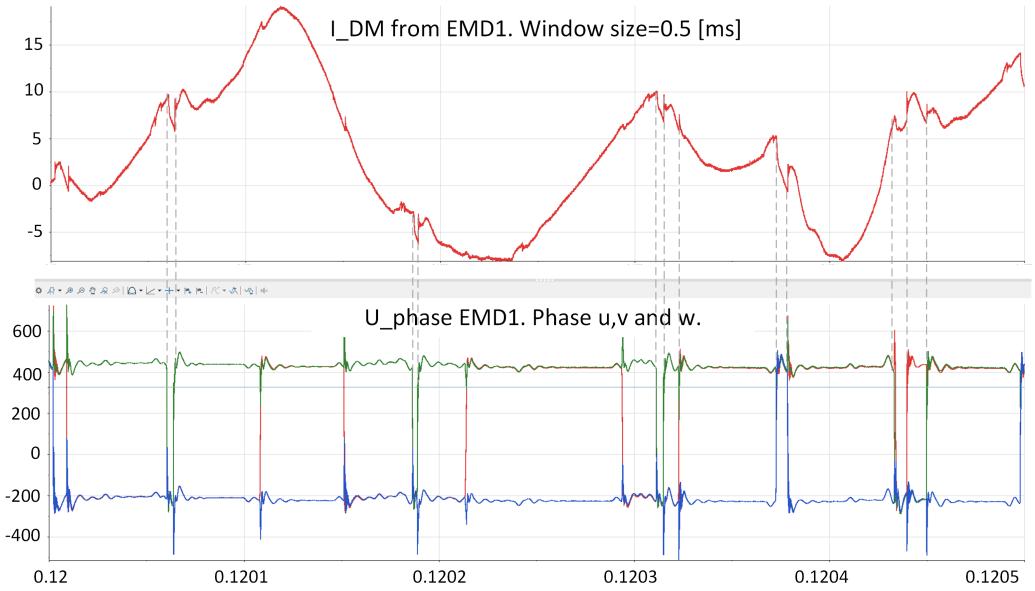


Figure 6.61: Measured DC differential-mode current i_{DM} on the DC side of EMD1 and the phase-to-chassis voltages u_{phase} of EM1. The grey dotted lines indicate the temporal relationship between switching events in the phase-to-chassis voltages and the resulting current response. The lower plot shows the three phase-to-chassis voltages of phases u, v, and w.

The measurements indicate that the DC DM current is strongly influenced by the switching behaviour of the EMD. To investigate this effect, simulations are performed both with and without the stray inductance L_s in the DC-link capacitor; see Figures 6.55 and 6.62.

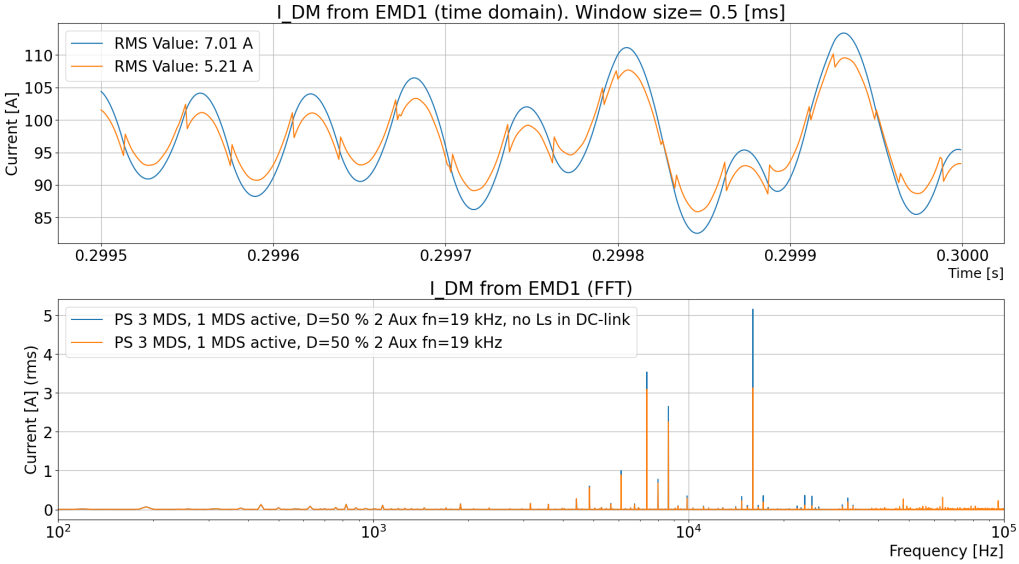


Figure 6.62: Simulated DC differential-mode current i_{DM} with and without the stray inductance L_s in the DC-link capacitor, illustrating the impact of L_s on the current waveform.

Comparing Figures 6.61 and 6.62, it is evident that the notch observed in the measured DC DM current also appears in the simulated waveform when the stray inductance L_s is included in the DC-link capacitor model. This feature is absent in simulations where L_s is neglected.

The strong agreement between measurements and simulations confirms that inclusion of the DC-link capacitor stray inductance is essential for accurately reproducing the observed DM current characteristics. These results provide experimental validation of the modelling approach used for DM simulations and form the basis for the overall conclusions presented in the following subsection.

Conclusion for the DM simulation model

Building on the analyses presented in Subsection 6.4.2, this subsection summarises the main findings from the differential-mode (DM) simulations and their validation through comparison with measured data.

The following comparisons are performed:

MDS representation: An MDS with active feedback control is compared with an MDS replaced by a controlled current source.

System variations: The DM current to the three-phase bridge, i_b, is evaluated for systems using ideal versus non-ideal components and when additional subsystems are included.

DC-link modelling: The impact of excluding or including the stray inductance L_s in the DC-link capacitor is analysed.

The comparisons demonstrate the following:

Controlled current source: A simulation model using a controlled current source governed by the current to the three-phase bridge, i_b, accurately reproduces the system behaviour.

Robustness of i_b: The current to the three-phase bridge, i_b, remains unaffected by variations in the surrounding system configuration.

DC-link stray inductance: The stray inductance in the DC-link capacitor, L_s, must be included to correctly model the DM DC-link voltage, u_{DM}.

Reference model: The model described in Subsection 6.4.2, with all subsystems from Figure 6.1 included, is hereafter referred to as **Model A**.

These findings provide a validated foundation for subsequent analyses of differential-mode behaviour at the system level and ensure consistency between simulation results and physical measurements.

6.4.3 Conclusion

The modelling framework developed in this section establishes a comprehensive basis for analysing differential-mode (DM) behaviour in the complete vehicle power system. Beginning with the simplification of individual subsystems in Subsection 6.4.1, the modelling strategy ensures that the most influential electrical interfaces, coupling paths, and parasitic effects are retained while computational complexity is minimised.

The subsequent system-level implementation in Subsection 6.4.2 integrates all subsystems into a unified PLECS environment. This enables the investigation of interactions between active and passive components, switching devices, and control algorithms under representative operating conditions. The validation studies confirm that the model accurately reproduces the dominant DM voltage and current behaviour, including switching-frequency harmonics and subsystem coupling phenomena.

Overall, the developed model—hereafter referred to as **Model A**—provides a validated and computationally efficient platform for studying electromagnetic interactions in complex electric-vehicle architectures. It serves as the analytical foundation for the subsequent examination of measurement and simulation results under varying load conditions in Section 6.5.

6.5 Differential-mode simulations compared to measurements in different load conditions

There is a well-known saying:
Simulations are believed by no one except those who conducted them.
Experimental results are believed by everyone except those who conducted them.
It illustrates the inherent challenge of simulations and measurements — what can truly be trusted?

This chapter explores these challenges by comparing simulated and measured differential-mode (DM) currents under varying load conditions. Several key differences between simulations and measurements are highlighted below:

- Vendor-supplied software is typically protected by intellectual property rights, which limits insight into internal algorithms and may cause discrepancies between simulated and measured system behaviour.
- In the simulations of the complete TVS, only the MDSs are actively simulated and operated under load conditions. The remaining subsystems are represented as passive loads, without drawing current or introducing disturbances into the system.
- The MDSs are not synchronised; for example, the phase of the PWM, even with the same switching frequency settings in all three MDSs, may drift over time, causing identical load conditions to produce varying measurement results.
- Components may behave differently depending on the frequency and magnitude of the current, but such dependencies are not included in the simulation models.

To illustrate these challenges, the steady-state load condition 14 *FM*1156 *SteadyState HighTorque FixGear*, see Table 6.2, is used as a representative example throughout the chapter. First, six steady-state measurements are presented to provide context, as listed in Table 6.2. Then, the behaviour observed in this specific case is analysed in detail, revealing significant current variations despite constant operating conditions. This is followed by simulations of the same case, initially using Model A. As shown, the results from Model A do not fully capture the behaviour observed in the measurements, prompting the development and evaluation of additional models.

The remainder of this section is structured as follows:

Subsection 6.5.1 Provides an overview of the measured load conditions and related DM current behaviour, establishing the context and identifying operating points with strong EMI characteristics.

Subsection 6.5.2 Highlights the practical and methodological difficulties in comparing simulated and measured DM currents due to drifting modulation, subsystem interactions, and load-dependent variations.

Subsection 6.5.3 Presents DM simulations of the representative high-torque operating point, comparing simultaneous and distributed switching of the EMDs and analysing their impact on DM current levels.

Subsection 6.5.4 Compares measurement and simulation for two representative switching cases, identifying key discrepancies such as missing harmonics and waveform distortion.

Subsection 6.5.5 Investigates the physical origin of the discrepancies using two targeted hypotheses: inductance asymmetry (second harmonic) and dead-time behaviour (sixth harmonic).

Subsection 6.5.6 Summarises the complete findings of Section 6.5 and motivates the introduction of DM-filter mitigation strategies in the next chapter.

6.5.1 Overview of different load conditions

This section provides an overview of the measured load conditions and the corresponding simulations that evaluate system behaviour under these scenarios. The purpose is to verify the developed simulation model and to examine how the system responds to varying load conditions. Particular attention is given to identifying worst-case operating scenarios regarding conducted electromagnetic interference (EMI) between subsystems.

The measurements include both steady-state operating points and acceleration phases, each conducted at low, medium, and high torque levels. Table 6.2 lists the steady-state measurements and corresponding load conditions. The base speed of the electric machines (EMs) is approximately 3000 rpm.

Figures 6.63 to 6.67 present an overview of extended measurement periods. These graphs display the measured differential-mode (DM) current, i_{DM}, on the DC side of all subsystems in the vehicle. The measurements are performed using Rogowski coils, which detect only the AC component of the current.

Table 6.2: Steady-state load conditions from measurements

Name of measurement	EMD1 T [Nm]	EMD1 n [rpm]	EMD2 T [Nm]	EMD2 n [rpm]	EMD3 T [Nm]	EMD3 n [rpm]
14 FM1156 SteadyState HighTorque FixGear	118	3487	107	2966	89	2550
15 FM1156 SteadyState MedTorque	38	3465	34	2955	29	2535
15B FM1156 SteadyState HighTorque	120	3564	109	3000	94	2588
17 FM1156 SteadyState HighTorque FixGear	233	4611	160	3863	144	3337
18 FM1156 SteadyState HighTorque FixGear	229	6407	257	5406	278	4669

Table 6.3 lists the load conditions recorded during acceleration from zero speed. The corresponding overview graphs are presented in Appendix C.3.

Table 6.3: Acceleration load conditions from measurements

Name of measurement
11A FM1156 Acc LowTorque
12A FM1156 Acc HighTorque
13A FM1156 Acc HighTorque
16 FM1156 Acc HighTorque
11 FM1156 RampUp LowTorque FixGear
12 FM1156 Acc HighTorque
13 FM1156 Acc HighTorque vxlAuto
14B FM1156 RampUp 35t vxlAut

An important observation from Table 6.2 is that the operating points differ across all measurements. Since both speed and torque vary, the measurements cannot be compared directly in terms of amplitude. This variation in operating points is intentional, aiming to highlight differences in EMI behaviour across the system.

The overview graphs in Figures 6.63 to 6.67 illustrate that DM currents vary over time. A steady-state load condition does not necessarily imply a stable current profile.

It is also important to note that the DCDC converter continuously operates during all measurements, supplying 24 VDC to the system. However, the load it supplies is neither constant between measurements nor stable over time. In contrast, the DCDC converter is modelled as a passive load in the simulations.

During acceleration, the DM currents fluctuate significantly. This is because power increases below base speed, while torque decreases above base speed. The corresponding acceleration graphs are shown in Figures C.37 to C.44 in Appendix C.3.

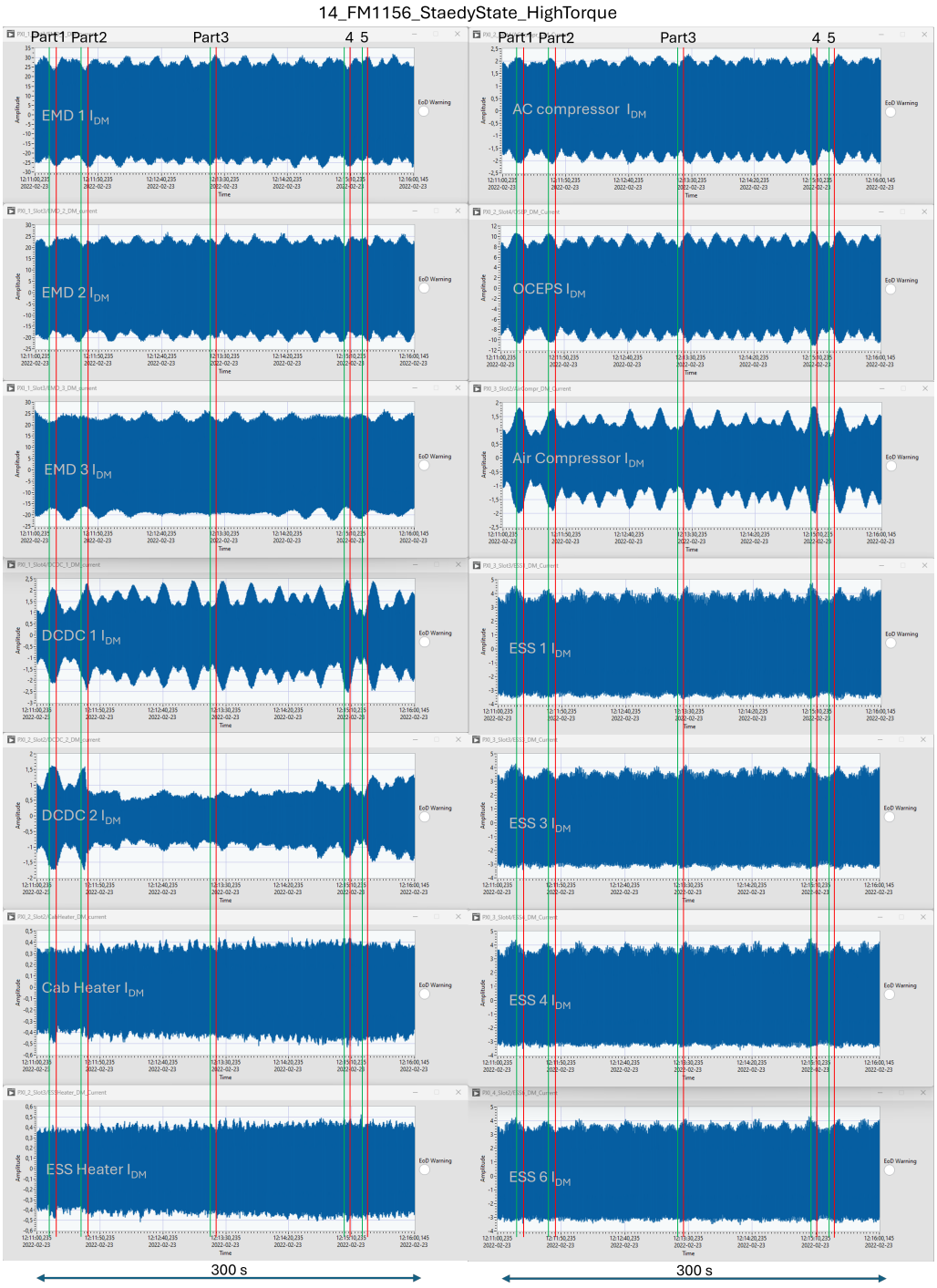


Figure 6.63: Measurement "14 FM1156 Steady State HighTorque FixGear", as listed in Table 6.2. The AirCompressor, DCDC1, and DCDC2 exhibit the highest ripple currents among the measurements in Table 6.3, with notably wide current variation. All currents are measured on the DC side, but only the AC component is visible, as the Rogowski coil measures the AC component of the current.

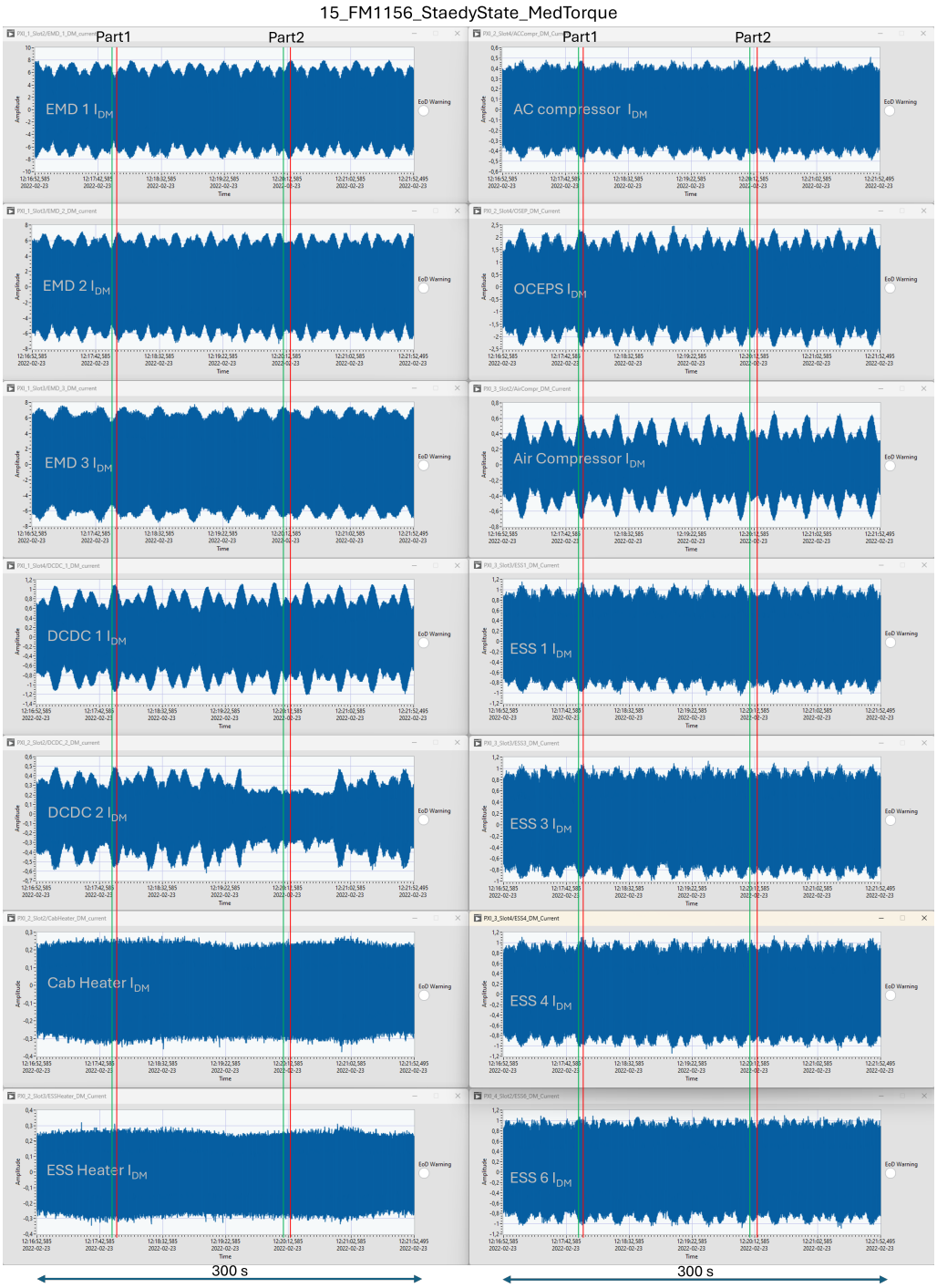


Figure 6.64: Measurement "15 FM1156 Steady State MedTorque FixGear" as listed in Table 6.2.
Similar to Figure 6.63, the AirCompressor, DCDC1, and DCDC2 show wide current variation, though with lower amplitude. Both measurements run at approximately the same speed but differ in torque. All currents are measured on the DC side, but only the AC component is visible, as the Rogowski coil measures the AC component of the current.

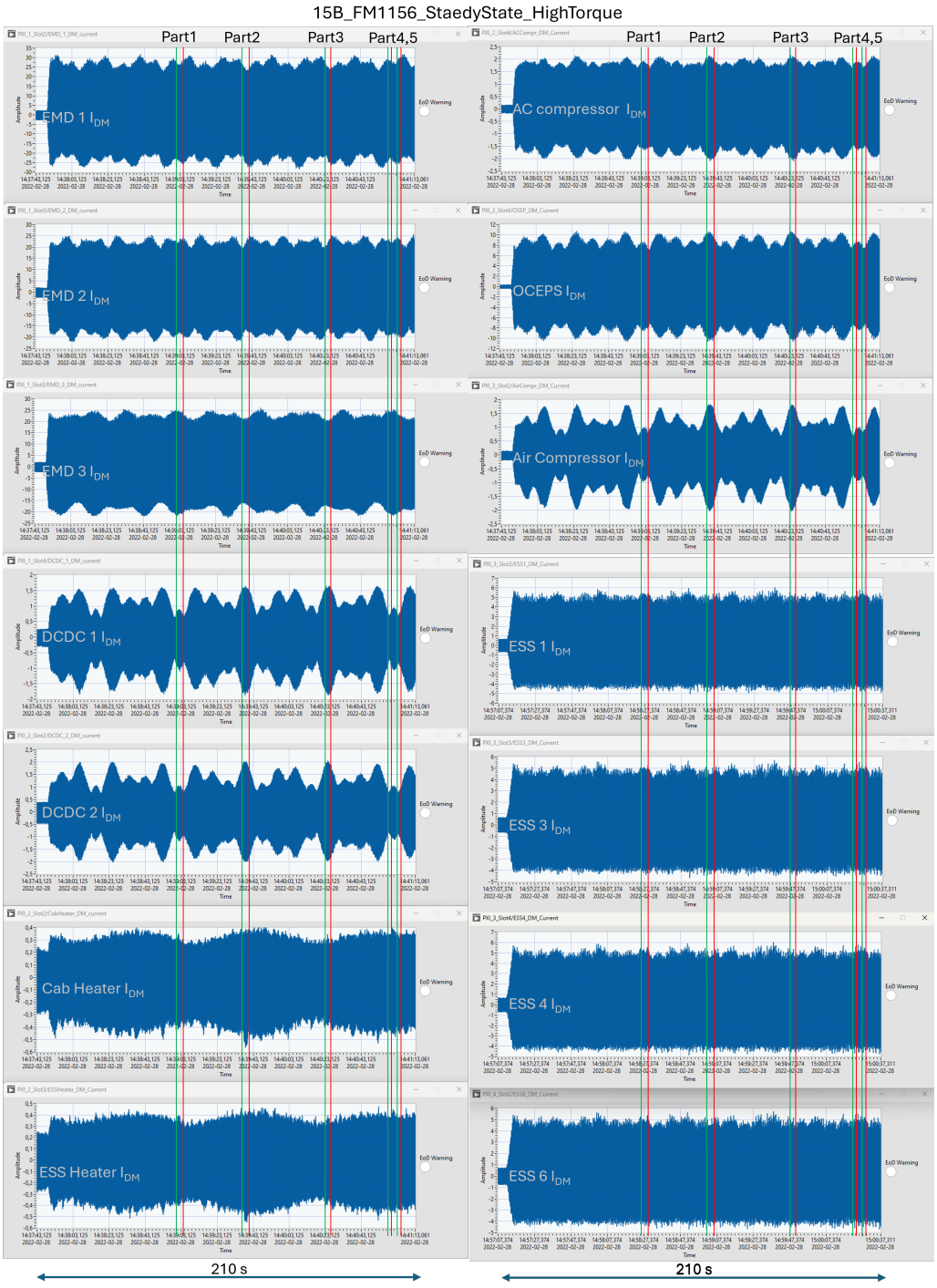


Figure 6.65: Measurement "15B FM1156 Steady State HighTorque FixGear" as listed in Table 6.2. All currents are measured on the DC side, but only the AC component is visible, as the Rogowski coil measures the AC component of the current.

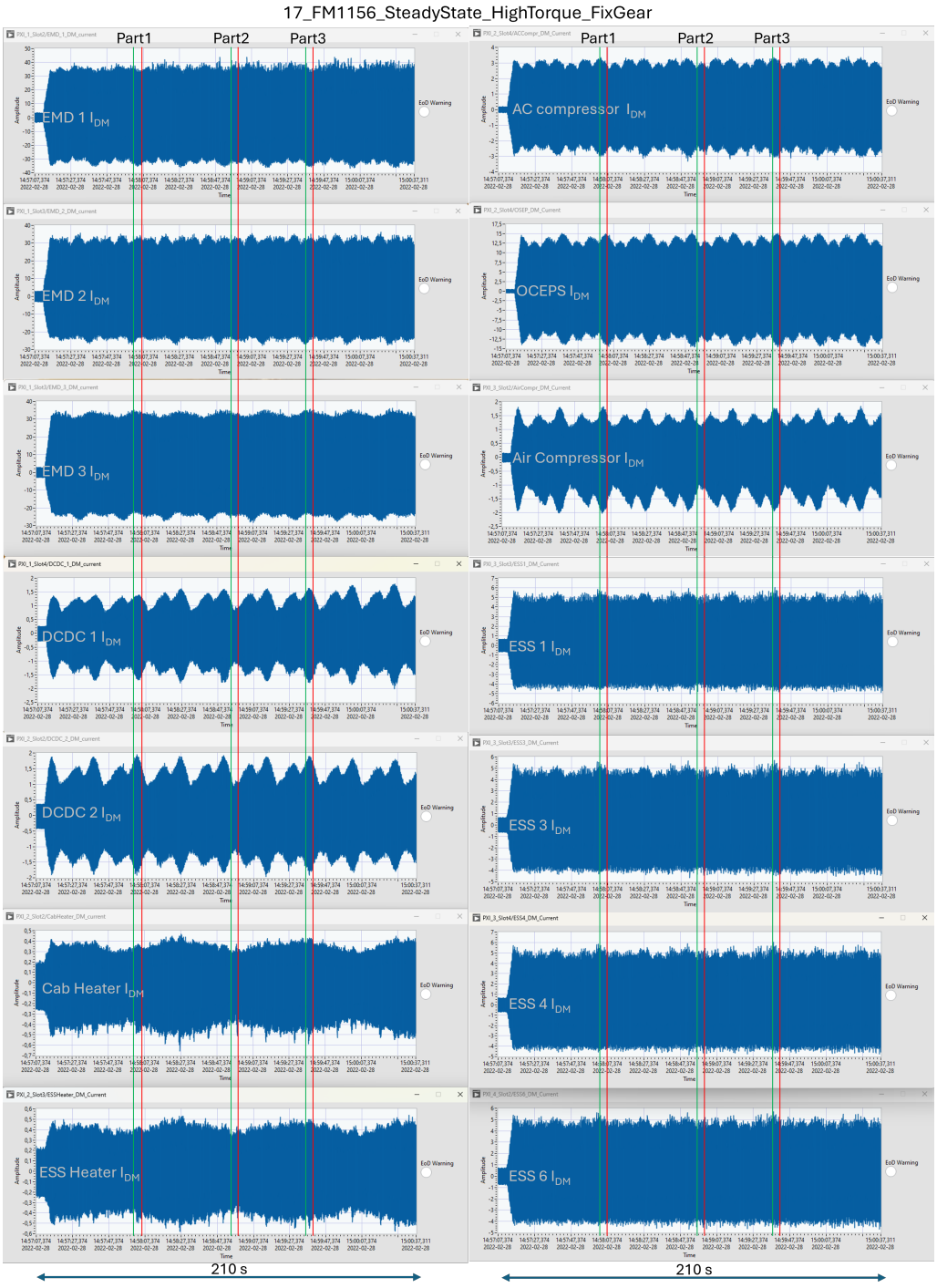


Figure 6.66: Measurement "17 FM1156 Steady State HighTorque FixGear" as listed in Table 6.2.
All currents are measured on the DC side, but only the AC component is visible, as the Rogowski coil measures the AC component of the current.

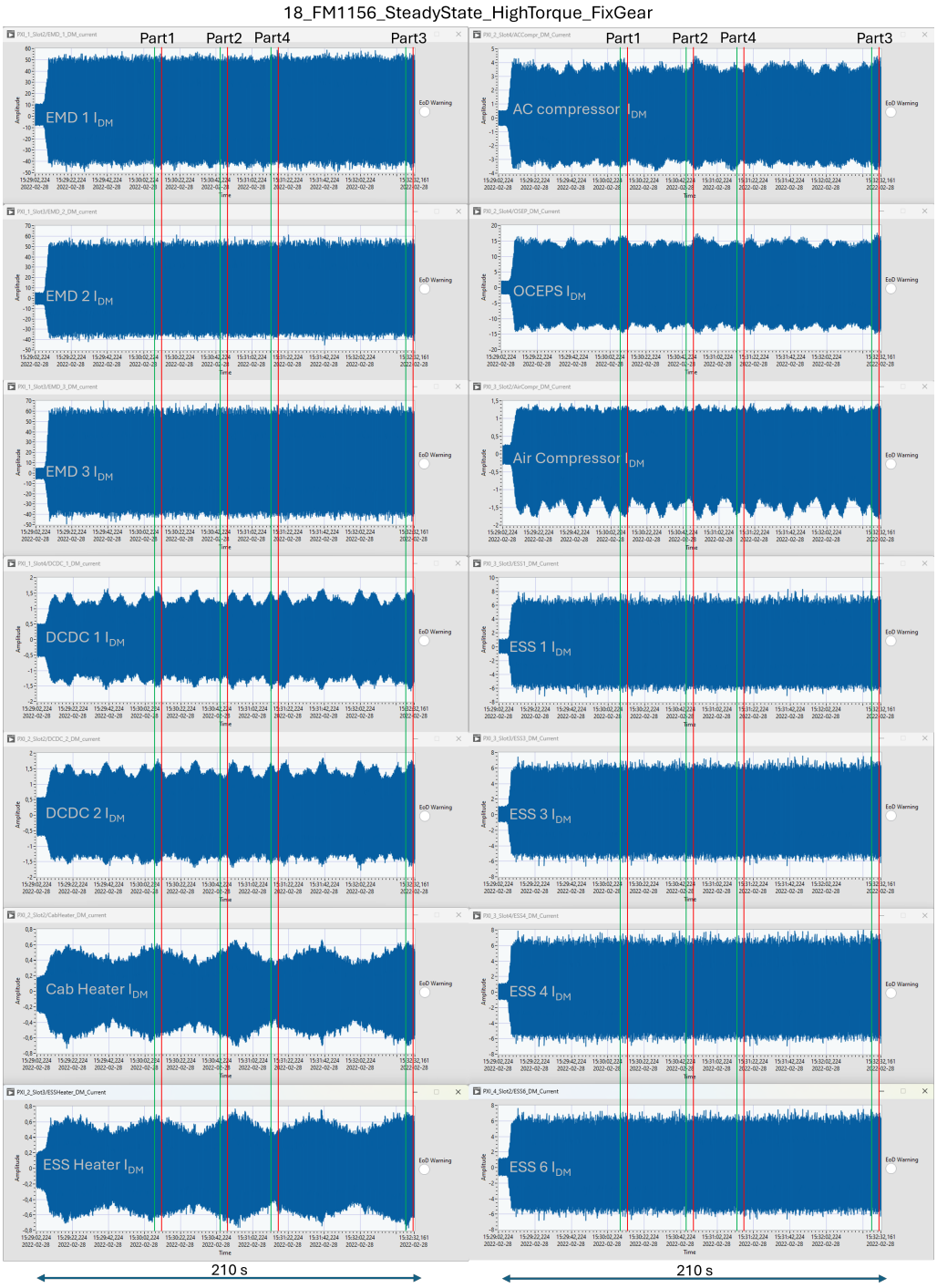


Figure 6.67: Measurement "18 FM1156 Steady State HighTorque FixGear" as listed in Table 6.2. All currents are measured on the DC side, but only the AC component is visible, as the Rogowski coil measures the AC component of the current.

Conclusion

In summary, this overview highlights how the measured differential-mode currents vary significantly across operating points and torque levels, even under nominally steady-state conditions. These observations form the baseline for the subsequent comparison between measured and simulated DM behaviour under different load scenarios, presented in the following section.

6.5.2 Challenge in comparing simulations of different load conditions

Building on the observations in Subsection 6.5.1, this analysis examines the practical and methodological challenges of reproducing measured differential-mode (DM) current behaviour in simulations. The measurements highlight significant variability in load conditions and electromagnetic interference (EMI), making it difficult to replicate real-world behaviour under controlled simulation settings.

This section focuses on the challenges observed in the measurements, which serve as a basis for understanding the limitations of the simulation models. The simulations themselves are presented in the following section, where steady-state conditions are used to explore the underlying mechanisms behind the observed EMI variations.

The system under study consists of standalone subsystems, each with independently operating PWM signals. While several subsystems share the same switching frequency, others operate at different frequencies. In all cases, the PWM signals are unsynchronised and may drift relative to one another.

An example illustrating the challenge of comparing modelling and measurements is shown for load condition 14 *FM*1156 *SteadyState HighTorque FixGear* in Figures 6.68 to 6.73. These figures represent the same operating point, but different segments of the five-minute recording exhibit distinct behaviours, as seen in Figure 6.63.

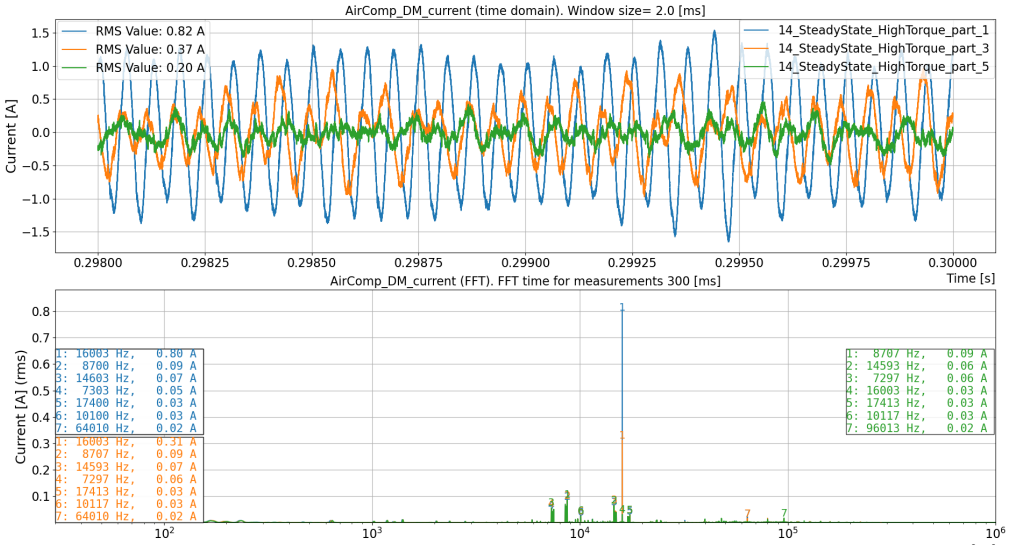


Figure 6.68: Differential-mode current in the Air Compressor, from measurement "14 FM1156 Steady State HighTorque FixGear", shown for parts 1, 3, and 5 in the same graph, as referenced in Figure 6.63. A notably wide current variation is observed. All currents are measured on the DC side, but only the AC component is visible, as the Rogowski coil measures the AC component of the current.

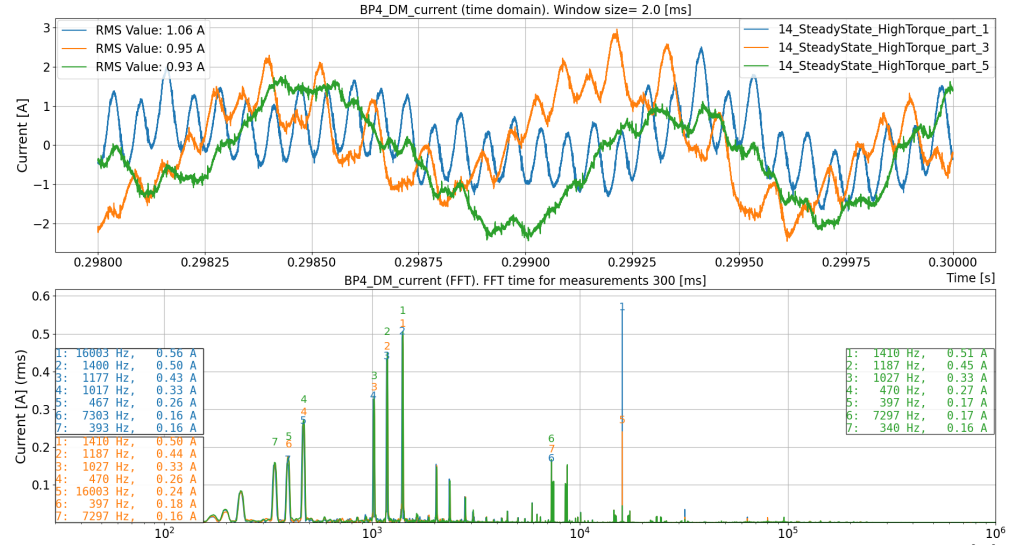


Figure 6.69: Differential-mode current in Battery 4, from measurement "14 FM1156 Steady State HighTorque FixGear", shown for parts 1, 3, and 5 in the same graph, as referenced in Figure 6.63. A notably wide current variation is observed. Unlike the Air Compressor in Figure 6.68, the RMS current remains approximately the same in all three cases, but the frequency content differs significantly. All currents are measured on the DC side, but only the AC component is visible, as the Rogowski coil measures the AC component of the current.

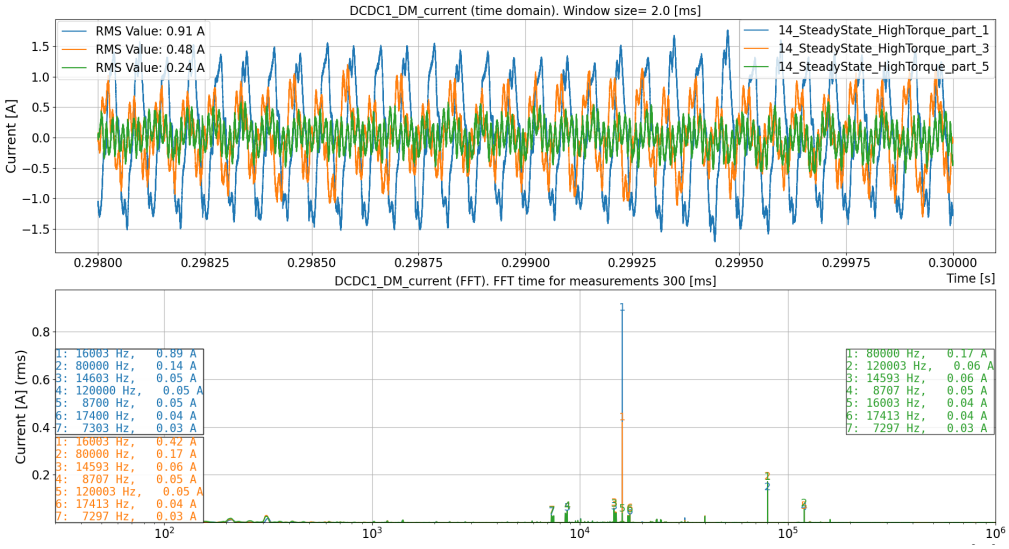


Figure 6.70: Differential-mode current in DCDC1, from measurement "14 FM1156 Steady State HighTorque FixGear", shown for parts 1, 3, and 5 in the same graph, as referenced in Figure 6.63. A notably wide current variation is observed. Similar to the Air Compressor in Figure 6.68, both the RMS current and the frequency content exhibit significant variation. All currents are measured on the DC side, but only the AC component is visible, as the Rogowski coil measures the AC component of the current.

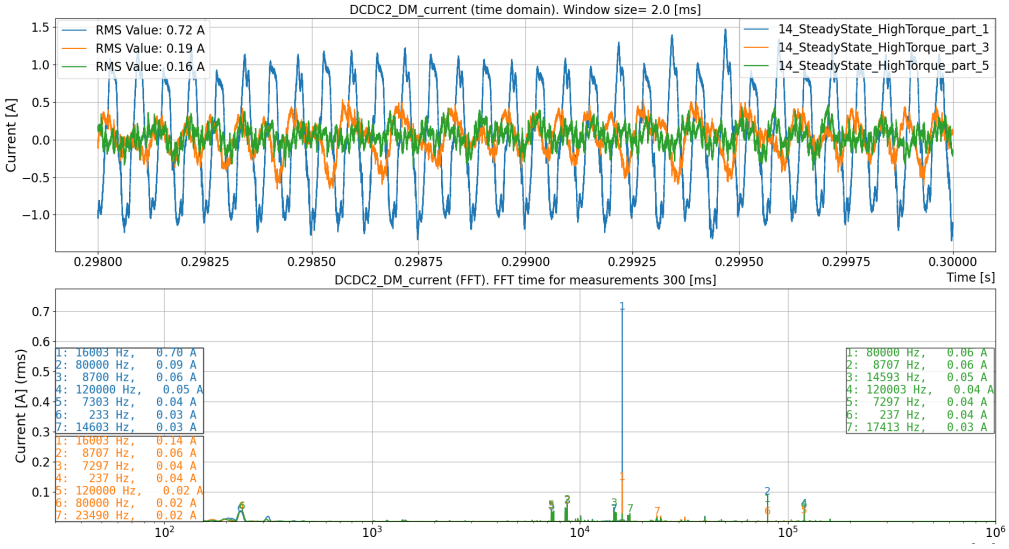


Figure 6.71: Differential-mode current in DCDC2, from measurement "14 FM1156 Steady State HighTorque FixGear", shown for parts 1, 3, and 5 in the same graph, as referenced in Figure 6.63. A notably wide current variation is observed. Similar to the Air Compressor and DCDC1 in Figures 6.68 and 6.70, both the RMS current and the frequency content show considerable variation. All currents are measured on the DC side, but only the AC component is visible, as the Rogowski coil measures the AC component of the current.

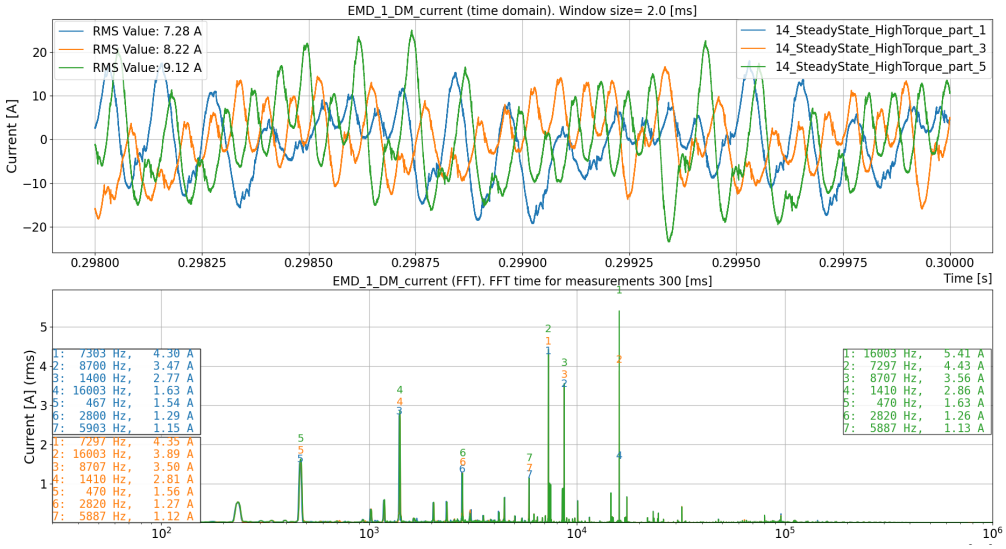


Figure 6.72: Differential-mode current in EMD1, from measurement "14 FM1156 Steady State HighTorque FixGear", shown for parts 1, 3, and 5 in the same graph, as referenced in Figure 6.63. A notably wide current variation is observed. In contrast to the Air Compressor, DCDC1, and DCDC2 in Figures 6.68, 6.70 and 6.71, the RMS current remains relatively stable across all three segments, while the frequency content varies significantly. All currents are measured on the DC side, but only the AC component is visible, as the Rogowski coil measures the AC component of the current.

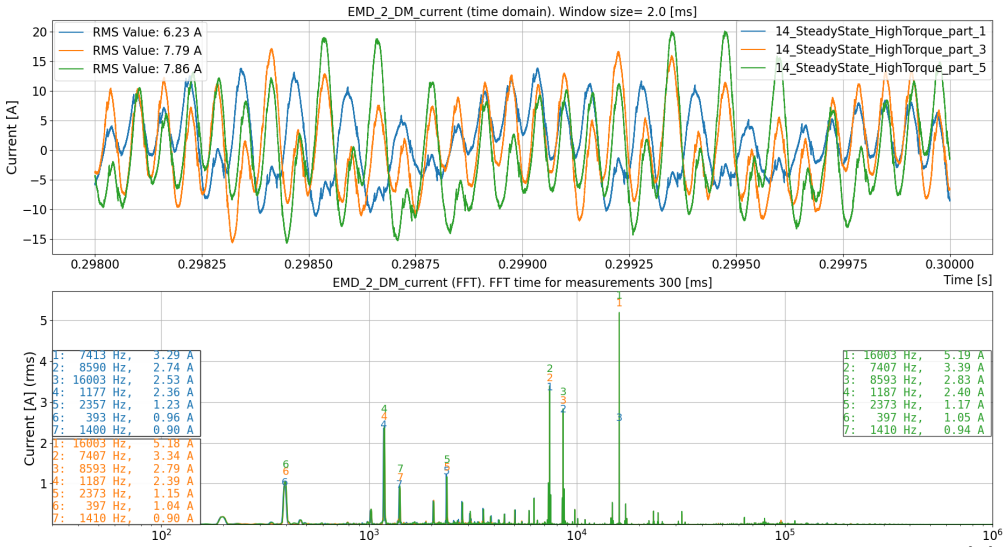


Figure 6.73: Differential-mode current in EMD2, from measurement "14 FM1156 Steady State HighTorque FixGear", shown for parts 1, 3, and 5 in the same graph, as referenced in Figure 6.63. A notably wide current variation is observed. In contrast to the Air Compressor, DCDC1, and DCDC2 in Figures 6.68, 6.70 and 6.71, the RMS current remains relatively stable across all three segments, while the frequency content varies significantly. All currents are measured on the DC side, but only the AC component is visible, as the Rogowski coil measures the AC component of the current.

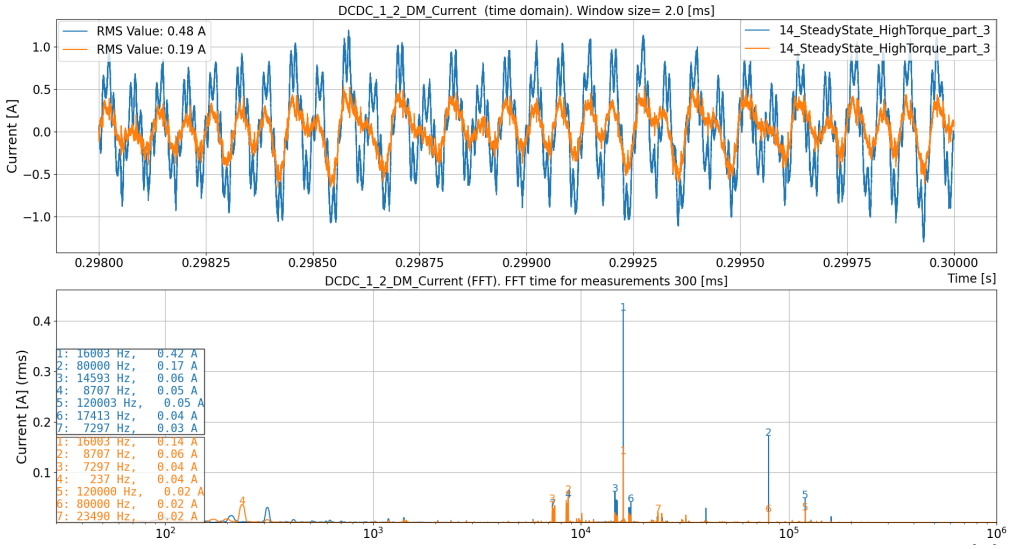


Figure 6.74: Differential-mode current in DCDC1 and DCDC2, from measurement "14 FM1156 Steady State HighTorque FixGear", shown for part 3 in the same graph, as referenced in Figure 6.63. Two identical subsystems operating side by side, but subjected to different loads from the 24 VDC system, exhibit significant variation in RMS current and in the distribution of FFT components. All currents are measured on the DC side, but only the AC component is visible, as the Rogowski coil measures the AC component of the current.

The 16 kHz component originates from the EMD switching at 8 kHz, and the 80 kHz component from the DCDC converters. It is challenging to simulate the load conditions and obtain comparable results, especially when the measurements show differences of up to a factor of four, as illustrated above.

The other challenge is the different behaviour in DCDC1 and DCDC2 in Figure 6.74, where the current differs significantly even though they are identical and located side by side.

Conclusion:

In summary, these variations highlight the difficulty of reproducing measured differential-mode behaviour under complex real-world load conditions. The next section therefore examines the simulation results for 14 *FM*1156 *SteadyState HighTorque FixGear* in more detail.

6.5.3 Simulation of load conditions 14 FM1156 SteadyState HighTorque FixGear

In Subsections 6.5.1 and 6.5.2, it is shown that the EMI varies significantly during steady-state conditions. The hypothesis is that when the EMDs switch simultaneously, the differential-mode (DM) voltage drops more, resulting in a larger DM current across all

subsystems at the double switching frequency. Conversely, the DM current is lower when the switching events are distributed in time.

Figures 6.75 to 6.79 present simulation results for two switching scenarios: minimum delay (simultaneous switching) and maximum delay (evenly distributed switching) between EMD1 and EMD2. The subsystems shown include the Air Compressor, Battery 4, and DCDC2 — which are not actively switching — as well as two of the three switching EMDs, namely EMD1 and EMD2.

The first simulations use the model described in Section 6.4, hereafter referred to as *Model A*.



Figure 6.75: Differential-mode current in the Air Compressor from "Simulation 14, Model A" with minimum delay (simultaneous switching) and maximum delay (evenly distributed switching) shown in the same graph. The RMS current remains relatively stable between the two simulations, while the frequency content varies significantly. The hypothesis is confirmed, as the 16 kHz component is substantially larger when switching is simultaneous. All currents are measured on the DC side, but only the AC component is visible, as the Rogowski coil measures the AC component of the current.

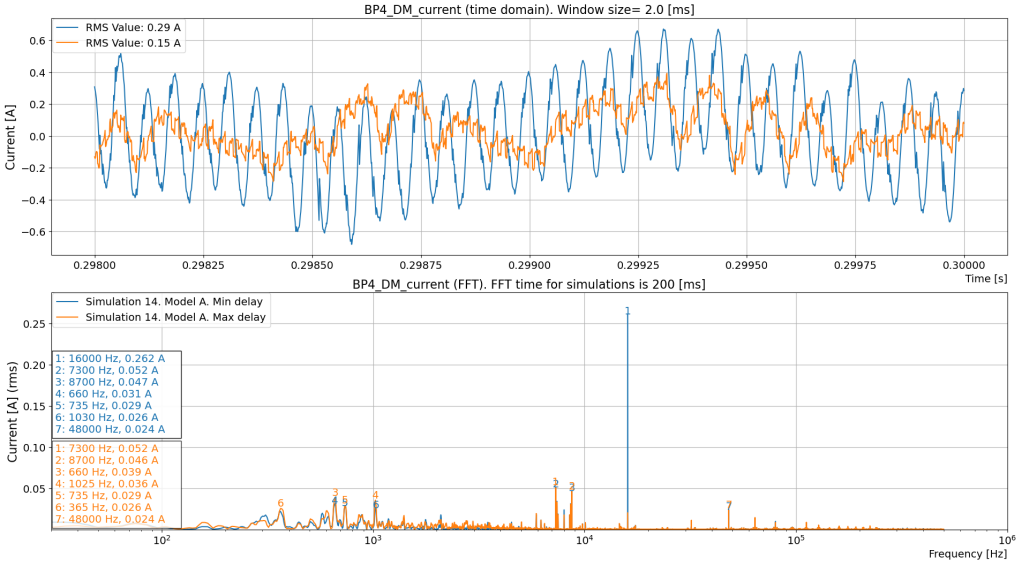


Figure 6.76: Differential-mode current in Battery 4 from "Simulation 14, Model A" with minimum delay (simultaneous switching) and maximum delay (evenly distributed switching) shown in the same graph. Both the RMS current and the 16 kHz component vary significantly between the two simulations. The hypothesis is confirmed, as the 16 kHz component is substantially larger when switching is simultaneous. All currents are measured on the DC side, but only the AC component is visible, as the Rogowski coil measures the AC component of the current.

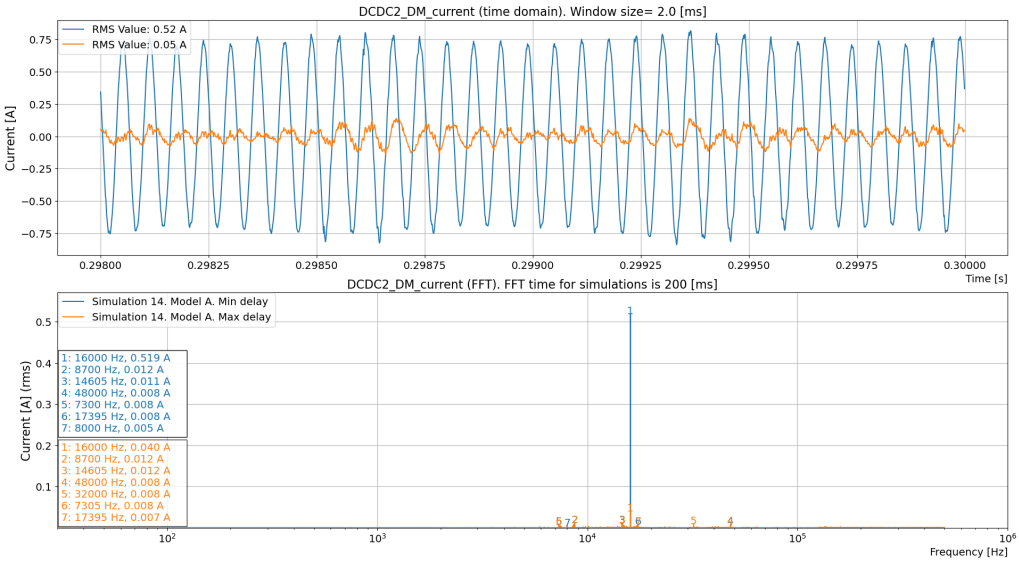


Figure 6.77: Differential-mode current in DCDC2 from "Simulation 14, Model A" with minimum delay (simultaneous switching) and maximum delay (evenly distributed switching) shown in the same graph. Both the RMS current and the 16 kHz component vary significantly between the two simulations, with even greater variation than observed for Battery 4. The hypothesis is confirmed, as the 16 kHz component is substantially larger when switching is simultaneous. All currents are measured on the DC side, but only the AC component is visible, as the Rogowski coil measures the AC component of the current.

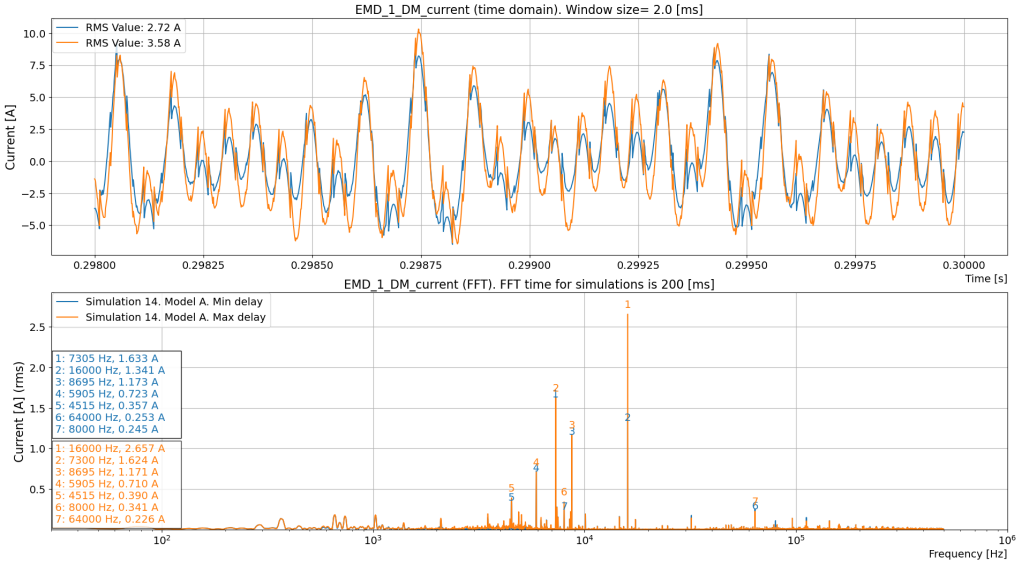


Figure 6.78: Differential-mode current in EMD1 from "Simulation 14, Model A" with minimum delay (simultaneous switching) and maximum delay (evenly distributed switching) shown in the same graph. Both the RMS current and the 16 kHz component in EMD1 increase with maximum delay, indicating that this subsystem is less affected by simultaneous switching compared to the passive subsystems. All currents are measured on the DC side, but only the AC component is visible, as the Rogowski coil measures the AC component of the current.

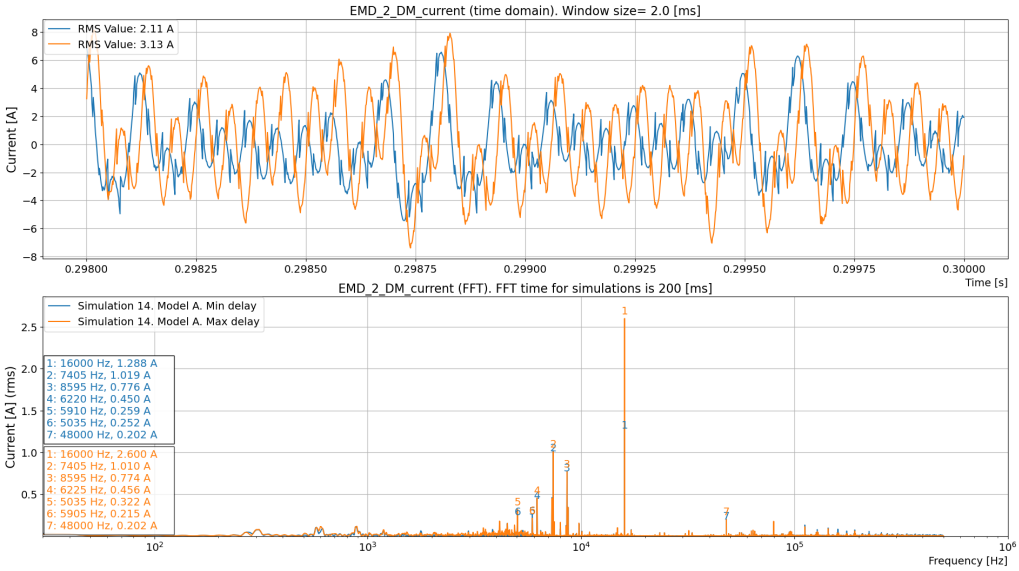


Figure 6.79: Differential-mode current in EMD2 from "Simulation 14, Model A" with minimum delay (simultaneous switching) and maximum delay (evenly distributed switching) shown in the same graph. EMD2 behaves similarly to EMD1, with both the RMS current and the 16 kHz component increasing with maximum delay, indicating less sensitivity to simultaneous switching. All currents are measured on the DC side, but only the AC component is visible, as the Rogowski coil measures the AC component of the current.

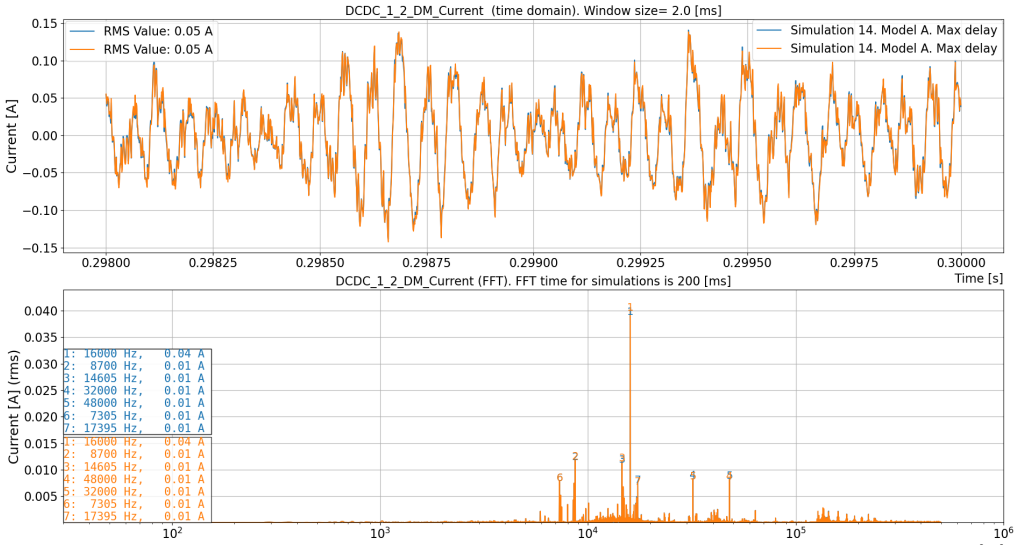


Figure 6.80: Differential-mode current in DCDC1 and DCDC2 from "Simulation 14, Model A" with maximum delay (evenly distributed switching) shown in the same graph. In contrast to Figure 6.74, the simulated currents in DCDC1 and DCDC2 are identical. All currents are measured on the DC side, but only the AC component is visible, as the Rogowski coil measures the AC component of the current.

The results presented in Figures 6.75 to 6.79 support the hypothesis that simultaneous switching of the EMDs increases the differential-mode (DM) current across all subsystems. However, a key discrepancy arises when comparing measurements and simulations of DCDC1 and DCDC2. As shown in Figure 6.74, the measured DM currents differ significantly between the two converters, despite their identical hardware and placement, due to load-dependent behaviour and individual load control. In contrast, the simulated results in Figure 6.80 show no such difference. This indicates that the simulation model does not capture the load-dependent behaviour observed in the physical system, highlighting a limitation in accurately replicating real-world load conditions.

Subsequently, the simulations are compared to the corresponding measurements to further validate the findings.

Conclusion

The simulation results confirm that simultaneous switching of the EMDs amplifies DM currents throughout the system, particularly at the 16 kHz, double switching frequency. Passive subsystems such as Battery 4 and DCDC2 exhibit the largest variations, while actively switching units like EMD1 and EMD2 are less affected. The discrepancy between simulated and measured currents in DCDC1 and DCDC2 underscores that Model A does not fully capture load-dependent current asymmetries. These limitations motivate the direct comparison between measurement and simulation presented in the following section.

6.5.4 Comparison of measurement and simulation for load condition 14 FM1156 SteadyState HighTorque FixGear

The results presented in Subsections 6.5.2 and 6.5.3 demonstrate a substantial difference in EMI currents between simultaneous and evenly distributed switching. The model described in Subsection 6.4.2 is referred to as **Model A**. The simulation of load condition 14 FM1156 SteadyState HighTorque FixGear is subsequently denoted as **Model A**14. Within this context, the scenarios involving simultaneous and distributed switching are hereafter referred to as **Model A**14 **min** and **Model A**14 **max**, respectively.

The following figures compare measurements and simulations for two switching scenarios: part 1 of the 14 FM1156 SteadyState HighTorque FixGear condition using **Model A**14 **min** (simultaneous switching), and part 5 using **Model A**14 **max** (distributed switching). These cases represent the extremes in EMI behaviour under steady-state conditions.

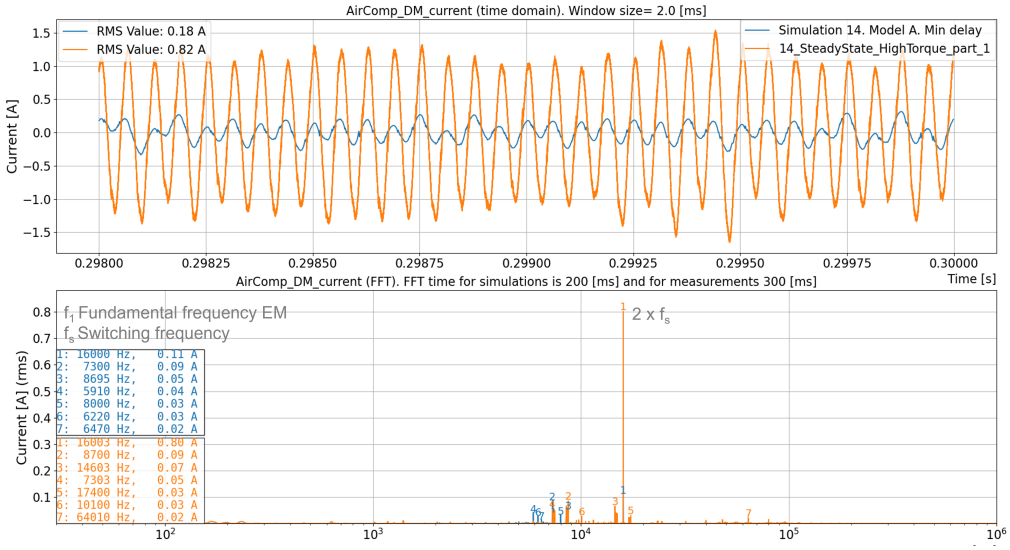


Figure 6.81: DM current in the Air Compressor from simulation (A14 min) and measurement (part 1). RMS and 16 kHz ($2f_s$) components differ substantially. All currents are measured on the DC side, but only the AC component is visible, as the Rogowski coil measures the AC component of the current.

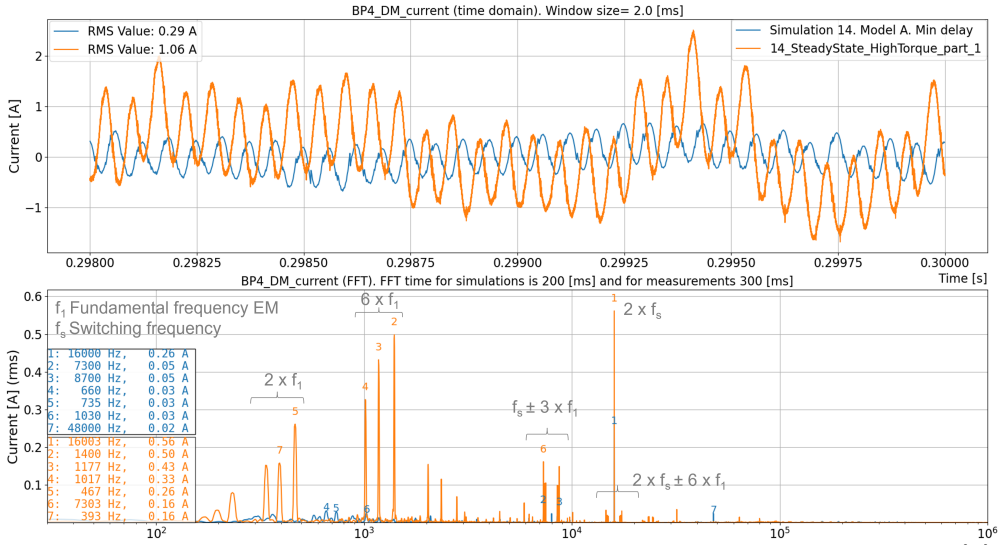


Figure 6.82: DM current in Battery 4 from simulation (A14 min) and measurement (part 1). RMS and 16 kHz differ; harmonics at $2 \times f_1$, $6 \times f_1$, and sidebands of f_s and $2 \times f_s$ are visible in the measurement. All currents are measured on the DC side, but only the AC component is visible, as the Rogowski coil measures the AC component of the current.

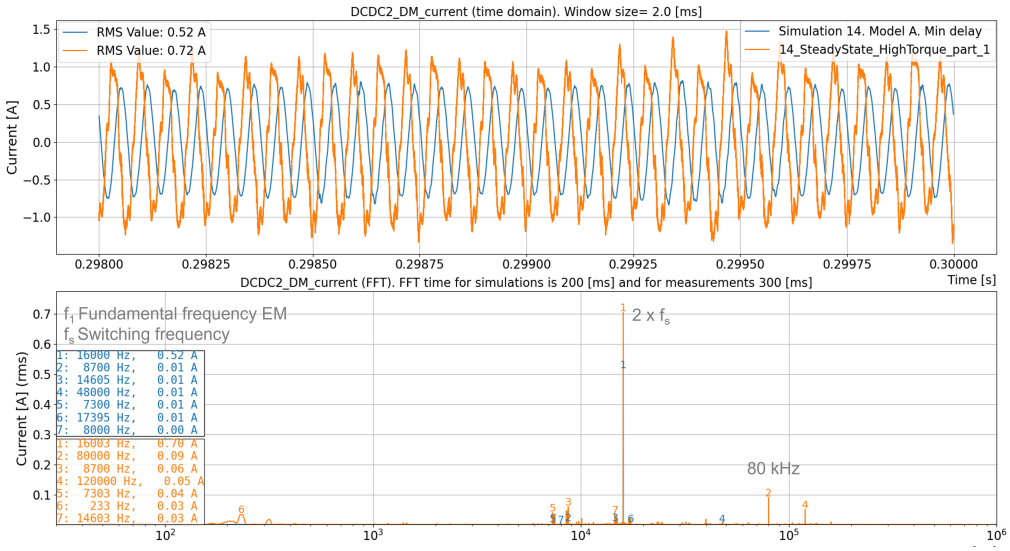


Figure 6.83: DM current in DCDC2 from simulation (A14 min) and measurement (part 1). RMS and 16 kHz show better agreement; an 80 kHz component appears only in the measurement. All currents are measured on the DC side, but only the AC component is visible, as the Rogowski coil measures the AC component of the current.

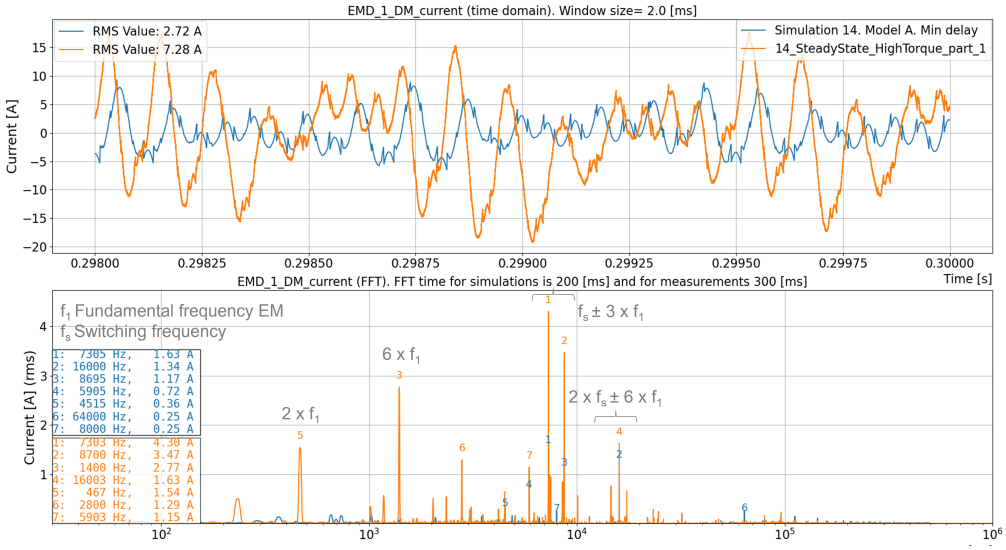


Figure 6.84: DM current in EMD1 from simulation (A14 min) and measurement (part 1). RMS and 16 kHz differ; harmonics at $2 \times f_1$ and $6 \times f_1$ are present in the measurement. All currents are measured on the DC side, but only the AC component is visible, as the Rogowski coil measures the AC component of the current.

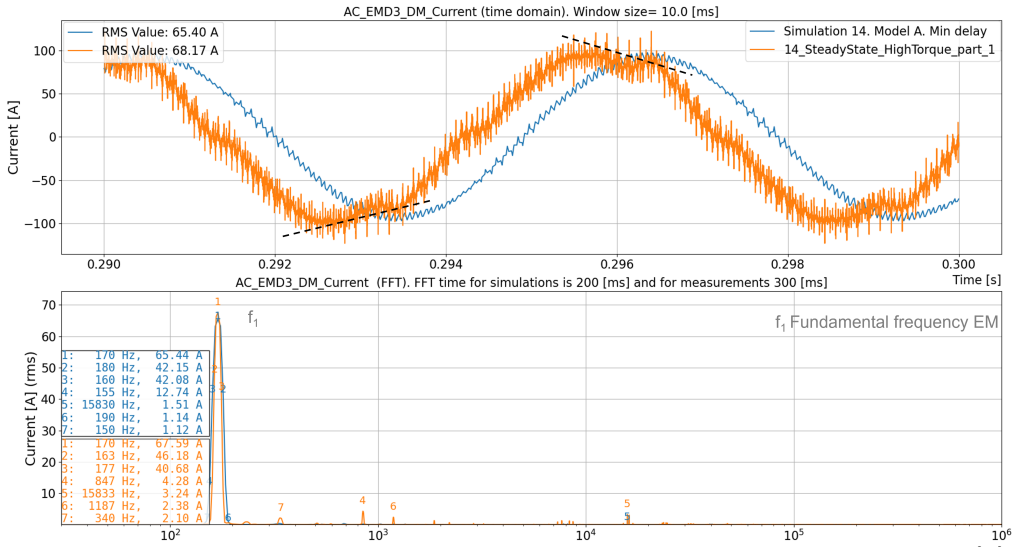


Figure 6.85: DM current to EM3 from EMD3, simulation (A14 min) and measurement (part 1). The measured waveform is distorted twice per period. All currents are measured on the AC side with a Rogowski coil.

To complement the previous results, the next set of figures compares part 5 with simulation model *A14 max*, representing the case with maximum delay and reduced EMI.

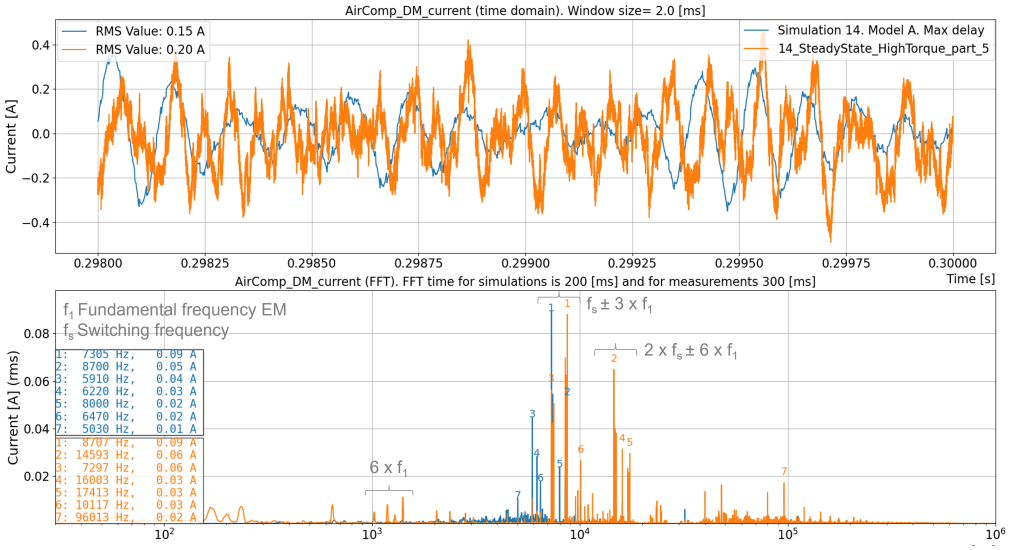


Figure 6.86: DM current in the Air Compressor from simulation (A14 max) and measurement (part 5). RMS matches better than in part 1, but FFT components differ. All currents are measured on the DC side, but only the AC component is visible, as the Rogowski coil measures the AC component of the current.

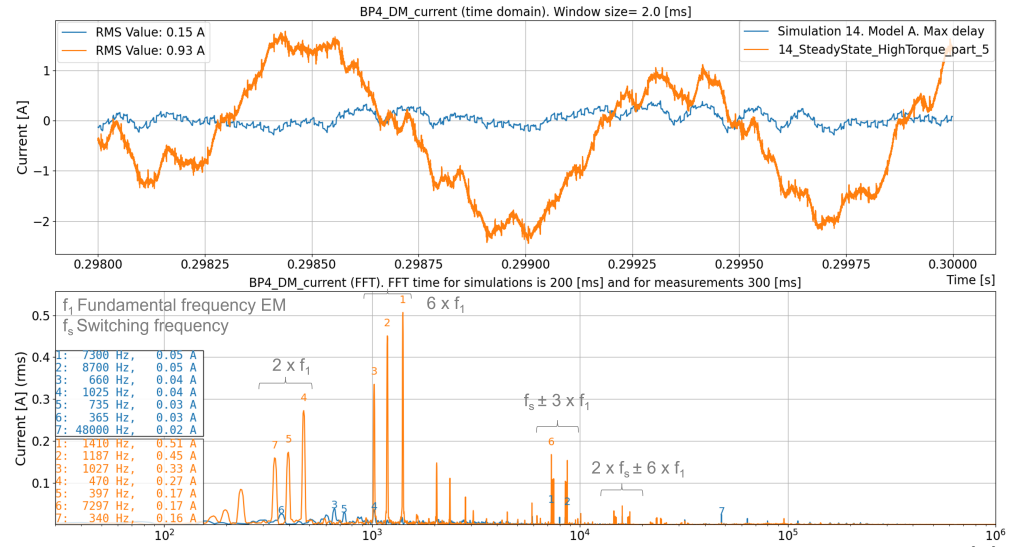


Figure 6.87: DM current in Battery 4 from simulation (A14 max) and measurement (part 5). RMS differs; harmonics and sidebands similar to part 1 are dominant. All currents are measured on the DC side, but only the AC component is visible, as the Rogowski coil measures the AC component of the current.

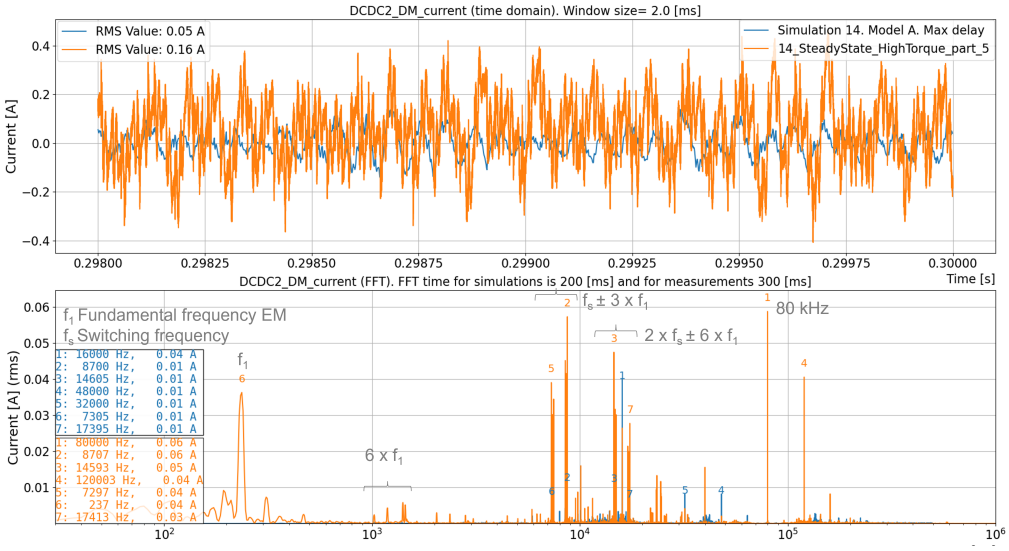


Figure 6.88: DM current in DCDC2 from simulation (A14 max) and measurement (part 5). An 80 kHz component appears only in the measurement. All currents are measured on the DC side, but only the AC component is visible, as the Rogowski coil measures the AC component of the current.

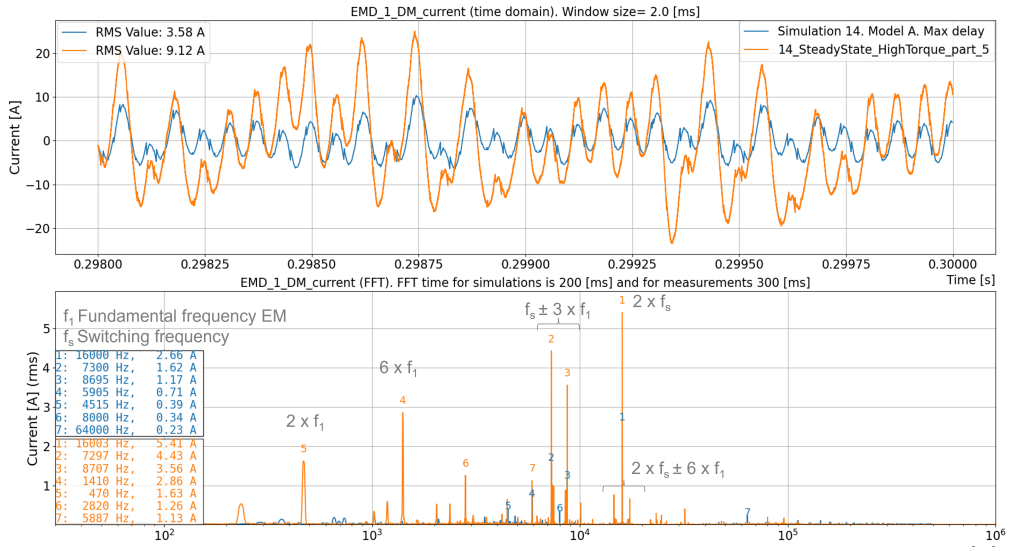


Figure 6.89: DM current in EMD1 from simulation (A14 max) and measurement (part 5). RMS and 16 kHz differ; harmonics at $2 \times f_1$ and $6 \times f_1$ are visible in the measurement. All currents are measured on the DC side, but only the AC component is visible, as the Rogowski coil measures the AC component of the current.

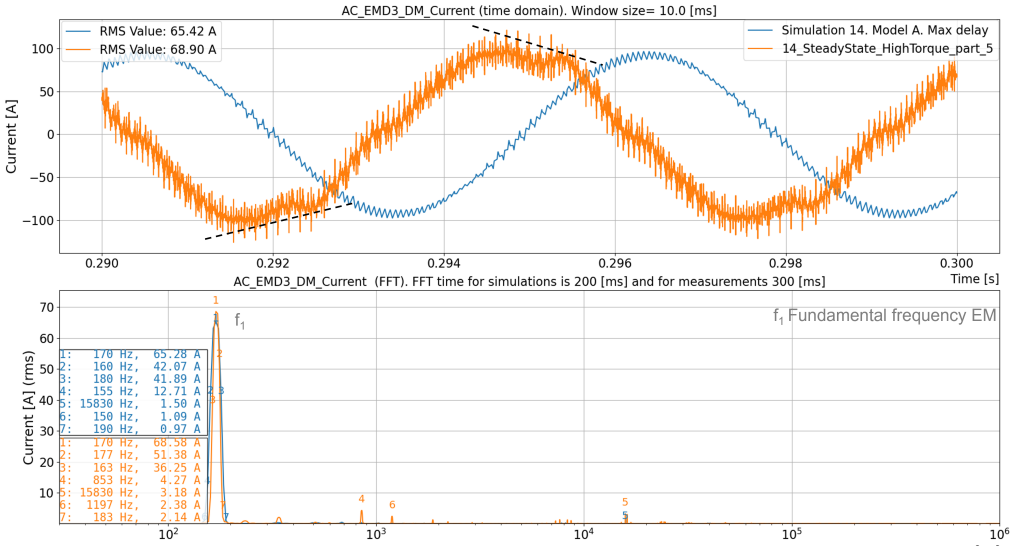


Figure 6.90: DM current to EM3 from EMD3, simulation (A14 max) and measurement (part 5). The measured waveform is distorted twice per period. All currents are measured on the AC side with a Rogowski coil.

Conclusion

The comparison between measurement and simulation for Load Condition 14 FM1156 SteadyState HighTorque FixGear reveals several key discrepancies:

- Missing harmonics at $2 \times f_1$ in the simulation, observed in Battery 4 for all three EM fundamental frequencies; see Figures 6.82 and 6.87.
- Missing harmonics at $6 \times f_1$ in the simulation, also visible in Battery 4 for all three EM fundamental frequencies; see Figures 6.82 and 6.87.
- Significant distortion in the measured AC current waveform compared to the simulated waveform, occurring twice per period; see Figures 6.85 and 6.90.

These differences are further investigated in the following section.

6.5.5 Analysis of discrepancies between simulation and measurement

In Subsection 6.5.4, a detailed harmonic analysis of the measured and simulated waveforms reveals notable discrepancies, particularly in the DC-link current. These deviations persist despite accurate modelling and parametrisation efforts, suggesting that certain physical phenomena may not be fully captured in the baseline simulation model. This section

investigates two potential sources of these discrepancies, each explored through a dedicated hypothesis and corresponding simulation model.

Hypothesis: inductance asymmetry and the second harmonic

The first hypothesis concerns the presence of the second harmonic of the fundamental frequency in the DC-link current. In an ideal three-phase converter-fed motor system, such harmonics are typically absent due to the symmetry of the electrical and magnetic circuits. However, slight asymmetries in the motor winding inductance, arising from manufacturing tolerances, magnetic saturation, or rotor geometry, may disrupt this symmetry. This distortion can produce a second-harmonic component, as described in [16].

To test this hypothesis, a modified motor model (hereafter referred to as **Model B**), based on Model A according to Figure 6.54, is introduced. This model incorporates an intentional inductance imbalance between the phases. The aim is to assess whether this asymmetry can account for the observed second harmonic in the measured DC-link current and improve the correlation between simulation and measurement.

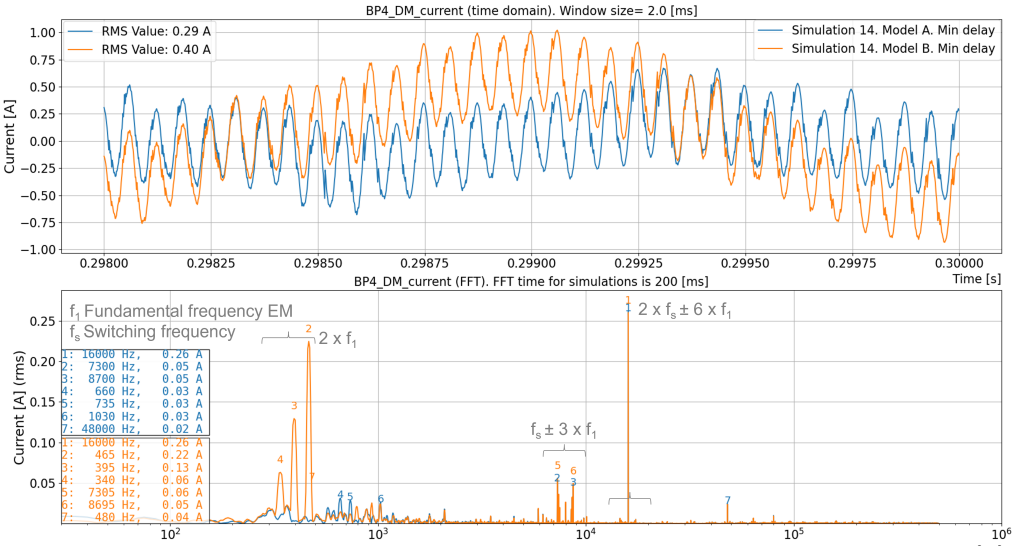


Figure 6.91: DM current in Battery 4 from simulations A14 and B14 min. The triplet at $2f_1$ is now observed in Model B, with asymmetric inductance added to one phase in the EM. This triplet arises from the contributions of MDS1-3 (Motor Drive System). All currents are measured on the DC side, but only the AC component is visible, as the Rogowski coil measures the AC component of the current.

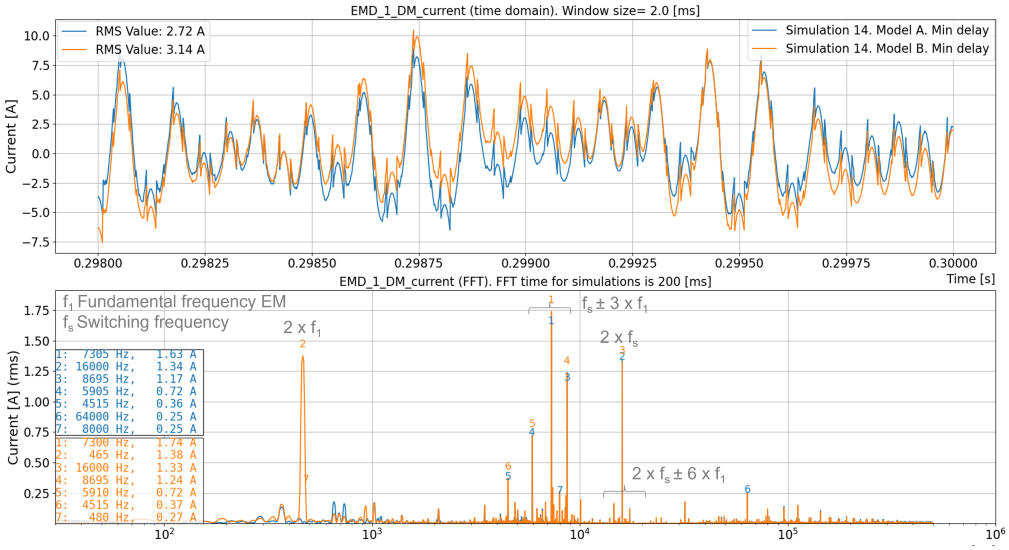


Figure 6.92: DM current in EMD1 from simulations A14 and B14 min. The component at $2f_1$ is now observed in Model B, with asymmetric inductance added to one phase in the EM. All currents are measured on the DC side, but only the AC component is visible, as the Rogowski coil measures the AC component of the current.

Conclusion

The results shown in Figures 6.91 and 6.92 confirm that the second harmonic of the fundamental frequency appears when inductance asymmetry is introduced in Model B. The hypothesis is therefore supported. However, while the qualitative trend aligns with the measurements, the magnitude and consistency across all load cases remain unverified and require further analysis.

Hypothesis: dead-time control and the sixth harmonic

The second hypothesis concerns the recurring presence of a sixth-harmonic component in the measured DC-link current. This phenomenon is rarely discussed in the literature for standard two-level converter topologies, yet it is clearly identifiable in the measurement data. It is hypothesised that the observed sixth harmonic in the DC-link current may be linked to the behaviour of the converter's dead-time control. Specifically, certain switching patterns associated with dead-time handling may introduce periodic disturbances in each phase during the electrical cycle. In a three-phase system, these disturbances can combine to form a sixth-harmonic component in the DC-link current. Additionally, such effects may contribute to distortion in the three-phase output currents.

The exact dead-time implementation in the commercial converter is proprietary and therefore not disclosed. To investigate this hypothesis, a modified dead-time strategy is implemented in simulation (referred to as **Model C**, with Model B as baseline; see Subsection 6.5.5). This model is designed to reflect modified control behaviour without revealing proprietary details. The results are analysed to determine whether the sixth harmonic can be reproduced and whether the modified strategy introduces the expected distortion patterns.

For reference, the baseline model (**Model B**) represents the dead-time control used in the standard simulation converter model. It does not exhibit the sixth harmonic in the DC-link current and therefore serves as the reference for evaluating Model C.

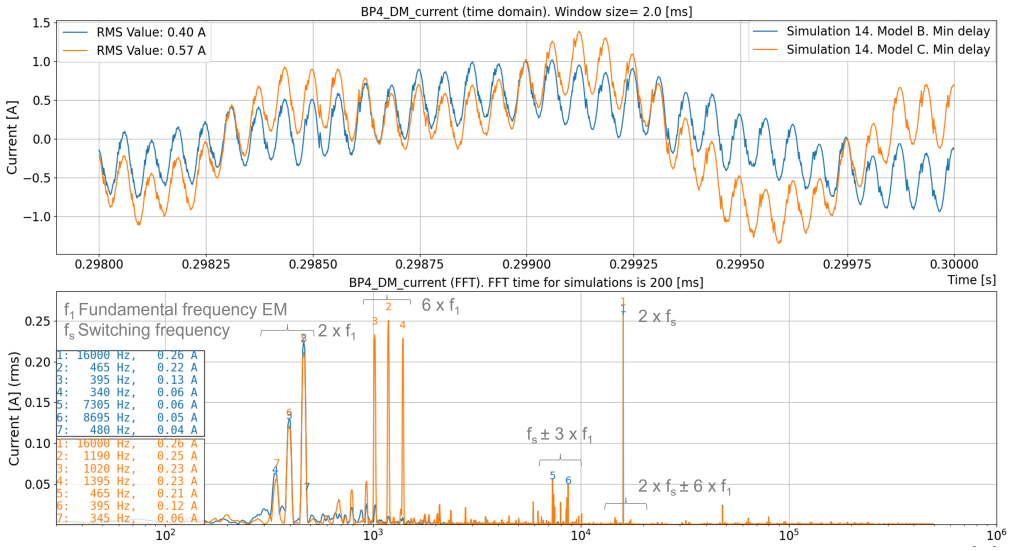


Figure 6.93: DM current in Battery 4 from simulations B14 and C14 min. The triplet at $6f_1$ is now observed in Model C, with modified dead-time control. This triplet arises from the contributions of MDS1-3 (Motor Drive System). All currents are measured on the DC side, but only the AC component is visible, as the Rogowski coil measures the AC component of the current.

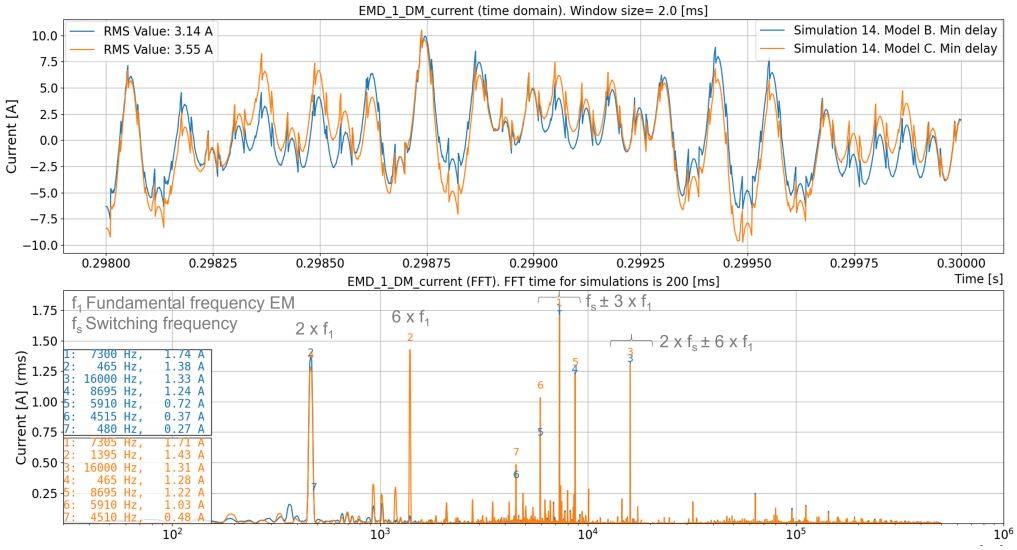


Figure 6.94: DM current in EMD1 from simulations B14 and C14 min. The $6f_1$ component is now observed in Model C, with modified dead-time control. All currents are measured on the DC side, but only the AC component is visible, as the Rogowski coil measures the AC component of the current.

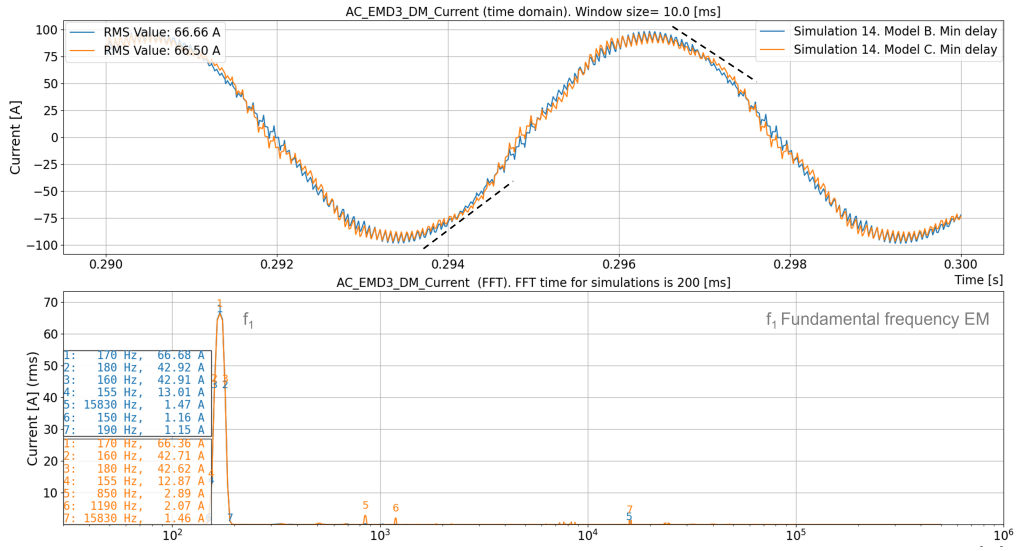


Figure 6.95: DM current to EM3 from EMD3, simulations B14 and C14 min. The measured waveform exhibits two distortions per period, but less than in Figure 6.90. This current is measured on the AC side, and the full waveform is visible.

Conclusion

In Figures 6.93 and 6.94, the sixth harmonic of the fundamental frequency is observed in Model C. In Figure 6.95, the three-phase current is distorted, although less than in Figure 6.90. The hypothesis regarding the impact of dead-time control on the sixth harmonic of the fundamental frequency is supported by the simulation results. However, while the trend in the simulation aligns with expectations, the magnitude and validation across all load cases are not confirmed.

Qualitative validation of simulation Model C against measurements

Recent simulations using Model C reveal trends that align with expected harmonic behaviour. Specifically, components at both the second and sixth harmonics of the fundamental frequency are observed. This section presents a qualitative comparison between the updated simulation Model C and measured waveforms, focusing on the presence and pattern of these harmonic components rather than exact magnitude matching.

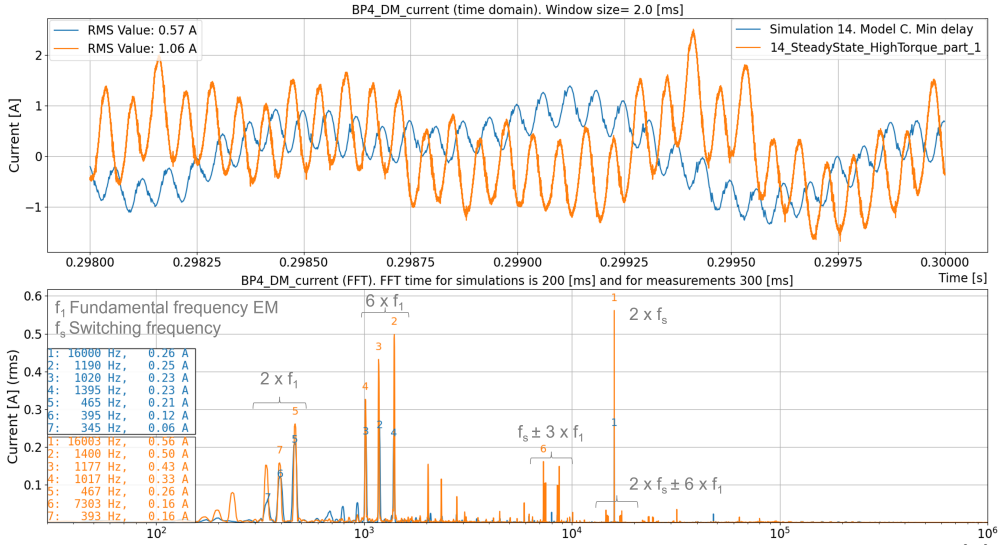


Figure 6.96: DM current in Battery 4 from simulation (C14 min) and measurement (part 1). The component at $2f_1$, resulting from the added asymmetry in the EM inductance, and the triplet at $6f_1$, observed as a result of the modified dead-time control, are both present in Model C. While the harmonic patterns are similar, the magnitude still differs between simulation and measurement. All currents are measured on the DC side, but only the AC component is visible, as the Rogowski coil measures the AC component of the current.

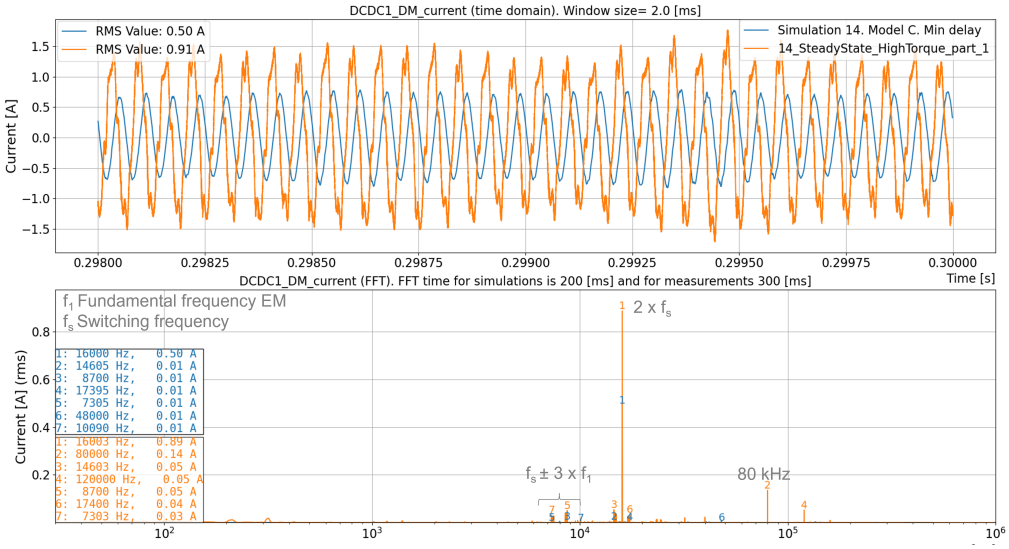


Figure 6.97: DM current in DCDC1 from simulation (C14 min) and measurement (part 1). A distinct 80 kHz component appears only in the measurement, indicating a phenomenon not captured by the simulation model. All currents are measured on the DC side, but only the AC component is visible, as the Rogowski coil measures the AC component of the current.

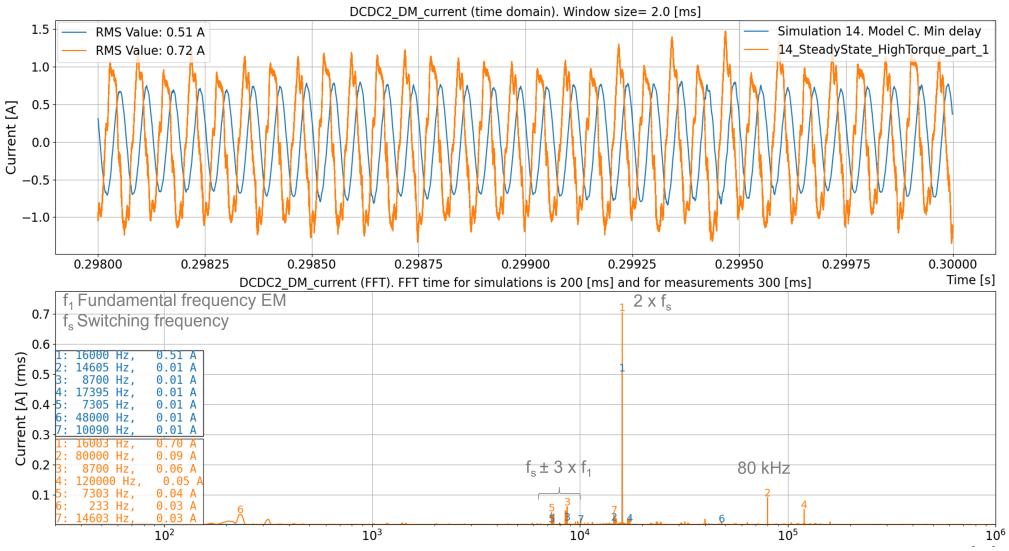


Figure 6.98: DM current in DCDC2 from simulation (C14 min) and measurement (part 1). In comparison to Figure 6.97, both simulations for DCDC1 and DCDC2 show similar values, whereas the measurements differ significantly. This highlights the challenge of accurately reflecting measured behaviour in the simulation. All currents are measured on the DC side, but only the AC component is visible, as the Rogowski coil measures the AC component of the current.

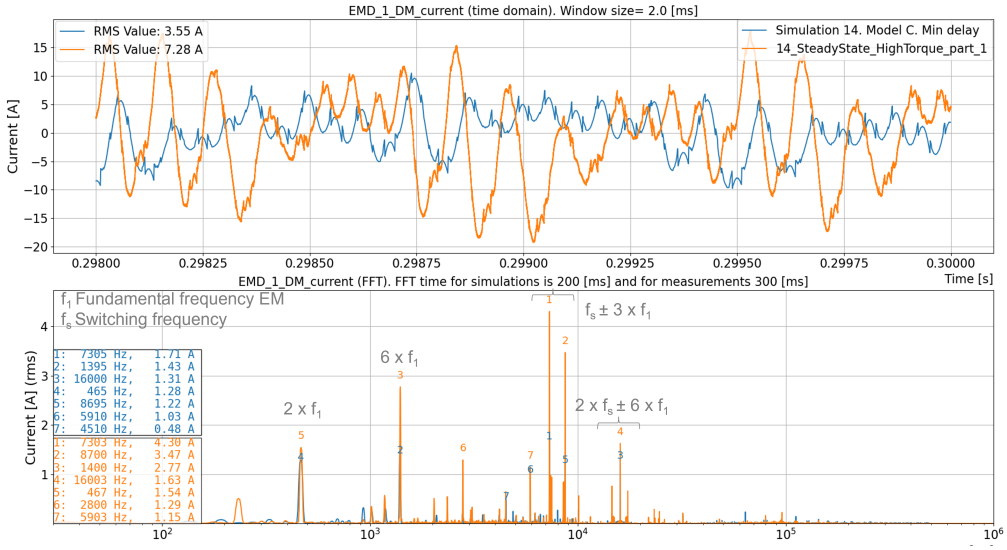


Figure 6.99: DM current in EMD1 from simulation (C14 min) and measurement (part 1). The component at $2f_1$, resulting from the added asymmetry in the EM inductance, and $6f_1$, observed as a result of the modified dead-time control, are both present in Model C. While the harmonic patterns are similar, the magnitude still differs between simulation and measurement. All currents are measured on the DC side, but only the AC component is visible, as the Rogowski coil measures the AC component of the current.

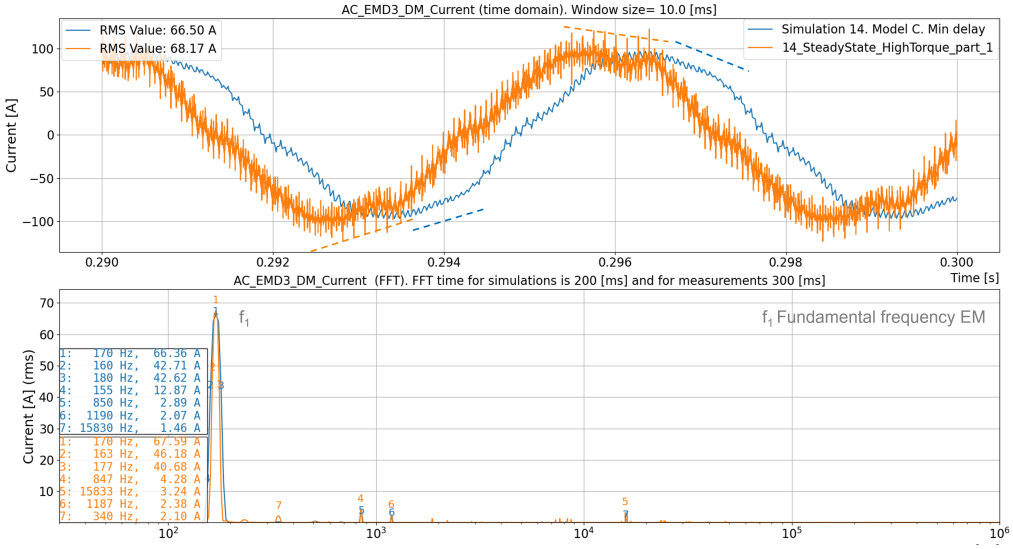


Figure 6.100: DM current to EM3 from EMD3 from simulation (C14 min) and measurement (part 1). The measured and simulated waveforms exhibit two distortions per period. FFT current components in simulation and measurement are similar. This current is measured on the AC side, and the full waveform is visible.

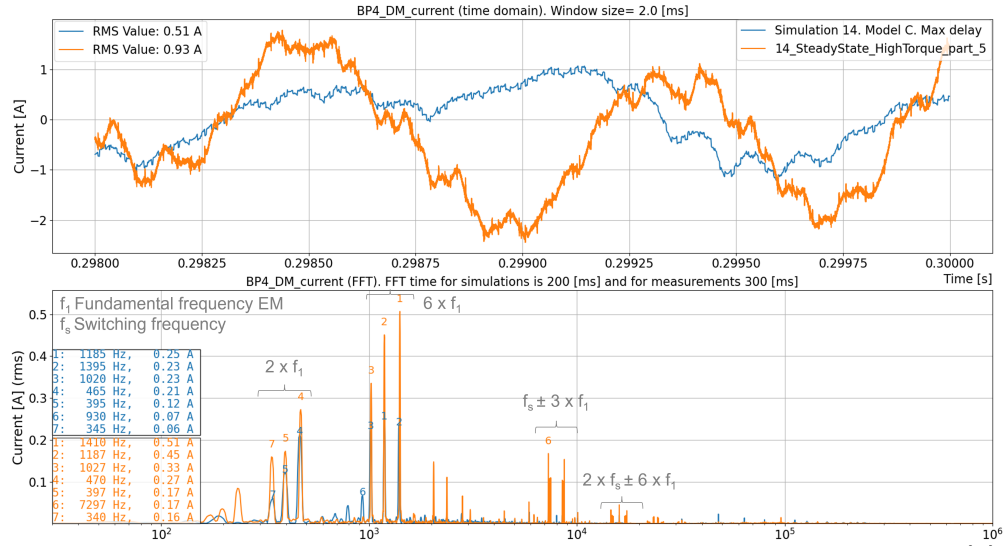


Figure 6.101: DM current in Battery 4 from simulation (C14 max) and measurement (part 5). The component at $2f_1$, resulting from the added asymmetry in the EM inductance, and the triplet at $6f_1$, observed as a result of the modified dead-time control, are both present in Model C. While the harmonic patterns are similar, the magnitude still differs between simulation and measurement. All currents are measured on the DC side, but only the AC component is visible, as the Rogowski coil measures the AC component of the current.

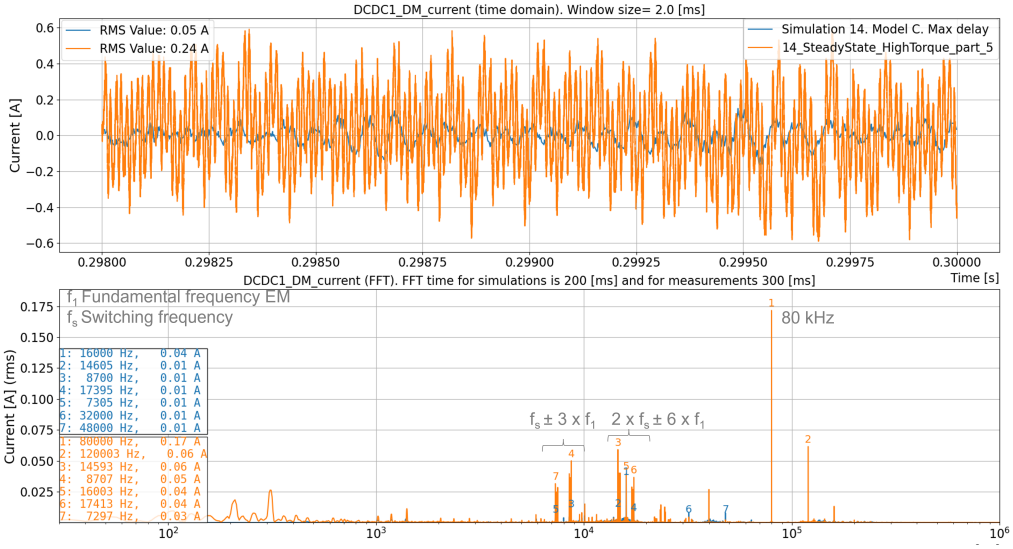


Figure 6.102: DM current in DCDC1 from simulation (C14 max) and measurement (part 5). A distinct 80 kHz component appears only in the measurement, indicating a phenomenon not captured by the simulation model. All currents are measured on the DC side, but only the AC component is visible, as the Rogowski coil measures the AC component of the current.



Figure 6.103: DM current in DCDC2 from simulation (C14 max) and measurement (part 5). The simulation shows similar values to DCDC1, while the measurement differs, indicating variation not captured by the model. All currents are measured on the DC side, but only the AC component is visible, as the Rogowski coil measures the AC component of the current.

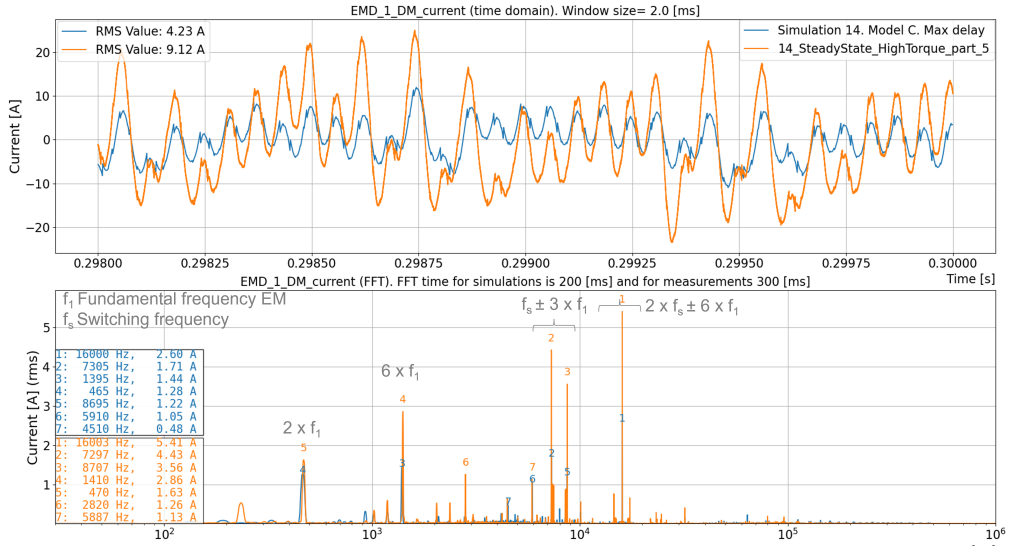


Figure 6.104: DM current in EMD1 from simulation (C14 max) and measurement (part 5). The component at $2f_1$, resulting from the added asymmetry in the EM inductance, and $6f_1$, observed as a result of the modified dead-time control, are both present in Model C. While the harmonic patterns are similar, the magnitude still differs between simulation and measurement. All currents are measured on the DC side, but only the AC component is visible, as the Rogowski coil measures the AC component of the current.

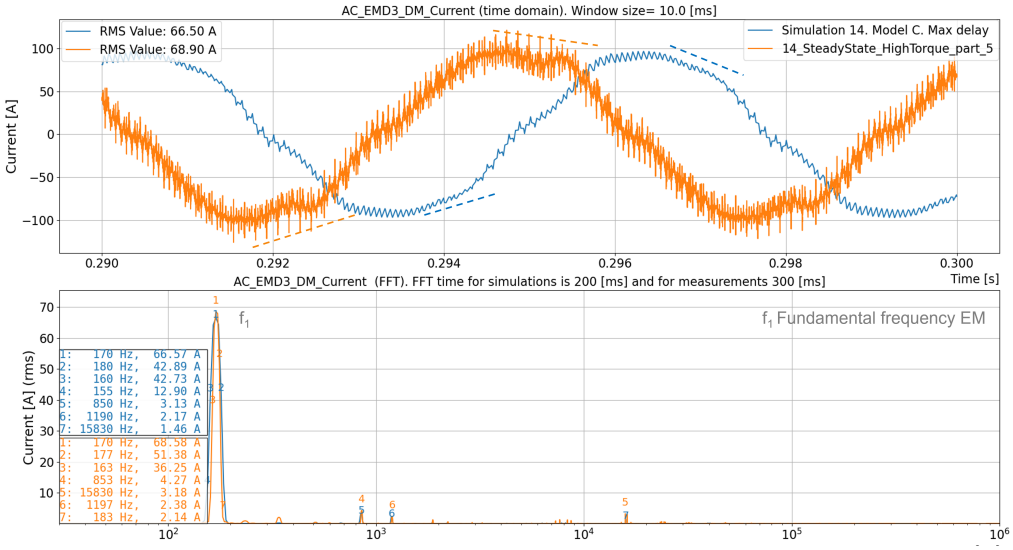


Figure 6.105: DM current to EM3 from EMD3 from simulation (C14 max) and measurement (part 5). The measured and simulated waveforms exhibit two distortions per period. FFT current components in simulation and measurement are qualitatively similar. This current is measured on the AC side, and the full waveform is visible.

Conclusion

The introduction of asymmetric EM inductance and modified dead-time control results in FFT components in the simulation that exhibit similar trends to those observed in the measurements. However, noticeable differences in amplitude remain.

These results confirm that combining inductance asymmetry and modified dead-time control improves the qualitative agreement between simulation and measurement. Nevertheless, quantitative discrepancies remain, particularly in amplitude, motivating further investigation.

To further investigate these amplitude discrepancies, a sensitivity analysis is presented in the following section.

Sensitivity analysis of the simulation model following the removal of Break Out Boxes

Break Out Boxes (BoBs) are integrated into the truck's wiring to facilitate measurements. The impedance of the BoBs is modelled and incorporated into simulation models A–C. The vehicle's orange cable system, including junction boxes, exhibits low inductance, making it highly sensitive to small changes that can cause substantial variations in current.

The following sensitivity analysis compares models C14 and E14 with measurements, where BoBs are removed in E14.

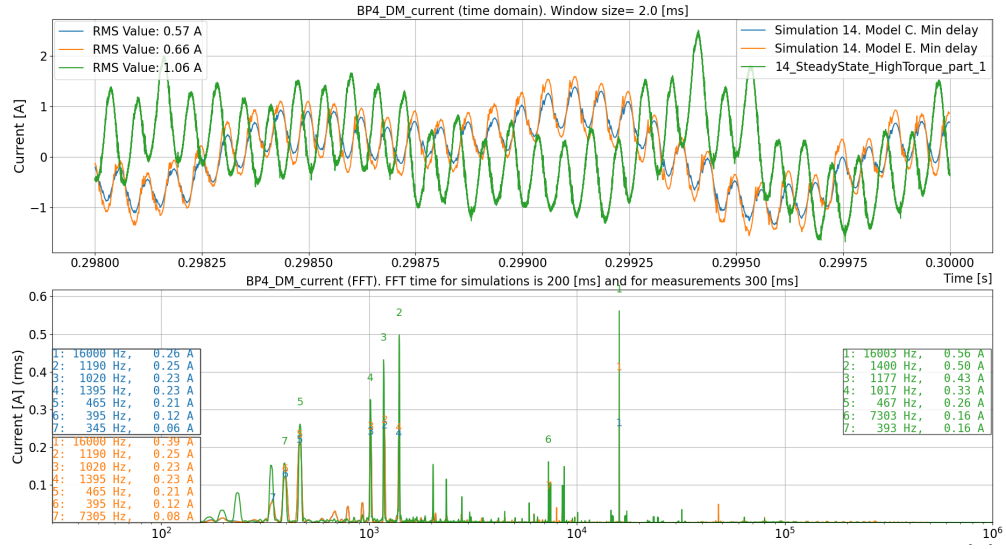


Figure 6.106: DM current in Battery 4 from simulations (C14 and E14 min) and measurement (14 part 1). Model E shows an increase in EMI current when the BoB and corresponding cables are removed. This increase is more pronounced at higher frequencies. The RMS current in simulation model E14 remains lower than the measured values. All currents are measured on the DC side, but only the AC component is visible, as measured by the Rogowski coil.

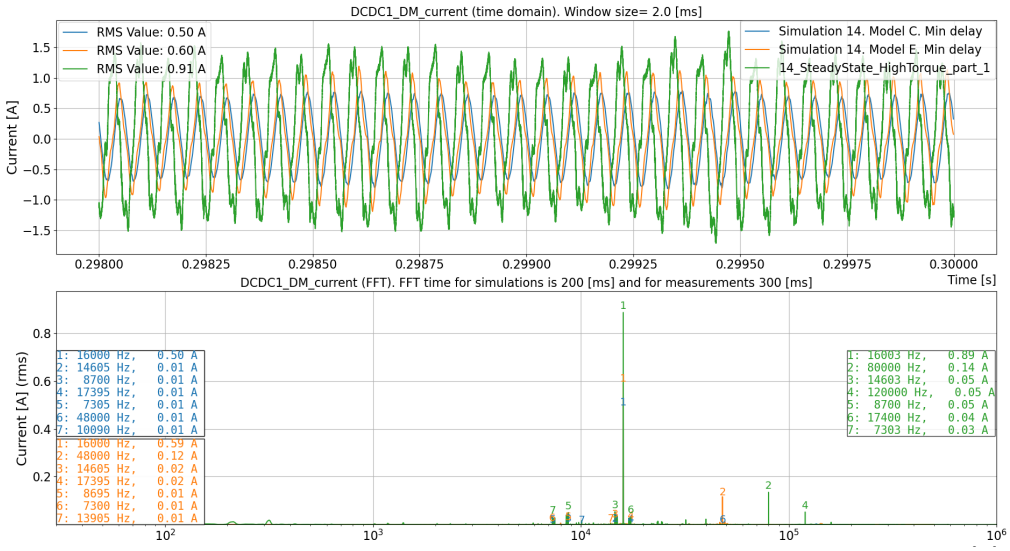


Figure 6.107: DM current in DCDC1 from simulations (C14 and E14 min) and measurement (14 part 1). A similar trend to BP4 is observed, where the RMS current in E14 remains lower than the measured values. All currents are measured on the DC side, but only the AC component is visible.

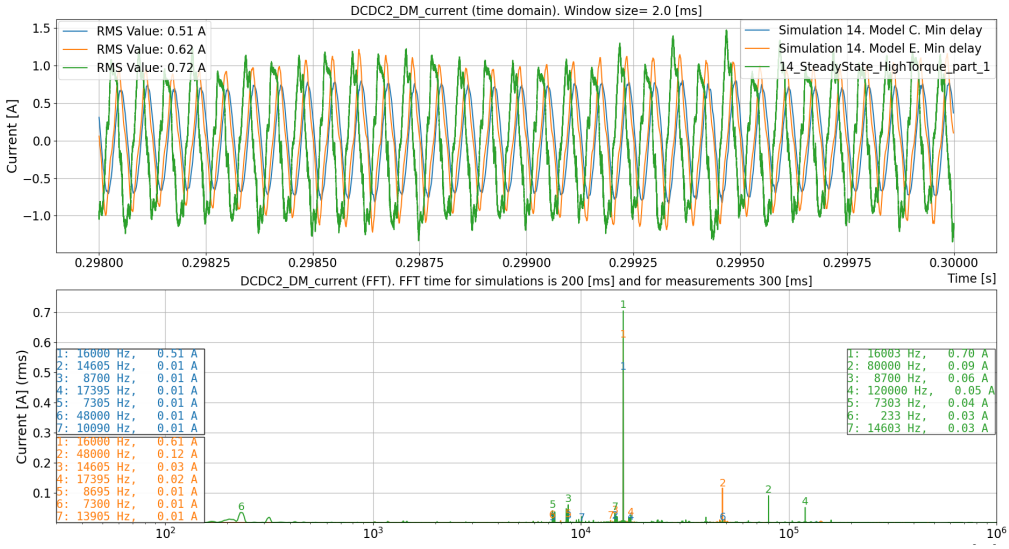


Figure 6.108: DM current in DCDC2 from simulations (C14 and E14 min) and measurement (14 part 1). The E14 simulations more closely resemble the RMS current observed in measurements. All currents are measured on the DC side, but only the AC component is visible.

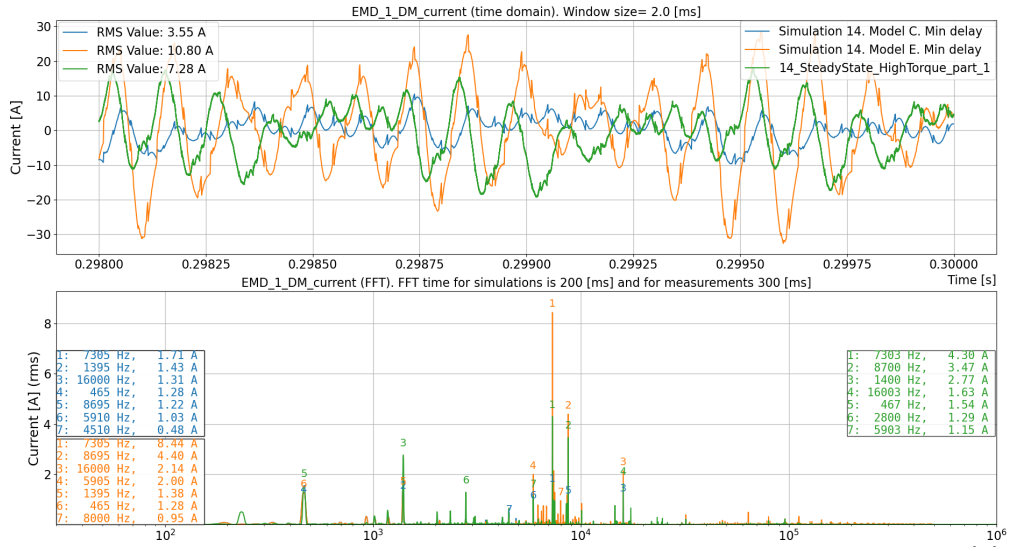


Figure 6.109: DM current in EMD1 from simulations (C14 and E14 min) and measurement (14 part 1). Model E shows a substantial increase in EMI current, more pronounced at higher frequencies. The RMS current increases threefold when the BoB is removed, raising concerns about the validity of measurements performed with such devices. The simulation E14 shows higher currents than measurements. All currents are measured on the DC side, but only the AC component is visible.

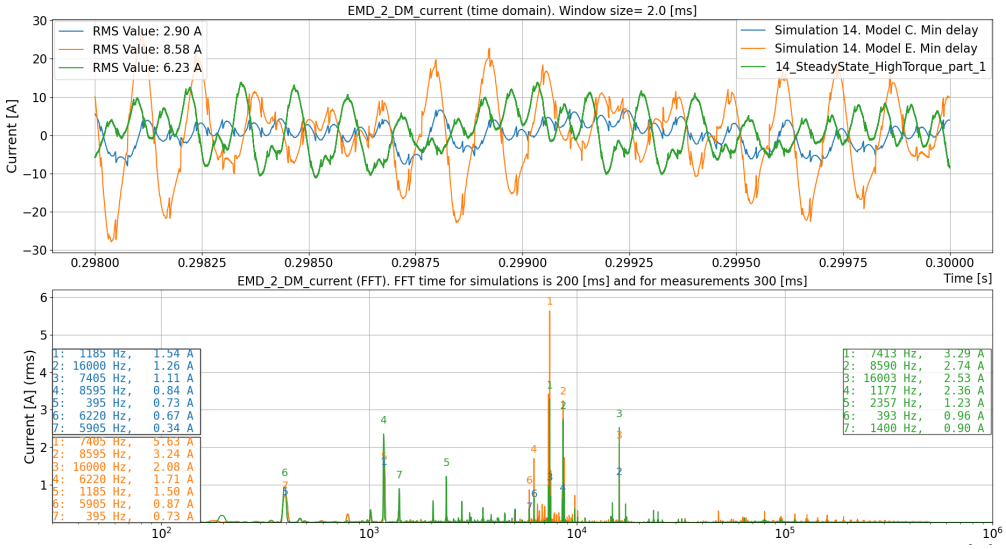


Figure 6.110: DM current in EMD2 from simulations (C14 and E14 min) and measurement (14 part 1). Model E shows a substantial increase in EMI current, especially at higher frequencies. The RMS current increases threefold when the BoB is removed. Simulation E14 shows higher currents than measurements. All currents are measured on the DC side, but only the AC component is visible.

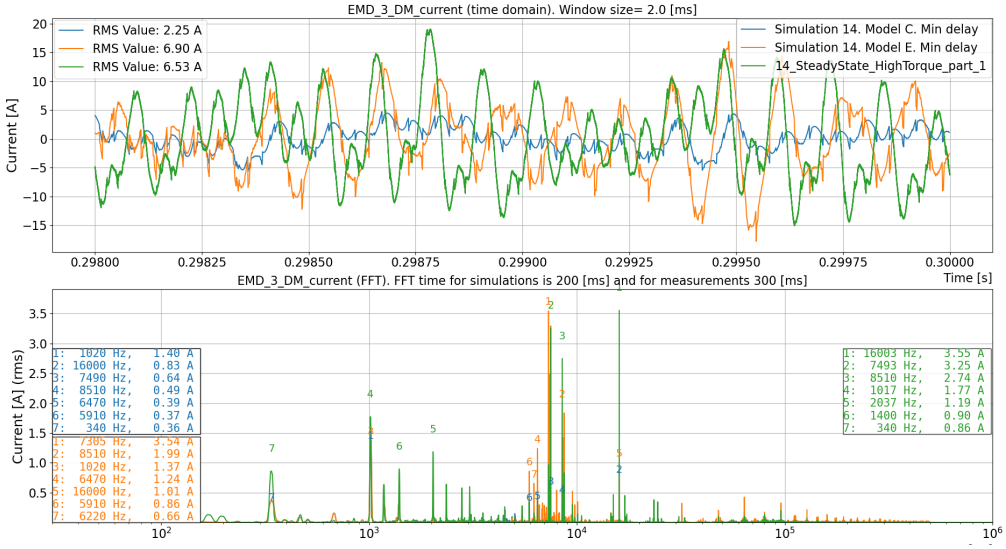


Figure 6.111: DM current in EMD3 from simulations (C14 and E14 min) and measurement (14 part 1). Model E shows a substantial increase in EMI current, particularly at higher frequencies. The RMS current increases threefold when the BoB is removed. Simulation E14 shows higher currents than measurements. All currents are measured on the DC side, but only the AC component is visible.

Conclusion

Removing the Break Out Boxes significantly increases EMI currents across all subsystems. The increase becomes more pronounced with frequency, and in several cases the simulated currents exceed measured values. This demonstrates that measurement equipment can suppress the true EMI behaviour of the system. While qualitative trends agree with measurements, amplitudes derived from measurement data underestimate actual EMI levels.

6.5.6 Conclusion

The system is highly sensitive to changes in impedance, as illustrated in Figures 6.106 to 6.111. While simulations do not replicate the absolute values observed in measurements, the overall trends remain consistent. For instance, the synchronisation or separation of switching events clearly influences the $n \cdot f_s$ components, which increase or decrease accordingly.

Measurement results may underestimate the system's true behaviour, as the presence of measurement equipment can suppress EMI effects. Simulations conducted without the Break Out Box (BoB) and associated cables reveal significantly higher EMI currents, suggesting that actual system performance may be worse than indicated by measurements.

Removing the Break Out Box (BoB) and its associated cables in simulations leads to a substantial increase in EMI currents—greater than the discrepancy observed between simulation and measurement results. This indicates that the presence of this measurement equipment may mask the system's true behaviour.

These findings underscore the need for robust EMI mitigation strategies that are resilient to variations in system layout and measurement setup. By understanding how test equipment influences observed behaviour, future designs can more accurately reflect the system's true electromagnetic performance.

The preceding analyses support the following key findings:

- Inductance asymmetry contributes to the emergence of the second harmonic in the DC-link current, as demonstrated by Model B.
- Modified dead-time control influences the sixth harmonic, improving alignment between simulation and measurement, as demonstrated in Model C.
- Model C, which combines both effects, qualitatively reproduces the harmonic patterns observed in measurements, although amplitude discrepancies remain.
- The presence of measurement equipment, such as Break Out Boxes and cables, significantly affects observed EMI behaviour, potentially masking the true system response.

Together, these findings highlight the limitations of conventional simulation models and measurement setups and underscore the need for refined modelling and robust EMI mitigation strategies.

The following section presents EMI mitigation strategies using differential-mode filtering.

6.6 EMI mitigation with differential-mode filters

The preceding analysis highlights the impact of measurement equipment and system impedance on the observed EMI behaviour. This section addresses these challenges by exploring mitigation strategies based on differential-mode (DM) filtering. The objective is to reduce EMI currents in a manner that is robust against variations in cable length, junction box configuration, and test setup, thereby improving the electromagnetic compatibility of the system under realistic operating conditions.

This section does not seek to define specific filter designs, but instead demonstrates that the presence of DM filters substantially reduces EMI levels. The examples presented here underscore the importance of requiring DM filters in subsystems, particularly in large commercial vehicles where system layout and cable routing vary widely. The design of the filters remains the responsibility of the subsystem supplier, but the results support the adoption of DM filtering as a system-level requirement.

The remainder of this section is structured as follows:

Subsection 6.6.1 Introduces DM filters, outlines their operating principles, and demonstrates how they influence EMI currents through impedance shaping.

Subsection 6.6.2 Examines how DM filtering shifts and damps subsystem resonance points, reducing sensitivity to switching-frequency variation.

Subsection 6.6.3 Evaluates the sensitivity of EMI behaviour to cable length and junction-box configuration, both with and without DM filters applied.

6.6.1 Introduction of differential-mode (DM) filters and their effect on EMI currents

In these simulations, parallel damped filters are adopted in each subsystem, with configurations tailored to the specific characteristics of each subsystem. The filters implemented here are solely intended for immunity purposes, not for emission suppression. Suppliers shall, of course, implement emission filters as well. A generic undamped and parallel damped filter is shown in Figure 6.112 [23].

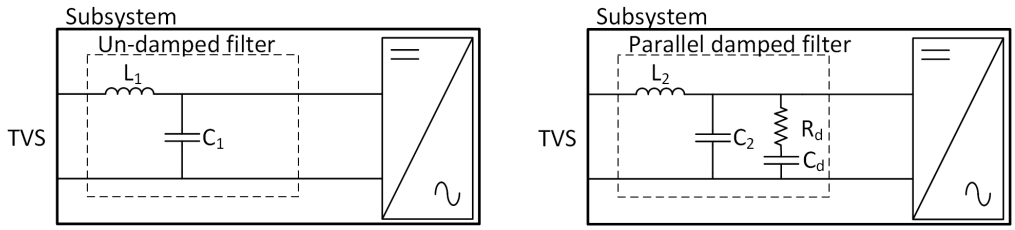


Figure 6.112: Undamped and parallel damped filter within a subsystem.

The resonance frequency f_0 for the undamped filter in Figure 6.112 is:

$$f_0 = \frac{1}{2\pi\sqrt{L_1 C_1}} \tag{6.16}$$

The resonance frequency f_0 for the damped filter in Figure 6.112 is set to 2 kHz for illustrative purposes. The original filter $L_1 C_1$ is replaced by $L_2 C_2$ to achieve a resonance frequency f_2 of 2 kHz. The damping resistor R_d and damping capacitor C_d are, according to [23]:

$$f_2 = \frac{1}{2\pi\sqrt{L_2 C_2}} \tag{6.17}$$

$$R_d = \sqrt{\frac{L_2}{C_2}} \tag{6.18}$$

$$C_d = 4C_2 \tag{6.19}$$

To illustrate the improvements, two subsystems — DCDC and OCEPS (Onboard Charger and Electrical Power Supply) — are presented in Figures 6.113 and 6.114, along with their impedance versus frequency responses. These highlight the resonance points for the original DM filter and a damped DM filter with a cut-off frequency of 2 kHz for the lowest resonance point.

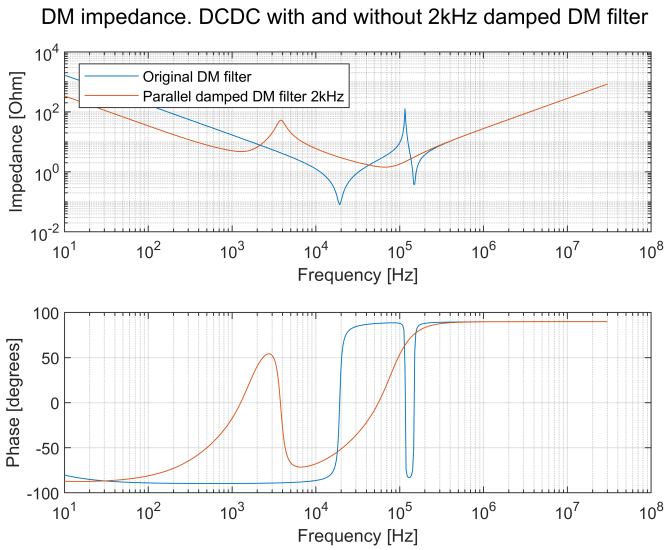


Figure 6.113: The original DM filter in the DCDC (blue) and a parallel damped filter with a cut-off at 2 kHz and another at 95 kHz (red). The resonance at 19.2 kHz is damped to 2 kHz, and the 150 kHz resonance is damped to 95 kHz.

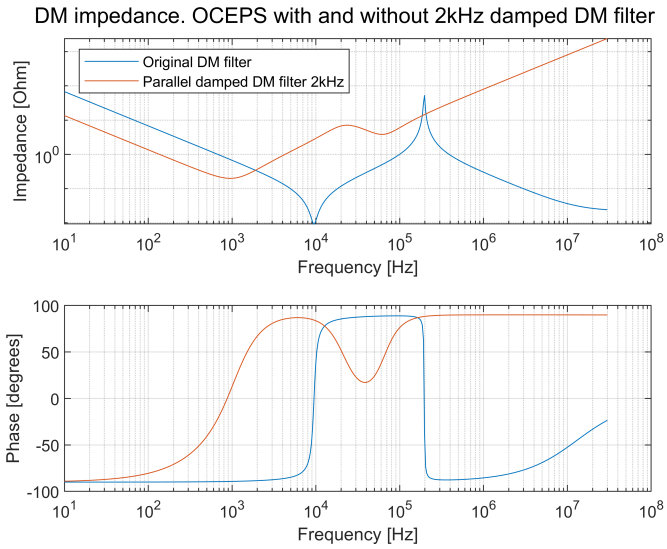


Figure 6.114: The original DM filter in the OCEPS (blue) and a parallel damped filter with a cut-off at 2 kHz and another at 60 kHz (red). The resonance at 9.7 kHz is damped to 2 kHz, and the anti-resonance at 150 kHz remains damped.

It is evident for both the DCDC and OCEPS subsystems that the resonance is shifted and damped to 2 kHz. Additionally, the overall impedance above 2 kHz increases. As previously mentioned, the filter design used here is intentionally simple and serves only to

illustrate the general effect. No further optimisation is carried out, nor is the filter intended to suppress emissions — its sole purpose is to demonstrate the impact on immunity.

A comparison between the following configurations:

- Model C: used as the baseline. Includes the Break Out Box (BoB) and its associated cables, the introduced inductance asymmetry, and the modified dead-time control.
- Model H: identical to Model C, but equipped with damped filters at 2 kHz.

is shown in Figures 6.115 and 6.116 for both simultaneous and distributed (min/max) switching. Although the individual details in each graph may appear visually dense, the primary purpose is not to highlight fine distinctions but to illustrate the overall progression from a poor operating condition to a significantly improved one. In this context, the graphical representation communicates the improvement more effectively than a detailed verbal explanation.

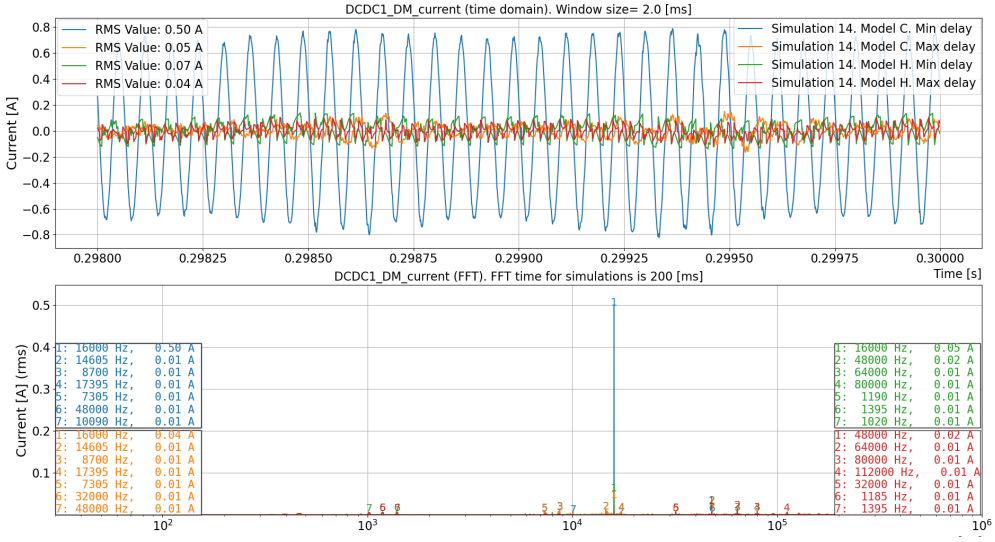


Figure 6.115: DM current in DCDC1 from simulations (C14 min/max and H14 min/max). In terms of RMS current, the reduction with the DM filter (Model C min to Model H min) is comparable to that achieved through distributed switching (Model C min to max). The further reduction from Model H min to max is 50 %, although the initial level is already low.

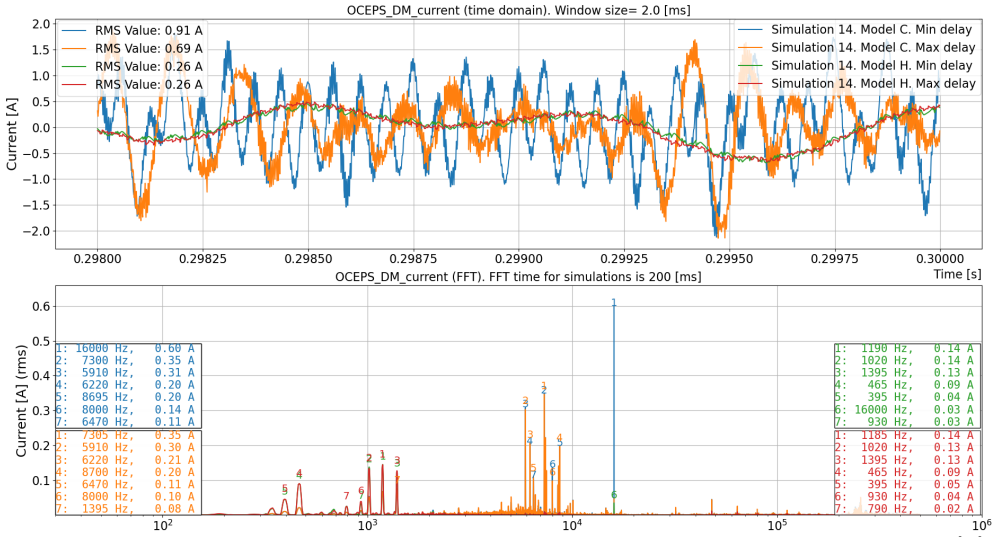


Figure 6.116: DM current in OCEPS from simulations (C14 min/max and H14 min/max). The RMS current reduction with the DM filter (Model C min to Model H min) is greater than that from distributed switching (Model C min to max). No further reduction is observed from Model H min to max.

The high-power subsystems such as the batteries and EMD cannot feasibly incorporate DM filters due to their high rated currents. **NB!** Model H therefore lacks DM filters in the EMD and battery subsystems, but includes them in all other subsystems.

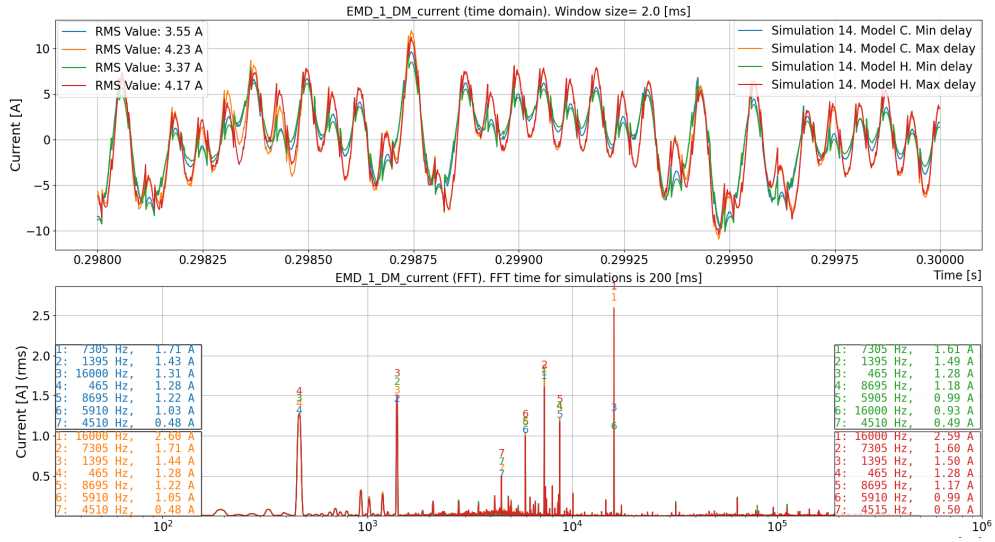


Figure 6.117: DM current in EMD1 from simulations (C14 min/max and H14 min/max). The RMS current remains unchanged as no filtering is applied in the EMD.

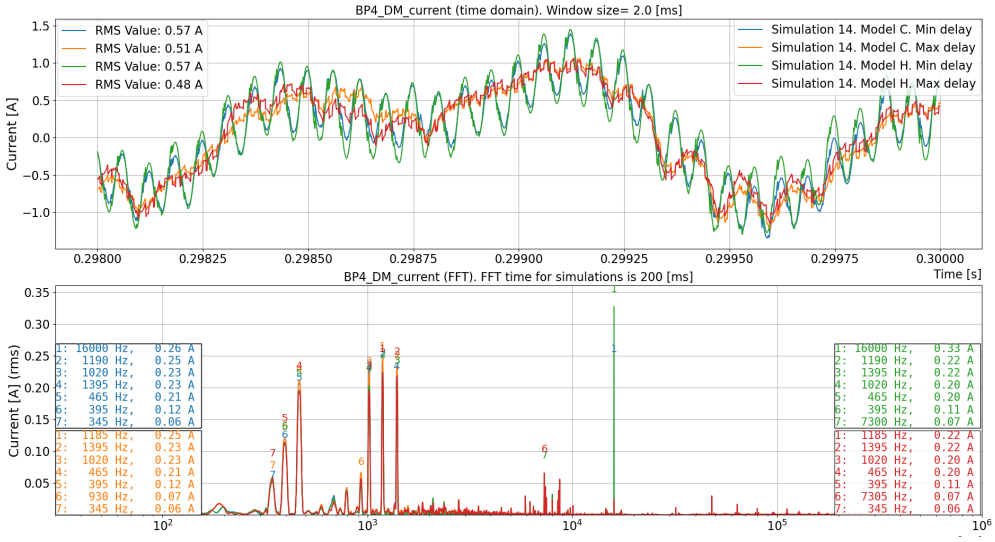


Figure 6.118: DM current in BP4 from simulations (C14 min/max and H14 min/max). The RMS current remains unchanged as no filtering is applied in the BP subsystem.

Conclusion

For the DCDC subsystem, the DM filter results in an EMI reduction comparable to that achieved through distributed switching. When both techniques are combined, EMI is further reduced, although the incremental improvement from distributed switching is relatively small. In the OCEPS subsystem, the DM filter alone achieves a greater reduction than distributed switching, lowering EMI to 30 % compared to 75 %. This indicates that the DM filter provides a significantly more effective means of EMI reduction.

Moreover, implementing distributed switching in the EMDs would require coordination between units, which may not be feasible for the supplier. No reduction in EMI currents is observed in the EMD, as no DM filter is applied. The battery remains exposed to emissions from the EMD; however, according to [2], AC harmonics do not adversely affect capacity fade or power fade.

6.6.2 Analysis of how DM filtering influences the system's resonance point

The switching frequency $2f_s$ from a three-phase converter typically appears as $2f_s$ on the DC side. In the nominal case, the switching frequency f_s is 8 kHz, resulting in a 16 kHz component on the DC side. Suppose the EMD supplier modifies the switching frequency to 4.85 kHz without a DM filter. As shown in Figure 6.114, the resonance point of the

OCEPS subsystem without DM filtering is 9.7 kHz, almost exactly twice the new switching frequency.

In Figure 6.119, two new models are introduced: Model J, which is identical to Model C but with the switching frequency changed to 4.85 kHz, and Model K, which adds damped DM filters.

- Model J: identical to Model C, but with the switching frequency changed from 8 kHz to 4.85 kHz.
- Model K: identical to Model J, but with added DM filters.

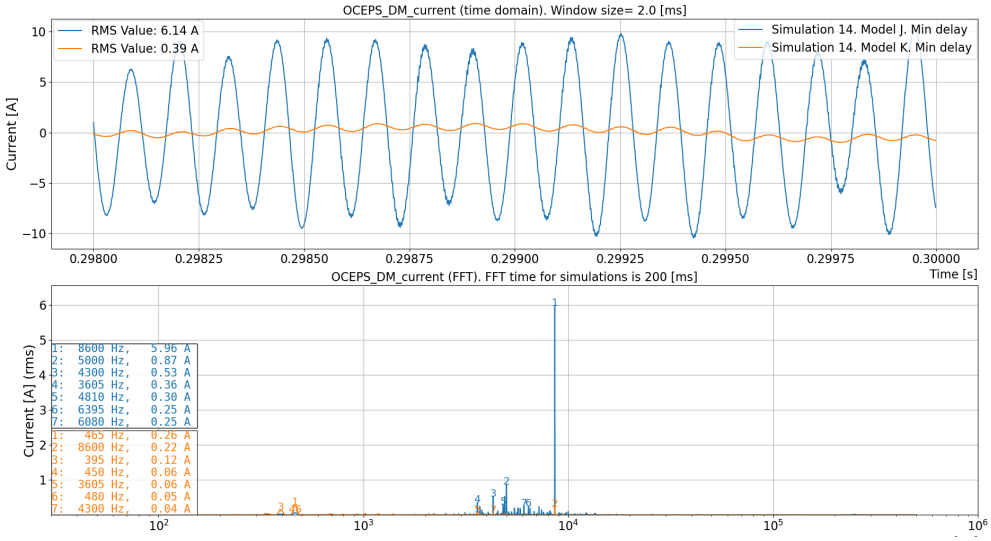


Figure 6.119: DM current in OCEPS from simulation (J14 min and K14 min). The doubled switching frequency coincides with the resonant frequency in the OCEPS, potentially stressing or damaging the DC-link capacitor. The RMS current is substantially reduced when comparing Model K to Model H. All currents are measured on the DC side, but only the AC component is visible, as the Rogowski coil measures AC current.

Conclusion

No further examples are required, as the necessity of the DM filter is evident. The DM filter protects the subsystem against switching-frequency variation by shifting and damping resonance points, thereby supporting its suitability as a platform-level solution.

6.6.3 Sensitivity analysis for cable length and junction box configuration

In the previous section, it was demonstrated that removing the Break Out Box (BoB) and its associated cables in simulations results in a substantial increase in EMI currents, exceeding

the discrepancy observed between simulation and measurement results. This indicates that the presence of measurement equipment may obscure the system's actual behaviour.

The following four models are evaluated in Figures 6.120 to 6.124:

- Model C: used as the baseline. Includes the Break Out Box (BoB) and its associated cables, the introduced inductance asymmetry, and the modified dead-time control.
- Model E: identical to Model C, but without the BoB and its associated cables.
- Model H: identical to Model C, but equipped with damped filters at 2 kHz.
- Model I: identical to Model C, but without the BoB and its associated cables, and equipped with damped filters at 2 kHz.

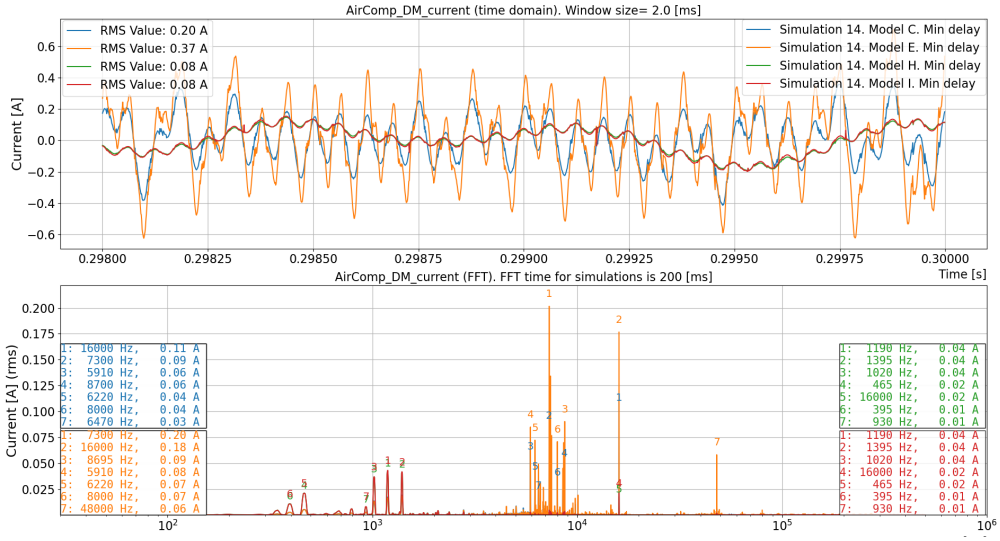


Figure 6.120: DM current in the Air Compressor from simulation (C14 min, E14 min, H14 min, and I14 min). The RMS current increases by 85 % when removing the BoB and its associated cables (Model C to Model E). Adding the DM filter (Model C to Model H) reduces the RMS current to 40 %. No change in current is observed when removing the BoB and its associated cables from Model H to Model I.

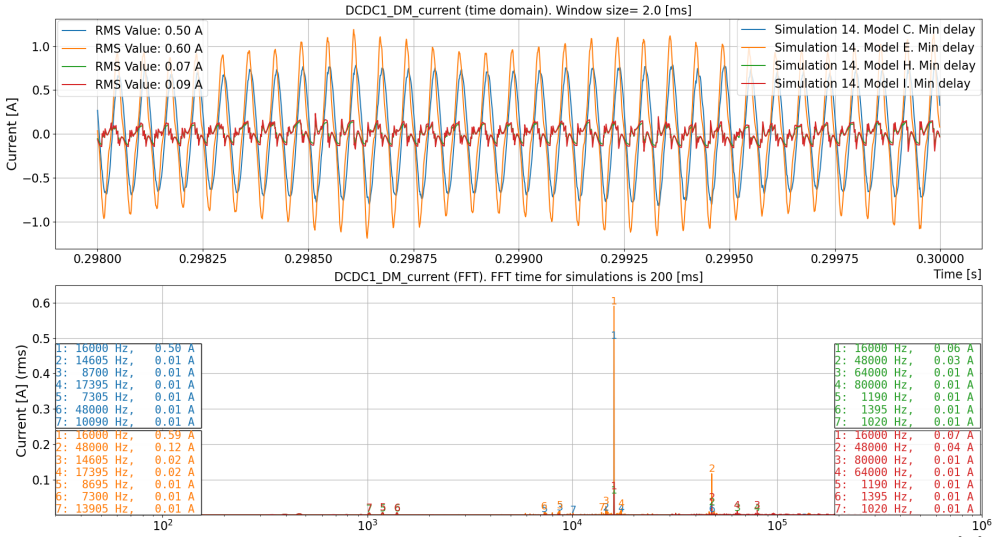


Figure 6.121: DM current in the DCDC from simulation (C14 min, E14 min, H14 min, and I14 min). The RMS current increases by 20 % when removing the BoB and its associated cables (Model C to Model E). Adding the DM filter (Model C to Model H) reduces the RMS current to 14 %. Removing the BoB and its associated cables from Model H to Model I increases the current by 28 %, but the level remains only 18 % of that in Model C.

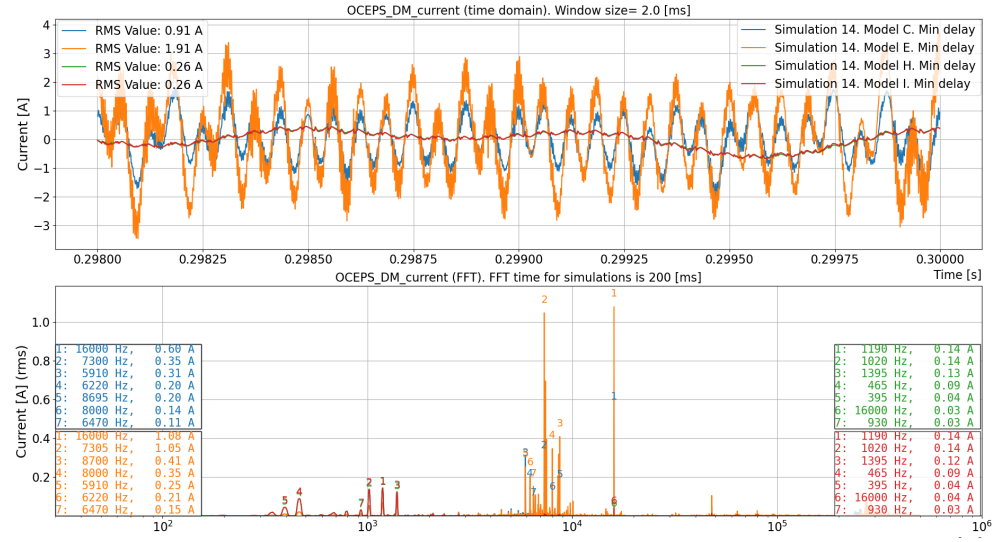


Figure 6.122: DM current in the OCEPS from simulation (C14 min, E14 min, H14 min, and I14 min). The RMS current increases by 110 % when removing the BoB and its associated cables (Model C to Model E). Adding the DM filter (Model C to Model H) reduces the RMS current to 29 %. No change in current is observed when removing the BoB and its associated cables from Model H to Model I.

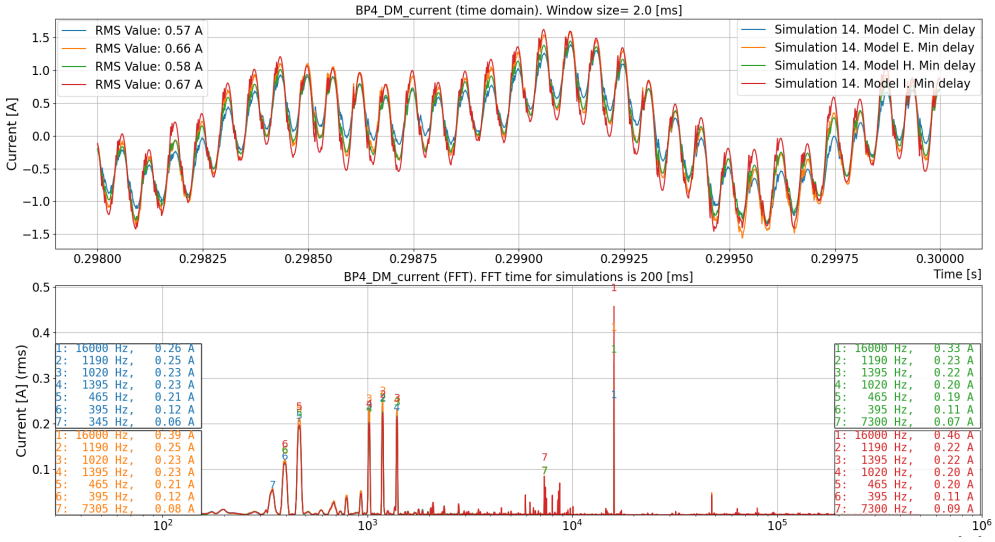


Figure 6.123: DM current in BP4 from simulation (C14 min, E14 min, H14 min, and I14 min). When DM filters are introduced, the current in BP4 remains unchanged. Removing the BoB and its associated cables from Model H to Model I increases the current by 16 %. According to [2], this behaviour does not adversely affect battery capacity fade or power fade.

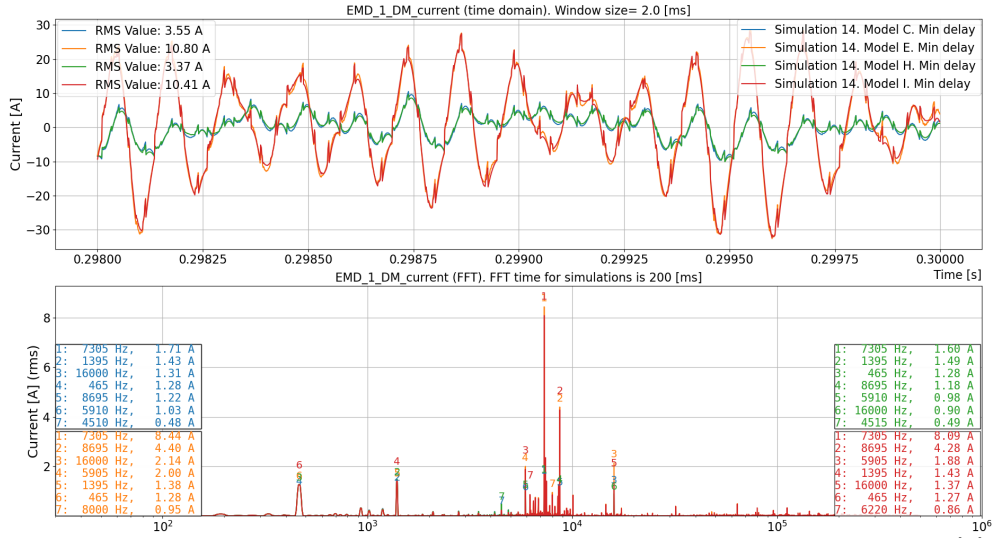


Figure 6.124: DM current in EMD1 from simulation (C14 min, E14 min, H14 min, and I14 min). With DM filters added, the current in EMD1 remains largely unchanged. Removing the BoB and its associated cables from Model H to Model I increases the current by 200 %. However, the EMD itself generates the current ripple, and the DC-link capacitor is designed to withstand this ripple.

Conclusion

The introduction of differential-mode (DM) filters substantially reduces EMI currents and improves system-level immunity. In addition to lowering current levels, the filters damp resonance points and reduce sensitivity to variations in switching frequency, cable configuration, and the presence of measurement equipment.

This robustness makes DM filtering well suited for platform-level integration, where subsystem layouts, cable lengths, and switching strategies vary. The results demonstrate that DM filters promote consistent electromagnetic behaviour across configurations, supporting their adoption as a system-level requirement.

6.6.4 Conclusion

The analyses in Section 6.6 collectively demonstrate that Differential Mode (DM) filters provide robust and system-wide improvements to the vehicle's electromagnetic behaviour. Beyond reducing RMS current levels in individual subsystems, the DM filters also damp resonance points, reduce sensitivity to switching-frequency variation, and mitigate the influence of cable routing and junction-box configurations.

Across all evaluated models, the implementation of DM filtering consistently stabilises the system response, even in cases where measurement equipment or structural differences introduce asymmetries. The results therefore confirm that DM filtering is not only effective for local EMI mitigation but also enhances platform-level immunity, making it a strong candidate for standardisation within future system designs.

6.7 Summary and conclusion

This chapter has combined the validated subsystem models developed in Chapter 5 into complete vehicle-level simulation models for both common-mode (CM) and differential-mode (DM) behaviour. The work demonstrates how system-level electromagnetic behaviour in a large traction voltage system (TVS) can be reproduced, analysed, and understood through a combination of detailed modelling, targeted model reduction, and comparison with full-vehicle measurements.

For CM behaviour, the chapter shows that accurate simulation requires explicit representation of parasitic capacitances, cable-shield return paths, junction-box impedances, semiconductor switching dynamics, and measurement-equipment effects. Several focused investigations confirm that idealised component models — particularly simplified IGBT switching behaviour or reduced cable or junction-box representations — lead to incorrect CM predictions. Despite this sensitivity, the chapter demonstrates that carefully reduced CM models reproduce the full-model behaviour up to 2–3 MHz, enabling computationally feasible system-level simulations without compromising the dominant physical mechanisms. The CM simulations also replicate all measurement phenomena presented earlier:

the generation of the common-mode DC offset, its dependence on the X factor, the cancellation of CM currents under 180-degree phase-shifted switching, the amplification of CM currents during in-phase switching, and the reduction of transient CM peaks when the switching instants of the phase legs are intentionally staggered.

For DM behaviour, the required modelling bandwidth is substantially lower. The chapter evaluates several DM model variants and shows that a reduced model — with electric machine drives represented as controlled current sources and the remaining subsystems described by their reduced DM impedance — captures the relevant behaviour up to 200 kHz. System-level DM simulations reproduce the dominant harmonic content and ripple behaviour measured in the vehicle, including the characteristic second and sixth harmonics. Remaining amplitude discrepancies are explained by the influence of the measurement hardware, particularly the Break Out Boxes, which attenuate the true ripple in the TVS; this effect is confirmed through comparison of simulations with and without the Break Out Boxes in place.

The chapter further shows that damped DM filters provide an effective means of reducing ripple currents and increasing system robustness. These filters suppress resonance peaks, reduce RMS ripple levels, and make the system less sensitive to variations in cable routing, subsystem placement, and switching frequency. While such filters cannot be applied to high-power units such as the traction converters and batteries, their implementation in the remaining TVS subsystems yields substantial system-level benefits.

Taken together, the results of this chapter demonstrate that a validated and computationally tractable set of CM and DM system models can reproduce the measured EMI behaviour of a large commercial electric vehicle. The findings clarify the dominant resonance mechanisms, the influence of subsystem interactions, and the role of measurement equipment in shaping observed waveforms. This provides the system-level understanding required before assessing how subsystems should be verified during early development phases.

The next chapter shifts focus from analysing EMI mechanisms and mitigation within a complete vehicle to the question of how subsystems can be meaningfully verified before they are integrated into the traction voltage system. Chapter 7 examines the use of artificial networks, particularly standardised line impedance stabilisation networks, and investigates how well such networks replicate the electrical environment a subsystem experiences when connected to an actual vehicle. This transition moves the discussion from system-level EMI behaviour to early-phase verification methods, establishing the link between vehicle-representative impedance characteristics and the test conditions used during subsystem development.

Chapter 7

Line impedance stabilization network (LISN)

Building on the system-level simulations in Chapter 6, this chapter examines how early-phase subsystem verification relates to the impedance environment of the traction voltage system (TVS). The analysis in Chapter 6 shows that subsystem behaviour depends strongly on surrounding converters, cables, and batteries, which means that verification outside the vehicle context is non-trivial. This motivates the need to evaluate how standardised artificial networks represent the TVS during early testing.

In Chapter 5, subsystem models are developed, reduced, and validated with the aim of enabling system-level simulations of a complete electric vehicle. These models capture the electrical behaviour of individual subsystems and their interconnections, but they do not, by themselves, determine how a subsystem is verified when no vehicle-level context is available. In particular, the electrical environment seen by a subsystem during bench testing may differ significantly from that of the final installation, both in magnitude and in resonance behaviour.

A complete electric vehicle is ideally tested in terms of the voltage and current ripple at the connection point of a subsystem to the TVS. However, when a prototype vehicle is built, the available time before start of production is limited, and testing all subsystems in a fully representative configuration is often not feasible. A method for early-phase verification is therefore required.

An artificial network, also known as a line impedance stabilization network (LISN), is a standardised method used in EMC testing for conducted and radiated emissions. The artificial network is described in [12]. The purpose of the LISN is to define a standardised input impedance presented to the device under test (DUT), enabling repeatable and comparable test results. In Figure 7.1, the perceived input impedance is denoted by "Z" for the DUT connected to a LISN. A description in [12] states: "*This test describes a standardised test setup and test method to enable comparability of the generated voltage ripple of voltage class*

B components."

An artificial network provides the defined impedance for the generated ripple test, as illustrated in Figure 7.1.

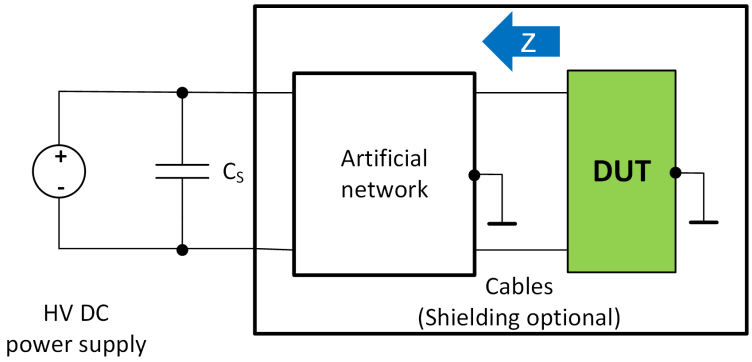


Figure 7.1: Ripple test setup with an artificial network/LISN, according to [12], and the device under test (DUT). The blue arrow, marked with "Z", indicates the perceived impedance from the artificial network/LISN towards the DUT.

The LISN defined in [12] is shown in Figure 7.2.

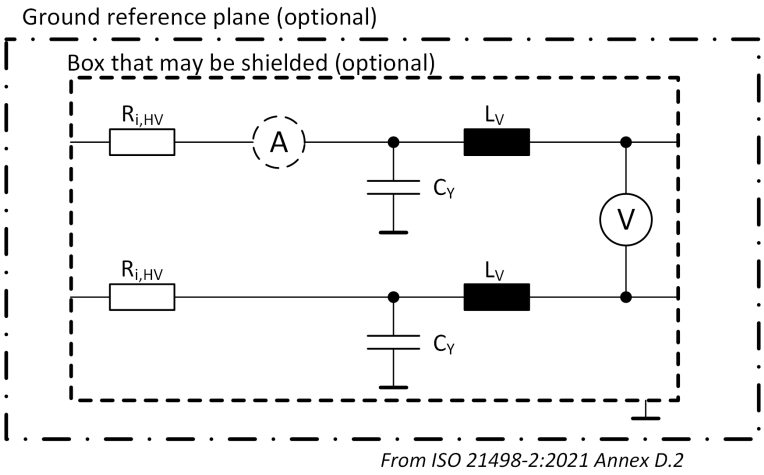


Figure 7.2: LISN according to [12].

$\mathbf{R_{i,HV}}$ Internal resistance of the power supply.

$\mathbf{L_V}$ Internal inductance of the vehicle, mainly originating from the vehicle power supply and cables.

$\mathbf{C_Y}$ Capacitor between HV+/HV− and ground used to limit EMC emissions.

$\mathbf{C_s}$ Decoupling capacitor.

7.1 Characteristics of a TVS

The purpose of using an LISN is to foresee disturbances that occur during operation of a traction voltage system (TVS). The TVS consists of batteries, converters, and cables of different designs and configurations. The main electrical properties of these subsystems are as follows:

- Battery: Ideal voltage source, internal resistance, common-mode (CM) and differential-mode (DM) inductance, and CM parasitic capacitance towards ground.
- Converter: DC-link capacitance, filter inductance, and CM capacitance C_Y.
- Cables: Resistance and inductance.

The combined properties of the subsystems result in multiple impedance and resonance circuits in the TVS.

To compare differences in impedance between two differently configured vehicles, the analysis uses a frequency sweep of the simulation model. Both vehicle models include identical auxiliary loads but differ in the number of batteries and electrical machine drives. The vehicle shown in Figure 6.1 is used as a reference to illustrate how system configuration affects the impedance characteristics.

In the study, EMD1 is replaced with the Device Under Test (DUT) as part of the model configuration. The perceived impedance of the TVS is then investigated from both the DM and CM perspectives. The large vehicle configuration is shown in Figure 7.3, while the smaller vehicle configuration is shown in Figure 7.4.

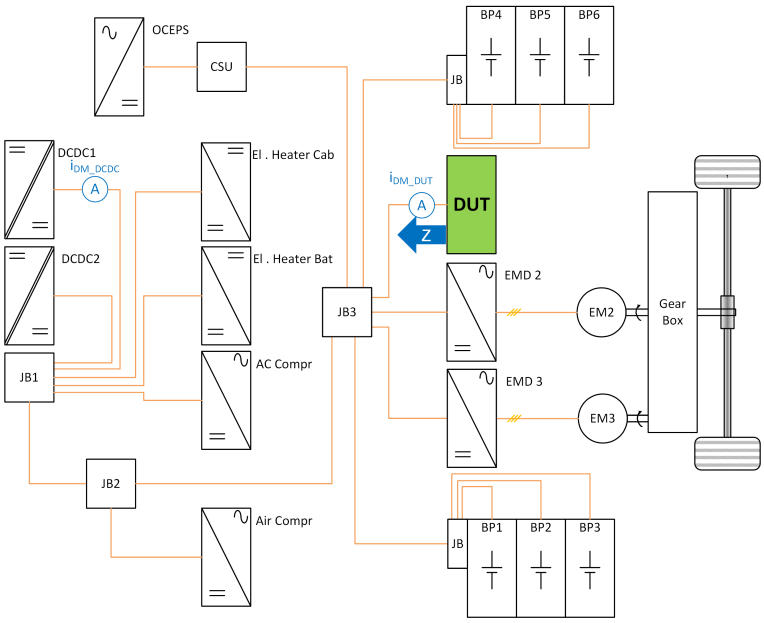


Figure 7.3: Simulation model of the large vehicle FM1156 where EMD1 is replaced by the DUT. The blue arrow, marked with "Z", indicates the perceived impedance from the artificial network/LISN to the DUT.

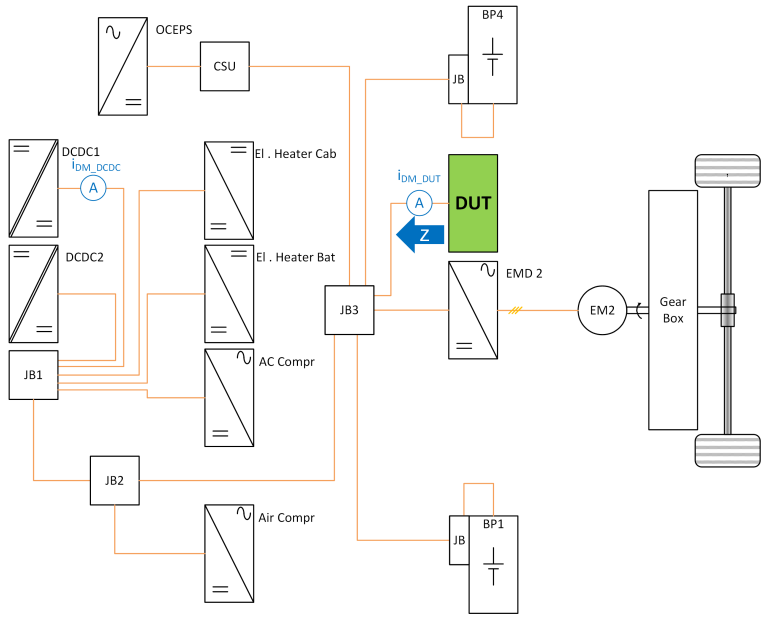


Figure 7.4: Simulation model of the small vehicle FM1156 where EMD1 is replaced by the DUT. The blue arrow, marked with "Z", indicates the perceived impedance from the artificial network/LISN to the DUT.

In the simulation model, the internal impedance of the TVS is denoted by "Z" at the connection point of the DUT, as indicated in Figures 7.3 and 7.4. The retrieved impedance Z from the PLECS simulations is shown for the DM case in Figure 7.5 and for the CM case in Figure 7.6.

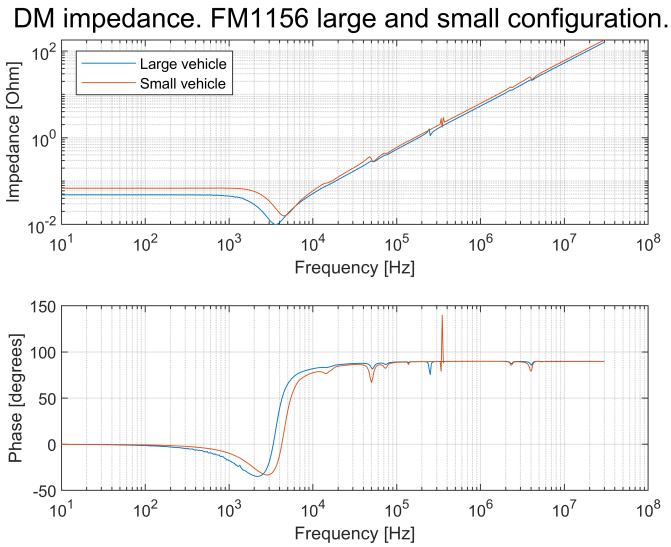


Figure 7.5: Simulation of the DM impedance retrieved from the DUT in Figures 7.3 and 7.4.

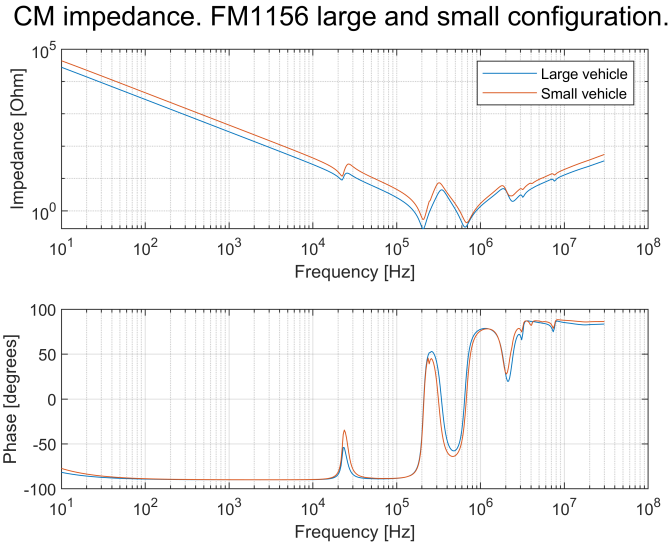


Figure 7.6: Simulation of the CM impedance retrieved from the DUT in Figures 7.3 and 7.4.

Conclusion

The results demonstrate that the perceived impedance of a TVS at the connection point of a subsystem is strongly dependent on the overall vehicle configuration. Changes in the number and type of connected subsystems significantly alter both the DM and CM impedance characteristics. This variability highlights that a standardized artificial network, such as an LISN, does not inherently represent the impedance conditions of a specific vehicle. Consequently, care must be taken when interpreting LISN-based measurements, as they may differ substantially from the impedance environment encountered in an actual vehicle installation.

7.2 Characteristics of a LISN

Figure 7.2 shows the LISN defined in [12]. According to [12], the standard defines four different use cases for an LISN. In three of these use cases, the internal resistance of the high-voltage power supply is specified, while the fourth use case is left open to be agreed between the customer and the supplier.

The parameters corresponding to Figure 7.2 are listed in Table 7.1.

Table 7.1: Use cases from Annex D in [12].

Use case	$R_{i,HV}$ [mΩ]	L_V [μH]	C_Y [μF]
A	10	1	1
B	25	1	1
C	100	1	1
Z	To be agreed between customer and supplier.	To be agreed between customer and supplier.	To be agreed between customer and supplier.

According to [12], the standard specifies that the decoupling capacitance C_S is 10 mF or greater. The value of 10 mF represents a larger capacitance compared with the DC-link capacitance of the vehicles considered in this study.

The frequency-dependent impedance of the LISN for use cases A–C in Figure 7.1 is shown in Figure 7.7 for the DM impedance and in Figure 7.8 for the CM impedance.

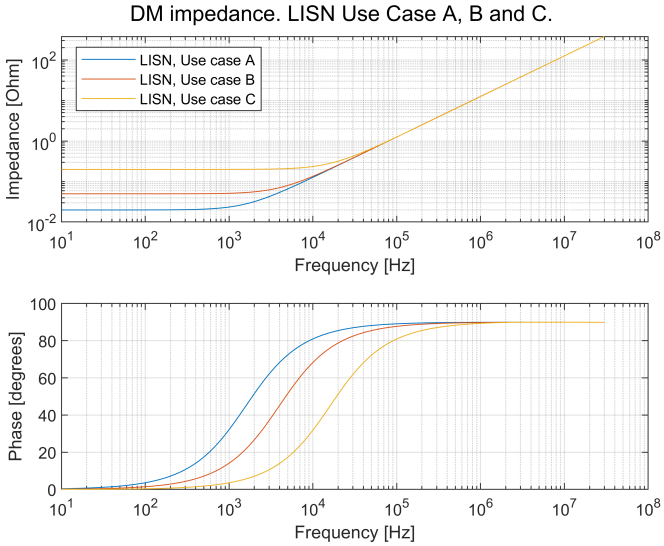


Figure 7.7: DM impedance of the LISN for use cases A, B, and C.

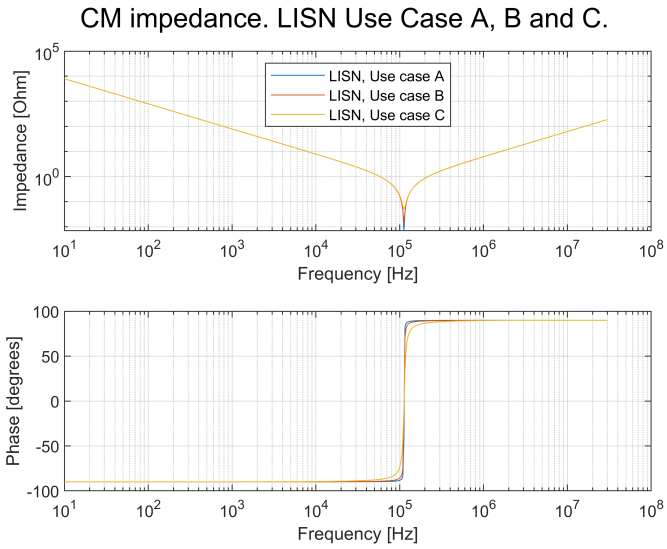


Figure 7.8: CM impedance of the LISN for use cases A, B, and C.

Conclusion

The defined LISN use cases provide a standardized impedance environment for conducted emission and ripple testing. However, the significant variation in impedance characteristics

between the use cases demonstrates that the LISN does not represent a unique or vehicle-specific electrical environment [26]. Instead, the LISN defines a bounded and repeatable test condition, which may differ substantially from the impedance characteristics of an actual traction voltage system. This observation motivates further investigation of how well standardized LISN configurations reflect real vehicle conditions.

7.3 Impedance comparison of an artificial network, a LISN, and measurements on a real truck

The Device Under Test (DUT) is a component intended to be integrated into a vehicle. The behaviour of the DUT when tested using an artificial network or a LISN is expected to reflect how the DUT behaves when connected to the vehicle traction voltage system (TVS). The impedance-based comparison methodology applied in this section follows the modelling and analysis framework presented in [31].

A frequency sweep is performed for three different configurations representing the input impedance perceived by the DUT:

- the input impedance "Z" of the TVS as seen from the DUT in the large vehicle configuration shown in Figure 7.3, consisting of three MDSs and six BPs;
- the input impedance "Z" of the TVS as seen from the DUT in the small vehicle configuration shown in Figure 7.4, consisting of two MDSs and two BPs;
- the input impedance "Z" of the TVS as seen from the DUT when connected to an LISN, as shown in Figure 7.1, using LISN use case B according to Table 7.1.

The resulting impedances are shown in Figure 7.9 for the differential-mode (DM) case and in Figure 7.10 for the common-mode (CM) case.

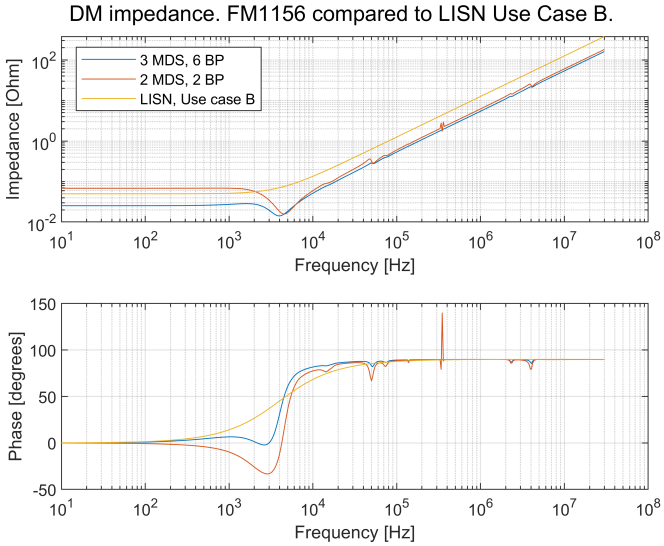


Figure 7.9: DM impedance comparison between an LISN and an FM1156 truck with large and small configurations. The large configuration consists of three MDSs and six BPs, and the small configuration consists of two MDSs and two BPs.

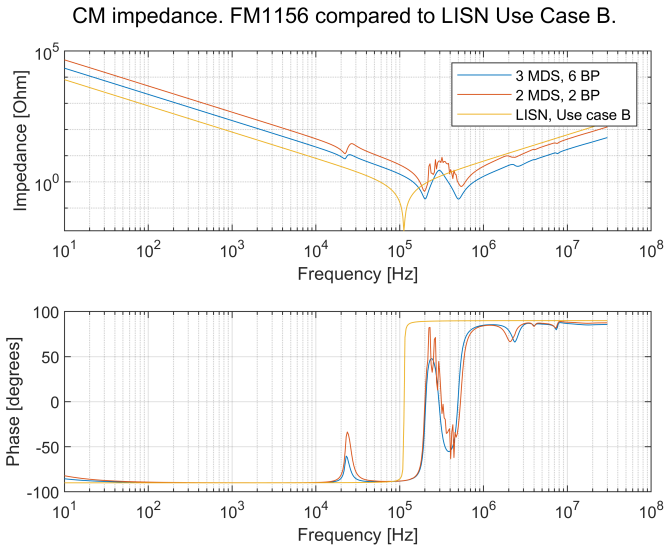


Figure 7.10: CM impedance comparison between an LISN and an FM1156 truck with large and small configurations. The large configuration consists of three MDSs and six BPs, and the small configuration consists of two MDSs and two BPs.

It can be observed from Figures 7.9 and 7.10 that the input impedance perceived by the DUT differs for both DM and CM between the small and large vehicle configurations. However, the difference between the vehicle configurations and the LISN is considerably

larger.

A distinct resonance can be observed in the vehicle models at frequencies around 4–6 kHz. In addition to this dominant resonance, several other resonances are present but are less pronounced.

Conclusion

The comparison demonstrates that a standardized LISN does not accurately represent the impedance characteristics of a real traction voltage system (TVS). Both the magnitude and the resonance behaviour of the impedance perceived by the DUT differ significantly between the LISN and the vehicle configurations, for both DM and CM.

These results indicate that LISN-based testing may lead to conclusions that are not representative of in-vehicle operation [14]. Consequently, the development of alternative artificial networks is recommended. It is proposed that OEMs define a limited set of LISN variants that better reflect different vehicle configurations, enabling suppliers to perform more representative early-phase validation of subsystems intended for integration into electric vehicles.

7.4 Alternative LISN

In Section 7.3, it was shown that the standardized LISN does not sufficiently represent the impedance characteristics of the TVS at the connection point of a subsystem. The LISN is intended to provide a defined and repeatable impedance towards the DUT; however, the TVS consists of multiple interacting subsystems, including batteries, converters, and cables, which together form a more complex impedance profile than that imposed by the standardized LISN.

From a differential-mode perspective, the battery can be represented as an ideal voltage source with series resistance and inductance. At low frequencies, the impedance is dominated by resistive behaviour, whereas inductive behaviour dominates at higher frequencies, as illustrated in Figure 6.55. A converter primarily contributes a DC-link capacitance at low frequencies, while stray inductances in the DC-link capacitor and the common-mode input inductors dominate at higher frequencies, also shown in Figure 6.55.

The standardized LISN does not exhibit pronounced resonance behaviour. This is mainly due to the relatively high internal resistance $R_{i,HV}$ in Figure 7.2, which damps the impedance and suppresses low-impedance resonance points. One possible modification to mitigate this effect is to relocate the decoupling capacitor C_S, shown in Figure 7.1, such that it is placed between L_V and $R_{i,HV}$, as illustrated in Figure 7.11. By moving C_S, the influence of $R_{i,HV}$ on the resonance behaviour is reduced. However, this modification deviates from the standardized test setup defined in Figure 7.1.

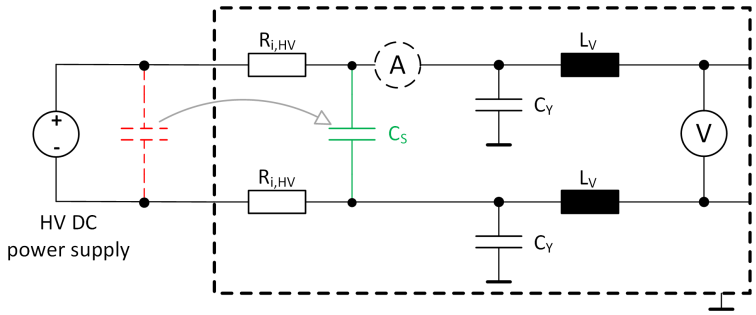


Figure 7.11: Modified LISN with the decoupling capacitor relocated to reduce the damping effect of the internal resistance.

A comparison of the DM and CM impedance between the standardized LISN and the modified LISN is shown in Figures 7.12 and 7.13.

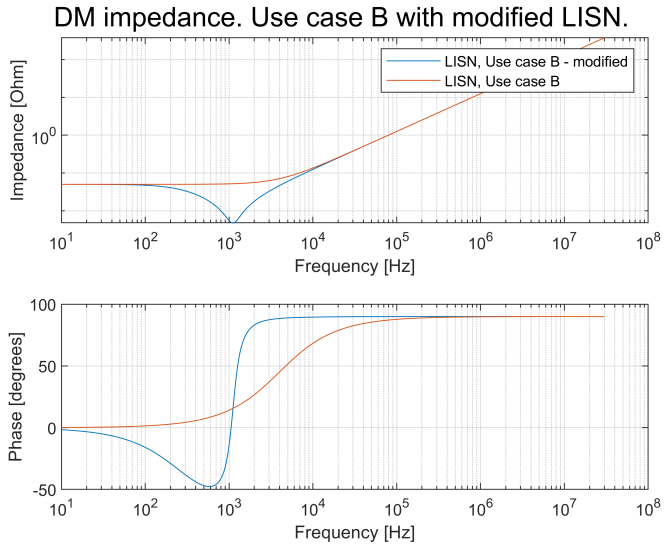


Figure 7.12: DM impedance comparison between the standardized LISN and the modified LISN.

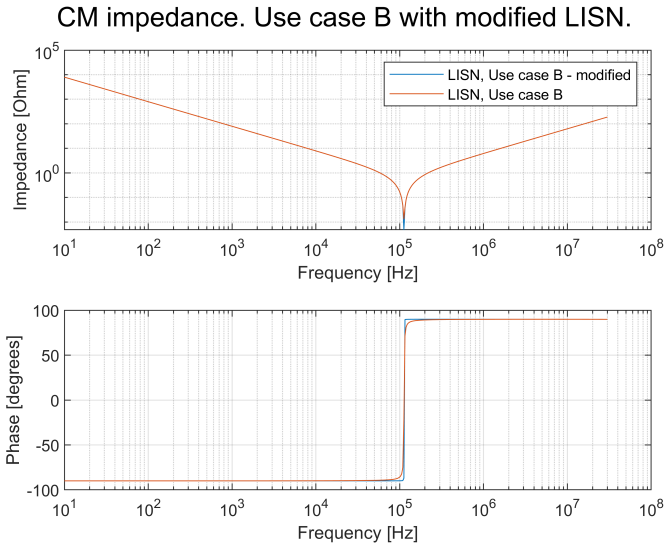


Figure 7.13: CM impedance comparison between the standardized LISN and the modified LISN.

In the modified LISN, a single resonance point is present in the DM impedance, as shown in Figure 7.12, and this resonance point is not present in the standardised configuration. The CM impedance, however, remains largely unchanged because capacitive coupling dominates this behaviour, making it less sensitive to the relocation of C_S. According to Table 7.1, use case Z specifies that the parameters $R_{i,HV}$, L_V, and C_Y may be selected by agreement between customer and supplier. Even with such parameter changes, the LISN topology results in only a limited number of resonance phenomena.

By adjusting L_V to better correspond to the vehicle inductance and selecting a value of C_S that improves agreement with the vehicle model, the result gives better agreement with the vehicle impedance. A comparison between the modified LISN with adjusted values of L_V and C_S and the vehicle impedance is shown in Figure 7.14.

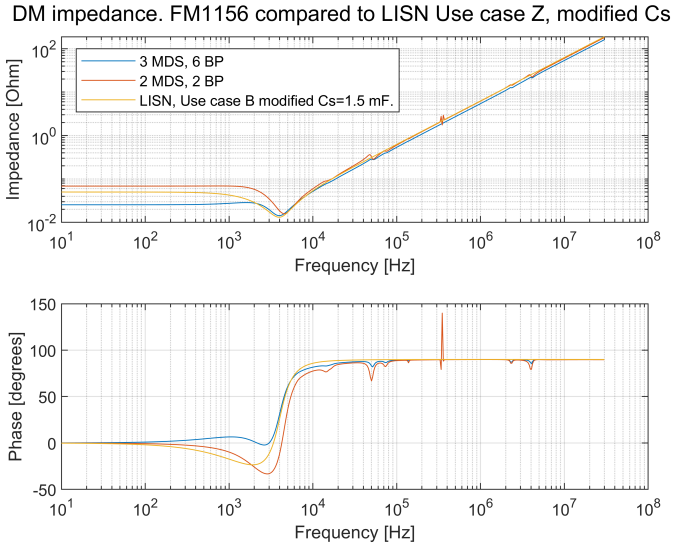


Figure 7.14: DM impedance comparison between the modified LISN and the TVS for small and large vehicle configurations.

Conclusion

The results show that the standardized LISN defined in current EMC test standards does not adequately represent the impedance characteristics of a vehicle TVS at the subsystem connection point. While modifications to the LISN topology and parameter values can improve agreement for specific cases, such adaptations deviate from the standardized test setup and remain limited in their ability to reproduce the multiple resonance phenomena observed in real vehicle configurations.

This section shows that a single standardized LISN does not capture the wide variation in vehicle architectures. Instead, the development of a limited set of alternative LISN configurations, tailored to representative vehicle impedance characteristics, would enable more realistic and vehicle-relevant early-phase validation of subsystems intended for integration into electric vehicles.

7.5 Conclusion

This chapter has examined the applicability of standardized artificial networks, in particular LISNs, for evaluating the conducted voltage and current ripple of subsystems intended for integration into electric vehicles. By analysing the impedance characteristics of a traction voltage system (TVS), the results show that the electrical environment perceived by a subsystem is strongly dependent on the vehicle configuration, including the number and type of energy storage units, converters, and interconnecting cables [31].

The impedance comparisons show that a standardized LISN does not reproduce either the magnitude or the resonance behaviour of a real vehicle TVS, for both differential-mode and common-mode conditions. Consequently, LISN-based testing can show results that are not representative of in-vehicle operation, especially when subsystem behaviour is sensitive to impedance-dependent resonance phenomena.

Furthermore, as shown by the subsystem interaction analyses presented earlier in this work, resonant behaviour can arise between subsystems within the TVS without being directly observable at the subsystem connection point. In such cases, a component can significantly influence internal current paths and resonance conditions while having only a limited impact on the impedance perceived by the DUT. This further limits the ability of LISN-based testing to capture system-level interactions.

The investigation of modified and alternative LISN configurations further shows that, while certain adaptations can improve agreement for specific cases, a single standardized network does not capture the wide variation in vehicle architectures. This supports the use of vehicle-representative impedance models and the concept of defining a limited set of alternative artificial networks tailored to typical vehicle configurations.

Overall, the results in this chapter demonstrate that the actual vehicle impedance environment must be considered when validating subsystems in early development phases. This provides a necessary foundation for the experimental investigations and verification methods presented in the subsequent chapter, where measurement results are analysed in relation to the modelling and impedance characteristics established in this work.

It is important to clarify that the purpose of this chapter is not to propose or develop a new LISN concept for BEV applications. The intention is solely to demonstrate the limitations of existing standardized LISN implementations when applied to heavy-duty electric vehicles, and thereby clarify why vehicle-representative impedance environments are required for meaningful subsystem verification.

Chapter 8

Conclusion, discussions and future work

In this thesis, depth is achieved through breadth, where system-level understanding is prioritised over isolated component model optimisation. Although individual converters, cables or subsystems can be analysed in great detail, the work shows that their electromagnetic behaviour cannot be understood—or predicted—without considering the complete traction voltage system (TVS). The CM and DM phenomena observed in the vehicle arise not from any single unit, but from the interaction between parasitic elements, cable impedances, switching sequences, ground paths and subsystem placement. The thesis demonstrates that system-level measurements, high-bandwidth modelling and targeted model reduction are all required to understand how disturbances originate, propagate and couple within a commercial BEV architecture. A key result is how the X-factor introduced in this thesis fundamentally shapes the common-mode DC voltage and the resulting current paths, and that realistic representation of non-ideal semiconductor behaviour is essential for reproducing measured CM currents. The work also shows that measurement interfaces, such as Break-Out Boxes, introduce non-negligible impedance and must be included in both analysis and simulation. What you measure might not be what is the operation condition without measurement equipment such as break out boxes and sensors.

Building on the objectives formulated in Chapter 1, this chapter returns to the central questions of how CM and DM disturbances are generated in the traction voltage system, how they propagate through the vehicle and how predictive capability can be achieved through system-level modelling and measurement. The analyses in the preceding chapters address these questions from complementary perspectives, and the results provide a coherent system-level understanding of the underlying mechanisms. Chapter 8 therefore synthesises how the thesis answers these research questions and clarifies their implications for modelling, measurement and EMI-aware design.

8.1 Conclusions

This thesis demonstrates that conducted electromagnetic disturbances in a battery-electric vehicle cannot be understood from isolated component behaviour alone. Common-mode (CM) and differential-mode (DM) disturbances originate in individual subsystems, yet their magnitude, propagation and interaction depend on the complete traction voltage system (TVS). The distributed parasitic elements, cable impedances, converter switching and subsystem placement determine how disturbances travel through the vehicle and how they influence neighbouring units.

The work addresses a commercial battery-electric vehicle and fills a gap in publicly available system-level EMI analysis. Existing studies primarily investigate isolated converters, cables or machines, whereas this thesis evaluates how disturbances propagate across a complete commercial TVS. In a heavy-duty truck or bus, the number of high-voltage subsystems is significantly larger than in a passenger car, and the TVS contains substantially longer cables, more junction boxes and more distributed return paths. This increases the complexity of the system-level EMI behaviour and the need for physically based modelling and full-vehicle measurements.

A central finding is that the relationship between symmetric CM capacitance and asymmetric parasitic capacitance fundamentally shapes the CM behaviour. The CMDC voltage depends on the X-factor defined by this capacitance ratio. A recommended target is $X = 50$, which ensures that the symmetric CM capacitance dominates the parasitic capacitances during switching events.

Although the CMDC voltage depends only on the X-factor and not on the physical placement of the symmetric CM capacitance, the resulting CM current distribution depends strongly on where this capacitance is located. Increasing the X-factor at the electric machine drive confines the CM current locally at the disturbance source and prevents large CM currents from propagating through cables, junction boxes and traction batteries. When the X-factor is evaluated with respect to the EMD, it is denoted X_{EMD}, and a recommended target is $X_{\mathrm{EMD}} = 50$. Measurements and simulations confirm that this placement-dependent X-factor governs whether the CM current closes locally around the EMD or spreads throughout the TVS.

Accurate CM simulation also requires non-ideal semiconductor models. Idealised switching devices do not reproduce the measured CM behaviour because they omit the parasitic capacitances, rise and fall times and stray inductances that drive CM currents during switching events. Non-ideal IGBTs are therefore required to reproduce both the CM waveforms and the resulting CM current paths in the vehicle.

Measurements show that the measurement system influences the electrical behaviour of the TVS. The impedance introduced by Break-Out Boxes and associated cabling alters both CM and DM quantities, particularly in low-impedance DM paths. Consequently, the measured quantities represent the combined behaviour of the TVS and the measurement interface, which must be included in simulations to obtain correlation with measurements.

Measurements also show that the electromagnetic behaviour is not static even when the operating conditions appear steady. Two situations are observed. When the vehicle that has more than one traction machine drive is at standstill but the electric machine drives are activated, no differential-mode current flows in the DC-link, yet the common-mode current fluctuates because small differences in switching frequency between the drives create low-frequency beating. The largest CM peaks appear when the switching patterns of two or more EMDs momentarily align in phase. During driving at a steady-state operating point, both CM and DM quantities vary, but due to different mechanisms: CM varies because of the same switching-frequency drift between EMDs, while DM varies because the AC component of the load-dependent DM current in the DC-link can increase or decrease depending on the instantaneous phase relationship between the drives. These two effects are independent but occur simultaneously during steady-state operation.

The required modelling bandwidth cannot be assumed from converter topology alone. The CM spectral content reaches up to approximately 2 MHz on the DC side and 3 MHz on the AC side of the electric machine drive, while the DM spectral content remains below approximately 200 kHz. These bandwidths must be measured on the actual vehicle before the subsystem models are defined. The measured frequency range forms the basis for the subsystem model reduction used in this thesis.

The modelling approach developed in this work introduces a systematic method for reducing subsystem complexity while preserving the resonant behaviour within the required CM and DM bandwidth. This reduction enables simulations of the complete TVS using physically based models of all major subsystems, cable impedances, junction boxes and measurement interfaces. The results show that cable shields form the actual CM return path, whereas the vehicle chassis exhibits significantly higher impedance. Junction boxes and Break-Out Boxes introduce inductance comparable to several metres of high-voltage cable and must be included explicitly in the simulation model when correlating with measurements.

Standardised artificial networks such as LISNs do not represent the impedance environment of a commercial vehicle and therefore cannot predict TVS-level CM or DM behaviour.

Overall, this thesis establishes a system-level methodology for analysing conducted CM

and DM behaviour in commercial battery-electric vehicles. Measurement and simulation complement each other: measurements define the relevant bandwidth and calibration, while simulations provide insight into how subsystem interactions shape system-level behaviour. Robust EMI performance requires accurate measurement of the complete vehicle and physically consistent modelling of the TVS as an integrated electrical system.

8.2 Discussion

The discussion relates the results to the objectives formulated in Chapter 1, namely to understand how CM and DM disturbances are generated, how they propagate through the traction voltage system and how predictive capability can be achieved through system-level modelling and measurement. It therefore interprets the findings with direct reference to these research questions and clarifies their implications for EMI-aware design and analysis. This section discusses the implications of the results presented in this thesis and places them in a broader system-level context. The focus is on how the findings should be interpreted, how they relate to the characteristics of commercial heavy-duty vehicle platforms, and what they imply for modelling, measurement and engineering practice. The discussion does not repeat the conclusions but highlights the insights that affect design decisions, development workflows and the understanding of conducted EMI in a traction voltage system.

System-level knowledge and interpretation of measurements

The results of this thesis show that system-level knowledge is essential for interpreting measurements in a commercial traction voltage system (TVS). Conducted CM and DM disturbances cannot be understood from isolated subsystem behaviour but must be analysed in the context of how parasitic elements, cable impedances and converter switching interact across the full vehicle. Measurements alone do not provide insight unless the engineer understands the electrical topology, the current return paths and how the operating point affects the switching patterns of the electric machine drives (EMDs). Without this understanding, there is a risk of misinterpreting results or drawing incorrect conclusions about the root cause of observed behaviour.

The work demonstrates that even steady operating conditions do not produce static measurement results. At standstill with active EMDs, CM currents fluctuate due to small differences in switching frequency between converters, and the largest CM peaks occur when their switching patterns momentarily align in phase. During steady-state driving, CM and DM quantities vary due to separate mechanisms: CM due to switching-frequency drift and DM due to the rippel on the load-dependent DC-link current. This illustrates that correct interpretation requires not only measurement competence but also knowledge

of the switching strategies and their interaction.

The measurement system itself influences the results. Break-Out Boxes (BOBs), added cabling and the instrumentation interface introduce impedance that alters CM and especially DM currents, since the DM path typically exhibits very low impedance. The measured quantities therefore represent the combined behaviour of the TVS and the measurement setup. This reinforces the need for system knowledge to distinguish physical effects from measurement artefacts.

Platform dependency and vehicle-level complexity

The TVS in a heavy-duty truck or bus differs significantly from that of a passenger car. The number of high-voltage subsystems is larger, cable lengths are longer and the return-path structure is more distributed. The findings in this thesis confirm that such platform differences have substantial impact on the CM and DM behaviour. The interaction between subsystems, the impedance of junction boxes and the shielding configuration of long cable harnesses all contribute to a more complex propagation of disturbances.

This complexity also affects design decisions. Improvements that are inexpensive at subsystem level may become difficult or costly to implement due to supplier integration, packaging constraints or platform architecture. Conversely, system-level improvements such as the placement of symmetric CM capacitance or shielding strategies can be highly effective when informed by whole-vehicle understanding. The results show that focusing on system architecture early in the development process is essential for avoiding costly late-stage design changes.

Validation and limitations of the simulation models

The simulation results correlate with measurements when non-ideal semiconductor models, cable shields, junction-box impedances and measurement interfaces are included. However, the work also demonstrates the limits of physically detailed simulations. A complete high-fidelity model of all subsystems, including detailed switching behaviour and distributed parasitics, becomes too complex to simulate for full-vehicle studies, and the required simulation time can increase from minutes to days — if the solver converges at all — as the wide separation between the lowest and highest frequencies in the state-space matrix can make the system unsolvable in PLECS.

This necessitates model reduction. The required frequency range for CM and DM simulation must be established from measurements before the models are defined. By reducing subsystem models to preserve resonant behaviour only within the relevant bandwidth, the

simulation becomes computationally feasible while maintaining physical accuracy. This highlights that validation is not about matching every detail of a waveform but about preserving the mechanisms that govern trends, sensitivities and system interactions.

Integration of simulation and measurement

A key insight from this work is that simulations and measurements serve complementary purposes. Measurements establish the real system behaviour, reveal operating-point dependencies and identify the relevant bandwidth and impedance levels. Simulations, in contrast, make it possible to isolate mechanisms, test modifications rapidly and examine configurations that cannot easily be realised in hardware.

A physically based simulation model that includes all relevant impedances can reproduce trends and current-distribution mechanisms observed in measurements. When both approaches are combined, the engineer can understand not only what happens but why. This integrated perspective is essential for developing design strategies in the absence of comprehensive standards for conducted EMI on heavy-duty vehicles.

Recommended workflow for TVS EMI engineering

The findings of this thesis point to a recommended workflow for EMI analysis in commercial vehicles.

1. **System-level measurements:** Perform system-level measurements to establish the relevant frequency range, operating-point behaviour and subsystem interactions.
2. **Reduced subsystem models:** Derive reduced subsystem models that preserve the resonant behaviour within the required CM and DM bandwidth.
3. **TVS-level simulation integration:** Integrate these models into a TVS-level simulation that includes cable shields, junction-box impedances and the measurement interfaces used in the hardware tests.
4. **Evaluation of design alternatives:** Evaluate design alternatives such as the placement of symmetric CM capacitances, CM filters, DM filters, switching frequencies and modified cable configurations.

This workflow balances measurement effort, modelling accuracy and engineering practicality. It acknowledges that EMI is not governed by strict rules but by system-level interactions and platform-specific behaviour. A structured approach enables engineers to

identify improvements early, avoid costly late corrections and make design decisions with a clear understanding of their impact on the complete vehicle.

8.3 Future work

A meaningful continuation of this work requires broader organisational understanding of EMI, its origin and its system-level behaviour. Developing additional models or performing more simulations is of limited value unless the underlying EMI mechanisms are understood by engineers and suppliers. As highlighted throughout this thesis, publicly available research remains limited, and strengthening competence is therefore the foundation for any further progress. Once this foundation is established, or developed in parallel, the following research directions can be pursued.

Bearing and gearbox currents

This thesis has focused primarily on conducted EMI on the DC side of the traction voltage system. The EM model is simplified and does not consider bearing currents, gearbox currents or the possibility that the mechanical coupling between rotor and gearbox may contribute to radiated EMI. These aspects warrant further investigation.

Measurements and more measurements

Measurements on additional vehicles with subsystems not included in this thesis are essential. The findings must be repeatable across different platforms and configurations to establish their generality.

Simulations and more simulations

The simulation platform should be extended with new subsystem models derived from future measurements. These models should then be simplified to remain computationally efficient, enabling combined measurement and simulation studies that deepen system-level understanding.

EMD configuration to reduce conducted DM and CM EMI

An open question is whether multiple EMDs or other subsystems can be integrated into a combined converter to confine both DM and CM EMI within the converter instead of allowing disturbances to propagate into the traction voltage system. Alternative converter topologies may also reduce EMI generation and should be explored.

Conducted vs. radiated EMI

Future work should examine radiated EMI at vehicle level and then apply conducted EMI mitigation to assess how radiated behaviour changes. Establishing the relationship between conducted and radiated EMI is crucial, although addressing radiated EMI at full-vehicle level occurs late in the development process, when subsystem design changes may no longer be feasible.

V2G

If vehicle-to-grid functionality is desired, the EMI behaviour associated with bidirectional power flow must be analysed. Present standards and system architectures are not fully aligned with EMI requirements for V2G applications, and further work is needed to clarify these constraints.

Alternative LISN

The development of a BEV-representative LISN lies outside the scope of this thesis. However, the limitations of existing LISN standards for heavy-duty electric vehicles suggest that alternative LISN concepts should be investigated.

The results collectively provide a system-level foundation for modelling, measurement and EMI mitigation in heavy-duty electric vehicles.

Appendix

Appendix A

How to derive the parameters in the models from measurements with Zview

To build accurate subsystem models, software tools are required in addition to the measurement equipment. This appendix introduces the tools used for parameter extraction and illustrates how impedance measurements translate into equivalent model parameters. PLECS [21] supports the system-level modelling, and Zview [36] supports the extraction of parameters from impedance measurements.

This appendix presents the procedure for deriving model parameters from LCR-based impedance measurements using Zview. When a component is measured with the LCR instrument, the resulting impedance magnitude and phase versus frequency must be translated into an equivalent circuit model. The example in this appendix uses a capacitor.

Figure A.1 shows the equivalent model of a capacitor.

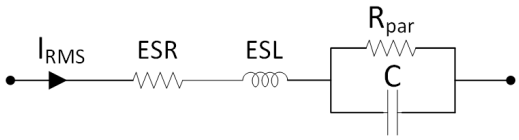


Figure A.1: Equivalent model of a capacitor.

Figure A.2 shows the measured impedance and phase from 100 Hz to 30 MHz. A distinct resonance occurs at approximately 1 MHz. The behaviour is capacitive below this resonance and inductive above it. At frequencies above 10 MHz, additional resonances are present in the measurement that are not captured by the equivalent model. As discussed in Appendix 5, measurements above 10 MHz are difficult to obtain with sufficient accuracy, and the resulting parameter extraction therefore becomes uncertain in this range.

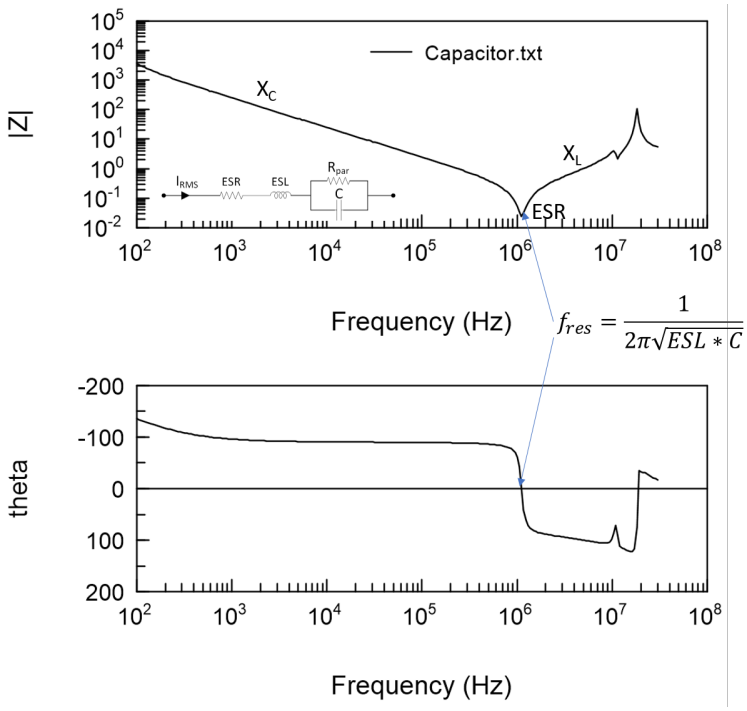


Figure A.2: Measured capacitor with a frequency sweep from 100Hz to 30MHz.

The parameters are derived using Zview by constructing the model shown in Figure A.3. Zview is configured to run fitting in the frequency range 100 Hz to 10 MHz. The fitted parameter values, corresponding to the equivalent model elements, appear below the circuit in the Zview interface.

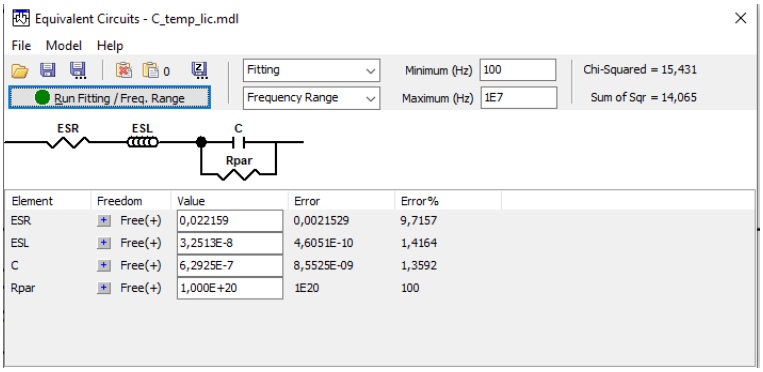


Figure A.3: Equivalent model in Zview with the parameters that responded to the run fitting.

Figure A.4 shows the simulated impedance from the equivalent model together with the measured values. Figure A.5 shows a simulation extended to 30 MHz. To generate the latter

figure, Zview runs in simulation mode; otherwise the fitting algorithm attempts to follow the higher-frequency resonances. As described in Subsection 5.1.3, the LCR instrument provides limited accuracy at low frequencies. Above 1 kHz, the correlation between model and measurement is close up to approximately 10 MHz.

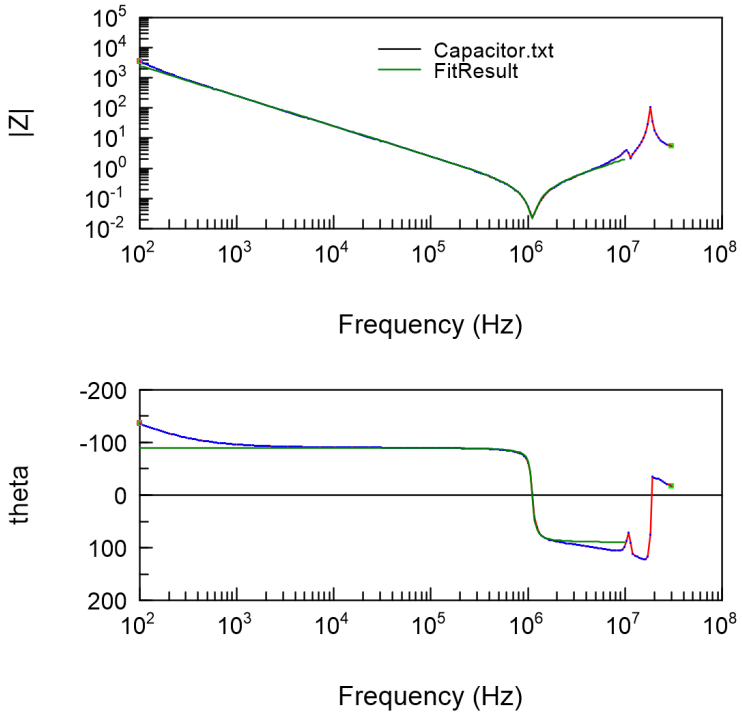


Figure A.4: Equivalent model simulated and shown together with the measured values.

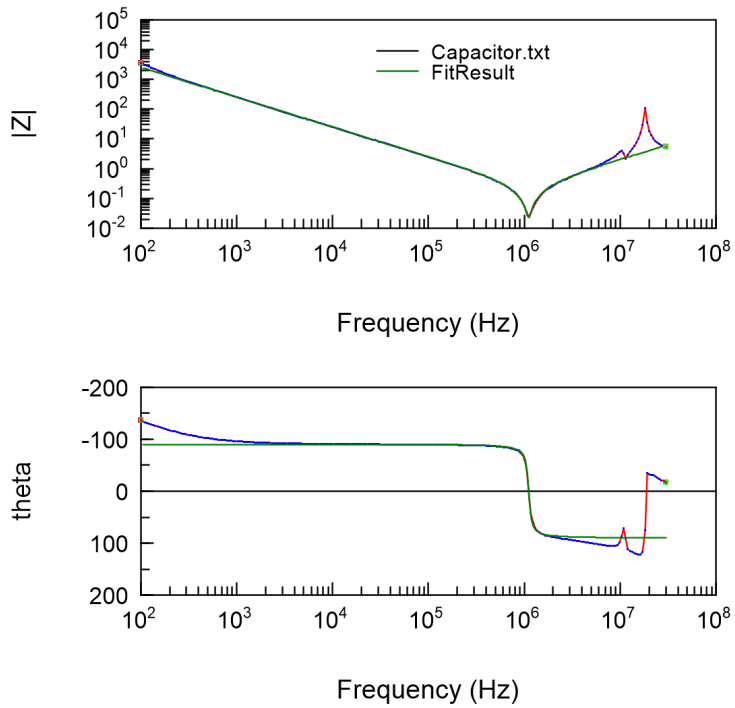


Figure A.5: Equivalent model simulated up to 30MHz and shown together with the measured values.

Appendix B

FFT of pulses, FFT windowing and axis scaling

B.1 Frequency-domain behaviour of short pulses.

The measured spectra in Figures B.1 and B.2 show the characteristic frequency-domain behaviour described in this appendix. These include broadband spectral content originating from short-duration pulses, harmonic structures induced by polarity alternation, and the influence of window functions and axis scaling on the interpretability of spectral magnitudes. The figures therefore serve as reference examples for the explanatory sections that follow.

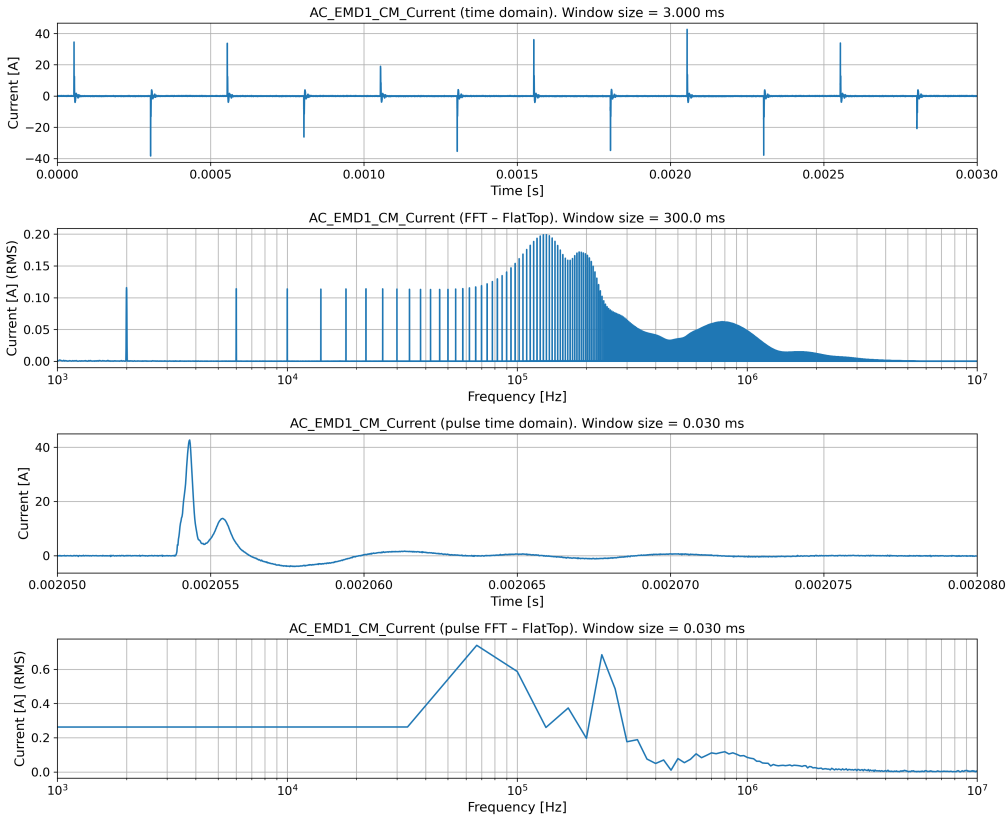


Figure B.1: Common-mode current spectrum of AC_EMD1_CM measured with a Flattop window and semilogarithmic scaling.

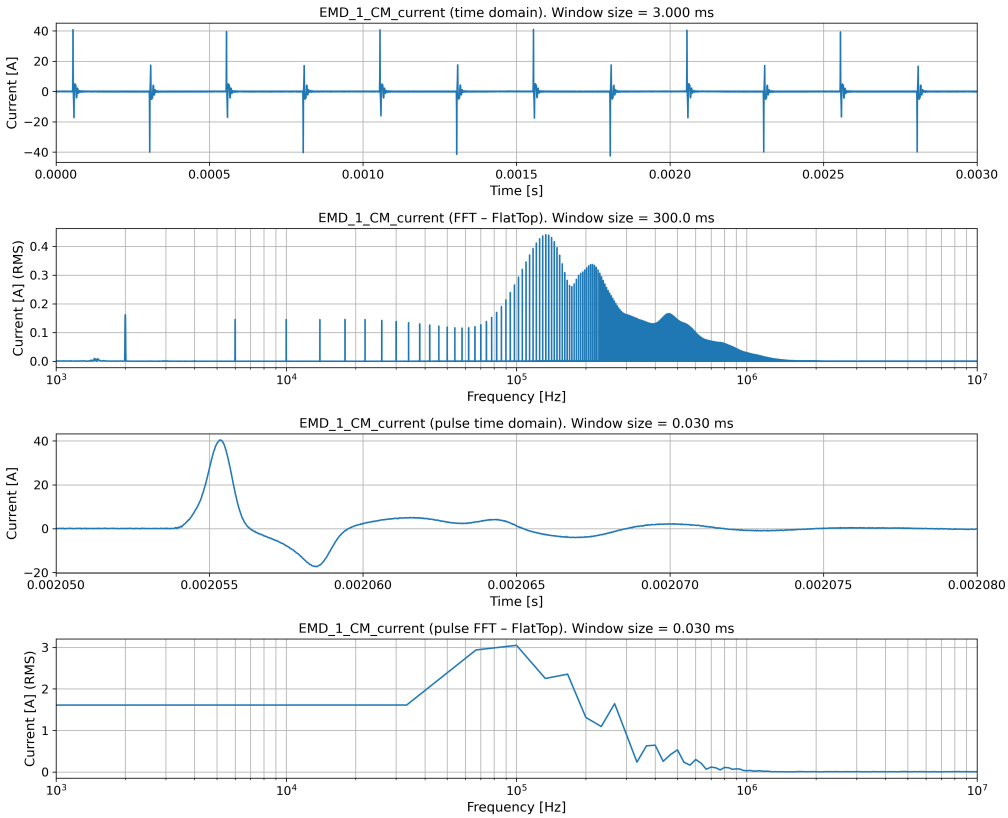


Figure B.2: Common-mode current spectrum of EMD_1_CM. The plot shows the difference between full-record FFT (periodicity-driven peaks) and pulse-segment FFT (broadband pulse response).

B.2 Spectral characteristics of short-duration current pulses

B.2.1 Broadband spectrum of a single short pulse

A short-duration current pulse of width τ produces a broadband spectrum. Fourier theory shows that the characteristic bandwidth is approximately $1/\tau$. A pulse of duration $\tau = 20\ \mu$s therefore produces wide spectral content up to approximately 50-100 kHz, followed by diminishing sidelobes. This behaviour follows from the transform of a rectangular-like waveform, often represented as a sinc-shaped magnitude response [8].

Conclusion

Short pulses inherently contain broadband spectral energy, and shorter pulses produce wider spectra.

B.2.2 Spectral behaviour of polarity-alternating pulse trains

When a switching converter produces a sequence of current pulses that alternate in polarity, the waveform repeats every second pulse. If pulses occur every 250 μs (corresponding to 4 kHz) and the sign alternates each time, the repeating pattern has a period of 500 μs, corresponding to 2 kHz.

This produces discrete spectral lines at 2 kHz and its odd harmonics (6, 10, 14 kHz, etc.), together with a component at the physical pulse repetition rate of 4 kHz. These features correspond to the spectral signature of full-polarity modulation, which is mathematically equivalent to amplitude modulation by a square wave of frequency 2 kHz [8, 17].

Conclusion

Polarity alternation doubles the effective repetition period, producing a dominant spectral line at half the pulse repetition frequency.

B.3 FFT windowing: Hanning and Flattop

B.3.1 Hanning window

The Hanning window is widely used in EMC measurements because it reduces spectral leakage effectively and produces smooth spectra. However, it underestimates amplitude and broadens peaks, which reduces the accuracy of magnitude estimation for discrete spectral components [18].

Conclusion

The Hanning window is suitable for identifying frequency components but not for precise amplitude estimation.

B.3.2 Flattop window

The Flattop window is designed for accurate amplitude estimation, typically within ± 0.1 dB, at the expense of lower frequency resolution. It is therefore appropriate for power electronics measurements in which the absolute magnitude of spectral components is essential, such as in the quantification of common-mode (CM) and differential-mode (DM) current excitation [17, 18].

Conclusion

The Flattop window provides amplitude accuracy within its specified range and is often preferable in switched-mode power conversion analysis.

B.4 Axis scaling: semilogx and loglog

B.4.1 Semilogx scaling

Semilogx scaling uses a linear amplitude axis and a logarithmic frequency axis. This representation preserves meaningful amplitude differences and enables clear identification of dominant frequency ranges. In the measurements considered here, the spectra contain measurable energy up to approximately 1 MHz for the EMD_1_CM current and up to approximately 2-3 MHz for the AC_EMD1_CM current. Above these ranges, the amplitude decreases to low levels. Semilogx scaling makes these transitions visually apparent.

Conclusion

Semilogx scaling enables meaningful amplitude comparison and clear identification of practical spectral cut-off frequencies.

B.4.2 Loglog scaling

Loglog scaling applies logarithmic axes to both frequency and amplitude, which amplifies very small values visually. This can obscure the interpretation of spectral decay, especially in broadband FFTs of short pulses.

Conclusion

Loglog scaling is suitable for examining very small spectral features over many decades but can obscure amplitude hierarchy in switched-pulse spectra.

B.5 Full-record FFT versus pulse-segment FFT

B.5.1 Full-record FFT

A full-record FFT emphasises periodicity, revealing spectral lines associated with pulse repetition and polarity alternation. Peaks at 2, 4, 6 and 10 kHz arise from these repeating structures.

Conclusion

Full-record FFTs highlight periodic structure and harmonic content.

B.5.2 Pulse-segment FFT

A pulse-segment FFT contains no information about the repetition rate, producing a broadband spectrum dominated by the pulse shape rather than the switching frequency. The absence of discrete spectral lines follows from the non-periodic nature of the isolated pulse.

Conclusion

Pulse-segment FFTs characterise the intrinsic spectral properties of individual switching events.

Appendix C

Complementary simulation and measurement graphs from Appendix 6

This appendix collects plots from Appendix 6 without further explanation. The purpose is to provide a collection of graphs without primary analytical interest while still allowing them to be reviewed as a complement to Appendix 6.

C.1 Graphs from common mode simulation of complete vehicle with full and reduced models

In this section all graphs follow the simulations in Subsection 6.3.1. The different models follow the descriptions in Subsection 6.3.1.

The following graphs are shown:

U_{cm} at EM1	see Figure C.1.
I_{cm} at EMD1	see Figure C.2.
U_{cm} at EMD1	see Figure C.3.
I_{cm} at EMD1	see Figure C.4.
U_{cm} at EMD2	see Figure C.5.
I_{cm} at EMD2	see Figure C.6.
U_{cm} at BP4	see Figure C.7.
I_{cm} at BP4	see Figure C.8.
U_{cm} at OCEPS	see Figure C.9.
I_{cm} at OCEPS	see Figure C.10.
U_{cm} at CAB_Heater	see Figure C.11.
I_{cm} at CAB_Heater	see Figure C.12.
U_{cm} at AC_Compr	see Figure C.13.
I_{cm} at AC_Compr	see Figure C.14.
U_{cm} at AirCompr	see Figure C.15.
I_{cm} at AirCompr	see Figure C.16.
U_{cm} at DCDC1	see Figure C.17.
I_{cm} at DCDC1	see Figure C.18.

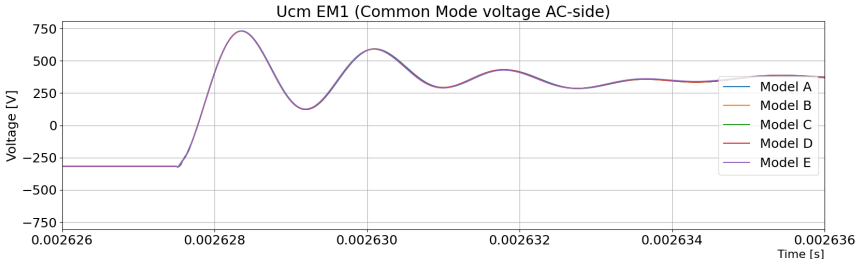


Figure C.1: Common mode voltage at the EM1 (AC side). This is the Z2 time span.

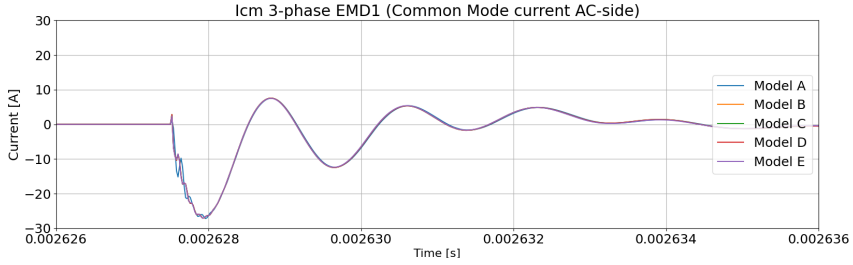


Figure C.2: Common mode current at the EM1 (AC-side). This is the Z2 time span.

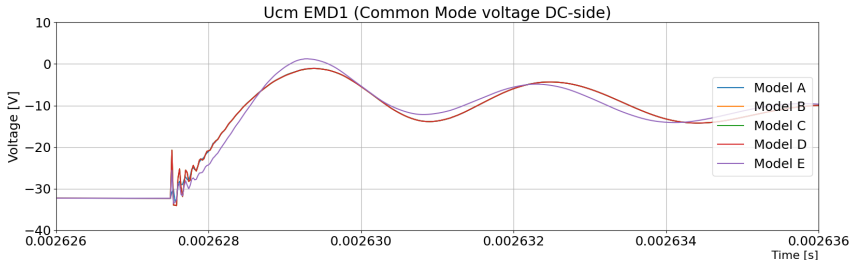


Figure C.3: Common mode voltage at the EMD1 (DC-side). This is the Z2 time span.

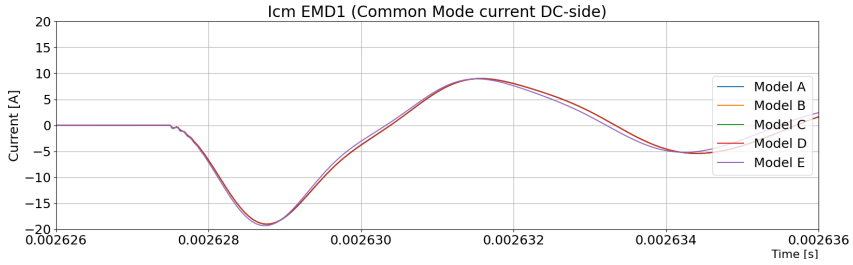


Figure C.4: Common mode current at the EMD1 (DC-side). This is the Z2 time span.

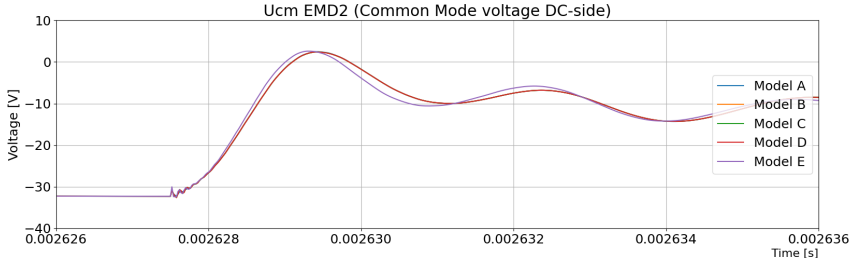


Figure C.5: Common mode voltage at the EMD2 (DC-side). This is the Z2 time span.

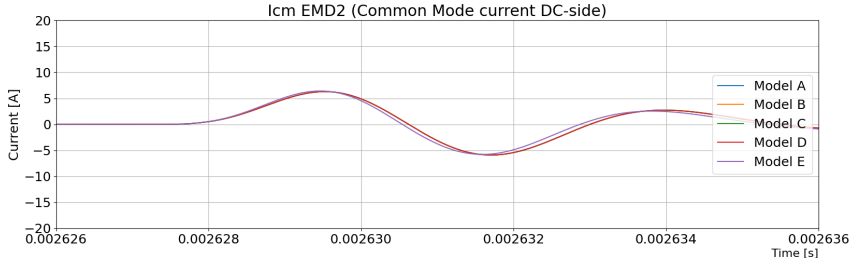


Figure C.6: Common mode current at the EMD2 (DC-side). This is the Z2 time span.

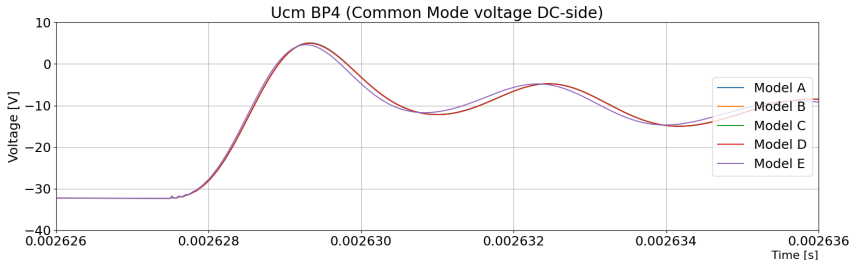


Figure C.7: Common mode voltage at the BP4 (DC-side). This is the Z2 time span.

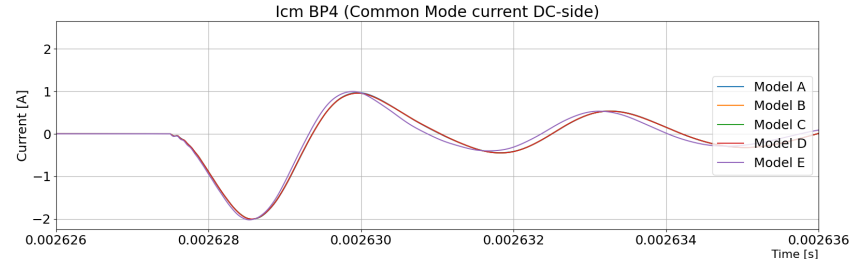


Figure C.8: Common mode current at the BP4 (DC-side). This is the Z2 time span.

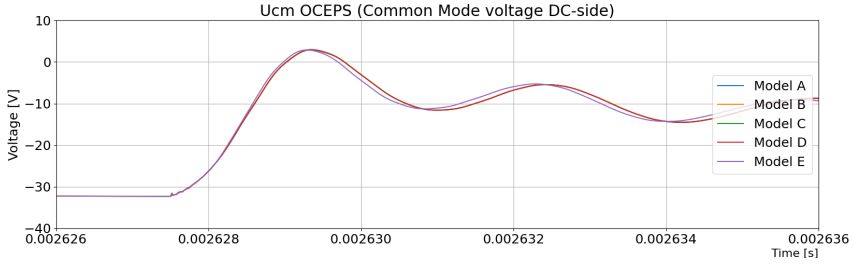


Figure C.9: Common mode voltage at the OCEPS (DC-side). This is the Z2 time span.

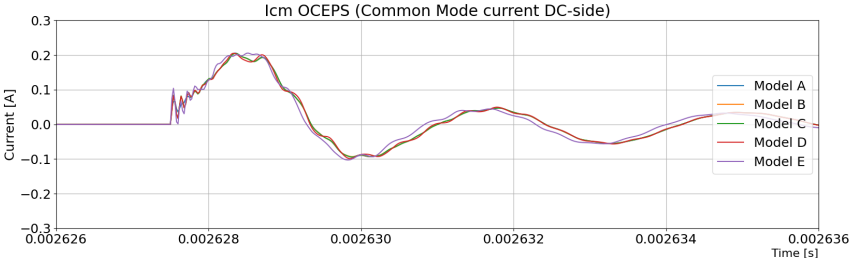


Figure C.10: Common mode current at the OCEPS (DC-side). This is the Z2 time span.

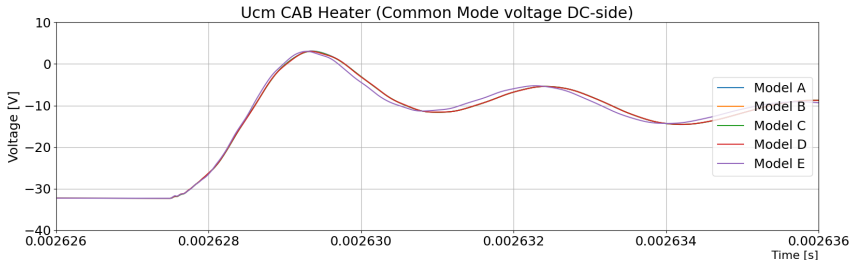


Figure C.11: Common mode voltage at the CAB Heater (DC-side). This is the Z2 time span.

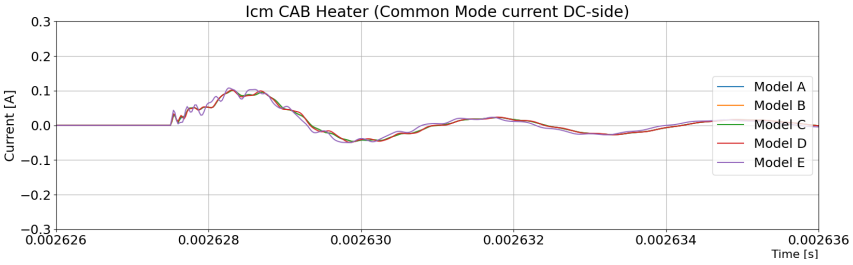


Figure C.12: Common mode current at the CAB Heater (DC-side). This is the Z2 time span.

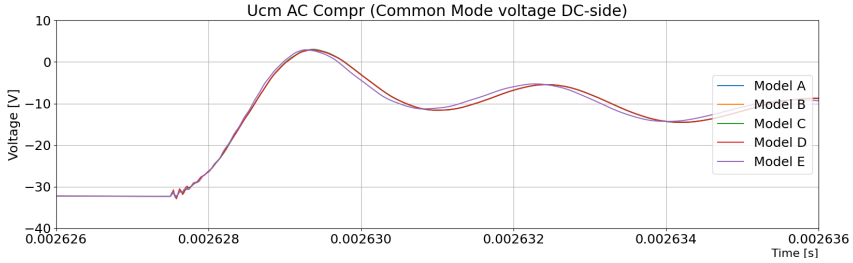


Figure C.13: Common mode voltage at the AC Compressor (DC-side). This is the Z2 time span.

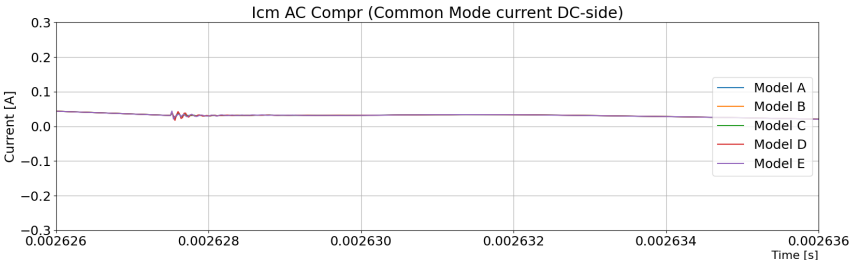


Figure C.14: Common mode current at the AC Compressor (DC-side). This is the Z2 time span.

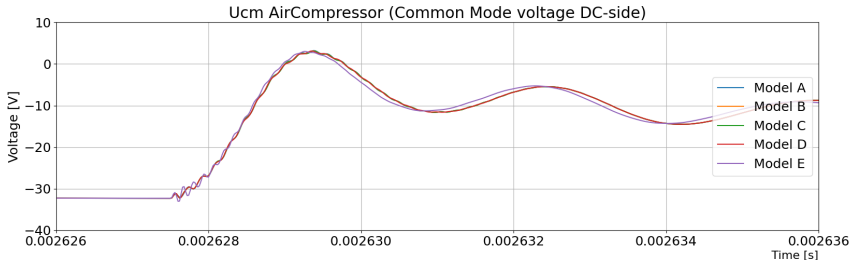


Figure C.15: Common mode voltage at the Air Compressor (DC-side). This is the Z2 time span.

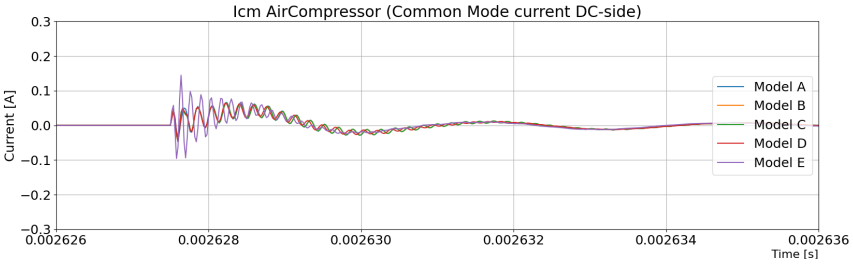


Figure C.16: Common mode current at the Air Compressor (DC-side). This is the Z2 time span.

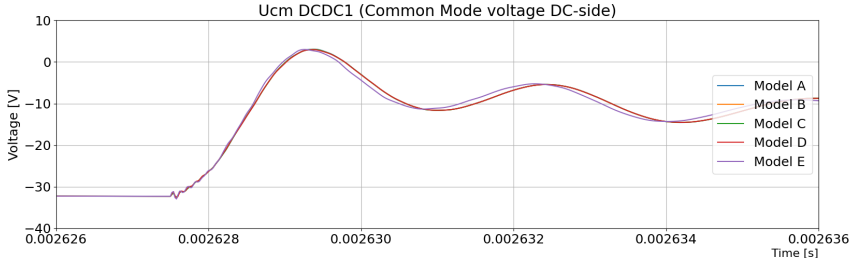


Figure C.17: Common mode voltage at the DCDC1 (DC-side). This is the Z2 time span.

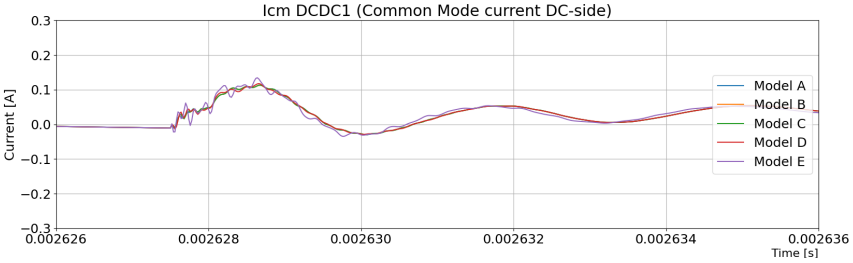


Figure C.18: Common mode current at the DCDC1 (DC-side). This is the Z2 time span.

C.2 Graphs from common mode simulation of part of the vehicle, with full and reduced models

In this section all graphs follow the simulations in Subsection 6.3.2. The different models follow the descriptions in Subsection 6.3.2.
The following graphs are shown:

U_{cm} at EM1	see Figure C.19.
I_{cm} at EM1	see Figure C.20.
U_{cm} at EMD1	see Figure C.21.
I_{cm} at EMD1	see Figure C.22.
U_{cm} at EMD2	see Figure C.23.
I_{cm} at EMD2	see Figure C.24.
U_{cm} at BP4	see Figure C.25.
I_{cm} at BP4	see Figure C.26.
U_{cm} at OCEPS	see Figure C.27.
I_{cm} at OCEPS	see Figure C.28.
U_{cm} at CAB_Heater	see Figure C.29.
I_{cm} at CAB_Heater	see Figure C.30.
U_{cm} at AC_Compr	see Figure C.31.
I_{cm} at AC_Compr	see Figure C.32.
U_{cm} at AirCompr	see Figure C.33.
I_{cm} at AirCompr	see Figure C.34.
U_{cm} at DCDC1	see Figure C.35.
I_{cm} at DCDC1	see Figure C.36.

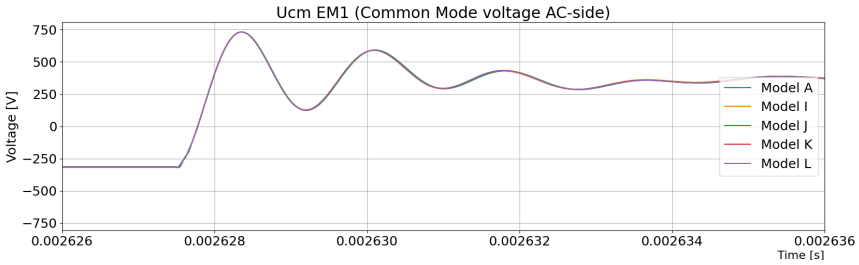


Figure C.19: Common mode voltage at the EM1 (AC side). This is the Z2 time span.

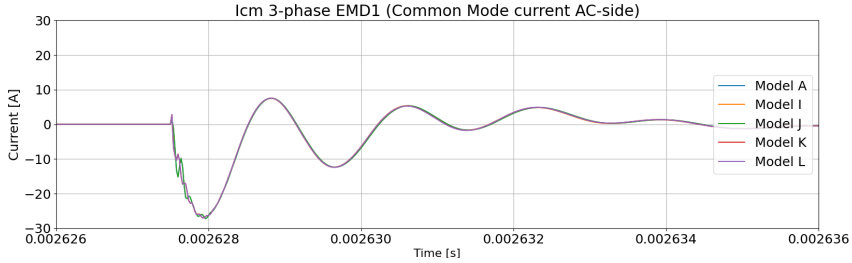


Figure C.20: Common mode current at the EM1 (AC-side). This is the Z2 time span.

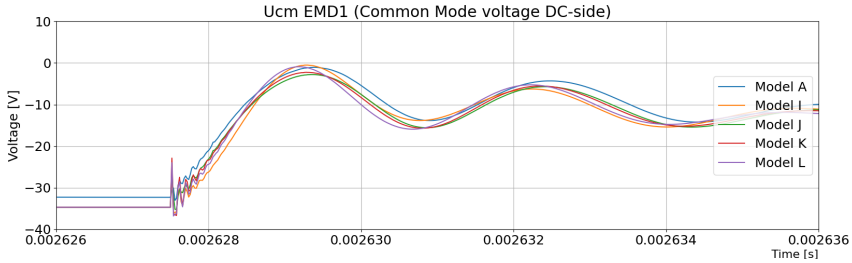


Figure C.21: Common mode voltage at the EMD1 (DC-side). This is the Z2 time span.

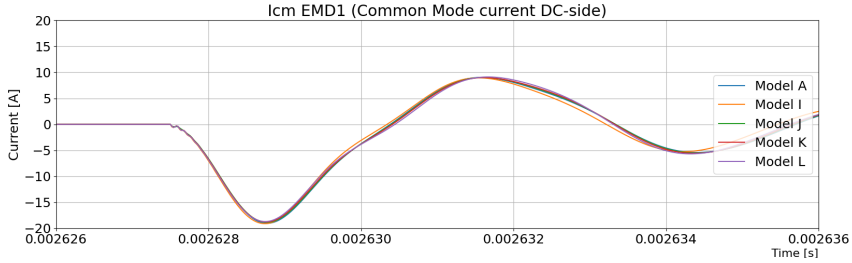


Figure C.22: Common mode current at the EMD1 (DC-side). This is the Z2 time span.

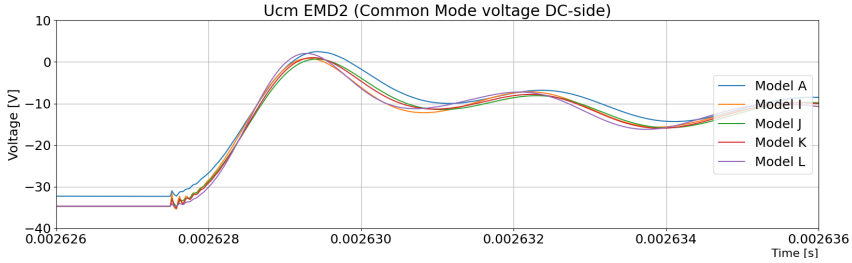


Figure C.23: Common mode voltage at the EMD2 (DC-side). This is the Z2 time span.

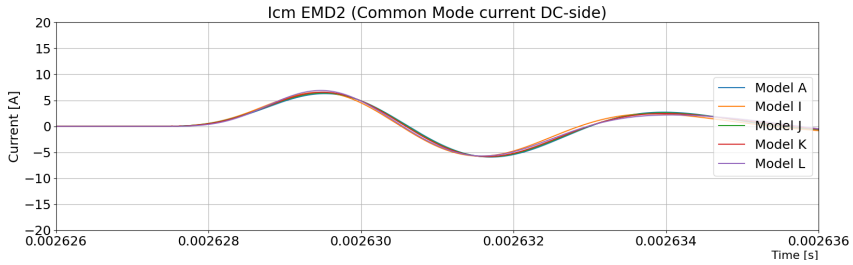


Figure C.24: Common mode current at the EMD2 (DC-side). This is the Z2 time span.

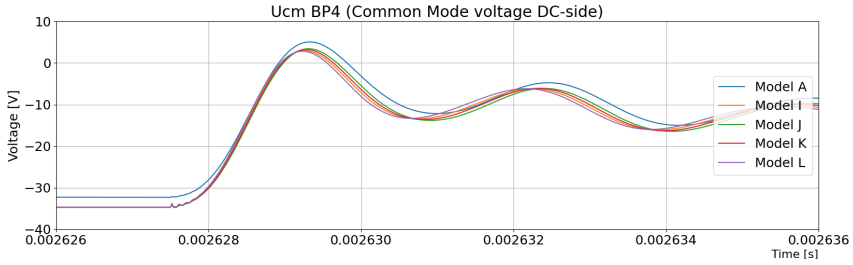


Figure C.25: Common mode voltage at the BP4 (DC-side). This is the Z2 time span.

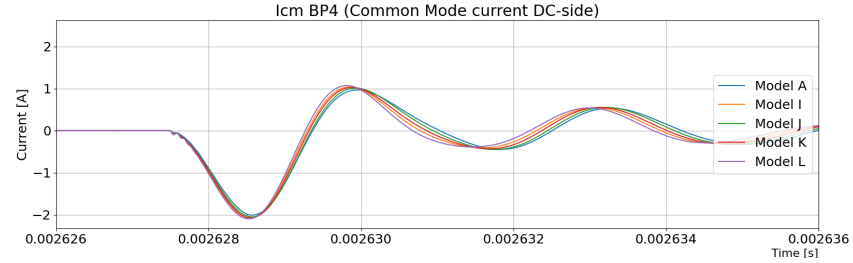


Figure C.26: Common mode current at the BP4 (DC-side). This is the Z2 time span.

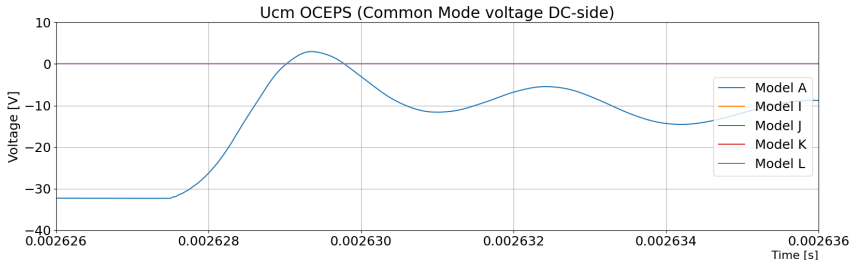


Figure C.27: Common mode voltage at the OCEPS (DC-side). This is the Z2 time span.

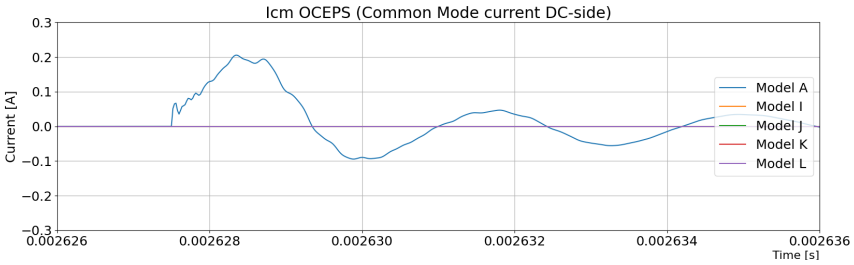


Figure C.28: Common mode current at the OCEPS (DC-side). This is the Z2 time span.

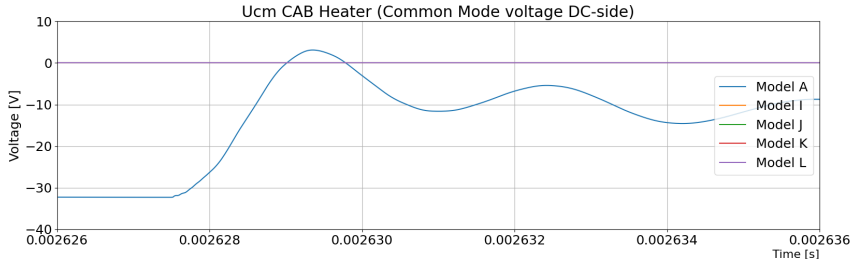


Figure C.29: Common mode voltage at the CAB Heater (DC-side). This is the Z2 time span.

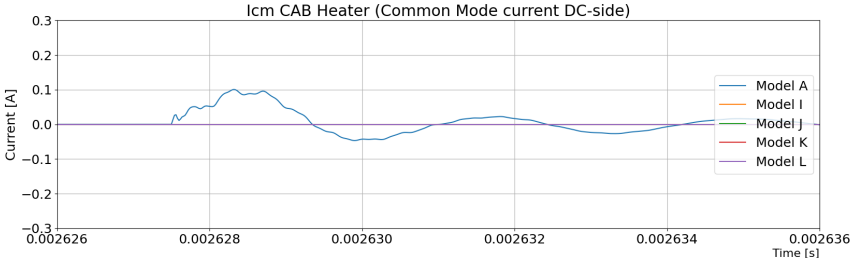


Figure C.30: Common mode current at the CAB Heater (DC-side). This is the Z2 time span.

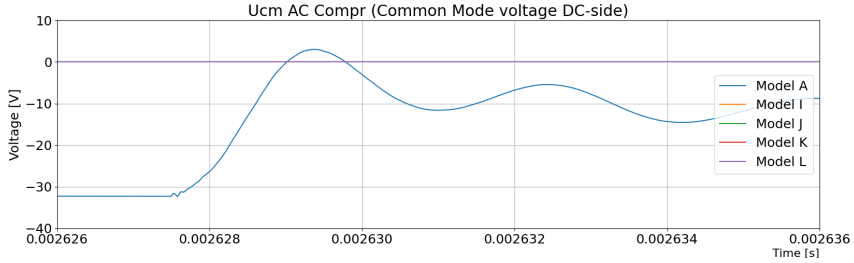


Figure C.31: Common mode voltage at the AC Compressor (DC-side). This is the Z2 time span.

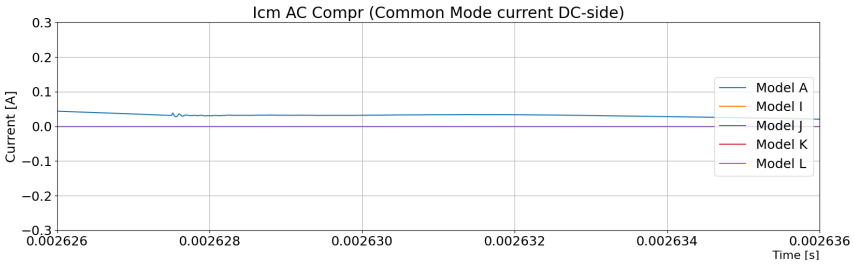


Figure C.32: Common mode current at the AC Compressor (DC-side). This is the Z2 time span.

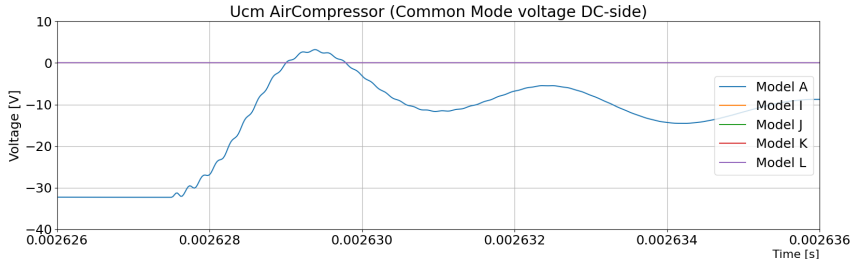


Figure C.33: Common mode voltage at the Air Compressor (DC-side). This is the Z2 time span.

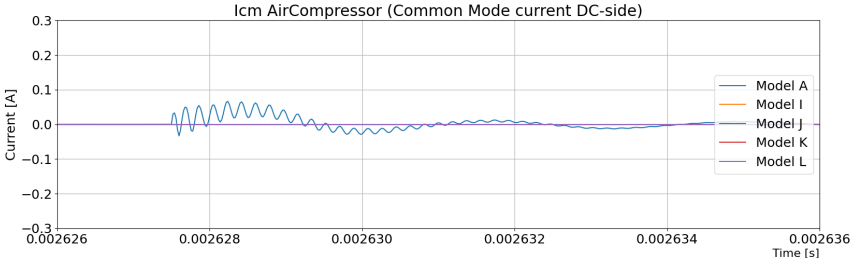


Figure C.34: Common mode current at the Air Compressor (DC-side). This is the Z2 time span.

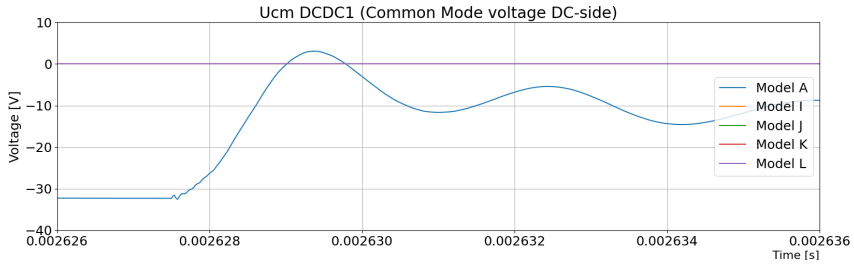


Figure C.35: Common mode voltage at the DCDC1 (DC-side). This is the Z2 time span.

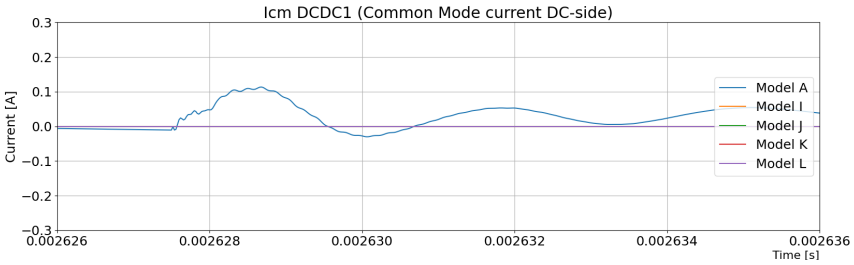


Figure C.36: Common mode current at the DCDC1 (DC-side). This is the Z2 time span.

C.3 Additional DM behaviour during dynamic operation (acceleration runs)

Subsection 6.5.1 presents various steady-state load conditions. This appendix complements that section by presenting the corresponding overview graphs for the acceleration load conditions listed in Table 6.3.

Figures C.37 to C.44 show a long measurement period. These graphs display the measured differential-mode (DM) current, i_{DM}, on the DC side of all subsystems in the vehicle. The measurements use Rogowski coils, which lack sensitivity to any DC component.

Note: The terms ”RampUp” and ”Acc” (acceleration) refer to the same type of operating condition. The naming variation results from inconsistencies during the measurement campaign.

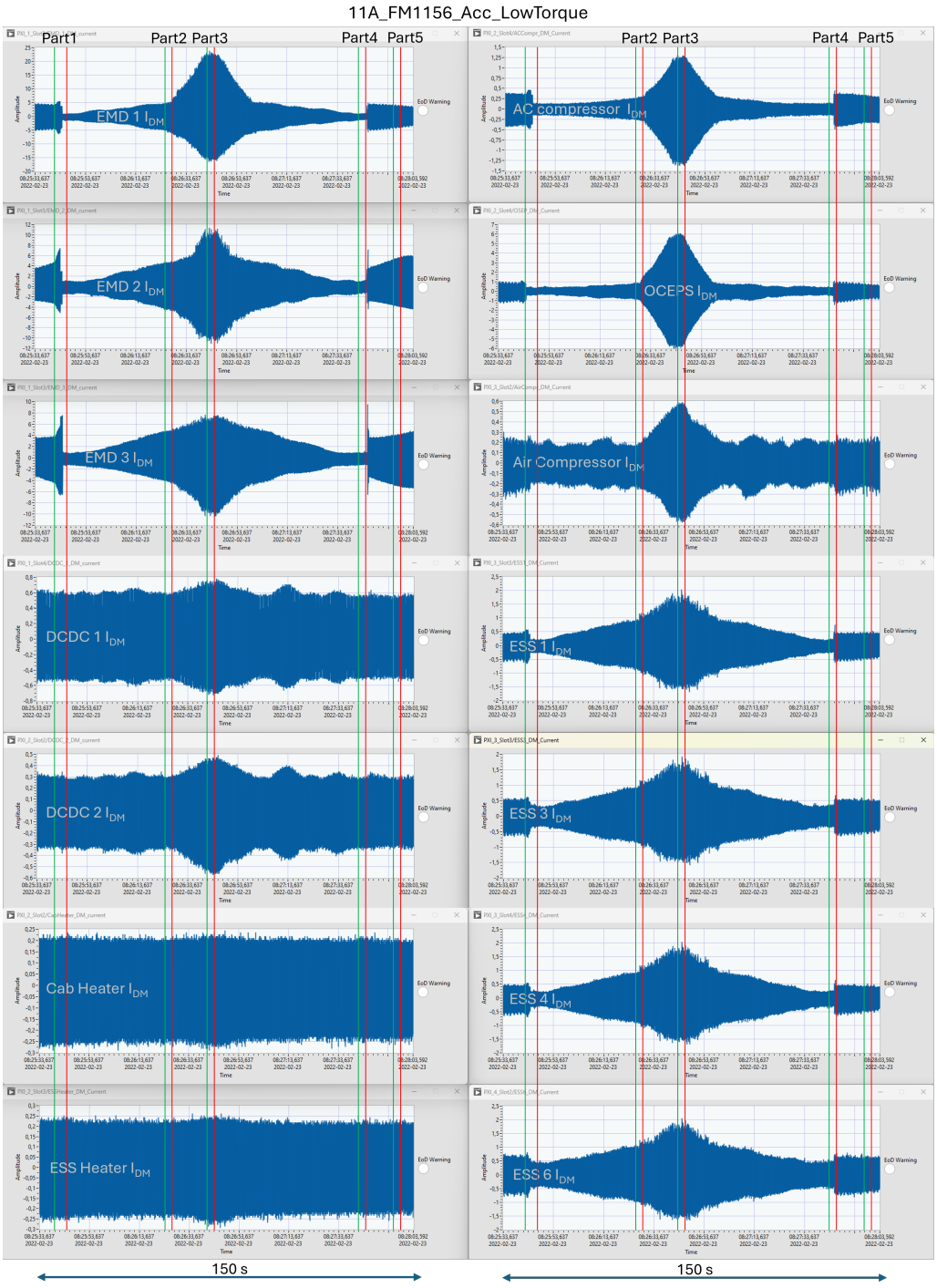


Figure C.37: Measurement "11A FM1156 Acc LowTorque" as listed in Table 6.3.

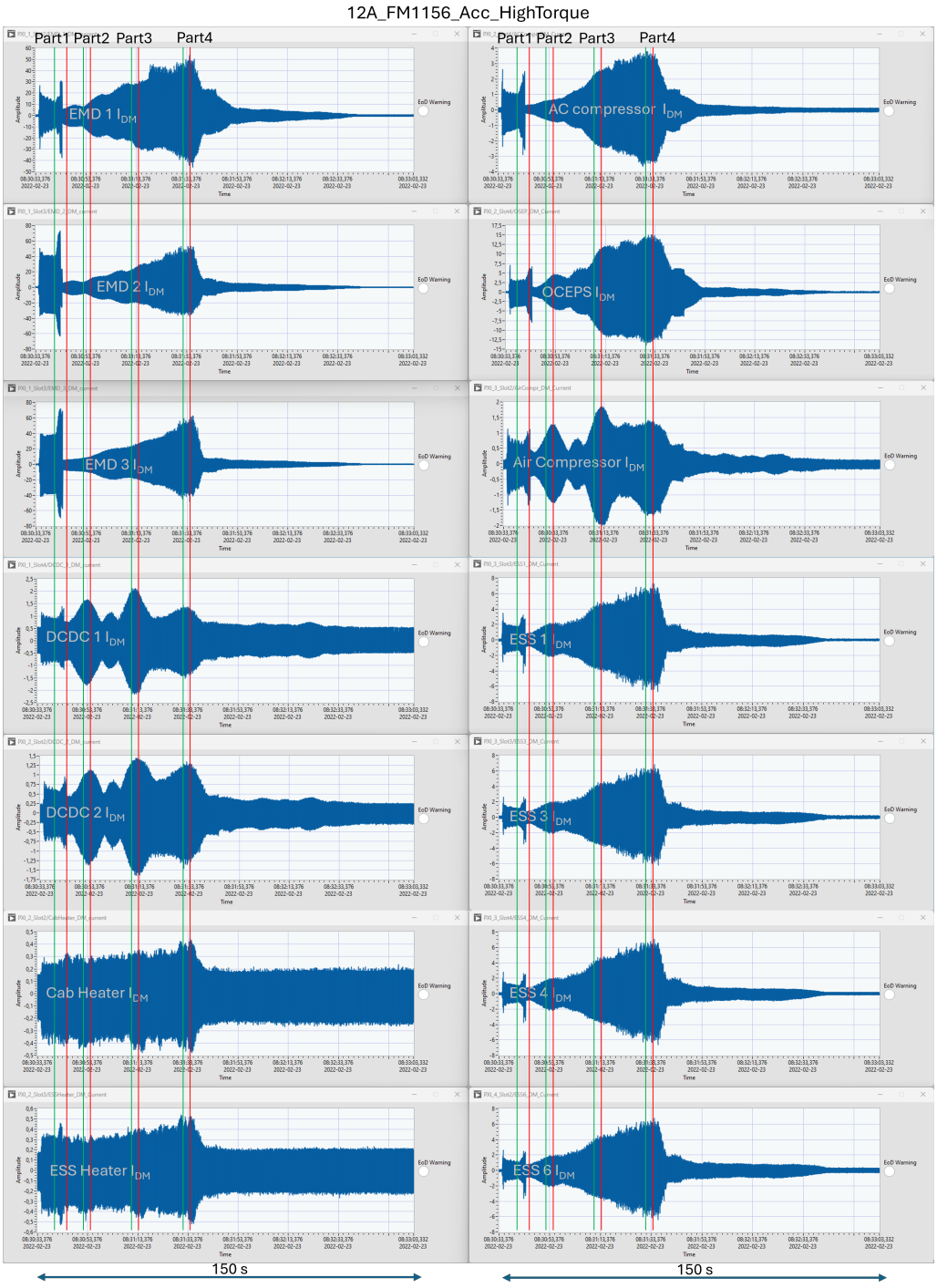


Figure C.38: Measurement "12A FM1156 Acc HighTorque" as listed in Table 6.3.

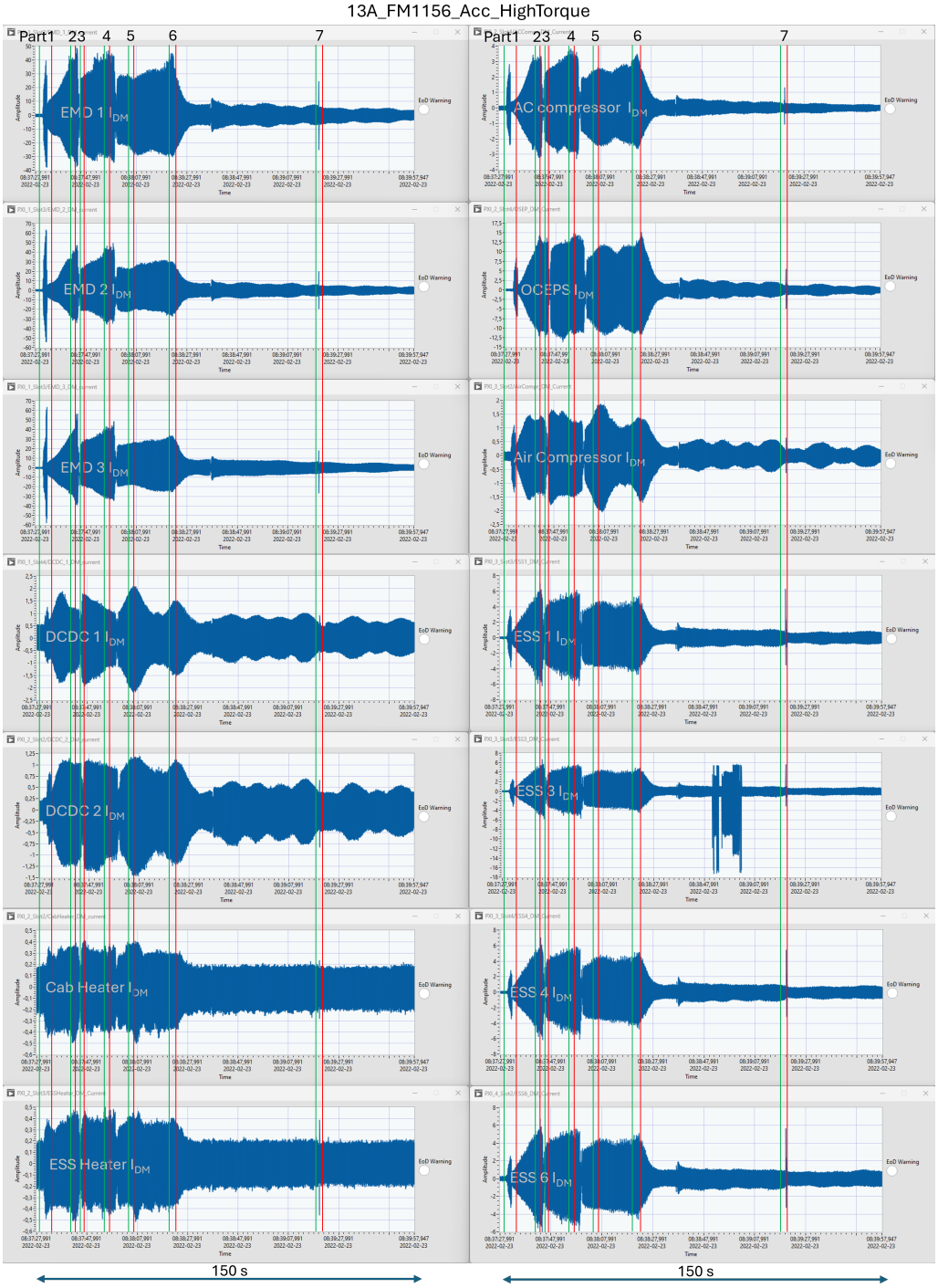


Figure C.39: Measurement "13A FM1156 Acc HighTorque" as listed in Table 6.3.

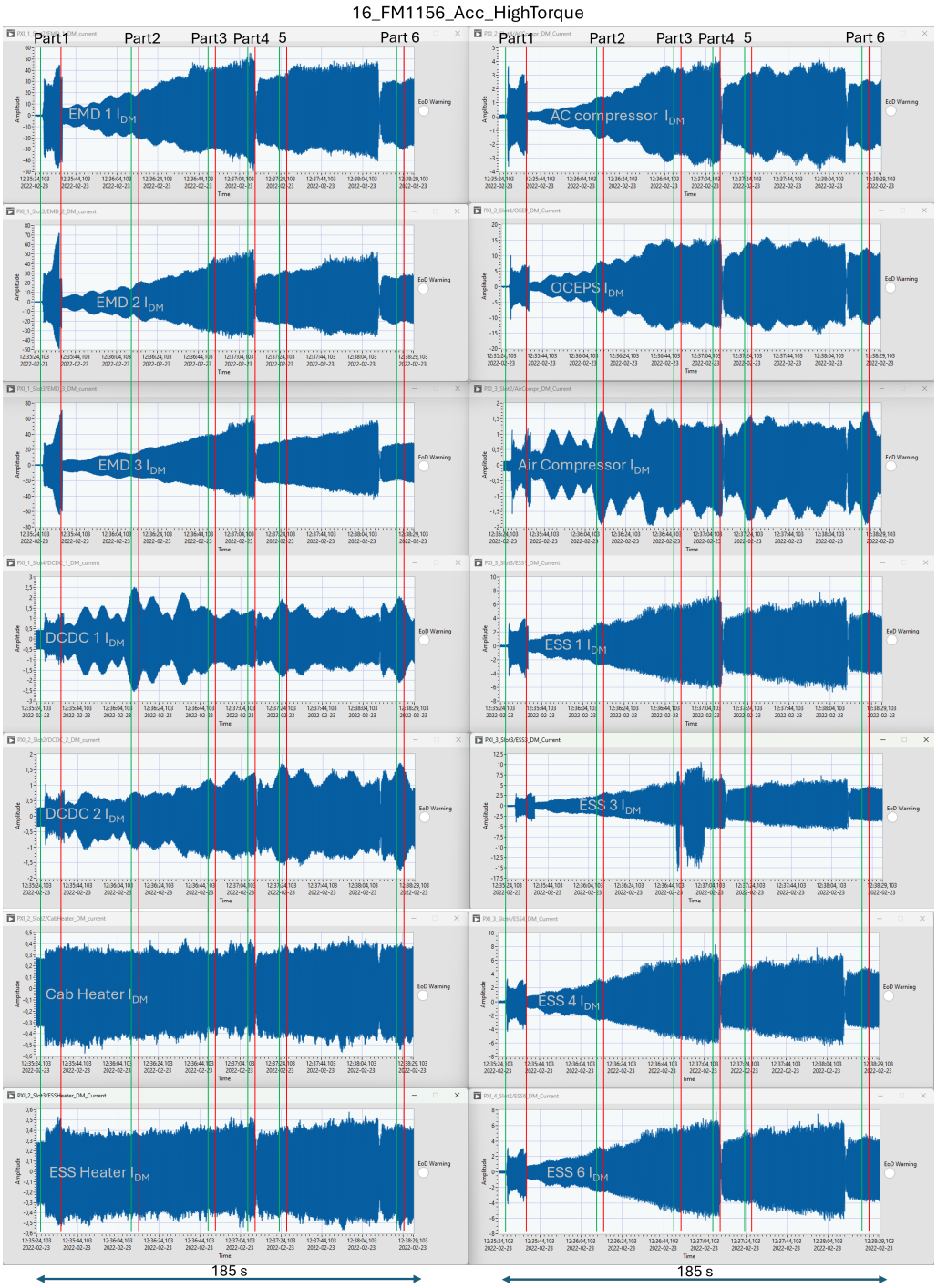


Figure C.40: Measurement "16 FM1156 Acc HighTorque" as listed in Table 6.3.

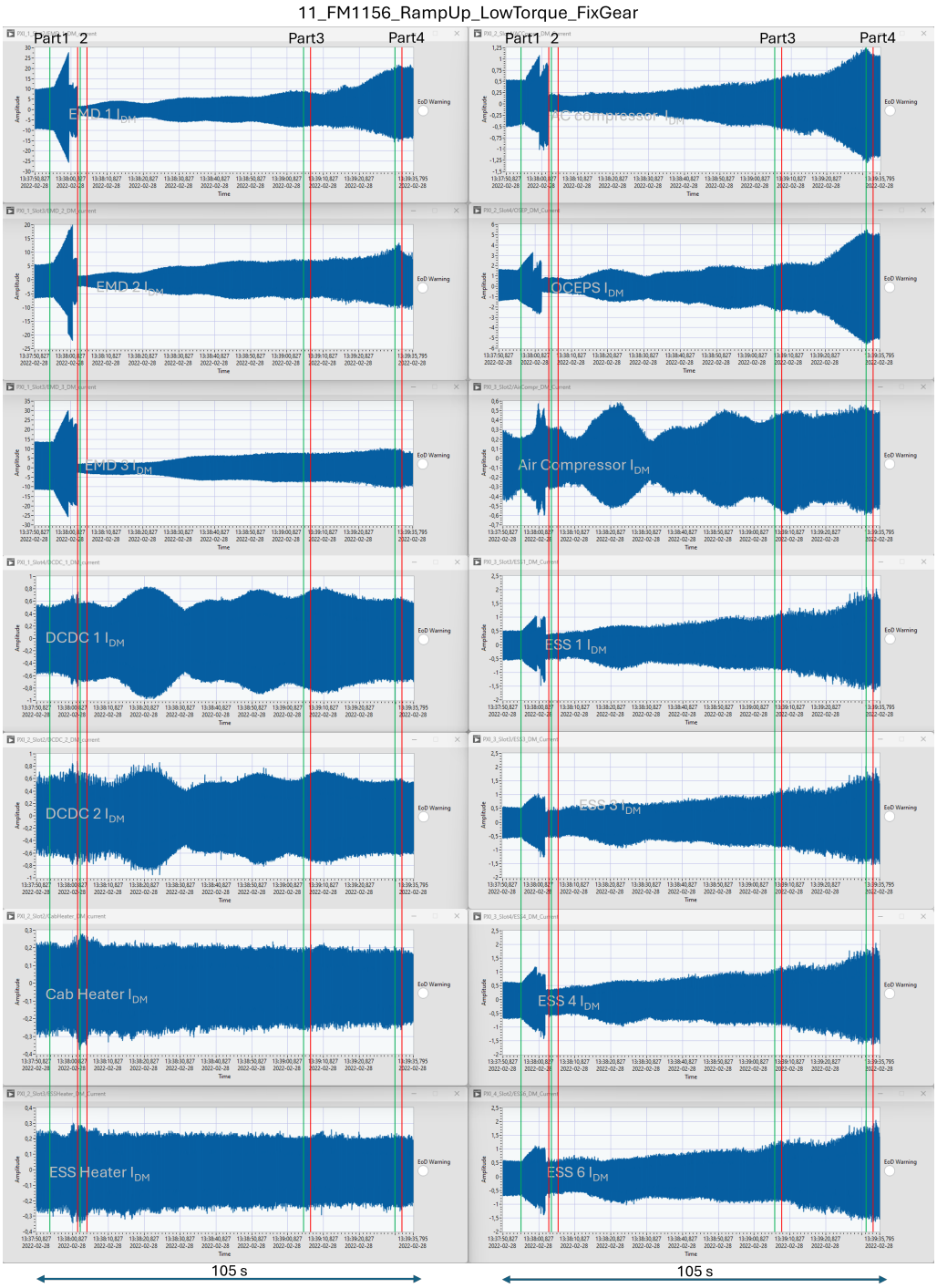


Figure C.41: Measurement "11 FM1156 RampUp LowTorque FixGear" as listed in Table 6.3.

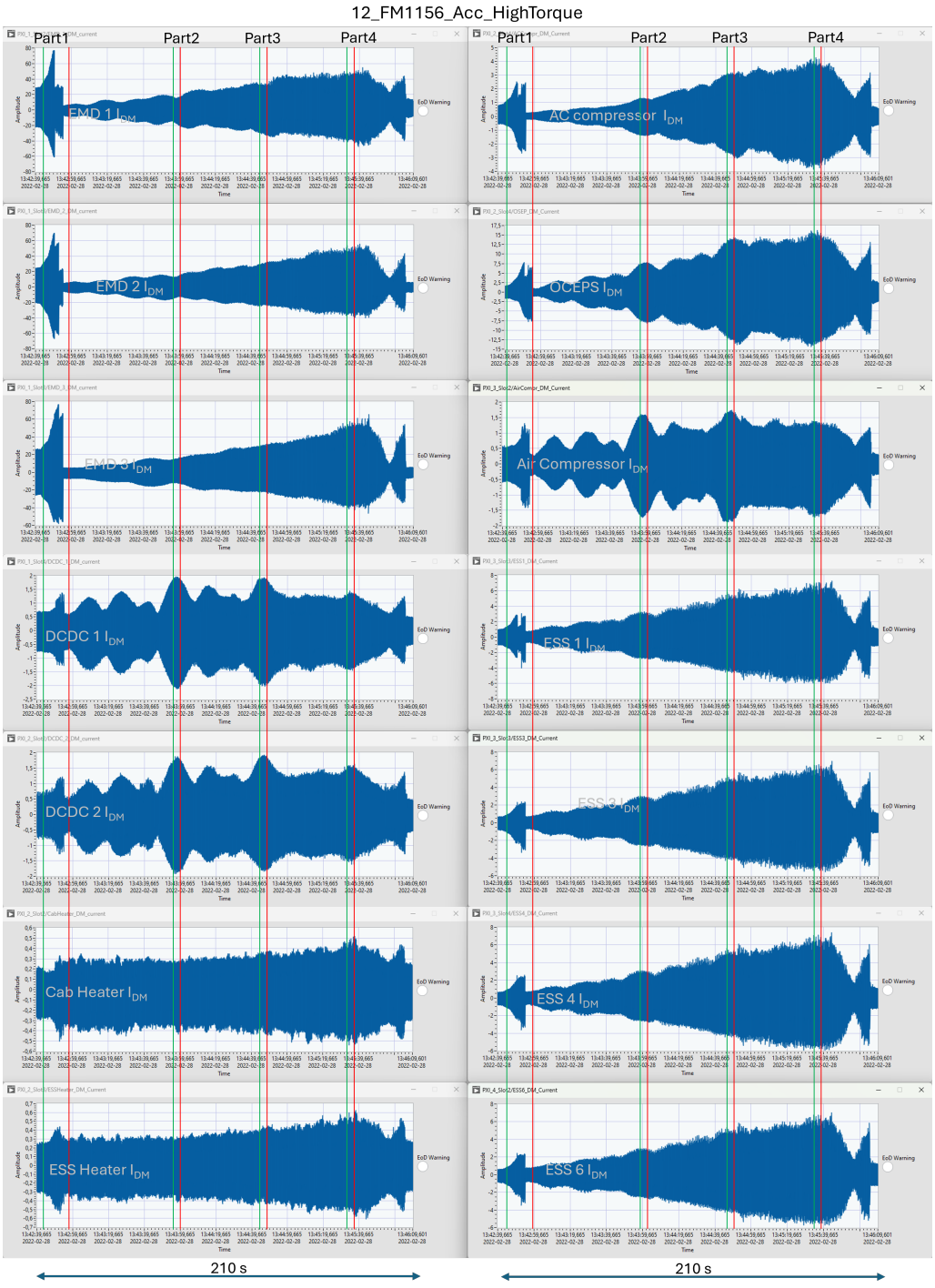


Figure C.42: Measurement "12 FM1156 Acc HighTorque" as listed in Table 6.3.

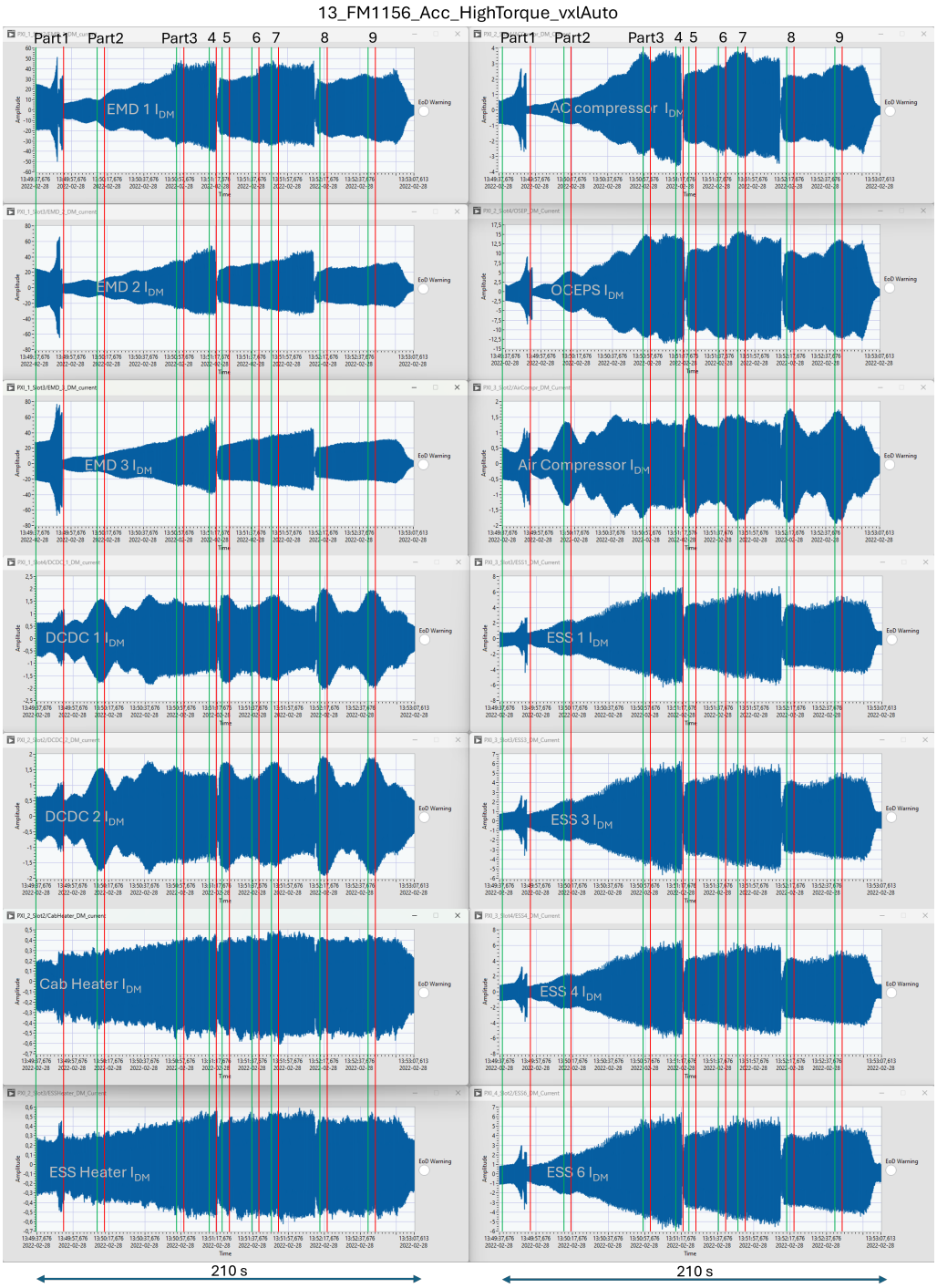


Figure C.43: Measurement "13 FM1156 Acc HighTorque vxlAuto" as listed in Table 6.3.

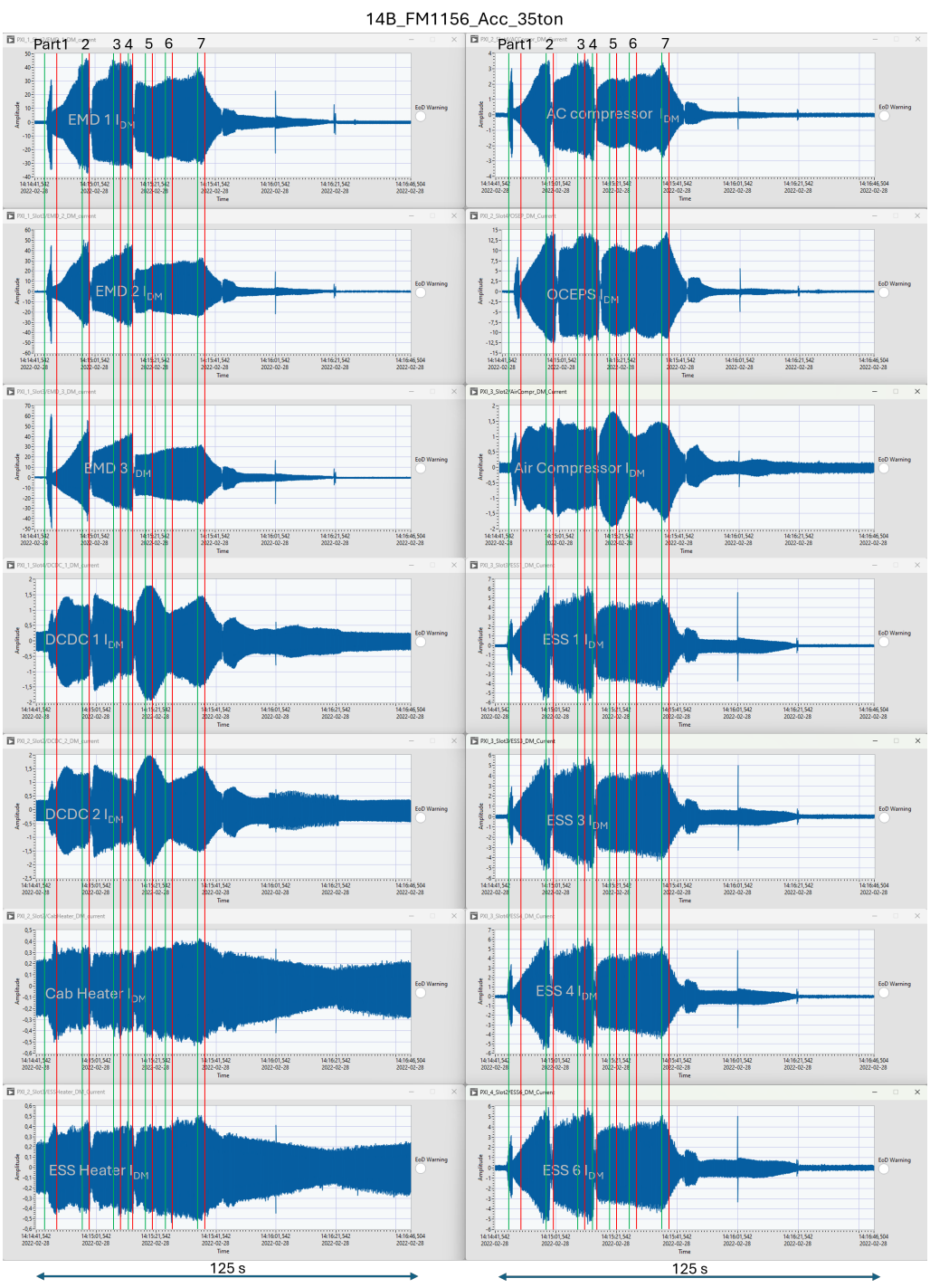


Figure C.44: Measurement "14B FM1156 RampUp 35t vxlAuto" as listed in Table 6.3.

References

[1] Mats Alaküla, Per Karlsson and Hans Bängtsson. *Power Electronics Devices, Converters, Control and Applications*. Course material in the EIEN75 course at Lund University (LTH). Access restricted to registered students. See https://kurser.lth.se/lot/course/EIEN75. Contact iea@iea.lth.se for access to the course material. 2019.

[2] Alexander Bessman et al. 'Aging effects of AC harmonics on lithium-ion cells'. In: *Journal of Energy Storage* 21 (Feb. 2019), pp. 741–749. ISSN: 2352-152X. DOI: 10.1016/J.EST.2018.12.016. URL: https://www.sciencedirect.com/science/article/pii/S2352152X18307035.

[3] *COMSOL Multiphysics® Software - Understand, Predict, and Optimize*. URL: https://www.comsol.com/comsol-multiphysics.

[4] Alan Cordic and Azka Wanitwijan. 'Cable modelling for electric vehicle drivetrains'. In: (2020). URL: https://odr.chalmers.se/handle/20.500.12380/304256.

[5] Pearson Electronics. *PEARSON CURRENT MONITOR MODEL 2877*. 1999. URL: http://pearsonelectronics.com/pdf/2877.pdf.

[6] Omar M.O. Gatous and J. Pissolato Filho. 'A new formulation for skin-effect resistance and internal inductance frequency-dependent of a solid cylindrical conductor'. In: *2004 IEEE/PES Transmission and Distribution Conference and Exposition: Latin America* (2004), pp. 919–924. DOI: 10.1109/TDC.2004.1432505. URL: https://ieeexplore.ieee.org/document/1432505.

[7] *Guide to FFT Analysis (Fast Fourier Transform) | Dewesoft*. URL: https://dewesoft.com/blog/guide-to-fft-analysis.

[8] Imperial College London. *Lecture 6: DFT and Windowing (slides)*. Lecture notes for undergraduate course in signal processing. URL: http://www.ee.ic.ac.uk/pcheung/teaching/DE2_EE/Lecture%206%20-%20DFT%20&%20Windowing%20%28slides%29.pdf.

[9] National Instruments. *Acquiring an Analog Signal: Bandwidth, Nyquist Sampling Theorem, and Aliasing*. 2016. URL: https://download.ni.com/evaluation/pxi/Acquiring_Analog_Signal.pdf (visited on 27/09/2021).

[10] National Instruments. *SPECIFICATIONS PXIe-5105*. URL: https://www.ni.com/pdf/manuals/374398d.pdf.

[11] ISO. *ISO - ISO 6469-3:2018/Amd 1:2020 - Electrically propelled road vehicles — Safety specifications — Part 3: Electrical safety — Amendment 1: Withstand voltage test for electric power sources*. 2011. URL: https://www.iso.org/standard/76885.html (visited on 18/05/2021).

[12] ISO. *ISO 21498-2:2021 - Electrically propelled road vehicles — Electrical specifications and tests for voltage class B systems and components — Part 2: Electrical tests for components*. URL: https://www.iso.org/standard/78210.html.

[13] ISO. *Standard - Electrically propelled road vehicles - Conductive power transfer - Safety requirements (ISO 17409:2020) SS-EN ISO 17409:2020 - Swedish Institute for Standards, SIS*. Mar. 2020. URL: https://www.sis.se/en/produkter/road-vehicles-engineering/electric-road-vehicles/ss-en-iso-174092020/.

[14] Arun Khilnani et al. 'Conducted Emissions Measurements in DC Grids: Issues in Applying Existing LISN Topologies and Possible Solutions'. In: *2021 IEEE 15th International Conference on Compatibility, Power Electronics and Power Engineering, CPE-POWERENG 2021* (2021). DOI: 10.1109/CPE-POWERENG50821.2021.9501169. URL: https://ieeexplore.ieee.org/document/9501169.

[15] Avinash Kishore et al. 'Investigation of common mode noise in electric propulsion system high voltage components in an electrified vehicle'. In: *2016 IEEE Transportation Electrification Conference and Expo, ITEC 2016* (July 2016). DOI: 10.1109/ITEC.2016.7520263. URL: https://ieeexplore.ieee.org/document/7520263.

[16] Yiyu Lai et al. 'Analysis of DC-Link Low-Frequency Current Harmonics in Multi-Source Multi-Three-Phase Electric Drives'. In: *Electronics 2024, Vol. 13, Page 2236* 13 (12 June 2024), p. 2236. ISSN: 2079-9292. DOI: 10.3390/ELECTRONICS13122236. URL: https://www.mdpi.com/2079-9292/13/12/2236.

[17] National Instruments. *The Fundamentals of FFT-Based Signal Analysis and Measurement*. Application Note 041. National Instruments Corporation, 2000. URL: https://www.sjsu.edu/people/burford.furman/docs/me120/FFT_tutorial_NI.pdf.

[18] National Instruments. *Understanding FFTs and Windowing Overview*. Technical Article. Backup mirror: https://turbosnu.files.wordpress.com/2015/04/ni-tutorial-4844-en.pdf. National Instruments Corporation, 2023. URL: https://download.ni.com/evaluation/pxi/Understanding%20FFTs%20and%20Windowing.pdf.

[19] Newtons4th. *IAI2 Impedance Analyzer - 10uHz to 50MHz*. URL: https://www.newtons4th.com/products/impedance-analyzers/impedance-analysis-interface-2/.

[20] Newtons4th. *PSM3750 Frequency Response Analyzer: 10µHz–50MHz – High Performance - Newtons 4th | Power Analyzers and Frequency Analyzers*. URL: https://www.newtons4th.com/products/frequency-response-analyzers/psm3750/.

[21] PLEXIM. *PLECS Standalone | Plexim*. URL: https://www.plexim.com/products/plecs/plecs_standalone.

[22] Malcom Stuart Raven. *(PDF) Experimental measurements of the skin effect and internal inductance at low frequencies*. URL: https://www.researchgate.net/publication/282988364_Experimental_measurements_of_the_skin_effect_and_internal_inductance_at_low_frequencies.

[23] Michele Sclocchi. *Input Filter Design for Switching Power Supplies*. Literature No. SNVA538. 2010. URL: https://www.ti.com/lit/an/snva538/snva538.pdf.

[24] TESTEC. *Instruction manual Testec - Differential probe TT-SI 9010.* 2021. URL: https://www.manualslib.com/manual/1424079/Testec-Tt-Si-9010.html (visited on 23/09/2021).

[25] 'Understanding FFTs and Windowing Overview'. In: (). URL: https://download.ni.com/evaluation/pxi/Understanding%20FFTs%20and%20Windowing.pdf.

[26] Lu Wan et al. 'Limitations in Applying the Existing LISN Topologies for Low Frequency Conducted Emission Measurements and Possible Solution'. In: *Proceedings of the 2021 Asia-Pacific International Symposium on Electromagnetic Compatibility, APEMC 2021* (2021). DOI: 10.1109/APEMC49932.2021.9596980. URL: https://ieeexplore.ieee.org/document/9596980.

[27] Kunbo Wang et al. 'Modeling of System-Level Conducted EMI of the High-Voltage Electric Drive System in Electric Vehicles'. In: *IEEE Transactions on Electromagnetic Compatibility* 64.3 (2022), pp. 741–749. DOI: 10.1109/TEMC.2021.3139644. URL: https://ieeexplore.ieee.org/document/9715977.

[28] Per Widek. 'Modeling of electric power systems in electric vehicles'. In: (). URL: https://portal.research.lu.se/sv/publications/modeling-of-electric-power-systems-in-electric-vehicles/.

[29] Per Widek and Mats Alakula. 'Common Mode Current Measurements in Traction Systems for Electric Vehicles'. In: *IEEE Transactions on Industry Applications* 59 (2 Mar. 2023), pp. 2061–2068. ISSN: 19399367. DOI: 10.1109/TIA.2022.3223631. URL: https://ieeexplore.ieee.org/document/9956900.

[30] Per Widek and Mats Alakula. 'Modeling of electric power system in electric vehicles'. In: *2020 International Symposium on Power Electronics, Electrical Drives, Automation and Motion, SPEEDAM 2020* (June 2020), pp. 293–298. DOI: 10.1109/SPEEDAM48782.2020.9161884. URL: https://ieeexplore.ieee.org/document/9161884.

[31] Per Widek and Mats Alaküla. 'Methods for the Investigation and Mitigation of Conducted Differential-Mode Electromagnetic Interference in Commercial Electrical Vehicles'. In: *Energies 2025, Vol. 18, Page 859* 18 (4 Feb. 2025), p. 859. ISSN: 1996-1073. DOI: 10.3390/EN18040859. URL: https://www.mdpi.com/1996-1073/18/4/859.

[32] Per Widek and Jonas Ottosson. 'Common Mode Current Reduction in Traction Systems for Electric Vehicles'. In: *2024 International Symposium on Power Electronics, Electrical Drives, Automation and Motion (SPEEDAM)* (June 2024), pp. 742–749. DOI: 10.1109/SPEEDAM61530.2024.10609110. URL: https://ieeexplore.ieee.org/document/10609110/.

[33] Wikipedia. *RC time constant - Wikipedia*. URL: https://en.wikipedia.org/wiki/RC_time_constant.

[34] Quancheng Wu et al. 'Evaluating Electromagnetic Interference for Fault Analysis and Maintenance in New Energy Vehicles'. In: *Electrica* 23.2 (2023), pp. 357–365. DOI: 10.5152/electrica.2023.22120. URL: https://www.electricajournal.org/index.php/pub/article/view/1096/1093.

[35] Kai Zhou, Zhipeng Xu and Zheng Li. 'Modeling and prediction of conducted EMI in on-board charging system of electric vehicles'. In: *Electrical Engineering* 107.6 (2025), pp. 3119–3134. DOI: 10.1007/s00202-024-02701-4. URL: https://link.springer.com/article/10.1007/s00202-024-02701-4.

[36] *ZView® For Windows - Scribner Associates*. URL: https://www.scribner.com/software/#analysis-visualization/.